

Edited by Umit S. Ozkan

 WILEY-VCH

Design of Heterogeneous Catalysts

New Approaches based on Synthesis, Characterization
and Modeling



Design of Heterogeneous Catalysts

Edited by

Umit S. Ozkan

Related Titles

Ding, K., Uozumi, Y. (eds.)

Handbook of Asymmetric Heterogeneous Catalysis

2008

ISBN: 978-3-527-31913-8

Kolasinski, K.

Surface Science

Foundations of Catalysis and Nanoscience

2008

ISBN: 978-0-470-03304-3

Ertl, G., Knözinger, H., Schüth, F., Weitkamp, J. (eds.)

Handbook of Heterogeneous Catalysis

8 Volumes

2008

ISBN: 978-3-527-31241-2

Chorkendorff, I., Niemantsverdriet, J. W.

Concepts of Modern Catalysis and Kinetics

2007

ISBN: 978-3-527-31672-4

Niemantsverdriet, J. W.

Spectroscopy in Catalysis

An Introduction

2007

ISBN: 978-3-527-31651-9

Cornils, B., Herrmann, W. A., Muhler, M., Wong, C.-H. (eds.)

Catalysis from A to Z

A Concise Encyclopedia

2007

ISBN: 978-3-527-31438-6

van Santen, R. A., Neurock, M.

Molecular Heterogeneous Catalysis

A Conceptual and Computational Approach

2006

ISBN: 978-3-527-29662-0

Design of Heterogeneous Catalysts

New Approaches based on Synthesis,
Characterization and Modeling

Edited by
Umit S. Ozkan



WILEY-
VCH

WILEY-VCH Verlag GmbH & Co. KGaA

The Editor

Professor Umit S. Ozkan

Department of Chemical and
Biomolecular Engineering
Ohio State University
140 W 19th Avenue
Columbus, OH 43210
USA

Cover Description: The cover provides an artistic illustration of using dendrimers to design and fabricate heterogeneous catalysts. In this scheme, organic dendrimers are used as nanoscale reactors to assemble metal complexes. Treatment with a reducing agent converts the metal complexes into nanoparticles. The dendrimer templated nanoparticles are then deposited onto a support and the organic template is thermally removed, yielding supported nanoparticle catalysts. This method presents new opportunities for catalyst design. Metal combinations unavailable through traditional catalyst preparation techniques became accessible through dendrimer mediated synthesis, and nanoparticle sizes and stoichiometries can be controlled. Dendrimer illustration was kindly provided by Bert Chandler and is reproduced with his permission.

All books published by Wiley-VCH are carefully produced. Nevertheless, authors, editors, and publisher do not warrant the information contained in these books, including this book, to be free of errors. Readers are advised to keep in mind that statements, data, illustrations, procedural details or other items may inadvertently be inaccurate.

Library of Congress Card No.: applied for

British Library Cataloguing-in-Publication Data

A catalogue record for this book is available from the British Library.

**Bibliographic information published by
the Deutsche Nationalbibliothek**

The Deutsche Nationalbibliothek lists this publication in the Deutsche Nationalbibliografie; detailed bibliographic data are available on the Internet at <http://dnb.d-nb.de>.

© 2009 WILEY-VCH Verlag GmbH & Co. KGaA, Weinheim

All rights reserved (including those of translation into other languages). No part of this book may be reproduced in any form – by photoprinting, microfilm, or any other means – nor transmitted or translated into a machine language without written permission from the publishers. Registered names, trademarks, etc. used in this book, even when not specifically marked as such, are not to be considered unprotected by law.

Typesetting Thomson Digital, Noida, India

Printing betz-druck GmbH, Darmstadt

Binding Litges & Dopf GmbH, Heppenheim

Cover Adam-Design, Weinheim

Printed in the Federal Republic of Germany

Printed on acid-free paper

ISBN: 978-3-527-32079-0

Contents

Preface XIII

List of Contributors XV

1	Use of Oxide Ligands in Designing Catalytic Active Sites	1
	<i>Edward L. Lee and Israel E. Wachs</i>	
1.1	Introduction	1
1.2	Molecular Structural Determination of Supported Metal Oxide Catalysts with <i>In Situ</i> Raman Spectroscopy	3
1.3	Characterization of AlO_x , TiO_x , and ZrO_x Surface-Modified SiO_2	3
1.4	Anchoring Site of Surface M_1O_x Species on Supported $\text{M}_2\text{O}_x/\text{SiO}_2$	5
1.5	Molecular Structure of Dehydrated Supported $\text{V}_2\text{O}_5/\text{SiO}_2$ and $\text{V}_2\text{O}_5/\text{M}_2\text{O}_x/\text{SiO}_2$ Catalyst Systems	5
1.6	Molecular Structure of Dehydrated Supported $\text{MoO}_3/\text{SiO}_2$ and $\text{MoO}_3/\text{M}_2\text{O}_x/\text{SiO}_2$ Catalyst Systems	8
1.7	Molecular Structure of Dehydrated Supported $\text{Re}_2\text{O}_7/\text{SiO}_2$ and $\text{Re}_2\text{O}_7/\text{M}_2\text{O}_x/\text{SiO}_2$ Catalyst Systems	11
1.8	Electronic Structure of Dehydrated Supported MO_x/SiO_2 and $\text{M}_1\text{O}_x/\text{M}_2\text{O}_x/\text{SiO}_2$ Catalysts via <i>In Situ</i> UV-Vis Spectroscopy	14
1.9	Determination of Surface Kinetic Parameters	15
1.10	Redox Surface Reactivity of Model Supported $\text{M}_1\text{O}_x/\text{SiO}_2$ Catalysts	16
1.11	Redox Surface Reactivity of Supported $\text{M}_1\text{O}_x/\text{M}_2\text{O}_x/\text{SiO}_2$ Catalysts	16
1.12	Conclusions	18
	References	19
2	Optimal Design of Hierarchically Structured Porous Catalysts	25
	<i>Marc-Olivier Coppens and Gang Wang</i>	
2.1	Introduction	25
2.1.1	Intrinsic Catalytic Activity and Selectivity: the Atomic and the Nanoscale	25
2.1.2	Catalyst Particle Size and Geometry: A Question of Reactor Engineering	26

2.1.3	Porous Catalyst Architecture and Optimization Methods	27
2.1.4	Learning from Nature	28
2.2	Optimizing Mesopore Connectivity and Shape	30
2.2.1	Topology, Order, and Randomness	30
2.2.2	Surface Roughness and Fractal Morphology	32
2.3	Optimizing Catalysts by Macroscopic Distributions in Activity	34
2.4	Optimal Design of the Highway Network	36
2.4.1	Novel Capabilities in Synthesizing Hierarchical Pore Spaces	37
2.4.2	Theoretical Optimization Studies: Opportunities for Optimal Design	39
2.4.3	Application to the Design of a Bimodal Porous Catalyst for NO _x Abatement	47
2.5	Conclusions	49
	References	50
3	Use of Dendrimers in Catalyst Design	59
	<i>Bert D. Chandler, Jeong-Kyu Lee, Harold H. Kung, and Mayfair C. Kung</i>	
3.1	Introduction	59
3.2	Modified Dendrimer Catalysts	60
3.2.1	Dendrimer Synthesis	60
3.2.2	Dendrimer Properties Important for Catalysis	61
3.2.3	Cooperative Catalysis	61
3.2.4	Site Isolation	64
3.3	Indirect Effects of Dendrimer Architecture	66
3.3.1	Polarity Gradients	66
3.3.2	Steric and Diffusion Effects	67
3.3.3	Comparing Dendrimers with Soluble Polymers	68
3.3.4	Other Novel Dendrimer Effects	70
3.4	Catalysis by Dendrimer Encapsulated Nanoparticles	72
3.4.1	Nanoparticle Synthesis	72
3.4.2	Catalysis by Monometallic DENs	73
3.4.3	Bimetallic Nanoparticles	73
3.4.4	Catalysis by Bimetallic DENs	75
3.5	Dendrimer Templated Nanocages	77
3.6	Conclusion	79
	References	79
4	Rational Design Strategies for Industrial Catalysts	83
	<i>Saeed Alerasool, C.P. Kelkar, and Robert J. Farrauto</i>	
4.1	Introduction	83
4.2	The First Stages Toward Commercialization of a Catalyst	84
4.3	Catalyst Discovery to Commercialization	84
4.3.1	Catalyst Preparation	84
4.3.2	Catalyst Testing	85
4.3.3	Advanced Testing in Accordance to the Duty Cycle	86

4.3.4	Aging Studies	86
4.3.5	Kinetics	87
4.3.6	Catalyst Scale-Up	88
4.3.7	Quality Control	89
4.4	Example 1: Automobile Pollution Abatement Catalyst System	89
4.4.1	The Quality of the Fuel	90
4.4.2	Base Metals Versus Precious Metals	90
4.4.3	Particulate Versus Monolithic Structures	91
4.4.4	The First Generation	91
4.4.5	The Final Test	92
4.5	Example 2: Dehydrogenation of Light Alkanes	93
4.5.1	Understanding Reaction Kinetics, Thermodynamics, and Process Constraints	94
4.5.2	Formulating the Catalyst	95
4.5.3	Pilot Plant Testing	97
4.5.4	Field Testing	98
4.5.5	Commercial Launch	99
4.6	Example 3: Petroleum Refining – Fluid Catalytic Cracking	100
4.6.1	Understanding Deactivation	101
4.6.2	Age Distribution	105
4.6.3	Attrition	105
4.6.4	Feed Effects	107
4.6.5	Scale-Up and Commercialization	109
4.7	Conclusions	109
	References	110
5	Chiral Modification of Catalytic Surfaces	113
	<i>Zhen Ma and Francisco Zaera</i>	
5.1	Introduction	113
5.2	Modification of Metal Surfaces by Cinchona Alkaloid and Related Compounds	115
5.2.1	General Background	115
5.2.2	Ordering Within the Adsorbed Layers	116
5.2.3	Modifier–Substrate Interactions	118
5.2.4	Adsorption Geometry	120
5.2.5	Influence of Reaction Conditions	122
5.2.6	Competitive Adsorption of Modifiers	125
5.3	Modification of Metal Surfaces by Tartaric Acid and Related Compounds	127
5.3.1	General Background	127
5.3.2	Long-Range Order Within the Adsorbed Layers	127
5.3.3	Local Chirality on the Surface	130
5.3.4	Identification of Chiral Sites on Surfaces	132
5.4	Conclusions	134
	References	136

6	Catalytic Nanomotors	141
	<i>John Gibbs and Yiping Zhao</i>	
6.1	Introduction	141
6.1.1	Biological Motors	142
6.1.2	Artificial Catalytic Nanomotors	142
6.2	The Propulsion Mechanism of Catalytic Nanomotors	144
6.2.1	Diffusiophoresis	144
6.2.2	Self-Electrophoresis	145
6.2.3	Bubble Propulsion	148
6.2.4	Interfacial Tension Gradients	149
6.2.5	Bioelectrochemical Propulsion	150
6.3	Advanced Design of Catalytic Nanomotors	151
6.3.1	Dynamic Shadowing Growth	151
6.3.2	Rotary Si–Pt Nanorod Nanomotors	151
6.3.3	L-Shaped Nanorod Nanomotors	152
6.3.4	Rolling Nanospring	153
6.3.5	Hinged Nanorods	154
6.4	Applications, Challenges, and Perspectives	157
	References	158
7	Rational Design and High-Throughput Screening of Metal Open Frameworks for Gas Separation and Catalysis	161
	<i>David Farrusseng and Claude Mirodatos</i>	
7.1	Introduction	161
7.2	MOF General Features and Brief State of the Art	162
7.2.1	A Building Block Construction	162
7.2.2	Robust Open, Functionalized, and Sizeable Frameworks	162
7.2.3	MOFs Synthesis	164
7.2.4	Adsorption Properties of MOF	166
7.2.5	Rational Strategies to Design MOFs for Targeted Applications	167
7.3	Combinatorial Design of MOF for CO ₂ Capture in a PSA Process	167
7.3.1	Process Specifications	167
7.3.2	General Properties of MOFs for CO ₂ Adsorption	168
7.3.3	MOF Design for CO ₂ Capture	171
7.3.3.1	“Structural” Route for Design Strategy	171
7.3.3.2	“Functionalization” Route for Design Strategy	172
7.3.4	Combinatorial Screening Methodology at IRCELYON	173
7.3.5	Combinatorial Synthesis	174
7.3.5.1	Protocol	174
7.3.5.2	Method Validation	174
7.3.5.3	Screening of Metal-BTC System	175
7.3.6	Characterization of Representative Samples	177
7.3.7	HT Testing and CO ₂ –CH ₄ Isotherms of Selected Samples	178
7.4	MOF Design for Catalytic Application	179

7.4.1	Properties of MOF in Catalysis	179
7.4.1.1	Lewis Acid Catalysis	180
7.4.1.2	Brönsted Acid Catalysis	181
7.4.1.3	Basic and Enantioselective Catalysis	182
7.4.1.4	C–C Coupling	183
7.4.1.5	Metal Catalysis	183
7.4.1.6	Wall Functionalization	183
7.4.1.7	Postfunctionalization	184
7.4.2	MOFs – Are They “Heterogenized” Catalysts or Solid Catalysts?	185
7.4.2.1	Engineering of Structural Defects in MOF	185
7.4.2.2	Probing Acid Centers by Alkylation Reactions	185
7.4.2.3	Catalyst Characterization	187
7.4.2.4	General Statements on MOF Application for Catalysis	188
7.5	Conclusion	188
	References	189
8	Design of Bimetallic Catalysts: From Model Surfaces to Supported Catalysts	195
	<i>Jeffrey P. Bosco, Michael P. Humbert, and Jingguang G. Chen</i>	
8.1	Introduction	195
8.2	Experimental and Theoretical Methods	196
8.2.1	Experimental Techniques	196
8.2.2	DFT Modeling	199
8.3	Results and Discussion	199
8.3.1	UHV and DFT Studies on Pt-Ni Model Surfaces	199
8.3.1.1	Adsorption and Desorption of Hydrogen	200
8.3.1.2	Disproportionation and Hydrogenation of Cyclohexene	202
8.3.2	Characterization and Reactor Studies of Supported Pt-Ni Catalysts	205
8.3.2.1	TEM and EXAFS Characterization of Ni/Pt/Al ₂ O ₃ Catalysts	205
8.4	Conclusions	211
	References	211
9	Self-Assembled Materials for Catalysis	213
	<i>Kake Zhu, Donghai Wang, and Jun Liu</i>	
9.1	Introduction	213
9.2	Mesocale Design	214
9.2.1	Inclusion of Heteroatoms	216
9.2.1.1	Acid Sites	216
9.2.1.2	Dispersed Metal Oxides	219
9.2.2	Embedded Nanoparticles	220
9.2.3	Nonsiliceous Mesoporous Materials	221
9.2.3.1	Molecule Self-Assembly to Mesoporous Catalysts	222
9.2.3.2	Nanoparticles Self-Assembly to Mesoporous Catalysts	222

9.2.4	Self-Assembly of Zeolite Seeds into Mesophase	223
9.2.5	Organic Functional Groups as Catalysts	224
9.3	Designing Catalysts at the Nanoparticle Surfaces	225
9.3.1	Polyoxometalates: Nanoparticles with Cations	225
9.3.2	Dendrimer-Stabilized Metal Nanoparticles	226
9.4	Perspectives	226
	References	227

10 Theory-Aided Catalyst Design 231

Matthew Neurock

10.1	Introduction	231
10.2	Catalytic Descriptors	234
10.2.1	Electronic Descriptors	234
10.2.2	Energetic Descriptors	235
10.2.3	Adsorption Energies or Binding Energies	236
10.2.4	High-Throughput Screening	238
10.3	High-Throughput Simulation and Design	242
10.3.1	NO Decomposition	244
10.3.2	Vinyl Acetate (VAM) Synthesis	249
10.4	Controlled Patterning	252
10.5	Catalyst Synthesis and Stability	252
10.6	Conclusions	253
	References	254

11 Use of *In Situ* XAS Techniques for Catalysts' Characterization and Design 259

Christophe Geantet and Jean-Marc M. Millet

11.1	Introduction	259
11.2	The X-Ray Absorption Techniques	260
11.2.1	Principles and Feasibility	260
11.2.2	Data Acquisition	262
11.2.3	Spectral Analysis and Interpretations	263
11.3	Recent Applications of X-Ray Absorption Techniques to the Design of Heterogeneous Catalysts	265
11.3.1	Time Resolution	265
11.3.2	High-Resolution XANES	271
11.3.3	High Detection Sensitivity	277
11.3.4	Spatial Resolution	278
11.3.5	Coupling of Techniques	280
11.4	Perspective	285
11.4.1	Time-Resolved Ultrafast X-Ray Absorption Spectroscopy	286
11.4.2	X-Ray Emission Spectroscopy (XES) and Resonant Inelastic X-Ray Scattering Spectroscopy (RIXS)	287
11.5	Conclusions	290
	References	291

12	Catalyst Design Through Dual Templating	295
	<i>Moises A. Carreon and Vadim V. Guliants</i>	
12.1	Introduction	295
12.2	Surfactant-Assisted Self-Assembly of Mesoporous Metal Oxides	297
12.2.1	Fundamentals	297
12.2.2	Thermal Stability Considerations	297
12.2.3	Mesostructuring via Evaporation-Induced Self-Assembly	299
12.3	Colloidal Sphere Templating of Macroporous Metal Oxides	301
12.4	Dual Templating of Metal Oxides	303
12.5	Catalytic Applications	305
12.5.1	Mesoporous Metal Oxides	305
12.5.2	Macroporous Metal Oxides	310
12.5.3	Metal Oxides Obtained via Dual Templating	311
12.6	Concluding Remarks	312
	References	313
	Index	315

Preface

As we face increasing challenges in economy, energy, and protection of the environment, the role of catalysis to provide some of the answers to these challenges has become more important than ever. With this increased importance, novel approaches have emerged for rational design of catalysts. Many of these approaches are based on new advances in synthesis, characterization, and modeling. They involve an understanding of the structure–function relationships and allow a molecular level control of the catalyst surfaces, thus taking catalyst development from being a semiempirical process to one that uses a rational design strategy, grounded in first principles.

This book presents several examples of this new paradigm in catalyst design, ranging from bioinspired approaches all the way to theory-aided design. Although no book can be comprehensive enough to cover all possible approaches to catalyst design, I believe the broad range of topics included in this volume will provide the reader with an insight into the realm of possibilities that now exist in catalyst development. It is also my hope that this book will stimulate further research in this exciting area.

I would like to express my deepest appreciation to all the authors who shared my excitement in preparing this book and contributed unique examples that illustrate the depth and breadth of the approaches now available in designing catalysts.

The Ohio State University
January 2009

Umit S. Ozkan

List of Contributors

Saeed Alerasool

BASF Catalysts
LLC
25 Middlesex Essex Tpk
Iselin
NJ 08830
USA

Jeffery P. Bosco

Department of Chemical Engineering
Center for Catalytic Science and
Technology (CCST)
University of Delaware
Newark
DE 19716
USA

Moises A. Carreon

Department of Chemical Engineering
University of Louisville
Louisville
KY 40292
USA

Bert D. Chandler

Department of Chemistry
Trinity University
1 Trinity Place
San Antonio
TX 78212
USA

Jingguang G. Chen

Department of Chemical Engineering
Center for Catalytic Science and
Technology (CCST)
University of Delaware
Newark
DE 19716
USA

Marc-Olivier Coppens

Rensselaer Polytechnic Institute
Howard P. Isermann Department of
Chemical and Biological Engineering
Troy
NY 12180
USA

Robert J. Farrauto

BASF Catalysts
LLC
25 Middlesex Essex Tpk
Iselin
NJ 08830
USA

David Farrusseng

Institut de Recherche sur la Catalyse et
l'Environnement de Lyon
UMR 5256 CNRS/Université Lyon 1
2 Avenue Albert Einstein
69626 Villeurbanne Cedex
France

Christophe Geantet

Institut de Recherches sur la Catalyse
et l'Environnement de Lyon
UMR 5256 CNRS/Université Lyon 1
2 Avenue Albert Einstein
69626 Villeurbanne Cedex
France

John Gibbs

Department of Physics and Astronomy
University of Georgia
Athens
GA 30602-2451
USA

Vadim V. Guliants

Department of Chemical & Materials
Engineering
University of Cincinnati
Cincinnati
OH, 45221
USA

Michael P. Humbert

Department of Chemical Engineering
Center for Catalytic Science and
Technology (CCST)
University of Delaware
Newark
DE 19716
USA

C.P. Kelkar

BASF Catalysts
LLC
25 Middlesex Essex Tpk
Iselin
NJ 08830
USA

Harold H. Kung

Chemical and Biological Engineering
Department
Northwestern University
Evanston
IL 60208
USA

Mayfair C. Kung

Chemical and Biological Engineering
Department
Northwestern University
Evanston
IL 60208
USA

Edward L. Lee

Operando Molecular Spectroscopy &
Catalysis Laboratory
Chemical Engineering Department,
Lehigh University
Bethlehem
PA 18015
USA

Jeong-Kyu Lee

Chemical and Biological Engineering
Department
Northwestern University
Evanston
IL 60208
USA

Jun Liu

Pacific Northwest National Laboratory
Richland
WA 99252
USA

Zhen Ma

Department of Chemistry
University of California
Riverside
CA 92521
USA

Jean-Marc M. Millet

Institut de Recherches sur la Catalyse et
l'Environnement de Lyon
UMR5256 CNRS/Université Lyon 1
2 Avenue Albert Einstein
69626 Villeurbanne Cedex
France

Claude Mirodatos

Institut de Recherches sur la Catalyse et
l'Environnement de Lyon
UMR 5256 CNRS/Université Lyon 1
2 Avenue Albert Einstein
69626 Villeurbanne Cedex
France

Matthew Neurock

Department of Chemical Engineering
and Chemistry
University of Virginia
Charlottesville
VA 22904-4741
USA

Israel E. Wachs

Operando Molecular Spectroscopy &
Catalysis Laboratory
Chemical Engineering Department
Lehigh University
Bethlehem
PA 18015
USA

Donghai Wang

Pacific Northwest National Laboratory
Richland
WA 99252
USA

Gang Wang

Rensselaer Polytechnic Institute
Howard P. Isermann Department of
Chemical and Biological Engineering
Troy
NY 12180
USA

Francisco Zaera

Department of Chemistry
University of California
Riverside
CA 92521
USA

Yiping Zhao

Department of Physics and Astronomy
University of Georgia
Athens
GA 30602-2451
USA

Kake Zhu

Pacific Northwest National Laboratory
Richland
WA 99252
USA

1

Use of Oxide Ligands in Designing Catalytic Active Sites

Edward L. Lee* and Israel E. Wachs

1.1

Introduction

Oxides of the group 5–7 metals (V, Nb, Ta, Cr, Mo, W, and Re) supported on a high surface area oxide material (SiO_2 , Al_2O_3 , TiO_2 , ZrO_2 , etc.) are recognized as industrially important catalysts for numerous chemical reactions [1–11]. For example, these catalysts are utilized for *o*-xylene oxidation to phthalic anhydride [12, 13], methane/methanol oxidation to formaldehyde [14], and selective catalytic reduction (SCR) of NO with ammonia to N_2 over supported vanadia catalysts [15–19]; SCR of NO with ammonia and selective oxidation of methane over supported molybdena catalysts [20–22]; olefin metathesis and hydrocarbon isomerization reactions over tungsta catalysts; and metathesis of olefins and alkanes over supported rhenia catalysts [23–25]. These supported metal oxide catalysts consist of highly dispersed surface metal oxide species – the catalytic active sites – anchored to the underlying oxide support. Over the decades, there have been many successful methods of controlling and anchoring the molecularly dispersed metal oxide phase by chemical vapor deposition (CVD) [26–28], incipient wetness impregnation [29–34], and precipitation [35–37]. The surface coverage of the metal oxide overlayer can vary from below to above monolayer coverage or the maximum dispersion limit, that is, maximum metal oxide dispersion before formation of crystalline metal oxide nanoparticles (NPs). Below monolayer surface coverage, only surface isolated (or monomeric) and surface polymeric metal oxide species are present on the support. At low surface coverage, only isolated surface metal oxide species are generally present [38]. Above monolayer coverage or maximum dispersion limit, crystalline metal oxide NPs are also present and reside on top of the molecularly dispersed surface metal oxide monolayer. Therefore, monolayer coverage or maximum dispersion limit is a critical parameter that allows distinguishing between two-dimensional molecularly dispersed surface metal oxide species and the three-dimensional NPs

*Present Work Address: The Dow Chemical
Company Core Research and Development
1776 Building, Midland, MI 48674, USA

present in supported metal oxide materials. For the purposes of simplifying and focusing the discussion, only SiO_2 -supported metal oxide catalysts at submonolayer coverages will be discussed in this chapter since the catalysis literature has demonstrated that only isolated surface metal oxide species are present at low coverage for supported MO_x/SiO_2 catalysts [14, 38–56].

The surface metal oxide species of supported metal oxide catalysts control the overall catalytic performance such as activity and selectivity. Thus, understanding the interactions of the surface metal oxide catalytic active sites with their environment (e.g., the underlying oxide support material and reactive environments) provides the ability to control and design these catalytic active sites. By spreading the catalytic active oxide layer over the underlying oxide support layers, the interfacial interaction of these “monolayer” catalysts results in different structures and catalytic properties than their bulk metal oxide counterparts [57, 58]. Therefore, recent studies have focused on characterizing the bridging $\text{M}-\text{O}$ –support bond for the design and control of the catalytic performance. The focus of this chapter will be to systematically surface modify the SiO_2 support with surface AlO_x , TiO_x , and ZrO_x species (the oxide ligands). The group 5–7 transition metal oxides (V_2O_5 , MoO_3 , and Re_2O_7) will then be anchored onto the surface-modified SiO_2 support by means of incipient wetness impregnation of soluble precursors and calcination. The V_2O_5 , MoO_3 , and Re_2O_7 catalytic active sites were chosen because of their dominant redox characteristics that will allow comparison of their reactivity properties. These “multilayered” supported $\text{M}_1\text{O}_x/\text{M}_2\text{O}_x/\text{SiO}_2$ catalysts will then be characterized and examined for their surface chemistry against the model supported MO_x/SiO_2 systems to understand the influence of the oxide ligands on the molecular/electronic structures and catalytic performance of the surface metal oxide species.

In keeping with the theme of the book for new approaches to synthesis and characterization of heterogeneous catalysts, this chapter will focus on the oxide ligand of the “multilayered” supported $\text{M}_1\text{O}_x/\text{M}_2\text{O}_x/\text{SiO}_2$ catalysts by characterizing the surface M_1O_x molecular and electronic structures and investigating the catalytic reactivity for oxidative dehydrogenation of methanol to formaldehyde. The molecular and electronic structures of the supported $\text{M}_1\text{O}_x/\text{M}_2\text{O}_x/\text{SiO}_2$ catalysts will be determined with *in situ* Raman and UV–Vis diffuse reflectance spectroscopy (DRS) spectroscopy, respectively, under various environments (e.g., dehydrated, oxidative, reductive, and isotopic exchange) to investigate the fundamental interactions between the surface metal oxide overlayer (M_1O_x) and the surface oxide modifiers (M_2O_x) on the silica support. Time-resolved Raman spectra for reductive and isotopic oxygen exchange studies will provide additional insights into the dynamic nature of these catalytic active sites. The catalytic surface reactivity will be chemically probed via CH_3OH temperature-programmed surface reaction (CH_3OH -TPSR) spectroscopy that will provide the surface kinetics and nature of the catalytic active sites (redox, acidic, or basic). Theoretical modeling results via computational density functional theory (DFT) from the literature will be referenced where appropriate. This systematic approach to supported metal oxide catalysts will assist in the establishment of molecular structure–reactivity relationship for designing and controlling surface metal oxide catalytic active sites.

1.2

Molecular Structural Determination of Supported Metal Oxide Catalysts with *In Situ* Raman Spectroscopy

Raman spectroscopic studies in the late 1970s first reported the detection of surface metal oxide species for supported MoO_3 [59–61], WO_3 [62], V_2O_5 [63, 64], and Re_2O_7 [65] catalysts. These studies were followed by *in situ* Raman measurements in the early 1980s, where the gas phase environment and temperature of the catalyst could be controlled [66–70]. Detection of the reversible surface structures when exposed to hydrated and dehydrated conditions was demonstrated during this period [66]. These earlier experimental breakthroughs and with further advances in Raman technology allowed for the characterization of the surface structures of mixed metal oxide catalysts [58]. New approaches for *in situ* Raman spectroscopic measurements of catalytic surfaces are now undertaken via measurements under reductive, isotopic D_2O – H_2O and ^{16}O – ^{18}O exchange environments coupled with time-resolved spectroscopy. These approaches provide new fundamental insights that enable the molecular structural determination of the catalytic active surface metal oxide sites present in supported metal oxide catalysts.

It is important to recall that isotopic ^{16}O – ^{18}O exchange results in band splitting. Based on vibrational theory, monoxo species are expected to exhibit two Raman vibrations ($\text{M}=\text{O}$ and $\text{M}=\text{O}$); dioxo species are projected to give rise to three Raman vibrations ($^{16}\text{O}=\text{M}=\text{O}$, $^{18}\text{O}=\text{M}=\text{O}$, and $^{18}\text{O}=\text{M}=\text{O}$); and trioxo species are expected to exhibit four Raman vibrations ($\text{M}(=\text{O})_3$, $^{18}\text{O}=\text{M}(=\text{O})_2$, $(^{18}\text{O})_2\text{M}=\text{O}$, and $\text{M}(=\text{O})_3$) [71–75]. The position of the vibrational shifts can be estimated using a simple M – O diatomic oscillator model for the isotopic ratio:

$$\left[\frac{\nu_{\text{O-M}}^{16}}{\nu_{\text{O-M}}^{18}} \right] = \frac{\frac{1}{2\pi c} \sqrt{\left(k \left(\frac{1}{m_{\text{M}}} + \frac{1}{m_{16}} \right) \right)}}{\frac{1}{2\pi c} \sqrt{\left(k \left(\frac{1}{m_{\text{M}}} + \frac{1}{m_{18}} \right) \right)}} = \frac{\sqrt{\left(\frac{1}{m_{\text{M}}} + \frac{1}{m_{16}} \right)}}{\sqrt{\left(\frac{1}{m_{\text{M}}} + \frac{1}{m_{18}} \right)}} \quad (1.1)$$

where ν is the frequency of the M – O bond (cm^{-1}), k is the force constant, and m is the mass of the transition metal ion or oxygen [71, 73].

1.3

Characterization of AlO_x , TiO_x , and ZrO_x Surface-Modified SiO_2

The surface of SiO_2 was modified by the deposition on the surface of M_2O_x (AlO_x , TiO_x , or ZrO_x) species. For each supported $\text{M}_2\text{O}_x/\text{SiO}_2$ system, the surface-modified SiO_2 support consists of 5% $\text{M}_2\text{O}_x/\text{SiO}_2$, which is below the maximum dispersion limit for these oxides on SiO_2 . The *in situ* Raman spectra of the dehydrated supported $\text{M}_2\text{O}_x/\text{SiO}_2$ samples are presented in Figure 1.1 (left) and do not exhibit any new significant spectral features as compared to the original SiO_2 support, with the exception of $\text{TiO}_x/\text{SiO}_2$, which will be discussed below. The deposition of alumina, titania, and zirconia on the silica support causes a decrease in the intensity of the band

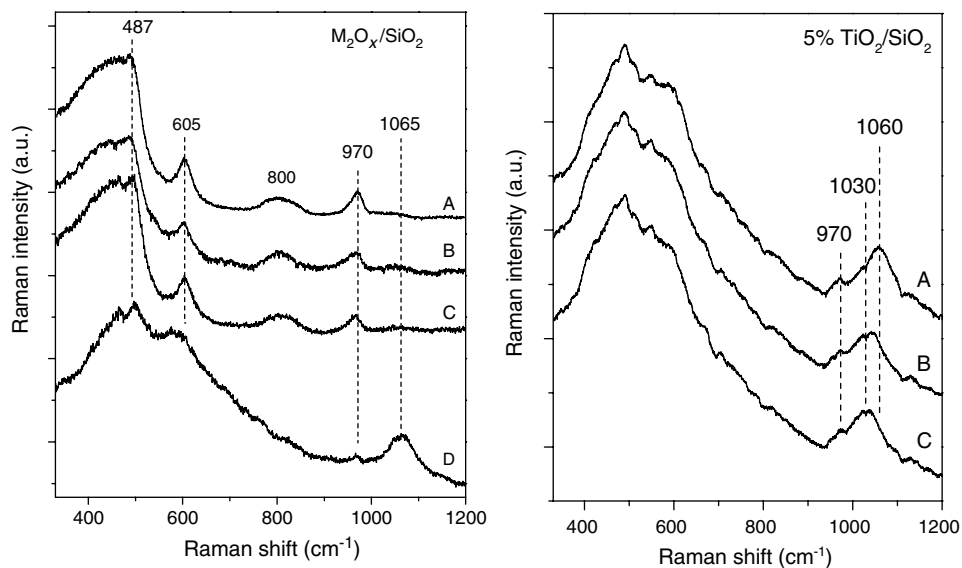


Figure 1.1 (Left) *In situ* Raman spectra of (A) pure and unmodified SiO_2 and surface-modified SiO_2 with (B) 5% ZrO_x , (C) 5% AlO_x , and (D) 5% TiO_x oxide ligands using 325 nm excitation energy at 500 °C. (Right) Time-resolved *in situ* Raman spectra of 5% TiO_x/SiO_2 during $H_2^{18}O$ exposure after (A) 0 min, (B) 30 min, and (C) 80 min.

at 970 cm⁻¹ of the Si–OH vibration and indicates consumption of the Si–OH surface hydroxyls. This decrease is further confirmed by *in situ* near-IR DRS at 7315 cm⁻¹ (2v). The surface modification of the SiO_2 surface by the deposited oxides leads to direct interactions with the silica surface hydroxyl groups, resulting in the broadening of the 970 cm⁻¹ band, and in the ZrO_2/SiO_2 spectrum, its shift toward lower wavenumbers (~940 cm⁻¹), which is suggestive of bridging Zr–O–Si linkages. Therefore, the AlO_x , ZrO_x , and TiO_x surface modifiers anchor to the silica at the Si–OH site to create a surface metal oxide layer with residual exposed Si–OH species also present.

Additional Raman features are present, however, for the supported TiO_x/SiO_2 sample in Figure 1.1 (left). The transverse-optical (TO) mode of the silica network at 1065 cm⁻¹, assigned to perturbed $Si(-O^-)_2$ and $Si-O^-$ silica vibrations from the formation of Ti–O–Si bridging bond, appears to be resonance Raman enhanced with the 325 nm excitation, and the broad band at 550–600 cm⁻¹ is suggestive of a small amount of polymeric Ti–O–Ti species. The supported TiO_x/SiO_2 sample was exposed to isotopic $^{18}O_2$ and monitored with time-resolved *in situ* Raman, see Figure 1.1 (right), to determine if the ~1065 cm⁻¹ band is related to the TO mode of the silica network or possibly the Ti=O bond. The isotopic oxygen exchange resulted in the band shift from ~1060 to ~1030 cm⁻¹, which exactly corresponds to that of the TO vibration [76] since $Ti=^{18}O$ should shift to 1015 cm⁻¹ for a simple Ti–O diatomic oscillator (see Equation 1.1).

Extensive characterization experiments under dehydrated conditions have also been conducted by means of *in situ* IR, UV–Vis DRS, XPS, XANES, and ^{27}Al NMR,

which provide additional molecular information about the supported MO_x phases on SiO_2 [77–80]. The supported 5% TiO_2/SiO_2 and 5% ZrO_2/SiO_2 samples consist of 100% dispersed surface TiO_x and ZrO_x species on the SiO_2 support. The surface TiO_x species are present as TiO_4 and TiO_5 coordinated species and the former dominates at the lower TiO_x content (such as 5% TiO_2/SiO_2). The coordination environments of the dehydrated surface ZrO_x species have yet to be determined. The supported 5% Al_2O_3/SiO_2 sample primarily contains surface AlO_4 coordination with a minor amount of surface AlO_5 species [77]. In summary, supported 5% TiO_2/SiO_2 sample consists of $(OH)-Ti-(O-Si)_3$, and the 5% Al_2O_3/SiO_2 consists of $(O^-)-Al-(O-Si)_3$ where the extra proton (Bronsted acid site) is on the bridging oxygen in the $Al-O-Si$ bond.

1.4

Anchoring Site of Surface M_1O_x Species on Supported M_2O_x/SiO_2

The supported M_1O_x phases are all found to be present as two-dimensional surface metal oxide species on the M_2O_x/SiO_2 supports, as will be shown below with Raman spectroscopy. The anchoring site of the surface M_1O_x species takes place on exposed surface $-OH$ sites and is related to the acidic/basic nature of the surface $-OH$ groups. It is well established that anchoring of acidic surface M_1O_x initially occurs at the most basic surface $-OH$ groups, followed by the neutral surface $-OH$ groups, and finally, the most acidic surface $-OH$ groups [81]. The acidity of the surface $-OH$ groups is related to the electronegativity of the oxide support cation and increases with the support cation electronegativity ($Zr \sim Ti < Al < Si$) [82]. Consequently, the acidic surface M_1O_x species preferentially anchor to the more basic surface $Zr-OH$, $Ti-OH$, and $Al-OH$ sites over the more acidic surface $Si-OH$ sites. This preferential anchoring is best demonstrated by the Raman spectra of the supported WO_x/SiO_2 and $WO_x/AlO_x/SiO_2$ catalytic systems, as shown in Figure 1.2. The supported WO_3/SiO_2 gives rise to a dominant Raman band at 982 cm^{-1} (dioxo $\nu_s(W(=O)_2)$) and a minor Raman band at 1014 cm^{-1} (monoxo $\nu_s(W=O)$) that transform to monoxo $\nu_s(W=O)$ species with a Raman band at 1020 cm^{-1} for the supported $WO_3/Al_2O_3/SiO_2$ catalyst system. Furthermore, the monoxo $\nu_s(W=O)$ Raman band position at 1020 cm^{-1} matches that for monoxo $\nu_s(W=O)$ species present in the supported WO_3/Al_2O_3 catalysts [83]. These Raman spectral changes clearly reflect the preferential anchoring of the surface WO_x species at the surface AlO_x sites over exposed SiO_2 sites on the surface-modified SiO_2 support. The preferential anchoring of the surface M_1O_x species at the surface M_2O_x species over the exposed SiO_2 support sites is a general phenomenon for anchoring of group 5–7 transition metal oxides on the surface-modified SiO_2 support.

1.5

Molecular Structure of Dehydrated Supported V_2O_5/SiO_2 and $V_2O_5/M_2O_x/SiO_2$ Catalyst Systems

The surface vanadium oxide species in the dehydrated V_2O_5/SiO_2 catalyst exhibit a sharp and intense Raman vibration at 1038 cm^{-1} , as shown in Figure 1.3 (left), curve

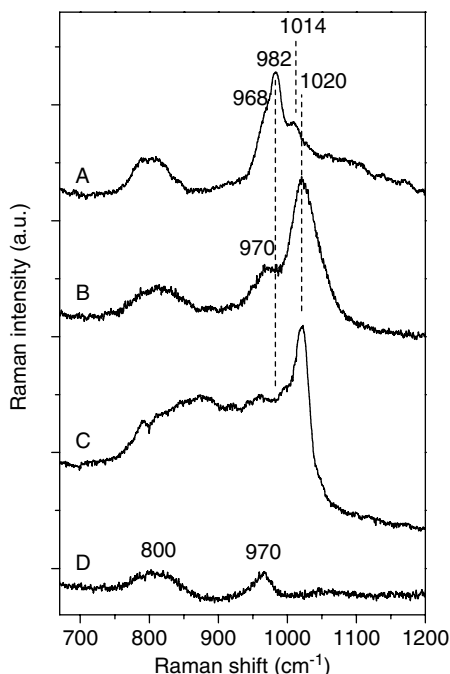


Figure 1.2 *In situ* Raman spectra under oxidizing conditions using 532 nm excitation energy of (A) 6% WO_3/SiO_2 , (B) 3% $\text{WO}_3/5\%$ $\text{Al}_2\text{O}_3/\text{SiO}_2$, (C) 20% $\text{WO}_3/\text{Al}_2\text{O}_3$, and (D) pure SiO_2 for reference.

labeled A, and has been assigned to the terminal $\nu_s(\text{V}=\text{O})$ stretch of isolated surface VO_4 species [39–45]. This Raman band position is also independent of exposure to D_2O at elevated temperatures indicating that there are no $\text{V}-\text{OH}$ functionalities (not shown for brevity). The position of the terminal $\text{V}=\text{O}$ vibration at 1038 cm^{-1} is consistent with the monoxo $\text{V}=\text{O}$ structure present in $\text{H}_3\text{SiMo}_{11}\text{VO}_{40}$ Keggin structure (1034 cm^{-1}) and $(\text{Ph}_3\text{SiO})_3\text{V}=\text{O}$ (1022 cm^{-1}), as well as with DFT calculations ($1038\text{--}1047\text{ cm}^{-1}$) for the simple gas phase monomer structure, $\text{O}=\text{V}(\text{OCH}_3)_3$ and monomeric polyhedral oligomeric silsesquioxanes [84–86]. Furthermore, dioxo $\text{O}=\text{V}=\text{O}$ structures vibrate at a wavenumber ~ 970 (ν_s)/ 960 (ν_{as}) cm^{-1} [73]. The terminal $\nu_s(\text{V}=\text{O})$ vibration is accompanied by weaker bands at 340 and 905 cm^{-1} , assigned to the bending (δ) $\text{V}-\text{O}$ and stretching $\text{V}-\text{O}-\text{Si}$ modes, respectively. The weak shoulder band at 1070 cm^{-1} is characteristic of the silica network TO mode and has been assigned to perturbed $\text{Si}(-\text{O}^-)_2$ and $\text{Si}-\text{O}^-$ silica vibrations that are also indicative of the formation of bridging $\text{V}-\text{O}-\text{Si}$ bonds [40]. The partial reduction of the 1038 , 905 , and 340 cm^{-1} Raman bands at 600°C under the reducing H_2 environment, shown in curve B of Figure 1.3 (left), confirms the assigned $\text{V}=\text{O}$, $\text{V}-\text{O}-\text{Si}$ and bending $\text{V}-\text{O}$ vibrations to surface $\text{V}-\text{O}$ vibrations [43]. Comparison of the Raman spectra for the reduced supported $\text{V}_2\text{O}_5/\text{SiO}_2$ catalyst sample with that of the SiO_2 support (see curve C of Figure 1.3 (left)) reveals the decrease of the silica 970 and 605 cm^{-1} bands relative to the silica 800 cm^{-1} band upon deposition of

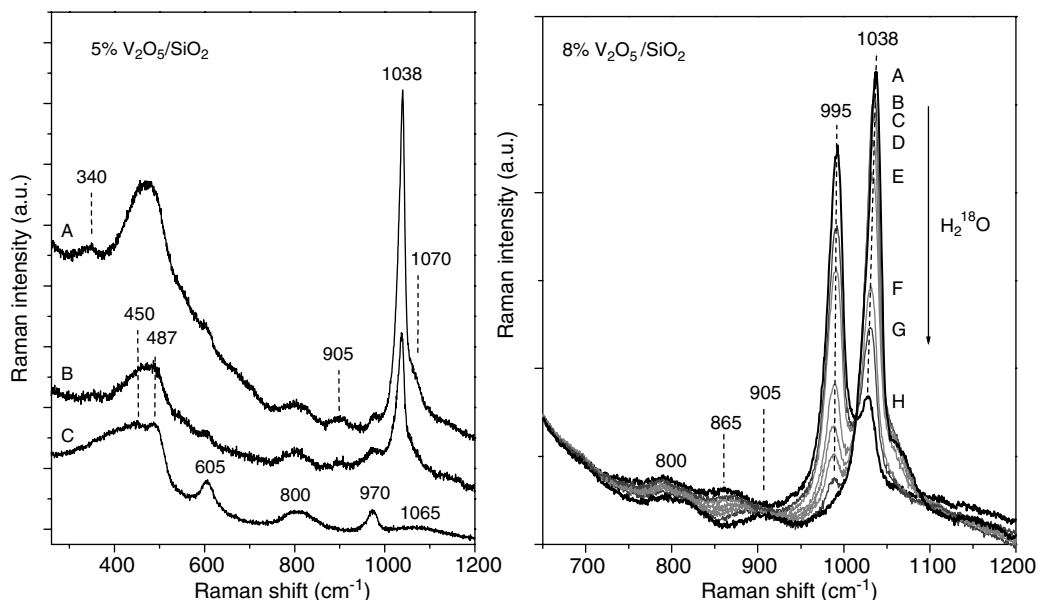


Figure 1.3 (Left) *In situ* Raman spectra of supported 5% $\text{V}_2\text{O}_5/\text{SiO}_2$ using 532 nm excitation energy under (A) oxidizing conditions at 450 °C and (B) hydrogen reducing conditions (5% H_2/Ar at 600 °C). The dehydrated SiO_2 support is shown for reference in (C).

Reproduced from Ref. [55]. (Right) Time-resolved *in situ* Raman spectra of supported 8% $\text{V}_2\text{O}_5/\text{SiO}_2$ during H_2^{18}O exposure after (A) 0 min, (B) 10 min, (C) 20 min, (D) 30 min, (E) 40 min, (F) 70 min, (G) 90 min, and (H) 130 min. Reproduced from Ref. [56].

surface vanadia species, indicating the preferential anchoring of the surface vanadia species at the isolated SiO_2 support surface hydroxyls and the three-membered siloxane rings, respectively. Deuterated water experiments result in a shift of the 970 cm^{-1} band to $\sim 955\text{ cm}^{-1}$ due to the exchange of $\text{Si}-(\text{OH})$ to $\text{Si}-(\text{OD})$ as seen with the pure silica [55]. Additional insight is provided by time-resolved isotopic oxygen exchange of the dehydrated supported $\text{V}_2\text{O}_5/\text{SiO}_2$ catalyst, shown in Figure 1.3 (right), and results in splitting of the surface $\text{V}=\text{O}$ band to 1038 and 995 cm^{-1} (assigned to $\nu_s(\text{V}=\text{O})$ and $\nu_s(\text{V}=\text{O})$, respectively) and shifting of the $\text{V}-\text{O}-\text{Si}$ vibration from 905 to 865 cm^{-1} [56, 72]. The time-resolved Raman spectra reveal that the two symmetric $\text{V}=\text{O}$ bands remain at the same wavenumber during the exchange process. The shift from 1038 to 995 cm^{-1} closely matches the theoretical $\text{V}=\text{O}$ vibration at 993 cm^{-1} of a simple diatomic oscillator model [56].

The Raman spectra of the dehydrated supported $\text{V}_2\text{O}_5/\text{TiO}_2/\text{SiO}_2$, $\text{V}_2\text{O}_5/\text{ZrO}_2/\text{SiO}_2$, and $\text{V}_2\text{O}_5/\text{Al}_2\text{O}_3/\text{SiO}_2$ catalysts are presented in Figure 1.4 (left) and give rise to a single sharp band at $\sim 1035\text{ cm}^{-1}$ from the $\nu_s(\text{V}=\text{O})$ stretching mode of the dehydrated surface VO_x species. The similarity of the terminal $\nu_s(\text{V}=\text{O})$ vibrations for the supported $\text{VO}_x/\text{M}_2\text{O}_x/\text{SiO}_2$ catalysts to that of the model supported VO_x/SiO_2 catalyst indicates that all these catalysts contain the same monoxo $\text{V}=\text{O}$ species. The constancy of the $\text{V}=\text{O}$ vibration indicates that the surface structure stays monoxo even with the addition of the surface modifiers, as depicted in Figure 1.4 (right).

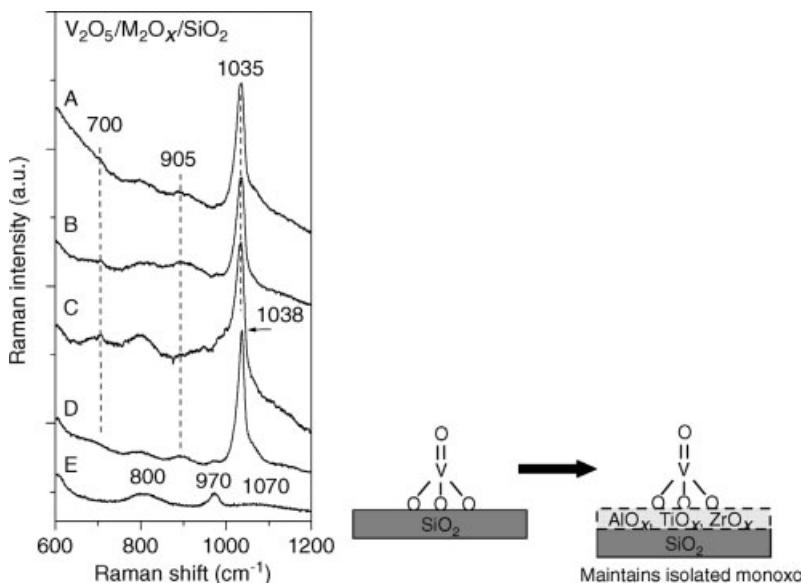


Figure 1.4 (Left) *In situ* Raman spectra (532 nm) of dehydrated supported (A) 5% $V_2O_5/TiO_x/SiO_2$, (B) 5% $V_2O_5/ZrO_x/SiO_2$, (C) 5% $V_2O_5/AlO_x/SiO_2$, and (D) 5% V_2O_5/SiO_2 catalysts under oxidizing conditions at 600 °C. Pure dehydrated SiO_2 spectrum (E) is provided for reference. Reproduced in part from refs. [44, 77, 87–90]. (Right) Schematic of dehydrated supported VO_x species on SiO_2 and surface-modified silica.

Furthermore, there is no apparent ligand effect of the surface modifiers on the molecular structure of the surface VO_x species. A new weak Raman band at $\sim 700\text{ cm}^{-1}$ is also present for the supported $VO_x/M_2O_x/SiO_2$ catalysts, which becomes more intense with increasing vanadia and additive concentrations and is tentatively assigned to the stretching mode of the corresponding $V-O-Al/V-O-Zr/V-O-Ti$ bridging bonds.

1.6

Molecular Structure of Dehydrated Supported MoO_3/SiO_2 and $MoO_3/M_2O_x/SiO_2$ Catalyst Systems

The *in situ* Raman spectrum of dehydrated supported MoO_3/SiO_2 is presented in curve A of Figure 1.5 (left). The dehydrated surface molybdenum oxide species possess dioxo $(O=)_2Mo(-O-Si)_2$ and monoxo $O=Mo(-O-Si)_4$ structures that give rise to Raman bands for $\nu_s(Mo(=O)_2)$ at $\sim 976\text{--}988\text{ cm}^{-1}$ and $\nu_s(Mo=O)$ at 1020 cm^{-1} , respectively [91–97]. The corresponding dioxo $\nu_{as}(Mo(=O)_2)$ stretch appears as a shoulder at $965\text{--}975\text{ cm}^{-1}$ and the weak vibration at 364 cm^{-1} is attributed to the bending $\delta(O-Mo-O)$ mode [20, 75, 94–97]. The surface MoO_x vibration at 1020 cm^{-1} is consistent with that of the monoxo $H_3SiMo_{12}O_{40}$ Keggin structure (1006 cm^{-1}) and DFT calculations predicting monoxo $(Si-O)_4Mo=O$ vibrations at $1014\text{--}1017\text{ cm}^{-1}$.

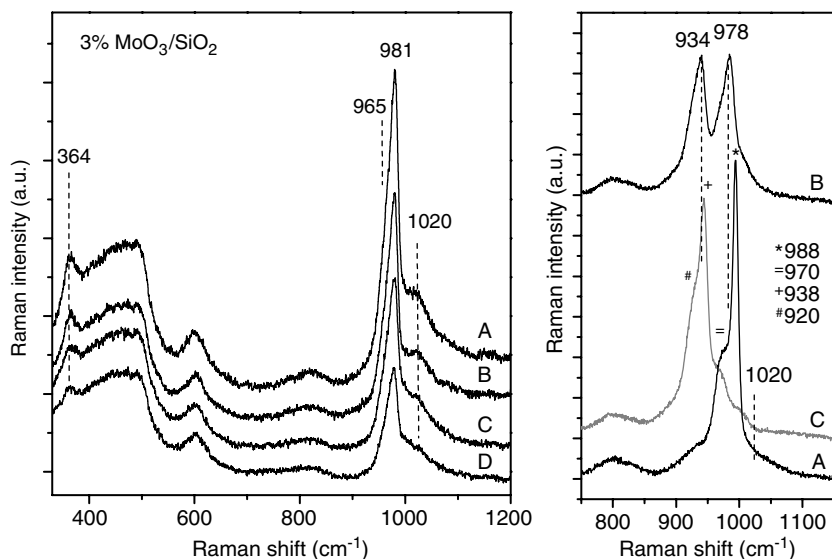


Figure 1.5 (Left) *In situ* Raman spectra (325 nm) of supported 3% $\text{MoO}_3/\text{SiO}_2$ under (A) oxidizing, dehydrated conditions at 500°C , (B) reoxidation after H_2 exposure, (C) 2% H_2/He exposure, and (D) 5% H_2/He exposure. Reproduced from Ref. [55]. (Right) Time-resolved *in situ* Raman spectra (325 nm) of supported 8% $\text{MoO}_3/\text{SiO}_2$ during H_2^{18}O exposure after (A) 0 min, (B) 13 min, and (C) 100 min.

Consequently, the surface molybdena vibrations present for the dehydrated supported $\text{MoO}_3/\text{SiO}_2$ catalyst samples at $976\text{--}988\text{ cm}^{-1}$ with the shoulder band at $965\text{--}975\text{ cm}^{-1}$ correspond to dioxo surface $\text{O}=\text{Mo}=\text{O}$ species, consistent with DFT calculations predicting the dioxo $(\text{Si}-\text{O})_2\text{Mo}(=\text{O})_2$ vibration located at $995(\nu_s)$ and $977(\nu_{as})$, respectively. The expected weak bridging $\text{Mo}-\text{O}-\text{Si}$ band is not readily observed in the $\sim 900\text{--}930\text{ cm}^{-1}$ region and may be overshadowed by the intense bands of the surface molybdena species. Upon exposure to reducing hydrogen environments, the surface $\nu_s(\text{Mo}(=\text{O})_2)$ vibration present in the *in situ* Raman spectrum of curve D of Figure 1.5 (left) reduces its intensity to about a quarter of the fully oxidized intensity, which indicates partial reduction. Additionally, the decrease in intensity of the Raman bands at 364 , ~ 965 , and 1020 cm^{-1} during the H_2 reduction treatments confirms that these assignments are associated with $\text{Mo}-\text{O}$ vibrations. Oxidation of the partially reduced supported $\text{MoO}_3/\text{SiO}_2$ catalysts restores all the surface MoO_x vibrations as shown in curve B of Figure 1.5 (left).

The surface dioxo ν_s and ν_{as} ($\text{Mo}(=^{16}\text{O})_2$) Raman bands at 988 and 970 cm^{-1} shift to 938 and 920 cm^{-1} , respectively, after almost complete isotopic oxygen exchange of the corresponding $\text{Mo}(=^{18}\text{O})_2$ species, and are presented in Figure 1.5 (right). The shift of approximately -50 cm^{-1} is consistent with earlier IR literature observations, that the 990 cm^{-1} band shifts to 940 cm^{-1} during isotopic exchange from Mo^{16}O to Mo^{18}O species [97] and that the 970 cm^{-1} band shifts to 935 cm^{-1} for the Mo^{16}O to Mo^{18}O species [98], and with Raman spectra studies that the 988 cm^{-1} band shifts to 938 cm^{-1} [99]. The Raman band of the surface monoxo $\nu_s(\text{Mo}^{16}\text{O})$ species at

1020 cm⁻¹ is not readily observed in Figure 1.5 (right) because of resonance enhancement of the vibrations of the surface dioxo species and the presence of a greater concentration of surface dioxo species at higher MoO_x loading (8 wt.%). Consequently, only the isotopic shift of for surface dioxo species will be discussed. At intermediate extent of isotopic oxygen exchange, the band splitting occurs at 978 cm⁻¹ of the $\nu_s(\text{Mo}(=\text{}^{16}\text{O})_2)$ vibration and at 934 cm⁻¹ of the $\nu_s(\text{Mo}(=\text{}^{18}\text{O})_2)$ species. Note that the $\nu_s(\text{Mo}(=\text{O})_2)$ vibration shifts from 988 cm⁻¹, when the surface MoO₄ contains ~100% ¹⁶O, to 978 cm⁻¹, when the surface MoO₄ is composed of a mixture of ¹⁶O and ¹⁸O. No shift of any surface species (Raman bands at ~965, 976–991, and 1020 cm⁻¹) is observed during H₂O–D₂O exchange or during injection of pure H₂O, which is consistent with the absence of an Mo–OH functionality. Therefore, shifting of the Raman bands is indicative of intermediate ¹⁶O=Mo=¹⁸O species, as suggested by DFT calculations. The DFT calculations predict that the Mo=O component shows a shift of not more than 5–7 cm⁻¹ (995 to ~988 cm⁻¹) from $\nu_s(\text{Mo}(=\text{}^{16}\text{O})_2)$ to $\nu_s(\text{}^{16}\text{O}=\text{Mo}=\text{}^{18}\text{O})$ and one that is larger, ~32 cm⁻¹ (~988 to ~956 cm⁻¹), from $\nu_s(\text{}^{16}\text{O}=\text{Mo}=\text{}^{18}\text{O})$ to $\nu_s(\text{Mo}(=\text{}^{18}\text{O})_2)$. Experimentally, the Mo=O component shows an initial shift of 5–10 cm⁻¹ (981–988 to 976–978 cm⁻¹) followed by a larger one, of almost –40 cm⁻¹, to ~933–938 cm⁻¹, which represents the shift from $\nu_s(\text{Mo}(=\text{}^{16}\text{O})_2)$ to $\nu_s(\text{}^{16}\text{O}=\text{Mo}=\text{}^{18}\text{O})$ to $\nu_s(\text{Mo}(=\text{}^{18}\text{O})_2)$. The $\nu_{as}(\text{Mo}(=\text{}^{16}\text{O})_2)$ shoulder vibration at 970 cm⁻¹ that shifts 40–50 cm⁻¹ to lower wavenumbers also closely follows the DFT calculations, where it is predicted that the shift of $\nu_{as}(\text{Mo}(=\text{}^{16}\text{O})_2)$ to $\nu_{as}(\text{Mo}(=\text{}^{18}\text{O})_2)$ is –43 cm⁻¹ (977 to ~934 cm⁻¹) after complete exchange. The shoulder at ~920 cm⁻¹ is also consistent with $\nu_{as}(\text{Mo}(=\text{}^{18}\text{O})_2)$ and not the Si–¹⁸OH vibration, which appears at 950 cm⁻¹ (not shown for brevity). Thus, consistent with predictions from the DFT calculations, the existence of the intermediate ¹⁶O=Mo=¹⁸O species allows for the conclusion that the dehydrated surface molybdenum oxide species exist as surface dioxo O₂Mo(=O)₂ species.

The dehydrated supported MoO₃/TiO_x/SiO₂, MoO₃/ZrO_x/SiO₂, and MoO₃/AlO_x/SiO₂ catalysts give rise to Raman bands in the 985–1002 cm⁻¹ assigned to dehydrated surface dioxo Mo(=O)₂ species, and are presented in curves A, B, and C, respectively, of Figure 1.6 (left) [88, 100]. These Raman spectra do not exhibit the Raman band at 1020 cm⁻¹ of the isolated surface monoxo M=O species, suggesting that the surface modifiers affected the ratio of the two dehydrated surface MoO_x species. The slight shift from 981 to 985–1002 cm⁻¹ indicates distortions of the dioxo surface Mo(=O)₂ species from interactions with the surface AlO_x, TiO_x, and ZrO_x additives on the surface-modified SiO₂ support, schematically depicted in Figure 1.6 (right). The somewhat higher wavenumber value of 1002 cm⁻¹ for the supported MoO₃/AlO_x/SiO₂ system may reflect the presence of some monoxo surface MoO₅ species. The corresponding surface dioxo $\nu_{as}(\text{Mo}(=\text{O})_2)$ band occurs as a shoulder at ~965–975 cm⁻¹ on the strong symmetric stretch and is most visible for the highly distorted supported MoO₃/AlO_x/SiO₂ catalyst at 973 cm⁻¹, however, surface hydroxyl groups and some surface dioxo species may also overlap in this region. The weak and broad bands at ~825–880 cm⁻¹ observed for supported MoO₃/AlO_x/SiO₂ and MoO₃/ZrO_x/SiO₂ catalysts are assigned to bridging M–O–Al and M–O–Zr bonds, respectively [95, 101, 102].

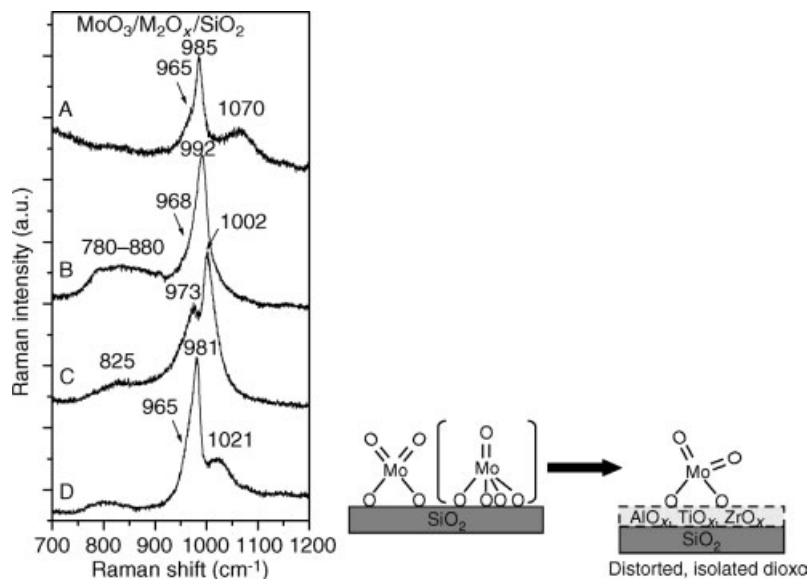


Figure 1.6 (Left) *In situ* Raman spectra (325 nm) of dehydrated supported (A) 3% $\text{MoO}_3/\text{TiO}_x/\text{SiO}_2$, (B) 3% $\text{MoO}_3/\text{ZrO}_x/\text{SiO}_2$, (C) 3% $\text{MoO}_3/\text{AlO}_x/\text{SiO}_2$, and (D) 3% $\text{MoO}_3/\text{SiO}_2$ under oxidizing conditions at 500 °C. (Right) Schematic of dehydrated supported MoO_x species on SiO_2 and on surface-modified silica.

1.7

Molecular Structure of Dehydrated Supported $\text{Re}_2\text{O}_7/\text{SiO}_2$ and $\text{Re}_2\text{O}_7/\text{M}_2\text{O}_x/\text{SiO}_2$ Catalyst Systems

The dehydrated surface rhenium oxide species on the supported $\text{Re}_2\text{O}_7/\text{SiO}_2$ catalyst are present as isolated trioxo surface $(\text{O}=\text{O})_3\text{Re}-\text{O}-\text{Si}$ species, giving rise to Raman bands for $\nu_s(\text{Re}(\text{=O})_3)$ at 1010 cm^{-1} , $\nu_{\text{as}}(\text{Re}(\text{=O})_3)$ at 977 cm^{-1} , and bending $\delta(\text{O}-\text{Re}-\text{O})$ at 343 cm^{-1} . The Raman spectrum is presented in curve A of Figure 1.7 (left) [103, 104]. The 977 cm^{-1} band from the surface ReO_x species of $\text{Re}_2\text{O}_7/\text{SiO}_2$ overlaps with the $\text{Si}-\text{OH}$ band at 970 cm^{-1} , as will be further shown below. The positions of these three surface ReO_x Raman bands coincide with the $\nu_s(\text{Re}(\text{=O})_3)$, $\nu_{\text{as}}(\text{Re}(\text{=O})_3)$, and $\delta(\text{O}-\text{Re}-\text{O})$ vibrations of the trioxo $\text{Re}(\text{=O})_3$ functionality of the gas phase $(\text{O}=\text{O})_3\text{Re}-\text{O}-\text{Re}(\text{=O})_3$ molecule at 1009, 972, and 341 cm^{-1} , respectively. However, the vibrations of the bridging $\text{Re}-\text{O}-\text{Re}$ bond at 456 (ν_s) and 185 (δ) cm^{-1} are absent, and this is consistent with the isolated nature of the surface rhenia species on the SiO_2 support. The bridging $\text{Re}-\text{O}-\text{Si}$ band, expected to give rise to a weak band at $\sim 900\text{ cm}^{-1}$, is not readily apparent in the vibrational spectrum. Upon exposure to reducing hydrogen environments, the dehydrated surface ReO_4 species on SiO_2 readily reduces, as shown in curve C of Figure 1.7 (left). The complete removal of the $\text{Re}-\text{O}$ vibrations under reducing environments followed by complete restoration of

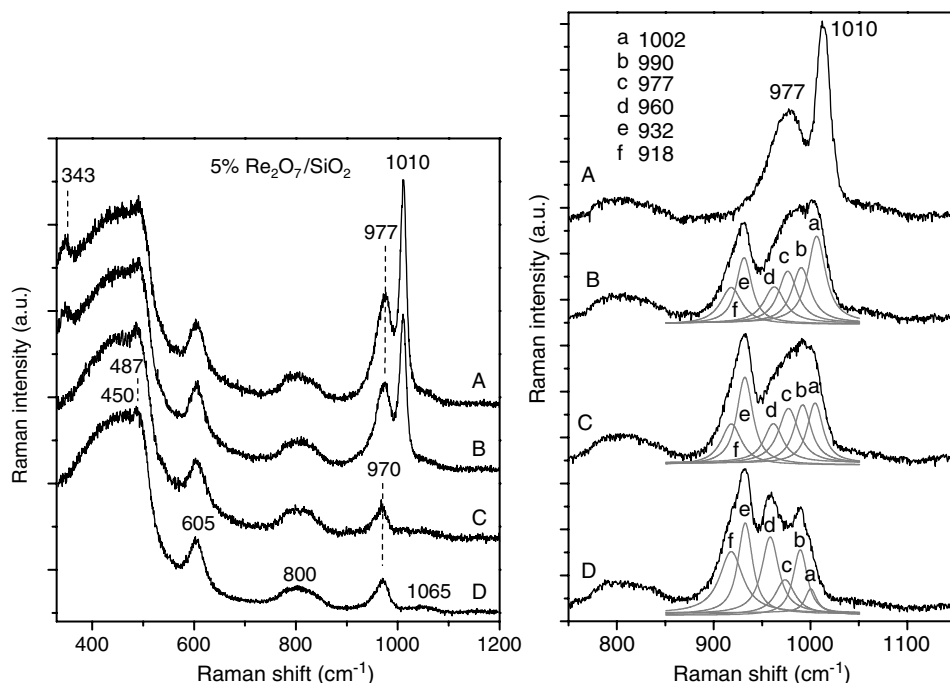


Figure 1.7 (Left) *In situ* Raman spectra (325 nm) of supported 5% Re₂O₇/SiO₂ under (A) oxygen environment at 450 °C, (B) reoxidation after hydrogen reduction at 2% H₂/Ar, and (C) after 40 min H₂ exposure. The SiO₂ support material is shown as reference (D). Reproduced from Ref. [55]. (Right) Time-resolved *in situ* Raman

spectra of supported 5% Re₂O₇/SiO₂ under H₂¹⁸O exposure after (A) 0 min, (B) 34 min, (C) 51 min, and (D) 123 min. The Raman spectra deconvolution are shown in gray and labeled with small letters, with the lower-case letters a, b, c, d, e, and f referring to specific band positions indicated in the figure.

the Re–O vibrations under oxidizing environments (Raman bands at 1010, 977, and 343 cm⁻¹) in curve B of Figure 1.7 (left) confirms that these vibrations are associated with the surface rhenia species. Note that the Raman spectrum of the reduced supported Re₂O₇/SiO₂ catalyst looks exactly like the Raman spectrum of the dehydrated SiO₂ support and demonstrates that the SiO₂ support is not reduced by the reduction treatments. In addition, the broadening of the 977 cm⁻¹ band to 968 cm⁻¹ and the lack of shift of the 343 and 1010 cm⁻¹ Raman bands during exposure to D₂O reflect that these vibrations are not associated with surface Re–OH species [55].

Isotopic H₂¹⁸O exchange of the dehydrated supported Re₂O₇/SiO₂ catalyst is shown in Figure 1.7 (right) and reveals the Raman band splitting of the Re(=O)₃ species. The initial $\nu_s(\text{Re}(=\text{}^{16}\text{O})_3)$ Raman band at 1010 cm⁻¹ rapidly decreases in intensity and shifts to lower wavenumbers because of the incorporation of ¹⁸O into the surface ReO₄ species and, concurrently, the $\nu_{as}(\text{Re}(=\text{}^{16}\text{O})_3)$ band at 977 cm⁻¹ also shifts to lower wavenumbers. The associated bending $\delta(\text{}^{16}\text{O}-\text{Re}-\text{}^{16}\text{O})$ mode shifts from 343 to ~335 cm⁻¹ as a consequence of incorporation of the ¹⁸O into the surface rhenia structure [56]. The time-resolved Raman spectroscopy during the isotopic oxygen

exchange allows for the resolution of the multiple band splitting of the symmetric and asymmetric vibrations, where the ν_s vibrations are deconvoluted at ~ 1002 , 990 , and $\sim 960\text{ cm}^{-1}$ and the ν_{as} vibrations are deconvoluted at 932 cm^{-1} , with a small shoulder at $\sim 918\text{ cm}^{-1}$. The Raman bands at ~ 1002 and 990 cm^{-1} are tentatively assigned to a single substituted- ^{18}O species, $^{18}\text{O}=\text{Re}(=\text{O})_2$, and a double substituted- ^{18}O species, $(^{18}\text{O})_2\text{Re}=\text{O}$, where the 990 cm^{-1} band grows at the expense of 1002 cm^{-1} . Furthermore, the 960 cm^{-1} vibration, which becomes distinct after prolonged exposure to isotopic oxygen and at the expense of the ~ 1002 and 990 cm^{-1} bands, is tentatively attributed to the triple substituted- ^{18}O species, $(^{18}\text{O})_3\text{Re}$. It is expected that if complete isotopic oxygen exchange were achieved beyond what is presented in curve D of Figure 1.7 (right), the 990 cm^{-1} would completely disappear and be replaced with the triply substituted $(^{18}\text{O})_3\text{Re}$ band at 960 cm^{-1} . For the initial $\nu_{as}(\text{Re}(=\text{O})_3)$ band at 977 cm^{-1} , isotopic exchange shifts the band to 932 cm^{-1} and a shoulder at 918 cm^{-1} , where both vibrations are tentatively assigned to a fully exchanged $\nu_{as}(\text{Re}(=\text{O})_3)$ vibration with various degrees of distortion. The detection of four surface rhenia isotopic vibrations ($\text{Re}(=\text{O})_3$ at 1010 cm^{-1} , $\text{Re}(=\text{O})(=\text{O})_2$ at $\sim 1002\text{ cm}^{-1}$, $\text{Re}(=\text{O})_2(=\text{O})$ at 990 cm^{-1} , and $\text{Re}(=\text{O})_3$ at 960 cm^{-1}) is consistent with the trioxo structure of the dehydrated surface ReO_4 species on SiO_2 .

The *in situ* Raman spectra of the dehydrated supported $\text{Re}_2\text{O}_7/\text{TiO}_x/\text{SiO}_2$, $\text{Re}_2\text{O}_7/\text{ZrO}_x/\text{SiO}_2$, and $\text{Re}_2\text{O}_7/\text{AlO}_x/\text{SiO}_2$ catalysts are presented in Figure 1.8

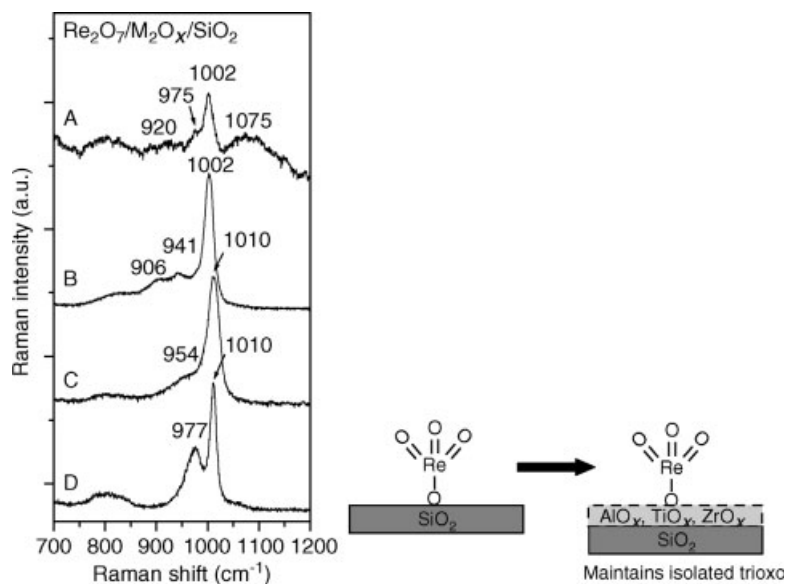


Figure 1.8 (Left) *In situ* Raman spectra (325 nm) of dehydrated supported (A) 3% $\text{Re}_2\text{O}_7/\text{TiO}_x/\text{SiO}_2$, (B) 3% $\text{Re}_2\text{O}_7/\text{ZrO}_x/\text{SiO}_2$, (C) 3% $\text{Re}_2\text{O}_7/\text{AlO}_x/\text{SiO}_2$, and (D) 3% $\text{Re}_2\text{O}_7/\text{SiO}_2$ (532 nm for 3% $\text{Re}_2\text{O}_7/\text{TiO}_x/\text{SiO}_2$ only) under oxidizing conditions at 450°C . (Right) Schematic of dehydrated supported ReO_x species on SiO_2 and on surface-modified silica.

(left) and give rise to strong bands at $\sim 1002\text{--}1010\text{ cm}^{-1}$ that is characteristic of the trioxo $\nu_s(\text{Re}(=\text{O})_3)$ functionality [88]. The corresponding asymmetric stretch appears between 941 and 975 cm^{-1} for the surface-modified SiO_2 catalysts. The bridging $\text{Re}\text{--O}\text{--Ti}$ and $\text{Re}\text{--O}\text{--Zr}$ vibrations are also observable at $\sim 905\text{--}920\text{ cm}^{-1}$. The similar band positions of the ν_s and $\nu_{as}(\text{Re}(=\text{O})_3)$ and bending mode of the model and surface-modified supported rhenia catalysts show that the surface oxide additives do not significantly alter the structure of the dehydrated surface ReO_x species that consists of the terminal trioxo $\text{Re}(=\text{O})_3$ functionality (see schematic in Figure 1.8 (right)).

1.8

Electronic Structure of Dehydrated Supported MO_x/SiO_2 and $\text{M}_1\text{O}_x/\text{M}_2\text{O}_x/\text{SiO}_2$ Catalysts via *In Situ* UV-Vis Spectroscopy

The corresponding UV-Vis DRS complements the surface Raman and IR spectroscopic vibrational information and provided local structural information (isolated monomer, dimer, polymeric chain, cluster, or 3D structure) of the supported metal oxide species. UV-Vis DRS monitors the surface metal oxide cation electronic structure via the ligand-to-metal charge transfer (LMCT) band position and the corresponding edge energy (E_g) value. The E_g values of the surface metal oxide species are determined by comparison against the electronic structures of well-defined metal oxide reference compounds [105–107]. In addition, each supported MO_x/SiO_2 catalyst system possesses unique spectral signatures through the LMCT band maxima that provide additional insights into their local molecular structures. It should be noted that the absorbance of a strong M_2O_x species, such as TiO_x for surface-modified $\text{TiO}_x/\text{SiO}_2$, may strongly overlap the contribution of the M_1O_x species, such as the $\text{Re}_2\text{O}_7/\text{TiO}_x/\text{SiO}_2$. Therefore, careful baseline subtraction must be performed to ensure proper band deconvolution. The *in situ* UV-Vis E_g values for the dehydrated surface M_1O_x ($\text{M}_1 = \text{V}, \text{Mo}, \text{and Re}$) species on native SiO_2 and surface-modified SiO_2 catalyst samples are scaled against well-defined reference compounds in Figure 1.9.

The dehydrated model supported $\text{M}_1\text{O}_x/\text{SiO}_2$ catalysts predominantly exist as isolated surface MO_x species on SiO_2 , which is reflected by the relatively high UV-Vis E_g values in Figure 1.9. The addition of the surface modifiers retains the high E_g values. For the surface molybdena catalyst system, the introduction of the surface M_2O_x modifiers eliminates the higher wavenumber, or lower energy, LMCT transition in the UV-Vis spectra for the surface M_1O_x species, which suggests a more isolated or distorted surface molybdena species [88]. This is in agreement with the Raman observations of the distortions of the surface MoO_x species in supported $\text{MoO}_x/\text{M}_2\text{O}_x/\text{SiO}_2$ catalysts and the suppression of the surface monoxo species. The lack of influence of the different surface M_2O_x ligands on the dehydrated surface $\text{O}_3\text{V}=\text{O}$ and $\text{ORE}(=\text{O})_3$ species reveals that these structures are not perturbed by the surface modification of the SiO_2 support.

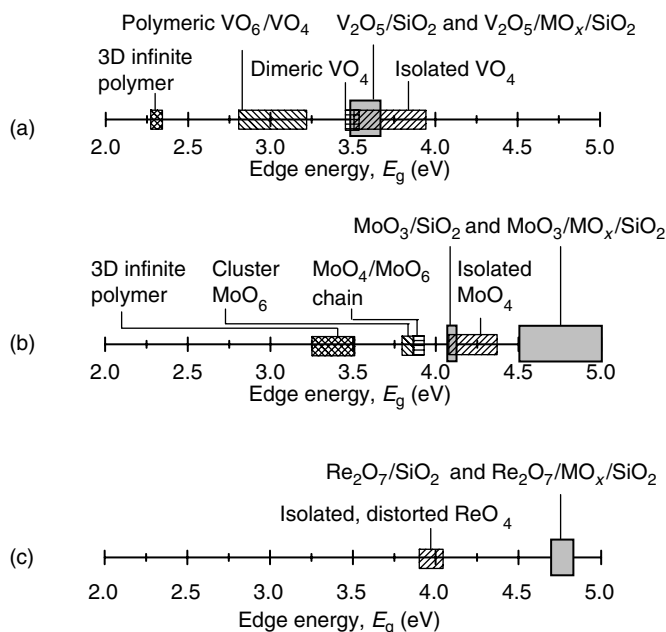


Figure 1.9 UV-Vis DRS edge energy, E_g , scale for well-defined reference compounds and measured E_g values for dehydrated SiO_2 -supported (A) VO_x [108–114], (B) MoO_x [115–120], and (C) ReO_x [115, 121–124] catalysts.

1.9

Determination of Surface Kinetic Parameters

The surface chemistry and reactivity of model supported MO_x/SiO_2 and $\text{M}_1\text{O}_x/\text{M}_2\text{O}_x/\text{SiO}_2$ catalysts can be determined by CH_3OH -TPSR spectroscopy since CH_3OH is a “smart” chemical probe molecule capable of distinguishing between surface acidic, redox, and basic sites [125]. By determining the nature of the catalytic active sites (redox, acidic, or basic), their specific surface reactivity (k_{rds}) toward methanol can be calculated, where k_{rds} represents the first-order kinetic constant of the rate-determining step (rds) [125–128]. The dissociative chemisorption of methanol forms surface methoxy (CH_3O^*) intermediate species, which is the most abundant reaction intermediate (MARI) [129, 130], and undergoes different reaction pathways that are dependent on the nature of the catalytic active site: formaldehyde (HCHO) from surface redox sites, dimethyl ether (CH_3OCH_3 , DME) from surface acidic sites, and CO/CO_2 from surface basic sites [125, 131]. H_2O formation is also a product of the CH_3OH surface chemistry. For the purposes of a focused discussion in this chapter, only the redox surface reactivity arising from methanol oxidative dehydrogenation to formaldehyde will be elaborated upon henceforth.

The surface kinetic parameters (E_{act} and k_{rds}) for the surface methoxy reactions to HCHO are directly obtained from the CH_3OH -TPSR spectra. The rds for the

unimolecular surface CH_3O^* dehydrogenation to HCHO involves breaking of the surface methoxy $\text{C}-\text{H}$ bond [34]. Applying the first-order Redhead equation [132] for the unimolecular decomposition reaction of the rds for the different reaction pathways allows for the determination of the E_{act} for the surface reactions:

$$\frac{E_{\text{act}}}{RT_p^2} = \left(\frac{\nu}{\beta}\right) \exp\left(\frac{-E_{\text{act}}}{RT_p}\right) \quad (1.2)$$

in which T_p is the CH_3OH -TPSR peak temperature of the reaction product, R is the gas constant ($1.987 \text{ cal mol}^{-1} \text{ K}^{-1}$), $\nu = 10^{13} \text{ s}^{-1}$ for first-order kinetics, and β is the heating rate ($10^\circ \text{C min}^{-1}$). The rate-determining step, k_{rds} (HCHO), for the conversion of the surface methoxy intermediate to HCHO is also a function of E_{act} (and hence T_p) and is determined by

$$k_{\text{rds}} = \nu \exp\left(\frac{-E_{\text{act}}}{RT}\right) \quad (1.3)$$

in which T is the reference temperature ($T = 230^\circ \text{C}$) that will be used for comparison of k_{rds} values.

1.10

Redox Surface Reactivity of Model Supported $\text{M}_1\text{O}_x/\text{SiO}_2$ Catalysts

The specific catalytic activities (k_{rds}) for the formation of HCHO of the model supported $\text{M}_1\text{O}_x/\text{SiO}_2$ and surface-modified $\text{M}_2\text{O}_x/\text{SiO}_2$ catalysts were determined with CH_3OH -TPSR and are compared to their corresponding unsupported bulk MO_x catalysts in Figures 1.10. The surface reactivity of the model silica-supported M_1O_x catalytic active sites is affected by anchoring of the M_1O_x transition metal oxides to the SiO_2 support. The specific activity of the surface M_1O_x ($\text{M}_1 = \text{V}$ or Mo) catalytic active sites on SiO_2 is generally lower, by several orders of magnitude, than that of their unsupported M_1O_x metal oxides. The same is also true for the supported ZrO_x species on SiO_2 . Whereas the surface AlO_x on silica is not affected by its anchoring to the SiO_2 support, with both exhibiting no redox activity, the surface TiO_x species on SiO_2 possess redox behavior while bulk TiO_2 does not exhibit redox characteristics. These differences reflect the changes resulting from anchoring isolated surface MO_x species onto the SiO_2 support surface via the bridging $\text{M}-\text{O}-\text{Si}$ linkages. Although some contribution may come from the different molecular structures present in the bulk and supported MO_x catalysts, the coordination of the surface M_1O_x and M_2O_x species to the silica support appears to be the major influence on the reactivity characteristics of the surface oxide anchored to the SiO_2 support.

1.11

Redox Surface Reactivity of Supported $\text{M}_1\text{O}_x/\text{M}_2\text{O}_x/\text{SiO}_2$ Catalysts

The introduction of the surface AlO_x , TiO_x , and ZrO_x modifiers onto the SiO_2 support dramatically enhances the k_{rds} redox values, by as much as a factor of $\sim 10^4$, of the

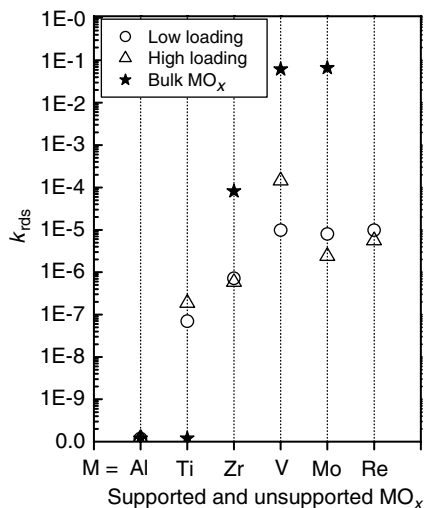


Figure 1.10 The k_{rds} values for HCHO formation from supported M_1O_x/SiO_2 and M_2O_x/SiO_2 catalysts at 230 °C for low and high (maximum dispersion) metal oxide coverage. The k_{rds} values of the unsupported bulk oxides are also shown for reference (with the star notation) [125–128].

supported M_1O_x catalytic active sites, as presented in Figure 1.11. These results are in agreement with steady-state CH_3OH oxidation studies, where the turnover frequency (TOF) significantly increases with the addition of the surface modifiers for the supported $M_1O_x/M_2O_x/SiO_2$ catalyst systems.

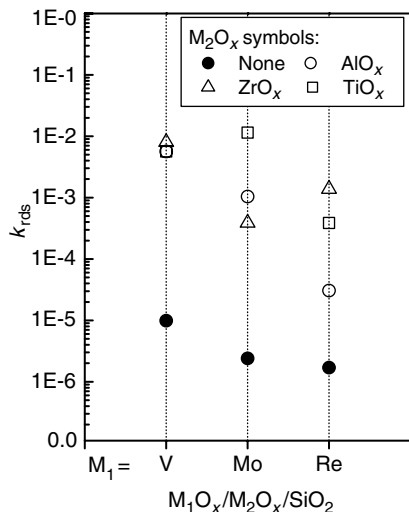


Figure 1.11 The k_{rds} values for supported 3% $M_1O_x/5\% M_2O_x/SiO_2$ catalysts ($M_1 = V, Mo, \text{ and } Re$; $M_2 = Al, Zr, \text{ and } Ti$) for decomposition of surface methoxy intermediate to HCHO.

Combining the molecular structural information with the corresponding reactivity studies allows for examination of possible molecular/electronic structure–activity relationships for the group 5–7 supported M_1O_x active sites. The multilayered supported $VO_x/M_2O_x/SiO_2$ and $ReO_x/M_2O_x/SiO_2$ catalyst systems contain the same surface monoxo VO_4 and trioxo ReO_4 structures, respectively, as their M_1O_x/SiO_2 counterparts. Consequently, the difference in reactivity is not related to a structural change of the surface M_1O_x species but is due to the different support ligands (M_2O_x and SiO_2). It is proposed that the enhanced surface redox activity is most likely related to the lower electronegativity of substrate oxide cations ($Si > Al > Ti \sim Zr$). Lowering of the oxide support ligand electronegativity increases the electron density on the oxygen of the bridging $M_1O_x-O-M_2O_x$ bond, which facilitates the dissociative chemisorption of methanol and decomposition of the surface methoxy intermediate to HCHO [133]. Several recent theoretical DFT/*ab initio* calculations have concluded that for the supported vanadia catalytic systems, the bridging V–O–support bond is the most energetically favorable methanol chemisorption site on the surface VO_x structure [84, 85, 134]. The bridging V–O–support bond has been shown to dramatically affect the steady-state TOF, defined as the number of HCHO molecules formed per surface VO_x sites per second [135] during steady-state CH_3OH oxidation. The TOF increases by two orders of magnitude with different supports, from 10^{-3} to $10^{-1} s^{-1}$ ($SiO_2 \ll Al_2O_3 \ll TiO_2 < ZrO_2$). Therefore, by substituting the bulk SiO_2 support with oxide ligands of lower electronegativity, the activity of the surface-modified vanadia catalyst systems was enhanced due to the formation of the bridging V–O–Al, V–O–Zr, and V–O–Ti bonds, which are the favorable active sites for methanol chemisorption. In addition, anchoring of the surface M_1O_x species onto the surface M_2O_x species may also change their local molecular structures and their related surface reactivity properties.

1.12

Conclusions

It is shown in this chapter that the activity of the supported catalytic active sites can be controlled and designed by oxide ligands. The molecular and electronic characterization of the model supported MO_x/SiO_2 and surface-modified supported $M_1O_x/M_2O_x/SiO_2$ catalyst systems were determined by *in situ* Raman and UV–Vis spectroscopy, respectively. The *in situ* Raman spectroscopy measurements were undertaken using various new approaches, such as time-resolved spectroscopy under reductive (H_2) and isotopic exchange ($^{18}O-^{16}O$ and D_2O-H_2O) environments. These new findings revealed that supported V_2O_5/SiO_2 system contains isolated monoxo $V=O$ surface species, supported MoO_3/SiO_2 consists of both isolated monoxo $M=O$ and dioxo $O=Mo=O$ surface species, and supported Re_2O_7/SiO_2 possesses isolated trioxo $Re(=O)_3$ surface species. The redox activity of these surface M_1O_x species is significantly reduced by their anchoring to the SiO_2 support. The oxide ligands of the surface-modified SiO_2 catalysts, on the other hand, did not significantly alter the molecular structures of the model systems, but did significantly increase the catalytic redox

reactivity performance by as much as a factor of $\sim 10^4$. This enhancement in redox surface activity is through the bridging M—O—support bonds and their relative electronegativity. The lower cation electronegativity values of the M_2O_x oxide ligands increase the electron density of the oxygen atom in the bridging M_1O_x —O— M_2O_x and, consequently, enhance its proton-accepting characteristics (CH_3O —H during chemisorption and *OCH_2 —H during the surface decomposition step).

Acknowledgments

The authors gratefully acknowledge the support from the United States Department of Energy – Basic Energy Sciences grant DEFG02-93ER14350.

References

- 1 McDaniel, M.P. (1985) *Advances in Catalysis*, **33**, 47.
- 2 Burwell, R.L., Haller, G.L., Taylor, K.C. and Read, J.F. (1969) *Advances in Catalysis*, **20**, 1.
- 3 Mol, J.C. and Moulijn, J.A. (1987) *Catalysis – Science and Technology*, Vol. 8 (eds J.R. Anderson and M. Boudart), Springer-Verlag, Berlin, p. 69.
- 4 Grzybowska-Swierkosz, B. and Haber, J. (1984) *Vanadia Catalysts for Processes of Oxidation of Aromatic Hydrocarbons*, Polish Scientific Publications, Warsaw.
- 5 Bosch, J. and Jansen, F. (1988) *Catalysis Today*, **2**, 369.
- 6 Knozinger, H. (1989) Proceedings of the 9th International Congress Catalysis, Calgary, Vol. 5 (eds M.J. Phillips and M. Ternan), The Chemical Institute of Canada, Ottawa, p. 20.
- 7 Prins, R., de Beer, V.H.J. and Somorjai, G.A. (1989) *Catalysis Reviews – Science and Engineering*, **31**, 1.
- 8 Hall, W.K. (1986) *Chemistry and Physics of Solid Surfaces* (eds R. Vanselow and R.F. Howe), Springer-Verlag, Berlin, p. 73.
- 9 Topsøe, H. (1983) *Surface Properties and Catalysis by Non-Metals* (eds J.P. Bonnelle, B. Delmon and E. Derouane), Reidel, Dordrecht, p. 329.
- 10 Delmon, B. (1979) Proceedings of the 3rd International Conference on Chemistry and Uses of Molybdenum (eds H.F. Barry and P.C.H. Mitchell), Climax Molybdenum Company, Ann Arbor, MI, p. 73.
- 11 Gates, B.C., Katzer, J.R. and Schuit, G.C.A. (1979) *Chemistry of Catalytic Processes* (eds R. Ciofallo, J. Marschall and B. Leap), McGraw-Hill, New York, p. 390.
- 12 Wachs, I.E., Saleh, R.Y., Chan, S.S. and Chersich, C.C. (1985) *Applied Catalysis A: General*, **15**, 339.
- 13 Grabowski, R., Grzybowska, B., Haber, J. and Sloczynski, J. (1975) *Reaction Kinetics and Catalysis Letters*, **2**, 81.
- 14 Deo, G. and Wachs, I.E. (1994) *Journal of Catalysis*, **146**, 323.
- 15 Mariscal, R., Galan-Fereres, M., Anderson, J.A., Alemany, L.J., Palacios, J.M. and Fierro, J.L.G. (1995) *Environmental Catalysis* (eds G. Centi *et al.*), SCI, Rome, p. 223.
- 16 Amiridis, M.D. and Solar, J.P. (1996) *Industrial & Engineering Chemistry Research*, **35**, 978.
- 17 Wauthoz, P., Machej, T. and Grange, P. (1991) *Applied Catalysis A: General*, **69**, 149.
- 18 Vogt, E.T.C., Boot, A., van Dillen, A.J., Geus, J.W., Janssen, F.J.J.G. and van den Kerkhof, F.M.G. (1988) *Journal of Catalysis*, **114**, 313.

- 19 Galan-Fereres, M., Mariscal, R., Alemany, L.J. and Fierro, J.L.G. (1994) *Journal of the Chemical Society, Faraday Transactions*, **90**, 3711.
- 20 De Boer, M., Van Dillen, A.J., Koningsberger, D.C., Geus, J.W., Vuurman, M.A. and Wachs, I.E. (1991) *Catalysis Letters*, **11**, 227.
- 21 Spencer, N.D., Pereira, C.J. and Grasselli, R.K. (1990) *Journal of Catalysis*, **126**, 546.
- 22 Banares, M.A., Fierro, J.L.G. and Moffat, J.B. (1993) *Journal of Catalysis*, **142**, 406.
- 23 Mel, J.C. and Moulijn, J.A. (1987) *Catalysis: Science and Technology*, Vol. 8 (eds. J.R. Anderson and M. Boudart), Springer-Verlag, Berlin, p. 69.
- 24 Xiaoding, X., Boelhouwer, C., Vonk, D., Benecke, J.I. and Mol, J.C. (1986) *Journal of Molecular Catalysis*, **36**, 47.
- 25 Banks, R.L. (1984) *Olefin Metathesis: Technology and Application. Applied Industrial Catalysis* (ed. B.E. Leach), Academic Press, New York, p. 215.
- 26 Haukka, S., Lakomaa, E. and Root, A. (1993) *The Journal of Physical Chemistry*, **97**, 5085.
- 27 Morrow, B.A. and Mcfarlan, A.J. (1990) *Journal of Non-Crystalline Solids*, **120**, 61.
- 28 Klaas, J., Schulz-Ekloff, G. and Jaeger, N.I. (1997) *The Journal of Physical Chemistry. B*, **101**, 1305.
- 29 Yoshida, S., Takenaka, S., Tanaka, T., Hirano, H. and Hayashi, H. (1996) Eleventh International Congress on Catalysis, *Studies in Surface Science and Catalysis*, **101**, 871.
- 30 Srinivasan, S., Datye, A.K., Hampden-Smith, M., Wachs, I.E., Deo, G., Jehng, J.M., Turek, A.M. and Peden, C.H.F. (1991) *Journal of Catalysis*, **131**, 260.
- 31 Srinivasan, S., Datye, A.K., Smith, M.H. and Peden, C.H.F. (1994) *Journal of Catalysis*, **145**, 565.
- 32 Deo, G., Turek, A.M., Wachs, I.E., Huybrechts, D.R.C. and Jacobs, P.A. (1993) *Zeolites*, **13**, 365.
- 33 Fernandez, A., Leyrer, J., Gonzalez-Elipe, A.R., Munuera, G. and Knozinger, H. (1988) *Journal of Catalysis*, **112**, 489.
- 34 Mariscal, R., Palacios, J.M., Galan-Fereres, M. and Fierro, J.L.G. (1994) *Applied Catalysis A: General*, **116**, 205.
- 35 Hanprasopwattana, A., Rieker, T., Sault, A.G. and Datye, A.K. (1997) *Catalysis Letters*, **45**, 165.
- 36 Hanprasopwattana, A., Srinivasan, S., Sault, A.G. and Datye, A.K. (1996) *Langmuir*, **12**, 3173.
- 37 Galan-Fereres, M., Alemany, L.J., Mariscal, R., Banares, M.A., Anderson, J.A. and Fierro, J.L.G. (1995) *Chemistry of Materials*, **7**, 1342.
- 38 Tian, H., Ross, E.I. and Wachs, I.E. (2006) *The Journal of Physical Chemistry. B*, **110**, 9593.
- 39 Das, N., Eckert, H., Hu, H., Wachs, I.E., Walzer, J.F. and Feher, F.J. (1993) *The Journal of Physical Chemistry*, **97**, 8240.
- 40 Gao, X., Bare, S.R., Weckhuysen, B.M. and Wachs, I.E. (1998) *The Journal of Physical Chemistry. B*, **102**, 10842.
- 41 Oyama, S.T., Went, G.T., Lewis, K.B., Bell, A.T. and Somorjai, G.A. (1989) *The Journal of Physical Chemistry*, **93**, 6786.
- 42 Resini, C., Montanari, T., Busca, G., Jehng, J.M. and Wachs, I.E. (2005) *Catalysis Today*, **99**, 105.
- 43 Banares, M.A., Cardoso, J.H., Agullo-Rueda, F., Correa-Bueno, J.M. and Fierro, J.L.G. (2000) *Catalysis Letters*, **64**, 191.
- 44 Gao, X. and Wachs, I.E. (2002) *Topics in Catalysis*, **18**, 243.
- 45 Went, G.T., Oyama, S.T. and Bell, A.T. (1990) *The Journal of Physical Chemistry*, **94**, 4240.
- 46 Burcham, L.J., Datka, J. and Wachs, I.E. (1999) *The Journal of Physical Chemistry. B*, **103**, 6015.
- 47 Baltes, M., Kytokivi, A., Weckhuysen, B.M., Schoonheydt, R.A., van der Voort, P. and Vansant, E.F. (2001) *The Journal of Physical Chemistry. B*, **105**, 6211.

- 48 Kim, D.S. and Wachs, I.E. (1993) *Journal of Catalysis*, **142**, 166.
- 49 Jehng, J.-M., Tung, W.-C., Huang, C.-H. and Wachs, I.E. (2007) *Microporous and Mesoporous Materials*, **99**, 299.
- 50 Tanaka, T., Nojima, H., Yamamoto, T., Takenaka, S., Funabiki, T. and Yoshida, S. (1999) *Physical Chemistry Chemical Physics*, **1**, 5235.
- 51 Weckhuysen, B.M., Wachs, I.E. and Schoonheydt, R.A. (1996) *Chemical Reviews*, **96**, 3327.
- 52 Doornkamp, C., Clement, M., Gao, X., Deo, G., Wachs, I.E. and Ponec, V. (1999) *Journal of Catalysis*, **185**, 415.
- 53 Banares, M.A., Hu, H. and Wachs, I.E. (1995) *Journal of Catalysis*, **155**, 249.
- 54 Jehng, J.M., Hu, H., Gao, X. and Wachs, I.E. (1996) *Catalysis Today*, **28**, 335.
- 55 Lee, E.L. and Wachs, I.E. (2007) *The Journal of Physical Chemistry. C*, **111**, 14410.
- 56 Lee, E.L. and Wachs, I.E. (2008) *The Journal of Physical Chemistry. C*, **112**, 6487.
- 57 Mestl, G. and Srinivasan, T.K.K. (1998) *Catalysis Reviews – Science and Engineering*, **40**, 451.
- 58 Wachs, I.E. (2005) *Catalysis Today*, **100**, 79.
- 59 Brown, F.R., Makovsky, L.E. and Rhee, K.H. (1977) *Applied Spectroscopy*, **31**, 563.
- 60 Brown, F.R., Makovsky, L.E. and Rhee, K.H. (1977) *Journal of Catalysis*, **50**, 162.
- 61 Brown, F.R., Makovsky, L.E. and Rhee, K.H. (1977) *Journal of Catalysis*, **50**, 385.
- 62 Thomas, R., Moulijn, J.A. and Kerkhof, F.P.J.M. (1977) *Recueil des Travaux Chimiques des Pays-Bas*, **96**, 134.
- 63 Roozeboom, F., Mittelmeijer-Hazeleger, M.C., Moulijn, J.A., Medema, J., De Beer, V.H.J. and Gellings, P.J. (1980) *The Journal of Physical Chemistry*, **84**, 2783.
- 64 Roozeboom, F., Medema, J. and Gellings, P.J. (1978) *Zeitschrift fuer Physikalische Chemie*, **111**, 215.
- 65 Kerkhof, F.P.J.M., Moulijn, J.A. and Thomas, R. (1979) *Journal of Catalysis*, **56**, 279.
- 66 Chan, S.S., Wachs, I.E., Murrell, L.L., Wang, L. and Hall, W.K. (1984) *The Journal of Physical Chemistry*, **88**, 5831.
- 67 Cheng, C.P., Ludowise, J.D. and Schrader, G.L. (1980) *Applied Spectroscopy*, **34**, 146.
- 68 Wang, L. and Hall, W.K. (1983) *Journal of Catalysis*, **82**, 177.
- 69 Stencel, J.M., Makovsky, L.E., Sarkus, T.A., De Vries, J., Thomas, R. and Moulijn, J.A. (1984) *Journal of Catalysis*, **90**, 314.
- 70 Stencel, J.M., Makovsky, L.E., Diehl, J.R. and Sarkus, T.A. (1984) *Journal of Raman Spectroscopy*, **15**, 282.
- 71 Weckhuysen, B.M., Jehng, J.-M. and Wachs, I.E. (2000) *The Journal of Physical Chemistry. B*, **104**, 7382.
- 72 Banares, M.A. and Wachs, I.E. (2002) *Journal of Raman Spectroscopy*, **33**, 359.
- 73 Nakamoto, K. (1986) *Infrared and Raman Spectra of Inorganic and Coordination Compounds*, 4th edn, John Wiley & Sons, New York, NY.
- 74 Banwell, C.N. (1983) *Fundamentals of Molecular Spectroscopy*, 3rd edn, McGraw-Hill, London.
- 75 Busca, G. (2002) *Journal of Raman Spectroscopy*, **33**, 348.
- 76 Galeener, F.L. and Mikkelsen, J.C. Jr. (1981) *Physical Review B: Condensed Matter*, **23**, 5527.
- 77 Gao, X. and Wachs, I.E. (2000) *Journal of Catalysis*, **192**, 18.
- 78 Gao, X. and Wachs, I.E. (1999) *Catalysis Today*, **15**, 233.
- 79 Gao, X., Bare, S.R., Fierro, J.L.G., Banares, M.A. and Wachs, I.E. (1998) *The Journal of Physical Chemistry. B*, **102**, 5653.
- 80 Yudaev, I.V., Gan, Z., Paukshtis, E.A., Wachs, I.E. and Lapina, O.B., unpublished.
- 81 Turek, A.M., Wachs, I.E. and DeCanio, E. (1992) *The Journal of Physical Chemistry*, **96**, 5000.
- 82 Sanderson, R.T. (1988) *Journal of Chemical Education*, **65**, 112.
- 83 Ostromecki, M.M., Burcham, L.J. and Wachs, I.E. (1998) *Journal of Molecular Catalysis A: Chemical*, **132**, 59.

- 84 Dobler, J., Pritzsche, M. and Sauer, J. (2005) *Journal of the American Chemical Society*, **127**, 10861.
- 85 Magg, N., Immaraporn, B., Giorgi, J.B., Schroeder, T., Baumer, M., Dobler, J., Wu, Z., Kondratenko, E., Cherian, M., Baerns, M., Stair, P.C., Sauer, J. and Freund, H.J. 2004 *Journal of Catalysis*, **226**, 88.
- 86 Avdeev, V.I. and Zhidomirov, G.M. (2004) *Research on Chemical Intermediates*, **30**, 41.
- 87 Lee, E.L. and Wachs, I.E. (2008) *Journal of Catalysis*, **258**, 103.
- 88 Lee, E.L. and Wachs, I.E. (1991) *The Journal of Physical Chemistry*, accepted.
- 89 Gao, X., Fierro, J.L.G. and Wachs, I.E. (1999) *Langmuir*, **15**, 3169.
- 90 Gao, X., Bare, S.R., Fierro, J.L.G. and Wachs, I.E. (1999) *The Journal of Physical Chemistry B*, **103**, 618.
- 91 Banares, M.A., Spencer, N.D., Jones, D. and Wachs, I.E. (1994) *Journal of Catalysis*, **146**, 204.
- 92 Hardcastle, F.D. and Wachs, I.E. (1991) *The Journal of Physical Chemistry*, **95**, 10763.
- 93 Desikan, A.N., Huang, L. and Oyama, S.T. (1991) *The Journal of Physical Chemistry*, **95**, 10050.
- 94 Williams, C.C., Ekerdt, J.G., Jehng, J.-M., Hardcastle, F.D., Turek, A.M. and Wachs, I.E. (1991) *The Journal of Physical Chemistry*, **95**, 8781.
- 95 Hu, H., Wachs, I.E. and Bare, S.R. (1995) *The Journal of Physical Chemistry*, **99**, 10897.
- 96 Banares, M.A., Hu, H. and Wachs, I.E. (1994) *Journal of Catalysis*, **150**, 407.
- 97 Cornac, M., Janin, A. and Lavalley, J.C. (1986) *Polyhedron*, **5**, 183.
- 98 Seyedmonir, S.R. and Howe, R.F. (1988) *Journal of Catalysis*, **110**, 216.
- 99 Ohler, N. and Bell, A.T. (2005) *The Journal of Physical Chemistry. B*, **109**, 23419.
- 100 Chempath, S., Zhang, Y. and Bell, A.T. (2007) *The Journal of Physical Chemistry. C*, **111**, 1291.
- 101 Wachs, I.E. (1996) *Catalysis Today*, **27**, 437.
- 102 Vuurman, M.A. and Wachs, I.E. (1992) *The Journal of Physical Chemistry*, **96**, 5008.
- 103 Vuurman, M.A., Stufkens, D.J. and Oskam, A. (1992) *Journal of Molecular Catalysis*, **76**, 263.
- 104 Kim, D.S. and Wachs, I.E. (1993) *Journal of Catalysis*, **141**, 419.
- 105 Weber, R.S. (1995) *Journal of Catalysis*, **151**, 470.
- 106 Gao, X. and Wachs, I.E. (2000) *The Journal of Physical Chemistry. B*, **104**, 1261.
- 107 Ross-Medgaarden, E.I. and Wachs, I.E. (2007) *The Journal of Physical Chemistry. C*, **111**, 15089.
- 108 Wachs, I.E., Chen, Y., Jehng, J.-M., Briand, L.E. and Tanaka, T. (2003) *Catalysis Today*, **78**, 13.
- 109 Wright, A.C. (1984) *Philosophical Magazine B*, **50**, L23.
- 110 Ng, H.N. and Calvo, C. (1972) *Canadian Journal of Chemistry*, **50**, 3619.
- 111 Busca, G., Ricchiardi, G., Sam, D.S.H. and Volta, J.C. (1994) *Journal of the Chemical Society, Faraday Transactions*, **90**, 1161.
- 112 Marumo, F., Isobe, M., Iwai, S. and Kondo, Y. (1974) *Acta Crystallographica*, **B30**, 1628.
- 113 Evans, H.T. (1960) *Zeitschrift für Kristallographie*, **114**, 257.
- 114 Gopal, R. and Calvo, C. (1974) *Acta Crystallographica*, **B30**, 2491.
- 115 Wachs, I.E. (2005) Molecular structures of surface metal oxide species: nature of catalytic active sites in mixed metal oxides, in *Metal Oxides: Chemistry and Applications* (eds. J.L.G. Fierro and H. Heinemann), CRC Taylor & Francis Press.
- 116 Wells, A. (1984) *Structural Inorganic Chemistry*, Oxford University, London.
- 117 Greenwood, N.N. and Earnshaw, A. (1989) *Chemistry of the Elements*, Pergamon Press, Elmsford, NY.
- 118 Knopnadel, I., Hartl, H., Hunnius, W.D. and Fuchs, J. (1974) *Angewandte Chemie International Edition*, **86**, 894.

- 119 Hove, A.R., Bildsoe, H., Skibsted, J., Brorson, M. and Jakobsen, H.J. (2006) *Inorganic Chemistry*, **45**, 10873.
- 120 Hardcastle, F.D. and Wachs, I.E. (1990) *Journal of Raman Spectroscopy*, **21**, 683.
- 121 Spitaler, J., Ambrosch-Draxl, C., Nachbaur, E., Belaj, F., Gomm, H. and Netzer, F. (2003) *Physical Review B: Condensed Matter*, **67**, 115127.
- 122 Lock, C.J.L. and Turner, G. (1975) *Acta Crystallographica*, **B31**, 1764.
- 123 Pendharkar, A.V. and Mande, C. (1973) *Pramana*, **1**, 104.
- 124 Swainson, I.P. and Brown, R.J.C. (1997) *Acta Crystallographica*, **B53**, 76.
- 125 Badlani, M. and Wachs, I.E. (2001) *Catalysis Letters*, **75**, 137.
- 126 Wang, X. and Wachs, I.E. (2004) *Catalysis Today*, **96**, 211.
- 127 Kim, T., Burrows, A., Kiely, C.J. and Wachs, I.E. (2007) *Journal of Catalysis*, **246**, 370.
- 128 Wachs, I.E., Jehng, J.-M. and Ueda, W. (2005) *The Journal of Physical Chemistry. B*, **109**, 2275.
- 129 Burcham, L.J., Briand, L.E. and Wachs, I.E. (2001) *Langmuir*, **17**, 6164.
- 130 Burcham, L.J., Deo, G., Gao, X. and Wachs, I.E. (2000) *Topics in Catalysis*, **11/12**, 85.
- 131 Tatibouet, J.M. (1997) *Applied Catalysis A: General*, **148**, 213.
- 132 Redhead, P.A. (1962) *Vacuum*, **12**, 213.
- 133 Kim, T. and Wachs, I.E., Ph.D. Thesis.
- 134 Bronkema, J.L. and Bell, A.T. (2007) *The Journal of Physical Chemistry. C*, **111**, 420.
- 135 Boudart, M. (1995) *Chemical Reviews*, **95**, 661.

2

Optimal Design of Hierarchically Structured Porous Catalysts

Marc-Olivier Coppens and Gang Wang

2.1

Introduction

2.1.1

Intrinsic Catalytic Activity and Selectivity: the Atomic and the Nanoscale

Heterogeneous catalysis engineering involves length scales ranging from the atomic to the catalyst particle or pellet scale, integrated with the design of the reactor in which the catalyst is to be used [1–8].

The activity and selectivity of a catalyst depends on the atomic structure of its so-called active sites. The geometric and electronic properties of these sites determine how some species are bound and converted on the catalyst surface. The structure of the active sites governs the conversion rates toward different products and the probability for the products to detach from the surface [9–12]. The immediate, local environment of these active sites is also important. In porous solid catalysts, the pores through which reactants and products move are often very narrow and the local surface curvature is very large, which could influence the intrinsic reaction rates. An extreme example is that of a zeolite, a crystalline aluminosilicate traversed by pores typically less than 1 nm in diameter, which limits the formation of products that are larger than the pore size. This size and shape selectivity is very useful to zeolite catalysis, and calculations of the activation energy required to fit molecules in zeolite pore windows could be used to find the right type of zeolite for a particular reaction [13, 14]. Similar comments, essentially based on Fischer's century old lock-and-key hypothesis, could be made about enzymatic catalysis [15]. Catalysis at the active site level can be studied using increasingly powerful computational quantum chemical [16, 17] and experimental spectroscopic tools [10, 18], as discussed in other chapters of this book. Such tools help to rationally design active sites, in order to achieve a high intrinsic activity and desired selectivity toward particular products [19], preferably with only slow deactivation by site decomposition, poisoning, and site or pore blockage.

The active sites are of atomic dimensions or, at most, a few nanometers in size. In industrial chemical engineering, it is often desired that a homogeneous catalyst be heterogenized or supported on a porous material. The active sites lie on the surface of mesopores that constitute a vast network inside a solid particle, with sizes varying from micrometers to centimeters. For example, Pt nanoparticles may be dispersed on the internal surface of a porous $\gamma\text{-Al}_2\text{O}_3$ support. Other catalysts are already, intrinsically, micro- or mesoporous materials, such as zeolites or MCM-41. In the example of $\gamma\text{-Al}_2\text{O}_3$, with its acid surface sites, the porous material may serve as a support for metal particles (e.g., Pt) and catalytic material at the same time, so that Pt/ $\gamma\text{-Al}_2\text{O}_3$ is a multifunctional catalyst.

2.1.2

Catalyst Particle Size and Geometry: A Question of Reactor Engineering

There are multiple reasons why such heterogeneous, micro- or mesoporous catalysts are desired for practical applications, but perhaps the most important one is that the catalyst is more easily separated from fluid (gaseous or liquid) reactants and products. Indeed, solid particles can be packed inside a reactor vessel or tube, with fluids flowing through the packed (fixed) bed, or coated on the walls of macroscopic channel arrays or a reactor tube, as in monolith reactors and membrane reactors. Alternatively, they can be fluidized in a gas or liquid stream, as in fluidized beds and slurry reactors. These different reactor types pose different demands on particle size.

Particle size in riser and slurry reactors is typically less than 100 μm , so that these particles are mobile enough to be entrained with the flow. Also fouling or attrition concerns play a role in the choice of the particle size for multiphase processes [20, 21]. In fixed beds, on the other hand, particles should typically be millimeters or centimeters in size because a packing of too fine particles is so dense, with such narrow interstices, that the pressure drop over the reactor becomes prohibitive when the fluid reactants move at high flow rates through the catalyst bed. Particle size might also be determined by mechanical and environmental concerns, too small particles forming a potentially harmful dust.

In brief, particle size is typically set by chemical engineering, rather than by chemical requirements. Therefore, in catalyst optimization studies, it is natural to keep the particle size constant, and to concentrate on optimizing the interior of the particle, when it is not an option to change the reactor design. This optimization might focus on maximum yield, selectivity toward desired components, and stability, or a combination of these. In a completely new process design, it is worth exploring the new opportunities offered by structured reactors, and neither catalyst nor reactor optimization should be viewed in isolation but in an integrated fashion [3, 20–26]. As stated by Villiermaux [27], the classical analysis going from macroscopic down to microscopic scales should be completed by a systems approach integrating phenomena from microscopic up to macroscopic complex systems. This includes the temporal domain as well, since transient operation may offer significant advantages.

2.1.3

Porous Catalyst Architecture and Optimization Methods

A vast network of extremely narrow pores inside catalyst particles is desirable to achieve a high internal surface area per unit volume. The total surface area lining these so-called nanopores can be enormous, several hundreds of square meters per gram of catalyst particle being normal. Note that from now on, we will use the term catalyst particle to denote the entire porous particle or pellet, containing the active sites on its internal surface. Because of the high specific surface area, the concentration of active sites per unit volume could be extremely high as well, leading to very high turnover rates; however, this assumes that these active sites are accessible to the reactant molecules, which need to enter the catalyst particle from the external surface, diffuse through the narrow pores, and finally react on a site. Similarly, products desorbing from the sites need to diffuse through the pores to exit the particles into the bulk reactor volume.

Because the pores are so narrow, often less than one or a few nanometers, their surface area is high but diffusion is slow. There is a price for the high intrinsic activity, namely, slow diffusion. Eventually, this limits the overall activity, if the reactor design requires large particles. Therefore, the effective observed yield will be lower than the intrinsic yield, which is the yield if all active sites were immediately accessible. The sites deep inside a catalyst particle are less accessible or not at all. Furthermore, products that diffuse too slowly through the pores risk further reactions on other active sites on their way out of the catalyst particle, forming undesired side products. For example, instead of the desired partial oxidation products, complete oxidation leads to formation of CO_2 or oligomers and carbonaceous deposits (coke), rather than the desired monomers, dimers, or isomers. Elaborating on the drunkard's walk model of diffusion, this is like a drunk wandering through a town with too many bars along a maze of narrow streets and alleys: large and straight avenues with few diversions are needed to bring him home, or he will "deactivate" on the way!

Catalyst design should therefore also consider scales above nanoscale: large pore channels (mesopores or macropores) are needed as "highways" to facilitate the macroscopic motion of molecules across a catalyst particle, so as to counter deactivation and increase the overall activity and selectivity. Designing the optimal channel configuration or pore network architecture is not a trivial problem. The design should optimize molecular residence times. Reactant molecules should spend enough time inside the catalyst particle to collide sufficiently frequently with active sites *en route* to have a high chance to be converted, while products should quickly leave. Also, reactant molecules should fully, or as fully as possible, utilize the available catalytic volume. Too high porosity decreases the number of active sites, limiting the maximum achievable yield. Too low porosity underutilizes the catalytic material.

This chapter mainly addresses the question of catalyst pore channel network design, in order to affect the transport properties, so that the overall yield per unit volume is maximized. A similar methodology can be used with other objective functions, like a desired product distribution or slower deactivation: What should the

large-scale porosity be? Should the channels be distributed in a uniform or in a nonuniform way? Should they be of the same size or distributed in size according to an optimal distribution? How sensitive is the design to variations in these textural parameters? Computational and (semi-)analytical methods allow us to answer these questions.

Porous catalyst design involves an adequate representation of the porous structure, possibly as a function of time, multicomponent species transport, and an appropriate model capturing the reaction kinetics [28]. Multicomponent transport includes gaseous diffusion, flow, and surface diffusion [29, 30]; this mass transport is directly coupled to heat transport, so that, more generally, an equation for the energy or, to be precise, entropy generation, should be considered as well [31]. Langmuir–Hinshelwood–Hougen–Watson models are often remarkably effective to describe the reaction kinetics [4, 28], especially if derived on the basis of the mechanistically correct single events [12, 32]. Alternatively, microkinetic models that do not require the assumption of a rate-determining step can be applied [33, 34].

Solutions to this hierarchical, multiscale design problem are within reach, because of fast computational methods such as multigrid techniques. Furthermore, the insights gained from theoretical optimization are becoming applicable in practice because of the remarkable progress in nano- and microtechnology, in addition to the more conventional synthesis techniques, which allows synthesizing porous catalysts with an optimized hierarchical architecture. This is why we return to the optimization of the catalyst pore channel distribution in detail in Section 2.4. Before we do so, we discuss a few other methods to optimize the architecture of catalyst particles in Sections 2.2 and 2.3.

A less-explored way to optimize catalyst particles is to fine-tune the catalyst structure at mesoscopic scales, that is, the intermediate scales in between the microscopic active sites and their immediate environment, on the one hand, and macroscopic variables such as the spatial distribution of macropores and active sites, on the other hand. The morphology and connectivity of the pores are parameters whose influence on diffusion-reaction problems has been studied extensively for decades [35], but which have not been applied so much in the context of catalyst design [36, 28]. In Section 2.2, we will point out some opportunities to optimize the catalyst mesostructure: pore surface roughness, and pore connectivity.

Instead of changing the pore space architecture, another interesting, complementary method to increase overall catalyst efficiency is to distribute the active sites in a desired way over the particle volume. In Section 2.3, we briefly review such studies on the optimization of site distributions, and refer to a book by Morbidelli *et al.* [37] for a more detailed overview.

2.1.4

Learning from Nature

Catalysis plays an important role in nature. Remarkably active and selective enzymes are crucial to life. Their geometric and electronic properties are an excellent source of ideas to design new catalytic complexes. Biomimetics was the driving force

behind the Graetzel photovoltaic cell, which operates in a catalytic way using dye molecules as photon absorbers, supported by mesoporous titania. As observed in green leaves, light absorption is separated from the transport of the photogenerated charge carriers, and a nanostructure with a huge surface area increases overall efficiency [38].

Impressive as these molecular and nanoscale examples are, we can draw lessons from nature at larger length scales as well. In biology, the nanoscale is linked to the macroscopic world in a remarkably efficient way; all scales matter in the workings of nature. A tree is a reactor relying on photosynthesis, but it depends on more than chlorophyll alone. The veins of the leaves form a ramified network through which nutrients and products flow, and they are fed through a crown that grows in a self-similar way. A fractal structure interpolates between the stem and the twigs [39]. As in organs like lungs or kidneys, the cells are size-independent, yet the fractal branching network extends over many generations, connecting the stem to a huge surface area. The number of generations depends on size, that is, on total volume, while cell or twig size remains invariant. The scalability of natural reactors and transport devices is considerably helped by the fractal structure of their transportation networks, very different from traditional reactor engineering. These scaling properties were the source of inspiration behind the design of fractal fluid distributors in chromatography or as a functional substitute for turbulence [40], and in fluid injection devices in fluid multiphase processes [41]. Scaling-up and uniform distribution of fluids over a large volume or surface area, from a single inlet or “stem,” are some of the attractive characteristics of these devices.

Beyond the nanoscale, a nature-inspired chemical engineering approach allows one to guide the multiscale design of novel materials and reactors [42, 43]. The change in fractal scaling properties of the lung beyond a certain number of branching generations, from the bronchial tree down to the alveolar sponge, corresponds to a change in the dominant transport mechanism from pressure-driven flow to diffusion. In general, the optimal architecture is linked to the physicochemical properties, which are scale-dependent, and optimal structure–function relationships are present in nature at all length scales. Likewise, tree crowns and the leaves they carry have a different architecture. Nonequilibrium thermodynamics offers additional insight into the link between the structure of lungs, and their remarkable efficiency in terms of minimum energy dissipation [44, 45]. This concept can be taken one step further, by relating optimal thermodynamic efficiency to an underlying tree-like architecture in nature and engineering [46]. However, as illustrated in Section 2.4, such optimization problems need to be carefully considered on a case-by-case basis, because the optimum depends on several constraints, including precise boundary and initial conditions. The “optimal” fractal structure of the lung is prone to asthma due to its high sensitivity to geometrical variations [47]. Likewise, robustness toward catalyst deactivation might not yield the same optimal design as that for maximum yield in the absence of deactivation. In other words, geometries in nature are an excellent source of ideas, and investigating their efficiency lends us tremendous insight, but this should not be used as a dogma when searching for optimal designs.

2.2

Optimizing Mesopore Connectivity and Shape

2.2.1

Topology, Order, and Randomness

Straightening the pores obviously reduces the average residence time spent by molecules in the pores. A reduction in pore tortuosity and constrictions by using materials such as MCM-41 [48] or SBA-15 [49, 50] instead of disordered amorphous silica might be attractive, although even in these materials, with their regular arrays of pores, these pores can be curved and macroscopically tortuous, depending on the synthesis route. With the explosion in literature on ordered mesoporous materials, it is important to realize that, for the sake of catalysis, periodicity in the arrangement of the pores is not as important as pore size and connectivity [51], as confirmed by early theoretical studies comparing random and ordered networks of the same average connectivity [52, 53]. Other studies, however, showed that periodicity could play a significant role, depending on the connectivity and on whether the catalytic reaction is diffusion limited or not.

In the case of a single chemical reaction, diffusion limitations are conveniently monitored by means of the Thiele modulus, ϕ . For a first-order reaction with reaction rate constant k , and effective diffusivity of the reactant, D_e , the Thiele modulus is defined by $\phi = L\sqrt{k/D_e}$, where L is a characteristic length scale, for example, half the thickness of a catalytic slab, or one-third the radius of a spherical catalyst particle. In this expression, D_e is assumed constant. When $\phi > 1$, diffusion limitations arise. The effective diffusivity of a species is sometimes expressed as $D_e = \varepsilon D_m / \tau$, where D_m is its bulk diffusivity, ε is the catalyst porosity and τ is the tortuosity factor, lumping various geometrical (and, possibly, also nongeometrical) factors that influence diffusion in a porous material. Sharratt and Mann [54] showed that the tortuosity factor, τ (or, equivalently, D_e) of a random pore network could depend on the Thiele modulus, that is, on whether there are diffusion limitations. This means that τ is not a purely geometrical factor. Hollewand and Gladden [55] found that $\tau(\phi)$ or the effective diffusivity, D_e , not only depends on ϕ but also differs between random and regular pore grids when the average connectivity is 6 or lower. As expected, τ and D_e do not strongly depend on the Thiele modulus for well-connected random networks because in this case the mean-field limit is approached, in which the explicit topology of the network is not accounted for. However, Hollewand and Gladden's [55] simulations show that for a periodic, cubic array of pores, τ changes from 3 to 9 when the reaction is increasingly diffusion limited (larger ϕ). For random networks, they discovered that $\tau \rightarrow 4$.

These results appear to indicate that a random pore network would be more robust than a regular one. Pore connectivity changes as a result of pore blockage due to coking or other deactivation mechanisms. Catalyst deactivation by site coverage and pore blockage affects overall diffusivities and yields in a complex way, depending on the pore network structure [56]. The effective diffusivity drops to zero when only a portion of the pores is blocked (the so-called percolation threshold) because open

areas surrounded by blocked pores are no longer accessible [57, 58]. Percolation theory [59] allows studying effects originating from pore blockage or from a distribution in pore size, which leads to a distribution in pore diffusivity [60]. Extensive reviews by Sahimi *et al.* [35] and Keil [61] discuss the influence of pore-network structure on diffusion and reaction in porous materials, both in terms of continuum and (explicit) network models.

Gavalas and Kim [177] derived analytical expressions for the diffusivity in regular pore networks, and analyzed the validity of the smooth field approximation (SFA), which neglects the effect of local concentration fluctuations on the macroscopic fluxes. The application of effective medium and renormalization group theories is particularly useful to solve diffusion-reaction problems in random pore networks with distributed pore sizes [35]. Burganos and Sotirchos [62] constructed models based on a combination of an effective medium approach (EMA), to account for the pore size distribution, and the smooth field approximation (SFA). The EMA replaces the disordered, heterogeneous medium (or network) by a homogeneous one with effective local properties, so that this replacement does not induce any changes in the volume-averaged, global properties [35, 63]. While SFA by itself would be inaccurate, the combination with EMA is very effective because of this homogenization, which removes the average effect of fluctuations. Note that such an approach can be extended to more complex pore models, should the need arise. Zhang and Seaton [64, 65] concluded from their simulations that continuum models, with appropriately evaluated effective diffusivities, can be used in situations sufficiently far removed from a percolation threshold, when the broadest pores are well connected, and when diffusion limitations are not too severe, so that molecules permeate a representative fraction of the pore space.

These theoretical studies were mostly carried out to study the effects of catalyst texture on diffusion and reaction for already existing porous catalysts, and much less for catalyst design purposes. The textural parameters needed to evaluate these models are estimated from nitrogen adsorption and mercury porosimetry measurements, or from computer reconstructions of materials, based on electron microscopy images [66, 67] and models mimicking the catalyst formation process [68–70]. When constructing a model for a porous material, using the measured pore size distribution, care has to be taken with regard to the way in which the pores are spatially distributed. For porous materials with a bimodal nanopore or macropore size distribution, as further discussed in Section 2.4, an uncorrelated random assignment of pore sizes to cylinders on a (regular or random) particle-spanning lattice, as done in several studies, is rarely representative of a real porous catalyst [71]. Furthermore, such network representations might lead to unrealistically high values for the tortuosity. Typically, a catalyst pellet consists of smaller, compacted nanoporous particles. The spaces in between these particles form the macropores. More realistic, therefore, is a macropore network embedding a nanoporous catalyst, with connections between macropores and nanopores.

Catalyst design is aided by this wealth of information on pore network models, which show what textural parameters have a large influence on effective diffusivities and reaction rates. When designing a new catalyst, we are not as much faced with

the challenge of representing a random material but have, within the bounds of synthetic capabilities, the freedom to construct a network that is most suitable to achieve high catalytic performance. Progress in synthesis of materials is shifting the boundaries of what is realizable, although many of the proposed routes in the chemical and materials science literature involve expensive additives or templates, or multiple steps, which limits their economical viability. There is a need for more research on routes that are scalable to industrially relevant quantities. In any case, computational speed is now seldom the limiting factor in solving three-dimensional pore network models or correctly coarse-grained continuum models, even in situations involving multiple reactions between multiple components, transported by flow and molecular, Knudsen and surface diffusion [28].

2.2.2

Surface Roughness and Fractal Morphology

Another issue is pore shape. Networks of cylindrical pores and/or spherical cavities might be amenable to easier analytical or computational treatments, but are often no accurate representations of reality, when confronting these models to electron microscopy images [67, 66]. Arguably, such models are able to account for pore diameter distribution and pore connectivity, but real amorphous porous media are generally more complex. Pore constrictions, for example, play a role, as does the pore surface morphology. Aggregates of partially overlapping spheres are a better first-order approximation when representing many mesoporous supports, because such models mimic the aggregation of sol particles during a frequently used synthesis route of catalyst supports [72].

When molecules are only slightly smaller than the local pore size, true nanoeffects come into play. The micropores, or small mesopores, can then be properly called nanopores because their geometry directly influences reaction kinetics, as a result of size and/or shape selectivity. This is almost always the case in zeolites, but also in some mesoporous materials. When pores are wider than a few molecular diameters, so that the molecules do not significantly interact with the pore walls at all times, changes in pore morphology can still affect product distributions in catalysis.

In catalytic reactions involving liquids, intermolecular interactions within the liquid may be perturbed by confinement inside a nanopore, so that the molecular diffusivity of reacting species is affected by the nanopore size and shape. In catalytic reactions involving gases, the mean free path is longer than the nanopore size at not too high pressures or too low temperatures. In this case, Knudsen diffusion dominates diffusion through the voids.

To accurately model transport in nanopores, especially when the pores are chemically and geometrically heterogeneous, is an ongoing challenge, requiring statistical mechanical methods (Monte Carlo and molecular dynamics simulations, first-passage time calculations, etc.) and correct estimates of interatomic potentials. Structural modifications at this nanoscopic level could simultaneously affect the intrinsic kinetics, a topic beyond the scope of this chapter.

Many porous amorphous catalysts and catalyst supports, including amorphous silica, γ -alumina, and zirconia, were shown to have a surface that is fractal over a range of length scales [δ_{\min} , δ_{\max}] including the size of typical molecules [36, 73–75]. The accessible surface area depends on the molecular diameter, δ , following a power law $\sim \delta^{2-D}$, where D is the fractal dimension of the surface [39], a number between 2 (smooth surface, like graphite) and 3 (space-filling surface). This means that small molecules will see a much larger surface area than large ones. A very convoluted internal catalyst surface of high fractal dimension, analogous to the Norwegian coastline with its cascades of fjords, has the potential to considerably increase the conversion per unit catalyst volume, as compared to the situation where the pores are smooth. However, reactant access to this tortuous surface is not necessarily uniform.

The fractal scaling range is usually too narrow to significantly influence molecular diffusion, but it has a large effect on Knudsen diffusion, since molecules get trapped inside the “fjords” alongside the surface, increasingly so if they are smaller. Traditional catalyst pore network representations in terms of smooth cylinders or spheres, such as the ones discussed earlier, ignore this surface roughness, but roughness can be included by superimposing a fractal perturbation, leading to more realistic models [76, 77]. The effect of fractal surface roughness on the Knudsen diffusivity D_K of a molecule of diameter δ can be calculated analytically [77] and verified by Monte Carlo simulations [78]. To a first (mean-field) approximation, $D_K/D_{K0} = \delta^{D-2}$, in which D_{K0} is the Knudsen diffusivity if the pore space were smooth, D is the fractal dimension of the surface, and $\delta' = \delta/d$, where d is the local pore diameter – this should be δ_{\max} rather than d if the upper bound of the fractal scaling regime, $\delta_{\max} > d$. A more correct analytical expression, based on a first-passage time analysis, accounts for the nonuniform accessibility of the surface, and includes two parameters, one of which is the fractal dimension and the other one a measure for this nonuniform accessibility [77]. The Knudsen self-diffusivity indeed decreases with increasing (fractal) dimension D and decreasing molecular diameter, δ . If the fractal regime is narrow, effects are smaller [78]. Extending upon work by Derjaguin [178], Levitz [79, 80] derived general expressions for the Knudsen diffusivity in random porous media, in terms of the pore chord length distribution; these are very useful in combination with continuous-time random walk simulations [81, 82].

Because of the opposite effects of surface roughness on the Knudsen diffusivity, on the one hand, and on the active surface area per unit volume (as compared to smooth pores), on the other hand, surface roughness should be considered in catalyst design. When applied to vinyl acetate production, conversion can be increased in rough fractal pores [83]. Catalytic reforming of naphtha on PtRe/ Al_2O_3 leads to higher octane gasoline when raising the fractal dimension of the alumina surface above the current value of $D = 2.3$. However, the hydrogen production peaks at $D = 2.6$ because diffusion limitations cause the light hydrogen molecules to be trapped in the fractal fjords along the pores, leading to excessive and undesired hydrogenolysis and hydrocracking side reactions [84].

Also if surface diffusion on the mesopore surface is the dominating transport mechanism, as could be the case in very narrow pores, or at sufficiently high

pressures and low temperatures, roughness will clearly affect product distributions and should be included in the optimization study [28, 70].

If the fractal scaling range is particularly broad, as in certain aerogels, diffusion limitations in the vicinity of the surface could arise for intrinsically fast catalytic reactions. The effective reaction rate depends on the fractal dimension and other fractal parameters describing the surface, as well as on the distribution of the active sites over the surface. This interesting problem, reminiscent of oxygen transport and exchange in the fractal lung, has been studied by numerous researchers, including: Nyikos and Pajkossy [85], who investigated the mathematically similar electrochemical problem of fractal electrodes; Meakin [86], who studied molecular diffusion in the vicinity of and reaction on diffusion-limited aggregates as a model fractal object; Gutfraind *et al.* [87] and Seri-Levy and Avnir [88], who modeled diffusion toward and reaction or adsorption on fractal sets. This is only a small sample of the considerable literature on this subject. We refer to Sheintuch [158] and to Coppens [36] for reviews on the effects of fractal geometry on diffusion and reaction, including studies in which the catalyst itself (and not only its surface) is fractal. In Section 2.4, we will return to the potential of fractal pore size distributions for catalyst design, since the same concepts can be applied at larger length scales – those of the large pore channels traversing the catalyst.

Pfeifer and Sapoval [89] introduced a “land surveyor approximation,” which uses scaling arguments to evaluate how much of the surface is effectively screened, as a function of the diffusivity and the intrinsic reaction rate constant of a first-order reaction. Interestingly, their analysis also holds for nonfractal rough surfaces. It was applied by Sapoval *et al.* [90] to capture effects of fractal roughness in an effective reactivity, rather than in an effective diffusivity.

Giona *et al.* [91, 92] developed comprehensive solutions for the problem of molecules moving and reacting on a fractal. Diffusion is anomalous in this case, meaning that the molecular mean-squared displacement is not proportional to time (Einstein’s law) but involves a fractional exponent, the so-called “spectral dimension” (Havlin and Ben-Avraham [176]). As a result of this, reactions on fractals may appear to be of fractional order and show anomalous behavior [93, 94].

Much of the literature on fractal models in catalysis assumes a very broad scaling regime for the catalyst itself, its surface, or its pore volume. While these conditions are uncommon for typical catalyst supports, with the important exceptions of some aerogels [75] and porous carbons [95], progress in materials synthesis makes the special properties of fractal morphologies of considerable interest for the design of new catalysts, also in the context of fuel cells, batteries, photovoltaics [38], and enzymatic catalysis.

2.3

Optimizing Catalysts by Macroscopic Distributions in Activity

The accessibility of active sites in a nanoporous catalyst can be improved by distributing the sites in a macroscopically nonuniform way. For instance, accessibility is

enhanced when the sites are concentrated within an area close to the external surface of the catalyst, forming an “eggshell” catalyst. Eggshell catalysts are attractive to counter significant heat and intraparticle mass transfer limitations. Several researchers have reviewed the design and preparation of porous catalysts with a nonuniform distribution of catalytic sites [20, 21, 37, 96–99].

A considerable effort was made to find theoretically the optimal activity profile in a catalyst pellet under various conditions, and with respect to various optimization objectives. Morbidelli *et al.* [100] optimized the activity profile in a catalyst pellet with an isothermal, bimolecular Langmuir–Hinshelwood reaction, and under no external mass transfer resistance. They found that the effectiveness factor is maximized by concentrating all the catalytic material at a precise location in the pellet. They showed that if the catalyst is deposited in a band, centered at this optimal location, then the effectiveness factor remains virtually the same when the width of the active zone is less than 5% of the pellet dimensions. Morbidelli *et al.* [100] also found that the effectiveness factor decreases gradually if the actual location deviates from the optimal location in a direction toward the center of the catalyst, but that it decreases drastically if the actual location moves closer to the external surface of the catalyst. Their analysis was extended to cases with external mass transfer resistance and a nonisothermal reaction [101, 102]. Vayenas and Pavlou [103] optimized the activity profile in a catalyst pellet for single reactions with general kinetics. They also found that the optimal profile is an appropriately chosen Dirac δ -distribution. Vayenas and Pavlou [104, 105] optimized the activity profile in a catalyst pellet with the aim to maximize the selectivity of parallel and consecutive reactions. Morbidelli *et al.* [106, 107] optimized the activity profile in catalyst pellets in a fixed-bed reactor.

In addition to these theoretical efforts, porous catalysts with different activity profiles have been prepared and compared. Summers and Hegedus [108] studied Pt–Pd catalysts for automobile emission control, and compared five different distributions: Pt(exterior)–Pd(interior), Pd(exterior)–Pt(interior), Pt–Pd(exterior), Pd(exterior) and Pt(exterior). Experimental results show that the Pt–Pd catalyst is the best in terms of catalytic activity and lifetime. Wu *et al.* [109] studied methanation ($\text{CO} + 3\text{H}_2 \rightarrow \text{CH}_4 + \text{H}_2\text{O}$) accompanied by coking on Ni–Al₂O₃ catalysts and found that the coking is suppressed when the catalytic materials are located subsurface. They attributed this observation to the fact that the H₂–CO ratio is higher subsurface than at the external surface of the catalyst. Gavrilidis and Varma [110] studied ethylene epoxidation on an Ag– α -Al₂O₃ catalyst, and found that for optimum selectivity and yield to ethylene oxide, the silver catalyst should be placed in a thin layer at the external surface of the pellet. Au *et al.* [111] studied the Ni-catalyzed hydrogenation of benzene. Five different distributions, ranging from preferential shell loading, to uniform, to preferential core loading were compared under isothermal conditions. It was found that the discrepancy in the performance of the five catalysts was amplified at increased Thiele modulus.

Finally, in the spirit of an integrated catalysis engineering approach, it should be noted that the same principle of invoking a nonuniform distribution of active sites to increase activity, selectivity, and stability could be used on a reactor scale as well, in particular in the case of structured reactors, like monoliths [7].

2.4

Optimal Design of the Highway Network

Nanoporous catalysts, like zeolites, have an extremely large internal surface area, which contributes to their high intrinsic catalytic activity. However, molecular transport in nanopores is slower than in the bulk and can be blocked as a result of catalyst deactivation. This has triggered significant interest in the introduction of large pore channels (i.e., macropores and large mesopores), which act as “highways” into nanoporous catalysts, so as to facilitate molecular transport, and, consequently, improve overall catalyst performance. Without these highways, accessibility to the catalyst interior may be severely limited; van Donk *et al.* [172] illustrated how hydrocarbon molecules could permeate only about 200 nm of a mordenite crystal.

The need for methods to include large pore channels in a better controlled way is beautifully demonstrated by the work by de Jong and coworkers, who used electron tomography (3D transmission electron microscopy) to reveal the interior of dealuminated faujasite (zeolite Y). This catalyst is used on a gigantic scale in catalytic cracking of gas oil. Steaming and acid leaching are used to extract and displace Al, thereby influencing the intrinsic catalytic activity and selectivity. This also generates large mesopores, which are often assumed to reduce diffusion limitations. However, the 3D TEM images of Janssen *et al.* [179] clearly show that the mesopores are unequally distributed, and are mostly present as cavities, not all of which are connected to each other or to the catalyst exterior. The importance of this is accentuated by recent pulsed-field gradient (PFG) NMR results by Kortunov *et al.* [173] who showed that the intracrystalline diffusivity of relevant hydrocarbon molecules is *not* affected by intracrystalline mesopores, in contrast to what had been commonly assumed.

Such effects are not isolated to zeolites. Hollewand and Gladden [113, 114] visualized pellets of amorphous alumina and silica, using NMR imaging and pulsed-gradient spin-echo NMR. These techniques revealed that the macropores in catalyst pellets are distributed in a highly nonuniform way, and that this considerably affects the effective diffusivity. These results stress the importance of aiming for catalysts that are macroscopically homogeneous, to obtain higher effective diffusivities.

It can be concluded that: (1) large pore channels are often necessary for transporting molecules in and out of nanoporous catalysts; (2) their position is not well controlled in current typical synthesis methods; (3) it is worthy to investigate if structuring these large pore channels can increase catalyst performance; (4) independent control of intrinsic activity and pore architecture is highly desirable.

In the following, we briefly review some of the staggering progress in the synthetic capabilities of hierarchical pore architectures, followed by a theoretical study on the opportunities offered by controlling the “highway network” in nanoporous catalysts, including some new results.

2.4.1

Novel Capabilities in Synthesizing Hierarchical Pore Spaces

The hierarchical pore system might be an intrinsic part of a multifunctional catalyst, for example, in cracking reactions in which large molecules are cracked in mesopores and smaller molecules in zeolite pores. The amorphous silica SBA-15 contains a hexagonal array of mesopores, of a size that can be tuned between approximately 5 and 30 nm, and is made by micellar templating [49]. Its walls are typically traversed by micropores, with a microporosity that could be separately tuned [115, 116]. Since the walls are quite thin (a few nanometers), the micropores can allow small molecules to move from one mesopore to an adjacent one, obviating the need for a three-dimensional network of mesopores. The diffusion tensor depends on the way in which SBA-15 was synthesized [117]. Active sites in both the micropores and the mesopores can play a role in the intrinsic kinetics of SBA-15-based catalysts. For large molecules, the micropores form a considerable, perhaps impenetrable, barrier, and three-dimensionally periodically connected mesoporous materials, such as MCM-48, SBA-1, or SBA-16 should be considered.

Latex (polystyrene) spheres, disordered or ordered to form colloidal crystals, can be used as “hard” templates to introduce large pores (macropores and large mesopores), after having been removed by extraction or calcination [118, 119]. To generate structured surface layers, soft lithography, which uses a patterned elastomer as the mask, stamp, or mold, has revolutionized microfabrication: it is cheaper than photolithography; can also be applied to nonplanar surfaces; and employs a broad variety of materials that can be easily functionalized [120]. It has thus been used to create two-dimensional porous oxides with a controlled pore structure at multiple length scales [121]. Ha *et al.* [122] used a microprinting technique to assemble micrometer-sized zeolites into a two-dimensional lattice with a size of 5–20 μm .

Oil-in-water emulsions can be combined with surfactant templating at the emulsion interface to create hierarchically structured mesoporous materials in various morphologies, governed by the shape of the interface [123]. Using a dual supramolecular templating–scaffolding route, Sun *et al.* [124] introduced large mesopores into MCM-41, a nanoporous silica with a tailored pore diameter of 3–10 nm; the size of the large mesopores could be independently controlled over a broad range, without affecting the size of the nanopores. An interesting new route adopted by Su and coworkers generates a wide variety of hierarchical mesoporous oxides with oriented, funnel-like macropores, using a single nonionic surfactant [125, 126]. Several novel methods to synthesize structured mesoporous–macroporous materials were recently reviewed by Yuan and Su [127].

Various methods to synthesize mesostructured zeolites, containing mesopores of a controlled size as well as zeolite, thus attempting to combine the hydrothermal stability of zeolite crystals with large pore channels for transport, were reviewed by van Donk *et al.* [112], Hartmann [128], Tao *et al.* [129], and Egeblad

et al. [130]. The use of small carbon particles [131] or carbon aerogels [129] as templates is particularly attractive, also from the economical point of view. Carbon is encapsulated by zeolites while they are crystallizing, and is removed by combustion at the end, leaving behind mesopores within each zeolite crystal. Such “nanocasting” methods are powerful methods to create a variety of nanostructured porous materials [132]. The carbon template can even be generated *in situ* from, for example, sugar decomposition [133], while the zeolite forms around it. By partial zeolitic recrystallization, grafting, or deposition of zeolite seeds on the walls of mesoporous materials (such as MCM-41 or SBA-15, which has thicker walls), catalyst acidity and stability are improved, while molecular transport, especially of larger species, is simultaneously enhanced [134–138]. Self-assembly of zeolite seeds around supramolecular templates generates mesoporous–microporous composite catalysts of higher hydrothermal stability as well [139]. Groen *et al.* [140] used desilication to create mesopores without displacing aluminum, in this way separating activity and mesopore control. Wang *et al.* [141, 142] introduced two new methods to form meso-structured zeolite composites, by using the zeolite template also as a structure-directing agent to generate large pore channels, obviating the need for (and the cost of) a second template.

The performance of nanoporous catalysts with and without large pore channels has been measured and compared. Christensen *et al.* [143] found an improved activity and selectivity for zeolites used in catalytic benzene alkylation when mesopores were introduced. Kärger and Vasenkov [144] achieved higher cracking conversions in faujasites of higher mesoporosity. Choi *et al.* [145] introduced mesopores with a tunable pore diameter of 2.1–7.4 nm into zeolites. They found that zeolites containing mesopores were more active than those without, for catalytic reactions involving large organic molecules. Likewise, Waller *et al.* [137] showed that a composite incorporating nanosized zeolite Beta inside the three dimensionally connected mesoporous material TUD-1 led to higher cracking rates of *n*-hexane. Groen *et al.* [146] found that diffusivity in zeolites increased more than two orders of magnitude when mesopores were introduced by their novel desilication route.

Therefore, these advances in the synthesis of hierarchically structured porous catalysts present us with a great opportunity, namely, the possibility to optimize overall performance of catalyst particles of a desired macroscopic size. This is especially so when the nanopores, the transport channels, and their connectivity, can be controlled independently. Certainly, optimization requires experimentation, but it can be aided by theoretical calculations, as the remainder of this section will attempt to demonstrate. Notice that optimization will depend on the system at hand, and on what exactly is being optimized: activity, selectivity, catalytic or mechanical stability, or a combination of all of these? Our examples will focus on maximum yield, but the objective function and boundary conditions can be modified, while preserving the described methodology.

2.4.2

Theoretical Optimization Studies: Opportunities for Optimal Design

On the theoretical side, both continuum and pore network models have been used to study diffusion and reaction in a bimodal porous catalyst, that is, a catalyst containing both nanopores and large pore channels.¹⁾ Dogu [147] presented a comprehensive review on this subject. In continuum models, effective macroscopic properties are used to lump all the effects of the pore space geometry. Continuum models are easiest to use, not only because they are more familiar to engineers, but also because they are free of complex detail about real pore networks. However, the effective properties can be defined only over homogeneous volume elements that are sufficiently large compared with individual pores and sufficiently small compared with the catalyst particle size. As a result, heterogeneity at length scales comparable to either individual pores or the catalyst size is invisible in continuum models. As discussed in Section 2.2, homogeneous continuum models are invalid for poorly connected and fractal networks and in other situations where long-range correlations are present [35, 65, 158]. Pore network models can explicitly account for the texture but require more detailed information to describe the geometric complexity (e.g., pore shapes, pore orientations, and connectivity) and are computationally more demanding.

A popular continuum approach to study diffusion and reaction in bimodal porous catalysts is the Pellet–Particle model, in which nanopores and large pore channels are assumed to be two distinctive continua [148–153]. Based on this approach, Carberry [148, 149] studied the effects of diffusion on selectivity for a sequential reaction $A \rightarrow B \rightarrow C$ in a bimodal porous catalyst and evaluated the effectiveness factor of a bimodal porous catalyst for a reversible reaction. Ors and Dogu [150] used the Pellet–Particle model to calculate the effectiveness factor of a first-order reaction in a bimodal porous catalyst. Kulkarni *et al.* [151], Jayaraman *et al.* [152], and Namjoshi *et al.* [153] extended this calculation to cases exhibiting nonlinear kinetics: power-law rate equations and Langmuir–Hinshelwood kinetics. The Pellet–Particle model predicts a new asymptote, $r \sim k^{1/4}$ (where, k is the rate constant and r the reaction rate), when severe diffusion limitations exist in both nanopores and large pore channels, as opposed to the classical one, $r \sim k^{1/2}$. This prediction makes sense because a weak k -dependence is a result of strong diffusion limitations. Interestingly, some researchers observed this asymptote ($r \sim k^{1/4}$) on fractal catalysts [154–158]. They recommended taking advantage of this feature to develop a deactivation-resistant catalyst, since the reaction rate is more k -insensitive in the regime of $r \sim k^{1/4}$ than in the regime of $r \sim k^{1/2}$. However, this deactivation-resistant design may

1) In much of the literature, the pores on two distinctive length scales in a bimodal porous catalyst are called macropores and micropores. Because these two words clash with the terminology of the International Union of Pure and Applied Chemistry, an alternate pair,

“channels” and “nanopores”, is used here to avoid confusion and to stress the difference between what are essentially transportation pores, as against pores that are principally tied to the intrinsic catalytic performance.

come at a cost, at least for nonfractal bimodal porous catalysts, because this k -insensitivity is tied to a low effectiveness factor (because of severe diffusion limitations in both nanopores and large pore channels), typically less than 1%, as predicted by the Pellet–Particle model. It should be stressed that the Pellet–Particle model is valid only when the large pore channels connect the external surface of the catalyst to its center, because the continuity equation for the large pore channels and its boundary condition on the external surface of the catalyst do not hold without that condition.

Another widely used continuum approach to study diffusion and reaction in a bimodal porous catalyst is based on the assumption that a bimodal porous catalyst can be treated as a single continuum, as opposed to double continua in the Pellet–Particle model. In this single-continuum approach, diffusion in nanopores and large pore channels in a bimodal porous catalyst is characterized by a single effective diffusivity. The equation of Wakao and Smith [159] is often used to calculate the effective diffusivity from the respective volume fractions and the diameters of the nanopores and the large pore channels. This equation assumes volume-averaged parallel and serial contributions of large channels and nanopores. Hegedus [160] optimized these structural variables of a bimodal porous catalyst for automobile emission control, under shell-progressive deactivation, based on a one-dimensional single-continuum model. Pereira *et al.* [161] used a similar approach to optimize a catalytic converter after 1000 h of operation in the presence of poisons. Beeckman and Hegedus [162] optimized volume fractions and diameters of nanopores and large pore channels of a bimodal porous catalyst for power plant NO_x emission control. They developed a new type of catalyst guided by the optimizations. The 50% improvement in activity predicted in the optimizations was also observed in experiments.

Pore network models were also used to simulate diffusion and reaction in bimodal porous catalysts [55, 71, 163–166]. One popular pore network model is the bond–node pore network model, which is derived in the following way: consider a pore network, consisting of a number of cylindrical pores, and formulate a one-dimensional diffusion-reaction equation for each pore, with the boundary conditions that the concentrations at the two ends of each pore are equal to the concentration at the corresponding node where two or more pores intersect. The concentration at each node is determined simultaneously by requiring that the sum of the fluxes at each node is zero. The bond–node pore network model can be used to study not only bimodal porous catalysts, but also catalysts with arbitrary pore size distribution.

Keil and Rieckmann [164] used a bond–node pore network model to study the catalytic hydrodemetallation of crude oil over a bimodal $\text{CaO-MoO}_3/\text{Al}_2\text{O}_3$ catalyst. The catalytic hydrodemetallation is used to remove organic compounds containing nickel and vanadium in crude oil. One salient feature of this process is that metals (e.g., nickel and vanadium) in crude oil deposit within the pores of the catalyst as metal sulfides, and that the accumulation of metal deposits blocks the pores and active sites of the catalyst, yielding irreversible catalyst deactivation. Keil and Rieckmann [164] optimized the nanopore radius and nanoporosity of the bimodal catalyst with the aim to maximize the reaction rate over a certain period of time. They showed that catalyst performance could be improved considerably by tuning the pore

structure. Keil and Rieckmann [174] extended their earlier approach by including multicomponent diffusion and viscous flow in the pore network under the framework of the dusty-gas model. The books by Jackson [30] and by Mason and Malinauskas [29] discuss the dusty-gas model in detail. Keil and Rieckmann [174, 175] applied their approach to two cases: (1) the deactivation of a bimodal ZSM-5 catalyst due to coke formation and (2) the selective hydrogenation of 1,2-dichloropropane to propane and hydrochloric acid over a bimodal Pd/Al₂O₃/SiO₂ catalyst. For the second case, they found good agreement between experimental measurements and model predictions.

El-Nafaty and Mann [165] simulated the regeneration of a heavily coked FCC catalyst. They treated the coke burn-off by a shrinking-core model and imposed a pseudo-steady-state assumption to calculate the concentration profile in the catalyst using a bond-node pore network model. They found that regeneration time would significantly shorten by structuring the catalyst in a hierarchical way, with a large pore channel network spanning across the catalyst, and nanoporous clusters (i.e., local nanopore networks) connected to the large pore channel network. They also found that a random pore network, which is often used to characterize catalyst particles, shows relatively poor burn-off kinetics. The reader is reminded of the 3D TEM images by van Donk *et al.* [112], discussed in Section 2.2, which showed the nonuniformity and poor connectivity of large pore channels inside zeolite particles used in the FCC process.

Prachayawarakorn and Mann [166] used a bond-node pore network model to calculate the effectiveness factor of a first-order reaction in a bimodal porous catalyst. They compared four bimodal pore structures that have the same porosity and numbers of nanopores and large pore channels but different pore architecture. They showed that the effectiveness factors of these four structures are very different and that a structure in which large pore channels are placed in the exterior shell of the catalyst, with nanopores in the interior, is the best of all and gives a 800% higher catalytic activity than its random counterpart, with randomly distributed nanopores and large pore channels.

Coppens and coworkers studied the general features of optimal large pore channel networks in bimodal porous catalysts [167–171]. This optimization problem differs from those in which the nanopore size is varied, and is practical in view of the fact that the features at the nanoscale typically determine the desired intrinsic kinetics, which we would like to preserve. Therefore, the texture at all length scales larger than the narrowest pores should be optimized with regard to efficient molecular transport in a bimodal porous catalyst.

Wang *et al.* [169] optimized the spatial distribution of volume fractions occupied by large pore channels and channel diameters of a square-shaped bimodal porous catalyst, based on a continuum model. As shown in Figure 2.1, the studied catalyst model is an assembly of $N \times N$ internally homogeneous square-shaped substructures, where N is an arbitrary positive integer, typically between 1 and 100. The large pore channels have an identical diameter in each substructure, but channel diameters and volume fractions occupied by large pore channels are allowed to differ from one substructure to another. Therefore, the optimizations allow for increasingly broader spatial variations in channel diameters and volume fractions occupied by

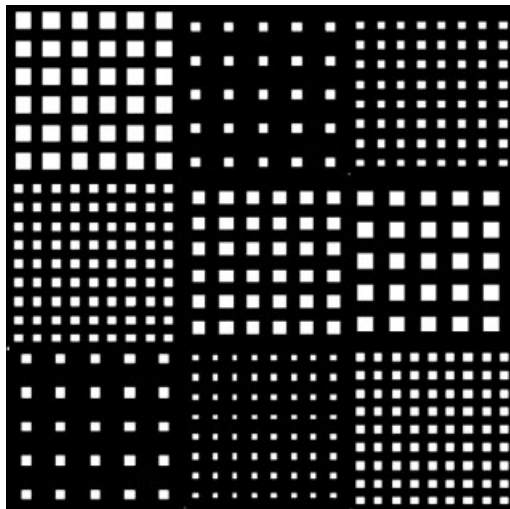


Figure 2.1 Diagram of the studied bimodal catalyst. The bimodal pore structure is an assembly of $N \times N$ internally homogeneous square-shaped substructures of equal size; $N = 3$ is for illustration only. The nanoporous, catalytically active materials is shown in white and the large pore channels in black.

large pore channels as N increases. Surprisingly, only a maximum of 5% difference in terms of the effectiveness factor was found between the optimal catalyst with a 1×1 substructure and those with $N \times N$ substructures ($N > 1$), indicating that a broad distribution of channel diameters and volume fractions occupied by large pore channels is *not* needed. This is important information from the point of view of catalyst synthesis, since Section 2.4.1 discussed various means to introduce large pore channels of an identical diameter into a nanoporous catalyst. It was also found that the optimal bimodal porous catalyst had a much higher effectiveness factor than the nanoporous catalyst (without large pore channels) for diffusion-limited reactions. In the optimal structures, the dominant transport pathway essentially reduces to two diffusion processes in series: (1) diffusion in the large pore channels over a characteristic length scale on the order of the catalyst particle size and (2) local diffusion in the nanoporous walls, that is, the nanoporous catalyst in between two neighboring large pore channels. Among these two processes, the rate-determining step is diffusion in the *large* pore channels, because, in the optimal catalyst, the covered diffusion distance is orders of magnitude longer in the large pore channels than within the nanopores. Interestingly, this corresponds to results based on PFG NMR measurements by Kärger and Vasenkov [144], who found that diffusion at reaction temperatures in composite faujasite-containing particles, used as FCC catalysts, is governed by diffusion in the large pore channels, and *not* in the intracrystalline micropores, as had often been assumed.

Johannessen *et al.* [170] used optimal control theory to optimize a periodic bimodal porous catalyst, shown in the left of Figure 2.2, based on a two-dimensional hybrid

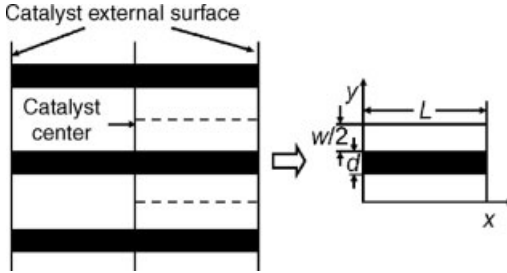


Figure 2.2 Diagram of the bimodal catalyst (left) and a subunit (right). The bimodal pore structure is formed by repeating the subunit in the y (vertical) direction. The nanoporous, catalytically active material is shown in white and the large pore channels in black. (From Ref. [171]).

pore network model. The large pore channels were considered explicitly, whereas the nanoporous catalytically active material was treated as a continuum. This structure was formed by repeating its subunit, shown in the right part of Figure 2.2, in the y (vertical) direction. The optimization variables were the channel diameter, d , and the channel wall thickness, w , as labeled in Figure 2.2. The objective was to maximize the effectiveness factor, η , of the bimodal porous catalyst, defined as

$$\eta = \frac{\int_V r(c) dV}{r(c_0) V_{\text{tot}}}$$

where, c_0 is the external concentration; $r(c)$ is the reaction rate as a function of reactant concentration (for a reaction where the kinetics depend on one reactant concentration only, a condition that can be relaxed); V is the volume (3D) or area (2D) occupied by nanoporous material; and V_{tot} is the volume (3D) or area (2D) occupied by both nanoporous material and the large pore channels. It was found that concentration gradients vanish in the y (vertical) direction, when the channel diameter and the channel wall thickness are optimized. This result is consistent with the conclusion reached by Wang *et al.* [169]. The optimal bimodal porous catalyst is much more active than the nanoporous catalyst for diffusion-limited reactions. A one-dimensional effective (continuum) model was also developed, which predicted the performance of the optimal bimodal porous catalyst with almost equal accuracy to the two-dimensional hybrid pore network model.

Wang and Coppens [171] found that the generalized distributor Thiele modulus, Φ_0 , governs the optimal effectiveness factor, η_{opt} , obtained by Johannessen *et al.* [170], when Φ_0 is defined in a way analogous to the generalized Thiele modulus, Φ , typically employed in chemical engineering [4], but using the diffusivity in the *large* pore channels, D_m , rather than the effective diffusivity in the nanoporous material, D_e . In other words, Φ_0 is defined as

$$\Phi_0 = \frac{V_{\text{tot}}}{S} \frac{r(c_0)}{\sqrt{2}} \left[\int_{c_c}^{c_0} D_m r(c) dc \right]^{-1/2}$$

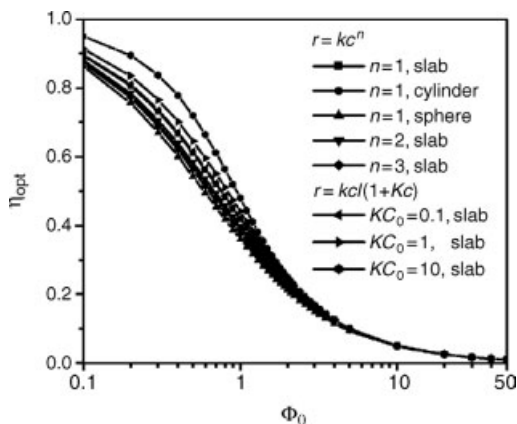


Figure 2.3 Optimal effectiveness factor η_{opt} of the bimodal catalyst as a function of the generalized distributor Thiele modulus, Φ_0 , for a single reaction with different chemical kinetics and for various catalyst shapes. (From Ref. [171]).

where, S is the external surface area (3D) or perimeter (2D) of the catalyst particle and c_c is the concentration at the center of the catalyst particle, typically assumed to be zero for an irreversible reaction or the equilibrium concentration for a reversible reaction. As Figure 2.3 shows, the $\eta_{\text{opt}} - \Phi_0$ relation is essentially independent of chemical kinetics and catalyst shape. Furthermore, Figure 2.4 shows that this relation holds regardless of the ratio of the molecular diffusivity in the large pore channels to the effective diffusivity in the nanoporous material, when this ratio is greater than 30. Deviations appear only at high Knudsen numbers in the large channels. This relation

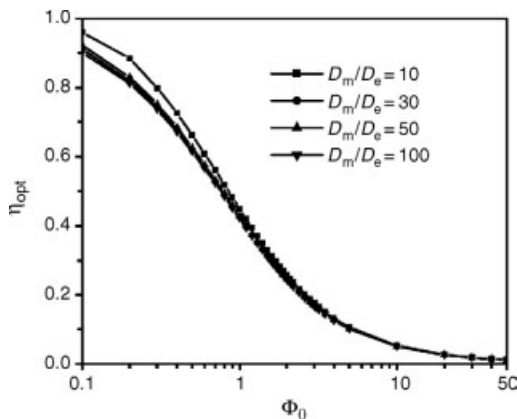


Figure 2.4 Optimal effectiveness factor, η_{opt} , of the bimodal catalyst as a function of the generalized distributor Thiele modulus, Φ_0 , at different values of D_m/D_e , the ratio of the molecular diffusivity in the large pore channels to the effective diffusivity in the nanoporous material. A first-order reaction in the bimodal catalyst slab is considered. (From Ref. [171]).

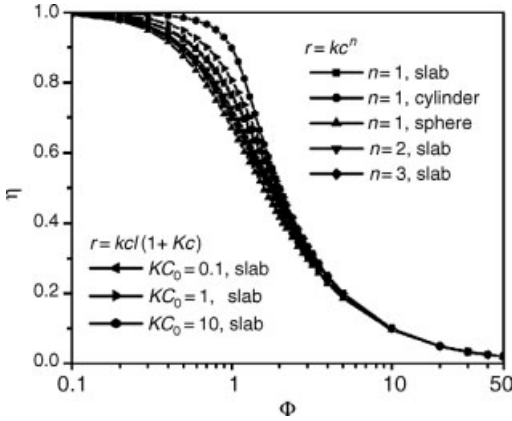


Figure 2.5 Effectiveness factor of a porous catalyst, η , as a function of the generalized Thiele modulus, Φ , for a single reaction with different chemical kinetics and for various catalyst shapes. (From Ref. [171]).

is analogous to the classical, universal $\eta - \Phi$ relation for porous catalysts, shown for comparison in Figure 2.5. Therefore, this yields a back-of-the-envelope approach to design a bimodal porous catalyst, since the effectiveness factor, η_{opt} , of the optimal bimodal porous catalyst could reasonably well be estimated *solely* from the value of Φ_0 , according to the $\eta_{\text{opt}} - \Phi_0$ relation, without need for case-by-case optimizations. This is very useful information to guide industrial catalyst synthesis. Wang and Coppens [171] applied this approach to the design of a bimodal catalyst for power plant NO_x emission control, as discussed in Section 2.4.3. Also other researchers [147] examined the effectiveness factors of bimodal porous catalysts, using the Pellet–Particle model in the limit where diffusion limitations vanish locally inside the nanoporous materials. They found that the shape-generalized pellet Thiele modulus (which was defined in their papers in a way similar to the generalized distributor Thiele modulus here) governs the effectiveness factors of bimodal catalysts in this limiting case. However, it was not pointed out that the optimal bimodal porous catalyst belongs to this limiting case, since these studies did not aim to optimize the design of a bimodal catalyst.

Three variations on the large pore channel network topology, shown in Figure 2.6, were optimized as well. The universal $\eta_{\text{opt}} - \Phi_0$ relation was found to remain valid for the optimized large pore channel networks, as shown in Figure 2.7. Also, the optimal effectiveness factor is essentially the same, no matter whether the large pore channels are restricted to have an identical diameter or not. This result is consistent with the conclusion of Wang *et al.* [169], but is in remarkable contradiction to earlier calculations for structure B (using the nomenclature of Figure 2.6) by Gheorghiu and Coppens [168], who had shown an increased efficiency when large pore channel networks with a broad distribution in channel diameter are used. The reason for this discrepancy is that Gheorghiu and Coppens [168] performed structural optimizations only for relatively small numbers of large pore channels that were fixed

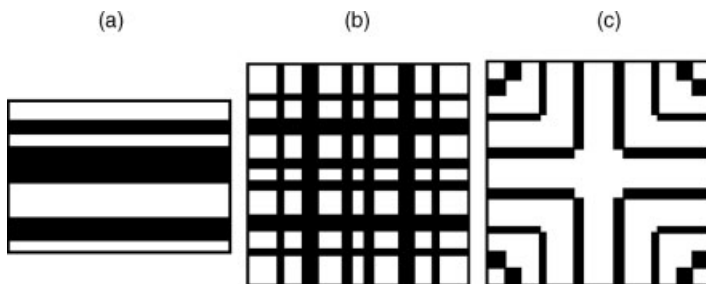


Figure 2.6 Diagram of the studied bimodal catalysts. The external surface of the catalyst is on the left and right sides of the rectangle for structure A and on the four sides of the square for structures B and C. Structure A repeats itself infinitely in the vertical direction. For all structures, the number of large pore channels can be freely optimized. The nanoporous, catalytically active material is in white and the large pore channels in black.

a priori. Fixing the number of pore channels clearly affects the results. Also, an analytical study by Coppens and Froment [167] indicated that nanoporous catalysts with a fractal, self-similar large-channel network could be much more active than if networks with a constant large-channel size were used. This work assumed that gradients in concentration are mostly present in the nanoporous material, while the global optimization study by Wang *et al.* [169] showed that the gradients are actually most significant in the large pore channels. Jointly, these results demonstrate the importance of the boundary conditions and the assumption of what is constant in the optimization.

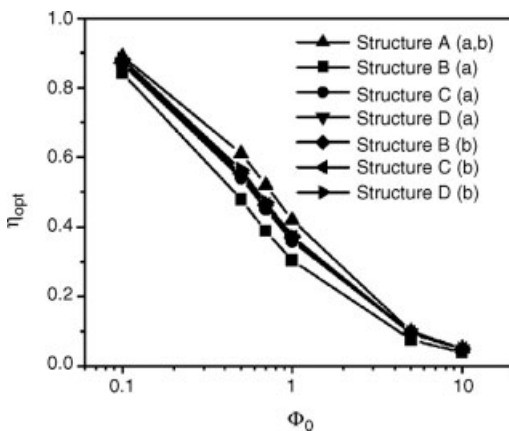


Figure 2.7 Optimal effectiveness factor η_{opt} of the bimodal catalyst as a function of the generalized distributor Thiele modulus, Φ_0 . Structures A, B, and C are shown in Figure 2.6 and structure D in Figure 2.1. (a) All the large pore channels are restricted to have an identical diameter and distribute evenly across the structure. (b) The diameter and position of each large pore channel are independently optimized.

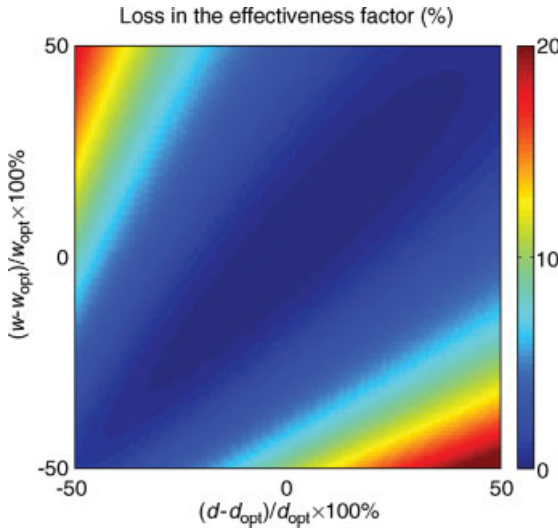


Figure 2.8 Sensitivity of the effectiveness factor to structural variations. The colors indicate the loss in effectiveness factor (expressed as a percentage of the optimal effectiveness factor) due to the following variations: the channel diameter, d , and the channel wall thickness, w , as labeled in Figure 2.2, vary in a range of 50–150% of their respective optimal values, d_{opt} and w_{opt} .

We also studied the sensitivity of the optimal catalyst performance to structural variations, since the true optima demanded from the optimizations might not be exactly reproduced in practical synthesis, and the textural parameters might change due to, for example, deactivation. The following variations were considered: the channel diameter d and the channel wall thickness w , as labeled in Figure 2.2, vary in a range of 50–150% of their respective optimal values, d_{opt} and w_{opt} . As shown in Figure 2.8, the loss in effectiveness factor is less than about 5% in a rather large region around the optimum. It is only when the pores are much thicker and the walls thinner, or vice versa, that the catalyst loses efficiency on a total-volume basis. This result is crucial from a practical point of view, since it gives information on how tightly the pore structure should be controlled in catalyst synthesis.

2.4.3

Application to the Design of a Bimodal Porous Catalyst for NO_x Abatement

A bimodal porous catalyst for power plant NO_x emission control was optimized using these principles [171]: NO_x is a precursor of acid rain and a contributor to near-ground ozone formation, which is a hazard to human health. Selective catalytic reduction (SCR) using ammonia could be used to abate NO_x emissions. This process, SCR, is usually carried out in a honeycomb monolith reactor, which consists of a bundle of parallel channels (a catalytic converter used for automobile emission control is an example of a monolith reactor). Porous catalysts are coated on the

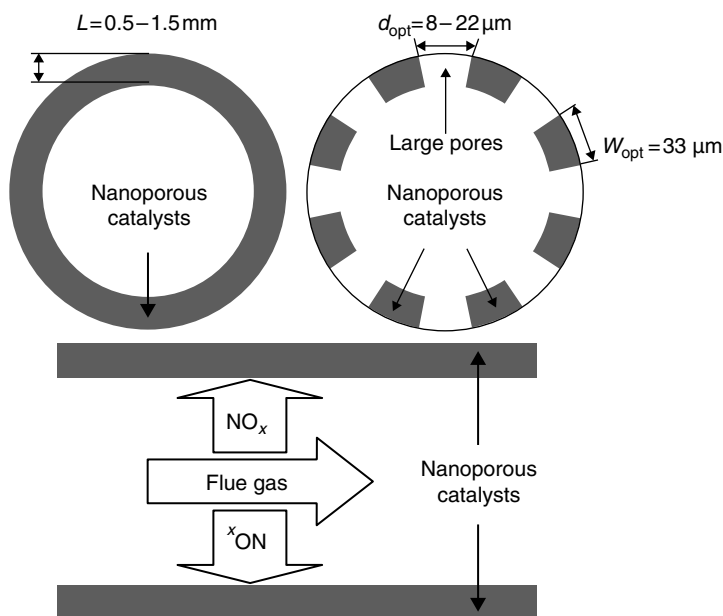


Figure 2.9 End view (top) and side view (bottom) of a single channel in a honeycomb monolith reactor. The top left shows nanoporous catalysts and the top right the optimal bimodal porous catalysts. (Adapted from Ref. [171]).

internal surface of the channels. Figure 2.9 presents a single channel in a monolith reactor. When flue gas flows through the channels, NO_x molecules diffuse into the catalyst and react on its internal surface. $\text{V}_2\text{O}_5\text{--TiO}_2$ catalysts are usually used. Data from Beeckman and Hegedus [162] were used in this optimization study. The reaction temperature is 300–400 °C. A typical monolith reactor is 70–100 cm long. The porous catalyst layer is 0.05–0.15 cm thick. Although performing SCR in a monolith reactor is a proven strategy for NO_x emission control, the performance of the monolith reactor needs to be improved, in order to meet imminent, increasingly strict regulations on environmental protection in a cost-effective manner. For instance, the *Clear Skies Initiative* sets a goal to reduce NO_x emissions from power plants in the United States by 67%, from the emissions of 5 million tons in 2002 to a cap of 2.1 million tons in 2008, and to 1.7 million tons in 2018.²⁾ An excellent way to improve the performance of the monolith reactor is to use rationally designed bimodal catalysts, rather than purely nanoporous catalysts. As shown in Figure 2.10, overall catalytic activity in a mesoporous deNO_x catalyst with a median pore size of 32.5 nm could be increased by a factor of 1.8–2.8 simply by introducing 8–22 μm wide pores, and, meanwhile, keeping pore walls (consisting of the same mesoporous catalytic material) 33 μm thick. The optimal volume fraction occupied by large pore channels is 20–40%, implying that the optimal bimodal porous catalyst uses 20–40%

2) <http://www.whitehouse.gov/news/releases/2002/02/clearskies.html>.

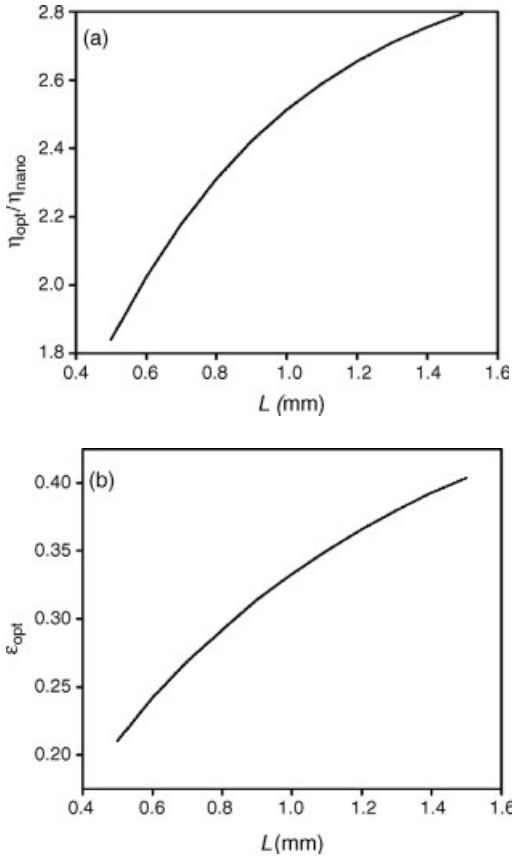


Figure 2.10 (a) The ratio of the effectiveness factor η_{opt} of the optimal bimodal porous catalyst to the effectiveness factor η_{nano} of the nanoporous catalyst (without large pores) and (b) the optimal volume fraction occupied by the large pores ϵ_{opt} versus the porous catalyst layer thickness L . (From Ref. [171]).

less catalytic material than its nanoporous counterpart. Figure 2.9 shows the optimal bimodal porous structure, which could potentially be made by extrusion.

2.5 Conclusions

Catalyst design is a multiscale effort. The active site and its immediate, nanoscopic environment is the heart of a good catalyst, like the chlorophyll of a tree, or the engine of a racecar. Inadequate catalyst design at the nanoscale cannot be compensated by modifying macroporosity. However, without the right macroscopic design, a tree cannot grow; a car is unstable and underperforms; and so does a catalyst. At present,

the rational design of mesoscopic features to optimize catalyst performance has not received as much attention as it should: properties like surface roughness and pore network topology play an important role in product distribution, activity, and protection against deactivation. Catalyst efficiency can also be increased by optimizing the macroscopic activity distribution. Furthermore, optimizing the pore network at larger length scales offers remarkable opportunities to increase conversion with less of catalyst, as discussed in some detail. The optimization of the fraction and location of large pore channels is such that it reduces the amount of nanoporous catalyst in between large pore channels, just so much that the local (generalized) Thiele modulus does not rise above 1. In doing so, the catalyst is efficiently used, preserving its intrinsic kinetics under the local conditions in the adjoining broad pore channels. The latter are just so broad as to allow quick transport, yet not more, so that the catalytic activity per unit volume is maximized. With the advent of micro- and nanotemplating methods to accurately control catalyst architecture at all length scales, truly rational catalyst design guided by computational and theoretical methods is no longer a distant dream.

Acknowledgments

Rensselaer Polytechnic Institute and the Delft Centre for Computational Science and Engineering are gratefully acknowledged for funding the research of G.W. MOC also thanks the Norwegian Academy of Science and Letters for a Guest Professorship at the Center for Advanced Studies in Oslo.

References

- 1 Hegedus, L.L. (ed.) (1987) *Catalyst Design*, John Wiley & Sons, Inc., New York.
- 2 Bell, A.T. (1990) Impact of catalyst science on catalyst design and development. *Chemical Engineering Science*, **45**, 2013–2026.
- 3 Hegedus, L.L. and Pereira, C.J. (1990) Reaction engineering for catalyst design. *Chemical Engineering Science*, **45**, 2027–2044.
- 4 Froment, G.F. and Bischoff, K.B. (1990) *Chemical Reactor Analysis and Design*, 2nd edn, John Wiley & Sons, Inc., New York.
- 5 Davis, M.E. (1994) Reaction chemistry and reaction-engineering principles in catalyst design. *Chemical Engineering Science*, **49**, 3971–3980.
- 6 Van Santen, R.A., van Leeuwen, P.W.N.M., Averill, B.A. and Moulijn, J.A. (2000) *Catalysis: An Integrated Approach*, 2nd edn, *Studies in Surface Science and Catalysis*, Vol. 123, Elsevier, Amsterdam.
- 7 Cybulski, A. and Moulijn, J.A. (eds) (2005) *Structured Catalysts and Reactors*, 2nd edn, CRC Press, New York.
- 8 Ertl, G., Knözinger, H., Schüth, F. and Weitkamp, J. (2008) *Handbook of Heterogeneous Catalysis*, 2nd edn, Wiley-VCH Verlag GmbH, Weinheim.
- 9 Boudart, M. and Mariadassou, G.D. (1984) *Kinetics of Heterogeneous Catalytic Reactions*, Princeton University Press, Princeton, NJ.
- 10 Somorjai, G.A. (1994) *Introduction to Surface Chemistry and Catalysis*, John Wiley & Sons, Inc., New York.
- 11 Thomas, J.M. and Thomas, W.J. (1996) *Principles and Practice of Heterogeneous*

- Catalysis*, Wiley-VCH Verlag GmbH, Weinheim.
- 12 Froment, G.F. and Waugh, K.C. (eds) (1997) Dynamics of surfaces and reaction kinetics in heterogeneous catalysis. *Studies in Surface Science and Catalysis*, 109.
 - 13 Gounaris, C.E., Floudas, C.A. and Wei, J. (2006) Rational design of shape selective separation and catalysis: I. Concepts and analysis. *Chemical Engineering Science*, **61**, 7933–7948.
 - 14 Gounaris, C.E., Wei, J. and Floudas, C.A. (2006) Rational design of shape selective separation and catalysis: II. Mathematical model and computational studies. *Chemical Engineering Science*, **61**, 7949–7962.
 - 15 Behr, J.-P. (ed) (1994) *Perspectives in Supramolecular Chemistry: The Lock-and-Key Principle*, Vol. 1, John Wiley & Sons, Inc., New York.
 - 16 Van Santen, R.A. and Neurock, M. (2006) *Molecular Heterogeneous Catalysis: A Conceptual and Computational Approach*, John Wiley & Sons, Inc., New York.
 - 17 Nilsson, A., Pettersson, L.G.M. and Norskov, J. (eds) (2007) *Chemical Bonding at Surfaces and Interfaces*, Elsevier, Amsterdam.
 - 18 Niemantsverdriet, J. (2000) *Spectroscopy in Catalysis: An Introduction*, 2nd edn, John Wiley & Sons, Inc., New York.
 - 19 Bell, A.T. (2003) The impact of nanoscience on heterogeneous catalysis. *Science*, **299**, 1688–1691.
 - 20 Centi, G. and Perathoner, S. (2003) Novel catalyst design for multiphase reactions. *Catalysis Today*, **79**, 3–13.
 - 21 Centi, G. and Perathoner, S. (2003) Integrated design for solid catalysts in multiphase reactions. *CATTECH*, **7** (3), 78–89.
 - 22 Krishna, R. and Sie, S.T. (1994) Strategies for multiphase reactor selection. *Chemical Engineering Science*, **49**, 4029–4065.
 - 23 Lerou, J.J. and Ng, K.M. (1996) Chemical reaction engineering: a multiscale approach to a multiobjective task. *Chemical Engineering Science*, **51**, 1595–1614.
 - 24 Dudukovic, M.P. (1999) Trends in catalytic reaction engineering. *Catalysis Today*, **48**, 5–15.
 - 25 Coppens, M.-O. (2005) Structuring catalyst nanoporosity, in *Structured Catalysts and Reactors* 2nd edn (eds A. Cybulski and J.A. Moulijn), CRC Press, New York, pp. 779–806.
 - 26 Liu, W. (2007) Multi-scale catalyst design. *Chemical Engineering Science*, **62**, 3502–3512.
 - 27 Villermaux, J. (1993) Future challenges for basic research in chemical engineering. *Chemical Engineering Science*, **48**, 2525–2535.
 - 28 Keil, F.J. (1999) Diffusion and reaction in porous networks. *Catalysis Today*, **53**, 245–258.
 - 29 Mason, E.A. and Malinauskas, A.P. (1983) *Gas Transport in Porous Media: The Dusty Gas Model*, Elsevier, Amsterdam.
 - 30 Jackson, R. (1977) *Transport in Porous Catalysts*, Elsevier, Amsterdam.
 - 31 Kjelstrup, S., Bedeaux, D. and Johannessen, E. (2006) *Elements of Irreversible Thermodynamics for Engineers*, 2nd edn, Tapir Academic Press, Trondheim.
 - 32 Froment, G.F. (1999) Kinetic modeling of acid-catalyzed oil refining processes. *Catalysis Today*, **52**, 153–163.
 - 33 Dumesic, J.A., Rudd, D.F., Aparicio, L.M., Rekoske, J.E. and Trevino, A.A. (1993) *The Microkinetics of Heterogeneous Catalysis*, American Chemical Society, Washington, DC.
 - 34 Broadbelt, L.J. and Snurr, R.Q. (2000) Applications of molecular modeling in heterogeneous catalysis research. *Applied Catalysis A-General*, **200**, 23–46.
 - 35 Sahimi, M., Gavalas, G.R. and Tsotsis, T.T. (1990) Statistical and continuum models of fluid solid reactions in porous-media. *Chemical Engineering Science*, **45**, 1443–1502.
 - 36 Coppens, M.-O. (1999) The effect of fractal surface roughness on diffusion and reaction in porous catalysts: from fundamentals to practical applications. *Catalysis Today*, **53**, 225–243.

- 37 Morbidelli, M., Gavrilidis, A. and Varma, A. (2001) *Catalyst Design: Optimal Distribution of Catalyst in Pellets, Reactors and Membranes*, Cambridge University Press, Cambridge, U.K.
- 38 Graetzel, M. (2001) Molecular photovoltaics that mimic photosynthesis. *Pure and Applied Chemistry*, **73**, 459–467.
- 39 Mandelbrot, B.B. (1983) *The Fractal Geometry of Nature*, 2nd edn, Freeman, San Francisco.
- 40 Kearney, M.M. (2000) Engineered fractals enhance process applications. *Chemical Engineering Progress*, **96**, 61–68.
- 41 Coppens, M.-O. (2005) Scaling up and down in a nature inspired way. *Industrial & Engineering Chemistry Research*, **44**, 5011–5019.
- 42 Coppens, M.-O. (2003) *Nature Inspired Chemical Engineering*, Delft University Press, Delft.
- 43 Coppens, M.-O. (2004) Nature inspired chemical engineering – learning from the fractal geometry of nature in sustainable chemical engineering. in *Fractal Geometry and Applications: A Jubilee of Benoit Mandelbrot* Proceedings of Symposia in Pure Mathematics (eds M.L. Lapidus and M. van Frankenhuijsen), Vol. 72(2), 507–532.
- 44 West, G.B., Brown, J.H. and Enquist, B.J. (1997) A general model for the origin of allometric scaling laws in biology. *Science*, **276**, 122–126.
- 45 Gheorghiu, S., Kjelstrup, S., Pfeifer, P. and Coppens, M.-O. (2005) Is the Lung an Optimal Gas Exchanger? in *Fractals in Biology and Medicine* (eds T.F. Nonnenmacher G.A. Losa and E.R. Weibel), Springer.
- 46 Bejan, A. (2000) *Shape and Structure, from Engineering to Nature*, Cambridge University Press, Cambridge.
- 47 Mauroy, B., Filoche, M., Weiber, E.R. and Sapoval, B. (2004) An optimal bronchial tree may be dangerous. *Nature*, **427**, 633–636.
- 48 Kresge, C.T., Leonowicz, M.E., Roth, W.J., Vartuli, J.C. and Beck, J.S. (1992) Ordered mesoporous molecular sieves synthesized by a liquid-crystal template mechanism. *Nature*, **359**, 710–712.
- 49 Zhao, D.Y., Feng, J.L., Huo, Q.S., Melosh, N., Fredrickson, G.H., Chmelka, B.F. and Stucky, G.D. (1998) Triblock copolymer syntheses of mesoporous silica with periodic 50 to 300 angstrom pores. *Science*, **279**, 548–552.
- 50 Zhao, D.Y., Huo, Q.S., Feng, J.L., Chmelka, B.F. and Stucky, G.D. (1998) Nonionic triblock and star diblock copolymer and oligomeric surfactant syntheses of highly ordered, hydrothermally stable, mesoporous silica structures. *Journal of the American Chemical Society*, **120**, 6024–6036.
- 51 Rolison, D.R. (2003) Catalytic nanoarchitectures: the importance of nothing and the unimportance of periodicity. *Science*, **299**, 1698–1701.
- 52 Winterfeld, P.H., Scriven, L.E. and Davis, H.T. (1981) Percolation and conduction of random two-dimensional composites. *The Journal of Physical Chemistry*, **14**, 2361–2376.
- 53 Jerauld, G.R., Hatfield, J.C. Scriven, L.E. and Davis, H.T. (1984) Percolation and conduction on voronoi and triangular networks: a case study in topological disorder. *The Journal of Physical Chemistry*, **17**, 519–1529.
- 54 Sharratt, P.N. and Mann, R. (1987) Some observations on the variation of tortuosity with thiele modulus and pore size distribution. *Chemical Engineering Science*, **42**, 1565–1576.
- 55 Hollewand, M.P. and Gladden, L.F. (1992) Modeling of diffusion and reaction in porous catalysts using a random three-dimensional network model. *Chemical Engineering Science*, **47**, 1761–1770.
- 56 Beeckman, J.W. and Froment, G.F. (1980) Catalyst deactivation by site coverage and pore blockage. *Chemical Engineering Science*, **35**, 805–815.
- 57 Reyes, S. and Jensen, K.F. (1985) Estimation of effective transport

- coefficients in porous solids based on percolation concepts. *Chemical Engineering Science*, **40**, 1723–1734.
- 58 Sahimi, M. and Tsotsis, T.T. (1985) A percolation model of catalyst deactivation by site coverage and pore blockage. *Journal of Catalysis*, **96**, 552–562.
 - 59 Stauffer, D. and Aharony, A. (1994) *Introduction to percolation theory*, revised 2nd edn, Taylor & Francis, London.
 - 60 Sahimi, M. (1994) *Applications of Percolation Theory*, Taylor & Francis, London.
 - 61 Keil, F.J. (1996) Modelling of phenomena within catalyst particles. *Chemical Engineering Science*, 1543–1567.
 - 62 Burganos, V.N. and Sotirchos, S.V. (1987) Diffusion in pore networks: effective medium theory and smooth field approximation. *AIChE Journal*, **33**, 1678–1689.
 - 63 Kirkpatrick, S. (1973) Percolation and conduction. *Reviews of Modern Physics*, **45** (4), 574–588.
 - 64 Zhang, L. and Seaton, N.A. (1992) Prediction of the effective diffusivity in pore networks close to a percolation threshold. *AIChE Journal*, **38**, 1816–1824.
 - 65 Zhang, L. and Seaton, N.A. (1994) The application of continuum equations to diffusion and reaction in pore networks. *Chemical Engineering Science*, **49**, 41–50.
 - 66 Adler, P.M. (1992) *Porous Media: Geometry and Transport*, Butterworth-Heinemann, Stoneham.
 - 67 Dullien, F.A.L. (1992) *Porous Media: Fluid Transport and Pore Structure*, 2nd edn, Academic Press, New York.
 - 68 Gelb, L.D. and Gubbins, K.E. (1998) Characterization of porous glasses: simulation models, adsorption isotherms, and the Brunauer-Emmett-Teller analysis method. *Langmuir*, **14**, 2097–2111.
 - 69 Gelb, L.D. and Gubbins, K.E. (1999) Pore size distributions in porous glasses: a computer simulation study. *Langmuir*, **15**, 305–308.
 - 70 Sahimi, M. and Tsotsis, T.T. (2003) Molecular pore network models of nanoporous materials. *Physica B*, **338**, 291–297.
 - 71 Hollewand, M.P. and Gladden, L.F. (1992) Representation of porous catalysts using random pore networks. *Chemical Engineering Science*, **47**, 2757–2762.
 - 72 Reyes, S.C. and Iglesia, E. (1991) Effective diffusivities in catalyst pellets – new model porous structures and transport simulation techniques. *Journal of Catalysis*, **129**, 457–472.
 - 73 Pfeifer, P. and Avnir, D. (1983) Chemistry in noninteger dimensions between two and three. I. Fractal theory of heterogeneous surfaces. *Journal of Chemical Physics*, **79**, 3558–3565.
 - 74 Avnir, D., Farin, D. and Pfeifer, P. (1983) Chemistry in noninteger dimensions between two and three. II. Fractal surfaces of adsorbents. *Journal of Chemical Physics*, **79**, 3566–3565.
 - 75 Avnir, D. (ed.) (1989) *The Fractal Approach to Heterogeneous Chemistry*, John Wiley & Sons, Ltd, Chichester.
 - 76 Coppens, M.-O. and Froment, G.F. (1995) Diffusion and reaction in a fractal catalyst pore: I. Geometrical aspects. *Chemical Engineering Science*, **50**, 1013–1026.
 - 77 Coppens, M.-O. and Froment, G.F. (1995) Knudsen diffusion in porous catalysts with a fractal internal surface. *Fractals*, **3**, 807–820.
 - 78 Malek, K. and Coppens, M.-O. (2001) Effects of surface roughness on self- and transport diffusion in porous media in the Knudsen regime. *Physical Review Letters*, **87**, 125505.
 - 79 Levitz, P. (1993) Knudsen diffusion and excitation transfer in random porous media. *The Journal of Physical Chemistry*, **97**, 3813–3818.
 - 80 Levitz, P. (1997) From Knudsen diffusion to levy walks. *Europhysics Letters*, **39** (6), 593–598.
 - 81 Montroll, E.W. and Weiss, G.H. (1965) Random walks on lattices. II. *Journal of Mathematical Physics*, **6**, 167–183.
 - 82 Klafter, J. and Silbey, R. (1980) Derivation of the continuous-time random-walk

- equation. *Physical Review Letters*, **44**, 55–58.
- 83 Coppens, M.-O. and Froment, G.F. (1994) Diffusion and reaction in a fractal catalyst pore: III. Application to the simulation of vinyl acetate production. *Chemical Engineering Science*, **49**, 4897–4907.
 - 84 Coppens, M.-O. and Froment, G.F. (1996) Catalyst design accounting for the fractal surface morphology. *Chemical Engineering Journal*, **64**, 69–76.
 - 85 Nyikos, L. and Pajkossy, T. (1985) Fractal dimension and fractional power frequency-dependent impedance of blocking electrodes. *Electrochimica Acta*, **30**, 1533–1540.
 - 86 Meakin, P. (1986) Simulation of the effects of fractal geometry on the selectivity of heterogeneous catalysts. *Chemical Physics Letters*, **123**, 428–432.
 - 87 Gutfraind, R., Sheintuch, M. and Avnir, D. (1991) Fractal and multifractal analysis of the sensitivity of catalytic reactions to catalyst structure. *Journal of Chemical Physics*, **95**, 6100.
 - 88 Seri-Levy, A. and Avnir, D. (1993) Kinetics of diffusion-limited adsorption on fractal surfaces. *The Journal of Physical Chemistry*, **97**, 10380–10384.
 - 89 Pfeifer, P. and Sapoval, B. (1995) Optimization of diffusive transport to irregular surfaces with low sticking probability. *Materials Research Society Symposium Proceedings*, **366**, 271–277.
 - 90 Sapoval, B., Andrade, J.S. and Filoche, M. (2001) Catalytic effectiveness of irregular interfaces and rough pores: the “land surveyor approximation”. *Chemical Engineering Science*, **56**, 5011–5023.
 - 91 Giona, M., Schwalm, W.A., Schwalm, M.K. and Adrover, A. (1996) Exact solution of linear transport equations in fractal media – I. renormalization analysis and general theory. *Chemical Engineering Science*, **51**, 4717–4729.
 - 92 Giona, M., Schwalm, W.A., Schwalm, M.K. and Adrover, A. (1996) Exact solution of linear transport equations in fractal media – II. Diffusion and convection. *Chemical Engineering Science*, **51**, 4731–4744.
 - 93 Lindenberg, K., Sheu, W.-S. and Kopelman, R. (1991) Scaling properties of diffusion-limited reactions: fractals. *Physical Review A*, **43**, 7070–7072.
 - 94 Shlesinger, M.F., Zaslavsky, G.M. and Klafter, J. (1993) Strange kinetics. *Nature*, **363**, 31–37.
 - 95 Pfeifer, P., Ehrburger-Dolle, F., Rieker, T.P., González, M.T., Hoffman, W.P., Molina-Sabio, M., Rodríguez-Reinoso, F., Schmidt, P.W. and Voss, D.J. (2002) Nearly space-filling fractal networks of carbon nanopores. *Physical Review Letters*, **88**, 115502.
 - 96 Lee, S.Y. and Aris, R. (1985) The distribution of active ingredients in supported catalysts prepared by impregnation. *Catalysis Reviews: Science and Engineering*, **27**, 207–340.
 - 97 Komiyama, M. (1985) Design and preparation of impregnated catalysts. *Catalysis Reviews: Science and Engineering*, **27**, 341–372.
 - 98 Dougherty, R.C. and Verykios, X.E. (1987) Nonuniformly activated catalysts. *Catalysis Reviews: Science and Engineering*, **29**, 101–150.
 - 99 Gavrilidis, A., Varma, A. and Morbidelli, M. (1993) Optimal distribution of catalyst in pellets. *Catalysis Reviews: Science and Engineering*, **35**, 399–456.
 - 100 Morbidelli, M., Servida, A. and Varma, A. (1982) Optimal catalyst activity profiles in pellets. 1. The case of negligible external mass-transfer resistance. *Industrial & Engineering Chemistry Fundamentals*, **21**, 278–284.
 - 101 Morbidelli, M. and Varma, A. (1982) Optimal catalyst activity profiles in pellets. 2. The influence of external mass-transfer resistance. *Industrial & Engineering Chemistry Fundamentals*, **21**, 284–289.
 - 102 Morbidelli, M., Servida, A., Carra, S. and Varma, A. (1985) Optimal catalyst activity profiles in pellets. 3. The non-isothermal case with negligible external transport

- limitations. *Industrial & Engineering Chemistry Fundamentals*, **24**, 116–119.
- 103 Vayenas, C.G. and Pavlou, S. (1987) Optimal catalyst activity distribution and generalized effectiveness factors in pellets – single reactions with arbitrary kinetics. *Chemical Engineering Science*, **42**, 2633–2645.
 - 104 Vayenas, C.G. and Pavlou, S. (1987) Optimal catalyst distribution for selectivity maximization in pellets – parallel and consecutive reactions. *Chemical Engineering Science*, **42**, 1655–1666.
 - 105 Vayenas, C.G. and Pavlou, S. (1988) Optimal catalyst distribution for selectivity maximization in non-isothermal pellets – the case of parallel reactions. *Chemical Engineering Science*, **43**, 2729–2740.
 - 106 Morbidelli, M., Servida, A. and Varma, A. (1986) Optimal catalyst activity profiles in pellets. 4. Analytical evaluation of the isothermal fixed-bed reactor. *Industrial & Engineering Chemistry Fundamentals*, **25**, 307–313.
 - 107 Morbidelli, M., Servida, A., Carra, S. and Varma, A. (1986) Optimal catalyst activity profiles in pellets. 5. Optimization of the isothermal fixed-bed reactor. *Industrial & Engineering Chemistry Fundamentals*, **25**, 313–321.
 - 108 Summers, J.C. and Hegedus, L.L. (1978) Effects of platinum and palladium impregnation on performance and durability of automobile exhaust oxidizing catalysts. *Journal of Catalysis*, **51**, 185–192.
 - 109 Wu, H., Yuan, Q. and Zhu, B. (1990) An experimental study of optimal active catalyst distribution in pellets for maximum selectivity. *Industrial & Engineering Chemistry Research*, **29**, 1771–1776.
 - 110 Gavrilidis, A. and Varma, A. (1992) Optimal catalyst activity profiles in pellets. 9. Study of ethylene epoxidation. *AIChE Journal*, **38**, 291–296.
 - 111 Au, S.S., Dranoff, J.S. and Butt, J.B. (1995) Nonuniform activity distribution in catalyst particles – benzene hydrogenation on supported nickel in a single pellet diffusion reactor. *Chemical Engineering Science*, **50**, 3801–3812.
 - 112 van Donk, S., Janssen, A.H., Bitter, J.H. and de Jong, K.P. (2003) Generation, characterization, and impact of mesopores in zeolite catalysts. *Catalysis Reviews: Science and Engineering*, **45**, 297–319.
 - 113 Hollewand, M.P. and Gladden, L.F. (1995) Transport heterogeneity in porous pellets – I. PGSE NMR studies. *Chemical Engineering Science*, **50** (2), 309–326.
 - 114 Hollewand, M.P. and Gladden, L.F. (1995) Transport heterogeneity in porous pellets – II. NMR imaging studies under transient and steady-state conditions. *Chemical Engineering Science*, **50** (2), 327–344.
 - 115 Miyazawa, K. and Inagaki, S. (2000) Control of the microporosity within the pore walls of ordered mesoporous silica SBA-15. *Chemical Communications*, 2121–2122.
 - 116 Yang, C.M., Zibrowius, B., Schmidt, W. and Schüth, F. (2003) Consecutive generation of mesopores and micropores in SBA-15. *Chemistry of Materials*, **15**, 3739–3741.
 - 117 Naumov, S., Valiullin, R., Kaerger, J., Pitchumani, R. and Coppens, M.-O. (2008) Tracing pore connectivity and architecture in nanostructured silica SBA-15. *Microporous and Mesoporous Materials*, **110**, 37–40.
 - 118 Velez, O.D., Jede, T.A., Lobo, R.F. and Lenhoff, A.M. (1997) Porous silica via colloidal crystallization. *Nature*, **389**, 447–448.
 - 119 Holland, B.T., Blanford, C.F., Do, T. and Stein, A. (1999) Synthesis of highly ordered, three-dimensional, macroporous structures of amorphous or crystalline inorganic oxides, phosphates, and hybrid composites. *Chemistry of Materials*, **11** (3), 795–805.
 - 120 Xia, Y. and Whitesides, G.M. (1998) Soft lithography. *Angewandte Chemie-International Edition*, **37** (5), 550–575.
 - 121 Yang, P., Deng, T., Zhao, D., Feng, P., Pine, D., Chmelka, B.F., Whitesides, G.M. and Stucky, G.D. (1998) Hierarchically ordered oxides. *Science*, **282**, 2244–2246.

- 122 Ha, K., Lee, Y.J., Jung, D.Y., Lee, J.H. and Yoon, K.B. (2000) Micropatterning of oriented zeolite monolayers on glass by covalent linkage. *Advanced Materials*, **12**, 1614–1617.
- 123 Schacht, S., Huo, Q., Voigt-Martin, G., Stucky, G.D. and Schüth, F. (1996) Oil–water interface templating of mesoporous macroscale structures. *Science*, **273**, 768–771.
- 124 Sun, J.H., Shan, Z., Maschmeyer, T. and Coppens, M.-O. (2003) Synthesis of bimodal nano-structured silicas with independently controlled small and large mesopore sizes. *Langmuir*, **19**, 8395–8402.
- 125 Blin, J.-L., Léonard, A., Yuan, Z.-Y., Gigot, L., Vantomme, A., Cheetham, A.K. and Su, B.-L. (2003) Hierarchically mesoporous/macroporous metal oxides templated from polyethylene oxide surfactant assemblies. *Angewandte Chemie-International Edition*, **42** (25), 2872–2875.
- 126 Yuan, Z.-Y., Ren, T.-Z., Vantomme, A. and Su, B.-L. (2004) Facile and generalized preparation of hierarchically mesoporous-macroporous binary metal oxide materials. *Chemistry of Materials*, **16** (24), 5096–5106.
- 127 Yuan, Z.-Y. and Su, B.-L. (2006) Insights into hierarchically meso–macroporous structured materials. *Journal of Materials Chemistry*, **16**, 663–677.
- 128 Hartmann, M. (2004) Hierarchical zeolites: a proven strategy to combine shape selectivity with efficient mass transport. *Angewandte Chemie-International Edition*, **43** (44), 5880–5882.
- 129 Tao, Y.S., Kanoh, H., Abrams, L. and Kaneko, K. (2006) Mesopore-modified Zeolites: preparation, characterization, and applications. *Chemical Reviews*, **106**, 896–910.
- 130 Egeblad, K., Christensen, C.H., Kustova, M. and Christensen, C.H. (2008) Templating mesoporous zeolites. *Chemistry of Materials*, **20** (3), 946–960.
- 131 Jacobsen, C.J.H., Madsen, C., Houzvicka, J., Schmidt, I. and Carlsson, A. (2000) Mesoporous zeolite single crystals. *Journal of the American Chemical Society*, **122**, 7116–7117.
- 132 Schüth, F. (2003) Endo- and exotemplating to create high-surface-area inorganic materials. *Angewandte Chemie-International Edition*, **42**, 3604–3622.
- 133 Kustova, M., Egeblad, K., Zhu, K. and Christensen, C.H. (2007) Versatile route to zeolite single crystals with controlled mesoporosity: in situ sugar decomposition for templating of hierarchical zeolites. *Chemistry of Materials*, **19**, 2915–2917.
- 134 Kloetstra, K.R., van Bekkum, H. and Jansen, J.C. (1997) Mesoporous material containing framework tectosilicate by pore-wall recrystallization. *Chemical Communications*, 2281–2282.
- 135 Mokaya, R. (1999) Ultrastable mesoporous aluminosilicates by grafting routes. *Angewandte Chemie-International Edition*, **38** (19), 2930–2934.
- 136 Trong On, D. and Kaliaguine, S. (2002) Ultrastable and highly acidic, zeolite-coated mesoporous aluminosilicates. *Angewandte Chemie-International Edition*, **41** (6), 1036–1040.
- 137 Waller, P., Shan, Z., Marchese, L., Tartaglione, G., Zhou, W., Jansen, J.C. and Maschmeyer, T. (2004) Zeolite nanocrystals inside mesoporous TUD-1: a high-performance catalytic composite. *Chemistry – A European Journal*, **10** (20), 4970–4976.
- 138 Wang, J., Vinu, A. and Coppens, M.-O. (2007b) Synthesis and structure of silicalite-1/SBA-15 composites prepared by carbon templating and crystallization. *Journal of Materials Chemistry*, **17**, 4265–4273.
- 139 Liu, Y., Zhang, W. and Pinnavaia, T.J. (2000) Steam-stable aluminosilicate mesostructures assembled from zeolite type Y seeds. *Journal of the American Chemical Society*, **122** (36), 8791–8792.
- 140 Groen, J.C., Moulijn, J.A. and Perez-Ramirez, J. (2006) Desilication: on the controlled generation of mesoporosity in

- MFI zeolites. *Journal of Materials Chemistry*, **16**, 2121–2131.
- 141 Wang, J., Groen, J.C., Yue, W., Zhou, W. and Coppens, M.-O. (2007) Single-template synthesis of zeolite ZSM-5 composites with tunable mesoporosity. *Chemical Communications*, 4653–4655.
 - 142 Wang, J., Groen, J.C., Yue, W., Zhou, W. and Coppens, M.-O. (2008) Facile synthesis of ZSM-5 composites with hierarchical porosity. *Journal of Materials Chemistry*, **18** 468–474.
 - 143 Christensen, C.H., Johannsen, K., Schmidt, I. and Christensen, C.H. (2003) Catalytic benzene alkylation over mesoporous zeolite single crystals: improving activity and selectivity with a new family of porous materials. *Journal of the American Chemical Society*, **125**, 13370–13371.
 - 144 Kärger, J. and Vasenkov, S. (2005) Quantitation of diffusion in zeolite catalysts. *Microporous and Mesoporous Materials*, **85**, 195–206.
 - 145 Choi, M., Cho, H.S., Srivastava, R., Venkatesan, C., Choi, D.H. and Ryoo, R. (2006) Amphiphilic organosilane-directed synthesis of crystalline zeolite with tunable mesoporosity. *Nature Materials*, **5**, 718–723.
 - 146 Groen, J.C., Zhu, W.D., Brouwer, S., Huynink, S.J., Kapteijn, F., Moulijn, J.A. and Perez-Ramirez, J. (2007) Direct demonstration of enhanced diffusion in mesoporous ZSM-5 zeolite obtained via controlled desilication. *Journal of the American Chemical Society*, **129**, 355–360.
 - 147 Dogu, T. (1998) Diffusion and reaction in catalyst pellets with bidisperse pore size distribution. *Industrial & Engineering Chemistry Research*, **37**, 2158–2171.
 - 148 Carberry, J.J. (1962) The micro-macro effectiveness factor for the reversible catalytic reaction. *AIChE Journal*, **8**, 557–558.
 - 149 Carberry, J.J. (1962) Mass diffusion and isothermal catalytic selectivity. *Chemical Engineering Science*, **17**, 675–681.
 - 150 Ors, N. and Dogu, T. (1979) Effectiveness of bidisperse catalysts. *AIChE Journal*, **25**, 723–725.
 - 151 Kulkarni, B.D., Jayaraman, V.K. and Doraiswamy, L.K. (1981) Effectiveness factors in bidispersed catalysts – the general nth order case. *Chemical Engineering Science*, **36**, 943–945.
 - 152 Jayaraman, V.K., Kulkarni, B.D. and Doraiswamy, L.K. (1983) A simple method for the solution of a class of reaction diffusion problems. *AIChE Journal*, **29** (3), 521–523.
 - 153 Namjoshi, A.N., Kulkarni, B.D. and Doraiswamy, L.K. (1984) Initial value approach to a class of reaction-diffusion systems. *AIChE Journal*, **30** (6), 915–924.
 - 154 Villiermaux, J., Schweich, D. and Authelin, J.-R. (1987) Transfert et Reaction à une Interface Fractale Représentée Par le «Peigne du Diable». *C.R Acad Sci Sér*, **2**, 304, 399–404.
 - 155 Mougin, P., Pons, M. and Villiermaux, J. (1996) Reaction and diffusion at an artificial fractal interface: evidence for a new diffusional regime. *Chemical Engineering Science*, **51**, 2293–2302.
 - 156 Giona, M., Schwalm, W.A., Adrover, A. and Schwalm, M.K. (1996a) First-order kinetics in fractal catalysts: renormalization analysis of the effectiveness factor. *Chemical Engineering Science*, **51**, 2273–2282.
 - 157 Sheintuch, M. (2000) On the intermediate asymptote of diffusion-limited reactions in a fractal porous catalyst. *Chemical Engineering Science*, **55**, 615–624.
 - 158 Sheintuch, M. (2001) Reaction engineering principles of processes catalyzed by fractal solids. *Catalysis Reviews: Science and Engineering*, **43**, 233–289.
 - 159 Wakao, N. and Smith, J.M. (1962) Diffusion in catalyst pellets. *Chemical Engineering Science*, **17**, 825–834.
 - 160 Hegedus, L.L. (1980) Catalyst pore structure by constrained nonlinear optimization. *Industrial & Engineering Chemistry Product Research and Development*, **19**, 533–537.

- 161 Pereira, C.J., Kubsh, J.E. and Hegedus, L.L. (1988) Computer-aided-design of catalytic monoliths for automobile emission control. *Chemical Engineering Science*, **43**, 2087–2094.
- 162 Beeckman, J.W. and Hegedus, L.L. (1991) Design of monolith catalysts for power-plant NO_x emission control. *Industrial & Engineering Chemistry Research*, **30**, 969–978.
- 163 Loewenberg, M. (1994) Diffusion-controlled, heterogeneous reaction in a material with a bimodal pore size distribution. *Journal of Chemical Physics*, **100**, 7580–7589.
- 164 Keil, F.J. and Rieckmann, C. (1994) Optimization of three-dimensional catalyst pore structures. *Chemical Engineering Science*, **49**, 4811–4822.
- 165 El-Nafaty, U.A. and Mann, R. (1999) Support-pore architecture optimization in FCC catalyst particles using designed pore networks. *Chemical Engineering Science*, **54**, 3475–3484.
- 166 Prachayawarakorn, S. and Mann, R. (2007) Effects of pore assembly architecture on catalyst particle tortuosity and reaction effectiveness. *Catalysis Today*, **128**, 88–99.
- 167 Coppens, M.-O. and Froment, G.F. (1997) The effectiveness of mass fractal catalysts. *Fractals*, **5**, 493–505.
- 168 Gheorghiu, S. and Coppens, M.-O. (2004) Optimal bimodal pore networks for heterogeneous catalysis. *AIChE Journal*, **50**, 812–820.
- 169 Wang, G., Johannessen, E., Kleijn, C.R., de Leeuw, S.W. and Coppens, M.-O. (2007) Optimizing transport in nanostructured catalysts: a computational study. *Chemical Engineering Science*, **62**, 5110–5116.
- 170 Johannessen, E., Wang, G. and Coppens, M.-O. (2007) Optimal distributor networks in porous catalyst pellets. I. Molecular diffusion. *Industrial & Engineering Chemistry Research*, **46**, 4245–4256.
- 171 Wang, G. and Coppens, M.-O. (2008) Calculation of the optimal macropore size in nanoporous heterogeneous catalysts and its application to DeNO_x catalysis. *Industrial & Engineering Chemistry Research*, **47**, 3847–3855.
- 172 van Donk, S., Bitter, J.H., Verberckmoes, A., Versluijs-Helder, M., Broersma, A. and de Jong, K.P. (2005) Physicochemical characterization of porous materials: spatially resolved accessibility of zeolite crystals. *Angewandte Chemie-International Edition*, **44** (9), 1360–1363.
- 173 Kortunov, P., Vasenkov, S., Kärger, J., Valiullin, R., Gottschalk, P., Fé Elía, M., Perez, M., Stöcker, M., Drescher, B., McElhiney, G., Berger, C., Gläser, R. and Weitkamp, J. (2005) The role of mesopores in intracrystalline transport in USY zeolite: PFG NMR diffusion study on various length scales. *Journal of the American Chemical Society*, **127**, 13055–13059.
- 174 Keil, F.J. and Rieckmann, C. (1997) Multicomponent diffusion and reaction in three-dimensional networks: general kinetics. *Industrial & Engineering Chemistry Research*, **49**, 3275–3281.
- 175 Keil, F.J. and Rieckmann, C. (1999) Simulation and experiment of multicomponent diffusion and reaction in three-dimensional networks. *Chemical Engineering Science*, **54**, 3485–3493.
- 176 Havlin, S. and Ben-Avraham, D. (1992) Diffusion in disordered media. *Advances in Physics*, **51** (1), 187–292.
- 177 Gavalas, G.R. and Kim, S. (1981) Periodic capillary models of diffusion in porous solids. *Chemical Engineering Science*, **36**, 1111–1122.
- 178 Derjaguin, B.C. (1946) Measurement of the specific surface of porous and disperse bodies by their resistance to the flow of varified gases. *Compt. Rend. Acad. Sci. U RSS*, **53**, 626–626.
- 179 Janssen, A.H., Koster, A.J. and de Jong, K.P. (2001) Three-dimensional transmission electron microscopic observations of mesopores in dealuminated zeolite Y. *Angewandte Chemie-International Edition*, **40**, 1102–1104.

3

Use of Dendrimers in Catalyst Design

Bert D. Chandler, Jeong-Kyu Lee, Harold H. Kung, and Mayfair C. Kung

3.1

Introduction

Dendrimers are a specific class of hyperbranched polymers that emanate from a single core and ramify outward with each subsequent branching unit [1–4]. They have well-defined and nearly monodisperse architectures that arise from the regular nature of their repeat units. Several classes of dendrimers are known, including polypropyleneimine (PPI), polyamidoamine (PAMAM), and Fréchet-type polyether dendrimers [1, 2]. Many dendrimers are now commercially available, making them convenient building blocks for a variety of nanoscale architectures. Many classes of dendrimers are readily functionalized to terminate in diverse moieties such as primary amines, carboxylates, hydroxyls, or hydrophobic alkyl chains. Since dendrimer composition, size, and end groups can be varied, they are typically named by their generation (G1, G2, etc.), building blocks (PAMAM, PPI, etc.), and exterior functionality ($-\text{NH}_2$, $-\text{OH}$).

Higher generation dendrimers (G4 and larger) adopt roughly spherical or globular structures, with exterior branches becoming increasingly intertwined. The interweaving of dendrimer branches is distinct from the cross-linked branches that are found in many polymeric colloid stabilizers. The macromolecular dendritic architecture gives rise to a relatively open interior pocket for high-generation dendrimers, while maintaining a closed, porous exterior. The presence of these open spaces within the dendrimer's interior and the synthetic control over dendrimer composition, architecture, and interior/exterior functionalities creates an environment that affords opportunities to build unique molecular architectures and facilitate trapping guest species [5, 6].

In this article, we focus on structure–functions relationships in the use of dendrimers as templates or as catalysts. It is not intended to be a comprehensive review of dendrimers as catalysts, as supports for catalysts, or as a vehicle for the synthesis of catalysts. There are a number of excellent recent reviews covering different aspects of dendrimers in catalysis, including a recent volume of *Topics in Organometallic Chemistry* [7–9]. The focus of this article will be to highlight several

examples from the literature of how structural features unique to the dendrimer architecture have been harnessed when dendrimers were used as catalysts and catalyst templates. In doing so, we explore how various research groups have used dendrimers to control catalytic structures, and how dendrimer structure and control of the active site impacts catalytic activity.

3.2

Modified Dendrimer Catalysts

One motivation for using dendrimers as templates to construct catalytic structures is the desire to capture the unique properties and functionalities of enzymes in artificial structures. Enzymes are among the most active and selective catalysts known. The functional groups that comprise the catalytic active site are often situated in a hydrophobic pocket and in a configuration conducive to multiple cooperative interactions between the enzyme and substrate(s). These complex interactions are tailored to favor binding between enzyme and specific substrate(s). This substrate specificity, for example, has been illustrated using methane monooxygenase to selectively oxidize a series of alkanes (ethane to pentane) to the corresponding alcohols. The rate constants relative to that of ethane were found to decrease steadily with increasing alkane chain length [10].

3.2.1

Dendrimer Synthesis

Dendrimer architectures and their uses in catalysis are derived largely from the synthetic strategies employed in their preparation, so a brief discussion of relevant synthetic schemes is warranted. A dendrimer is constructed from AB_n building blocks, where A and B are monomer groups of orthogonal chemical reactivity, and n is the number of B functional groups on the branching unit. These focal points dictate how the dendrimer branches, and provide for a controlled and specific branching mechanism that differentiates dendrimers from other highly branched polymers. The orthogonal reactivity is similarly critical and may be designed such that A and B are inherently different, or that B is a profunctional or a protected functional group that can be activated as necessary in the course of dendrimer synthesis.

In the commonly used divergent synthesis, a dendrimer is built from the core outward to the periphery. The branches are attached to the core through reaction of A with functionalities issuing from the core, which is a molecule containing several B units. A generation zero (G0) dendrimer is formed when the first AB_n unit is attached to each core functionality. A first-generation (G1) dendrimer is formed by reacting the activated B functional groups at the periphery of the branches of G0 with other AB_n monomers. Through this iterative growth process, multiple generations of dendrimers can be constructed. This process is nominally reversed for the convergent synthesis, where several dendritic subunits are assembled onto a single core molecule (which also may be a low-generation dendrimer).

3.2.2

Dendrimer Properties Important for Catalysis

There are several advantages to using dendrimers as catalysts or as platforms for catalysts. The highly branched architecture and repeating composition of dendrimers permit high catalyst loadings when the active components are either in/on the branches or at the periphery of the structure. Dendrimers can be solubilized in a variety of different solvents by derivatizing the periphery, thereby retaining the advantages of homogeneous catalysts but avoiding potential pore diffusion limitations in heterogenized systems. Yet dendrimers are small polymer molecules that can be separated from the reaction medium with nanofiltration or membrane reactors [11]. When properly derivatized, the periphery can coordinate and concentrate substrates, hence increasing the overall reaction rates [12] or create an environment more conducive to reaction [13].

3.2.3

Cooperative Catalysis

The functional groups in a dendrimer are usually closely situated and preorganized in relatively well-defined spatial orientations. These attributes foster cooperative catalysis in a manner similar to what occurs in the molecular cavity of an enzyme. Cooperativity can result when one functional group(s) in the catalytic center enhances the reactivity of another functional group(s) through nonbonding interactions, orients the substrates, and/or stabilizes the transition state. Enhanced catalytic performance can also occur when multicatalytic centers act in concert to effect a reaction. These concepts are illustrated in the examples below.

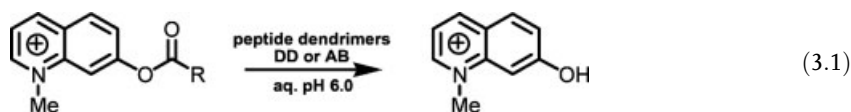
The dense packing of functional groups at the periphery of higher generation dendrimers creates opportunities for these groups to act in concert. Simultaneous activation of a substrate and a nucleophile can occur on closely situated functional groups. Thus, significantly accelerated reaction rates result because the reacting groups are brought close to each other.

Asymmetric epoxide ring opening is an example of a reaction that can proceed through cooperative bimetallic catalysis [14]. Over these catalysts, one metal complex serves as the binding site for the epoxide while another metal complex activates the nucleophile. Breinbauer *et al.* [15] derivatized the periphery of a PAMAM dendrimer with chiral $[\text{Co}^{\text{III}}\text{--}(\text{salen})]$ complexes and investigated their catalytic activity. Using the kinetic hydrolytic resolution of (rac)-1,2 epoxyhexane as a probe reaction, the activity of a monomeric $[\text{Co}^{\text{III}}\text{--}(\text{salen})]$ complex was compared to a PAMAM dendrimer with four Co-salen complexes and a dimeric analog of the dendrimer catalyst. The derivatized dendrimer outperformed the dimeric model compound (on a per Co basis), and the control monomer was inactive under the test condition.

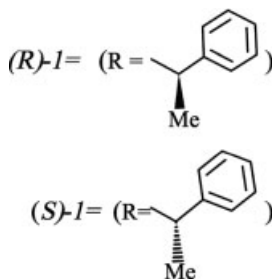
In another example, the hydrolysis of phosphate diesters with a dinuclear Zn complex was found to be faster than its mononuclear analog. The difference has been attributed to the cooperative role of the ions in stabilizing the transition state and in altering the $\text{p}K_{\text{a}}$ of the H_2O bound to the Zn complex [16]. Martin *et al.* [17] prepared

a series of catalysts with varying degrees of derivatization of the peripheral groups of a G3 DAB (poly(propylene imine)) dendrimer with triazacyclononane (TACN) ligands that bind Zn^{II} complexes. The remaining NH_2 groups on the periphery were then inactivated by reaction with acetic anhydride. When this series of dendrimers was tested for the cleavage of 2-hydroxypropyl-*p*-nitrophenyl phosphate (HPNPP), a model substrate of a RNA phosphodiester, they observed a faster-than-statistical increase in the hydrolysis activity with an increase in the density of peripheral TACN complexes. This nonlinear dependence indicated that more than one Zn complex acted in a cooperative manner in the cleavage of HPNPP. The DAB dendrimers with fully functionalized peripheries are among the most active catalysts reported for the cleavage of the RNA model substrate HPNPP.

Cooperativity between different amino acids in the branching units of peptide dendrimers is among the most convincing evidence of the importance of precise positioning of functional groups. Reymond and coworkers prepared a series of peptide dendrimers as model esterases using solid-state synthesis with 1,3-diaminoisopropoxyacetic acid as the branching units that conferred dendritic architecture [18]. In the hydrolysis of 7-acetoxy-1-methylquinolinium sulfate (Equation 3.1 where $\text{R} = \text{CH}_3$), they observed that catalytic activity was associated with the presence of histidine residues at the outermost positions of the dendrimers. The rate of catalysis for the most active peptide dendrimer is ~ 1000 times that of the uncatalyzed reaction.



They extended this initial study to a combinatorial series of 21 different peptide dendrimers distributed in the scheme shown in Figure 3.1 [19]. Employing solid-phase peptide synthesis, second-generation peptide dendrons with the amino acid cysteine at the apex were synthesized using Fmoc-protected 3,5-diaminobenzoic acid as the branching unit (B). Amino acids aspartate, histidine, and serine (D, H, S) were placed at variable positions A^1 , A^2 , and A^3 to form six different dendrons (A to F). Coupling of two dendrons at the cysteine units resulted in dendrimer D1. With these six dendrons, there are 21 possible pairing, and thus 21 possible dendrimer compositions. These dendrimers were used to catalyze the aqueous hydrolysis of 7-acetoxyhydroxy-*N*-methyl esters (where $\text{R} = \text{CH}_3$ in Equation 3.1). They found that only dendrimers D1-AB and D1-DD were effective ester hydrolysis catalysts. Common to both dendrimers is the histidine at the A^2 position.



Fmoc amino acids (A^1 , A^2 , A^3 = His, Asp, Ser), Fmoc-3,5 diaminobenzoic acid

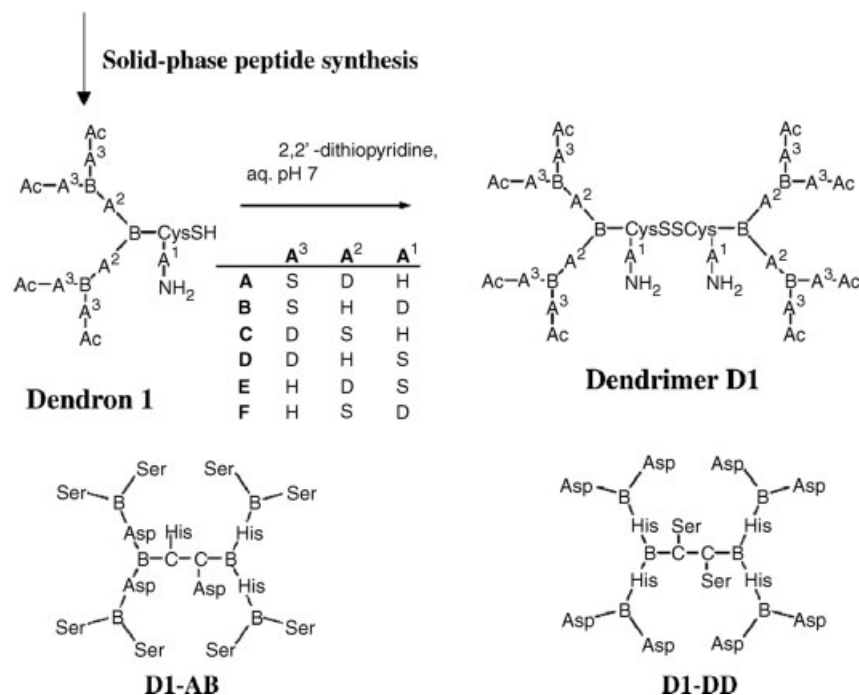


Figure 3.1 Combinatorial scheme of 21 peptide dendrimers synthesized to investigate cooperativity in the hydrolysis of 7-acetoxyhydroxy-*N*-methyl esters. Adapted from [19]. The letters S, H, and D stand for serine, histidine, and aspartate, respectively. **D1-AB** and

D1-DD are examples of the dendrimers formed through heterodimerization of monomers **A** and **B** and homodimerization of monomers **D**, respectively. Reprinted with permission. Copyright 2004 American Chemical Society.

Dendrimer **D1-DD** was tested to see whether it could discriminate between the (*S*)-1 and (*R*)-1 enantiomers of 2-phenylpropionate ester. The catalyst showed substrate selectivity, with (*S*)-enantiomer reacting 2.8 times faster than the (*R*) enantiomer. Cooperativity of histidine at the A^2 position was tested by its systematic replacement in dendrimer **D1-DD** with alanine. When all four histidines in the A^2 position were replaced, the dendrimer became inactive. Surprisingly, the catalytic efficiency was reduced by 75% even with just one histidine replaced by alanine. Furthermore, dendrimers with one, two or three histidines in the A^2 position showed comparable reactivities. A proposed mechanism for the cooperativity involves one histidine acting as the nucleophile while the other histidines serve to stabilize the oxyanion in the tetrahedral intermediate. Another possible contributing factor to the rate enhancement involves the possible modulation of pK_a values via interactions between the various histidines.

Complete replacement of serine in the A^1 position had little effect on the catalytic activity, suggesting that it is not essential for catalysis. Dendrimers **D1-DD** and

D1-BB both have histidine at the A² position, but differ in that the amino acids in A¹ and A³ positions are switched. Dendrimer **D1-BB** does not catalyze ester hydrolysis, implying that the aspartate at position A³ is important for catalysis. A proposed role for the anionic aspartate is that it is involved in the molecular recognition of the cationic quinolinium ester. Thus, this work demonstrated how multiple amino acids in the dendrimer architecture cooperate to effect catalysis: the periphery aspartate amino acids are involved in substrate recognition and the four histidine residues on the branches in the interior of the dendrimer act to effect nucleophilic attack and stabilize the transition state.

3.2.4

Site Isolation

A common approach to increasing the stability of a homogeneous catalyst is encapsulation in a polymeric matrix. Encapsulation in a dendrimer matrix offers more precise control of the environment around the active site than random encapsulation in a soluble polymer with poorly defined topology. In this application, the catalytic unit of interest is often installed as the core of the dendrimer and dendritic branches are constructed around it to optimize its stability via steric isolation. Many examples are present where metal complexes installed as the core of the dendrimer exhibit enhanced stability. For example, Pd^{II} complexes stabilized by para-substituted pyridine ligands derivatized with a 2,3,4,5-tetraphenylphenyl substituent and its higher dendritic units were found to be excellent catalysts for the air oxidation of alcohols. Formation of Pd black was completely suppressed [20]. In another example, Hu *et al.* [21] used a G2 chiral binaphthyl-based rigid dendrimer as catalyst for the addition of diethyl zinc to benzaldehyde. The high activity of this catalyst relative to the parent BINOL was attributed to the prevention of formation of Zn–O–Zn aggregates due to steric constraint of the rigid and bulky dendrimer arms.

Ni complexes bearing bidentate (P,O) ligands such as *o*-diphenylphosphinophenol **2** (Figure 3.2) are catalytically active for the oligomerization of ethylene when they are in the chelated monomeric form (**2b**) but are inactive when they dimerize to form the bis(P,O) complex (**2c**). Olefin oligomerization activity was compared for Ni complexed to **2** and to *o*-diphenylphosphinophenol installed as the core of a carbosilane dendrimer (dendrimer **D2**, Figure 3.2) [22]. In a nonpolar solvent, Ni with the dendritic ligand is site isolated and thus suppressing the formation of the bis(P,O) Ni complex and resulting in a more productive catalyst relative to Ni complexed to **2**. In a polar solvent such as methanol, a medium that favors the bis(P,O) Ni complexes, Ni complexed to **2** is inactive. Ni complexed to **D2** is still able to effect catalysis, albeit at a lower rate, due to the ability of the bis(P,O) Ni complex to dissociate into the monoligated form under reaction conditions.

N-Heterocyclic carbene (NHC) ligands form stronger bonds to metals than more conventional ligands such as phosphines [23]. Tsuji's group studied ketone hydrosilylation using dendrimer **D3**, in which an Rh–NHC complex was installed as a core. The initial study utilized a Fréchet-type polybenzyl ether dendrimer (R = **3b**). The product yield was 4–8 times higher than the Rh–NHC complexes not encapsulated

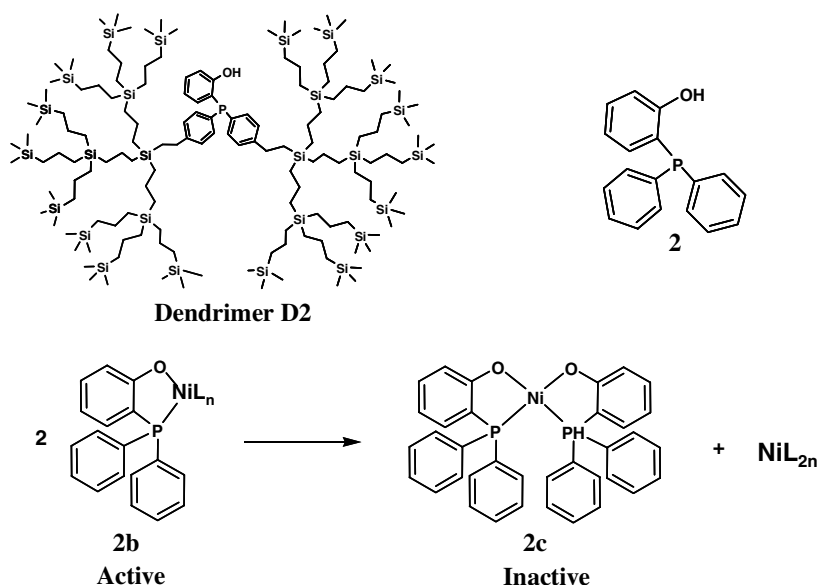


Figure 3.2 Core-functionalized dendritic P,O ligand (**dendrimer D2**) and the smaller parent ligand (**2**) used to chelate Ni to catalyze oligomerization of ethylene. Reprinted with permission from [22]. Copyright 2004 American Chemical Society.

by dendritic branches. Furthermore, the yield enhancement increased with the generation number of the dendrimer.

The researchers extended the study to investigate the effect of dendrimer branch flexibility on the catalytic performance of a Rh–NHC complex (Figure 3.3) [24].

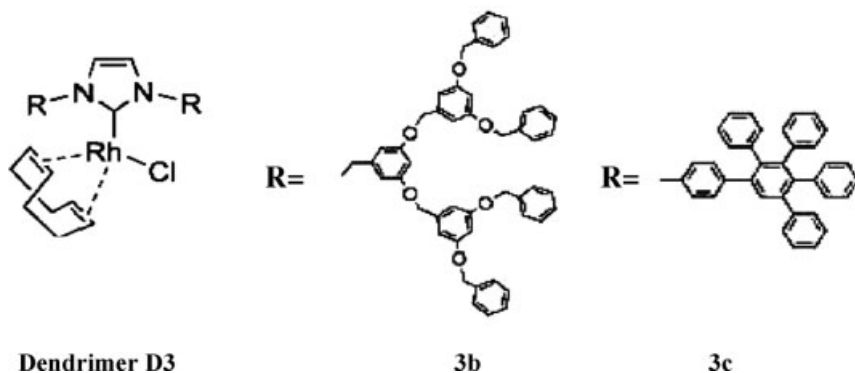
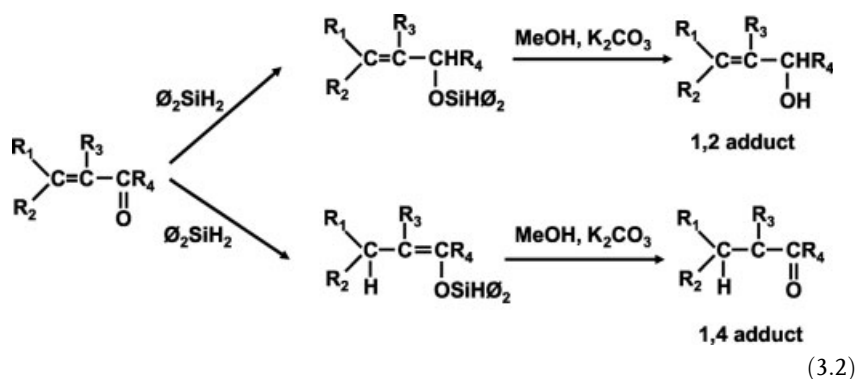


Figure 3.3 Dendrimer **D3**, Rh complexed to NHC ligands installed as the core and surrounded by dendrons constructed using polybenzyl ether (**3b**) or 2,3,4,5-tetraphenylphenyl (TPPh) (**3c**). These dendrimers are used for the hydrosilylation of ketones. Adapted from [24]. Reprinted with permission. Copyright 2007 RSC Publishing.

Hydrosilylation of α,β -unsaturated ketones with Ph_2SiH_2 followed by methanolysis will result in 1,4 and 1,2 adducts (Equation 3.2). The hydrosilylation–methanolysis of 2-cyclohexen-1-one with Ph_2SiH_2 in the presence of homogeneous catalysts such as Rh-NHC complexes and $\text{RhH}(\text{PPh}_3)_4$ resulted in 1,2 adduct (2-cyclohexen-1-ol) selectivity of 92 and 100%, respectively. When this reaction was conducted using **D3** constructed with flexible dendrons ($\text{R} = \mathbf{3b}$) as the catalyst, the product selectivity was 61% 1,2-adduct. In contrast, when the dendritic branches are rigid (e.g., $\text{R} = \mathbf{3c}$), the major product (91% selectivity) was the 1,4 adduct (cyclohexanone). The flexible dendrons are known to fold back around the active site and thus the Rh active sites have characteristics closer to that of Rh solution complexes. It is intriguing that the rigid branches around the active site can cause a reversal in the regioselectivity.



3.3

Indirect Effects of Dendrimer Architecture

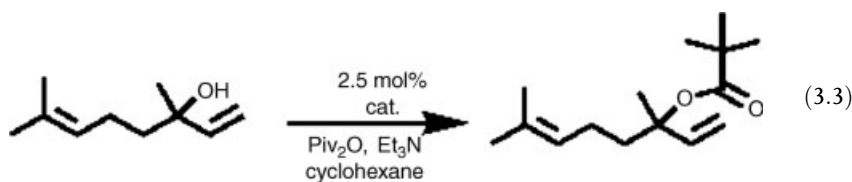
Beyond the ability to carefully control catalyst and active site synthesis, dendrimers offer a number of more general properties that are potentially advantageous for catalysis. Properties like backbone rigidity, polarity gradients from the dendrimer exterior to interior, and diffusion through the dendrimer branches may all have important effects on catalytic activity – either positively or negatively. While many of these properties are very attractive, some of them can also be achieved by appropriate soluble polymers, which are generally easier to prepare than dendrimers. Thus, the choice of using a dendrimer versus soluble polymer depends on the balance between gains in catalytic performance with the difficulty in their synthesis.

3.3.1

Polarity Gradients

Judicious choices of core, branching units, and end groups of a dendrimer can generate a controlled gradient of polarity from the core to the periphery. This precise control of the nanoenvironment can be utilized to affect the course of a reaction.

Fréchet's group has investigated this extensively. Fréchet-type benzyl ether and aliphatic ester dendrimers were constructed from a common trivalent core containing three 4-(dimethylamino) pyridine (DMAP) groups and were used as catalysts for the acylation of linalol, a tertiary alcohol, with pivalic anhydride (Equation 3.3) [25]. The preferential partition of the alcohol from the cyclohexane solvent into the polar interior of the polyester dendrimer created a local, high concentration of the substrates at the active centers at the core and dramatically enhanced the reactivity compared to the DMAP control. In addition, the product, being substantially less polar than the alcohol, is likely to partition into the nonpolar solvent, further affecting the reaction in a positive manner. The polyester platform appeared to be more effective than a benzyl ether one.



This theme of difference in polarity between the dendrimer's interior and exterior was also explored for the elimination of tertiary halides in nonpolar solvents using a tetradecyl chain terminated poly(benzyl ether) dendrimer [26]. The polar halides are concentrated near the active center and the nonpolar alkenes are partitioned into the nonpolar medium. In addition, the interior hydroxymethyl functional groups on the branches can stabilize the transition state. As a consequence of these favorable features, an impressive turnover number of approximately 17 400 was observed.

3.3.2

Steric and Diffusion Effects

It is often observed that when a catalytic unit is placed in the interior of a dendrimer, the reaction rate decreases with increasing generation number [27]. This effect is due to steric crowding at the dendrimer periphery, reducing accessibility of the catalytic site [28]. A detailed quantitative analysis of this adverse dendritic effect was conducted by Zubia *et al.* [29]. They installed a single tertiary amine catalytic core into a series of dendrimers with different inert branches. Figure 3.4 shows the various G2, structurally related, trialkylamine dendrimers with different indices of branching. The effect of generation number and branching indices on the rate of the Henry (nitroaldo) reaction was then examined, and they observed a decrease in the rate with increasing generation number and branching index. Supported by molecular dynamics simulation, the observation could be explained by the accessibility of the catalytic core to the reactants. Having steric bulk at the dendrimer periphery can also have advantages for reactant selectivity, preferentially catalyzing reactions of smaller, more mobile molecules over larger molecules that have difficulty diffusing through the dendrimer branches (see Section 3.4.2)

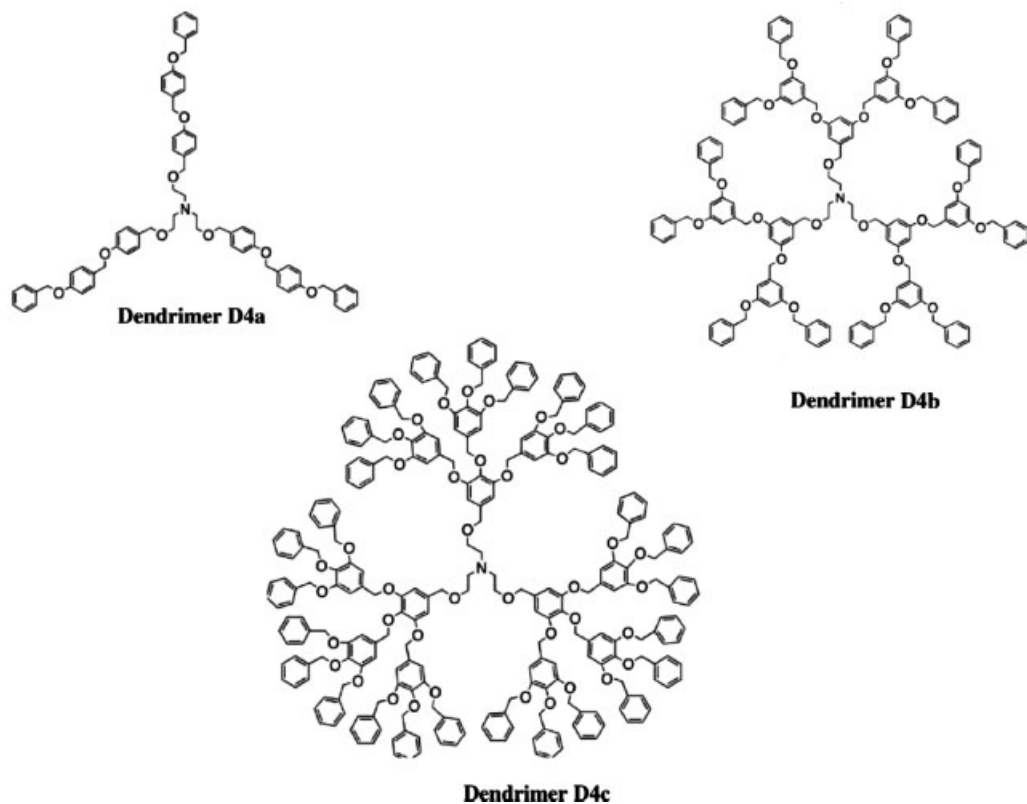
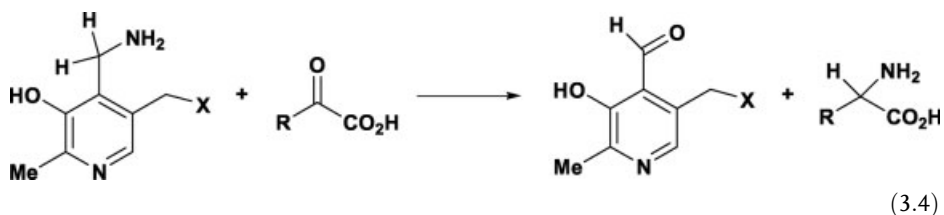


Figure 3.4 G2 dendrimers with a common tertiary amine catalytic core surrounded by dendritic branches with different degrees of branching. Adapted from [29]. Copyright 2004 American Chemical Society.

3.3.3

Comparing Dendrimers with Soluble Polymers

Since dendrimers are highly branched polymers that are nearly monodisperse, it is of interest to compare and contrast them with soluble polymers as platforms for catalysis. The example of α -keto acid reaction with pyridoxamine to form amino acid and pyridoxal (Equation 3.4) will be used for this purpose:



This reaction is the first stage of the two-stage transamination reaction in the biological system [30]. Through a general acid–base catalysis mechanism assisted by the coenzyme pyridoxamine, the lysine residue of an aminotransferase transforms an α -keto acid to an amino acid. In this stage of the reaction, the pyridoxamine is converted to pyridoxal, which is then regenerated in the second stage by reaction with a sacrificial amino acid. Both stages require the two catalytic components (the catalytic amino group and coenzyme pyridoxamine/pyridoxal) to be in a hydrophobic environment and work in synchrony.

Breslow's group extensively examined the first stage of transamination, the stoichiometric reaction of α -keto acid with pyridoxamine (Equation 3.4). They compared pyridoxamine attached to a polyimine polymer (PEI–PM) [31, 32] with one installed as the core of an NMe₂ terminated PAMAM dendrimer (PAMAM–PM) [33]. The ratio of amino groups to pyridoxamine amine is 3:1 in PEI–PM, whereas it varies as a function of 2^n in PAMAM–PM, where n is the generation number. Pyruvic acid ($R = -CH_3$) and phenylpyruvic acid ($R = -CH_2Ph$) were the α -keto acids investigated using both the PEI–PM and PAMAM–PM systems; Michaelis–Menten kinetics were observed in all cases.

Pyruvic acid transformation to alanine was dramatically faster in the PEI–PM system compared with the control system of pyridoxamine in aqueous buffer [31, 32] because pyridoxamine was sequestered from the aqueous environment in the polymer matrix and because an effective general acid–base catalyst (another amine) was absent in the control system. Phenylpyruvic acid and pyruvic acid exhibited comparable reactivities with PEI–PM, but the former reacted significantly faster with G6 PAMAM–PM. When the hydrophobicity around pyridoxamine was increased further through laurylating 10% and methylating 90% of the amine groups of the PEI polymer, there was a modest increase in the observed rate constant with pyruvic acid but a dramatic increase for phenylpyruvic acid [32]. This was due to the attractive interaction between the phenyl group of the substrate and the lauryl group of the polymer. In contrast, modification of NMe₂ with lauryl groups had little effect on the rates of the transamination reactions. The observed differences in G6 PAMAM–PM and PEI–PM indicate that the dendritic architecture of a higher generation PAMAM dendrimer, as compared with a soluble polymer, is better able to isolate the pyridoxamine from the surrounding medium and create a hydrophobic nanoenvironment so that discrimination between substrates of different hydrophobicity is possible.

Acetylation of NH₂ groups at the periphery of the PAMAM dendrimer caused a precipitous drop in the reaction rates without affecting K_M . This suggests that the terminal NMe₂ are much more effective general acid–base catalysts than the internal tertiary amines surrounding pyridoxamine at the core. This type of information is only obtainable with a topologically well-defined system like the dendrimer and is invaluable for understanding structure–reactivity relationships.

The cooperativity of the pyridoxamine and the periphery amino groups in the PAMAM–PM system is proposed to occur by the folding of the flexible chains of the dendrimer into the void space near the core [34]. This is supported by the observation of enantioselectivities when the terminal amino groups are chiral [35]. Such a manner

of accessing the core by terminal amines is sterically demanding. Consequently, experiments conducted with PAMAM-PM have to be conducted at 60 °C instead of at 30 °C with PEI-PM. Thus, steric factors play a large role in decreasing the activities of dendrimer based catalysts.

3.3.4

Other Novel Dendrimer Effects

Several examples of large reactivity enhancements using dendrimer-based catalysts may have practical implications, although they are not yet fully understood. One example involves *in situ* generation of active sites. Drake *et al.* observed a dramatic dendrimer effect when they used a Frechét-type dendrimer terminating in $-\text{O}(\text{CH}_2)_2\text{SePh}$ as a catalyst for the bromination of cyclohexene with H_2O_2 and NaBr [36]. They attributed the large rate enhancement (normalized per Se) to autocatalysis: Br^+ formed from the noncatalyzed reaction of H_2O_2 with NaBr oxidized a peripheral SePh to a catalytically active $\text{Se}(=\text{O})\text{Ph}$ [37]. This oxidized Se, besides being the active species for cyclohexene bromination, also catalyzes the formation of Br^+ that is used to activate a neighboring Se. Interestingly, the catalytic activity in bromination of cyclohexene for selenoxides associated with G3 dendrimers was higher than for monomeric $\text{PhO}(\text{CH}_2)_2\text{SePh}$, suggesting that additional cooperative effects might be involved.

Another example involves the construction of heterometallic dendrimers (dendrimer **D5a**) in which the placement of the various redox groups can be controlled [38]. The cyclic voltammogram of dendrimer **D5a** showed two diffusion-controlled, reversible oxidation processes at about $E_{1/2} = 0.51 \text{ V}$ and $E_{1/2} = 0.93 \text{ V}$ (versus SCE), ascribed to the oxidation of iron and chromium centers, respectively. The $E_{1/2}$ value for the oxidation of the iron centers is slightly higher for **D5a** than that of the related homometallic dendrimer **D5b** due to the electron-withdrawing nature of the silicon-linked adjacent $(\eta^6\text{-C}_6\text{H}_5)\text{Cr}(\text{CO})_3$ moieties. Although no catalytic results were presented, these dendrimers may be useful in redox catalysis (Figure 3.5).

Another promising catalytic system that is not fully understood is Cu chelated to a phosphorous dendrimer. Figure 3.6 shows such a G3 dendrimer where the periphery *N*-[(1*E*)-pyridin-2-ylmethylene]-aniline functional groups were used to complex Cu(I) [39]. Different generations of dendrimer **D6** were used to catalyze the coupling of 3,5-dimethylphenol with phenol iodide (Equation 3.5). While the catalytic activity of Cu chelated to G1, G2, or a monomeric ligand **4** was comparable, the yield of diarylether was 40% higher with G3. In the arylation of pyrazole with bromobenzene, the yield of phenylpyrazole was 2, 40, 44, and 80% with the Cu catalyst complexed to **4**, G1, G2, and G3, respectively. The comparable performance of G1 and G2 and the significant enhancement in the catalytic performance of G3 dendrimer is puzzling. The fact that this reaction could be conducted under very mild conditions using dendritic catalysts suggests that further understanding of the dendritic effect may be fruitful.

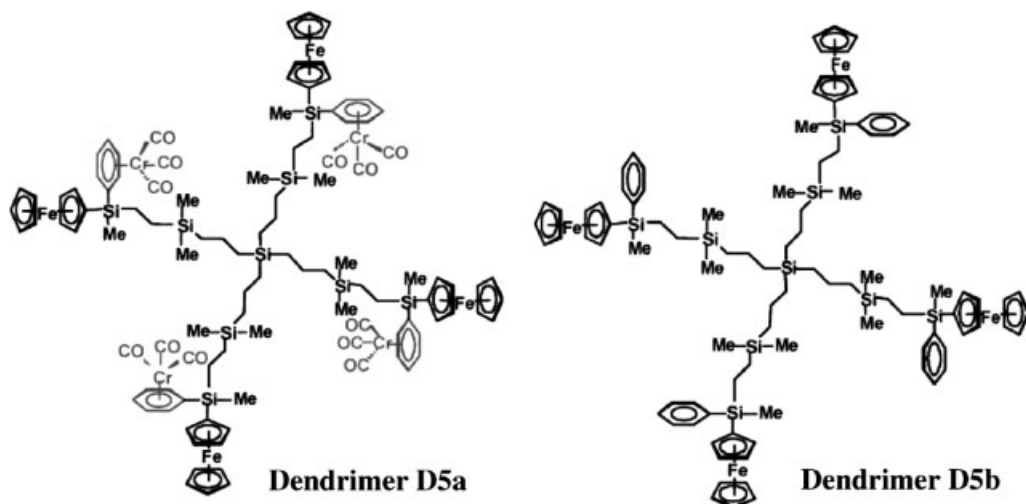


Figure 3.5 Heterometallic dendrimer **D5a** and its related homometallic dendrimer **D5b**. Adapted from [38]. Reprinted with permission from Copyright 2007. American Chemical Society.

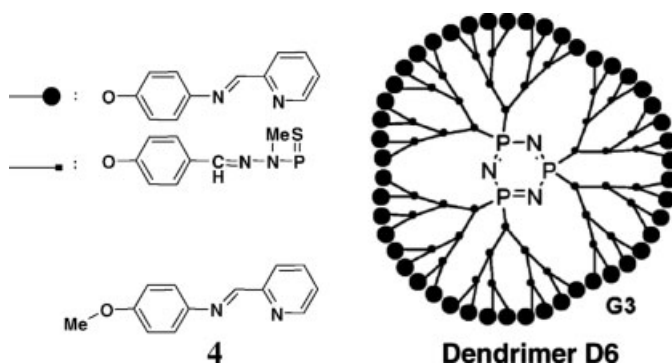
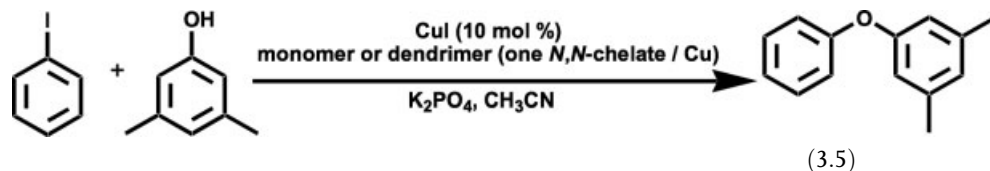


Figure 3.6 G3 of dendrimer **D6**; an imino pyridine-capped phosphorus dendrimer and ligand **4**, which is used to chelate Cu as control catalyst. Adapted from [39]. Reprinted with permission. Copyright 2006 American Chemical Society.



3.4

Catalysis by Dendrimer Encapsulated Nanoparticles

Beyond the ability to design catalytic active sites at the molecular level, dendrimers have also been used to prepare nanoparticle catalysts, either in solution or on high surface area supports. There are a number of studies using dendrimer templated nanoparticles to evaluate structure–function relationships for heterogeneous catalysts [40–42] and electrocatalysts [43] (particularly bimetallic catalysts), and this topic has been recently reviewed. Below, we focus on studies of dendrimer encapsulated nanoparticles (DENs) in solution, particularly in the context of the themes in previous sections of this review.

3.4.1

Nanoparticle Synthesis

PAMAM dendrimers can be used to template and stabilize reduced (zero-valent) metal nanoparticles in solution [44, 45]. The most common preparative route for DENs is analogous to the “ship in a bottle” synthesis (Figure 3.7). In the first step, metal ions (e.g., Cu^{2+} , Pd^{2+} , Pt^{2+}) are intercalated through the porous exterior of a PAMAM dendrimer and complexed to the interior amine and/or amide groups. Electrons are added via reducing agents such as borohydride, ascorbic acid, or hydrogen [6, 46]. The reduced metal atoms, which are effectively trapped within the interior cavity, coalesce to form a nanoparticle. Hence, the dendrimer plays multiple roles, serving both as a template for the number (and type) of metal atoms and as a colloid stabilizer preventing agglomeration after the particles form. Purification is straightforward and reaction byproducts are readily removed with dialysis. A number of modifications to this general procedure are available, and readers are directed to recent reviews for more thorough discussions of dendrimer mediated nanoparticle syntheses [6, 46].

Dendrimer mediated nanoparticles (DENs) are typically named by the dendrimer from which they are prepared along with the metal–dendrimer stoichiometry used in the nanoparticle synthesis, for example, G5–OH(Pt_{50}). With careful synthetic techniques, nanoparticles with very narrow particle size distributions (1.3 ± 0.3 nm) can be selectively prepared inside cavities in the dendrimer’s interior. Provided that metal reoxidation is prevented, DENs are stable for long periods of time and do not

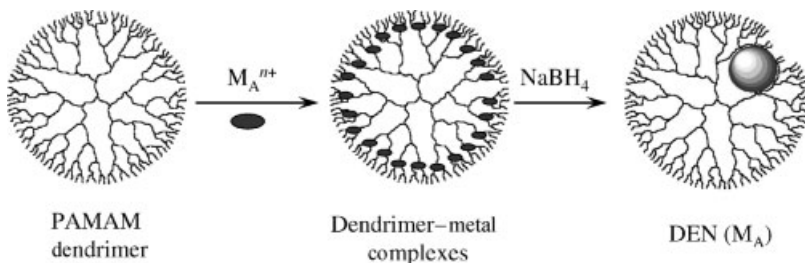


Figure 3.7 Scheme showing preparative route for dendrimer encapsulated nanoparticles (DENs).

agglomerate, since the nanoparticles are trapped within the dendrimer framework [6, 46]. Monometallic Pt, Au, Cu, Pd, and Ru have all been prepared [46], as well as a number of bimetallic systems (see below). The variability of dendrimer end groups has allowed for the preparation of DENs in aqueous, organic, fluorous, and supercritical solvents [46].

3.4.2

Catalysis by Monometallic DENs

The area of homogeneous catalysis by monometallic DENs, which was reviewed by Scott *et al.* [46] in 2005, has largely focused on a broad range of “proof-of-concept” experiments. As such, catalysis has primarily been used for test reactions to show changes and modifications to the nanoparticles or dendrimers. Pd DENs have been the most widely studied homogeneous catalysts, especially for carbon–carbon coupling catalysts. In Heck coupling reactions, Pd DENs show higher activities and selectivities relative to other colloidal Pd catalysts [47]. Pd catalyzed Stille [48] and Suzuki [49, 50] couplings have also been explored. Pd DENs also compare favorably with polymer stabilized nanoparticles for stability in Suzuki couplings, although the DENs exhibit lower turnover rates [50].

A few of the reported studies begin to probe some important structural considerations for these systems. Although the steric bulk of the dendrimer has been shown to slow reaction rates (see Section 3.3.2), that bulk can also impart favorable properties in terms of reactant selectivity. As homogeneous hydrogenation catalysts, the PAMAM dendrimer surface functions as a size- and shape-selective membrane for reactant molecules [46, 51–53]. Figure 3.8 shows conceptually how size selectivity of substrates can be accomplished using different dendrimer generations. The packing density of periphery groups increases with increasing generation and can be used to control access of the substrate to the encapsulated nanoparticle. Polypropyleneimine DENs also impart substantial selectivity towards polar substrates in competitive hydrogenation reactions [53]. In a clever set of experiments, the size selectivity of Pd DENs for alkene hydrogenation, coupled with molecular “rulers” (alkenes tethered to large cyclodextrin “stoppers”) has been used to estimate the distance of the Pd nanoparticle from the dendrimer surface [46]. This distance (0.7 ± 0.2 nm, on average) indicates that the nanoparticles are substantially displaced from the G4–OH dendrimer center (G4–OH radius ≈ 2.2 m) [46, 54]. Pd DENs have also been used to investigate particle size effects for allyl alcohol hydrogenation [55].

3.4.3

Bimetallic Nanoparticles

Bimetallic DENs can be prepared using methodologies comparable with those for monometallic DENs, although the synthetic details are somewhat more complicated for bimetallic DENs. Relative complexation and reduction rates are important additional considerations and can be used to control particle morphology (well-mixed or core–shell nanoparticles). These details are beyond the scope of this chapter,

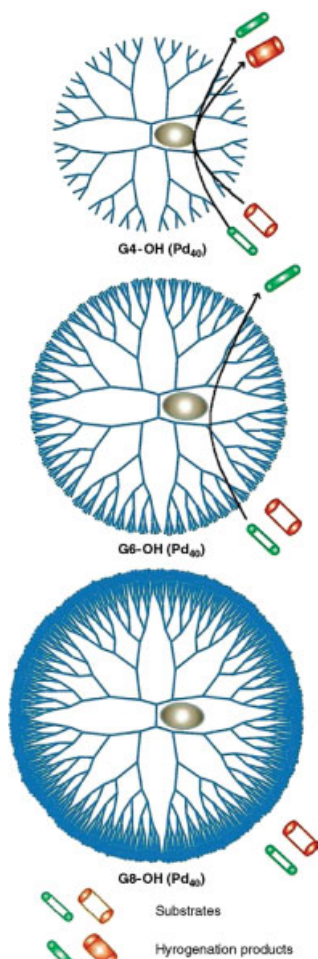


Figure 3.8 Size selective hydrogenation by Pd DENs. Reprinted with permission from [52]. Copyright 2001 American Chemical Society.

and readers are directed to recent reviews for a more thorough discussion [46, 56]. Unless specific synthetic steps are undertaken to prepare well-defined morphologies, bimetallic DENs are generally described as “well-mixed” bimetallic nanoparticles. The critical aspect of these descriptions is the random, intimate mixing of the two metals within individual nanoparticles. In some cases, bimetallic nanoparticles can be prepared throughout bulk miscibility gaps [42].

One method for preparing bimetallic DENs can be described as the “sequential reduction” method. This method, shown in the scheme depicted in Figure 3.9, involves the initial complexation and reduction of a “seed” metal (M_A), followed by the complexation and subsequent reduction of the second metal (M_B) to produce the $M_A M_B$ system. The synthetic utility of this method is that it provides the means to

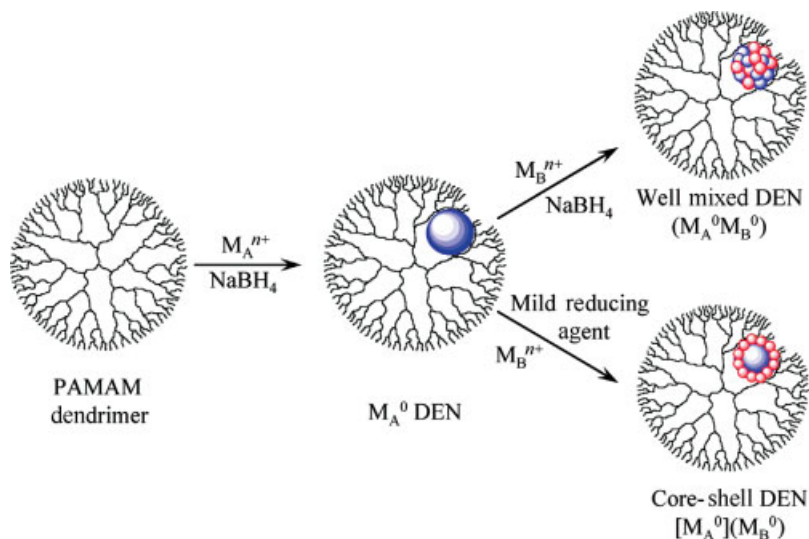


Figure 3.9 Scheme showing synthetic routes to bimetallic dendrimer encapsulated nanoparticles (DENS).

access both well-mixed and core-shell type DENS. When the reducing agent used for M_B is a mild reductant, such as H_2 or ascorbic acid, core/shell nanoparticles with a M_A core and a M_B shell can be selectively prepared. In the nomenclature for these core-shell nanoparticles, $[M_A]$ denotes the core metal(s) and (M_B) indicates the exterior metal shell. Several bimetallic DENS have been prepared in this manner, including AuAg [57, 58], $[Au](Pd)$ [59], $[Pd](Au)$ [59], $[Au](Ag)$ [58], $[AuAg](Au)$ [58].

3.4.4

Catalysis by Bimetallic DENS

Catalysis is a potentially sensitive probe for nanoparticle properties and surface chemistry, since catalytic reactions are ultimately carried out on the particle surface. In the case of bimetallic DENS, catalytic test reactions have provided clear evidence for the modification of one metal by another. DENS also provide the opportunity to undertake rational control experiments not previously possible to evaluate changes in catalytic activity as a function of particle composition. Several bimetallic DENS have been employed as homogeneous catalysts, predominately for hydrogenations. The most detailed studies have been with allyl alcohol hydrogenation [60] and the partial hydrogenation of 1,3-cyclooctadiene [61, 62] (1,3-COD). In these studies, turnover frequencies (TOFs), normalized per mole of nanoparticles, can be compared as functions of the metal atomic ratio in the DENS. Comparison to physical mixtures of monometallic DENS with the same net atomic ratio allows investigators to directly compare both the magnitude and direction of changes with rationally prepared control materials.

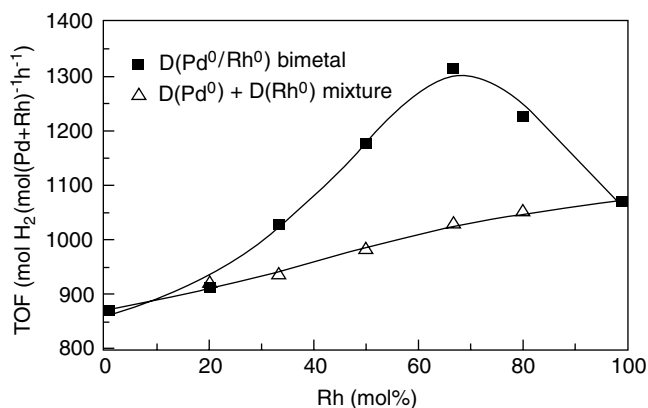


Figure 3.10 Dependence of the catalytic activity of the dendrimer-encapsulated PdRh bimetallic nanoparticles on its composition in partial hydrogenation of 1,3-cyclooctadiene. Reprinted with permission from [61]. Copyright 2003 Elsevier.

Figure 3.10 shows a plot of TOFs for the partial hydrogenation of 1,3-COD by PdRh DENs compared to TOFs for physical mixtures of Pd and Rh monometallic DENs [61]. As the mol % of Rh in the bimetallic DENs was increased, an increase in the TOF was observed that was *greater* than that of the physical mixtures. Importantly, the average particle size and distribution did not change as the mol% Rh increased, which was used to rule out the possibility that the TOF enhancement was a consequence of a systematic decrease in particle size. This allows for the conclusion that the bimetallic DENs truly are intimately mixed bimetallic nanoparticles and that a “synergistic” structure–activity effect is responsible for the catalytic rate enhancement.

Most of the homogeneous catalysis studies have reported some degree of catalytic rate enhancement when metals are intimately mixed in bimetallic nanoparticles. This synergistic effect was observed in the hydrogenation of allyl alcohol by PdAu [59] and PdPt [60] DENs, as well as the reduction of *p*-nitrophenol by AuAg [58] DENs. One particularly noteworthy study of this synergistic effect compared allyl alcohol hydrogenation by G6-Q₁₁₆(Pd_{55+n}) with G6-Q₁₁₆[Au₅₅](Pd_n) for values of *n* from 0 to 455 (see Figure 3.11). This study examined the effect of particle size and morphology on catalytic activity, and highlights the type of structural study for which DENs are uniquely suited.

The first interesting observation from this study is that TOF, normalized to the total number of metal atoms, actually increased with *n*. As particle size increases, the fraction of surface atoms decreases, therefore it is inferred that faster reaction rates are actually catalyzed by fewer surface atoms. The structure–activity relationship here is not easily interpreted, however. The dendrimer clearly plays an important role in mass transfer to the nanoparticle catalyst (*vide supra*). Because of this, it is not clear how much of this effect is due to particle size effects on the inherent catalytic activity of the nanoparticle surface and how much is due to larger nanoparticles affecting the dendrimer structure, which may reduce transport barriers or possibly free up more surface sites (fewer dendrimer amines may be bound to the nanoparticle. Thus,

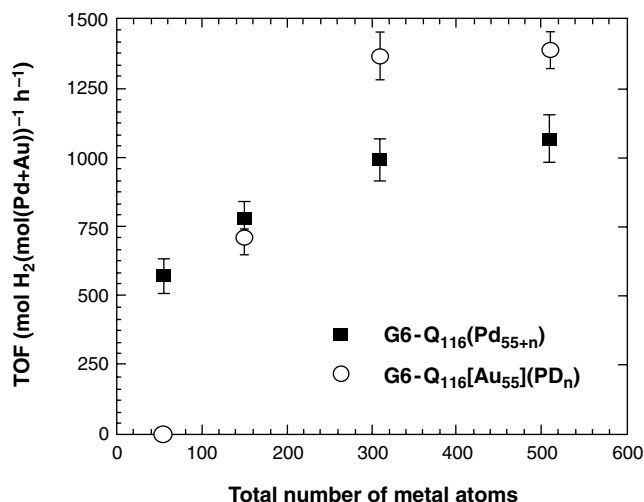


Figure 3.11 Turnover frequencies (TOFs) for the hydrogenation of allyl alcohol using G6-Q₁₁₆(Pd_{55+n}) and G6-Q₁₁₆[Au₅₅](Pd_n), which was prepared using the sequential-loading method, for $n = 0, 95, 255, 455$. Conditions: 22 °C, substrate:metal = 3300:1

[Pd + Au] = 150 μM. The ■ represents TOF data for Pd-only DENs, while the ○ represents data for the bimetallic DENs. Reprinted with permission from [59]. Copyright 2004 American Chemical Society.

the ultimate origin of the rate enhancement observed for these DENs is unclear, and some combination of structural and electronic effects is likely.

Figure 3.11 also shows that the Au core nanoparticles are more active catalysts than pure Pd particles containing the same total number of atoms. Since pure Au nanoparticles are inactive for alkene hydrogenation, this enhancement is likely due to a synergistic modification of Pd by Au. The nature of the synergistic rate enhancements, which have been well documented in the homogeneous and heterogeneous catalysis literature, are of fundamental interest and importance [63]. Particle size affects both surface geometries (e.g., curvature, size of extended planar surface) and electronic structure [64]. A dopant metal can potentially affect both of these parameters by donating or withdrawing electron density or epitaxially templating altered surface arrangements. Homogeneous catalysis studies have highlighted the magnitude and direction of these effects (at least for aqueous alkene hydrogenation), but assessing the relative importance of structural and electronic effects in the presence of the PAMAM dendrimer is difficult in these systems.

3.5

Dendrimer Templated Nanocages

As we have seen, the dendrimer architecture provides several attributes that make them ideal templates for catalytic structures. The near monodispersity of dendrimers

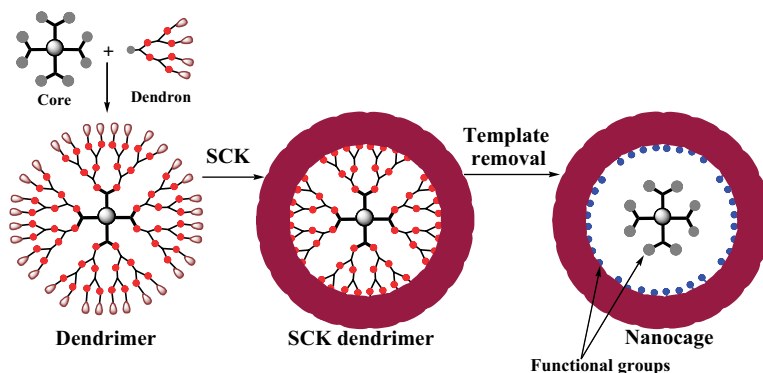


Figure 3.12 Formation of hollow nanocage with entrapped functionalized core and interior functional groups on the shell wall using dendrimer as template. Here, SCK stands for shell cross-linking.

enables the construction of precise structures and architectures, and the modular construct of dendrimers permits convenient variation of cage size. Figure 3.12 is a scheme showing one method to use a dendrimer as a template to generate a hollow nanocavity that has interior functionalities both on the shell wall and on the entrapped core. To achieve this, a dendrimer is chosen with the following properties: (i) The branching linkages can be disintegrated after the shell formation to generate a hollow interior, (ii) the periphery groups can be used to react with shell cross-linking agents to form a thin porous shell, and (iii) the dendrimer is globular in structure and has densely packed functional groups at the periphery to facilitate the formation of an intact shell. After shell cross-linking, disintegration of the dendrimer, and removal of the fragments, a hollow nanocage results with functionalities at the core and in the interior of the wall. The cavity size, which is dictated by the dendrimer size, can range from 2 to 10 nm. These cavities are small enough that the interior functional groups can interact with the substrates cooperatively, but large enough to accommodate molecules in most chemical reactions.

An example material synthesized with this scheme is a carbosilane nanocage with a 4.5 nm cavity [65]. It is synthesized using a G4 dendrimer with carbamate linkage bonds as template. Carbamate bonds are readily disintegrated by treatment with KOH or silyl iodide. The periphery of the dendrimer is populated with C=C such that shell cross-linking can be achieved with a hydrosilylation reaction. In this example, the starting core molecule was too small to be retained inside the nanocage, so a hollow cage was produced. Cleavage of the carbamate linkages leaves alcohol groups on the interior shell wall, which can be activated with *p*-nitrophenyl chloroformate to form carbonates. The interior surface carbonates react rapidly with smaller amines (e.g., allylamine) but sluggishly with bulky amines (e.g., tritylamine). This is because the carbosilane shell functions like a molecular sieve, that is, the nanocage exhibits size selectivity.

3.6

Conclusion

The architectural features unique to dendrimers, as well as their synthetic methodologies, can be utilized in designing dendrimer-based catalysts and catalyst templates. Many examples above show how these unique attributes were exploited in designing catalytically active sites at the molecular level. Important design features include backbone rigidity, polarity gradients from the dendrimer's exterior to interior and precise placement of functional groups on the branches. The combination of a relatively open interior pocket with a closed but porous exterior is one of the most attractive features of the dendrimer architecture. It permits metal complexes to be prepared at the dendrimer core and allows for the formation of DENs. In these very different types of catalysts, the role of the dendrimer in isolating one active site from another results in greater catalyst stability. The dense periphery groups can function as a size- and shape-selective membrane for reactant molecules. The close packing of the periphery groups is also conducive for cooperative catalysis between terminal groups.

The near monodispersity of dendrimers allows for the preparation of bimetallic DENs with very narrow size distributions. As a result of the narrow size distributions, the effects of particle composition (metal ratio) and morphology (well-mixed versus core-shell) can be studied independently from particle size effects. The near perfect structure of the dendrimer also makes them ideal templates for generating nanocages of uniform size. The modular construct of dendrimers is another attractive feature when tuning of template size is needed.

Potentially interesting uses of the dendrimer architecture in catalyst design have only begun; new additional uses are likely to follow. Some of these include *in situ* generation of active sites and integration of multiple redox centers on one dendritic structure. The modular construct can also allow for structures to be synthesized where the branches in different zones are of different rigidity. It thus appears that dendrimers have immense potential for future use in catalytic studies and technologies.

Acknowledgment

This work is supported by the US Department of Energy, Office of Science, Basic Energy Sciences, Grant No. DE-FG02-01ER15184. BDC thanks the Robert A. Welch Foundation (grant number W-1552) and the U.S. National Science Foundation (CHE-0449549) for financial support.

References

- 1 Fisher, M. and Vogtle, F. (1999) *Angewandte Chemie-International Edition*, **38**, 884.
- 2 Fréchet, J.M.J. and Tomalia, D.A.(eds) (2001) *Dendrimers and other Dendritic Polymers*, John Wiley & Sons, Ltd, West Sussex, UK.
- 3 Newkome, G.R., He, H. and Moorefield, C.N. (1999) *Chemical Reviews*, **99**, 1689.

- 4 Bosman, A.W., Janssen, H.M. and Meijer, E.W. (1999) *Chemical Reviews*, **99**, 1665.
- 5 Cooper, A.I., Londono, J.D., Wignall, G., McClain, J.B., Samulski, E.T., Lin, J.S., Dobrynin, A., Rubinstein, M., Burke, A.L.C., Fréchet, J.M.J. and DeSimone, J.M. (1997) *Nature*, **389**, 368.
- 6 Crooks, R.M., Zhao, M., Sun, L., Chechik, V. and Yeung, L.K. (2001) *Accounts of Chemical Research*, **34**, 181.
- 7 Kofoed, J. and Reymond, J.-L. (2006) *Current Opinion in Chemical Biology*, **9**, 656.
- 8 Liang, C. and Fréchet, J.M.J. (2005) *Progress in Polymer Science*, **30**, 385.
- 9 Gade, L.H. (ed) (2006) *Dendrimer Catalysis*, Vol. 20, Springer.
- 10 Elliott, S.J., Zhu, M., Tso, L., Nguyen, H.-H.T., Yip, J.H.-K. and Chan, S.I. (1997) *Journal of the American Chemical Society*, **125**, 9949.
- 11 Ribudao, F., van Leeuwen, P.W.N.M. and Reek, N.H.J. (2006) *Topics in Organometallic Chemistry*, **20**, 39.
- 12 Lee, J.J., Ford, W.T., Moore, J.A. and Li, Y. (1994) *Macromolecules*, **27**, 4632.
- 13 Murugan, E., Sherman, R.L., Jr Spivey, O. and Ford, W.T. (2004) *Langmuir*, **20**, 8307.
- 14 Jacobsen, E.N. (2000) *Accounts of Chemical Research*, **33**, 42.
- 15 Breinbauer, R. and Jacobsen, E.N. (2000) *Angewandte Chemie-International Edition*, **39**, 3604.
- 16 Iranzo, O., Kovalevsky, A.Y., Morrow, J.R. and Richard, J.P. (2003) *Journal of the American Chemical Society*, **125**, 1988.
- 17 Martin, M., Manea, F., Fiammengio, R., Prins, L.J., Pasquato, L. and Scrimin, P. (2007) *Journal of the American Chemical Society*, **129**, 6982.
- 18 Esposito, A., Delort, E., Lagnoux, D., Djojo, F. and Reymond, J.-L. (2003) *Angewandte Chemie-International Edition*, **42**, 1381.
- 19 Douat-Casassus, C., Darbre, T. and Reymond, J.-L. (2004) *Journal of the American Chemical Society*, **126**, 7817.
- 20 Iwasawa, T., Tokunaga, M., Obora, Y. and Tsuji, Y. (2004) *Journal of the American Chemical Society*, **126**, 6554.
- 21 Hu, Q.-S., Pugh, V., Sabat, M. and Pu, L. (1999) *The Journal of Organic Chemistry*, **64**, 7528.
- 22 Müller, C., Ackerman, L.J., Reek, J.N.H., Kärner, P.C.J. and van Leeuwen, P.W.N.M. (2004) *Journal of the American Chemical Society*, **126**, 14960.
- 23 Fujihara, T., Obora, Y., Tokunaga, M., Sato, H. and Tsuji, Y. (2005) *Chemical Communications*, 4526.
- 24 Sato, H., Fujihara, T., Obora, Y., Tokunaga, M., Kiyosu, J. and Tsuji, Y. (2007) *Chemical Communications*, 269.
- 25 Helms, B., Liang, C.O., Hawker, C.J. and Fréchet, J.M.J. (2005) *Macromolecules*, **38**, 5411.
- 26 Piotti, M.E., Rivera, F., Bond, R., Hawker, C.J. and Fréchet, J.M.J. (1999) *Journal of the American Chemical Society*, **121**, 9471.
- 27 Morao, I. and Cossío, F.P. (1997) *Tetrahedron Letters*, **38**, 6461.
- 28 Mak, C.C. and Chow, H.-F. (1997) *Macromolecules*, **30**, 1228.
- 29 Zubia, A., Cossío, F.P., Morao, I., Rieumont, M. and Lopez, X. (2004) *Journal of the American Chemical Society*, **126**, 5243.
- 30 Eliot, A.C. and Kirsch, J.F. (2004) *Annual Review of Biochemistry*, **7**, 383.
- 31 Liu, L. and Breslow, R. (2002) *Journal of the American Chemical Society*, **124**, 4978.
- 32 Liu, L., Rozenman, M. and Breslow, R. (2002) *Journal of the American Chemical Society*, **124**, 12660.
- 33 Liu, L. and Breslow, R. (2003) *Journal of the American Chemical Society*, **125**, 12110.
- 34 Liu, L. and Breslow, R. (2003) *Journal of the American Chemical Society*, **125**, 12110, supporting information.
- 35 Breslow, R., Wei, S. and Kenesky, C. (2007) *Tetrahedron*, **63**, 6317.
- 36 Francavilla, C., Drake, M.D., Bright, F.V. and Detty, M.R. (2001) *Journal of the American Chemical Society*, **123**, 57.
- 37 Drake, M.D., Bright, F.V. and Detty, M.R. (2003) *Journal of the American Chemical Society*, **125**, 12558.
- 38 Zamora, M., Alonso, B., Pastor, C. and Cuadrado, I. (2007) *Organometallics*, **26**, 5153.

- 39 Ouali, A., Laurent, R., Caminade, A.-M., Majoral, J.-P. and Taillefer, M. (2006) *Journal of the American Chemical Society*, **128**, 15990.
- 40 Chandler, B.D. and Gilbertson, J.G., (2008) *Nanoparticle Catalysis* (ed. D. Astruc), Wiley-VCH Verlag GmbH, Germany, pp. 129–160.
- 41 Hoover, N.N., Auten, B.J. and Chandler, B.D. (2006) *The Journal of Physical Chemistry. B*, **110**, 8606.
- 42 Lang, H., Maldonado, S., Stevenson, K.J. and Chandler, B.D. (2004) *Journal of the American Chemical Society*, **126**, 12949.
- 43 Ye, H. and Crooks, R.M. (2007) *Journal of the American Chemical Society*, **129**, 3627–3633.
- 44 Crooks, R.M., Lemon, B.I., Sun, L., Yeung, L.K. and Zhao, M. (2001) *Topics in Current Chemistry*, **212**, 82.
- 45 Ottaviani, M.F., Montalti, F., Turro, N.J. and Tomalia, D.A. (1997) *The Journal of Physical Chemistry. B*, **101**, 158.
- 46 Scott, R.W.J., Wilson, O.M. and Crooks, R.M. (2005) *The Journal of Physical Chemistry. B*, **109**, 692–704.
- 47 Yeung, L.K. and Crooks, R.M. (2001) *Nano Letters*, **1**, 14.
- 48 Garcia-Martinez, J.C., Lezutekong, R. and Crooks, R.M. (2005) *Journal of the American Chemical Society*, **127**, 5097.
- 49 Pittelkow, M., Moth-Poulsen, K., Boas, U. and Christensen, J.B. (2003) *Langmuir*, **19**, 7682.
- 50 Li, Y. and El-Sayed, M.A. (2001) *The Journal of Physical Chemistry. B*, **105**, 8938–8943.
- 51 Zhao, M. and Crooks, R.M. (1999) *Angewandte Chemie-International Edition*, **38**, 364.
- 52 Niu, Y.H., Yeung, L.K. and Crooks, R.M. (2001) *Journal of the American Chemical Society*, **123**, 6840.
- 53 Ooe, M., Murata, M., Mizugaki, T., Ebitani, K. and Kaneda, K. (2002) *Nano Letters*, **2**, 999.
- 54 Gröhn, F., Bauer, B.J., Akpalu, Y.A., Jackson, C.L. and Amis, E.J. (2000) *Macromolecules*, **33**, 6042–6050.
- 55 Wilson, O.M., Knecht, M.R., Garcia-Martinez, J.C. and Crooks, R.M. (2006) *Journal of the American Chemical Society*, **128**, 4510.
- 56 Chandler, B.D. and Gilbertson, J.D. (2006) *Topics in Organometallic Chem.*, Vol. 21 (ed. Gade, L.), Springer, p. 97.
- 57 Wilson, O.M., Scott, R.W.J., Garcia-Martinez, J.C. and Crooks, R.M. (2005) *Journal of the American Chemical Society*, **127**, 1015.
- 58 Endo, T., Yoshimura, T. and Esumi, K. (2005) *Journal of Colloid and Interface Science*, **286**, 602–609.
- 59 Scott, R.W.J., Wilson, O.M., Oh, S.-K., Kenik, E.A. and Crooks, R.M. (2004) *Journal of the American Chemical Society*, **126**, 15583.
- 60 Scott, R.W.J., Datye, A.K. and Crooks, R.M. (2003) *Journal of the American Chemical Society*, **125**, 3708.
- 61 Chung, Y.-M. and Rhee, H.-K. (2003) *Journal of Molecular Catalysis A: Chemical*, **206**, 291.
- 62 Chung, Y.-M. and Rhee, H.-K. (2003) *Catalysis Letters*, **85**, 159.
- 63 Sinfelt, J.H. (1983) *Bimetallic Catalysts: Discoveries, Concepts, and Applications*, John Wiley & Sons, Inc., New York.
- 64 Schloegl, R. and Abd Hamid, S.B. (2004) *Angewandte Chemie-International Edition*, **43**, 1628.
- 65 Lee, J.K., Kung, M.C., Suh, Y.-W. and Kung, H.H. (2008) *Chemistry of Materials*, **20**, 373.

4

Rational Design Strategies for Industrial Catalysts

Saeed Alerasool, C.P. Kelkar, and Robert J. Farrauto

4.1

Introduction

Design and commercialization of industrial catalysts require steps that are often overlooked. The focus of many published reports in catalyst journals is on identifying new catalyst formulations for emerging applications of interest or claiming superior features of newly developed formulations for existing processes. The reported performance is often based on testing on a very small scale using laboratory prepared quantities of powder catalyst and using high purity feedstock. Often lacking in such studies is a thorough understanding of process conditions and the required diligence in performing catalyst evaluations under conditions close to the industrial environment [1].

Existing petroleum and chemical processes generally operate at steady-state conditions with trained professionals monitoring performance and making the appropriate adjustments when necessary. Therefore the duty cycle for operation, deactivation and regeneration is more or less well understood. For the automotive catalytic converter, the consumer was the first to determine the duty cycle. Similarly, residential fuel cell systems with integrated fuel reformers to generate hydrogen can have variable and extremely demanding duty cycles, as do portable electronics powered by fuel cells. Regardless of the final product desired, it is essential to understand the critical process parameters and their range variability over the life of the catalyst (or duty cycle) to develop and optimize a catalyst for a particular application each of which is likely to be different.

Thus, different demands are made of the catalyst and the process, which has a profound influence on how the catalyst manufacturer approaches the development of commercial products and how to ensure its acceptable performance once it is in the hands of the end-user.

This brief review article will give an insight into how a few representative products are developed from a catalyst manufacturer's point of view. The scope will include the initial development and scale-up phases to production and ultimately to commercialization.

4.2

The First Stages Toward Commercialization of a Catalyst

Establishing goals and timing with process developers or potential end-users is an essential part of determining the technical approach to be taken. Several key unit operations issues should be considered prior to starting catalyst development:

1. Reactor configuration: fixed-bed, particulate or monolith, fluid-bed, slurry phase.
2. Minimum requirements for catalyst activity, selectivity, and life dictated by the overall process economics.
3. Process operating conditions: temperature, pressure, feed rate, fluid phase (vapor, liquid, or mixed phase), and the expected variability in these conditions.
4. Expected feed impurities that may result in reversible or irreversible catalyst poisons.
5. Regeneration requirements.

Once the baseline information is known, a thorough review of the existing patent and journal literature is essential before establishing a team of scientists and engineers to begin the development process.

4.3

Catalyst Discovery to Commercialization

4.3.1

Catalyst Preparation

A plan for catalyst development, in today's world, will likely include combinatorial (high throughput experimentation or "HTE") screening for candidate catalyst materials. High throughput experimentation provides a rapid estimate of initial activity and selectivity for a large number of candidate material formulations. Most effective HTE approaches consist of intelligent choices of most likely combinations of active components based on fundamental understanding of reaction requirements and reported information in the literature combined with the use of "design of experiments" not only aimed at identifying the optimum composition but also optimizing key synthesis parameters and post treatment conditions. With recent advances in automation, rapid high resolution analytical techniques, and powerful computer software and hardware technologies, HTE has established itself as a valuable tool for accelerating catalyst development – particularly for new reactions for which limited prior research and development has been carried out.

The catalyst preparation scientists will make laboratory preparations of some of the most promising candidates developed from the high throughput testing. These materials are often made into specific structures (particulates, powders, monolithic structures, etc.) depending on the application with catalyst precursors and products known to be acceptable (safe, environmentally acceptable, and cost effective).

There is a constant feedback network required between preparation and testing during the development phase in optimizing the final catalyst composition and method of preparation. Scientists will continuously modify the preparation procedures, including the type and concentrations of active components and promoters as well as shape and size of the catalyst and its mechanical strength, required for the end-use in a given industrial process. The goal is to constantly improve activity, selectivity, and life using the most cost-effective methods of manufacture.

4.3.2

Catalyst Testing

Rapid screening of formulations for activity and selectivity is accomplished through high throughput testing. Literally, hundreds of new formulations are prepared and tested rapidly in specially designed high throughput systems. Once candidates are identified, they are subjected to more advanced and reliable tests in laboratory reactors designed to simulate the end-use process conditions including feed composition, temperature, pressure, and space velocity and their effect on activity, selectivity, and short-term life. These test results will be used for the next phase of down-selecting candidates. The most common test conducted is to generate a conversion–selectivity versus temperature plot at a series of space velocities as shown in Figure 4.1. Conversion is the percentage conversion of a reactant. Selectivity is defined as the number of moles of desired product produced divided by the theoretical maximum for a given conversion expressed in percentage.

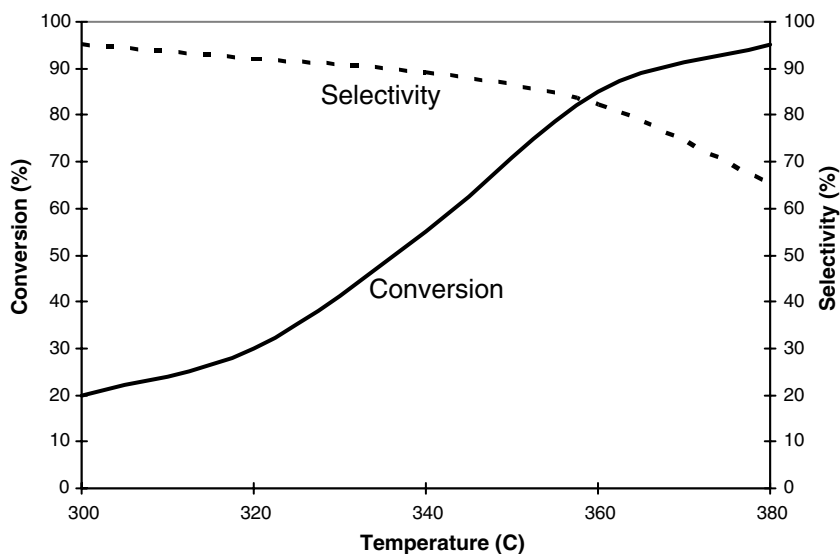


Figure 4.1 A conversion–selectivity profile as function of temperature as a preliminary performance test.

A very important question is related to the best method for activating the catalyst – does the catalyst have to be oxidized or reduced? It is preferable that this be done in the catalyst manufacturing plant but often, it has to be done in the commercial reactor as part of the pre-startup activities. Successful candidates then move on to the next phase of advanced testing which usually involves aging in simulated process feed streams.

4.3.3

Advanced Testing in Accordance to the Duty Cycle

The effect of extreme conditions on performance includes the impact of poisons, and upset conditions expected in the duty cycle. It is also important to identify aging mechanisms and effective ways to regenerate catalysts. To further prolong catalyst effectiveness, it is also important to focus on reducing aging by making process design changes. These include incorporation of guard beds upstream of the reactor. For this to be effective, the impact of feed impurities and their poisoning effects (i.e., reversible or irreversible) should be thoroughly studied and understood. The range of space velocities, temperatures, and pressures under which the catalyst is operating also needs to be clearly understood. This is particularly important in automotive emission control where the catalyst is expected to abate pollutants over a wide range of driving conditions (i.e., varying space velocities and temperatures). These considerations are important to proper design and sizing of the catalyst to ensure that viable process economics is achieved.

4.3.4

Aging Studies

During various phases of long-term testing catalyst samples are removed and characterized by standard instrumental methods to establish the main causes of deactivation [2]. The feed gas should closely simulate that which is expected in the commercial process. Routine characterization tests of the aged or spent catalyst are conducted to understand how the catalyst has changed. The reader is referred to the “ASTM D-32 ‘Committee on Catalysis’, third edition, 1988” for standardized test procedures used in the catalysis community [3]. Several bulk and surface techniques can be used to determine likely causes of catalyst deactivation. Presence of contaminants on the catalyst surface can be investigated using optical and electron microscopy and X-ray photoelectron spectroscopy (XPS) to identify, characterize, and quantify and nature of foreign components on the catalyst. X-ray diffraction (XRD), electron microscopy, and nuclear magnetic resonance are used to assess structural changes of the catalyst. Mechanical attrition is a particular problem in applications where the catalyst grinds against itself, as in fluid-bed or slurry-phase process. Here one measures the quantity of fines generated through various standardized attrition tests. Sintering of the carrier is measured by BET or XRD while catalytic component sintering is measured by selective chemisorption techniques, XRD, or TEM.

The next critical task is establishing the major causes of deactivation and by attempting to eliminate the various expectant causes. For example, if poisoning is observed, evaluate the catalyst under the anticipated duty cycle but in the absence of the poison. This will facilitate an understanding of poisoning effects in catalyst deactivation. It is likely that many structural and chemical changes will occur but only the most important will cause significant deactivation. If thermally induced aging is expected based on observed sintering or phase changes of the carrier and catalytic components, the catalyst can be exposed to these extreme temperature conditions and it can be studied whether the activity is lower than the fresh catalyst [4]. In processing hydrocarbons, it is common for coke to deposit (e.g., mask) on the catalyst covering its surface of the catalyst and blocking pores preventing reactants from interacting with the active sites. A simple coke burn-off in diluted O_2 followed by an activity test will establish if the catalyst can be regenerated and under what conditions.

Slip stream testing is a reliable approach to determining catalyst effectiveness. A small fraction of the process steam is passed through the catalyst. Periodically samples are withdrawn and evaluated in the laboratory for performance using a model activity test simulating the molecules and conditions to be used in the real process. Characterization of this sample is also required, since unexpected conditions often occur. Careful analysis of performance and the associated catalyst characterization data, along with history of the plant operation during that time period, allows further direction to the process engineers and catalytic scientists to make adjustments for optimum performance. Furthermore, it provides the necessary deactivation modes to permit the development of accelerated tests by amplifying those modes that lead to deactivation.

4.3.5

Kinetics

Successful design of an industrial catalyst is much more easily accomplished when armed with an in-depth understanding of reaction kinetics. It is important to identify the rate-limiting step in the actual process and to reduce its activation energy. Once the rate-limiting step is identified, the catalyst scientist or engineer can optimize the chemical and physical properties of the catalyst and to optimize the process. For kinetically controlled reactions, one can increase the concentration of active sites by increasing dispersion of the catalytic components or simply increasing the concentration of the catalytic component, or a combination of both. Increasing the temperature will also favor the rate, since kinetically controlled reactions have higher activation energies compared to the physically rate-limiting modes of mass transfer [5].

For a reaction expected to be controlled by pore diffusion, the pores of the carrier can be made larger or the active catalytic components can be deposited nearer the surface of the particulate carrier. Smaller particles also decrease the diffusion path thereby favoring an increase in rate but this creates greater pressure drop for fixed-bed processes and makes catalyst separation from the reaction medium more problematic for slurry-phase processes. Some manufacturers use

ring, or “donut,” shaped supports to decrease the diffusion path without sacrificing pressure drop.

For reactions controlled by mass transfer, an increase in the geometric area of the catalyst (i.e., smaller particles, roughened surface, or a greater number of channels in a monolith favors the rate. Enhancing turbulence by reactor design is also a common tool used by the engineers to enhance reaction rates. Thus, knowledge of kinetics gives both the scientist and engineer tools to make further performance improvements.

4.3.6

Catalyst Scale-Up

In recent decades, many important advances have been made toward understanding fundamental aspects of catalyst design, including better elucidation of the nature of active sites through the use of more sophisticated characterization tools. In addition, high throughput and combinatorial techniques have led to the discovery of several new and improved catalyst formulations for various industrially important reactions. However, little research has gone toward understanding and improving the scale-up of laboratory scale catalyst discoveries. As a result, catalyst scale-up has continued to remain mostly an “art” that resides behind the walls of catalyst manufacturers. This process has basically evolved into empirical relationships developed through many years of experience [6].

Laboratory synthesis of catalysts is generally much less challenging than large-scale production. For large volume production, there are many engineering considerations that must be factored into the design. Laboratory syntheses are almost always carried out at very small scales, using high-purity reagents and with elaborate well-controlled treatment steps, usually without a consideration for feasibility of transferring the recipe to commercial scale. There are many questions to be answered before a catalyst recipe can be transferred to manufacturing. Do the precursors lead to unsafe conditions for the plant operators? Will the decomposition of the precursor salts result in emissions that require new abatement conditions? Are there less-expensive precursors that can be used? Does the order of addition of reagents allow for smooth plant operations? These are some of the factors that must be addressed before cost-effective production is possible.

Issues of component mixing and heat generation need to be controlled to avoid hot spots and inhomogeneous mixing. Forming the catalyst into its final structure with the proper size, shape, strength, and adhesion (for wash coats to monoliths) is critical to meet performance specifications. The final heat treatment must allow for sufficient drying and calcination without disrupting the structure of the carrier or support.

The question of manufacturing cost of the catalyst is an important aspect of any scale-up effort. Recipes using expensive high-purity precursors often become prohibitive therefore less-expensive, commercially available materials with equivalent performance must be found. Precursors that lead to excessive wastage either

during the initial synthesis or during the required post-treatment steps should also be avoided.

4.3.7

Quality Control

It is necessary to understand the limitations of the plant in the manufacture of the catalyst, regarding composition tolerances. Can the catalyst be repeatedly made within specifications? For example, if the catalyst prepared and tested in the lab and the field has a composition of 0.5% Pt with 0.05% Fe deposited on an Al_2O_3 carrier, how reliably can the plant produce this composition? How much tolerance is allowed before the performance begins to suffer? Thus, it is important for the team to understand the performance–composition tolerances that are acceptable, to meet the specifications of the customers. From this information, quality control specifications are set between the catalyst manufacturer and the customer, recognizing that these are tentative until real data from real use are understood.

Most manufacturers have in-process monitoring to ensure the product meets specifications, so as to avoid making an unacceptable product. Finally, what are the tests to be used to ensure that the catalyst meets plant and customer specifications. Often, a model activity test is used to ensure that each batch of catalyst is consistent. It is also common to have a few fast and relatively simple characterization tests such as chemical analysis, chemisorption for metal dispersion, and sometimes XRD for ensuring proper carrier structure.

4.4

Example 1: Automobile Pollution Abatement Catalyst System

It is difficult to imagine an application where the duty cycle is as demanding as in the automobile catalyst for pollution abatement. When the issue of controlling emissions from automobile internal combustion engines was first discussed in the early 1970s, the use of a catalyst was quickly dismissed by most of the automobile companies. They understood the emissions from the car and the quality of the fuel, but most importantly they understood the duty cycle of a car and the driving and maintenance habits of the consumers. They concluded that catalysts would not have the durability in this heroic environment to meet federal regulations. Catalyst companies, however, took on the challenge and continually identified key issues that had to be addressed [4].

1. Carbon monoxide, unburned hydrocarbon, and nitric oxide emissions had to be reduced to meet 1975 U.S. regulations. The oxides of nitrogen emissions were to be handled with engine modifications, leaving the oxidation catalyst as the main challenge. The generic reactions (unbalanced) are shown below





2. The quality of the fuel, especially, the presence of lead in gasoline, used to enhance octane, was known to be a permanent poison to catalysts.
3. Stability of the catalyst in a severe high-temperature steam environment known to accelerate the process of sintering of both catalyst carriers and its catalytic components was expected..
4. The impact of thermal shock on the mechanical integrity of the catalyst due to rapid transients when the vehicle undergoes rapid changes in temperature from high-speed highway driving to low speeds in urban areas had to be considered.
5. Flow resistance caused by installing a catalyst in the exhaust of the vehicle, would surely add pressure drop, effecting driving performance and fuel economy.
6. Sulfur, present in gasoline, was a well known poison to most catalyst materials, especially base metal oxidation catalysts such as copper, chromium, nickel, cobalt, manganese, and so on. Inorganic oil additives such as phosphorous, zinc, calcium, and other inorganic species which could mask the catalyst surface [4], varying flow had to be addressed.

The challenge was to address each of these with the current knowledge of the catalyst data base, how to modify them and how to establish new test facilities to meet the new U.S. federal emission regulations for this new application.

4.4.1

The Quality of the Fuel

Very quickly, it became apparent to both car companies and catalyst manufacturers that lead was permanently deactivating all catalyst candidates; thus petitions were made to the U.S. government, which passed legislation mandating the fuel companies to reduce lead in the gasoline. In 1975, lead levels were dramatically reduced, setting the stage for the implementation of a catalytic solution for meeting the regulations.

4.4.2

Base Metals Versus Precious Metals

Catalyst preparation and testing facilities, including engine and chassis dynameters, were built and commissioned in catalyst and automobile companies to develop the solutions. Laboratories were equipped with reactor systems capable of generating pollutants concentrations at flow rates comparable to the most extreme conditions anticipated during driving cycles. Of particular importance were the high-temperature steam-containing environments not previously experienced in supported catalytic processes. Reactors were equipped with feed gases simulating anticipated poisons such as sulfur and oil additives to evaluate the promising new catalyst candidates.

Although it was well known that precious metals were more active and robust than base metal oxides, their expense and limited availability became a major obstacle. Thus, the search for less-expensive materials began. Definitive statements were made that precious metals would not be used. Research then accelerated, looking for the correct composition of base metals that would have sufficient activity and durability to meet the duty cycles required [7–10]. After a couple years of intensive research, it became apparent that base metal oxides lacked the thermal stability and poison resistance to ever be viable candidates for the converter [4].

4.4.3

Particulate Versus Monolithic Structures

All attention then turned to precious metals and the carrier and supports needed to fix them in the automobile exhaust. High surface area particulate carriers such $\gamma\text{-Al}_2\text{O}_3$ were well known as catalyst carriers in the chemical and petroleum processing fields so it was natural to consider them. Plants already existed for their manufacture, generic catalyst preparation procedures were well known and mechanical and flow models had been developed.

However, other automobile companies were concerned about increased pressure drop and particulate attrition issues and began exploring new ceramic monolithic structures (cordierite) upon which catalysts could be deposited as wall coating or washcoats. Ceramic monoliths had multicellular channels in parallel with open frontal areas of over 70% ensuring low pressure drop. The walls had low surface areas so a washcoat of catalyst had to be deposited [4]. The washcoat was composed of combinations of precious metals dispersed on a high surface area carrier such as $\gamma\text{-Al}_2\text{O}_3$. Aqueous slurry of the catalyzed carrier was deposited onto the walls of the monolith by a dipping process, dried and calcined to remove precursor salts and to ensure washcoat–monolith adhesion. The washcoated monolith had to have sufficient thermal shock resistance to meet the mechanical integrity requirement of extreme temperature transients.

4.4.4

The First Generation

Work continued pursuing the use of both particulate catalysts, Pt and Pd, on $\gamma\text{-Al}_2\text{O}_3$ beads and Pt- and Pd-containing washcoated monoliths [11]. Progress in stabilizing $\gamma\text{-Al}_2\text{O}_3$ against hydrothermal sintering using metal oxide stabilizers was forthcoming. Varying combinations of Pt and Pd were used. Extensive accelerated aging tests, based on knowing the major causes of deactivation, were established, greatly providing simulated durability data needed for modifications of the catalyst and reactor design. Within about 5 years, automobile fleet testing demonstrated that the regulations could be met with both precious metal particulate designs in radial flow (pancake) type reactors and precious metal washcoats on monoliths. The first catalytically equipped vehicles were on the road in 1975.

4.4.5

The Final Test

In the hands of American drivers problems began to arise, especially for those cars equipped with particulate catalysts. Attrition due to abrasion between particles became a dominant life-shortening issue that ultimately led to the adoption of all monolith solutions in the late 1970s. So, in spite of all the extensive laboratory and field testing done by experienced chemical and mechanical engineers, the driving habits of the consumer ultimately provided the final direction for monoliths systems, which are exclusively used today throughout the world.

The modern exhaust converter represents one of the crowning achievements in catalyst technology today. The modern three-way catalyst (TWC) simultaneously converts carbon monoxide, unburned hydrocarbons, and oxides of nitrogen to extremely low levels with a proven life of 150 000 miles. Its success is derived from thoroughly understanding the duty cycles of the vehicle and solving all the critical issues using accelerated aging tests. Figure 4.2 shows a schematic of the modern three-way converter equipped with oxygen sensors that measure the O_2 content of the exhaust, which is then fed back to the engine, controlling the air-to-fuel ratio within a stoichiometric window permitting simultaneous conversion of CO, HC, and NO_x . The modern TWC catalyst contains a combination of Pt, Pd, and Rh on a stabilized high surface area washcoat of $\gamma-Al_2O_3$. Compounds containing CeO_2 are added, to buffer perturbations in the O_2 content of the exhaust and allow optimum performance caused by variations in the air to fuel ratio due to time delays in the feedback control system [12].

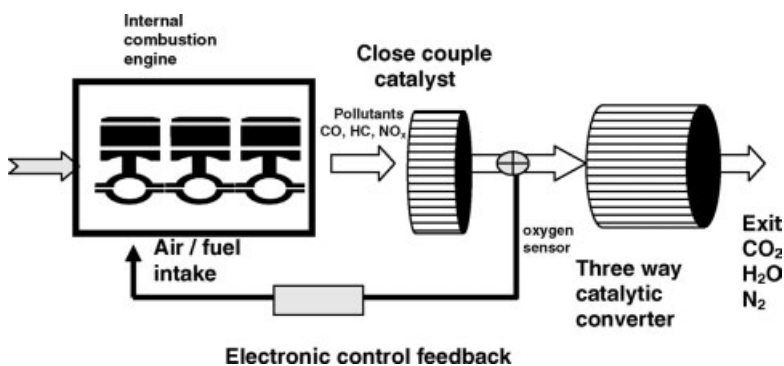


Figure 4.2 The three-way catalytic converter positioned in the exhaust of the internal combustion engine. The O_2 sensors provide a feedback to the engine to maintain the air-to-fuel ratio close to stoichiometric. A close-coupled catalyst is positioned up against the engine to ensure rapid light-off during the cold start portion of the driving cycle.

4.5

Example 2: Dehydrogenation of Light Alkanes

Production of C_3 and C_4 olefins has continued to attract attention in recent decades. Prior to concerns surrounding the use of MTBE as a gasoline additive, isobutylene – used in the esterification process to make MTBE – enjoyed enormous growth driven by the Clean Air Act of 1990. In recent years, due to the banning of MTBE in the United States, and its uncertain future in the rest of the world [14], isobutane dehydrogenation capacities have remained flat-to-declining. Propylene demand, on the other hand, continues to enjoy rapid growth throughout this decade with a projected rate of 5% per year from 2006 to 2011 [15] such that demand will almost certainly outpace supply. Units of FCC are increasing their propylene production through the use of zeolite-based additives as well as changes in the operating regimes and mechanical revamps. In addition to FCC-based propylene, on-purpose production of this monomer is also taking on a larger role in fulfilling the eminent increase in demand. As a result, dedicated “on-purpose” catalytic processes such as dehydrogenation and ethylene–butylene metathesis have proven to be viable routes to economically bridging the gap between supply and demand of propylene and Isobutene for the production of polypropylene and isooctane, respectively. For the on-purpose processes to remain competitive with other routes such as FCC, improvements in process efficiency and reliability have been made. One important aspect of these improvements is the development of more robust catalysts delivering an acceptable performance, both in terms of activity and selectivity as well as catalyst life.

The focus of this section is to introduce an example of how an understanding of fundamental catalytic properties can be combined with practical aspects of catalyst development in order to successfully develop a catalyst that provides the best combination of performance and cost in a commercial reactor. Pilot plant and commercial data presented will demonstrate that improvement in catalyst technology can play a key role in making the economics of the process more attractive and competitive.

As mentioned before, a prerequisite for designing the optimum catalyst for a given process is establishing a thorough understanding of the process conditions. This should include not only the reactor in which the catalyst operates but also the downstream and upstream unit operations which can in turn impose additional constraints on the catalyst. For this particular example, the industrial fixed-bed multireactor Houdry[®] process is selected. This process is designed to operate at high temperatures (580–610 °C) and subatmospheric pressures. A typical commercial unit includes three to eight parallel reactors. As the reaction proceeds, rapid coke buildup necessitates an air-regeneration step at 640–660 °C [16]. To facilitate this, a number of reactors operate the reaction cycle while others are either being regenerated in air or are being reduced and purged. A complete reaction–reduction–regeneration cycle lasts between 15 and 25 min. Catalysts used in this process are typically chromium based and their expected life is around 18–24 months depending on the operating philosophy that determines the severity

of process conditions. Due to the severity of the operation, hydrothermal stability of the catalyst is a key requirement. If the catalyst is to deliver acceptable performance for two years, it needs to survive over 600 000 reaction–regeneration cycles at temperatures exceeding 600 °C. This means the catalyst should maintain a slow activity and selectivity decay while maintaining its physical integrity. Although the catalyst formulation may be robust enough to maintain the activity and selectivity of the active sites throughout its expected life, the catalyst pellets may not be able to withstand these severe process conditions. If the catalyst fails to maintain its physical integrity, formation of dust or broken pellets can lead to elevated pressure drop, which in turn forces reduced throughput levels or unplanned and costly shut-downs.

Selectivity to the desired product (propylene, isobutylene, or butadiene) is also important, since specific feedstock consumption is a key component of process economics. In addition to the obvious need to maximize selectivity toward the desired products, selectivity toward undesirable components such as coke and carbon oxides play can directly impact the operation of the plant. Too much coke during the dehydrogenation cycle can lead to excessive heating during the regeneration cycle, which in turn results in the catalyst being exposed to higher than desired localized temperatures, formation of “hot spots,” and accelerated irreversible deactivation. Excessive production of carbon dioxide, on the other hand, can put limitations on the operation of the “cold box” and the degree to which residual products can be recovered by the downstream equipment. Elevated carbon dioxide production can sometimes (particularly during the startup phase) force the operator to flare valuable propylene (or isobutene) instead of recovering it as the product.

Development of a catalyst that can deliver the required performance under the above-described severe operating conditions is a challenging task and requires a rational and systematic approach to catalyst development. Performance targets can only be achieved if the most critical catalyst synthesis parameters are understood and optimized. This is accomplished through a systematic approach to catalyst development, scale-up and commercialization. In the following paragraphs, the implementation of such an approach, which ultimately led to the advent of a superior catalyst platform for the fixed-bed dehydrogenation process, is demonstrated.

4.5.1

Understanding Reaction Kinetics, Thermodynamics, and Process Constraints

Dehydrogenation is an endothermic reaction and limited by equilibrium with increasing reaction pressure. The reaction favors elevated temperatures and lower pressures. These thermodynamic aspects are well established and their implications on reactor and catalyst design are known. However, developing a thorough understanding of reaction mechanisms and the nature of active sites is a challenging task; even for such seemingly simple reactions as propane or butane dehydrogenation, recent studies using more sophisticated characterization tools continue to contribute to our understanding of these fundamental aspects. While it is ideal to first establish such an understanding and then embarking on the design of an industrial catalyst, in

the real world this is not easily accomplished. Usually, catalysts are commercialized without establishing these fundamental understandings. It is however imperative that these new fundamental insights are incorporated into the approach toward the design of new catalytic materials in order to succeed in pushing the boundaries of the performance envelope. These new insights can often lead to shifting of the old paradigms and challenging widely accepted assumptions. In the case of chromia on alumina catalyst, the structures and dehydrogenation behavior of such catalysts have been studied extensively in an attempt to elucidate structure–activity relationships. Up until recently, it was widely believed that the trivalent chromium species are the only set of active sites, and maximizing their surface concentration can lead to a catalyst with the highest dehydrogenation activity. While this is still partially the case, recent studies have attributed the dehydrogenation activity not only to the coordinately unsaturated redox and nonredox Cr^{3+} ions, but also to the oxygen ions in the catalyst [17]. These findings have important implications on whether the catalyst should be pre-reduced with hydrogen or carbon monoxide prior to loading in the reactor. On the hand, recent results by Nijhuis *et al.* suggest that a small amount of coke improves its activity, most likely because of an improved adsorption of propane on the catalyst, but the activity of the catalyst drops when the amount of coke exceeds a certain value [18].

4.5.2

Formulating the Catalyst

Armed with most recent fundamental findings regarding kinetics and the active site centers, the next step is to identify the optimum active metal(s), support, promoters, and stabilizers and to optimize their composition. With respect to the design of this particular catalyst, enough is known about the chemistry and process requirements to rule out non-chromium metals and other supports besides alumina. For this reason, HTE will likely not be applicable here. The challenge, however, is to develop a new formulation involving these metals that delivers superior performance to that already practiced in the field. Tailor-making the alumina support with the right phase structure, surface acidity, and porosity is a key requirement for achieving hydrothermal stability, minimizing side reactions and possible mass diffusion effects. The critical importance of the starting alumina phase structure in providing hydrothermal stability cannot be over-stated. While different types of hydrated aluminas (e.g., Gibbsite, boehmite, pseudoboehmite, and bayerite) can be used to prepare a catalyst with acceptable initial activity and selectivity, there are only specific types that will lead to a catalyst with good hydrothermal stability. Furthermore, even after proper choice of starting alumina, thermal and hydrothermal treatment steps have to be fine tuned in order to achieve maximum stability. Figure 4.3 compares the stability of two alumina-supported chromia catalysts prepared from two different types of hydrated aluminas. Figure 4.4 shows the impact of Lewis acidity of the alumina support on the selectivity of the catalyst. As Lewis acidity is decreased, the selectivity improves until it reaches an optimal level. Lewis acid sites are known for the ability to catalyze undesirable side reactions such as cracking.

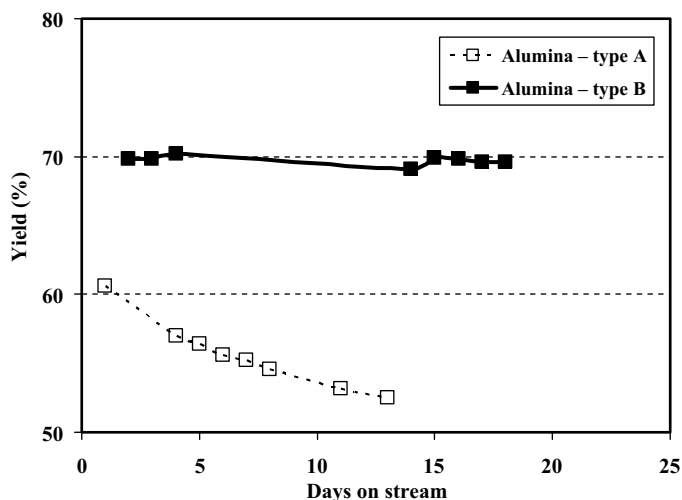


Figure 4.3 Impact on alumina type on hydrothermal stability and deactivation.

The next step is to incorporate the active metal (i.e., chromium) into the support and to optimize metal loading, crystal size, and to control the location of the metal crystallites within the alumina support to maximize dehydrogenation activity.

Another important aspect of catalyst development is the assessment of the hydrothermal stability long term performance of the new catalyst formulations. Since the commercial catalyst is expected to have a life time of at least two years, a new catalyst formulation should not only have good initial performance but it should also possess a very high degree of hydrothermal stability under severe operating conditions (i.e., temperatures greater than 650 °C). To simulate such severe conditions, a

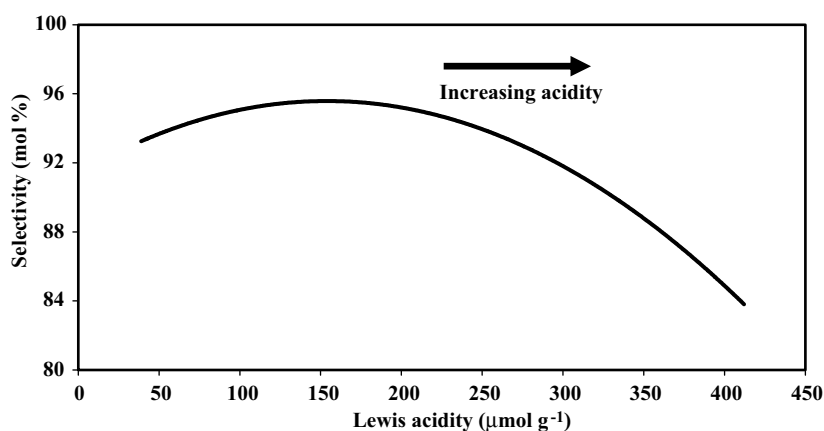


Figure 4.4 Impact of support acidity on selectivity. Acidity was measured by pyridine DRIFTS.

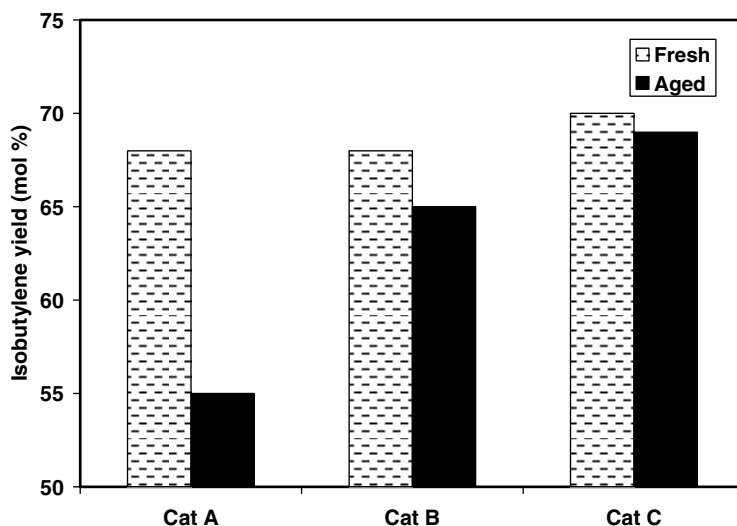


Figure 4.5 Comparison of fresh and aged catalysts.

simulated aging protocol was developed that is capable of distinguishing between catalysts with different degrees of hydrothermal stability. Figure 4.5 shows the hydrothermal stability of three different catalyst formulations. Although all three catalysts exhibit similar activity prior to aging, their performances differ widely upon aging. Clearly, Catalyst C is the most stable of the three formulations, closely followed by Catalyst B. However, Catalyst A has unacceptably low stability and is expected to rapidly deactivate in a commercial reactor.

4.5.3

Pilot Plant Testing

Having developed the optimal catalyst formulation and verified its superior performance through screening tests, performance of the catalyst should be demonstrated at the pilot plant scale prior to placing the catalyst in commercial use. Failure to demonstrate long-term viability of the catalyst under conditions similar to those encountered in the commercial reactor can potentially expose the plant operator to significant financial risks. This is particularly the case for fixed-bed processes, in which process economics assume a minimum of one year, but more often two years, of catalyst life. Pre-mature failure of the catalyst can result in several days of production loss, additional reactor change out cost as well as increased catalyst replacement cost. For this reason, it is imperative that every measure is taken to minimize such risks. In this particular example, the new formulation was evaluated in pilot reactors for several days (see Figure 4.6) using the same isobutane feed used in a commercial isobutane dehydrogenation reactor. This means the feed contained impurities including up to 5% paraffins (such as propane, *n*-butane, and *n*-pentane),

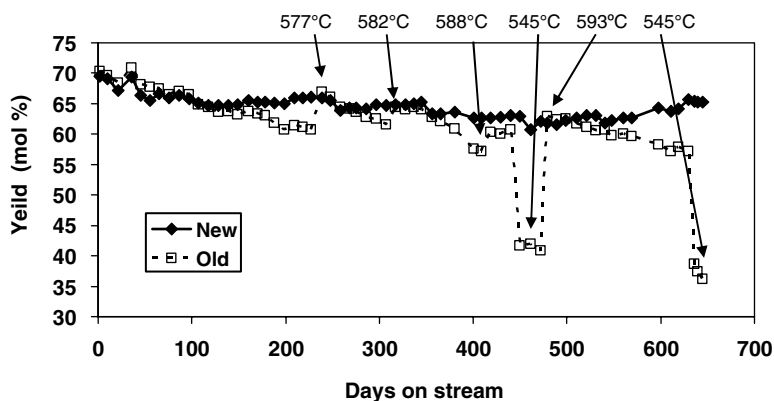


Figure 4.6 Pilot plant performance of the new versus the old catalyst.

olefins such as various isomers of butenes as well as potential reversible and irreversible poisons such as sulfur and halogens. A sample of previous generation catalyst was used as a reference. Both the standard catalyst and the new one were placed in reactors with independent temperature controls. The new catalyst was operated isothermally at 545 °C throughout the entire test while the temperature of the old generation catalyst was adjusted upwards to compensate for its declining activity. As shown in Figure 4.6, the new catalyst showed virtually no decline in performance throughout the 645-day period, while the standard catalyst gradually declined in performance. To compensate for the activity loss of the standard catalyst, temperature was increased four times to 577, 582, 588, and 593 °C after 230, 300, 400, and 480 days on stream, respectively. After about 450 days on stream, the temperature of the old generation catalyst was lowered to 545 °C (same as that of the new catalyst). This resulted in a 17% lower isobutylene yield for the standard catalyst compared to that of newly developed formulation. When the same was repeated after 645 days on stream, the difference in the isobutylene yield of the two catalysts had increased to nearly 30%. These results clearly indicate that the new catalyst not only has higher intrinsic activity than the standard commercial catalyst, it is also able to maintain this activity for a much longer period.

4.5.4

Field Testing

Armed with convincing pilot reactor data, the new catalyst was loaded into one of the seven reactors of a commercial seven-reactor system. This was done as a final confirmation of the superior performance prior to a full commercial trial. In this single-reactor trial, the performance of the reactor containing the new catalyst was compared to the average of the other six reactors containing the standard catalyst. Once again, results confirmed the higher activity and stability of the new formulation. As shown in Figure 4.7, after 500 + days of operation, the reactor containing

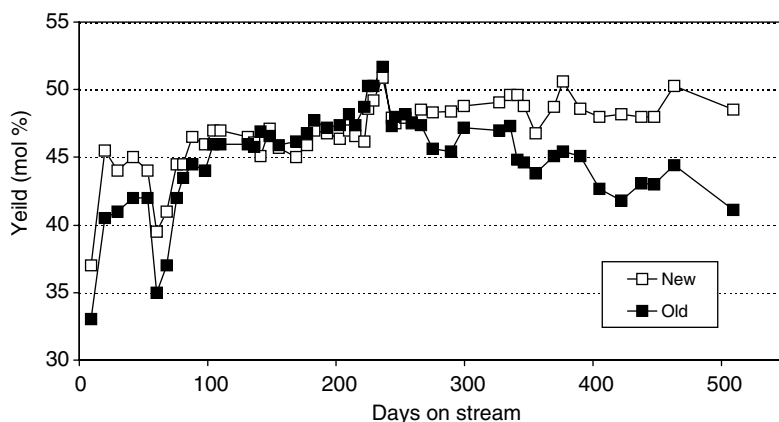


Figure 4.7 Single-reactor trial of the new catalyst in a commercial dehydrogenation unit.

the new catalyst showed about 8% higher isobutylene yield compared to the average performance of the other six reactors. It should be noted that in order to assess the individual reactor performances, the effluent of each reactor was analyzed on a weekly basis and results were tabulated.

4.5.5

Commercial Launch

Upon successful completion of the single-reactor trial of the new catalyst, a full commercial charge was loaded in the commercial isobutene dehydrogenation unit. This was the first time an entire commercial dehydrogenation unit was loaded completely with the new catalyst. A thorough assessment of this trial was critical to its future success. To perform a meaningful evaluation, results of the trial with the new catalyst were compared with the most recently completed run using the industry-standard catalyst. The first trial of the catalyst lasted for 617 days while the previous run with the standard catalyst was terminated after 589 days. Table 4.1 compares the

Table 4.1 Comparison of commercial performance of the new with the old catalyst.

Cumulative Average 589 d on stream	New Catalyst	Old Catalyst	Advantage
Fuel gas addition ($\text{m}^3 \text{h}^{-1}$)	60	133	73
Average feed rate, LHSV	1.13	1.06	0.07
Average feed temperature ($^{\circ}\text{C}$)	600	602	2
Average air temperature ($^{\circ}\text{C}$)	641	643	2
Average yield (mol%)	51.2	48.2	3.0
I = C4 production	—	—	5% ^a

^aProduction advantage normalized to equivalent feed rate.

overall operating conditions between the two runs. The new catalyst operated at lower air and feed temperatures while resulting in 5% boost in isobutylene production. A comparable, or even slightly lower, hydrocarbon feed and air temperatures, the new catalyst was able to deliver higher isobutene yield. Injection of fuel gas to the reactors, which in some units is used as an additional heat source, started later than previous practice and total fuel gas usage was considerably less than before (Table 4.1). Despite operating at up to 7% higher conversion, higher selectivity was achieved with the new catalyst than with the standard catalyst. The combination of markedly higher conversions and slightly higher selectivity led to significantly higher isobutylene yield. It was precisely because of the higher yield values that a 5% increase in isobutylene production was achieved.

4.6

Example 3: Petroleum Refining – Fluid Catalytic Cracking

Petroleum refining plays a very significant role in supplying our growing energy demands. Although alternate sources of energy are hotly debated and pursued, energy from crude oil is going to continue to supply a very large portion of our energy needs. Refining of crude oil to yield useful products such as LPG olefins, gasoline, diesel, and so on is a complex operation that involves several catalytic processes such as cracking, hydrocracking, isomerization, hydrotreating, and so on. Refining industry faces a dichotomy of feed getting heavier and product slate becoming more stringent. This dichotomy creates a challenge and an opportunity for improved and novel catalysis and processes. Each of these catalytic applications brings its own unique challenges which we will illustrate by utilizing Fluid Catalytic Cracking (FCC) as an illustrative example.

Fluid Catalytic Cracking can justifiably be called as the heart of a typical refinery. It is the largest volume process that results in molecular weight reduction from C7 to C25 + to gasoline range (C5–C11) and diesel range (C11–C17). More recently, FCC is being also used to increasingly generate lighter LPG olefins such as propylene and butylenes, which can be used as chemical feedstocks. An FCCU consists of a riser reactor and a regenerator. Feed to the FCCU is preheated and contacted with hot regenerated catalyst at the base of the riser. The mixture of feed and catalyst is pneumatically transferred up the riser in a plug flow manner along with simultaneous reaction. In the process, gas oil feed is cracked to a series of products with decreasing boiling points such as heavy cycle oil, light cycle oil (diesel), gasoline, LPG, dry gas, and hydrogen along with coke which is deposited on the catalyst. At the top of the riser the liquid and gaseous products are stripped from the catalyst and sent to a fractionation column. Spent catalyst containing about 1 wt% coke is sent to the regenerator. The major purpose of the regenerator is to oxidize the coke on the spent catalyst to CO₂ and H₂O. Another purpose of the regenerator is to utilize the heat of combustion of coke to heat the catalyst to upto ~740 °C and provide heat of reaction for the endothermic reaction. Heat for the endothermic reaction of cracking is provided by the hot catalyst entering the base of the riser.

The commercially used FCC catalyst is in the form of microspheres with an average particle size of 70 μm . It is a complex mixture of different catalytic components sometimes in the same microsphere but often in separate microspheres. Although, in recent years, several “additives” are being used for variety of catalytic applications, the heart of the process remains rare earth exchanged Y or ultra-stable Y zeolite. Several papers and books have described the role of Y zeolite in catalytic cracking and its mechanism [19].

This section will focus on three aspects of FCC catalyst development that make the task seem even more onerous: (a) understanding deactivation; (b) attrition; and (c) feedstock effects, in addition to discussing scale-up and commercialization aspects.

4.6.1

Understanding Deactivation

Understanding of deactivation is a key aspect of any industrial catalyst development program but provides unique challenges in an FCCU. As opposed to most other applications where a fresh batch of catalyst is put into industrial service or under a car and deactivates over time, fresh FCC catalyst is continuously being added to the unit and an approximately equal amount withdrawn. Commercial performance in a unit is a result of a mixture of microspheres with an infinite range of ages, from fresh to fully deactivated ones. This catalyst is called equilibrium catalyst or Ecat. In a typical unit, about 2–5% of the total catalyst in the inventory is replaced daily with fresh catalyst. Developing a commercially successful catalyst for the application will require a thorough understanding of “how” the catalyst ages and what the performance of a representative age will be.

Two types of deactivations will be discussed: (a) deactivation due to the presence of steam and temperature and (b) deactivation due to presence of contaminant metals such as Ni and V. In both the cases, more advanced strategies around age distribution will be introduced.

The primary component of FCC catalysts, Y zeolite deactivates in the presence of steam and temperature. Under conditions present in the FCC regenerator thermal deactivation is relatively a slow step and hydrothermal deactivation dominates. Activity or selectivity of an FCC catalyst is a function of the zeolites content or zeolites surface area and the UCS of the zeolites. O'Connor and Pouwels [20] systematically evaluated the effect of steam partial pressure and temperature on zeolite surface area (Figure 4.8). Figure 4.8 shows that, under FCC regenerator conditions, thermal deactivation of catalysts is minimal. The first 25% of steam has significant impact of zeolite retention. Zeolite retention continues to decline with steam partial pressure, temperature, and time. Figure 4.9 shows the effect of temperature and time on UCS at 100% steam partial pressure. Compared to surface area, equilibration of UCS is much more rapid. Typically, within the first 30 min of deactivation, the UCS decreases to the equilibrated value and is more a function of temperature than time. The choice of which variable to choose in deactivating fresh catalyst down to Ecat properties (surface area, UCS) is not clear cut. In majority of the cases, the approach has been to a priori fix the steam partial pressure at 100%. The

Surface area retention

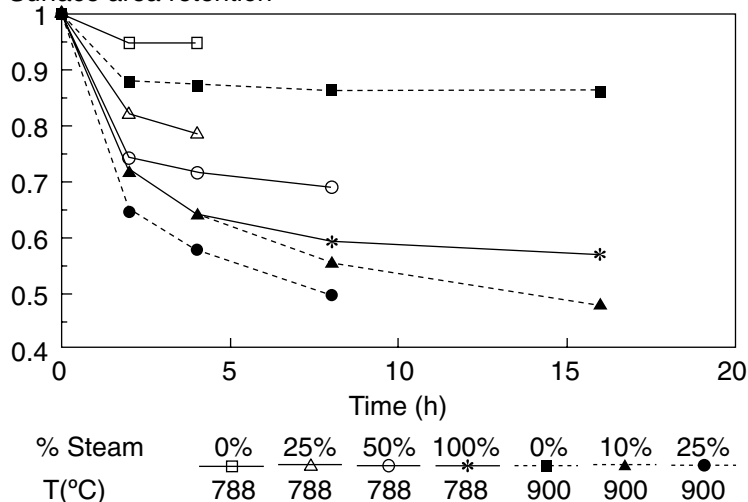


Figure 4.8 Effect of temperature and steam partial pressure on surface area retention as function of time for a typical FCC catalyst.

most common temperature employed has been either 788 or 815 °C and time is used as the “free” variable to deactivate the fresh catalyst until Ecat properties are matched.

Deactivation is even more challenging when it comes to resid FCC catalysts. The two primary contaminant metals, Ni and V, impact the catalyst activity and selectivity

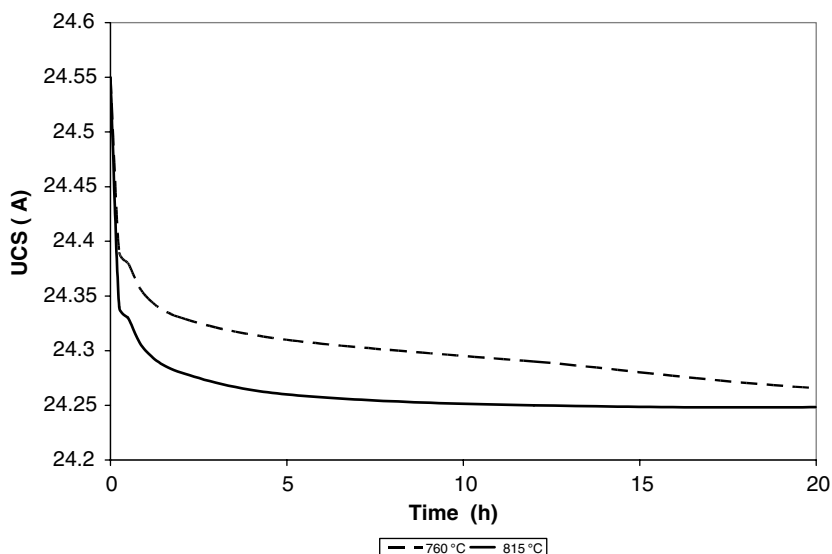


Figure 4.9 Effect of temperature at 100% steam partial pressure on Unit Cell Size (Å) as a function of time for a 1 wt% REO containing FCC catalyst.

differently. Both metals are excellent dehydrogenation catalysts and in the reductive environment in the riser, lead to H_2 and coke. Under laboratory conditions the impact of both metals is similar but in a commercial unit, V demonstrates only quarter of the propensity of Ni to catalyze dehydrogenation reaction. In addition to dehydrogenation, V also catalyzes destruction of zeolite Y and is also known to be mobile under hydrothermal conditions. A typical feed going to the unit has anywhere from 0.5 to 10 ppm of total contaminant metals which cumulatively accumulate 3000 to over 10 000 ppm on the catalysts over hundreds of cycles. How to correctly simulate the performance of such a catalyst? Industrially several strategies have been developed and they in order of increasing difficulty are

- (a) Mitchell method impregnation with steaming,
- (b) Mitchell method deposition with CPS steaming,
- (c) cyclic deposition with steaming.

The easiest and simplest approach first described by Mitchell [21] was to impregnate the catalyst with the desired amounts of Ni and V to match Ecat metals, followed by calcination and steaming. Some air, typically 10–20%, is added to the steamer to permit V to remain in the +5 state and to allow it to remain mobile. Table 4.2 [22] compares the performance of Ecat with a Mitchell method deactivated catalyst. Although both metals catalyze dehydrogenation to produce H_2 and coke, H_2 is in most cases a more sensitive measure of the dehydrogenation activity of contaminant metals. Simple Mitchell method deactivation resulted in 35% higher H_2 yield compared to Ecat, indicating that Ni and V are more active and better dispersed. There are several concerns with Mitchell method: (a) metals have not been exposed to the redox environment present in FCC; (b) the distribution of the metals does not match that of Ecat, where Ni is predominantly distributed along the rim; and (c) all the metals have been deactivated to the same extent. An attempt to correct the first concern was to introduce deactivation by Cyclic Propylene Steaming (CPS) [23]. CPS replaces gas oil as a reducing hydrocarbon with more easily manageable propylene as a laboratory reductant. Post impregnation with the Mitchell method, the catalyst is

Table 4.2 MAT catalyst–oil ratios and yields at 75% conversion after Mitchell method, CDU deactivations in comparison with equilibrium catalyst.

	Mitchell method	CDU	Ecat
C/O ratio	5.3	5.3	5.6
H_2 (wt%)	0.84	0.75	0.62
Dry gas (wt%)	3.44	3.26	2.91
LPG (wt%)	10.6	10.9	10.9
Gasoline (wt%)	50	50	50
LCO (wt%)	18.6	18.5	17.3
HCO (wt%)	7.7	8.6	9.5
Coke (wt%)	9.4	9.1	10.0

Table 4.3 Typical CPS deactivation protocol.**Heat up phase**

Room temperature to 733 °C
 29 cycles of the cycle described below at 788 °C
 10 min, 50% nitrogen + 50% steam
 10 min, 50% nitrogen (containing 5% propylene) + 50% steam
 10 min, 50% nitrogen + 50% steam
 10 min, 50%, 4000 ppm SO₂ in air + 50% steam
 30th cycle
 10 min, 50% nitrogen + 50% steam
 10 min, 50% nitrogen (containing 5% propylene) + 50% steam
 Cool down under nitrogen flow

deactivated by cycling between an environment of propylene and air along with steam. Standard protocol, as described in the above reference, is shown in Table 4.3. Since then, several modifications have been proposed but the basic redox principle remains the same.

Although CPS provides for a simulated redox mechanism, it does not lead to nonuniform decomposition of Ni, as has been observed commercially. The preferential deposition caused because the Ni-porphyrins contained in a real feed are very bulky molecules that have slow rate of diffusion even in the macropores. It is believed that the Ni-porphyrin once deposited on the surface, whether a zeolite or amorphous matrix, will remain there and be eventually burned off as coke, leaving nickel oxide on the surface of the catalyst in the regenerator. Nickel oxide will be reduced to metallic nickel in the riser.

Cyclic deposition conceptually comes closest to the real deactivation experienced by the catalyst in an FCC unit. Ni-octaoate and V-naphthanete are dissolved in light gas oil and is used as a feedstock for cracking. Their levels are chosen such that the target Ecat metal levels can be achieved in about 20–50 cycles. CDU's are designed to be fixed-fluid bed units. Typical run cycle consists of cracking of metal doped gas oil (30–90 s), stripping with N₂ (~10 min), regeneration (~10 min), and steaming (30 min). CDU protocol attempts to answer two concerns with the Mitchell method. Since metals are “cracked-on” it is presumed the distribution of Ni will be more nonuniform, and since metals are cracking in small increments, albeit still larger than commercial operation – all the metals are not deactivated to the same extent. Table 4.2 shows that CDU deactivation lowers the H₂ yield compared to Mitchell method but it is still higher than a Ecat. This is due to multitude of reasons. One of them is that the molecule used to crack is smaller than the porphyrin. This molecule could be penetrating deeper into the microsphere. A second reason could be the specific CDU protocol described in this work is milder compared to Ecat. Analogous to CPS, laboratories have continued to modify the CDU protocol.

In addition to the above protocols, industrial laboratories continue to work on developing new techniques to better mimic deactivation, especially as materials other

than Y zeolite are of interest. One of the more elegant of these approaches is the λ -sweep method [24] where the ratio of the oxidizing to reducing gases is being changed continuously as opposed to in stages as is the case with CPS.

Which of these protocols is the correct one to choose when developing industrial catalysts? The answer lies in balancing the need for speed and accuracy. Most catalyst development programs will utilize all the above protocols and sometimes use them in combination with each other. The most commonly used approach will be to utilize the simpler Mitchell method deactivation early on in a development program where speed in screening different formulations is more critical. Later on in the program, where the objective will change to obtaining the proof of principle or maybe targeting a key customer or scale-up it will be necessary to use more metal cracking such as CDU.

4.6.2

Age Distribution

The other facet of FCC catalyst deactivation is age distribution. Single-mode deactivations cannot reproduce the complex profiles of ages and levels of deactivations present in an Ecat. Beyerlein *et al.* [25] performed a systematic desegregation of an Ecat based on density differences. The younger fractions had lower density. Evaluation of catalytic activity of the different age fractions showed that the youngest 15% of the Ecat contributes 45% of the cracking activity. How to accurately replicate such an effect in the laboratory? There are no easy answers, especially since there could and would be a different answer for every FCC unit.

Stockwell and Wieland [26] have attempted to put forth a self-consistent and rational methodology on how to approach age distribution based upon modeling of zeolites' surface area, matrix surface area, and UCS. They utilized that model to replicate Ecat from a gas oil unit using three different weight fractions of 20%/40%/40%. The youngest 20% fraction was steamed at 788 °C, the second 40% was steamed at 815 °C, and the last 40% was steamed at 843 °C. Trials were needed to set the steaming time for each temperature. Their work has shown that attempting to develop complex age distribution models are not feasible and even with significant effort it is not clear that a single solution will be attained. Nevertheless, in developing commercial catalysts it is necessary to be cognizant of that.

A simpler approach that has been utilized by many laboratories is to use a single deactivation to match the zeolites and matrix surface area of an Ecat. Anywhere from 2 to 5% of fresh catalyst is added to the deactivated catalyst and this 95/5 blend is used for catalytic evaluation. This type of approach has the benefit of simplicity along with permitting the fresh catalyst to play a role in defining activity and selectivity.

4.6.3

Attrition

Commercial success of any new catalyst developed for this application requires that the active materials be part of an attrition-resistant microsphere. In a typical FCC

unit, about ~ 0.1 – 0.5 wt% of the fresh catalyst added is lost through the stack as fines. Attrition is important for two reasons: (a) refiners do not want to lose valuable catalyst and (b) in many cases, environmental regulations prohibit refiners from emitting particulates through the stack. Particulates refer to total solids being emitted from the stack. Cyclones in the FCC units are designed to retain greater than 95% of particles in excess of $\sim 20\text{ }\mu\text{m}$ and all the particles in excess of $\sim 40\text{ }\mu\text{m}$.

Sources of attrition in a fluidized FCC unit are the air grid, gas bubbles within the bed, cyclones, the bends in the piping, and so on. There are many different types of attrition testing equipment currently in use. Most of these tests are proprietary. One of the more common methods to measure attrition of FCC catalysts in the laboratory is the air jet method [27, 28]. A sample of dried and humidified catalysts is attrited in a cylindrical tube 710 mm long with an inside diameter of 35 mm, by means of three high-velocity air jets. The outlet of the tube is connected to a separation chamber that is wider in diameter and serves to retain all microspheres larger than $20\text{ }\mu\text{m}$. Microspheres smaller than that are removed by elutriation and collected in a thimble. Fines generated by measuring the weight of the thimble 1 and 5 h into the test. The air jet index is calculated from the elutriated fines to obtain a relative estimate of attrition resistance of a catalyst.

A binder is employed to glue the active zeolite crystals into a microspherical that is resistant to attrition. At present, four binder systems are used in commercial production of FCC catalysts [29]. Table 4.4 shows the four binder types and their main characteristics. Silica sol binder is a relative inert binder produced by mixing sodium silicate and acidified aluminum sulfate solution. A clear, low-viscosity sol that is very sensitive to pH and has a short shelf life is what results. The sol is mixed with active components such as Y zeolite, and spray dried to produce an attrition-resistant microsphere. In contrast, aluminum sol binders prepared from aluminum chlorhydrol (ACH) is a hydroxylated aluminum sol with chloride as the counter ion. This sol can also be used to bind active components but needs calcination before the microsphere gains the necessary strength. A third binder is pseudoboehmite alumina peptized with monoprotic acids such as formic acid. An advantage of this type of binder is that it converts to γ -alumina upon calcination, which itself provides Lewis acid sites that can participate in the cracking cycle. A completely different class of binding technology called *in situ*. In this method, kaolin platelets are spray dried into microspheres and then Y zeolite is grown within the pores, utilizing the Si and Al leached from the kaolin. The intras-structural Y zeolite in effect acts as a binder.

Table 4.4 Typical commercial binders.

Type	Surface area	Activity
Silica sol	$20\text{ m}^2\text{ g}^{-1}$	Very low
Aluminum chlorhydrol	$60\text{--}80\text{ m}^2\text{ g}^{-1}$	Moderate
Peptized alumina	$300\text{ m}^2\text{ g}^{-1}$	High
Self-binding (<i>in situ</i>)	—	High

In most cases, the choice of binder is dictated by manufacturing constraints, but it is useful to be knowledgeable about the different binders and their effect on both the attrition and catalytic selectivity.

4.6.4

Feed Effects

Another aspect of commercializing catalyst is evaluation of their performance under commercially relevant feeds. Unlike chemical reactors, which are operated within very tight feed specifications, an FCC catalyst needs to be designed for continuously varying feeds. One source of feed variation is obviously the variation of the crude oil source entering the refinery. In a hypercompetitive refining environment, a refiner is always on the lookout for the most economical feedstock available. A second source of variation is an upset or normal duty cycle variation at another unit upstream of the FCCU, for example, feed hydrotreater. As the feed hydrotreater nears the end of its cycle, the FCC unit will experience feed with higher metals, sulfur and polynuclear aromatics. An FCC catalyst has to be designed to handle such normal variations. The complexity of FCC feeds is exemplified by two typical feeds from commercial units shown in Table 4.5. Feed B is a resid feed, as typified by order of magnitude higher Ni and V content as well as higher Conradson carbon which is a measure of unreactive species in the feed. Even though the final boiling points of the two feed are identical, careful perusal of the boiling point distribution reveals that a greater fraction of feed B boils at higher temperatures. The nature of the feed molecules is characterized by several tests such as pour point and API. The lower the pour point the lower the paraffin content and greater aromatic content; API is somewhat related to inverse of the specific gravity. The higher the specific gravity, which implies lower API, the more suggestive it is of greater aromatic content.

Table 4.5 Characterization of two typical FCC feeds.

Type	Feed A Gas Oil	Feed B Resid
Ni (ppm)	0.3	6.6
V (ppm)	0.2	5.1
S (wt%)	0.74	0.65
Conradson Carbon (wt%)	0.26	4.57
Total N (ppm)	978	2209
Basic N (ppm)	298	630
API @ 60 °F	24.19	21.24
Pour point (°F)	102	80
Initial BP	267	566
30% Off	729	790
50% Off	805	850
75% Off	904	944
Final BP	1122	1123

Clearly, the complexity of a commercial feed cannot be duplicated by synthetic feed mixtures prepared from model compounds. All industrial catalyst development programs will rely on commercial feed samples. During catalytic testing, the choice of feeds should include variations in boiling point range and nature of hydrocarbon molecules, that is, paraffins versus aromatics. The metal content in the feed will play a minor role, since the amount of metal being cracked on a catalyst is trivially small compared to the metals already deposited during the deactivation period.

The above two feeds, A and B, were dramatically different and will require different approaches in developing appropriate catalyst. In contrast, feeds C and D, shown in Table 4.6 are very similar. Performance of a commercial equilibrium catalyst is compared with feeds C and D and the results at a constant coke of 10 wt% are also shown in Table 4.6. Feed D results in about 1.5 wt% lower gasoline and 1.2 wt% lower LCO. Considering that LCO is often used as blending component of diesel, change from feed C to feed D has the potential of resulting in 2.5 wt% less in liquid products that are of value to a refiner. The only noticeable difference between the two feeds is the 26% higher basic N in feed D. These basic N species are probably too bulky to enter the pores of the Y zeolite but can chemisorb on to matrix Lewis acid sites and result in higher coke yield. It can also be hypothesized that by poisoning the matrix acid sites which lead to bottoms upgrading resulting in lower LCO yields. This typical example demonstrates that feed effects in FCC are significant and play an important role in both catalyst development and selection.

Table 4.6 Catalytic cracking data of a typical Ecat with two very similar feeds in ACE microactivity unit constant coke of 10 wt%.

Type	Feed C Resid	Feed D Resid
Ni (ppm)	4.4	4.8
V (ppm)	4.1	3.9
Sulfur (wt%)	0.42	0.40
Basic N (ppm)	489	665
Conradson carbon (wt%)	5.2	5.1
API @ 60 °F	22.3	22.5
Pour point (°F)	82	80
	Yields at constant coke of 10 wt%	
H ₂ (wt%)	0.33	0.35
Dry gas (wt%)	2.26	2.19
LPG (wt%)	14.72	13.66
Gasoline (wt%)	48.28	46.68
LCO (wt%)	15.58	16.75
HCO (wt%)	8.83	10.36
Coke (wt%)	10.0	10.0

4.6.5

Scale-Up and Commercialization

The next step, once the recipe is successfully demonstrated in the laboratory, is scale-up and commercialization. Laboratory recipes are typically of the scale where 0.5–2 kg of “finished” catalyst is prepared for the different types of evaluations described above. At this scale, process variables such as type of mixer used to prepare the slurry, order of addition, and so on have less of an impact on product properties. An intermediate between the laboratory and commercial plant is the pilot plant. A typical FCC pilot plant will have the capability to produce ~5–10 kg of finished catalyst. A key difference between the pilot plant and laboratory other than just size will be the type of equipment. Process equipment in the pilot plant will be similar to that in the commercial plant. An example is while most of the calcination steps in the laboratory will be done in a standard muffle oven, pilot plant calcinations will be done in a rotary calciner. The catalyst will demonstrate subtle catalytic and maybe physical property differences dependent upon the type of calciner utilized. Also, in most cases, the pilot plant spray driers will be more reproducible in terms of physical characteristics such as particle size distribution. Due to the potentially significant impact of the scale-up step, most industrial laboratories do not distinguish between research steps and scale-up. Very often, both equipment and scale are employed very early on in the research to mitigate the effects of possible later surprises.

Industrial catalyst research is not considered to be successful until that catalyst has demonstrated the desired performance in a commercial unit. In the case of FCC, because of the variability of individual unit performance at the time of trial, performance demonstration in at least two units is desirable. Therefore, in most cases, it is desirable to manufacture ~100 t or more of finished FCC catalyst. The transition from 10 kg scale in the pilot plant to 100 t is quite challenging and the process may require some baby steps along the way. Prior history has shown which of the manufacturing operations are “scaleable” and which are more difficult to do so. In such a case, initial commercialization runs are carried out simultaneously both in the plant and the laboratory with samples from the “easy” step being bought back to the laboratory for the next process step.

4.7

Conclusions

All three examples of industrial catalysts described in this chapter demonstrate the importance of combining fundamental insight into catalyst surface and bulk properties and their impact on reaction kinetics with a thorough knowledge of process parameters. Test methods used in the laboratory are only relevant if they are conducted under conditions close to the commercial process. Rapid screening and microreactor testing should be followed or combined with tests that use real feeds containing both permanent and temporary contaminants. For fixed-bed processes using shaped catalysts, comparative testing is only valid if pellets or

extruded catalysts are used in the final evaluations. This ensures that mass transfer effects are properly accounted for. Since the catalysts in most fixed-bed processes are expected to last up to 2 to 5 years, the ability to devise meaningful accelerated aging tests that mimic the gradual aging in the commercial reactor is key to the ability to develop improved catalysts without having to perform the tests for hundreds of days before launching the new catalysts into commercial use. For fluid-bed processes, such as FCC, the ability to simulate the process is equally important.

References

- 1 Armor, J. (2005) *Applied Catalysis A: General*, **282**, 1–4.
- 2 Bartholomew, C.H. (2003) Catalyst deactivation and regeneration, in *Encyclopedia of Catalysis* (ed. I. Horvath), John Wiley & Sons, Inc., New Jersey.
- 3 ASTM D-32 (1988) *Committee on Catalysis*, 3rd edn. American Society of Testing Methods, Philadelphia, PA, USA.
- 4 Heck, R., Farrauto, R.J. and Gulati, S. (2002) *Catalytic Air Pollution Control: Commercial Technology*, 2nd edn, John Wiley & Sons, Hoboken, NJ.
- 5 Fogler, H. (1999) *Elements of Chemical Reaction Engineering*, Prentice-Hall, NJ.
- 6 Turaga, U. (2006) Chemical Engineering Progress, June 1.
- 7 Farrauto, R. and Wedding, B. (1974) Poisoning by sulfur oxides of some base metal oxide automotive exhaust catalysts. *Journal of Catalysis*, **33** (2), 249.
- 8 Yao, Y. (1975) The oxidation of CO and C₂H₄ over metal oxides. *Journal of Catalysis*, **39**, 104.
- 9 Kummer, J. (1980) Catalysts for automotive emission control. *Progress in Energy Combustion Science*, **6**, 177.
- 10 Taylor, K. (1990) Catalysts in cars. *Chemical Technology*, 551.
- 11 Acres, G., Cooper, B., Shutt, E., Malerbi, B. (1975) Platinum catalysts for exhaust emission control: The mechanism of catalyst poisoning by lead and phosphorous. ACS Series 143, in *Catalysis for Control of Automotive Pollutants* (ed J. McEvoy), American Chemical Society, Washington, D.C., p. 54.
- 12 Bartholomew, C. and Farrauto, R. (2005) *Fundamentals of Industrial Catalytic Processes*, Wiley and Sons, New Jersey.
- 13 Heck, R. and Farrauto, R. (2001) Automotive exhaust catalysts. *Applied Catalysis A: General*, **221**, 443.
- 14 SAR International (January 2008), p. 3.
- 15 Devanney, M.T. CEH Marketing Research Report.
- 16 Bhasin, M.M., McCain, J.H., Vora, B.V., Imai, T. and Pujado, P.R. (2001) *Applied Catalysis A: General*, **221**, 397–419.
- 17 Airaksinen, S.M.K. and Krause, A.O.I. (2004) Proceedings of the DGMK Conference (eds S. Ernst, A. Jess, J.A. Lercher, M. Marchionna, P. Prinz and E. Schwab), Munich, Germany, pp. 69–75.
- 18 Nijhuis, T.A., Tinnemans, S.T., Visser, T., Weckhuysen, B.M. (2004) *Chemical Engineering Science*, **59** (22–23), 5487–5492.
- 19 Wojciechowski, B.W. and Corma, A. (1986) *Catalytic Cracking: Catalysts, Chemistry and Kinetics*, Marcel Dekker, New York.
- 20 O' Connor, P. and Pouwels, A.C. (1994) *Studies in Surface Science and Catalysis*, **88**, 129–144.
- 21 Mitchell, M.M. (1980) *Industrial & Engineering Chemistry Product Research and Development*, **19**, 209–213.
- 22 Bendiksen, M., Tangstad, E., Myrstad, T. (1995) *Applied Catalysis*, **129**, 21–31.

- 23 Wallenstein, D., Roberie, T., Bruhin, T. (2007) *Catalysis Today*, **127**, 54–69.
- 24 Stockwell, D.M. (2007) *Studies in Surface Science and Catalysis*, **166**, 79–102.
- 25 Beyerlein, R.A., Tamborski, G.A., Marshall, C.L., Meyers, B.L., Hall, J.B. and Huggins, B.J. (1991) *Fluid Catalytic Cracking II, Concepts in Catalyst Design*, 109–143.
- 26 Stockwell, D.M. and Wieland, W. (2000) *American Chemical Society Division of Petroleum Chemistry*, **45** (2), 310–316.
- 27 ASTM D 5727-95 (1995) *Standard Test Method for Determination of Attrition and Abrasion of Powdered Catalysts by Air Jets*, ASTM, Philadelphia, PA.
- 28 Zhao, R., Goodwin, J.G., Jr. Jothimurugesan, K., Spivey, J.J., Gangwal, S.K. (2000) *Industrial and Engineering Chemistry Research*, **39**, 1155–1158.
- 29 Mitchell, M.M. and Magee, J.S. *Fluid Catal Crack Tech, Stud Surf Sci & Catal*, **76**, 117–120.

5

Chiral Modification of Catalytic Surfaces*Zhen Ma and Francisco Zaera*

5.1

Introduction

A tetrahedral carbon atom in a given molecule, when surrounded by four different ligands, can exist in two different and nonsuperimposable conformations; such a molecule is said to be chiral. The two possible conformers, called the (*R*) and (*S*) enantiomers (which stand for right, or rectus, and left, or sinister), are mirror images of each other, and display identical physical and chemical properties. Most synthetic routes for chiral compounds produce so-called racemic (50 : 50) mixtures, and their components are quite difficult to separate. Nevertheless, it is crucial to be able to separate them for biological and medical applications, because Nature has developed a preference for one family of enantiomers over the other [1]. For instance, while (*S*)-penicillamine is an effective antiarthritic medicine, (*R*)-penicillamine is highly toxic. Another example is that of thalidomide, of which the (*R*) enantiomer has a therapeutic effects for controlling morning sickness but the (*S*) counterpart causes severe birth defects. Ever since the thalidomide tragedy that led to tens of thousands of cases of malformations in the 1950–1960s, the importance of using enantiomerically pure chiral compounds in pharmaceuticals has received much public attention. Nowadays, pure chiral compounds are widely used in the synthesis of fine chemicals, pharmaceuticals, agrochemicals, flavors, and fragrances. The market for single enantiomers has recently reached the US \$160 billion mark, and accounts for close to half of the profits in the sales of medicines worldwide [2].

Many approaches are available for the manufacturing of chiral compounds. For instance, racemic mixtures can be separated by liquid chromatography or by reaction with other chiral compounds [3]. However, at best, these methods waste 50% of the original material and require the disposal of unreacted reagents. Enantioselective catalysis is a more promising approach, because the stereochemistry there can be controlled by using a small amount of a catalyst, thus minimizing the generation and need for disposal of side-products [4–6]. Although at present, homogeneous enantioselective catalysis by chiral metal complexes such as DIPAMP, BINAP, and

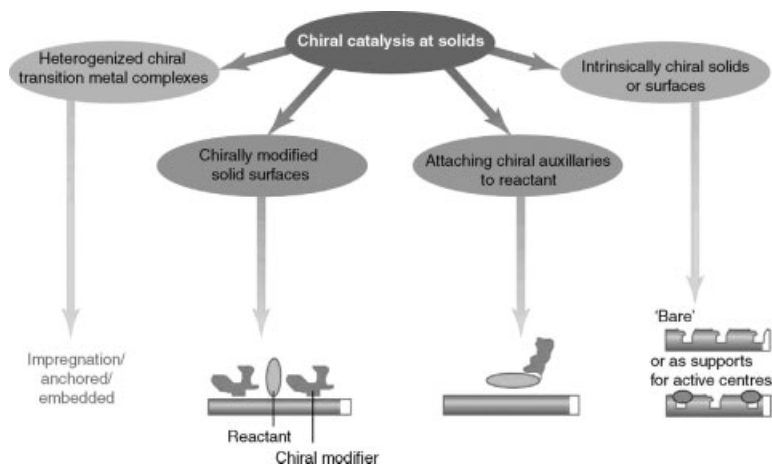


Figure 5.1 Different approaches to the design of heterogeneous enantioselective catalyst systems [7]. (Figure provided by Rasmita Raval, reproduced with permission of Springer.)

salene provides the most versatile venue for enantioselective synthesis, problems sometime arise because of the need for separation and recycling steps. It would be advantageous to use heterogeneous enantioselective catalysts instead, since those are easier to handle and recycle.

Heterogeneous enantioselective catalysts can, at least in principle, be prepared by following several strategies (Figure 5.1) [1, 7, 8]. For instance, natural chiral solids or metals deposited on chiral supports (e.g., quartz, silk, wool) may be used as catalysts. However, to date, this approach has been shown to lead to low or irreproducible enantioselectivity, or both [9, 10]. Alternatively, chiral metal complexes can be immobilized onto supports via covalent binding, ion-pair formation, or encapsulation [11, 12]. That method offers some versatility in terms of the choice of chiral complex and support that can be used, but it suffers from problems associated with leaching. In a third strategy, chirality is imparted to a metal catalyst by adsorbing a chiral modifier, which can be seen as a co-catalyst [13]. At present, this appears the most promising route to the achievement of chiral heterogeneous catalysis, as indicated by the two successful proven examples available so far, the use of cinchona alkaloid-modified platinum or palladium catalysts for the enantioselective hydrogenation of α -ketoesters [14–20], and the employment of tartaric acid-modified or aminoacid-modified nickel catalysts for the enantioselective hydrogenation of β -ketoesters [21–25]. These applications are quite limited, and the field of heterogeneous enantioselective catalysis is still in its infancy. Studies toward a better molecular-level understanding of the correlations among structure, function, and reaction mechanisms in this type of chiral modification processes are expected to facilitate the advance of the field and the development of other chiral-modified catalytic systems.

In this chapter, we summarize the recent progress that has been made in the understanding of chiral modification of catalytic surfaces from a fundamental perspective. In Section 5.2, we introduce the existing work on the enantioselective hydrogenation of α -ketoesters using cinchona alkaloid-modified platinum and palladium catalysts. In Section 5.3 we overview the data related to the enantioselective hydrogenation of β -ketoesters on tartaric acid-modified or aminoacid-modified nickel catalysts. There, we also highlight a few surface-science studies, which, although not directly connected to any existing catalytic systems, provide basic insight into surface chiral chemistry. Finally, in Section 5.4 we generalize what has been learned from these systems, comment on the advantages and limitations of these model studies, and provide some future prospects. Because there are already many excellent reviews available in the literature on the practical aspects of heterogeneous enantioselective catalysis [14–29], we will not cover any of the details associated with catalyst preparation or process design here. Instead, the focus of this review will be on the molecular characterization of the underlying surface chemistry. From this review, it is hoped that the reader gets an impression that fundamental studies can furnish deeper insights into these complex catalytic systems, and aid in the rational design of heterogeneous enantioselective catalysts.

5.2

Modification of Metal Surfaces by Cinchona Alkaloid and Related Compounds

5.2.1

General Background

Perhaps the best-studied chiral systems in heterogeneous catalysis are those that involve cinchona alkaloids. Cinchona alkaloids (e.g., quinine, quinidine, cinchonidine, and cinchonine) are typically distilled from the bark of cinchona trees, and have been long used to treat malaria and other diseases. They are also employed in organic chemistry to catalyze homogeneous reactions [30, 31]. In the late 1970s, Orito and coworkers reported that α -ketoesters can be enantioselectively hydrogenated on cinchona-modified platinum catalysts [32–34] and, after some hiatus, that system has been characterized further by several other research groups [14–19]. A prototypical reaction for this is the hydrogenation of ethyl pyruvate to (*R*)-ethyl lactate using cinchonidine as a chiral modifier for platinum catalysts, a process that can be carried out to purities of over 95% enantiomeric excess (ee). Using cinchonine (a near-enantiomer of cinchonidine) instead, ethyl pyruvate can be converted to (*S*)-ethyl lactate, also with more than 90% ee. The basic elements of this reaction, including the most typical chiral modifiers and catalysts used, are summarized in Figure 5.2 [14].

Over the last 30 years or so, the influence of the details of the catalyst preparation and pretreatment (e.g., choice of metal and support, metal dispersion, reduction temperature) as well as of the modification procedures and reaction conditions used (e.g., modifier concentration, modification sequence, solvent, reaction temperature,

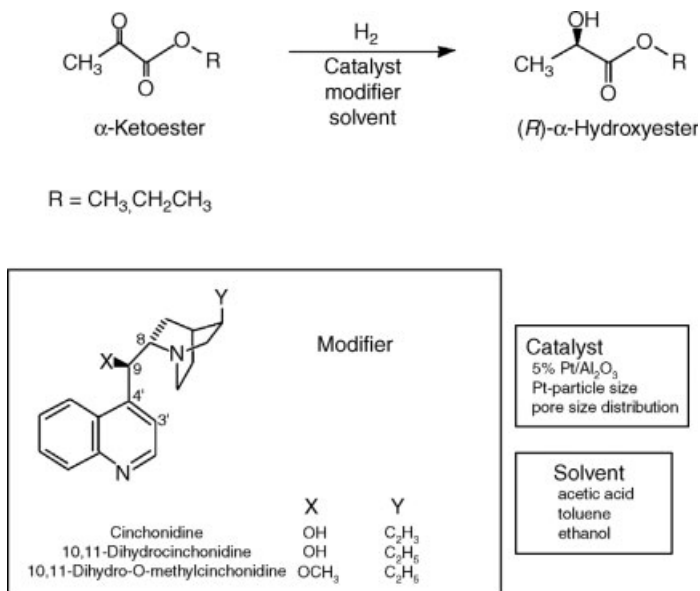


Figure 5.2 Main ingredients in the enantioselective hydrogenation of α -ketoesters over cinchona alkaloid-modified platinum metal [14]. (Figure provided by Alfons Baiker, reproduced with permission of Elsevier.)

hydrogen pressure) have been examined in great detail [14–19]. Much effort has also been placed on developing new modifiers and on extending this catalysis to a wider family of organic reactants. More recently, informative research involving experiments that rely on H–D exchange, transient modifier switching, and the use of modifier pairs has followed, and spectroscopic and surface science methods have been employed to characterize the chiral-modified catalysts. Quantum mechanics calculations and molecular modeling have been integrated into this research as well in order to get deeper insight into the physiochemical aspects of this catalysis.

5.2.2

Ordering Within the Adsorbed Layers

In their discussions on the mechanism by which cinchona alkaloids induce enantioselectivity, Wells and coworkers initially proposed a “template” model in which L-shaped cinchonidine molecules adopt a non-close-packed but ordered arrangement on Pt(100) surfaces (Figure 5.3a), leaving chiral Pt-atom ensembles uncovered. Those chiral empty sites were proposed to favor the adsorption of methyl pyruvate in a preferential configuration to promote the production of (*R*)-methyl lactate (Figure 5.3b); the formation of (*S*)-methyl lactate from methyl pyruvate on cinchonidine-modified platinum is not allowed because of steric hindrance (Figure 5.3c) [35]. Chemical interactions between methyl pyruvate and the modifier

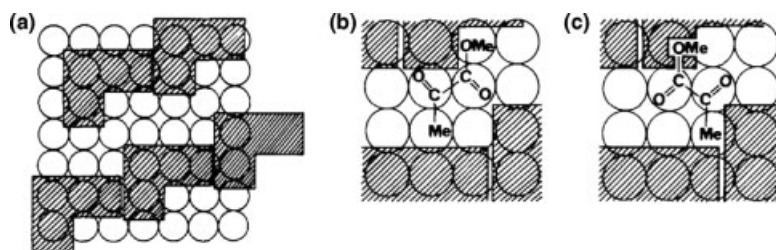


Figure 5.3 Template model proposed by Wells and coworkers to explain the chiral modification of Pt(100) surfaces for the enantioselective hydrogenation of methyl pyruvate [35]. (a) A representation of the suggested non-close-packed ordered array formed by cinchonidine molecules adsorbed on Pt(100). (b) Favorite adsorption of methyl pyruvate to yield *R*-methyl lactate upon hydrogenation. (c) Unfavorable adsorption of methyl pyruvate to produce *S*-methyl lactate. (Reproduced with permission of Elsevier.)

were not considered in this proposal, and the possibility of using bulkier reactant (e.g., ethyl-2-oxo-4-phenylbutyrate) was not addressed either.

In support of this model, Wan, Bai and coworkers showed, based on scanning tunneling microscopy (STM) data, that both cinchonidine and cinchonine form long-range ordered arrays with (4×4) symmetry on Cu(111), at least under electrochemical conditions (Figure 5.4a) [36, 37]. However, although those STM images are compelling, it is not clear whether such ordered layers also form on more relevant metal surfaces such as platinum. In fact, these authors used Cu(111) “because the mobility of adsorbates on the surface is helpful to form an ordered adlayer” [37]. Certainly, other adsorbates, including the chiral 2-phenylpropionamide [38], tyrosine [39], tartaric acid [40], and 1-(2-diphenylphosphthyl)isoquinoline [41], also form

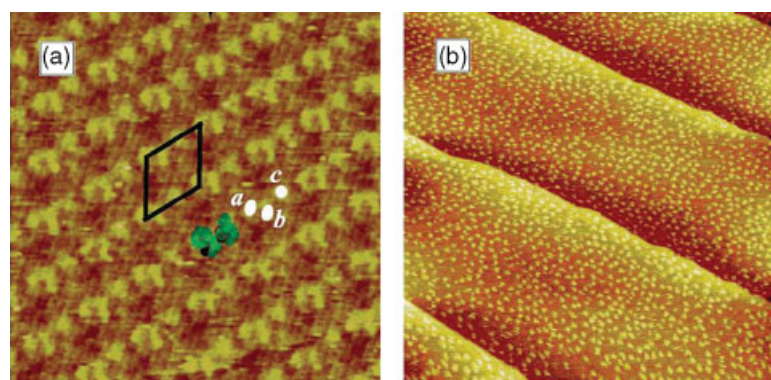


Figure 5.4 (a) High-resolution STM image of cinchonidine adsorbed on Cu(111) in 0.1 M HClO₄ (5 nm \times 5 nm) [36]. (Reproduced with permission of the American Chemical Society). (b) Adsorption of *S*-NEA on Pt(111) in the absence of H₂ at 298 K (50 nm \times 50 nm) [47]. Long-range ordering is seen in the first example but not in the more catalytically relevant second. (Figure provided by Richard Lambert, reproduced with permission of the American Chemical Society.)

ordered (4×4) adlayers on Cu(1 1 1) due to this same property, but more limited mobility and less ordering is typically seen on more reactive metals such as platinum. For instance, Wells, Roberts and coworkers found by low-energy electron diffraction (LEED) that while naphthalene (a polycyclic reference compound) forms an ordered (3×3) adlayer on Pt(1 1 1), neither quinoline (the anchoring ring of cinchona alkaloids) nor 10,11-dihydrocinchonidine form ordered layers on that surface [42, 43]. Similarly, Lambert and coworkers also reported no long-range ordering for quinoline on Pd(1 1 1) [44], and Ernst and coworkers could not observe ordered cinchonidine adlayers on Au(1 1 1) either [45].

Perhaps the more damning evidence against the “template” model is that arising from the study by Lambert and coworkers, who reported, based on STM images, that both quinoline [46] and (*S*)-naphthylethylamine (also a chiral modifier used in enantioselective hydrogenation) [47] adsorb randomly on Pt(1 1 1) (Figure 5.4b). Arx, Wahl, and coworkers also showed that cinchonidine molecules adsorb randomly on both Pt(1 1 1) and Pd(1 1 1) surfaces, and that cinchonine molecules adsorb randomly on Pt(1 1 1) as well [48, 49]. Put together, these LEED and STM data suggest not only that the ability of the adsorbed modifiers to order on the surface may depend on the nature of the metal (because the formation of ordered arrays depends strongly on the strength of the adsorbate–metal interactions [50, 51]), but also that such ordered modifier arrays are not necessary for chiral catalysis.

5.2.3

Modifier–Substrate Interactions

Nowadays, the “template” model for the way cinchona alkaloids impart chirality on metal surfaces is fairly discredited. Instead, a consensus has been reached in the literature on the chiral modifying properties of cinchona alkaloids as being the result of the formation of a 1 : 1 complex with the reactant, either prior to its adsorption onto the catalyst surface [7, 52] or once bonded to the solid [53]. This 1 : 1 complex has so far eluded experimental isolation, but has certainly been invoked in several homogeneous catalytic processes [30, 54]. Also, according to some theoretical calculations, the adsorption of α -ketoesters on cinchonidine-modified platinum surfaces via a specific configuration that favors the production of (*R*)-ethyl lactate is energetically more favorable than adsorption via the configuration needed for the production of (*S*)-ethyl lactate (Figure 5.5) [14].

In their study of the adsorption of methyl pyruvate on clean and naphthylethylamine-modified Pt(1 1 1), McBreen and coworkers have obtained fairly compelling evidence for the 1 : 1 complex-formation mechanism, and have provided additional details on how the catalytic reaction may occur. For one, they established, using reflection–absorption infrared spectroscopy (RAIRS), that while adsorption of the methyl pyruvate on Pt(1 1 1) at 110 K and low coverages leads to the formation of enediolate (a in Figure 5.6), at higher surface concentrations that is accompanied by the appearance of an additional perpendicularly adsorbed η^1 -trans species (b in Figure 5.6) [55]. The new η^1 -trans species was found to be thermally stabilized by the coadsorption of naphthylethylamine, presumably via the formation of the 1 : 1 complex required for catalysis

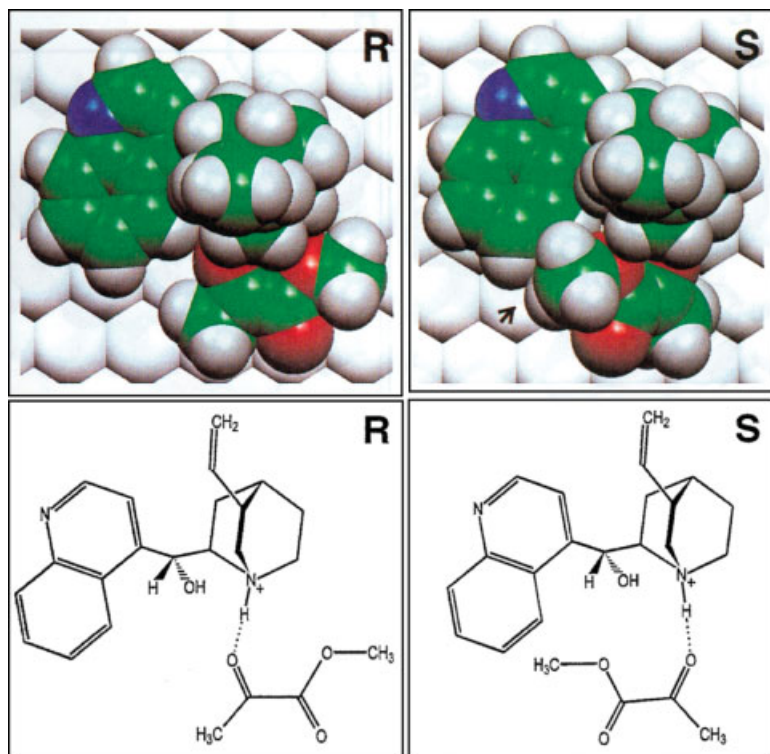


Figure 5.5 Proposed transition complexes between protonated cinchonidine and methyl pyruvate on platinum surfaces based on molecular modeling [14]. The adsorption of complex “R” (left) which leads to the production of *R*-methyl lactate is energetically more

favorable than that of complex “S” (right), which produces *S*-methyl lactate, presumably because of strong steric hindrance in the latter case. (Figure provided by Alfons Baiker, reproduced with permission of Elsevier.)

(c in Figure 5.6). The key point of this work was the finding that the 1 : 1 cinchona-pyruvate interaction occurs at the ester carbonyl of the *trans*-methyl pyruvate species oriented perpendicular to the surface. Additional TPD experiments highlighted the key role that the amine group plays in this [56].

In a separate study, McBreen and coworkers found that coadsorbed benzene converts the enediolate state of methyl pyruvate into a flat-lying species, even at low benzene coverages [57]. They proposed that this geometry change may be due to an aromatic-carbonyl interaction via $C-H \cdots O=C$ hydrogen bonding [57], as also suggested later for ethyl and methyl formate coadsorbed with unsubstituted arenes on Pt(1 1 1) [58]. These ideas were extended to advance a generalized two-point hydrogen-bonding model for enantioselective hydrogenation where the prochiral carbonyl moiety forms a $C-H \cdots O$ bond with the aromatic anchor of the modifier at the surface while the ester carbonyl fragment forms another hydrogen bond with the protonated tertiary amine group of the modifier above the surface [59].

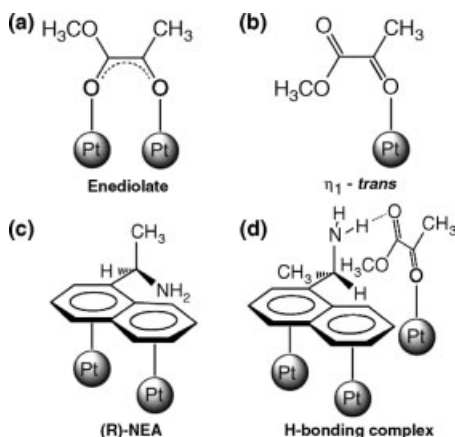


Figure 5.6 Schematic representation of the adsorption states of methyl pyruvate ((a) enediolate and (b) η^1 -trans) and *R*-naphthylethylamine (c) on Pt(111) and of the complex formation by the two on the surface (d) [55]. (Figure provided by Peter McBreen, reproduced with permission of the American Chemical Society.)

Direct interactions between the reactants and the cinchona alkaloids used as chiral modifiers have also been reported in more realistic systems. In particular, Baiker and coworkers, in their attenuated total reflection infrared (ATR-IR) spectroscopy study of the interaction between ketopantolactone and cinchonidine on a Pt-Al₂O₃ catalyst in a H₂-saturated CH₂Cl₂ solution [60], observed a broad band around 2580 cm⁻¹ that they ascribed to a N⁺–H···O hydrogen bond. As expected, the same band was not detected when coadsorbing ketopantolactone and *N*-methyl cinchonidine chloride, because no hydrogen bonding is expected in that case. In another report, Baiker and coworkers identified the interaction between ethyl pyruvate and cinchonidine on Pt-Al₂O₃ in the presence of supercritical CO₂ by a band at 1660 cm⁻¹ and two smaller signals at 1710 and 1050 cm⁻¹, which they also assigned to the formation of hydrogen bonding on the surface [61]. Independently, Muzin and coworkers reported the detection of hydrogen bonding between adsorbed cinchonidine and 1-phenyl-1,2-propanedione in their studies on Pt-Al₂O₃ catalysts by DRIFTS [62]. On the other hand, although some side reactions have been seen with ethyl pyruvate and the cinchonidine modifier on platinum catalysts [63–65], no studies of these have provided additional evidence for the formation of the 1 : 1 complex.

5.2.4

Adsorption Geometry

Another question relevant to the performance of cinchona alkaloids as chiral modifiers in heterogeneous catalysis relates to the orientation or geometry they adopt upon adsorption on the surface of the active metal phase. It has been reported that chiral modifiers with extended flat aromatic rings such as quinoline, naphthalene, and

anthracene may promote high enantioselectivity in α -ketoester hydrogenation, whereas those with non-flat rings like 1-(9-triptyceny)-2-(1-pyrrolidinyl)ethanol lead to racemic products instead [66]. It has also been observed that the ee in chiral catalysis decreases when the chiral modifier concentration exceeds an optimum value [67–69]. These observations have led to the postulation that it is the quinoline ring of the modifier that serves as the anchoring moiety on the surface of the catalyst, and that flat-lying adsorption geometry is required to achieve high enantioselectivities.

Several reports can be cited designed to test this hypothesis. For instance, Thornton and coworkers reported, based on near-edge extended X-ray absorption fine structure (NEXAFS) data, that the quinoline ring of 10,11-dihydrocinchonidine adsorbed on Pt(1 1 1) adopts an orientation nearly parallel to the surface plane, at least at 298 K and under ultrahigh vacuum (UHV) conditions [70]. Additional NEXAFS experiments by Lambert and coworkers, also under UHV, established that quinoline lies approximately flat on both Pt(1 1 1) and Pd(1 1 1) surfaces at 300 K (with tilted angles of about 15 and 18°, respectively). In contrast, lepidine (methylquinoline) and (*S*)-naphthylethylamine adopt greater tilted angles (32 and 46° on Pt(1 1 1), respectively), presumably because of steric effects [44, 46, 71]; theoretical calculations by Rauls and Hammer confirmed the tilted nature of (*S*)-naphthylethylamine on Pt(1 1 1) (tilt angle = 33°) [72]. Considering that ring substitutions are common in cinchona modifiers, the authors suggested that adsorption of the aromatic ring in strictly flat-lying geometry is not necessary for chiral induction [46].

More recently, several optical spectroscopies have been used to probe the adsorption of cinchona modifiers under more realistic conditions, namely, *in situ* at the solid–liquid interface, to take into account the effects the solvent may exert on the catalytic chiral modification. For one, Kubota and Zaera used *in situ* RAIRS to characterize the adsorption of cinchonidine from CCl₄ solutions onto the surface of a polycrystalline platinum disk [73, 74]. Significant differences were seen in the adsorption of quinoline and lepidine from solution versus in UHV, since both compounds dehydrogenate around room temperature under vacuum but not in solution, indicating that the solvent plays a crucial role in the overall chemistry of these systems [75, 76]. This contrast certainly casts some doubt on the validity of the previous UHV work. In addition, based on differences in the relative intensities among the different peaks in the spectra as a function of solution concentration, and using the so-called surface selection rule that applies to RAIRS with metals, Zaera *et al.* also concluded that the quinoline ring of several cinchona alkaloids adopts flat-lying geometry at intermediate solution concentrations but tilts to more upright geometry at higher concentrations [73, 76, 77]. A correlation was established between the cinchonidine concentrations needed for flat-lying adsorption and those that lead to optimum ee in catalysis [73].

Similar conclusions regarding the adsorption geometry that cinchona alkaloids adopt upon adsorption on platinum surfaces were reached by Bürgi and coworkers, in this case by using ATR-IR spectroscopy to characterize chiral-modified Pt-Al₂O₃ and Pd-Al₂O₃ supported catalysts in contact with a CH₂Cl₂ solution of cinchonidine (Figure 5.7) [78–80]. In additional studies, Williams and coworkers employed surface-enhanced Raman spectroscopy (SERS) to examine cinchonidine and dihydrocinch-

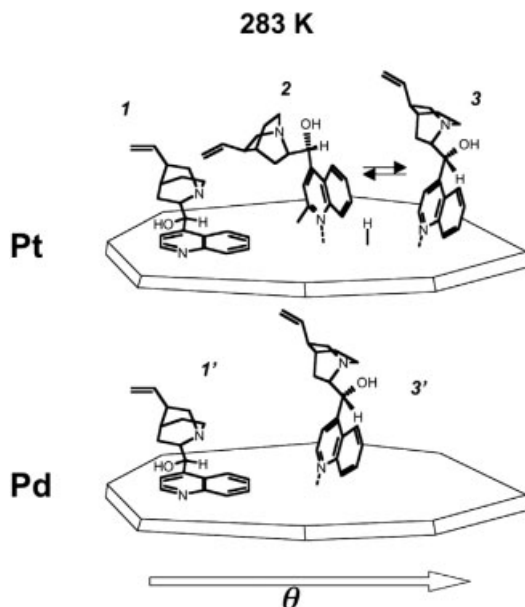


Figure 5.7 Types of cinchonidine adsorption modes proposed on Pt-Al₂O₃ and Pd-Al₂O₃ catalysts at 283 K. The evolution of these species as a function of modifier coverage (θ) is highlighted [80]. (Figure provided by Alfons Baiker, reproduced with permission of Elsevier.)

onidine adsorption from an ethanol phase on to a platinum film [77, 81, 82], and Richards and coworkers studied cinchonidine-modified platinum colloids by diffuse reflectance infrared Fourier transform spectroscopy (DRIFTS) [83]; all those groups observed behavior roughly mimicking those reported by the Zaera groups. Exceptions to this are the cases of Au-Al₂O₃ [84] and Rh-Al₂O₃ [85], where no transitions from flat-lying to tilted geometry were observed (only a tilted cinchonidine species was detected), but those two catalysts are generally not good for the promotion of enantioselective hydrogenation. Subtle differences have also been seen among the platinum- and palladium-based catalytic systems with respect to the nature of the metal surface, the modifier, and the solvent used [80], highlighting the complexity of this adsorption chemistry [86].

5.2.5

Influence of Reaction Conditions

The performance of chiral-modified catalysts is also influenced by the reaction conditions used. Certainly, things like the presence of gases in the solution, changes in the solvent used, and variations in reaction temperature, affect the final enantiomeric excesses obtained in chiral catalysis, and need to be considered when designing such process. For instance, Baiker and coworkers found that the ee obtained

for the hydrogenation of ethyl pyruvate on cinchonidine-modified $\text{Pt-Al}_2\text{O}_3$ is low in supercritical CO_2 , probably because of the formation of CO by a reverse water–gas shift reaction ($\text{CO}_2 + \text{H}_2 \rightarrow \text{CO} + \text{H}_2\text{O}$), but that the enantioselectivity increases significantly after switching to a H_2 -containing supercritical ethane solvent [87]. In another example, Li and coworkers found that in a fixed-bed reactor, the ee for the hydrogenation of ethyl pyruvate decreases over time when the ethyl pyruvate solution is made to flow through a $\text{Pt-Al}_2\text{O}_3$ catalyst pre-modified by cinchonidine [88]. The decrease in ee is most obvious with acetic acid as the solvent, less marked with ethanol, and the least extensive with toluene. Clear decreases in enantioselectivity have also been reported when the reaction temperature is raised above 40–50 °C [35, 89–91].

Again, modern surface-characterization experiments have been able to address this issue at a molecular level. For instance, Zaera and coworkers, in their work on the influence of dissolved gases on the adsorption of cinchonidine from a CCl_4 solution on to a platinum surface by *in situ* RAIRS, corroborated the dual role that H_2 plays in this reaction, cleaning the platinum surface and initially facilitating the adsorption of cinchonidine, but also removing some of the surface cinchonidine, possibly because of the hydrogenation of the quinoline ring [92]. Other gases, such as Ar, N_2 , O_2 , air, and CO_2 were determined to neither facilitate the adsorption of cinchonidine nor remove it once it adsorbs on surface, but CO was found to strongly poison the adsorption of cinchonidine. The adsorbed CO can be removed by either O_2 or H_2 , but only when hydrogen is used is it possible to ensure the subsequent uptake of cinchonidine [92]. This observation is consistent with the restoration of the ee seen after switching from supercritical CO_2 to a H_2 -saturated supercritical ethane solvent in the catalytic study mentioned earlier [87].

Ma and Zaera have also studied the influence of the nature of the solvent on the desorption of cinchonidine from a platinum disk into the liquid phase [75, 93]. The solubility of cinchonidine varies by as many as five orders of magnitude depending on the solvent used, and displays volcano-type correlations with respect to both the empirical polarity (E_T^N) and the dielectric constant of the solvent. Such solubility differences influence the adsorption–desorption equilibrium of the cinchonidine on metal surfaces [94], which shifts toward the solution with increasing dissolving power of the solvent (Figure 5.8) [75, 93]. Two main factors appear to control the stability of the adsorbate on the surface, namely, the strength of the bond between the adsorbate and the surface, and the solubility of the adsorbate in the solvent above the surface [76]. It is the balance between these two driving forces that determines the stability of the surface species. In any case, good solvents for the cinchona alkaloids seem to generally perform better in chiral catalytic processes [88, 89, 95], perhaps because they allow for a faster adsorption–desorption equilibrium, and with that an easier formation of complexes with the reactant.

In terms of temperature effects, Thornton and coworkers reported that 10,11-dihydrocinchonidine adsorbs nearly flat on $\text{Pt}(1\ 1\ 1)$ at 298 K but tilts to an angle of 60° at 323 K [70]. They ascribed the collapse in enantioselectivity seen at high temperatures to the change in the adsorption geometry of the modifier. On the other hand, Lambert and coworkers observed that quinoline adsorbs approximately flat on $\text{Pt}(1\ 1\ 1)$ and Pd $(1\ 1\ 1)$ throughout the temperature range between 300 and 360 K [44, 46]. They also

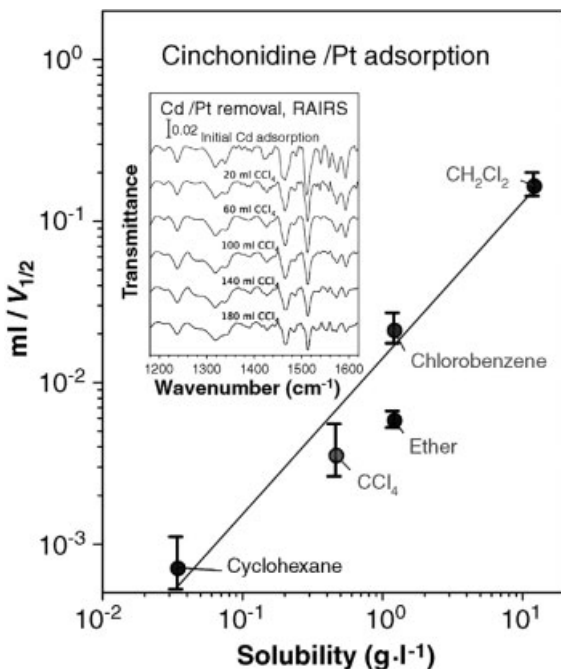


Figure 5.8 Correlation between the solubility of cinchonidine in different solvents and the ease of its desorption from platinum surfaces [93]. The latter was determined by RAIRS experiments such as those shown in the inset for CCl_4 , by measuring the volume of the pure solvent needed to reduce the RAIRS signal of the adsorbate to half that of a cinchonidine-saturated layer. The data indicate that, typically, the solvents that better dissolve cinchonidine are the ones that remove the adsorbate faster [75].

noticed an accumulation of quinoline molecules at the step edges of the $\text{Pt}(111)$ crystal upon heating to 350 K, and an accompanying increase in the number of unmodified platinum sites [46]. In another study, Lambert and coworkers observed an irreversible dimerization of (*S*)-naphthylethylamine on $\text{Pt}(111)$ in the absence of H_2 , and the destruction of the ethylamine moiety in the presence of H_2 above 320 K [47]. These observations suggest new mechanisms for the collapse of enantioselectivity upon increases in reaction temperature, even if the experiments were all carried out under UHV conditions and did not consider the effect of the solvent.

Williams and coworkers provided more detailed information on the effect of temperature in these reactions by studying the adsorption of cinchonidine and dihydrocinchonidine on platinum as a function of temperature *in situ* in the presence of an ethanol solvent [96]. The SERS bands of the modifier were seen to decrease with temperature, indicating desorption of the modifier. Also, the tilting of the quinoline ring was determined to increase significantly at elevated temperatures, as judged by the relative intensities of the peaks at 1587 and 784 cm^{-1} (Figure 5.9) [96]. The loss of modifier from the surface is consistent with the findings that the concentration of the modifier in solution increases with solution temperature [91], perhaps because of an increase in cinchonidine solubility [97].

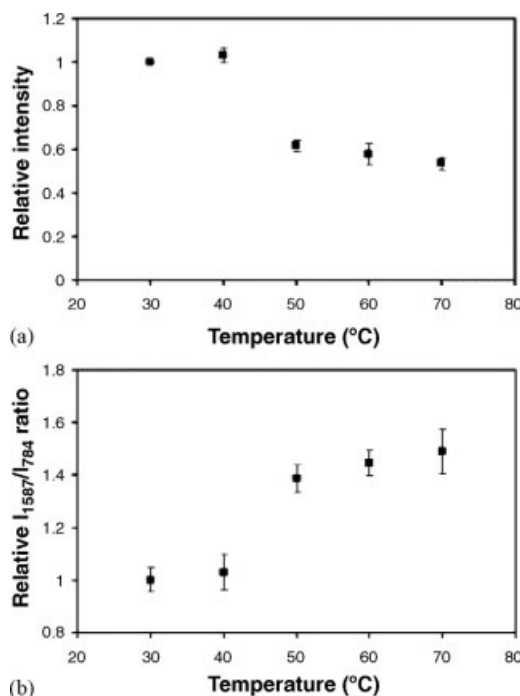


Figure 5.9 SERS characterization of cinchonidine–Pt in H₂-saturated ethanol as a function of temperature [96]. (a) Relative intensity of the 1357 cm⁻¹ in-plane ring stretching vibration, normalized to the peak intensity at 30 °C and (b) ratio of the 1587 cm⁻¹ in-plane band intensity to the 784 cm⁻¹

out-of-plane band intensity, normalized to the value of that ratio at 30 °C. The trends observed are consistent with increased tilting of the aromatic ring at high temperatures. (Figure provided by Christopher Williams, reproduced with permission of Elsevier.)

5.2.6

Competitive Adsorption of Modifiers

Further subtleties in the way cinchona alkaloids act as catalyst modifiers become evident when mixtures of two or more of those modifiers are used for chiral promotion. In such cases, nonlinear effects are seen, in terms of the dependence of the ee on the ratio of the concentration of the modifier. For instance, Baiker and coworkers found that cinchonidine prevails over *O*-phenylcinchonidine in this chiral-modifying function: the hydrogenation of ketopantolactone on a Pt-Al₂O₃ catalyst switches from 79% ee (*R*)-pantolactone to 52% ee (*S*)-pantolactone, when going from pure cinchonidine to pure *O*-phenylcinchonidine, but significant (*R*)-pantolactone excesses are also produced when using mixtures of the two modifiers with as little as 0.7% of cinchonidine [98, 99]. In another example, Wells and coworkers identified a clear preference for the production of (*R*)-methyl lactate when using mixtures of cinchonidine and cinchonine modifiers [100]. Additional coadsorption and transient modifier-switching experiments designed to test what

happens with the enantioselectivity in competitive environments have led to the general conclusion that, typically, one of the modifiers dominates the overall chemistry. These effects have been ascribed in those reports to the stronger adsorption of one of the modifiers on the surface [101–103].

Modern surface characterization experiments have provided direct evidence for this preferential adsorption in competitive environments with mixtures of cinchona chiral modifiers. For instance, Baiker and coworkers found by ATR-IR that, on a Pt-Al₂O₃ film, cinchonidine is able to displace *O*-phenylcinchonidine from the surface, but that the reverse removal of adsorbed cinchonidine by *O*-phenylcinchonidine does not occur [104]. These results indicate that cinchonidine adsorbs more strongly than *O*-phenylcinchonidine on the platinum surface, as inferred also from their catalytic data. Further research by the same group indicated that cinchonidine also bonds more strongly to platinum than quinidine [105, 106].

Ma and Zaera used displacement experiments to probe the relative adsorption strength of several modifiers on a platinum polycrystalline surface from CCl₄ solutions [107]. In some cases, the adsorption strengths were found to be so clearly different that the modifier that adsorbs the more strongly (e.g., cinchonidine) could be seen to easily displace the more weakly bound one (e.g., 6-methoxyquinoline), while the reverse could not be achieved (Figure 5.10a). However, in other instances (i.e., lepidine and quinoline) the adsorption strengths of both modifiers were close enough so that either modifier could display the other (Figure 5.10b). In the latter cases, additional coadsorption experiments such as those exemplified in Figure 5.10c were carried out to quantify the subtle difference in adsorption strength. Overall, in

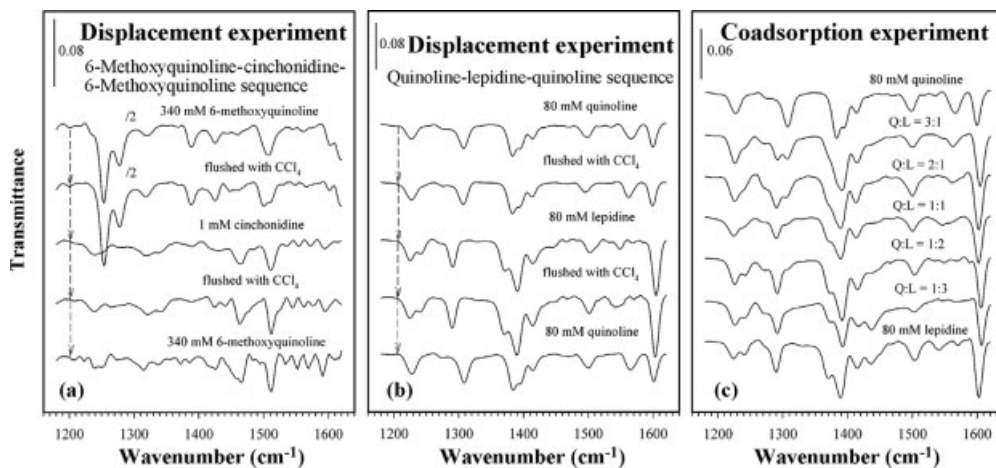


Figure 5.10 RAIRS data to test the competitive adsorption of several cinchona modifiers [107]. In these experiments, a platinum surface was exposed: (a) sequentially to CCl₄ solutions (from top to bottom) of 6-methoxyquinoline, cinchonidine, and back to 6-methoxyquinoline; (b) sequentially to CCl₄ solutions (from top to bottom) of quinoline, lepidine, and back to quinoline; and (c) to mixed quinoline + lepidine solutions of different compositions. The results allowed for the determination of the relative adsorption strengths of these compounds. (Figure provided by Francisco Zaera, reproduced with permission of the American Chemical Society.)

the presence of the CCl_4 solvent, the adsorption strength of the modifiers on platinum under competitive adsorption conditions was found to follow the sequence: quinine, quinidine > cinchonidine > cinchonine > 6-methoxyquinine > lepidine > quinoline [107]. Interestingly, separate studies on the uptake of each individual modifier on the surface lead to adsorption equilibrium constants that follow a slightly different sequence: cinchonine > quinidine > cinchonidine > quinine > 6-methoxyquinoline > lepidine > quinoline [76, 86]. Two factors were identified as key in explaining these trends, as mentioned before: (1) the solubility of the cinchona alkaloid in the solvent, and (2) the strength of the bond of the cinchona to the surface. With respect to this latter point, different bonding modes were also identified for cinchonidine, cinchonine, quinine, and quinidine, at least at high coverages [76, 86]. The sequences obtained from this work, and the underlying physical chemistry identified here, can account for some of the observations reported in the catalysis literature [49, 100, 108, 109].

5.3

Modification of Metal Surfaces by Tartaric Acid and Related Compounds

5.3.1

General Background

Another well-established chiral system in heterogeneous catalysis is that associated with the use of tartaric acid modifiers and nickel catalysts. Work on these systems started in 1958 with the report by Isoda and coworkers on the possibility of achieving enantioselective hydrogenation using Raney nickel modified with enantiopure aminoacids [110, 111]. At that time, enantioselectivities of only 2.5–36% were observed, but the promise unveiled by their observations led to more systematic studies of this catalytic system in subsequent years [21–24]. The most common modifiers used in these systems have been tartaric acid and aminoacids, and the most typical organic reactants have included β -ketoesters, β -diketones, and prochiral ketones. The nickel catalyst is most often used in the form of Raney nickel, but work has also been carried out with silica-supported nickel, nickel powders, and nickel black. Under optimized conditions, over 80% optical yields have been obtained, as in the case of the enantioselective hydrogenation of methylacetoacetate (MAA) on (*R,R*)-tartaric acid-modified nickel to produce (*R*)-methyl-3-hydroxybutrate (MHB). Figure 5.11 shows the basic features of this catalysis [7].

5.3.2

Long-Range Order Within the Adsorbed Layers

The enantioselective hydrogenation of methylacetoacetate has been proposed to occur according to the so-called “2P model,” in which two carboxylic acid groups of the tartaric acid modifier anchor onto the nickel surface, and two hydroxyl groups of the modifier form hydrogen bonds with two carbonyl groups of methylacetoacetate (Figure 5.11) [25]. This model is endorsed by the fact that replacing one of the $-\text{OH}$

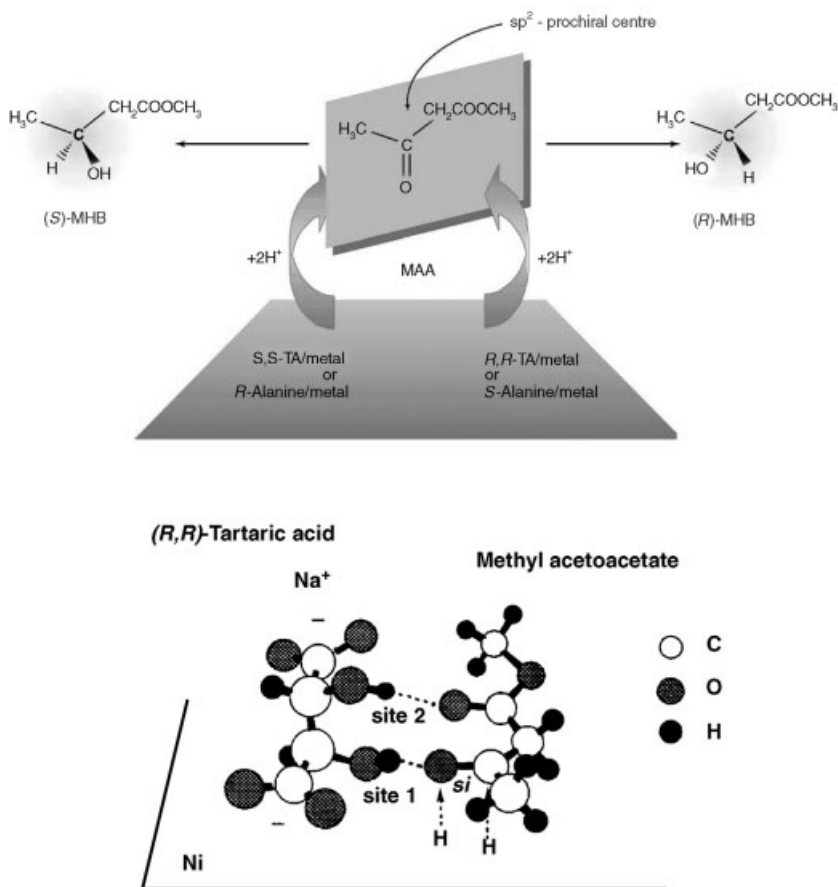


Figure 5.11 Top: Schematic illustration of the way by which the enantioselective hydrogenation of methylacetoacetate (MAA) on tartaric acid- (TA) or alanine-modified nickel catalysts occurs [7]. (Figure provided by Rasmita Raval, reproduced with permission of Springer). Bottom: 2P model proposed for the enantioselective hydrogenation of methylacetoacetate on tartaric acid-modified nickel [25]. (Reproduced with permission of Springer.)

groups in (*R,R*)-tartaric acid by $-OCH_3$ or $-OCOC_6H_5$ reduces the ee yield, measured by the polarizing activity of the products and comparing that to the expected optical activity of the pure enantiomers, from 83 to 68% and 65%, respectively. Replacing both reduces the optical yield to 0.2 and 8%, respectively, and replacing one $-COOH$ group by $-H$ or $-CH_3$ reduces the optical yield to 0 and 1.2% respectively [7, 21]. Apparently, both the carboxylic groups and the hydroxyl moieties of tartaric groups are important for this catalysis.

The bonding discussed above describes the interaction between the reactant and the chiral modifier, but does not necessarily explain the reasons for the enantioselectivity observed in these catalytic reactions. Here, the issue of the potential ordering of

the adsorbed layers comes into play again, because the molecular simplicity of the modifiers argues against a pure 1:1 complexation mechanism and suggests the possibility of a “template” model, along the lines of what was discussed in Section 5.2.2.

In searching for the long-range order that could account for the operability of the “template” model, Ravel and coworkers have carried out extensive studies on the adsorption of (*R,R*)-tartaric acid on Cu(1 1 0) surfaces by LEED, STM, and RAIRS [112]. A complex phase diagram, showing the two-dimensional ordered phases adopted by (*R,R*)-tartaric acid on Cu(1 1 0) as a function of coverage, temperature, and time, was established. Three phases were highlighted: a bitartrate phase at low coverages (Figure 5.12), a monotartrate phase at medium coverages, and a dimer–monomer

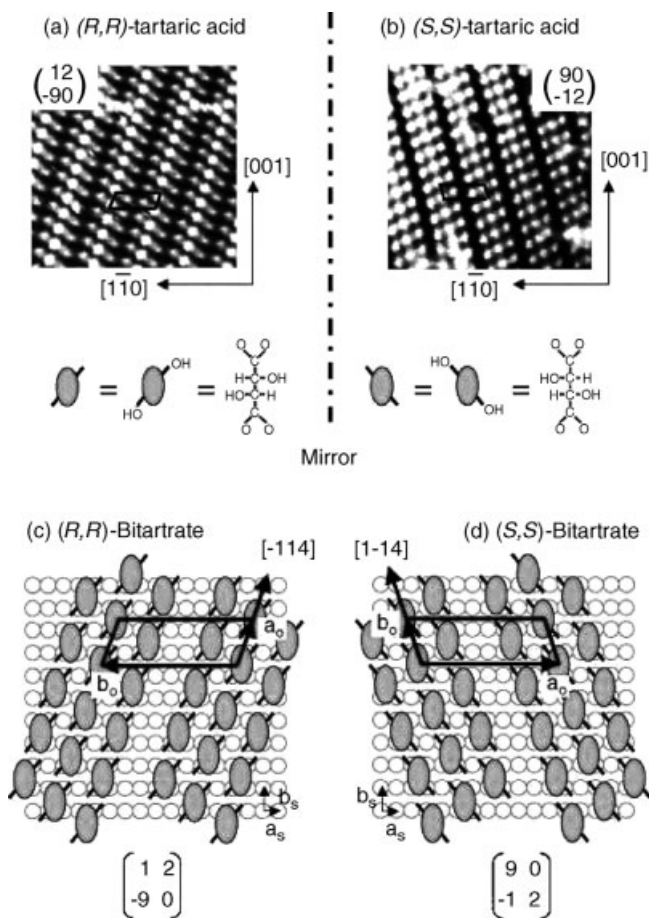


Figure 5.12 STM images and proposed ordering for the adsorption of chiral tartaric acid on Cu(1 1 0) [113]. It has been suggested that this type of chiral long-range ordering may be responsible for the chiral modification in some catalytic systems. (Figure provided by Rasmita Raval, reproduced with permission of Elsevier.)

phase at high coverages [112, 113]. The authors also showed by STM that it is possible for the monotartrate phase to be thermally transformed into a more catalytically relevant bitartrate phase [114]. Fasel, Ernst, and coworkers used angle-resolved X-ray photoelectron diffraction (XPD) to confirm the global chirality created by the adsorption of both (*R,R*)- and (*S,S*)-tartaric acid on Cu(1 1 0) [115], and models for the formation of chiral domains for tartaric acid on Cu(1 1 0), based on DFT calculations and kinetic Monte Carlo studies, have been proposed as well [116, 117]. These results are consistent with the effects identified in catalytic studies on enantioselectivity due to modification time, temperature, and modifier concentration.

Overall, the studies cited above have clearly established that under certain conditions, (*R,R*)-tartaric acid molecules form ordered chiral arrays on Cu(1 1 0), creating surfaces with extended chirality [112]. (*S,S*)-tartaric acid molecules were found to form exact mirror images of the structures seen with (*R,R*)-tartaric acid on Cu(1 1 0) (Figure 5.12) [112, 113], and similar extended chiral structures were also identified for (*R*)-alanine and (*S*)-alanine on Cu(1 1 0) [118, 119]. Those observations do give credence to the proposal of a “template” model where the formation of long-range ordered chiral domains may be responsible for the enantioselective hydrogenation of β -ketoesters. The idea is that those supramolecular structures may create chiral pockets where the hydrogenation takes place.

Other researchers have also attempted to produce and characterize long-range chirality on metal surfaces. For instance, Wan and coworkers found that both (*R,R*)- and (*S,S*)-tartaric acid also form a well-ordered adlayer with a (4×4) symmetry on Cu (1 1 1) surfaces under electrochemical conditions [40]. Pearl and coworkers, in their studies on the adsorption of (*R,R*)- and (*S,S*)-tartaric acid on Ag(1 1 1), determined that both molecules bind very weakly, and that stronger interadsorbate forces lead to the formation of ordered adlayers that are globally chiral [120]. Nevertheless, the same issues raised in the discussion of the cinchona systems reappear here. For one, it is not clear whether β -ketoester molecules with varied sizes can adsorb equally efficiently on the chiral sites. In addition, it is also not obvious that the adsorbed reactants can be enantioselectively transformed on such chiral-modified surfaces; recall that copper and silver are not good hydrogenation catalysts. Finally, it is somewhat dangerous to extrapolate results from studies with single crystals and under UHV conditions to catalytic systems.

5.3.3

Local Chirality on the Surface

To address the issue of the role of the nature of the metal in aiding the formation of ordered adsorbate layers, Raval and coworkers extended their initial studies on the adsorption of (*R,R*)-tartaric acid to a more-relevant Ni(1 1 0) surface. Unfortunately, they were not able to observe any long-range modifier ordered arrays on that substrate. On the other hand, a complex phase diagram for that system was identified here too, involving bi-acid and mono- and bi-tartrate surface species similar to those observed on copper [121]. Furthermore, DFT calculations showed that only one type of chiral footprint is favored by (*R,R*)-tartaric acid on Ni(1 1 0), with the mirror

adsorption site being unstable by 6 kJ mol^{-1} . Those results cast severe doubts on the need to form ordered chiral-modifier arrays in order to achieve chiral catalysis, and suggest that local chirality on the surface may be sufficient for this.

Collectively, all the observations mentioned above highlight the difficulty in determining the relative importance of long-range versus local chirality for bestowing chirality to hydrogenation catalysts. In fact, mixed results have been obtained in some cases. For instance, in the work of Baddeley and coworkers on the adsorption of (*R,R*)-tartaric acid on Ni(1 1 1), LEED experiments failed to indicate any ordered adsorbate structure, but STM data showed the formation of domains of two ordered phases with local coverages of 0.2 and 0.18 monolayers, respectively [122]. The authors of that study determined that the adsorption of methylacetoacetate can only take place in regions of lower (*R,R*)-tartaric acid coverages, but that, once adsorbed, methylacetoacetate locally rearranges the tartrate adsorbates to produce a two-dimensional ordered co-crystal (Figure 5.13) [123]. They proposed that one of the carbonyl moieties in the methylacetoacetate may interact with an α -hydroxyl group of a neighboring tartrate species in these structures. This certainly points to the dynamic and synergistic interaction between the chiral modifier and the reactant.

Additional work has also been carried out on the adsorption of (*S*)-glutamic acid on Ni(1 1 1) [124]. The interest in that system stems from the fact that the ee during the hydrogenation of methylacetoacetate using this modifier is greatly affected by temperature: modification at 273 K results in an excess of (*R*)-methyl-3-hydroxybutyrate, but when the modification is conducted above 350 K, a slight preference for the (*S*)-product is observed [22]. A combination of RAIRS and transmission electron microscopy (TEM) results led to the conclusion that at low coverage, adsorption of

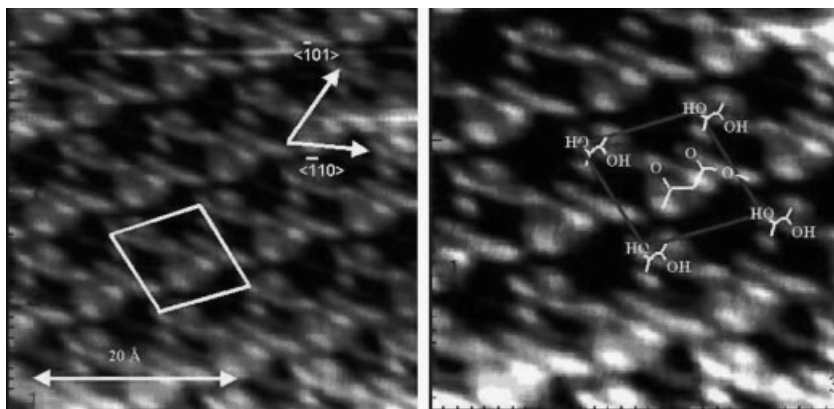


Figure 5.13 STM images of methylacetoacetate adsorbed on low-coverage *R,R*-tartaric acid-modified Ni(1 1 1) [123]. A local rearrangement occurs upon this coadsorption, presumably driven by an interaction between a carbonyl moiety in methylacetoacetate and an α -hydroxyl group in a neighboring tartrate. (Picture provided by Christopher Baddeley, reproduced with permission of Elsevier.)

(*S*)-glutamic acid on Ni(1 1 1) induces the formation of a zwitterionic species at 300 K but not at 350 K. The authors of that work reasoned that the NH_3^+ group of the zwitterions hydrogen bonds with methylacetoacetate in a way that favors the production of (*R*)-methyl-3-hydroxybutyrate. To complicate matters further, they also found that at 350 K, the modifier significantly corrodes the step edges of Ni(1 1 1). Since no such corrosion was observed at 300 K, that side reaction may also influence the enantioselectivity.

In their RAIRS studies on the adsorption of (*S*)-glutamic acid on Ni(1 1 1), both alone and coadsorbed with methylacetoacetate, Baddeley and coworkers reported that methylacetoacetate adsorbs on the Ni(1 1 1) surface in two tautomeric forms, diketo and enol [125, 126]. Since the diketo–enol ratio was found to decrease with temperature, they argued that the diketo tautomer of methylacetoacetate may be the precursor to (*R*)-methyl-3-hydroxybutyrate production. Interestingly, the sticking probability of methylacetoacetate on (*S*)-glutamic acid–saturated surfaces is close to zero; its adsorption can only occur at lower modifier coverages. Based on this observation, the authors proposed a 1 : 1 interaction model for this chiral-modified system. However, no infrared peak assigned to the proposed hydrogen bonding was identified.

5.3.4

Identification of Chiral Sites on Surfaces

Regardless of the molecular details on how the chiral modifier works in the tartaric acid and amino acid systems, surface chirality can be probed in those indirectly by using a second chiral adsorbate. This has been the approach pioneered by Tysoe and coworkers [127, 128] and also followed by Zaera and coworkers [129, 130].

In their initial work, Tysoe and coworkers chose 2-butanol, a chiral alcohol, as the chiral templating agent to modify Pd(1 1 1) surfaces, and propylene oxide, also a chiral molecule, to probe the potential formation of chiral sites on the surface [127]. The 2-butanol precursor decomposes on Pd(1 1 1) to form 2-butoxide, and anchors on the surface through the oxygen atom. The key observation that derived from that work is that the uptake of (*R*)-propylene oxide on (*R*)-2-butoxide-covered Pd(1 1 1) can be as much as twice that possible on (*S*)-2-butoxide-covered surfaces prepared under identical conditions. This effect is coverage dependent, peaking at a relative 2-butoxide coverage of 25% of saturation and disappearing at a coverage of 50% of saturation (Figure 5.14) [127]. Tysoe et al. then extended their work to 2-methylbutanoic acid as the precursor to modify the Pd(1 1 1) surface to test the generality of the observations derived above [128]. Surprisingly, the experiments on the adsorption of (*R*)- or (*S*)-propylene oxide on to (*R*)- or (*S*)-methylbutanoate-modified Pd(1 1 1) indicated no enantioselectivity. The authors explained this apparent contradiction by suggesting that the chiral butyl group sits farther away from the metal surface when bonded via a carboxylate than via an oxygen atom, and that this difference leads to a freer azimuthal rotation of the chiral center. Indeed, they also found that enantioselectivity is restored when the methyl group of methylbutanoate is replaced by an amine group (i.e., by using chiral 2-aminobutanoate as the template). They postulated

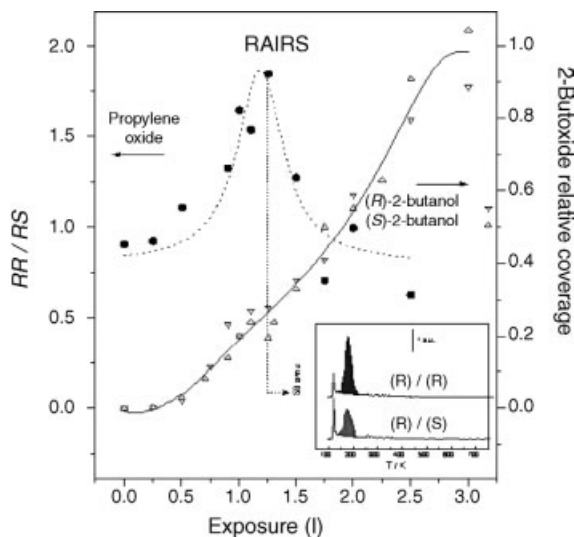


Figure 5.14 Test of enantioselectivity for R -propylene oxide adsorbed on S -2-butoxide modified $Pd(111)$ surfaces. Shown in the main figure are plots of the relative coverages of S -2-butoxide (Δ) and R -2-butoxide (∇) as a function of exposure on $Pd(111)$ (right axis), and of the ratio of the coverage of R -propylene oxide adsorbed on R -2-butoxide-covered $Pd(111)$ (RR) to the saturation coverage

of R -propylene oxide adsorbed on S -2-butoxide (RR/RS) (\bullet) (left axis) as a function of 2-butanol exposure. The inset shows typical propylene oxide desorption spectra from 2-butoxide-covered $Pd(111)$ [127]. (Figure provided by Wilfred Tysoe, reproduced with permission of the American Chemical Society.)

that the role of the amino group is to anchor the chiral group and to inhibit azimuthal rotation.

Lee and Zaera's experiments on $Pt(111)$ instead of $Pd(111)$ have provided some support for Tysoe's model but also raised new questions [129, 130]. Consistent with the findings of Tysoe *et al.*, the Zaera group found that (R)-propylene oxide adsorbs more extensively on (R)-butoxide-templated $Pt(111)$ and (S)-propylene oxide adsorbs more on (S)-butoxide-templated $Pt(111)$ than the other way around, namely, (S)-propylene oxide on (R)-butoxide-templated $Pt(111)$ or (R)-propylene oxide on (S)-butoxide-templated $Pt(111)$ [129]. However, in contrast, they also found a measurable enantioselectivity for the uptake of (S)-propylene oxide on (S)- versus (R)-2-methylbutanoate-templated $Pt(111)$ surfaces [129]. This observation brings into question the two-point anchoring model and highlights the differences induced by the nature of the metal. Unfortunately, because of the indirect way in which enantioselectivity is probed in these experiments, it is not clear whether the enantioselectivity imparted by the templating agent is due to long-range ordering or to the creation of local chiral environments on the surface by the chiral modifiers. What is evident is that the promotion is quite general: Tysoe and coworkers have identified enantioselectivity on palladium surfaces templated with several aminoacids, including alanine, norvaline, proline, and isoleucine. On the other hand, the effect is not universal: no enantioselectivity was seen with valine or leucine. Clearly,

the secondary structure of the modifier also plays a key role in aiding enantioselectivity [131]. Lee and Zaera have recently observed significant enantioselectivity with 1-naphthylethylamine on Pt(1 1 1) as well, although in that case differences in energy of adsorption were also evident. The question then arises on what the relative contributions of entropic ordering versus energetic 1 : 1 interactions are to the overall surface chiral bestowing effect. More work is needed to unravel these uncertainties.

5.4

Conclusions

In this chapter, we have briefly surveyed the recent progress made in the research of chiral modification of surfaces from a fundamental perspective. In particular, we have emphasized the studies that rely on the use of modern surface-science and spectroscopic techniques to provide molecular-level information on heterogeneous enantioselective catalysis. Examples were given above on adsorption systems related to the enantioselective hydrogenation of α -ketoesters on cinchona alkaloid-modified platinum and palladium catalysts and of β -ketoesters on tartaric acid- or aminoacid-modified nickel catalysts. Work has also been carried out on more basic systems dealing with patterns formed via adsorption of chiral molecules [50, 51], the adsorption and reaction of organic molecules on inherently chiral metal surfaces [132, 133], and the restructuring of metal surfaces by chiral adsorbates [134–136], but those fall outside the scope of this chapter, and were therefore not discussed here in any detail.

Valuable information can be extracted from the fundamental studies reviewed above. For one, it has been determined that the adsorption of chiral modifiers is the controlling factor in their behavior towards promoting enantioselectivity in catalysis, and that such adsorption is critically influenced by many operational parameters, including the temperature, the modifier concentration, the type of solvent, and the nature of metal utilized, to mention a few. These factors influence the adsorbate conformation, coverage, adsorption geometry, order on the surface, and adsorption–desorption equilibrium. It has been clear that the optimization of chiral modification in these enantioselective catalytic systems needs to be achieved by exerting proper control on the adsorption of the chiral modifiers as a function of those parameters. That requires the type of direct knowledge on the molecular details of the adsorption reported here, aided by spectroscopic characterization, surface-science techniques, and theoretical calculations.

Although a unified picture of the reaction mechanisms operative in the different chiral catalytic systems known to date is not yet available, it is already certain that the formation of ordered chiral modifier arrays is not necessary for chiral catalysis in either of the hydrogenation systems for which enantioselectivity has been observed. On the other hand, specific synergies among the reactant, the modifier, and the active metal surfaces are required to achieve enantioselectivity, probably controlled, at least in part, by hydrogen bonding and other acid–base interactions and by the favoring of particular molecular conformations and/or adsorption geometries [13]. According to

Baiker and Blaser, an enantioselective catalyst must fulfill two functions: it must be able to activate the different reactants, and it must control the stereochemical outcome of the reaction [16]. These functions imply the need of particular chemical interactions on the surface of the catalyst with high enantiospecificity. The direct outcome of such enantiospecificity is a differentiation in the activation energies for the formation of the appropriate intermediate structures within the two enantiomers of the product. These energetic effects do not need to be dramatic: it is estimated that at 25 °C, an energy difference of only 6–12 kJ mol⁻¹ is sufficient to lead to enantiomeric excesses of about 80–98% [16].

Entropic terms may also play a role in the chiral modification of catalysts. Besides the potential for long- or short-range ordering of the modifier, as discussed above, there is also the possibility for the chiral modifier to adopt many energetically close configurations on the surface, especially in the case of the cinchona alkaloids, or for the reactants to bind in different adsorption modes to the solid metal. It may also be concluded from the above literature survey that the modifier may require, besides one or more chiral centers, more than one key functional group to anchor to the surface and to interact with the reactant. Indeed, multiple interactions may be required between the modifier and the surface to render the chiral center rigid enough to allow its chirality to be expressed. That would contribute to both the entropy and enthalpy of the kinetics terms that explain the enantioselectivity [137–139]. It is also quite likely that the adsorbed chiral modifier must not adsorb in a close-packed mode on the surface to leave room for the adsorption and conversion of the reactant; hence the optimal chiral behavior seen at intermediate concentrations with cinchonidine, and at intermediate coverages in the case of the chiral probing experiments on the chiral-templated single-crystal surfaces.

Finally, we should point out that the current understanding of these systems is quite limited still, and that the fundamental work has not yet led to any significant predictions or to the developing of truly new chiral systems. These limitations are likely to be addressed in the near future. In particular, *in situ* spectroscopic characterization can be now conducted while monitoring the catalytic activity and enantioselectivity on real catalysts, and first-principle calculations and molecular modeling can be performed on fairly complex systems to take the contributions of the metal and the solvent into account. New catalytic systems for characterization studies can also be built up by increasing the complexity of the modifier and the reactant step by step [140–142]. The associated chemistry that takes place in the solution phase (e.g., the conformational fluctuations and the possible protonation of the modifier in different solvents) is also being explored [143, 144]. In more general terms, it needs to be acknowledged that most workers have so far been dealing with simplified models of these systems, typically including only two or three elements such as the modifier and either the solvent or the surface. To build up more realistic systems in the future, the interplay among all – the solvent, catalyst, modifier, reactant, and product – needs to be considered collectively in more complex model systems. With these advances, it is hoped that the synergy between catalysis and surface science will help advance our fundamental understanding of these systems and aid in the design of industrial catalysts for heterogeneous enantioselective hydrogenation [145].

References

- 1 Coman, S.M., Poncelet, G. and Parvulescu, V.I. (2006) in *Surface and Nanomolecular Catalysis* (ed. R. Richards), Taylor & Francis (CRC Press), New York, pp. 493–531.
- 2 Rouchi, A.M. (1999) *Chemical & Engineering News*, **77** (41), 101.
- 3 Collins, A.N., Sheldrake, G.N. and Crosby, J. (eds) (1997) *Chirality in Industry II*, John Wiley & Sons, Chichester.
- 4 Jacobsen, E.N., Yamamoto, A. and Pfaltz, A. (eds) (1999) *Comprehensive Asymmetric Catalysis*, Springer, Berlin.
- 5 Ojima, I. (ed.) (2000) *Catalytic Asymmetric Synthesis*, 2nd edn, Wiley-VCH, Weinheim.
- 6 Blaser, H.U. and Schmidt, E. (eds) (2003) *Large Scale Asymmetric Catalysis*, Wiley-VCH, Weinheim.
- 7 Raval, R. (2001) *Cattech*, **5**, 12.
- 8 Heitbaum, M., Glorius, F. and Escher, I. (2007) *Angewandte Chemie-International Edition*, **45**, 4732.
- 9 Akabori, S., Izumi, Y., Fujii, Y. and Sakurai, S. (1956) *Nature*, **178**, 323.
- 10 Studer, M. and Blaser, H.-U. (2001) *Journal of Molecular Catalysis A – Chemical*, **172**, 277.
- 11 Vankelecom, I.F.J. and Jacobs, P.A. (2000) in *Chiral Catalyst Immobilization and Recycling* (eds D.E. De Vos, I.F.J. Vankelecom and P.A. Jacobs), Wiley-VCH, Weinheim, pp. 19–42.
- 12 McMorn, P. and Hutchings, G.J. (2004) *Chemical Society Reviews*, **33**, 108.
- 13 Baiker, A. and Blaser, H.U. (1997) *Handbook of Heterogeneous Catalysis (Volume 4)* (eds G. Ertl, H. Knözinger and J. Weitkamp), VCH, Weinheim, pp. 2422–2436.
- 14 Baiker, A. (1997) *Journal of Molecular Catalysis A – Chemical*, **115**, 473.
- 15 Wells, P.B. and Wilkinson, A.G. (1998) *Topics in Catalysis*, **5**, 39.
- 16 Studer, M., Blaser, H.-U. and Exner, C. (2003) *Advanced Synthesis and Catalysis*, **345**, 45.
- 17 Murzin, D.Y., Mäki-Arvela, P., Toukoniitty, E. and Salmi, T. (2005) *Catalysis Reviews – Science and Engineering*, **47**, 175.
- 18 Hutchings, G.J. (2005) *Annual Review of Materials Research*, **35**, 143.
- 19 Barkók, M. (2006) *Current Organic Chemistry*, **10**, 1533.
- 20 Mallat, T., Orglmeister, E. and Baiker, A., (2007) *Chemical Reviews*, **107**, 4863.
- 21 Izumi, Y. (1971) *Angewandte Chemie-International Edition*, **10**, 871.
- 22 Izumi, Y. (1983) *Advances in Catalysis*, **32**, 215.
- 23 Osawa, T., Harada, T. and Tai, A. (1997) *Catalysis Today*, **37**, 465.
- 24 Tai, A. and Sugimura, T. (2000) *Chiral Catalyst Immobilization and Recycling* (eds D.E. De Vos, I.F.J. Vankelecom and P.A. Jacobs), Wiley-VCH, Weinheim, pp. 173–209.
- 25 Osawa, T., Harada, T. and Takayasu, O. (2000) *Topics in Catalysis*, **13**, 155.
- 26 Fish, M.J. and Ollis, D.F. (1978) *Catalysis Reviews – Science and Engineering*, **18**, 259.
- 27 Blaser, H.U., Jalett, H.P., Müller, M. and Studer, M. (1997) *Catalysis Today*, **37**, 441.
- 28 Sugimura, T. (1999) *Catalysis Surveys from Japan*, **3**, 37.
- 29 Baiker, A. (2000) *Journal of Molecular Catalysis A – Chemical*, **163**, 205.
- 30 Kacprzak, K. and Gawronski, J. (2001) *Synthesis*, 961.
- 31 Yoon, T.P. and Jacobsen, E.N. (2003) *Science*, **299**, 1691.
- 32 Orito, Y., Imai, S. and Niwa, S. (1979) *Nippon Kagaku Kaishi*, 1118.
- 33 Orito, Y., Imai, S., Niwa, S. and Nguyen, G.H. (1979) *Journal of Synthetic Organic Chemistry, Japan*, **37**, 173.
- 34 Orito, Y., Imai, S. and Niwa, S. (1980) *Nippon Kagaku Kaishi*, 670.

- 35 Sutherland, I.M., Ibbotson, A., Moyes, R.B. and Wells, P.B. (1990) *Journal of Catalysis*, **125**, 77.
- 36 Xu, Q.-M., Wang, D., Wan, L.-J., Bai, C.-L. and Wang, Y. (2002) *Journal of the American Chemical Society*, **124**, 14300.
- 37 Xu, Q.-M., Wang, D., Han, M.-J., Wan, L.-J. and Bai, C.-L. (2004) *Langmuir*, **20**, 3006.
- 38 Xu, Q.M., Wang, D., Wan, L.J., Wang, C., Bai, C.L., Feng, G.Q. and Wang, M.X. (2002) *Angewandte Chemie-International Edition*, **41**, 3408.
- 39 Wang, D., Xu, Q.M., Wan, L.J., Bai, C.L. and Jin, G. (2003) *Langmuir*, **19**, 1958.
- 40 Yan, H.J., Wang, D., Han, M.J., Wan, L.J. and Bai, C.L. (2004) *Langmuir*, **20**, 7360.
- 41 Han, M.J., Wang, D., Hao, J.M., Wan, L.J., Zeng, Q.D., Fan, Q.H. and Bai, C.L. (2004) *Analytical Chemistry*, **76**, 627.
- 42 Simons, K.E., Meheux, P.A., Griffiths, S.P., Sutherland, I.M., Johnston, P., Wells, P.B., Carley, A.F., Rajumon, M.K., Roberts, M.W. and Ibbotson, A. (1994) *Recueil des Travaux Chimiques des Pays-Bas-Journal of the Royal Netherlands Chemical Society*, **113**, 465.
- 43 Carley, A.F., Rajumon, M.K., Roberts, M.W. and Wells, P.B. (1995) *Journal of the Chemical Society – Faraday Transactions*, **91**, 2167.
- 44 Bonello, J.M., Lindsay, R., Santra, A.K. and Lambert, R.M. (2002) *The Journal of Physical Chemistry B*, **106**, 2672.
- 45 Behzadi, B., Ferri, D., Baiker, A. and Ernst, K.H. (2007) *Applied Surface Science*, **253**, 3480.
- 46 Bonello, J.M. and Lambert, R.M. (2002) *Surface Science*, **498**, 212.
- 47 Bonello, J.M., Williams, F.J. and Lambert, R.M. (2003) *Journal of the American Chemical Society*, **125**, 2723.
- 48 von Arx, M., Wahl, M., Jung, T.A. and Baiker, A. (2005) *Physical Chemistry Chemical Physics*, **7**, 273.
- 49 Wahl, M., von Arx, M., Jung, T.A. and Baiker, A. (2006) *The Journal of Physical Chemistry B*, **110**, 21777.
- 50 Humblot, V., Barlow, S.M. and Raval, R. (2004) *Progress in Surface Science*, **76**, 1.
- 51 Ernst, K.-H. (2006) *Topics in Current Chemistry*, **265**, 209.
- 52 Margitfalvi, J.L., Hegedüs, M. and Tfirst, E. (1996) *Studies in Surface Science and Catalysis*, **101**, 241.
- 53 Bürgi, T. and Baiker, A. (2004) *Accounts of Chemical Research*, **37**, 909.
- 54 Kolb, H.C. and Sharpless, K.B. (1998) *Transition Metals for Organic Synthesis* (eds M. Beller and C. Bolm), Wiley-VCH, Weinheim, Germany, pp. 243–260.
- 55 Lavoie, S., Laliberté, M.-A. and McBreen, P.H. (2003) *Journal of the American Chemical Society*, **125**, 15756.
- 56 Lavoie, S., Laliberté, M.-A. and McBreen, P. (2004) *Catalysis Letters*, **97**, 111.
- 57 Lavoie, S. and McBreen, P.H. (2005) *The Journal of Physical Chemistry B*, **109**, 11986.
- 58 Lavoie, S., Mahieu, G. and McBreen, P.H. (2006) *Angewandte Chemie-International Edition*, **45**, 7404.
- 59 Lavoie, S., Laliberte, M.A., Temprano, I. and McBreen, P.H. (2006) *Journal of the American Chemical Society*, **128**, 7588.
- 60 Bonalumi, N., Bürgi, T. and Baiker, A. (2003) *Journal of the American Chemical Society*, **125**, 13342.
- 61 Schneider, M.S., Urakawa, A., Grunwaldt, J.D., Bürgi, T. and Baiker, A. (2004) *Chemical Communications*, 744.
- 62 Busygin, I., Tkachenko, O.P., Nieminen, V., Borokov, V.Y., Sillanpää, R., Toukonniitty, E., Kustov, L.M., Murzin, D.Y. and Leino, R. (2007) *The Journal of Physical Chemistry C*, **111**, 9374.
- 63 Ferri, D., Bürgi, T. and Baiker, A. (2004) *The Journal of Physical Chemistry B*, **108**, 14384.
- 64 Ferri, D., Diezi, S., Maciejewski, M. and Baiker, A. (2006) *Applied Catalysis A: General*, **297**, 165.
- 65 Liu, Z.M., Li, X.H., Ying, P.L., Feng, Z.C. and Li, C. (2007) *The Journal of Physical Chemistry C*, **111**, 823.
- 66 Baiker, A. (2000) *Chiral Catalyst Immobilization and Recycling* (eds D.E. De Vos, I.F.J. Vankelecom and P.A. Jacobs), Wiley-VCH, Weinheim, pp. 155–171.

- 67 Schwalm, O., Minder, B., Weber, J. and Baiker, A. (1994) *Catalysis Letters*, **23**, 271.
- 68 Bond, G. and Wells, P.B. (1994) *Journal of Catalysis*, **150**, 329.
- 69 LeBlond, C., Wang, J., Andrews, A.T. and Sun, Y.K. (2000) *Topics in Catalysis*, **13**, 169.
- 70 Evans, T., Woodhead, A.P., Gutiérrez-Sosa, A., Thornton, G., Hall, T.J., Davis, A.A., Young, N.A., Wells, P.B., Oldman, R.J., Plashkevych, O., Vahtras, O., Ågren, H. and Carravetta, V. (1999) *Surface Science*, **436**, L691.
- 71 Bonello, J.M., Sykes, E.C.H., Lindsay, R., Williams, F.J., Santra, A.K. and Lambert, R.M. (2001) *Surface Science*, **482**, 207.
- 72 Rauls, E. and Hammer, B. (2006) *Catalysis Letters*, **106**, 111.
- 73 Kubota, J. and Zaera, F. (2001) *Journal of the American Chemical Society*, **123**, 11115.
- 74 Kubota, J., Ma, Z. and Zaera, F. (2003) *Langmuir*, **19**, 3371.
- 75 Ma, Z., Lee, I., Kubota, J. and Zaera, F. (2004) *Journal of Molecular Catalysis A – Chemical*, **216**, 199.
- 76 Ma, Z., Lee, I. and Zaera, F., (2007) *Journal of the American Chemical Society*, **129**, 16083.
- 77 Chu, W., LeBlanc, R.J., Williams, C.T., Kubota, J. and Zaera, F. (2003) *The Journal of Physical Chemistry B*, **107**, 14365.
- 78 Ferri, D., Bürgi, T. and Baiker, A. (2001) *Chemical Communications*, 1172.
- 79 Ferri, D. and Bürgi, T. (2001) *Journal of the American Chemical Society*, **123**, 12074.
- 80 Ferri, D., Bürgi, T. and Baiker, A. (2002) *Journal of Catalysis*, **210**, 160.
- 81 Chu, W., LeBlanc, R.J. and Williams, C.T. (2002) *Catalysis Communications*, **3**, 547.
- 82 LeBlanc, R.J., Chu, W. and Williams, C.T. (2004) *Journal of Molecular Catalysis A – Chemical*, **212**, 277.
- 83 Kraynov, A., Suchopar, A., D'Souza, L. and Richards, R. (2006) *Physical Chemistry Chemical Physics*, **8**, 1321.
- 84 Behzadi, B., Vargas, A., Ferri, D., Ernst, K.H. and Baiker, A. (2006) *The Journal of Physical Chemistry B*, **110**, 17082.
- 85 Schmidt, E., Ferri, D. and Baiker, A. (2007) *Langmuir*, **23**, 8087.
- 86 Mink, L., Ma, Z., Olsen, R.A., James, J.N., Sholl, D.S. and Zaera, F., (2008) *Topics in Catalysis*, **48**, 8349.
- 87 Minder, B., Mallat, T., Pickel, K.H., Steiner, K. and Baiker, A. (1995) *Catalysis Letters*, **34**, 1.
- 88 Li, X.H. and Li, C. (2001) *Catalysis Letters*, **77**, 251.
- 89 Blaser, H.U., Jalett, H.P., Monti, D.M., Reber, J.F. and Wehrli, J.T. (1988) *Studies in Surface Science and Catalysis*, **41**, 153.
- 90 Meheux, P.A., Ibbotson, A. and Wells, P.B. (1991) *Journal of Catalysis*, **128**, 387.
- 91 Augustine, R.L., Tanielyan, S.K. and Doyle, L.K. (1993) *Tetrahedron: Asymmetry*, **4**, 1803.
- 92 Ma, Z., Kubota, J. and Zaera, F. (2003) *Journal of Catalysis*, **219**, 404.
- 93 Ma, Z. and Zaera, F. (2005) *The Journal of Physical Chemistry B*, **109**, 406.
- 94 Parfitt, G.D. and Rochester, C.H. (eds) (1983) *Adsorption from Solution at the Solid/Liquid Interface*, Academic Press, London.
- 95 Török, B., Balázsik, K., Kun, I., Szöllösi, G., Szakonyi, G. and Bartók, M. (1999) *Studies in Surface Science and Catalysis*, **125**, 515.
- 96 LeBlanc, R.J. and Williams, C.T. (2004) *Journal of Molecular Catalysis A – Chemical*, **220**, 207.
- 97 Ma, Z. (2006) *Liquid-Solid Interfaces of Catalysis Relevance: In Situ Probing and Related Solution Chemistry*, University of California, Riverside, PhD Dissertation.
- 98 Diezi, S., Szabo, A., Mallat, T. and Baiker, A. (2003) *Tetrahedron: Asymmetry*, **14**, 2573.
- 99 Diezi, S., Mallat, T., Szabo, A. and Baiker, A. (2004) *Journal of Catalysis*, **228**, 162.
- 100 Simons, K.E., Meheux, P.A., Ibbotson, A. and Wells, P.B. (1993) *Studies in Surface Science and Catalysis*, **75**, 2317.
- 101 Huck, W.-R., Bürgi, T., Mallat, T. and Baiker, A. (2003) *Journal of Catalysis*, **216**, 276.

- 102 Huck, W.-R., Mallat, T. and Baiker, A. (2003) *Catalysis Letters*, **87**, 241.
- 103 Huck, W.-R., Mallat, T. and Baiker, A. (2003) *Advanced Synthesis and Catalysis*, **345**, 255.
- 104 Bonalumi, N., Vargas, A., Ferri, D., Bürgi, T., Mallat, T. and Baiker, A. (2005) *Journal of the American Chemical Society*, **127**, 8467.
- 105 Meier, D.M., Mallat, T., Ferri, D. and Baiker, A. (2006) *Journal of Catalysis*, **244**, 260.
- 106 Meier, D.M., Ferri, D., Mallat, T. and Baiker, A. (2007) *Journal of Catalysis*, **248**, 68.
- 107 Ma, Z. and Zaera, F. (2006) *Journal of the American Chemical Society*, **128**, 16414.
- 108 Blaser, H.U., Imhof, D. and Studer, M. (1997) *Studies in Surface Science and Catalysis*, **108**, 175.
- 109 Fietkau, N., Bussar, R. and Baltruschat, H. (2006) *Electrochimica Acta*, **51**, 5626.
- 110 Isoda, T., Ichikawa, A. and Shimamoto, T. (1958) *Rikagaku Kenkyusho Hokoku*, **34**, 134.
- 111 Isoda, T., Ichikawa, A. and Shimamoto, T. (1958) *Rikagaku Kenkyusho Hokoku*, **34**, 143.
- 112 Lorenzo, M.O., Baddeley, C.J., Murn, C. and Raval, R. (2000) *Nature*, **404**, 376.
- 113 Humblot, V. and Raval, R. (2005) *Applied Surface Science*, **241**, 150.
- 114 Lorenzo, M.O., Humblot, V., Murray, P., Baddeley, C.J., Haq, S. and Raval, R. (2002) *Journal of Catalysis*, **205**, 123.
- 115 Fasel, R., Wider, J., Quitmann, C., Ernst, K.H. and Greber, T. (2004) *Angewandte Chemie-International Edition*, **43**, 2853.
- 116 Barbosa, L.A.M.M. and Sautet, P. (2001) *Journal of the American Chemical Society*, **123**, 6639.
- 117 Hermse, C.G.M., van Bavel, A.P., Jansen, A.P.J., Barbosa, L.A.M.M., Sautet, P. and van Santen, R.A. (2004) *The Journal of Physical Chemistry B*, **108**, 11035.
- 118 Barlow, S.M., Louafi, S., Le Roux, D., Williams, J., Murn, C., Haq, S. and Raval, R. (2004) *Langmuir*, **20**, 7171.
- 119 Barlow, S.M., Louafi, S., Le Roux, D., Williams, J., Murn, C., Haq, S. and Raval, R. (2005) *Surface Science*, **590**, 243.
- 120 Lakhani, A.M., DeWitt, D.J., Sant'Agata, N.M. and Pearl, T.P. (2007) *The Journal of Physical Chemistry C*, **111**, 5750.
- 121 Humblot, V., Haq, S., Murn, C. and Raval, R. (2004) *Journal of Catalysis*, **228**, 130.
- 122 Jones, T.E. and Baddeley, C.J. (2002) *Surface Science*, **513**, 453.
- 123 Jones, T.E. and Baddeley, C.J. (2002) *Surface Science*, **519**, 237.
- 124 Jones, T.E., Urquhart, M.E. and Baddeley, C.J. (2005) *Surface Science*, **587**, 69.
- 125 Jones, T.E. and Baddeley, C.J. (2006) *Langmuir*, **22**, 148.
- 126 Jones, T.E., Rekasas, A.E. and Baddeley, C.J. (2007) *The Journal of Physical Chemistry C*, **111**, 5500.
- 127 Stacchiola, D., Burkholder, L. and Tysoe, W.T. (2002) *Journal of the American Chemical Society*, **124**, 8984.
- 128 Stacchiola, D., Burkholder, L., Zheng, T., Weinert, M. and Tysoe, W.T. (2005) *The Journal of Physical Chemistry B*, **109**, 851.
- 129 Lee, I. and Zaera, F. (2005) *The Journal of Physical Chemistry B*, **109**, 12920.
- 130 Lee, I. and Zaera, F. (2006) *Journal of the American Chemical Society*, **128**, 8890.
- 131 Burkholder, L.A., Stacchiola, D.J. and Tysoe, W.T. (2004) Abstracts of Papers. 228th ACS National Meeting, Philadelphia, PA, United States, August 22–26, 2004, COLL U474.
- 132 Attard, G.A. (2001) *The Journal of Physical Chemistry B*, **105**, 3158.
- 133 Horvath, J.D. and Gellman, A.J. (2003) *Topics in Catalysis*, **25**, 9.
- 134 Zhao, X.Y. (2000) *Journal of the American Chemical Society*, **122**, 12584.
- 135 Schunack, M., Lægsgaard, E., Stensgaard, I., Johannsen, I. and Besenbacher, F. (2001) *Angewandte Chemie-International Edition*, **40**, 2623.
- 136 Chen, Q. and Richardson, N.V. (2003) *Progress in Surface Science*, **73**, 59.
- 137 Zaera, F. (2002) *The Journal of Physical Chemistry B*, **106**, 4043.
- 138 Zaera, F. (2005) *Chemical Record*, **5**, 133.

- 139 Zaera, F. (2005) *Journal of Molecular Catalysis A-Chemical*, **228**, 21.
- 140 Vargas, A., Ferri, D., Bonalumi, N., Mallat, T. and Baiker, A. (2007) *Angewandte Chemie-International Edition*, **46**, 3905.
- 141 Bonalumi, N., Vargas, A., Ferri, D. and Baiker, A. (2007) *The Journal of Physical Chemistry C*, **111**, 9349.
- 142 Hoxha, F., Königsmann, L., Vargas, A., Ferri, D., Mallat, T. and Baiker, A. (2007) *Journal of the American Chemical Society*, **129**, 10582.
- 143 Bürgi, T. and Baiker, A. (1998) *Journal of the American Chemical Society*, **120**, 12920.
- 144 Olsen, R.A., Borchardt, D., Mink, L., Agarwal, A., Mueller, L.J. and Zaera, F. (2006) *Journal of the American Chemical Society*, **128**, 15594.
- 145 Ma, Z. and Zaera, F. (2006) *Surface Science Reports*, **61**, 229.

6

Catalytic Nanomotors

John Gibbs and Yiping Zhao

6.1

Introduction

Biological motors that have been evolving for millions of years convert stored chemical energy into mechanical work and provide necessary functions for the organism through the hydrolysis of adenosine triphosphate (ATP) [1]. By studying and observing these motor proteins, researchers gain insight into how form meets function. A wide variety of naturally occurring nanomotors exists that governs essential functions of biological organisms. These motors perform work at the cellular level such as muscle contraction, cellular repair, waste removal, disease control, respiration, and any type of function that involves transport [1]. Without these devices, life, as we know it on Earth, would not exist.

The design of artificial nanomotors to mimic the behavior and functionalities of biological nanomotors could have a tremendous impact in such fields as medicine, drug development, and various others involving manipulation at the cellular level. Implications of the artificial nanomotors could also extend beyond applications in biology and medicine. Manufacturing functional artificial nanomachines is one of the major goals for nanotechnology, and researchers have already begun to fabricate and study autonomously moving catalytic nanomotors. The fundamental design principle regarding artificial nanomotors mimics naturally occurring biological nanomotors.

There are three fundamental characteristics of biological nanomotors. First, autonomous motion is seen frequently in biological organisms at the micrometer scale and the nanometer scale, and this is a key for directional motion or targeted delivery. Second, the motion is driven by converting the chemical energy stored in the environment to mechanical energy through a catalytic reaction. No additional energy device is needed for the nanomotor. Third, to fulfill the mechanical motion structurally, the catalytic molecules are located asymmetrically around the nanomotor so that an unbalanced force or torque may be generated during the catalytic reaction. A good design of artificial nanomotors should possess these three unique features. Some current researchers attempt to mimic these naturally occurring nanomotors.

Nonautonomous manipulation of nanomotors with such techniques as controlling motion with electromagnetic fields or light pulses is relatively easy in comparison to achieving autonomous motion through catalysis. However, these techniques are not as practical as catalytically driven machines since, in practice, having various fields present to manipulate the nanomotors may not be possible. Very recently, researchers have successfully designed some simple catalytic nanomotor structures by either combining the biological nanomotors [2] with nanostructures or by using heterostructured nanorod systems through a simple catalytic reaction [3].

6.1.1

Biological Motors

The simplest design of an artificial nanomotor is achieved by coupling the existing biological motors to inorganic nanostructures to achieve certain mechanical motion. One excellent example is found in the work produced at Cornell University [2]. Montemango *et al.* fabricated nanopropellers fueled by an F_1 -ATPase biomolecular motor [2]. The rotation of the nanopropeller is activated by ATP and may be shut off by sodium azide [2]. This design uses preexisting biological machinery to propel inorganic devices. Biological motors exist naturally in biological organisms; these devices are protein machines that utilize ATP to gain mechanical work [1]. ATP consists of adenine bonded to ribose as a backbone and a tail with three tightly packed phosphate groups attached to the ribose [1]. Hydrolysis breaks the relatively unstable bonds between the phosphate groups and converts ATP to adenosine diphosphate (ADP), and releases a single phosphate group. This reaction is exergonic, which means energy is released along with the inorganic phosphate [1]. The energy released by this reaction provides the driving force for the mobility of the biomotors [1].

Three types of biological motors exist: kinesins, myosins, and dyneins [4]. The exact mechanisms for most of the subclasses of the above motors are still unknown, but the physical structure of the motor corresponds to how it will utilize ATP. In all three types of motors, conformational changes lead to motion. For example, in muscle cells, conformational changes caused by the hydrolysis of ATP drive parallel actin filaments and myosin past one another, causing the cell to shorten and leading to muscle contraction [1]. Dynein is a large protein that is used in bacterial flagella; the protein changes conformation through bending caused by the mechanism of dynein, which involves dynein arms “walking” along microtubules. All biomotors utilize chemical energy to do work, and the structure of the motors corresponds to the type of work the motor performs. Therefore, the shape and design of artificial catalytic nanomotors have important consequences on the type of motion achieved.

6.1.2

Artificial Catalytic Nanomotors

An artificial catalytic nanomotor employs similar principles as the biological nanomotor, and here, motion is driven by a catalytic reaction. The greatest challenge

regarding catalytic nanomotors is controlling autonomous motion. Creating machines that consume fuel is relatively simple, but to design a machine that converts energy from its environment into controlled motion is challenging. Specifically, autonomous motion through catalysis is desirable, since the machine extracts mechanical work from stored energy present within its environment. The motors will run indefinitely while chemical energy (or reactants) is present; since the nanomotors utilize a catalyst to gain motility, they do not break down themselves. The specific placement of the catalyst onto the nanomotor backbone dictates the type of motion exhibited, which may be rotational, translational, or combinations of the two. The catalyst decomposes a chemical such as hydrogen peroxide at a faster rate than spontaneous decomposition, causing a concentration gradient of reaction products; this gradient leads to autonomous motion in nanomotors that has been explained by various mechanisms.

Certain asymmetric structures are found in natural biomotors, and taking a cue from nature, asymmetrically designed motors effectively exploit the energy contained in its environment. The analogy between biological motors and artificial catalytic nanomotors is as follows: biological motors utilize asymmetrically placed ATP to gain conformational changes, thereby leading to autonomous motion; catalytic nanomotors rely upon an asymmetrically placed catalyst that leads to self-induced electric fields, reaction product concentration gradients, and so on to gain autonomous mobility.

Most current catalytic nanomotor research involves the reaction of splitting hydrogen peroxide into water and oxygen: $\text{H}_2\text{O}_2 \xrightarrow{\text{Catalyst}} \text{H}_2\text{O} + \text{O}_2$ [3, 4]. The catalyst is either platinum or silver primarily, but other metals such as magnesium or nickel may be used to speed up the decomposition of hydrogen peroxide. When nanomotors are designed, an emphasis is placed on asymmetrical distribution of the catalyst onto the motor backbone. For example, an Au–Pt heterogeneous nanorod can be fabricated through a template-directed electroplating method, which is half gold and half platinum, as shown in Figure 6.1 [5]. When this object is placed into a dilute solution

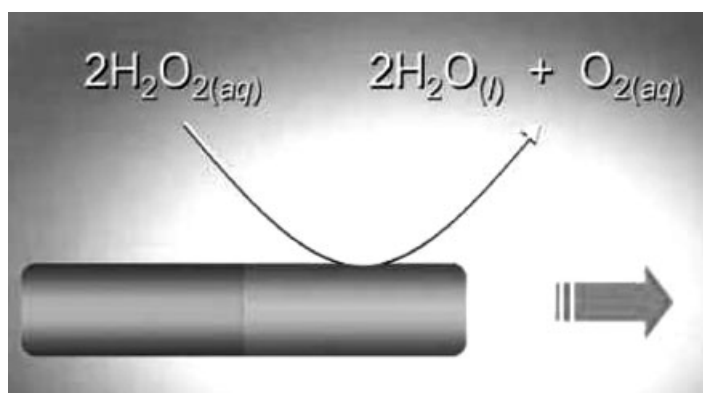


Figure 6.1 A catalytic Au–Pt nanorod nanomotor. The Pt acts as a catalyst to break down the H_2O_2 more rapidly at the platinum end. This asymmetry leads to autonomous motion [9].

of hydrogen peroxide, the above-mentioned catalytic reaction occurs more rapidly at the platinum side of the rod than at the gold side [5]. This phenomenon leads to autonomous translational motion of the nanorod, which will be described in detail in Section 6.2. The heterogeneous nanorod is the simplest example of a mechanism that leads to translational motion. One could easily imagine the limitless possibilities for catalytic nanomotor design with this simple example.

6.2

The Propulsion Mechanism of Catalytic Nanomotors

The design of nanomotors, the underlying physics and chemistry, and experimental observations all contribute simultaneously to the future creation of functional machinery at the nanometer scale. Some research workers take an engineering approach by creating novel nanomotors, nanomachines, micropumps, and other related devices, while some others study motion and motion mechanisms.

The interpretations of nanomotor motion through catalytic reactions include self-electrophoresis, bubble propulsion, interfacial tension gradients, and reaction product gradients. The concepts involved address tension forces, viscous drag, and electrochemistry. All explanations revolve around the gradients of reaction products created by the asymmetrically distributed catalyst and are closely related to diffusiophoresis.

6.2.1

Diffusiophoresis

Diffusiophoresis arises due to concentration gradients of reaction products in solution that may cause motion depending upon the interaction of the products with the particle surface. Through van der Waals and dipole forces, reaction molecules interact with the surfaces of objects in solution [6]. If a concentration gradient exists in solution, the system is not in equilibrium, and therefore, some action must take place in order for equilibrium to occur. If the solutes interact with the surface of a nearby particle, then the particle will move. Diffusiophoresis is one of the essential mechanisms leading to nanomotor motion. Catalytic nanomotors are propelled by diffusiophoresis, since, by design, they create concentration gradients in the solution through a catalytic reaction. Ajdari *et al.* designed a simple mathematical model to illustrate and analyze diffusiophoresis in which the reaction occurs on a spherical particle at the asymmetrically distributed enzymatic site, as shown in Figure 6.2 [7]. If the excess product particles are being released at a rate $\frac{dN_p(t)}{dt}$ and the density of excess product particles is given by

$$\frac{\partial}{\partial t} \rho(\vec{r}, t) - D \nabla^2 \rho(\vec{r}, t) = \frac{dN_p(t)}{dt} \delta^3(\vec{r} - \vec{r}_s) \quad (6.1)$$

where \vec{r}_s corresponds to the reaction site, and D is the diffusion constant for the particles. Then the density of excess particles, ρ , can be determined [7]. The velocity of

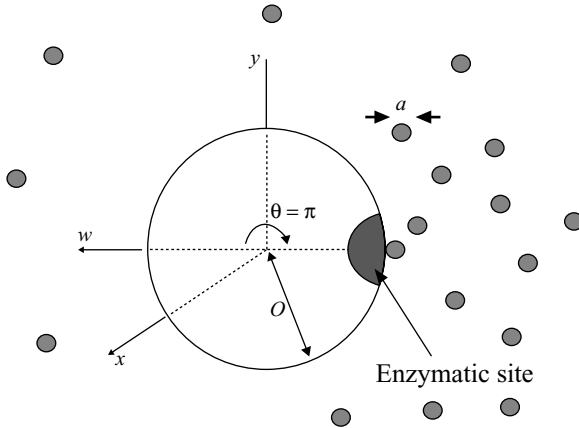


Figure 6.2 A simple model of a spherical particle in the presence of a reaction product gradient. The blue spheres represent the products that are of higher concentration near the catalyst [7].

propulsion in the z -direction is given by $v = -\frac{k_B T}{\eta} \frac{\lambda^2}{R} \rho$, where λ is a length scale that depends on the phoretic mechanism, η is the viscosity of the fluid, and R is the radius of the spherical particle. Combining Equation 6.1 with the above expression for v and using appropriate boundary-value conditions, one can have an expression for the velocity of the particle

$$v(t) = l \int \frac{d\omega}{2\pi} \frac{e^{-i\omega t} f(\omega) \left[1 - i \left(\sqrt{\frac{i\omega R^2}{D}} \right) \right]}{\left[1 - i \left(\sqrt{\frac{i\omega R^2}{D}} \right) - \frac{1}{2} \left(\sqrt{\frac{i\omega R^2}{D}} \right)^2 \right]} \quad (6.2)$$

where $f(\omega)$ is the Fourier transform of $\frac{dN_p(t)}{dt}$ and $l = a \left(\frac{3\lambda^2}{4R^2} \right)$, where a is the diameter of the excess product particle [7]. When the calculation of the above velocity expression is carried out, the value gives the correct order of magnitude for observed colloidal particle motion, which demonstrates that this model gives a reasonable approximation to particle motion behavior.

Diffusiophoresis is one of the mechanisms for nanomotor motion. For specific catalytic nanomotor systems, the mechanism for each is somewhat different. Self-electrophoresis is another mechanism in which the chemical reaction causes heterogeneous metallic conducting nanorods to create their own electric fields and effectively turn into electric dipoles.

6.2.2

Self-Electrophoresis

Electrophoresis, which arises due to electrochemistry, has been proposed as the mechanism for moving heterogeneous nanorods through a solution of hydrogen peroxide [5, 8]. When analyzing the heterostructured nanomotor made of two

sections of different metals, a popular explanation regarding how the catalytic reaction translates chemical energy into kinetic energy is self-electrophoresis [5, 8]. A self-induced electric field occurs as a result of a oxidation–reduction reaction, or a *redox reaction*; the reaction releases charged products into the solution surrounding the conductive material, which generates an electric field [5, 8]. The strength of the field naturally depends upon the type of conductive material used and the type of reaction occurring.

For example, for the Au–Pt nanorod motor, the decomposition of hydrogen peroxide is a redox reaction. It has been shown that platinum acts as the cathode by reducing hydrogen peroxide and consuming protons while the gold end of the nanorod acts as the anode that generates protons by oxidizing the hydrogen peroxide [5, 8, 9]. The above reaction occurs at both ends of the rod, which causes a proton gradient in the solution [5, 8, 9]. Since the Au–Pt rod is an electrical conductor, it responds to this gradient by allowing electrons to be collected at the end with the larger concentration of protons, and therefore, the rod becomes an electric dipole [5, 8]. The protons then move past the rod to the platinum section (cathode), where they are consumed [5, 8]. The motion of the protons drags the fluid adjacent to the rod, and causes a *slip velocity*, propelling the rod through the solution. A cartoon of this process is illustrated in Figure 6.3.

An application of the self-electrophoresis is to design micrometer-sized pumps [10]. These pumps exploit the process of self-electrophoresis differing only in the fact that the metals now are stationary [10]. The slip velocity caused by the migration of protons propels Au–Ag nanorods through the solution, but if the metals are stationary, only the fluid moves, and this flow in the direction of the cathode effectively creates a pump [10]. Figure 6.4 illustrates the redox reaction that occurs with a silver island placed atop an Au thin film. The generated protons migrate toward the silver and create an electroosmotic flow that can be visualized using tracer particles [9]. Kline *et al.* have successfully created pumps using self-electrophoresis at the micrometer scale [10]. Paxton *et al.* designed an apparatus to test the effect that the catalyst has on the micropump [9]. By designing a switch that turns the electrochemical reaction on and off, the relationship between the motion

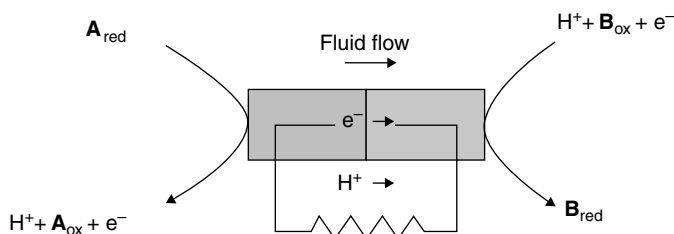


Figure 6.3 Self-electrophoresis occurs as protons are created when the A species is oxidized on the one end, and the protons are consumed at the other end as species B is reduced. The protons drag the fluid, causing a slip velocity propelling the rod in the opposite direction of the fluid flow [9].

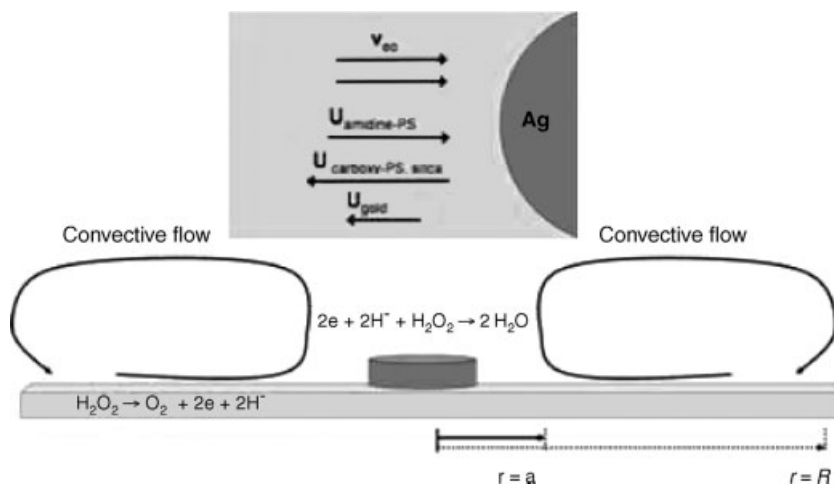


Figure 6.4 An island of Ag on a surface of Au served as a micropump. Since the metals are stationary, the protons create a fluid flow and effectively a micro-sized pump [5].

caused by the electrochemical reaction and the motion of the nonelectrochemical reaction can be compared [9]. Graphical representations of the fluid flow created by these Au–Pt micropumps are shown in Figures 6.5 and 6.6. Figure 6.5 illustrates the effect that the micropump has on an Au particle when the circuit is connected at

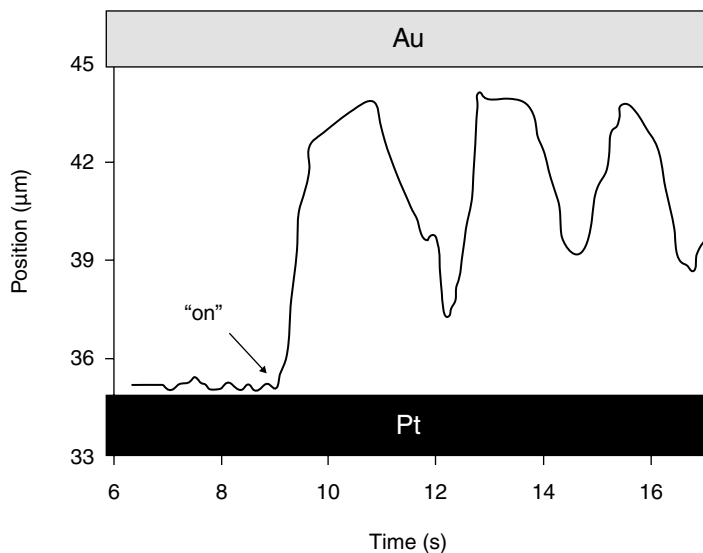


Figure 6.5 A 1D trajectory plot of a tracing Au nanorod in a switchable micropump. At roughly 8.8 s, the switch is turned on and the tracer particle begins to migrate toward the Au electrode. Once the tracer particle reaches the Au electrode, it migrates back toward the Pt, and the cycle continues [4].

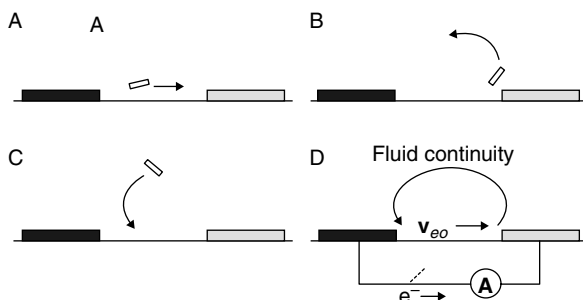


Figure 6.6 Fluid continuity of a Au–Pt micropump. The tracer particle moves toward the Au electrode of the pump on the pump plane and then is projected away from the plane back toward the Pt electrode, and a continuous cyclic flow is observed [4].

around 8.8 s. Some motion of the Au particle is seen before the pump is turned on, but the convection effect of the pump is clearly demonstrated by the trajectory of the particle once the pump is activated. Based upon empirical evidence, self-electrophoresis seems to accurately describe catalytic nanomotor behavior of heterometal nanorods.

6.2.3

Bubble Propulsion

Another possible mechanism for catalytic nanomotors is *bubble* propulsion. As the name implies, this mechanism suggests that tiny bubbles of oxygen propel an object through solution. Autonomous motion has been observed for macroscopic objects moving on the surface of hydrogen peroxide at the air/hydrogen peroxide interface [11]. Whitesides *et al.* created small, <1 cm, plates with platinum placed on one side, perpendicular to the solution surface. The catalytic reaction of hydrogen peroxide generates oxygen bubbles that nucleate on the catalyst (Pt) surface, aggregate, and eventually rupture, causing linear and rotational motion of the plates [11]. Whitesides used these particles to study particle aggregation in which the reaction increased the amount of particle collisions per unit time. Such a propulsion mechanism was also observed by Ozin *et al.* when studying the motion of the Au–Ni heteronanorods moving in a solution of hydrogen peroxide [12]. Figure 6.7 shows the trajectory of the oxygen bubble generated during the motion [12].

Feringa *et al.* designed a device that decomposes hydrogen peroxide via a manganese-based catalyst mimic that moves due to the nucleation of oxygen bubbles, as shown in Figure 6.8 [13]. This particular machine does not utilize asymmetrical distribution of the catalyst, but the machine's structure has asymmetrical properties [13]. The machine consists of an object that is attached to a catalyst by a tether; the asymmetric shape of the machine causes rotational and translational motion thought to be caused primarily by bubble propulsion. Macroscopic machines that move autonomously via bubble propulsion are relatively easy to create and observe, making them good candidates for research.

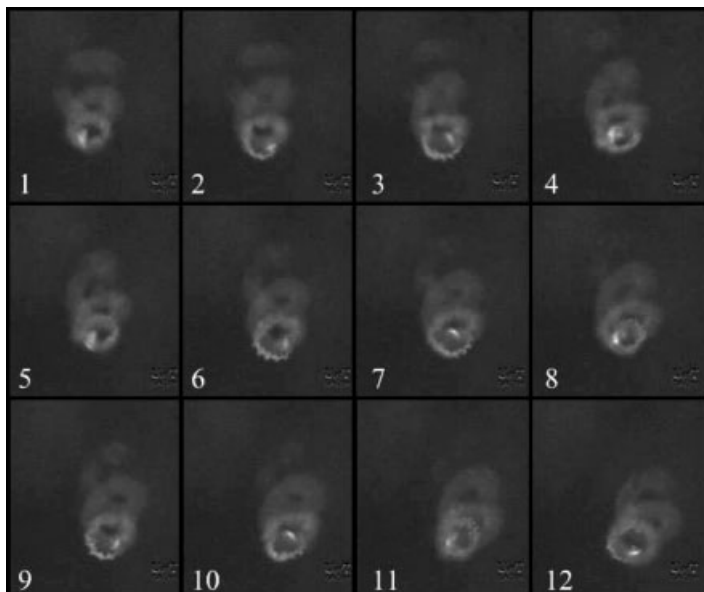


Figure 6.7 Time-lapse photography of Au–Ni nanorods, exhibiting corkscrew motion traced by the oxygen bubbles [12].

6.2.4

Interfacial Tension Gradients

Interfacial tension gradients have been proposed to propel nanomotors through a solution of hydrogen peroxide. When spatial dimensions are scaled down to the submicrometer sizes, these tension gradients begin to have a more significant effect than that at macroscopic dimension. Some observations have been made that cannot be described by the mechanisms described above. Paxton *et al.* observed the motion of Au–Pt nanorods at interfacial regions along with other novel nanomotors [14].

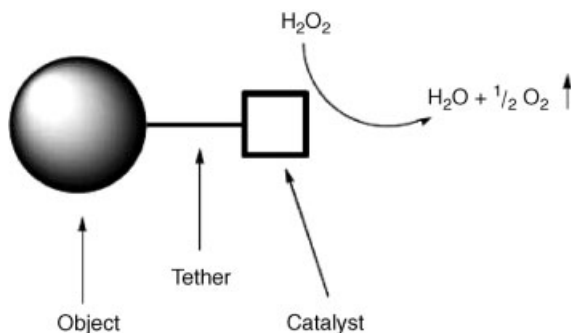


Figure 6.8 A machine designed by Feringa *et al.* that most likely moves as a result of bubble propulsion caused by the reaction at the catalyst attached to the object by a tether [13].

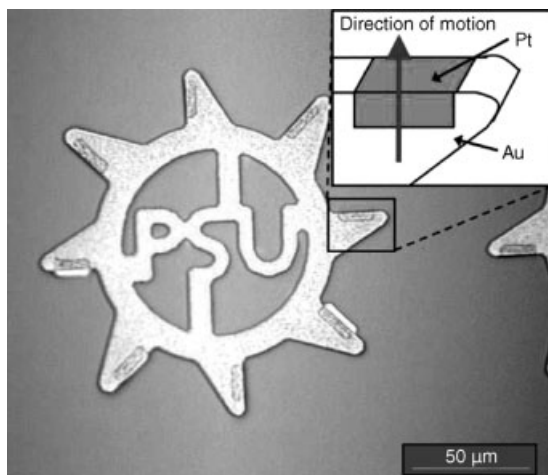


Figure 6.9 A gear of Au side coated with Pt and turning in the direction of the Pt catalyst in H_2O_2 solution, as shown in the upper right corner of the picture [9].

In Section 6.2.4, we described the phenomenon of *bubble propulsion* in which objects such as the ones designed by the Whitesides group are propelled away from the region with a higher concentration of oxygen. Catchmark *et al.* produced a result that contradicts this idea, and they have designed a device that moves in the direction of higher oxygen concentration that consists of asymmetrically placed platinum on the teeth of a gold gear [15]. The gear consists entirely of gold as shown in Figure 6.9, but a small amount of platinum is placed on the teeth of the gear. The first natural explanation of this motion was diffusiophoresis, discussed in Section 6.2.2, but calculations show that this mechanism would not be sufficient to propel the gold–platinum gear at the speeds observed, and more importantly, the theory predicts motion in the opposite direction [15]. An alternate suggestion was made in that an asymmetric tension gradient is induced through the decomposition of hydrogen peroxide, and concurrently, a slip velocity between the particle and the fluid is produced. By solving the diffusion–convection equation regarding oxygen production, a linear dependence of the velocity with respect to the oxygen production speed can be determined, and observations have verified this calculation [5].

6.2.5

Bioelectrochemical Propulsion

Thus far, only inorganic catalytic nanomotors have been discussed. Many applications will take place *in vivo*, so biologically based motors should be considered. Mano and Heller report man-made machines exhibiting locomotion via glucose–oxygen reactions [16]. The group fabricated a carbon fiber with one end containing bilirubin oxidase, which reduces oxygen, and the other end contains glucose oxidase, which catalyzes the oxidation of glucose. The flow of current through the carbon fiber runs from a glucose-oxidizing microanode to an oxygen-reducing microcathode. The drag

of ions through the solution propels the fiber along the water–oxygen interface at a speed of 1 cm s^{-1} . The motility is reduced as time passes and the solution becomes contaminated with reaction products. These fibers have been shown to exhibit linear and rotational motion. This reaction mimics metabolism in biological organisms.

6.3

Advanced Design of Catalytic Nanomotors

The specific design of a catalytic nanomotor determines the type of motion exhibited. The fundamental design method involves asymmetrically distributed catalyst on the nanomotor. Mallouk and Sen's group at Pennsylvania State University and Ozin's group at the University of Toronto both designed heterogeneous nanorod structures through template-directed electroplating (TDEP) method [3, 17]. This is a template method that is relatively inexpensive and easy to perform [18]. Both groups have successfully created nanomotors using TDEP and have studied important motion characteristics. However, this technique is somewhat limited in that usually only one type of motion, such as translational or rotational motion, is achieved, since the TDEP can only produce coaxial nanostructures. If the mass of the deposited structures is well balanced, in principle, only translational motion may be observed [18].

To create a wide variety of structures that have the ability to achieve several types of motion, a dynamic fabrication technique must be utilized. Currently, there is an alternative technique that can fulfill this requirement, and it is termed dynamic shadowing growth (DSG); this method is a vapor deposition technique that is fairly simple to implement, and it allows for a flexible design of catalytic nanomotors [19].

6.3.1

Dynamic Shadowing Growth

In a physical deposition system, a material is melted until vapor is released into a vacuum chamber. This vapor condenses onto a substrate and forms a thin film. If the substrate is tilted at a large angle ($\theta > 70^\circ$) with respect to the vapor incident direction, then an interesting phenomenon known as self-shadowing occurs; this method is known as oblique angle deposition (OAD) [20, 21]. The dynamic shadowing growth technique combines substrate rotation and the shadowing effect, which will be illustrated in detail below. This method is effective for the design of catalytic nanomotors since making heterogeneous nanostructures is simple, and just by alternating the material being deposited in the chamber, and intrinsically, the DSG could place the catalyst asymmetrically on nanomotor backbone.

6.3.2

Rotary Si–Pt Nanorod Nanomotors

First, we will look at the design of a rotary silicon–platinum nanorod nanomotor using the DSG technique. These heterogeneous nanomotors consist of a silicon backbone

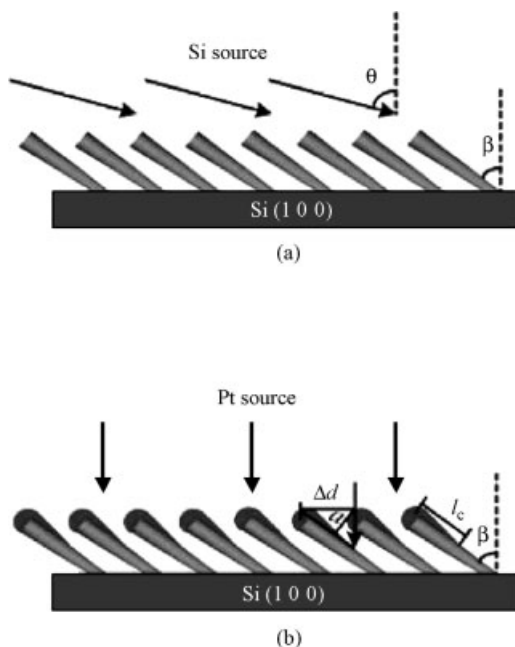


Figure 6.10 Fabrication of Si-Pt nanorod nanomotors [19].

that is generated using OAD, as discussed in the previous section [19]. Figure 6.10 illustrates the fabrication procedures. By rotating the substrate to an angle $\theta \approx 86^\circ$, silicon nanorod are fabricated at an angle $\beta < \theta$ due to the self-shadowing effect, which will serve as the backbones for the nanomotors [19]. Then a thin platinum catalyst layer is deposited onto one side of the silicon nanorod backbones by rotating the substrate back to $\theta = 0^\circ$. This process effectively creates rotary Si/Pt nanorod nanomotors, and the rotary motion of these nanorods has been observed as shown in Figure 6.11 [19]. A TEM image of a Si-Pt nanorod nanomotor can be seen in Figure 6.12. The heterogeneous nanorod nanomotor is probably the simplest example for DSG, but DSG allows for much more interesting and dynamic structures.

6.3.3

L-Shaped Nanorod Nanomotors

L-shaped nanorods were designed to break the symmetry of the nanorod and to determine the direction of the driving force applied to catalytic nanomotors when



Figure 6.11 Movie clips of a clockwise rotated Si-Pt nanorod nanomotor. The time interval between the adjacent clips is 0.1 s [19].

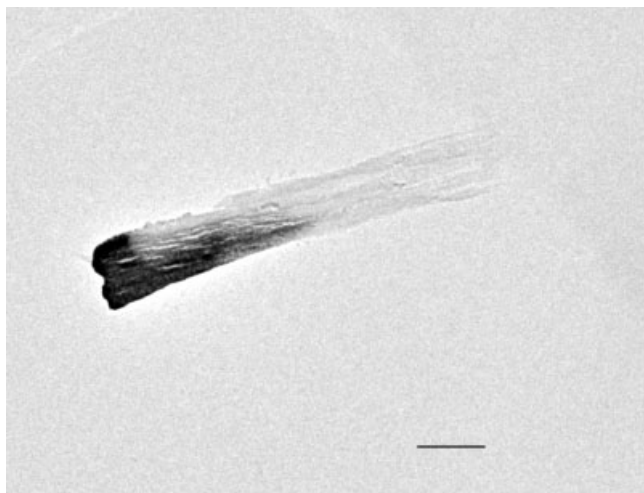


Figure 6.12 A TEM image of a Si-Pt nanorod. The scale bar represents 500 nm [19].

immersed in hydrogen peroxide solution. The shape of these nanomotors allows for the observation of their orientation and motion direction in solution [19]. As shown in Figure 6.13, the “L-shape” is achieved by first growing a short section of silicon nanorods using OAD, as discussed above, and then rotating the substrate 180° azimuthally to grow a long section of Si nanorods [19]. Once this process is complete, a thin layer of platinum is deposited at the upper side of the long Si nanorods. A TEM image of such a Si-Pt nanorod can be seen in Figure 6.14 in which the platinum is placed asymmetrically on the long arm of the L-shaped Si nanorod.

It has been shown that when these nanomotors are placed into a solution of 5% hydrogen peroxide, they all rotate from the long arm to the short arm, as shown in Figure 6.15, demonstrating that the L-shaped nanomotors are pushed from the platinum side. Therefore, the chemical reaction taking place at the platinum side of the nanomotor produces a propelling force that pushes the nanorod away from the reaction site. The reason for generation of this force is still not understood, but as Whitesides and Ozin suggested, this may occur due to the generation of tiny oxygen bubbles that propel the nanorod away from the reaction.

6.3.4

Rolling Nanospring

An interesting example of a complex nanomotor structure that DSG can design is the rolling nanospring. The idea is roughly the same as for the L-shaped nanorods discussed above, but instead of rotating the substrate azimuthally by 180° , after depositing a section of silicon nanorod and coating its top side with a thin layer of silver, the substrate is rotated azimuthally by 90° , and a similar section of Si-Pt nanorod structure is deposited again; repeating the deposition procedure three times results in the creation of a spring-like structure, as in Figure 6.16. As shown, the silver deposited on each section of the nanospring contributes the force supplied to moving

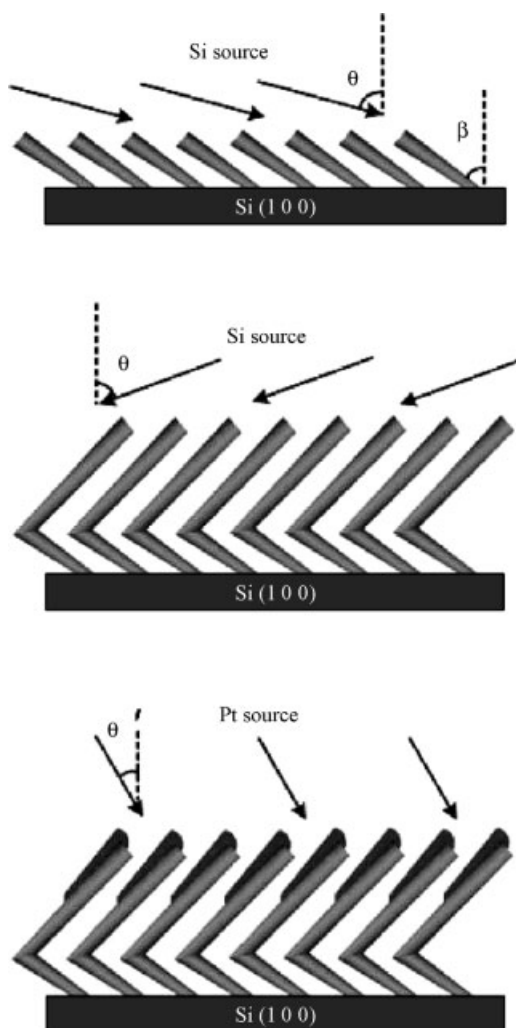


Figure 6.13 Fabrication of L-shaped Si–Pt nanorods [19].

the nanomotor. When these objects are placed into a 5% solution of hydrogen peroxide, they exhibit rolling translational motion that has been observed by movie analysis [19]. From force analysis, there will be a net downward force, as well as a net torque, since the actions of all of the forces are in four different planes as shown in Figure 6.16.

6.3.5

Hinged Nanorods

Integrating flexible components with catalytic nanomotors introduces another degree of freedom for designing complex nanomachinery. The Ozin group has

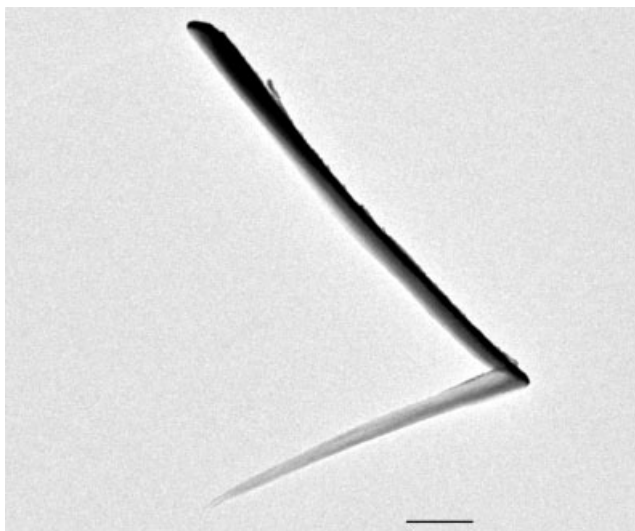


Figure 6.14 A TEM image of L-shaped Si-Pt nanorod. The scale bar represents 500 nm [19].

recently created multicomponent nanorods with multifunctionality [22]. They combined multiple nanofabrication procedures and produced nanorods consisting of polyelectrolyte hinges allowing for significant flexibility and bending; an SEM image is shown in Figure 6.17 [22]. The procedure for constructing such devices relies upon using self-assembled layered polyelectrolytes through electrostatic attraction followed by chemical etching [22].

Coaxial Pt-Au-Pt nanorods are created using electrodeposition, and a thin layer of silver is deposited surrounding each nanorod for electrical contact. The platinum is the catalyst for the reaction of hydrogen peroxide, just as discussed in the previous sections. The rods then are treated with mercaptoethanesulphonic acid (MESA), which renders a negative surface charge when dispersed in an aqueous medium [22]. The nanorods are completely covered with polyelectrolytes, creating a polymeric sheath encapsulating each nanorod. Then the nanorods are exposed to dilute nitric acid and the Ag backing is dissolved, and the gold segment is dissolved by aqueous KI/I₂. The final product consists of hinged nanorods with polyelectrolyte connections between platinum ends [22].

Brownian motion induced bending of these nanorods has been observed with video footage as shown in Figure 6.18 [22]. One conclusion reached is that as the

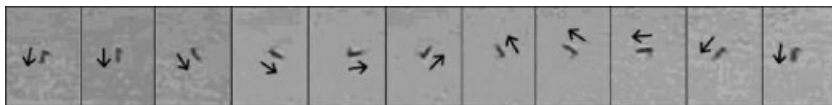


Figure 6.15 Movie clips of a rotary L-shaped Si-Pt nanorod. The time interval between the adjacent clips is 0.4 s [19].

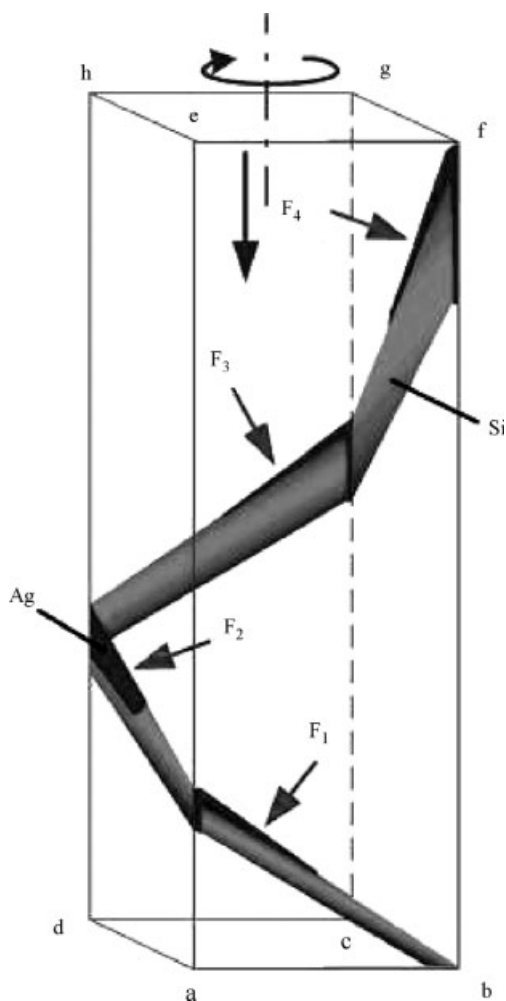


Figure 6.16 A drawing of the Si-Ag nanospring and corresponding force analysis when the structure is placed into a H_2O_2 solution [19].

number of layers increases, the flexibility decreases. Since each of the layers is added one at a time, controlling the number of layers and therefore the overall flexibility of the rods is possible. On adding hydrogen peroxide, the amplitude of bending increases, and the exposure of the hinge to hydrogen peroxide seems to have little effect on the structural integrity of the hinge [22].

This research demonstrates that creating flexible machinery at the nanoscale is achievable. It is also inferred that combining both dynamical fabrication techniques and other nanofabrication techniques may allow for the creation of complex, multifunctional catalytic nanomotors.

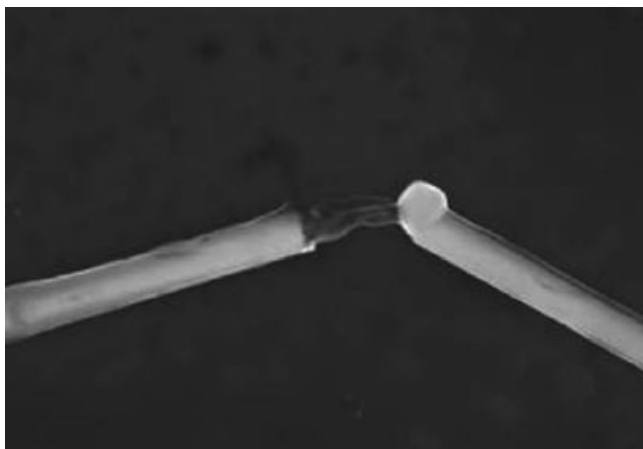


Figure 6.17 A SEM image of a Pt–Pt nanohinge connected with a polyelectrolyte sheath. The center section has been etched [22].

6.4

Applications, Challenges, and Perspectives

Fabrication of nanoscale autonomous motion objects is a relatively new field that has more unanswered questions than not. The future of smart nanomotor fabrication relies upon the combination of multiple nanofabrication techniques as exemplified by the nanohinge design. Before any practical applications may exist, the fundamental properties of these objects must be understood. Once more information has been extracted from experiment and theory, many exciting applications are expected to follow. Nanomotors will most likely find applications in biology, electronics, medicine, and other areas, but the possibilities are ultimately limitless.

Perhaps the most exciting application will pertain to medicine, in which nanomotors may interact intimately with individual cells. Naturally occurring nanomotors



Figure 6.18 Selected movie clips of a one-hinged nanorod [22].

complete complex tasks at the cellular level, and biomotors are vital to the survival of cells. Controlling artificial nanomotors will allow doctors to treat patients at the microscopic level with these machines delivering medicine, eliminating foreign objects, repairing tissue, removing infected cells, and so on. The applications to medicine are potentially staggering, but most importantly, we must first learn how to manipulate nanomotors and how to administer them without interfering with healthy functions in the body. Other applications exist in areas such as microelectronics, in which nanomotors may aid in the creation of ultrasmall circuits: steering, smart structures, actuators, and sensors. Overall, much more research is needed in order for these exciting future applications to become practical.

Acknowledgments

The authors would like to thank the financial support from DOE (DE-FG02-05ER46251) and NSF (ECS-0404066 and CMMI 0726770). The contributions from Dr. Yuping He, Mr. Justin Abell, and Mr. Wilson Smith are deeply appreciated.

References

- 1 Campbell, N.A. and Reece, J.B. (2002) *Biology* (ed. B. Wilbur) Pearson Education, Inc., San Francisco, CA.
- 2 Soong, R.K., Backand, G.D., Neves, H.P., Olkhovets, A.G., Craighead, H.G. and Montemango, C.D. (2000) *Science*, **290**, 1555–1558.
- 3 Fournier-Bidoz, S., Arsenault, A.C., Manners, I. and Ozin, G.A. (2005) *Chemical Communications*, 441–443.
- 4 Schliwa, M. and Woehlke, G. (2003) *Nature*, **422**, 759–765.
- 5 Paxton, W.F., Baker, P.T., Kline, T.R., Wang, Y., Mallouk, T.E. and Sen A. (2006) *Journal of the American Chemical Society*, **128**, 14881–14888.
- 6 Anderson, J.L. (1989) *Annual Reviews*, **21**, 61–99.
- 7 Golestanian, R., Liverpool, T.B. and Ajdari, A. (2005) *Physical Review Letters*, **94**, 220801–220804.
- 8 Paxton, W.F., Sundararajan, S., Mallouk, T.E. and Sen, A. (2006) *Angewandte Chemie International Edition*, **45**, 5420–5429.
- 9 Paxton, W.F., Sen, A. and Mallouk, T.E. (2005) *Chemistry – A European Journal*, **11**, 6462–6470.
- 10 Kline, T.R., Paxton, W.F., Wang, Y., Velegol, D., Mallouk, T.E. and Sen, A. (2005) *Journal of the American Chemical Society*, **127**, 17150–17151.
- 11 Ismagilov, R.F., Schwartz, R.B. and Whitesides, G.M. (2002) *Angewandte Chemie International Edition*, **41**, 652–654.
- 12 Ozin, G.A., Manners, I., Fournier-Bidoz, S. and Arsenault, A. (2005) *Advanced Materials*, **17**, 3011–3018.
- 13 Vicario, J., Eelkema, R., Browne, W.R., Meetsma, A., La Crois, R.M. and Feringa, B.L. (2005) *Chemical Communications*, 3936–3938.
- 14 Dhar, P., Fischer, T.M., Wang, Y., Mallouk, T.E., Paxton, W.F. and Sen, A. (2006) *Nano Letters*, **6**, 66–72.
- 15 Catchmark, J.M., Subramanian, S. and Sen, A. (2005) *Small*, **1**, 202–206.
- 16 Mano, N. and Heller, A. (2005) *Journal of the American Chemical Society*, **127**, 11574–11575.

- 17 Paxton, W.F., Kistler, K.C., Olmeda, C.C., Sen, A., St Angelo, S.K., Cao, Y., Mallouk, T.E., Lammert, P.E. and Crespi, V.H. (2004) *Journal of the American Chemical Society*, **126**, 13424–13431.
- 18 Kline, T.R., Tian, M.L., Wang, J.G., Sen, A., Chan, M.W.H. and Mallouk, T.E. (2006) *Inorganic Chemistry*, **45**, 7555–7565.
- 19 He, Y., Wu, J. and Zhao, Y. (2007) *Nano Letters*, **7**, 1369–1375.
- 20 Abelmann, L. and Lodder, C. (1997) *Thin Film Solids*, **305**, 1.
- 21 Robbie, K. and Brett, M.J. (1997) *Journal of Vacuum Science & Technology A-Vacuum Surfaces and Films*, **15**, 1460.
- 22 Mirkovic, T., Foo, M.L., Arsenault, A.C., Fournier-Bidoz, S., Zacharia, N.S. and Ozin, G.A. (2007) *Nature Nanotechnology*, **250**, 1–5.

7

Rational Design and High-Throughput Screening of Metal Open Frameworks for Gas Separation and Catalysis*David Farrusseng and Claude Mirodatos*

7.1

Introduction

Among the major objectives of modern industrial chemistry reflected in large international programs like the EU FP7 (<http://cordis.europa.eu/fp7/>), the effective integration of nanotechnology, materials science, design, and new production methods is proposed to achieve and maximize impacts for industrial transformation and, at the same time, support sustainable production and consumption. One perfect example of this strategy is illustrated at the nanoscale in areas such as nanostructured hybrid inorganic–organic systems (both catalysts and adsorbents), to be developed in the field of environmentally friendly, flexible, and efficient materials processing [1, 2].

Within this category of materials, the so-called “metal open frameworks” (MOFs) have recently attracted utmost interest for the above-mentioned reasons, as reflected by an explosion of papers in the open literature (2180 papers dealing with the “MOF” concept, with 500, 410, and 280 in 2007, 2006, and 2005, respectively). Indeed, when loosely defined, MOF may also mean “metal organic framework,” which creates an obvious confusion for reviewing the domain. Indeed, the latter do not necessarily exhibit an open architecture. Although an “open” framework does not preclude the robustness of the porous structure upon guest removal, in this chapter, we review materials with proven or presumed accessible porosity.

Applications of MOF materials for sensors, magnetism, conductivity, nonlinear optics, luminescent materials, gas storage, separation, and catalysis have been discussed in reviews [3–9]. A number of studies have addressed H₂ storage and can be found elsewhere [10–21]. In line with the theme of this handbook, “Design of Heterogeneous Catalysts,” we restrict this review to CO₂ capture and catalysis. While reviewing published open literature, we have paid special attention to the way materials are designed. The concept of “design” may have different meanings depending on the context. In this chapter, by “design” we mean defining appropriate material architectures for solving application issues. It is actually a two-step process. First, material specifications are addressed in terms of functions (such as working

capacity for separation and Lewis acidity for catalysis), in the context of the application targets and the chemical process. Then, appropriate material structures are proposed.

7.2

MOF General Features and Brief State of the Art

7.2.1

A Building Block Construction

In analogy to the framework of zeolites, the construction of inorganic–organic hybrid framework solids allows designing of specific framework geometries in the nanometer length scale, with specific pore structures [1, 2]. Unlike zeolites, which are made from TO4 tetragonal units, the considerable control exercised over complex geometry in coordination chemistry can then be extended for the design of infinite network assemblies [22–24]. These new porous materials can be classified into different families according to the dimensionality of the inorganic framework [25]: (i) organic–inorganic hybrid materials, where inorganic moieties can be organized either in (1D) chains or (2D) layers that are separated by organic pillars; (ii) Coordination polymers, which are made from (0D) “inorganic” clusters or isolated metal ions connected by bridging organic polytopic ligands. Polytopic organic ligands are generally nitrogen- and oxygen-donor rigid molecules such as bipyridine and multicarboxylic acids, respectively (Figure 7.1). The diversity in terms of ligands is infinite. For the latter, we account for more than 50 commercially available multidendate ligands. The simplest and most frequently used among these is terephthalic acid (benzene-1,4-dicarboxylic acid hereafter denoted 1,4DBC). The conceptual approach by which a metal–organic framework is assembled is termed reticular synthesis and is based upon identification of how the single building units (SBUs), or blocks, come together to form a net, or reticulate, with a specific spatial configuration [22, 23, 26–29]. The most common SBUs are (i) binuclear clusters called $M_2(CO_2)_4$ “paddle wheels” [30, 31] such as found in MOP-1 [32, 33] and $Cu_3(btc)_2$ (HKUST-1) and (ii) μ_4 -oxo $M_4O(CO_2)_6$ such as those found in IRMOF series. Extensive reviews on metal open framework structures and functionalities can be found here [31, 34–39].

7.2.2

Robust Open, Functionalized, and Sizeable Frameworks

The strategy to synthesize robust, truly porous MOFs must begin with an adequate choice of organic linking agent. Early use of rigid carboxylates such as benzene-1,3,5-tricarboxylate [40, 41] and benzene-1,4-dicarboxylate [42–45] yielded neutral, non-interpenetrated networks that were shown to maintain crystallinity during desorption and adsorption of guest molecules. Decomposition temperatures for many of these frameworks are in the range of 300–400 °C, leaving a comfortable domain of stability above the temperatures required for guest removal. The strength of these

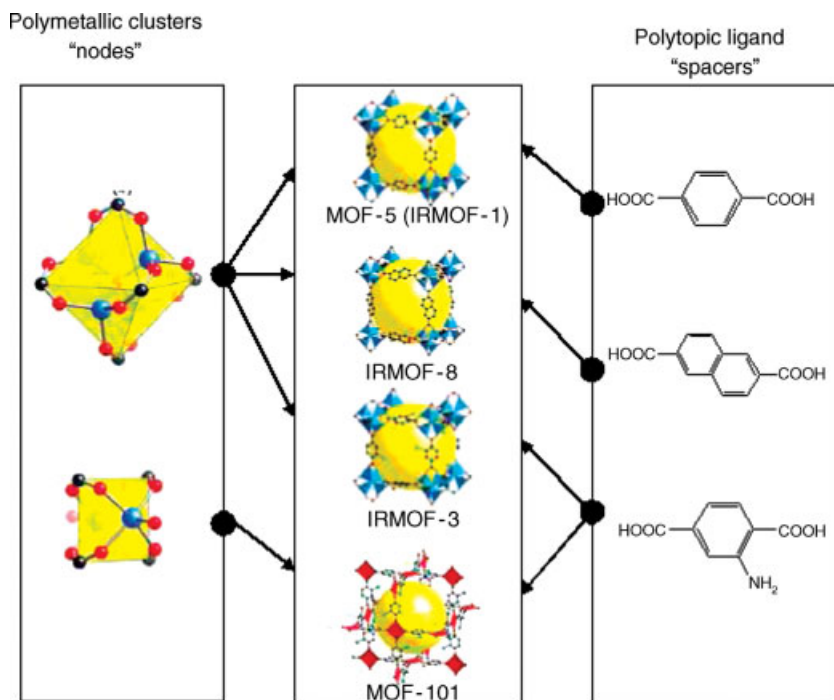


Figure 7.1 Self-assembly of polymetallic clusters and organic linkers yielding metal open frameworks (edited from Refs [31, 38]); (a) μ_4 -oxo $M_4O(CO_2)_6$, (b) $M_2(CO_2)_4$ paddlewheel.

frameworks arises from the inherent attributes of metal–carboxylate bonds: first, their energy is comparatively large due to enhanced electrostatic attraction, and second, the size of the carboxylate functionality permits bridging or chelating of metal cations, or a combination of both, to produce rigid, geometrically defined clusters.

In systems where the framework is sufficiently robust to display a permanent porosity, pore volumes and window diameters tend to significantly exceed those found in zeolites. For the series IRMOF based on MOF-5 structure, the pore size can be varied from 0.38 to 2.88 nm [46] by selecting linker of various sizes (Figure 7.2). The same holds for the 3D coordination polymer $Cu(OOC-R-COO)TEDA$ for which the pore size can be monitored to lie between 0.7 and 1.1 nm by playing with the length of the R group [47]. The largest cavities reported so far are those of MIL-100 and MIL-101 [48, 49] with cavities of 3.4 nm. Some of these materials have been prepared on pilot plant batch scale and have demonstrated outstanding storage capacity for rare gases [7], H_2 [13], and CO_2 [50].

The interest of this “node and spacer” approach is that it offers a route to functional networks with tuneable pore size [38, 46]. Nonoxide microporous materials are attractive as they are not, in principle, restricted to tetrahedral network topologies of zeolites; accordingly, their internal surfaces can have polarity, geometry, functionality, and reactivity quite different from the 3D aluminosilicate materials.

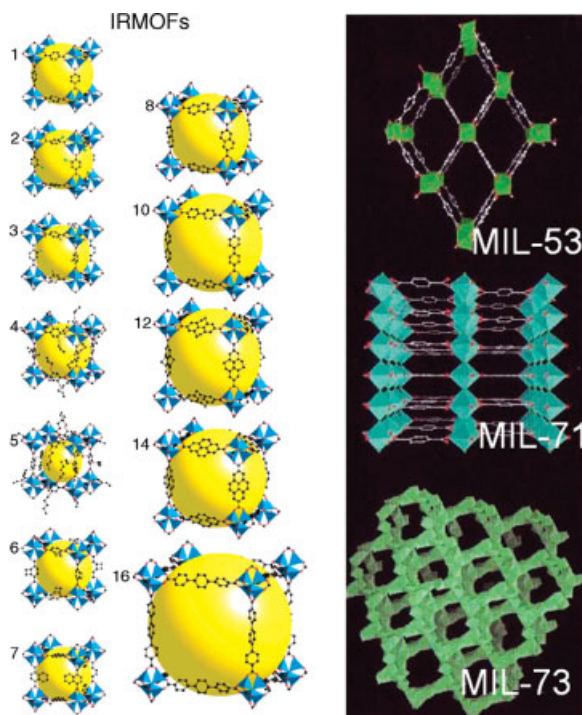


Figure 7.2 Example of 3D isoreticular compounds (IRMOFs) from references [46, 51] (left), example of 1D, 2D, and 3D porous structures (right).

7.2.3

MOFs Synthesis

Among the numerous factors to consider for the synthesis of a new metal–organic framework, the most important is the maintenance of the integrity of the building blocks. Where a desired SBU is to be generated *in situ*, the required synthetic conditions must be compatible with the preservation of the linking units. Typically, this is performed by precipitation from a solution of precursors.

Before a sufficient knowledge was established to elucidate the conceptual roots of reticular synthesis, the majority of studies were exploratory, with early attempts involving simple, highly soluble precursors, and labile metal ions of the late transition series. The assembly process of a MOF is akin to organic polymerizations, in that an insoluble entity is quickly formed that precludes recrystallization. The framework assembly occurs as a single synthetic step, and thus all of the desired attributes of the target material must be carried by the building blocks. Nevertheless, intermolecular forces may limit predictability, which requires identifying and modifying synthetic conditions that allow the assembly of the building units in the intended fashion. It has often been observed that minor changes in concentration, solvent polarity, pH, or temperature lead to poorer quality crystals, reduced yields, or

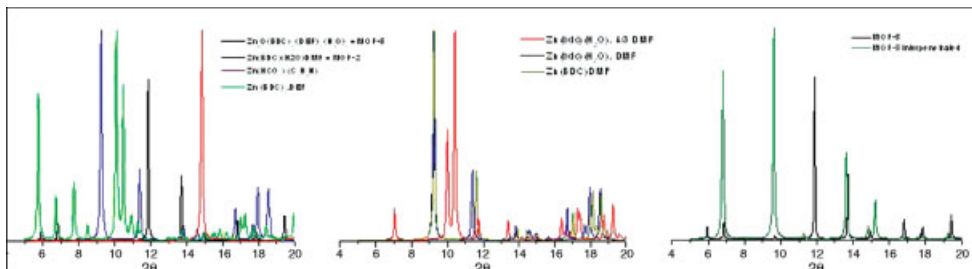


Figure 7.3 XRD patterns that can be obtained from the Zinc and 1,4-bdc system; different structures [43, 54, 58, 61] (left), effect of occluded solvent [54, 55] (middle) and effect of intercalation [62] (right).

the formation of entirely new phases. The system $\text{Zn}(\text{NO}_3)_2 \cdot x\text{H}_2\text{O}/1,4\text{-bdc}$ is an outstanding example of protocol sensitivity [52–54] (Figure 7.3). Whereas “dried” DMF yields MOF-5 [55, 56], MOF-2 and MOF-3 are obtained in DMF/toluene [57] and DMF/MeOH mixtures [58], respectively. When water is added to DMF, a different phase, MOF-69C, is obtained [45, 59]. The synthesis of MOF-5 is very moisture sensitive, since the level of hydration of the precursor (e.g., hexahydrate against tetrahydrate) as well as the “dryness” of the DMF may direct the synthesis toward MOF-5 or MOF-69C (or a mixture of the two) [60]. Use of high temperature leads to a degradation of DMF into formic acid, which is responsible for the formation of $\text{Zn}(\text{HCO}_2)_3(\text{C}_2\text{H}_8\text{N})$ [54]. The nature of the base has been shown to yield different phases such as PNM-1 [61] or a Zn nanocluster containing MOF-5 [62]. In addition to the numerous phases that can be obtained, experimentalists face pseudopolymorphism issues whereby structures obtained differ in the number or types of included solvent molecules [63]. Finally, XRD patterns are very sensitive to interpenetration and intercalation phenomena, which are favored by using high-precursor concentrations [38, 46, 63].

A variety of techniques were primarily used to grow crystals of simple inorganic salts, such as slow evaporation of a solution of precursors, layering of solutions, or slow diffusion of one component solution into another through a membrane or an immobilizing gel. For the synthesis of more robust frameworks, solvothermal techniques were found more appropriate [31]. The precursors are typically combined in the form of dilute solutions in polar solvents such as water, alcohols, acetone, or acetonitrile and heated in sealed vessels such as Teflon-lined stainless steel bombs or glass tubes, generating autogenous pressure. The different solubilities of organic and inorganic precursors may be a limit for the synthesis of materials in reasonable amounts for applications. It can be overcome by a biphasic solvothermal synthetic procedure, where the inorganic source is dissolved in water with the organic in immiscible alcohol [34]. Mixed solvent systems are often used to tune the solution polarity and the kinetics of solvent–ligand exchange, effecting enhanced crystal growth.

In cases where deprotonation of the linker is necessary, gradual neutralization of a solution can be performed by thermal decomposition of an amide cosolvent. Alkyl

formamides are particularly useful toward this end, as they are also excellent solubilizing agents. An alternative method is to slowly generate the desired link *in situ*, for example, by hydrolyzing nitriles or esters to yield carboxylates. Finally, when high yield is desired over crystal quality, reaction times can be greatly reduced by increased concentration and agitation of the solution. Generally, microcrystalline materials are formed under these conditions.

Although the design of MOF by a *reticular engineering* approach has attained considerable degree of achievement, we can, at best, direct rather than predict structures, that is, we can optimize the conditions under which a targeted structure may exist, but we cannot be certain of its formation or stability [31, 63].

7.2.4

Adsorption Properties of MOF

Generally speaking, knowledge of properties of MOFs is limited when it comes to zeolites. Permanent and robust microporous structures are characterized by isotherm shapes (N_2 at 77 K) of type I, with little or no hysteresis, as in the general case of zeolites. This is the case for examples of IRMOFs [31, 64] and HKUST-1 [65]. Sorption isotherms of organic vapors such as chloroform, benzene, or cyclohexane have also been used to estimate pore volumes and aperture sizes of rigid frameworks [53]. Even, if BET assumptions are not valid to measure surface areas of microporous materials, this method provides meaningful and accurate measurements in the case of MOF materials [66, 67]. As shown below, considerable increases in these values have been obtained in just a few years. Surface BET records are held by Cu(bdc)teda [68], MOF-177 [31, 69], MIL-101 [48], with surface areas of 4000, 4500, and $5300 \text{ m}^2 \text{ g}^{-1}$, respectively (Figure 7.4).

However, examples of robust microporous materials, as determined by N_2 (or Ar) isotherms at 77 K, are relatively limited when compared to the thousands of published coordination polymers. In addition to the examples mentioned above, we can cite $\text{CuSiF}_6(4,4'\text{-bipyridine})_2$ ($1350 \text{ m}^2 \text{ g}^{-1}$) [70] $\text{Cu}_2(\text{pzdc})_2(\text{bpy})$ [71], HKUST-1 ($1780 \text{ m}^2 \text{ g}^{-1}$), MOF-2 ($345 \text{ m}^2 \text{ g}^{-1}$), MOF-11 ($560 \text{ m}^2 \text{ g}^{-1}$) [72], MOF-505 ($1550 \text{ m}^2 \text{ g}^{-1}$), MOF-74 ($815 \text{ m}^2 \text{ g}^{-1}$) [50, 73], MOP-28 ($915 \text{ m}^2 \text{ g}^{-1}$) [33], IRMOF-51 (480) [74],

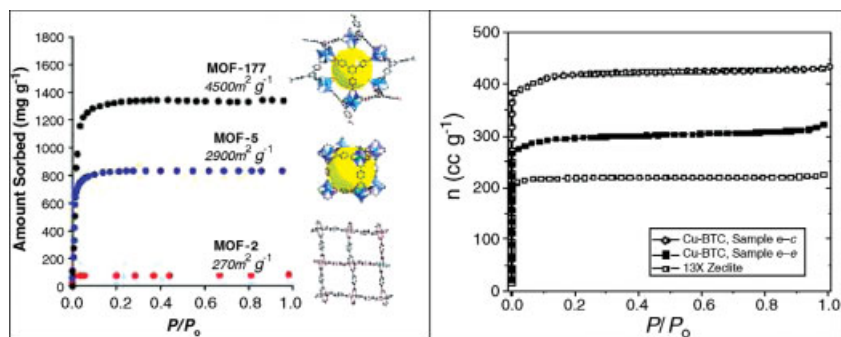


Figure 7.4 Examples of N_2 adsorption isotherms at 77 K from Refs [31, 65].

MIL-47 ($930 \text{ m}^2 \text{ g}^{-1}$) [75], MIL-53 ($1100 \text{ m}^2 \text{ g}^{-1}$) [9], MIL-68 ($600 \text{ m}^2 \text{ g}^{-1}$) [76], MIL-103 ($930 \text{ m}^2 \text{ g}^{-1}$) [77], $\text{Zn}_3(\text{bpd})_3(\text{bpy})$, $\text{Cu}(\text{hfpbb})(\text{H}_2\text{hfpbb})_{0.5}$, $\text{Co}(\text{ox})(\text{bpy})$ [78], $\text{Co}_2(\text{ndc})_2(\text{bipyen})$ ($230 \text{ m}^2 \text{ g}^{-1}$) [79], $\text{Rh}(\text{bdc})$ ($470 \text{ m}^2 \text{ g}^{-1}$) [80], TUDMOF-2 ($520 \text{ m}^2 \text{ g}^{-1}$) [81], JUC-48 ($880 \text{ m}^2 \text{ g}^{-1}$) [82], $\text{Ni}_{2.5}(\text{OH})(\text{L-Asp})_2$ ($157 \text{ m}^2 \text{ g}^{-1}$) [83], $\text{Ni}_2(\text{dhtp})(\text{H}_2\text{O})_2$ ($1083 \text{ m}^2 \text{ g}^{-1}$) [84], and $\text{Zn}_4\text{O}(\text{D}_2\text{-tcppda})_{1.5}$ [85] (* Langmuir surface area).

Very few types of probing molecule are also studied. Generally, only isotherms for H_2 , CO_2 , and CH_4 are investigated due to storage applications although vapor adsorption of hydrocarbons can provide useful insights on pore size and hydrophily–hydrophobia balance [53, 86]. For separation applications, much more insight is required concerning the changes in adsorption capacity with temperature and pressure, the effects of mixture of various gases for separation, that is, all information required for envisioning any industrial application for gas separation. The natural gas cleanup by means of CO_2 capture for pressure swing adsorption (PSA) will be treated later on, as a case study to illustrate a rational design of new generation of MOF adsorbents, including a specific literature survey.

7.2.5

Rational Strategies to Design MOFs for Targeted Applications

As derived from the above literature survey, a striking general feature of MOF syntheses and uses is the number of physicochemical variables involved, such as nature of ions clusters, linkers, solvent, operating conditions (precipitation, solvothermal, diffusion, ...) and so on, which makes their combination almost infinite [9]. Till now, mainly, simplified “try and error” approaches were applied for MOF synthesis. Fortunately, high-throughput techniques (HTTs), are now available, as routine lab equipments and can be used to accelerate the discoveries of new materials for targeted applications [87–91]. HTT have been used to investigate the parameter space of solvothermal conditions in order to discover new phases [92–98].

Two case studies, carried out in our laboratory, illustrate the development of HT experimentations combined with a rational material design for efficient separation and catalytic applications. In Section 7.3, we report the design and HT screening of MOF adsorbing materials for CO_2 capture by PSA process, as a major challenge for the environmental research. Outstanding pore shape selectivity for aromatic alkylation is described as part of MOF design in Section 7.4.

7.3

Combinatorial Design of MOF for CO₂ Capture in a PSA Process

7.3.1

Process Specifications

As produced from the gas fields, natural gas generally contains variable amounts of several contaminants such as water, C_{3+} hydrocarbons (mainly light paraffins and aromatics), carbon dioxide, nitrogen and sulfur-containing compounds. Before

supplying to processing plants and downstream customers, gas treating operations are usually mandatory, especially the removal of nitrogen and acid gases such as carbon dioxide and hydrogen sulfide. For large-volume treatments, the most frequent technology is scrubbing with liquid TriEthyleneGlycol (TEG). An alternative process is PSA, which can be applied to medium and small units. Separation of CO₂ from the field mixture is effected in PSA by cycling adsorption (at high pressure, 30–50 bars) and desorption (at low pressure, 2–5 bars) on a selective adsorbent. Here, the absence of chemicals (e.g., amine, solvents) generates considerable environmental benefits.

As for any adsorption separation processes, the key requirement is an adsorbent that preferentially adsorbs one component from a mixed feed. Main adsorbent criteria are (i) adsorption capacity of the gas to capture, that is, difference between the amount adsorbed and desorbed, (ii) adsorption selectivity (evaluated from Henry's law constants), (iii) regenerability, that is, the ability to desorb the captured gas at the desorption conditions, and (iv) access to diffusion kinetics such as mass and heat transport in the porous system.

In general, compromises have to be found between these criteria. In the case of CH₄/CO₂ separation, when adsorption selectivity is very high for CO₂, CH₄ can be recovered with high purity but at the expense of the energy balance to assist desorption of CO₂. Large pore size would favor high pore volume and, therefore, adsorption capacity and diffusion, whereas it would reduce interaction potential and, therefore, selectivity.

Despite numerous porous materials (e.g., activated carbons, zeolites, silica, silica–alumina, alumina, polymers) being available on the PSA market, there is still a large space for process improvement, which requires a strong coupling between process engineering and material science, as proposed in this integrated approach of MOF development.

7.3.2

General Properties of MOFs for CO₂ Adsorption

In terms of adsorption properties, MOF materials exhibit three major differences with respect to classical adsorbents.

- (i) Higher adsorption capacities due to very large microporous or mesoporous volumes: This is specially the case when considering high-pressure domains ($P > 25$ bars). For example, to compare with the reference 13X material at 50 bars, CO₂ adsorption capacities are twice and three times larger for MOF-177 and MIL-101, respectively [50]. This outstanding property can be advantageous for storage applications.
- (ii) Different adsorption potential observed at low pressure ($P < 5$ bars), due to their specific organic moieties: Adsorption proceeds mainly by van der Waals interactions instead of dipole–dipole interactions in the case of oxides. As a result, MOFs exhibit much lower heats of adsorption for CO₂, which can be observed by a low adsorption rate at low CO₂ pressures (Henry's constant).

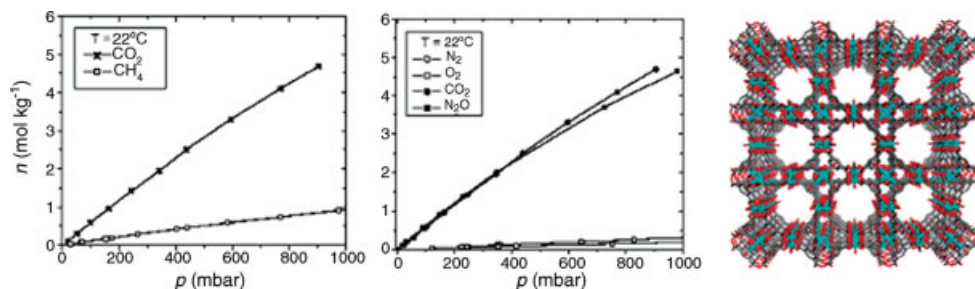


Figure 7.5 adsorption isotherms of Cu₃(btc)₂ at 22 °C from Ref. [65] and 3D structure from Ref. [78].

As an example, Cu₃(btc)₂ (also called HKUST-1) has a 3D porous structure of channels that intersect at cavities that are 1.32 and 1.11 nm in diameter, with apertures of 0.69 nm. The pore volume is about 0.4 cc/g with large pores of 0.8 nm [73]. Sorption isotherms for CO₂ and CH₄ at ambient temperature are nearly linear over a broad pressure range up to atmospheric pressure with a strong preferential sorption of CO₂ over CH₄ [65] (Figure 7.5).

(iii) Framework flexibility upon adsorption–desorption [99, 100]: In contrast with the permanent porosity typical of classical “rigid” adsorbents (carbons, zeolites), adsorption on MOF may evolve dynamically depending on the nature and quantity of host molecules. In many examples, it is observed that the sorption process can take place at different pressures depending on the adsorbed gas, leading to adsorption–desorption isotherms with hysteresis phenomena. In addition, the adsorption can also take place stepwise depending on the pressure. These phenomena, usually named “Gate Opening” arise from two properties; (i) the guest–host interactions, governed by coordination chemistry, is the driving force and (ii) flexibility of 1D, 2D porous networks. Adsorption of guest molecules at the nodes may result in different cluster geometry (different bond angles). At the network scale, it results in a distortion of the host structure, leading to changes in the porous structure in terms of pore sizes, shapes, and volumes.

The flexibility of coordination polymer frameworks [Cu(4,4'-bipy)(dhbc)2] has been used to activate access to the porosity using guest pressure [101] (Figure 7.6). This exploits either freedom to displace one interpenetrated network relative to another one or uses guest pressure to overcome the weakest framework-forming interaction in a low-dimensional system. The porous system is stable to guest loss, but the interlayer separation decreases to prevent nitrogen uptake at 77 K. However, N₂ sorption isotherm, performed at 25 °C, demonstrates an abrupt increase in uptake beyond 50 atm, referred to as the “gate-opening” pressure, which corresponds to a structural transition from the “closed” to the “open” form driven by interaction between the framework and the guest.

The presence of water can drastically change the structure and thus adsorption properties [102, 103]. For example, MIL-53 is built up from infinite chains of corner-sharing MO₄(OH)₂ octahedra (M=Cr³⁺, Al³⁺, Fe³⁺) interconnected by benzene

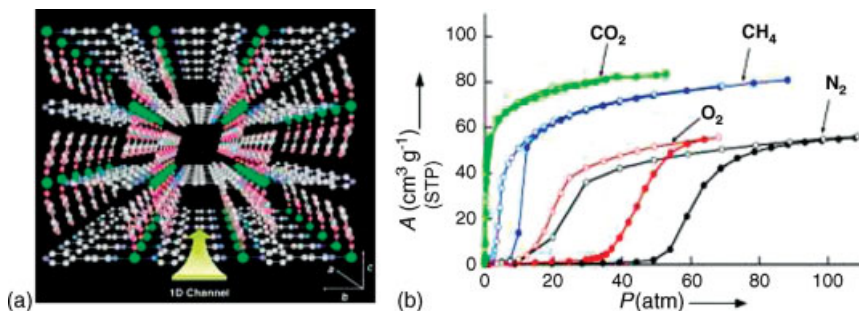


Figure 7.6 3D p-stacked pillared layer structure of [Cu(4,4'-bipy)(dhbc)2] (left), adsorption (filled circles) and desorption isotherms (open circles) at 25 °C (right) from Ref. [101].

dicarboxylate units. This results in MOF containing 1D diamond-shaped channel with pores of free diameter close to 0.85 nm. The MIL-53 (Cr³⁺, Al³⁺) solids exhibit a “breathing” phenomenon upon hydration/dehydration (Figure 7.7). In the hydrated form, the pores are slightly deformed owing to hydrogen-bond interactions. When dried, the structure becomes more open. Adsorption of CO₂ on the dehydrated MIL-53(Cr) sample takes place in a two-step process. On the other hand, the adsorption of CO₂ on the hydrated sample shows little uptake at pressures up to 10 bars, while a single uptake occurs at about 15 bars. Thus, CH₄ and CO₂ cannot be adsorbed in large amounts in moisture conditions at moderate pressure.

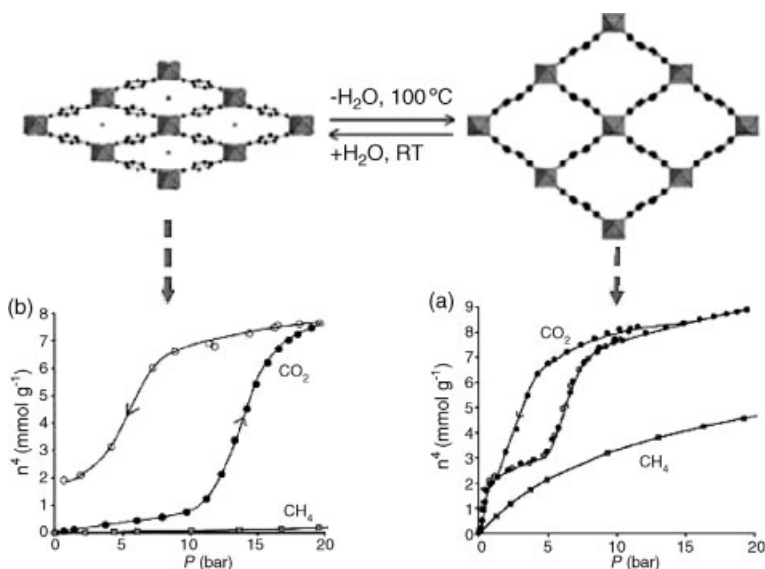


Figure 7.7 Breathing phenomena upon water adsorption and impact on CO₂ and CH₄ adsorption from Ref. [102].

7.3.3

MOF Design for CO₂ Capture

As already mentioned, high adsorption capacity at high pressure is not very useful for CO₂ capture, either for “flue” applications that operate at atmospheric pressure or for natural gas cleanup, since the gas fields’ partial pressure of CO₂ hardly exceeds 10 bars. The flexibility property is not appropriate for separation processes such as PSA because desorption takes place at lower pressure than adsorption, thus making the regeneration more energy intensive.

From the above statements, the nearly linear shape of the MOF isotherm at relatively low pressure (as for instance HKUST-1) is a key advantage over zeolites, especially in the desorption step. Indeed, MOF desorption can take place rapidly at atmospheric pressure whereas a significant quantity of CO₂ remains trapped in zeolite materials, which is detrimental to the working capacity. However, the heats of adsorption of CO₂ in a MOF are still too low to allow the separation to proceed with selectivity CO₂/CH₄ > 10. Therefore, MOF materials shall be designed to enhance interactions of CO₂ with MOF walls.

Two different strategies can be applied. (1) a “structural” route: It aims at reducing micropore size, usually quite large in case of MOF (>1.5 nm), to the size of medium- or large-pore zeolites (0.5–1.2 nm) in order to benefit from stronger wall–molecules interactions; (2) a “functionalization” route: It aims at changing the wall’s potential by increasing polarity.

7.3.3.1 “Structural” Route for Design Strategy

The design of MOF with intergrown networks is a promising route for producing a MOF with small pores. Yaghi *et al.* described different types of “network” for which two or more identical frameworks are intergrown, at the expense of pore volume. This may take the form of *interpenetration*, where the networks are maximally displaced from each other, or *interweaving*, where they are minimally displaced and exhibit close contact, which may result in mutual reinforcement. The former is commonly cited as one of the major obstacles to be overcome for developing a porous MOF [46]. The possibility of either of these events is directly dependent on the network topology or distortions thereof. Network interpenetration is a route to reduce the pore size while still retaining relatively high-porous volume. For example, IRMOF-9, 11, 13, and 15 are interpenetrated MOF-5 types with lower pore sizes with respect to their respective noninterpenetrated parent structure [46]. Another example is the triply interpenetrated CO₂(ndc)²(bipyen) which shows pore cross sections of 4.4 Å × 3.5 Å [79]. The advantage of constricting the pore dimensions in interpenetrated IRMOFs was demonstrated by larger Henry constant for H₂ adsorption [73].

Pillared networks: a route to design MOF with small pores Chen *et al.* [104] have very recently reported a rational design strategy to tune micropores for their highly selective sorption of small molecules. The basic strategy is to form 2D layers of paddle wheel cluster M₂(COO)₄ with bicarboxylate linkers and to add bidentate pillars between the layers to construct 3D porous primitive cubes [47]. As an example,

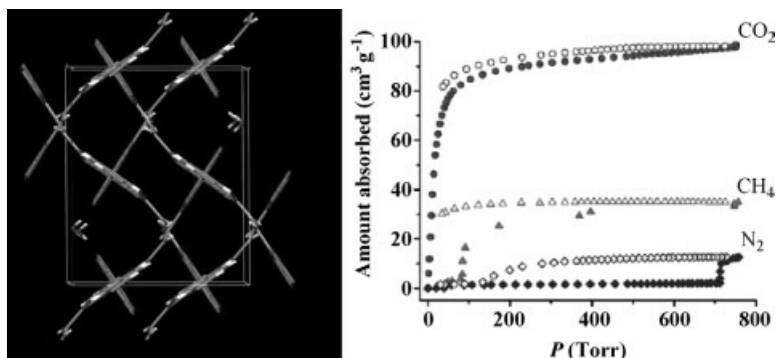


Figure 7.8 Crystal structures of frameworks Cu(fumarate)(4,4'-Bpe)_{0.5}·0.5H₂O (left), adsorption isotherms at 195 K from Ref. [104].

Zn(bdc)(4,4'-bipy)_{0.5} with micropores about 0.4 nm × 0.4 nm was applied to gas chromatographic separation of alkanes. For separation and purification of smaller gas molecules such as H₂, Ar, N₂, and CO₂, such micropores need to be further narrowed down. It can be done by selecting shorter ligands either carboxylates or pillars, or both. As an example, bdc can be replaced by fumaric acid (fma) and the pillar 4,4'-bipy trans-bis(4-pyridyl)ethylene occupying the axial sites of the Cu₂ paddle wheels to form 3D MOFs [104]. The network shows 1D channels of about 0.2 nm × 0.32 nm that interconnect the pore cavities of about 0.36 nm, which can accommodate two water molecules (Figure 7.8).

Large-to-very-large hysteresis curves were observed for CH₄ and N₂, respectively, while reversible desorption was observed for CO₂, indicating different gate-opening effects: CO₂ as guest, opens the host structure easily while CH₄ and N₂ do not interact as well with the host.

7.3.3.2 “Functionalization” Route for Design Strategy

Even if the linear shape of CO₂ isotherms is appropriate for maximizing the working capacity, the adsorption rate must be increased to get sufficient CO₂ selectivity for CO₂–CH₄ separation. “Thermodynamic” separation (i.e., depending on adsorption heats) can be optimized by tuning the chemical nature of the adsorbent. For example, zeolite polarity can be monitored by adjusting the Si/Al ratio. It can also be changed by postsynthesis treatments such as ion exchange, silylation, and dealumination. At IRCELYON, we have investigated two different approaches for framework functionalization: (i) at the linker and (ii) at the node.

We have taken advantage of linker functionalization on MOF-5 (or IRMOF-1) to insert out-of-plane amino groups into the pore channels, assuming that these basic centers would increase interaction potential with the acidic CO₂ molecules. Yaghi has shown that it was possible to substitute terephthalic acid with amino terephthalic acid for the synthesis of IRMOF-3 structure [46]. Thus, the porous structure remains very identical while having modified the basicity of the materials by introducing accessible –NH₂ groups from the channels. As can be seen in Figure 7.9, adsorption isotherms

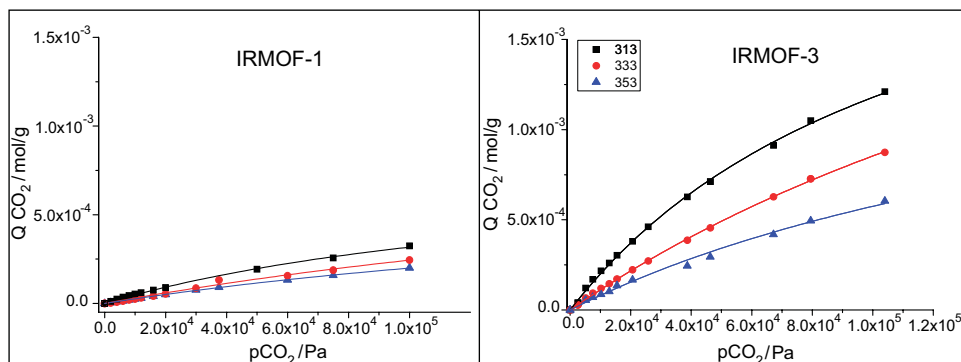


Figure 7.9 CO₂ adsorption isotherms of IRMOF-1 and -3 (submitted).

confirm the highest affinity for amino functionalized materials with CO₂ heats of adsorption of -15 and -17 kJ mol⁻¹, for IRMOF-1 and IRMOF-3, respectively.

Adsorption of CO₂ was recorded by DRIFT at different temperature on IRMOF-1 and IRMOF-3. Physisorption of CO₂ is revealed by the increase of peak intensity of ν_3 band (2320 cm⁻¹) as the temperature decreases. We have also observed weak peaks at 1609 and 1446 cm⁻¹, which can be assigned to carbamic species, arising from the condensation of CO₂ with the primary amine. Although the corresponding CO₂ amount was not quantified, this case study shows that stronger adsorption phenomena than van der Waals interactions can take place in functionalized MOF. We believe that the combination of both chemisorption and physisorption is a promising route for CO₂ capture.

The saturation of the coordination sphere for most of transition metal-based MOFs may limit strong adsorption of guest molecules. Hence, for IRMOFs, the strongest adsorption sites are located at the Zn₄O cluster with very limited interactions with the metal itself, and the adsorption force arises from weak interactions [105]. Because of their 4f electrons, lanthanides provide richer coordination chemistry and thus can overcome saturation issues, thus providing accessible adsorption sites [77, 106, 107].

7.3.4

Combinatorial Screening Methodology at IRCELYON

A modular, net-based approach is an essential part of crystal engineering, for both design and analysis of crystal structures. However, despite the increasing number of examples of true structure design, the limitations and challenges of this approach should not be ignored. At best, structures can be directed rather than predicted – that is, one can create the conditions under which it is possible that desired structures may form, though there is no certainty that they will do so [63].

As already stressed in the analysis of the state of the art, a number of known and unidentified parameters play a role in the synthesis of MOFs and subtle changes in the recipe may lead to an entirely different structure. For these reasons, an approach through combinatorial chemistry seems quite adapted to the synthesis of new MOFs,

by screening various synthesis protocols in a rational way. Such an approach would actually integrate a rational design of MOF components while accelerating their discovery, characterization, and testing by HT screening. However, instead of focusing on an “a priori selected” design, we prefer a “pragmatic” approach in which materials are ranked according to their testing performances rather than the usual “crystal engineering” approach in which the properties are assessed after the structure is determined.

7.3.5

Combinatorial Synthesis

The objectives of the combinatorial screening are (i) to accelerate the discovery of synthetic conditions that lead to desired structures, (ii) to discard samples that are not crystalline and water-temperature sensitive, as early as possible in the screening process.

7.3.5.1 Protocol

For the synthesis, the amounts of solvent and the precipitating agent are the two key parameters that are systematically varied whereas the temperature is fixed. As solvents, polar organic solvents (EtOH, DMSO, DMF) that have adapted properties to dissolve organic chemicals (linkers and base) as well as metal salts have been selected (Figure 7.10). The organic bases are selected according to their pK_a . Three bases covering a large range of basicity were selected, with pK_a ranging from 5 to 11 (pyridine, dabco, Et_3N). Precipitates are first washed with water in order to discard compounds that would be salts or would hydrolyze and then dried at $170^\circ C$ in order to check their capacity to maintain crystallinity upon thermal treatment for further gas adsorption treatments.

After precipitates are dried, they are all analyzed by powder x-ray diffraction. Identification of existing structures from the structural database can hardly be performed for reasons explained above. Structure resolution using Rietveld type method can also not be performed in a HT screening approach. Instead, we use a chemometric method (PCA analysis) in order to compare XRD patterns. This method is commonly used for the screening of drug molecules. It enables us to identify classes of samples. Using this fast method, it becomes easy to distinguish similar samples, mixtures of phases, and peculiar phases.

7.3.5.2 Method Validation

Usually, MOF compounds are synthesized by solvothermal methods to obtain single crystals for purposes of characterization. However, the yields and quantities that can be usually achieved using this method are too low to systematically evaluate their



Figure 7.10 Applied synthesis protocol selected for preparing MOFs libraries.

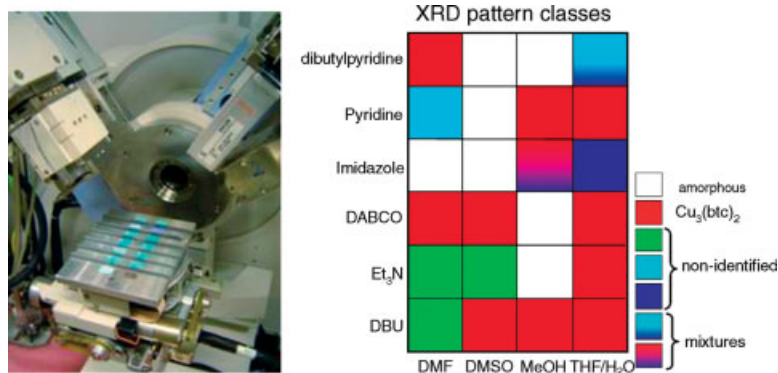


Figure 7.11 HT X-ray diffraction analysis performed on a MOF library of 16 samples.

sorption properties. As a consequence, the first step of this work was to develop a method to obtain a powder MOF quickly, in soft conditions, and in reasonable yields. The validation of the method was carried out on a reference MOF, namely, Cu₃(btc)₂. The objective is to check whether Cu₃(btc)₂ can be obtained by using a combinatorial method easy to implement. The precipitation method was selected with a screening method dealing with a systematic variation of the solvent and base nature.

The protocol selected in this work is to dissolve 1 g Cu(NO₃)₂·3H₂O in 25 mL of the given solvent and mixing it with 3 g of trimeric acid also dissolved in 25 mL of the same solvent. Subsequently, the organic amine dissolved in 25 mL of the same solvent is poured into the solution dropwise. A precipitate is obtained, which is washed, separated by centrifugation, and finally dried at 170 °C in air. To determine the influence of key parameters on the synthesis, six amines with different pK_a (5–12) and four solvents were tested, which gives 24 samples to test. X-ray diffraction patterns were recorded a Bruker D5005 apparatus which allow us to characterize a library of 16 samples in about 1 h (Figure 7.11).

Among the 24 experiments, 10 compounds show XRD pattern corresponding to Cu₃(btc)₂; three phases could not be identified; and two are mixtures of thereof. The remaining samples are mostly amorphous (Figure 7.11). These results reveal any obvious correlation between the screened parameters and the formation of Cu₃(btc)₂. The specific surface and porous volume, 1536 m² g^{−1} and 0.8 cm³ g^{−1}, respectively, are in good agreement with those reported by Wang *et al.* [65]. High-microporous volume is usually an indicator of sample quality. Indeed, amorphous compounds (such as Cu oxides) or other nonporous phase in low amounts may be present, which would reduce measured pore volume [108].

The material also shows that dehydration occurs at 100 °C and remains stable up to 300 °C, as reported by Kaskel *et al.* [108]. The heat of CO₂ adsorption was −12 kJ/mol as measured by gravimetric methods (TEOM balance) (Figure 7.12).

7.3.5.3 Screening of Metal-BTC System

More than 200 MOF samples were prepared, using mostly trimesic acid (H₃btc) as organic linker. Metals investigated are lanthanides (La, Ce, Pr, Nd, Sm, Gd, Tb) and

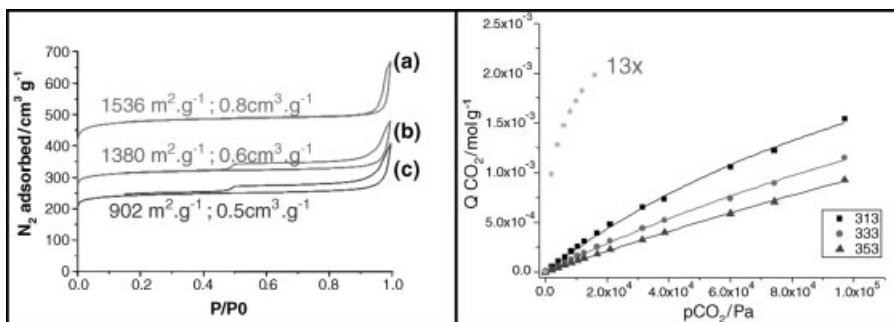


Figure 7.12 N_2 physisorption at 77 K of $Cu_3(btc)_2$ (left), CO_2 adsorption at different temperature and comparison with zeolite 13X on a TEOM oscillating thermobalance.

transition metals (Cu, Zn, Ni, Co, Ru). For each couple of metals, about 15 different synthesis procedures were carried out (3 different bases with 5 different solvents).

For Cu/ H_3btc and Zn/ H_3btc combinations, new XRD phases were evidenced in addition of phases reported in the literature. Neither Ni nor Co give crystalline phases. For the lanthanide series, about 90% precipitate and 40% show crystalline phases. The synthesis protocol did not lead to monocrystals that could be further analyzed. Alternative protocols for monocrystal synthesis are under development.

The issue then is to identify distinct classes of XRD patterns. Figure 7.13 shows the XRD patterns of about 40 Ln/ H_3btc samples. At first glance, similarities seem to exist, but these can hardly be quantified manually.

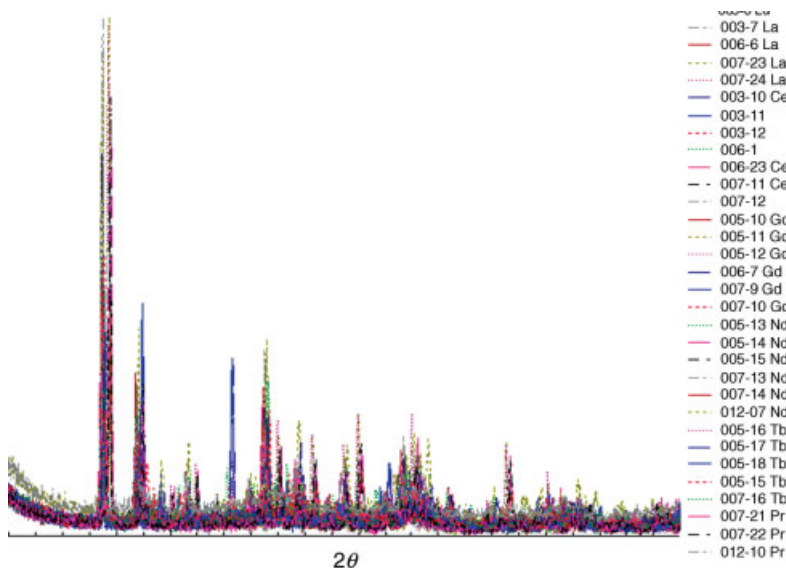


Figure 7.13 XRD patterns of Ln/ H_3BTC samples.

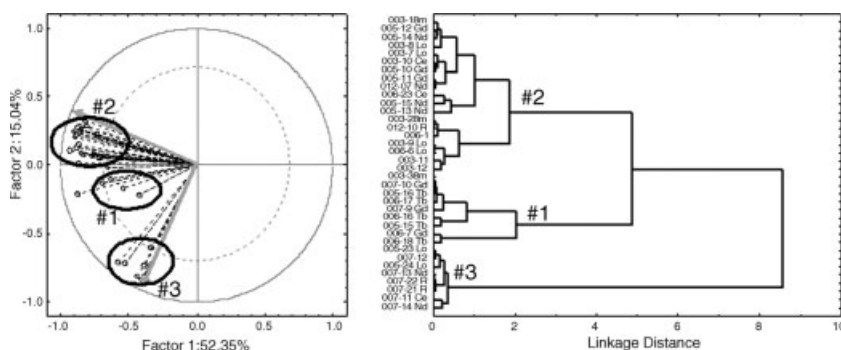


Figure 7.14 PCA and clustering analysis from XRD data; PCA (right) and hierarchical clustering (Left).

After validating the protocol, it was extended first to the system Ln–BTC. The lanthanide metals chosen were La, Ce, Pr, Nd, Sm, Gd, and Tb. In these experiments, the solvents were THF, DMF, H₂O/THF, H₂O/Et₂O and DMSO, while the bases were pyridine, dabco, and Et₃N. In a second step, different ligands were tested.

In order to classify the different kinds of crystalline phases, the XRD patterns were classified using PCA and clustering techniques, as implemented in Statistica (Figure 7.14). These techniques indicate that XRD patterns can be classified into three distinct families. Looking at the patterns in more detail, we notice that cluster #1 contains materials of low crystallinity whereas cluster #2 and cluster #3 are represented by well crystalline and distinct phases.

7.3.6

Characterization of Representative Samples

Figure 7.15 shows the XRD patterns of two representative samples between the two clusters, #2 and #3, characterized by two distinct highly crystalline compounds. On the one hand, it comes about that the compounds of cluster #2 are obtained in DMF while all compounds of cluster #3 are made in DMSO. This means that one synthesis parameter – the nature of solvent used – primarily directs the XRD structure. On the

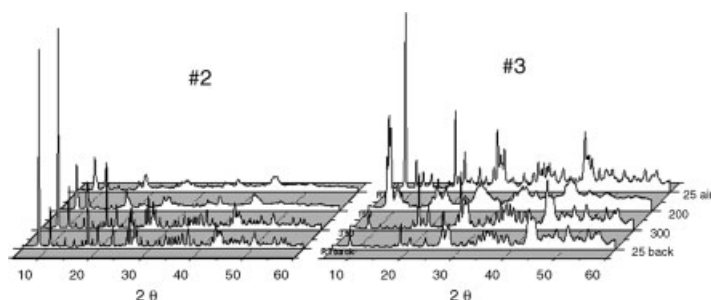


Figure 7.15 XRD patterns of two representatives of clusters #2 and #3 of MOFs materials.

other hand, elemental analysis, temperature-programmed XRD and TGA/TDA analyses indicate that these two classes of materials do not display the same properties (to be published). For examples, MOFs of cluster #2 are stable upto 400 °C whereas the other ones from cluster #3 are stable only upto 250 °C. Attempts to synthesize single crystals failed because structure resolution failed, but Rietveld refinement performed on the microcrystalline powder indicates that the structure of cluster #2 is close to Dy(btc)(H₂O)·DMF, recently reported by Guo *et al.* [109].

Another parameter investigated during this combinatorial approach is the loss of crystallinity upon time on stream and its possible recovery. High crystallinity was found to be recovered when heating at 350 °C under dry atmosphere. Upon heat treatment, water molecules bonded to Ln can be removed leading to accessibility of the metal site [109].

7.3.7

HT Testing and CO₂–CH₄ Isotherms of Selected Samples

The HT testing of porous material library (zeolites, MOFs) at IRCELYON is carried out by means of parallel breakthrough curve measurements on a SWITCH-16 apparatus. This system allows us to quantify transient adsorption phenomena on 16 different samples at various pressures and temperatures. Isotherms and isobars of pure component or mixtures can be obtained in a day for the sample library. Instruments and methods are reported elsewhere [110]. After a sample is identified as a “hit” under conditions close to the PSA application, isotherms of pure gases are recorded on a TEOM balance in order to study the kinetics of adsorption and desorption.

Sorption isotherms for CO₂ and CH₄ at ambient temperature were carried out on La(btc) (cluster #2). Nearly linear sorption isotherms were obtained up to atmospheric pressure, with a strong preferential sorption of CO₂ over CH₄ (Figure 7.16).

For thermodynamic separation, the two key criteria of adsorbent effectiveness are the working capacity (WC) and the working selectivity (WS). The definition of working capacity is given in Equation 7.1:

$$WC_A = Q_A(x, P, T)_{\text{ads}} - Q_A(x, P, T)_{\text{des}}, \quad (7.1)$$

$$WS = \frac{WC_A}{WC_B}, \quad (7.2)$$

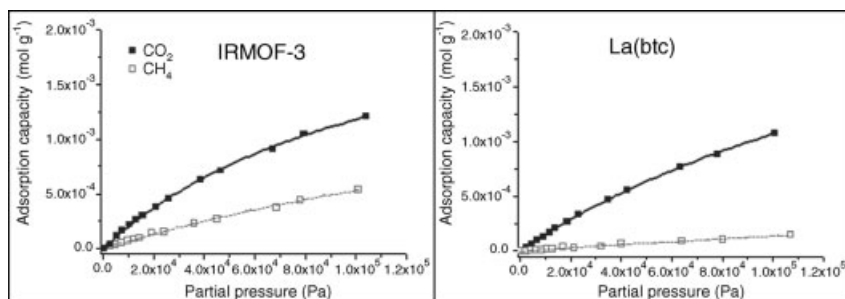


Figure 7.16 CO₂ and CH₄ adsorption at 313 K on IRMOF-3 (left) and La(btc) (right).

where $Q_A(x, P, T)_{\text{ads}}$ and $Q_A(x, P, T)_{\text{des}}$ are the equilibrium loadings of A (mol/g) corresponding to the gas-phase mole fraction (x), total pressure (P), and temperature (T) at adsorption and desorption steps, respectively. The working capacity physically represents the net amount of adsorbate transacted on and off with the adsorbent for each complete cycle, providing a good indication of the amount of adsorbent required for the separation. The working selectivity of component A relative to component B (defined in Equation 7.2) is a key indicator, since it represents the separation efficiency. The operating conditions will dictate the selectivity and hence the performances of the adsorbents.

Here, the adsorption parameters have been estimated assuming Langmuir model. For La(btc), the working selectivity CO_2/CH_4 is about 6 at 313 K ($P = 1\text{--}5$ bars), which is still lower than industrial targets. However, the desorption process takes place very rapidly, for example, in the same range as the adsorption step, which is a key property for fast PSA process.

7.4

MOF Design for Catalytic Application

7.4.1

Properties of MOF in Catalysis

Metal open framework materials can be regarded as a “new” class of catalytic materials at the frontier between active 3D inorganic frameworks such as the zeolites, with respect to their porous structure, and surface organometallic compounds, regarding their accessible metallic nanoclusters. The possible organization and functionalization of active sites on the nanoscale provides the basis to develop materials specifically adapted to catalytic challenges like complex chemo-, region-, or stereo-selectivity. Thus, polynuclear transition metal complexes are known to play a fundamental role in a number of catalytic chemical and biological processes. The metal open framework materials might mimic these complex active centers by means of adroit design of their polymetallic nodes and linkers.

Among their catalytic potential, MOF materials can, in principle, combine different catalytic functions, as schematized in Figure 7.17:

- (i) They combine Brönsted or Lewis acidity and basicity, or both, and redox centers, thus making possible “cascade” catalytic processes.
- (ii) Specific hydrophilic/hydrophobic properties might control adsorption of reagents, intermediates, and products, and thus drive catalytic selectivity.
- (iii) Their highly controlled 3D geometric organization at the nanoscale level can create outstanding synergetic effects. Confinement in a rigid structure of substrates according to a specific spatial arrangement of catalytic centers and functionalized walls will drive unseen chemo-selective and region-selective transformations, comparable to those encountered in enzymes and whole cells.

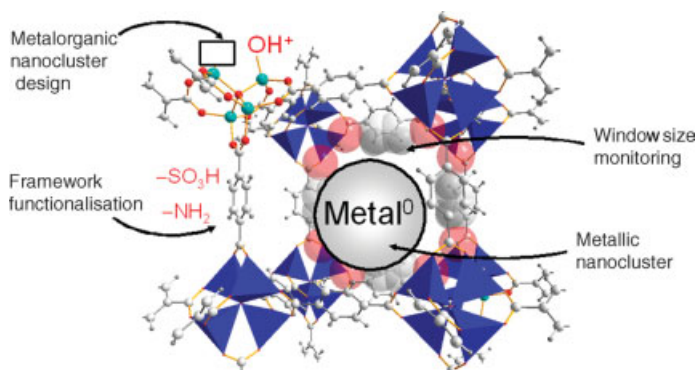


Figure 7.17 Scheme of potential functionalization and active centers in MOF materials.

- (iv) Their nanosized porosity permits shape selectivity by avoiding the production of undesired bulky intermediates or products and to impose ordered successive transformations in a sequence of reactions.

Although these potentialities of MOF for catalytic applications are extensively acknowledged, only a limited number of successful catalytic studies have been reported until now. They are reviewed here.

7.4.1.1 Lewis Acid Catalysis

The HKUST-1 that exhibits accessible Cu clusters is an outstanding proof of the concept of Lewis acid MOF [40, 108]. The structure $\text{Cu}_3(\text{btc})_2(\text{H}_2\text{O})$ consists of a binuclear Cu_2 paddle wheel [41]. The Cu^{2+} ions are connected through a weak bond and the second axial coordination site is filled by a weakly bonded water molecule which points toward the interior of the cavity. Thus, coordinated water can be removed easily with a heating treatment at 383 K making the Cu Lewis acid center directly accessible for reactant diffusing within the porous network. With respect to the texture, it is a 3D porous structure of channels that intersect at cavities that are 1.32 and 1.11 nm in diameter, with apertures of 0.69 nm, thus making accessible to large molecules [73]. Different model reactions for characterizing Lewis acidity were tested: benzaldehyde cyanosilylation [40], isomerization of alpha-pinene oxide, citronellal cyclization and rearrangement of ethylene acetal of 2-bromopropiophenone [108]. HKUST-1 was shown to be quite selective, typical of strong Lewis acid centers. Although the solid does not show Brönsted sites when properly activated, protic solvent may create Brönsted acidity, which can explain different properties when different solvents are used [111]. On the other hand, strongly coordinating solvents such as THF can bond the acidic Cu sites and thus prevent Lewis type reaction to take place [40].

It can be foreseen that other structures exhibiting such out-of-plane sites could be tested as well, $\text{Ni}_2(\text{dhtp})$ [84], $\text{Dy}(\text{btc})$ [109], MOF-2 [53, 58], MOF-101 [112], and Cu (5-methylisophthalate) [113] (Figure 7.18).

Lewis acid solids can also perform selective oxidations, such as Ti-silicate (TS-1) that selectively oxidizes alkenes into corresponding peroxides. Recently, Cu^{2+}

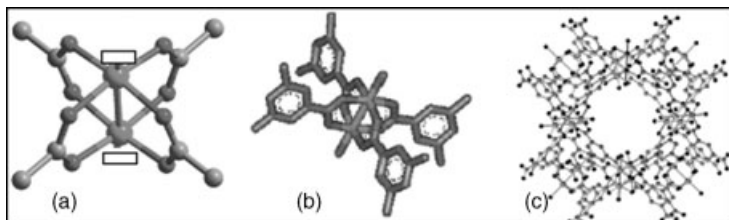


Figure 7.18 (a) Cu₂ Paddle wheel showing Lewis sites [11], (b) two water molecules are adsorbed on the sites [7], and (c) structure of the cavities from Ref. [40].

trinuclear networks have shown high activity and selectivity for the peroxidative oxidation of cyclohexane to corresponding alcohols and ketones (MeCN/H₂O/HNO₃ media) [114]. The structure is based on stable Cu₃(μ₃-OH)(μ-pyrazole) SBU for which the tetracoordinated metal is readily accessible as axial sites. Activity is comparable to best molecular systems such as copper and iron complexes (32% yield and TON of 44). Although the mechanism is still unclear, these trinuclear copper networks are the most efficient catalysts reported so far for the mild peroxidation of alkanes.

7.4.1.2 Brønsted Acid Catalysis

The reaction of Friedel–Crafts, currently applied for the manufacture of linear alkylbenzene (intermediate for laundry detergents) in a very large volume (3 million tons per year), is also routinely applied to probe acid centers of solids, especially for the characterization of zeolites acidity. Ferey *et al.* [115] have recently reported the catalytic activity of two different types of MIL-100 (Fe, Cr) for Friedel–Crafts benzylation. Although they have identical structure M₃OF_{0.85}(OH)_{0.15}(H₂O)₂(btc)₂, the Fe³⁺ structure shows much higher catalytic activity and even surpasses HBEA and HY zeolites. As evidenced by CO chemisorption at low temperature, MIL-100 (Cr³⁺) shows both Cr-OH Brønsted of medium acidity and several species of Lewis centers [111, 116]. Under moisture conditions, water molecules are coordinated to the Lewis center, thus creating other types of Brønsted acidity. However, unlike zeolites they are free from any interaction by H-bonding with adjacent oxygen, and do not dissociate to form hydroxyl groups. It is unclear which type of center is responsible for the catalytic activity i.e. either –M□, M-OH, or M-OH₂. In addition, the difference in induction time between the Cr³⁺ and Fe³⁺ MIL-100 deserves further studies. The synthesis of pure Brønsted MOF materials could eventually address mechanistic issues. For examples, Ferey and Coll have prepared other series of MIL materials that have well structurally identified hydroxyl centers, namely M(OH)(bdc) and Zn₃(OH)₂(bdc) also called MIL-53 [117] and MIL-69C [59], respectively. The MIL-53 is built from infinite chains of corner-sharing MO₄(μ₂-OH)₂ (M=Al³⁺, Cr³⁺) while MOF-69 consists of chains of ZnO₂(OH)₂ tetrahedron and ZnO₄(OH)₂ octahedron and with μ₃-OH as bridging species [45]. These materials might be highly efficient in acid catalysis for both liquid and gas phases.

7.4.1.3 Basic and Enantioselective Catalysis

The enantioselective transesterification was performed on a chiral MOF with free basic center (called POST-1) [118]. The self-assembly of D-tartaric acid and Zn^{2+} produces a trinuclear SBU $[\text{Zn}_3(\mu_3\text{-O})(\text{tartrate})]$, which are interconnected through coordinate Zn ions and some pyridyl groups, thereby generating an hexagonal porous system. Other pyridyl groups are pointing toward the center of large 1D chiral channels (13 Å). At the networking step, the ligand chirality induces also the structure chirality thus making selectively D-POST-1 or L-POST-1 materials. The transesterification of a racemic mixture of 1-phenyl-2-propanol in presence of D-POST-1 or the enantiomorphous L-POST-1 produces the corresponding esters with about 8% of enantiomeric excess in favor of S or R enantiomer, respectively. This is the first example of asymmetric induction mediated by MOF materials although a number of homochiral MOFs exist.

Nevertheless, examples of base catalysis with MOF materials are scant in the literature. This scarcity might arise from experimental issues in the synthesis of free pyridyl donating MOF materials. Indeed, when nitrogen-containing aromatic moieties in a carboxylic-based ligand (such as pyridine dicarboxylates, imidazole dicarboxylate) are used, the N electronic doublet usually coordinates strongly to the metal ion and, therefore, is not available for substrate activation. Recently, Yaghi and coworkers have experienced this issue by functionalizing the imidazole ligand with N-containing functions (called ZIF materials for Zeolite Imidazole Frameworks) [119]. The network backbone is formed by the N donor–metal ion bonds, while the other N functions remain uncoordinated. This approach leads to a large diversity of MOF materials with accessible Lewis basic groups, and may offer new opportunities in base catalysis (Figure 7.19).

Despite this proof of concept, homochiral MOF materials capable of enantioselective separation or catalysis, or a combination of both, are scarce in the literature [120–123]. Most homochiral MOFs are not robust enough to show permanent porosity, which makes this topic a still greater challenge. For the synthesis of homochiral MOF, three strategies have been applied: (i) the use of a rigid homochiral organic ligand as spacer (case of POST-1); (ii) the grafting of a homochiral ligand as an auxiliary pendant that does not directly participate in the framework backbone but induces a specific chirality of the structure; and (iii) the assembly of a metal ion with a readily available homochiral ligand to form homochiral SBUs that are further linked

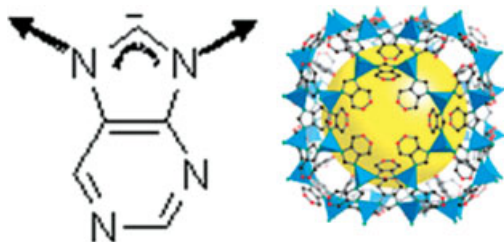


Figure 7.19 ZIF-20 from Ref. [119].

together by rigid spacers to build a network structure. The latter strategy was successfully implemented with the synthesis of $[\text{Zn}_2(\text{bdc})(\text{l-lac})(\text{DMF})]$, where *l-lac* (*l*-lactic acid) is the homochiral ligand and 1,4-dbc the rigid linker [124]. Although selective catalytic oxidation of thioethers to sulfoxides was observed, an asymmetric induction was detected.

7.4.1.4 C–C Coupling

The $\text{Pd}(\text{2-pymo})_{2n} \cdot 3\text{H}_2\text{O}$ materials is an outstanding example of MOF material design for catalytic applications (2-pymo = 2-hydroxypyridimidolate) [125]. The nodes consist of tetracoordinated Pd ions that are accessible from channels of two different sizes (4.8 and 8.8 Å) thus making possible the activation of substrates to form penta- or hexacoordinated intermediates. In addition, the material is stable in alkaline solutions (pH = 6), which makes it more attractive than carboxylate-based MOFs that are prone to hydrolysis in similar conditions. The C–C cross-coupling reaction between aryl halides and arylboronic acids known as Suzuki–Miyaura coupling is a benchmark reaction to rank palladium catalysts' activity. The Pd-based MOF has a TOF of 1230 h^{-1} at 150°C and can be reused without special treatments. On the other hand, the partial oxidation of cinnamyl alcohol in air takes place at 90°C with selectivity of 74%. Finally, selective hydrogenation of alkene is reported with shape selectivity when bulky substrates are tested.

7.4.1.5 Metal Catalysis

Because of their very high surface area, high metallic dispersion can be expected in MOF materials, which should enhance catalytic activity over metal particles and may also generate different selectivity. Chemical vapor infiltration of organometallic precursors was shown to be an appropriate method for dispersing metal particles such as Pt, Au, and Pd into the porosity of MOF-5 [126, 127]. For checking purposes, these supported metal catalysts were tested against CO oxidation with air. More recently, a chemical-based method was developed to prepare 1 wt% Pd supported MOF-5 by incipient wetness impregnation [56]. High activity was observed for hydrogenation of various alkenes in the liquid phase.

In some reactions for which oxides support are not appropriate, metal-supported MOF may be of particular interest. It is known that high selectivity on alkene oxidation with molecular O_2 in gas phase cannot be achieved on oxide supports such as alumina because of hydroxyl groups' epoxide ring-opening activity. Thus, the use of very high surface area MOF-5, which does not exhibit an acid center, is appropriate support. A process of propylene epoxidation in gas phase was patented on various Ag/MOF materials (BASF) [128].

7.4.1.6 Wall Functionalization

The porphyrin macrocycle functionalized at its four *meso* positions by 4-carboxyphenyl groups is an extremely versatile building block for the self-assembly of framework solids [5,10,15,20-tetra(carboxyphenyl) porphyrin (TCPP)]. Its square-planar symmetry with diverging carboxylic functions is perfectly suited for the construction of open quadrangular supramolecular networks [129–131]. A review

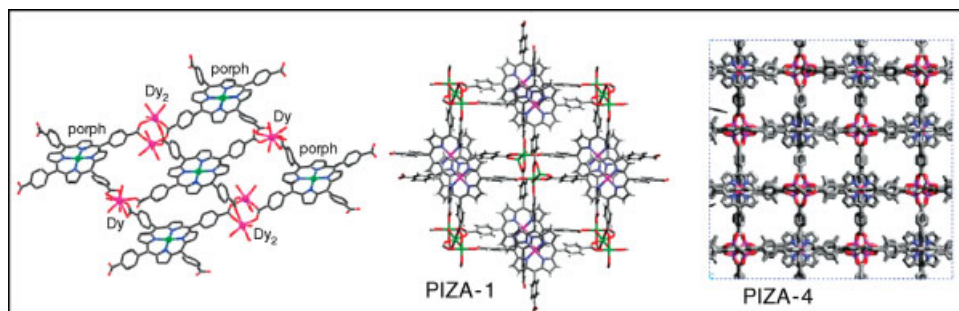


Figure 7.20 Different MOF structure using porphyrin carboxylate as linkers from Refs [129, 132].

of coordination polymers using porphyrin functionalized ligand can be found elsewhere [132]. The networking can take place by H-bonding, and single ions such as Na^+ , polymetallic transition metal ions, and ionic rare earth assembly. The two latter provide thermally stable MOF. It was shown that the 3D architecture can be designed by an adequate choice of metallic cluster nodes. The assembly of TCPP with the paddle wheel SBU Zn_4O generates a 3D porous MOF (PIZA-4) (Langmuir surface = $800 \text{ m}^2/\text{g}$) and thermally stable up to 400°C . It was shown that hydrophobic/hydrophilic balance is very sensitive to the structure, which is directed by the SBU (Figure 7.20).

Mori *et al.* [80, 133] have synthesized various Rh-TCCP coordination polymers with dinuclear Rh paddle wheel nodes. They show high activity in gas-phase hydrogenation of propene. From H_2 – D_2 exchange results at 100 K, the authors suggest that H_2 is activated on the metalloporphyrin while propene is adsorbed on the Rh-based node.

Similar microporous Ru(II,III) complexes having porphyrin $[\text{Ru}_2(\text{H}_2\text{TCPP})]\text{BF}_4$ show outstanding selectivity in the oxidation of primary aliphatic alcohols with dioxygen and air without any additives at room temperature [134, 135]. For example, the oxidation of benzyl alcohol gives the corresponding aldehyde with a selectivity of 95% and a TON of 10 for 24 h of reaction. The reaction pathway is believed to pass through the formation of an Ru–oxygen radical intermediate, which is due to the high affinity of diruthenium(II,III) sites for dioxygen.

Biomimetic MOF design was further extended to chiral (salen)Mn struts [136]. The salen Mn complex was incorporated by means of metal–pyridine bonding while biphenyldicarboxylate ligands were used as pillars. The pillared structure is a highly effective asymmetric catalyst for olefin epoxidation. The oxidation of 2,2 dimethyl-2H-chromene with iodosylbenzene as oxidant yields 82% of enantiomeric excess that rivals results of the molecular analogs. The catalyst can be separated from the media by filtration and reused without loss of activity.

7.4.1.7 Postfunctionalization

Examples of grafting molecular entities on to the walls of a porous network as in, for example, postfunctionalization, are scarce. The homochiral $\text{Cd}_3\text{Cl}_6(\text{L}_4)_3 \cdot 4\text{DMF} \cdot 6\text{MeOH} \cdot 3\text{H}_2\text{O}$ (L_4 is (R)-6,6'-dichloro-2,2'-dihydroxy-1,1'-binaphthyl-4,4'-bipyridine)

is a 3D network with large chiral channels of about $1.6 \text{ nm} \times 1.8 \text{ nm}$ and a specific surface area of $601 \text{ m}^2 \text{ g}^{-1}$ [137–139]. The dihydroxy groups that are readily accessible from the open channels are used to anchor the Ti alkoxide as isolated catalytic sites. The resulting catalyst performs the addition of diethylzinc to 1-naphthaldehyde to afford (*R*)-1-(1-naphthyl)propanol with complete conversion and 93% ee, which reveals with homogeneous analogs.

7.4.2

MOFs – Are They “Heterogenized” Catalysts or Solid Catalysts?

Generally, published papers on catalytic applications using MOF materials suffer from lack of characterization with respect to sample homogeneity and purity. In most cases, only powder XRD analysis are performed, although low quantity of amorphous metal oxides phases or other crystalline phases can be also formed, which may be responsible for observed catalytic activities [40, 108]. In addition, the homogeneity of samples at short range is usually not investigated even though catalysis phenomena take place at molecular level. Indeed it is well known that structural defects play a major role in catalysis. This is specially the case for zeolites [140]. For instance, the catalytic properties of ultrastable Y (USY) can be monitored by steaming treatments, which causes localized structural defects hardly detectable by powder XRD [141].

In analogy with zeolite properties, would it be possible that structural defects in MOF lead to catalytic properties? Also, can we envisage monitoring structural defects?

7.4.2.1 Engineering of Structural Defects in MOF

At IRCELYON, we have anticipated that the introduction of localized structural defects in MOF would lead to potential catalytic centers that could be of Brønsted or Lewis types [142]. We have further postulated that if a ligand would be missing between two nodes, it would create defects while not affecting the robustness of the framework significantly. However, MOF preparation methods that have been developed so far were designed for the synthesis of single crystals as well organized as possible for structure resolution purposes. These methods usually aim to slow down crystal growth while minimizing nucleation rate. In contrast, our strategy was to speed up the crystal growth so that structural defaults have higher probabilities to occur in the framework. The catalytic IRMOF-1 was prepared by precipitation, which consists of adding pure triethylamine to an aqueous solution of zinc nitrate and 1,4-bdc acid in DMF [143]. The white microcrystalline powder is obtained instantaneously upon addition of base at room temperature. This method was extended to the synthesis of IRMOF-8 by using 2,6-NDC as the ligand.

7.4.2.2 Probing Acid Centers by Alkylation Reactions

The activity and selectivity of MOF samples were studied for the alkylation of toluene and biphenyl with *t*-butylchloride (*t*BuCl) in batch reactor. Because of the size matching between alkylbiphenyl compounds and large pore zeolites, the alkylation of biphenyl is an appropriate model reaction to highlight pore shape selectivity properties (or selecto-forming) for acid catalysis, as depicted in Figure 7.21. The acid

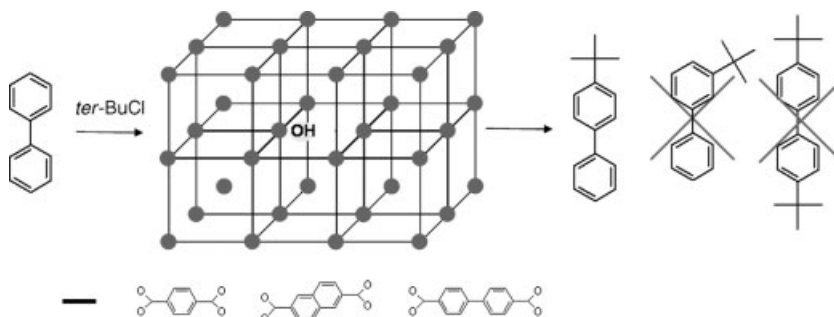


Figure 7.21 Scheme for selective alkylation of biphenyl with *t*-butylchloride (*t*BuCl) over Brønsted acid sites: only the *para* compound is expected to result from the alkylation due to steric hindrance limitations.

form of beta zeolite (denoted hereafter H-BEA) and AlCl_3 were used as reference catalysts.

As main results, IRMOF samples are shown to be as active as H-BEA and AlCl_3 , and reactions are completed within 2 h at 170 °C. Although all catalysts are active at much lower temperatures, selectivity data are presented in Table 7.1 in order to compare catalyst performances in similar *t*BuCl conversions ranging from 60 to 80%. For toluene alkylation, IRMOF samples exhibit good selectivity to the less bulky *para*-oriented products in the same range than H-BEA, whereas AlCl_3 produce mixtures of *ortho*- and *para*-oriented products in equivalent amount. On the other hand, the alkylation of biphenyl reveals exceptional selectivity to *para*-isomer 4-*tert*-butylbiphenyl for IRMOF samples with respect to H-BEA and AlCl_3 . Indeed, only traces of doubly alkylated products are detected for IRMOFs whereas H-BEA and AlCl_3 show much higher selectivity to the *ortho*-isomer and about 15% to di-alkylated products. For 1 h of reaction at 100 °C, 100% selectivity is obtained in the *para*-product with conversion of 20% for IRMOF-1, whereas H-BEA shows much lower selectivity of 55% (for 35% conversion). Those results point out outstanding selecto-forming properties of IRMOFs for large polyaromatics.

Table 7.1 Selectivity of *tert*-butylation reaction at 170 °C.

Catalyst	Toluene			Biphenyl		
	<i>para</i> ^a	<i>ortho</i>	di ^c	<i>para</i> ^b	<i>ortho</i>	di ^c
IRMOF-1	82	18	0	96	3	1
IRMOF-8	84	16	0	95	3	2
H-BEA	72	28	0	55	22	23
AlCl_3	46	54	0	51	38	11

Conversions are ranging from 60 to 80%. Reactions have been carried out for 2 h in decane with aromatic:*t*BuCl ratio of 2:1.

^a*p*-*tert*-butyltoluene.

^b4-*tert*-butylbiphenyl.

^cSum of dialkylated products.

Additional experiments (reuse of the catalyst after filtration, testing of the filtrate, and so forth) clearly demonstrated that the reaction proceeds only on the solid without any leaching favoring liquid-phase homogeneous reaction.

7.4.2.3 Catalyst Characterization

Surface areas, micropore volumes, and pore sizes correspond to those reported elsewhere with similar preparation procedures for IRMOF-1 [62, 143] and IRMOF-8 [12] (Table 7.2), confirming sharp pore size distributions. Calculated window diameter (“free space”) from structural data indicates, for example, that the window between the cages of IRMOF-1 has a van der Waals space of diameter approximately 7.8 Å. In contrast to zeolite pore sizes, these values shall be interpreted with care for MOF materials, especially when one wants to correlate structural features and properties. Indeed, in addition to their general flexibility properties, the aromatic rings of IRMOF can rotate, thus making feasible the diffusion of larger guests [99].

From experimental and theoretical data, there is, in principle, no steric hindrance for monoalkylated products to diffuse out of all porous solids, including H-BEA. Even very bulky products such as the doubly alkylated product 4,4'-di-*t*-butylbiphenylene (12.5 Å × 5.0 Å) can be formed in large quantities in H-BEA [145, 146]. Therefore, the shape selectivity properties observed for IRMOF sample cannot arise from diffusion hindrance of the most bulky products, since pore windows are even larger. For the reaction that takes place we suggest that the biphenyl is adsorbed in a specific manner to allow the formation of the transition state for the *para*-oriented product. Once alkylated, it cannot be activated in the same manner because of steric hindrance, and double alkylation cannot proceed. Because of porous structure similarity between IRMOF-1 and IRMOF-8, it is not surprising that similar selectivity is obtained.

Thorough structural (XRD, IR) and thermal (TGA) characterization of IRMOF-1 carried out on the tested samples, before and after testing, clearly revealed that the catalytic centers may arise either from Zn hydroxide clusters or from the presence of MOF-69c microcrystallites, or from structural defects as Zn–OH species formed at the synthesis step or upon water adsorption.

Thus, it has been demonstrated that MOFs can undergo highly shape-selective catalytic alkylation of large molecules. This opens new perspective for C–C coupling of polyaromatics or biomolecules that are too large to be converted by zeolites. It is

Table 7.2 N₂ physisorption results and comparison of pore sizes with structural data.

Sample	Surface area (m ² g ^{−1}) ^a	Micropore volume (cm ³ g ^{−1}) ^b	Pore diameter (Å) ^c	Window diameter (Å)
IRMOF-1	450	0.18	8.8	7.8 ^d
IRMOF-8	730	0.29	7.3/11.6	9.2 ^d
H-BEA	430	0.10	7.7	6.1 ^e

^aBET.

^b*t*-plot.

^cDFT.

^dFrom Ref. [46].

^eFrom Ref. [144].

further believed that the control of structural defects in MOF materials may lead to the generation of a new class of shape-selective catalysts with different acidity and hydrophilic properties from those encountered in zeolites.

7.4.2.4 General Statements on MOF Application for Catalysis

Despite a limited number of papers, proofs of concept have been demonstrated for both acid and base catalysis, metal catalysis, and chemo-, stereo-, and even enantio-selectivity properties. The scepticism to apply MOF in catalysis is essentially related to stability issues.

In *gas-phase processes* for hydrogenation and oxidation, thermal stability in hydrogen or air was shown to be effective under mild conditions, as shown for $[\text{Ni}_2(2,5\text{-dihydroxyterephthalic acid})]$ (250 °C) [84], MOF-5, HKUST-1, MIL-100 (350 °C), Dy (btc) (400 °C) [109].

In *liquid-phase processes*, the first issue is the dissolution of MOF in hot solvent when performing a reaction in batch reactor. Schlichte *et al.* [40] report dissolution of HKUST-1 in CH_2Cl_2 . For IRMOF in particular, Zn–O bonds can be readily hydrolyzed under moisture condition [56]. After a few hours of exposure to humid air, MOF-5 pore structure collapses, making MOF-5 and related materials hardly applicable for industrial applications. However, examples of stability and reusability after tests have been reported such as for $\text{Pd}(2\text{-pymo})$ [125] and $\text{Sc}(1,4\text{-bdc})$ [147] in liquid phase.

It may be pointed out that MOF materials, like other “new materials” in the past, are approaching the limit of the knowledge in catalysis. It would be questionable for the materials science community to regard MOF as only “extended” molecular materials and to evaluate them as a “molecular” assembly. In essence, MOFs are solids, which are complex systems, where interfaces, defects, medium-to-long range electronic effects and heterogeneity may play key catalytic roles, in contrast to isolated molecular sites.

7.5

Conclusion

In this chapter, we illustrate the combination of HT testing and the rational approach for the discovery of efficient materials in the field of separation and catalysis. A general overview of the state of the art for metal organic frameworks reveals (i) a much less documented domain as compared to the zeolites one, though that is rapidly evolving; (ii) a general trend to synthesize as pure as possible, new crystallographic structures, not necessarily adapted to potential industrial like gas separation and catalysis; (iii) a lack of integrated strategy combining the design concepts with the targeted applications and specifications. In addition, due to the large number of parameters to be fine-tuned that might direct the final properties of the new MOF structures, it is proposed that high-throughput technologies (HTTs) and combinatorial approaches are well adapted for MOF screening.

To illustrate that point of view, two cases studies were selected among the most promising potential application of MOF structures: natural gas separation and cleaning for PSA processes and various aspects of catalytic applications.

In both cases, a specific overview of properties of the MOF specific to each application was completed, and further on, exemplified by recent results obtained in the laboratory.

For gas separation, a combinatorial approach allowed us to discover efficient materials for CO₂ capture from methane by the PSA process.

For catalytic application, a nonconventional strategy was implemented, aiming at producing MOF structures with a maximized concentration of defects such as extra frameworks microcrystals or amorphous phases that could act as active and selective catalytic centers. This resulted in outstanding selecto-forming properties of IRMOFs for large polyaromatics alkylation.

In general, it was stated that exploring the huge potential of MOFs for industrial applications requires a multidisciplinary approach to be undertaken, by experts in organometallic chemistry, solid state and materials science, catalysis, and also chemical engineering. High-throughput technologies and combinatorial methodologies might also act as real boosters for this approach.

Acknowledgments

Part of this work was supported by the European research project “TOPCOMBI” (contract NMP2-CT2005-515792) and the ANR “MECAFI”.

Glossary

Btc	1,3,5-benzenetricarboxylate
teda	triethylenediamine
bpc	biphenyldicarboxylate
bpy	4,4'-bipyridine
H ₂ hfpbb	4,4-(hexafluoroisopropoxydene)-bis(benzoic acid)
ox	C ₂ O ₄ ²⁻
bipyen	trans-1,2-bis(4-pyridyl)-ethylene
dhtp	2,5-dihydroxyterephthalate
tcppda	N,N,N',N'-tetrakis(4-carboxyphenyl)-1,4-phenylenediamine

References

- 1 Barton, T.J., Bull, L.M., Klemperer, W.G., Loy, D.A., McEnaney, B., Misono, M., Monson, P.A., Pez, G., Scherer, G.W., Vartuli, J.C. and Yaghi, O.M. (1999) *Chemistry of Materials*, **11** (10), 2633–2656.
- 2 Sanchez, C., Soler-Illia, G.J.d.A.A., Ribot, F., Lalot, T., Mayer, C.R. and Cabuil, V. (2001) *Chemistry of Materials*, **13**, 3061–3083.
- 3 Maspoch, D., Ruiz-Molina, D. and Veciana, J. (2007) *Chemical Society Reviews*, **36** (5), 770–818.
- 4 Janiak, C. (1997) *Angewandte Chemie, International Edition in English*, **36** (13/14), 1431–1434.

- 5 Janiak, C. (2003) *Dalton Transactions*, **14**, 2781–2804.
- 6 Sanchez, C., Julian, B., Belleville, P. and Popall, M. (2005) *Journal of Materials Chemistry*, **15** (35–36), 3559–3592.
- 7 Mueller, U., Schubert, M., Teich, F., Puetter, H., Schierle-Arndt, K. and Pastre, J. (2006) *Journal of Materials Chemistry*, **16** (7), 626–636.
- 8 Dinolfo, P.H. and Hupp, J.T. (2001) *Chemistry of Materials*, **13**, 3113–3125.
- 9 Ferey, G. (2008) *Chemical Society Reviews*, **37** (1), 191–214.
- 10 Park, H., Britten, J.F., Mueller, U., Lee, J., Li, J. and Parise, J.B. (2007) *Chemistry of Materials*, **19** (6), 1302–1308.
- 11 Panella, B., Hirscher, M., Putter, H. and Muller, U. (2006) *Advanced Functional Materials*, **16** (4), 520–524.
- 12 Li, Y.W. and Yang, R.T. (2006) *Journal of the American Chemical Society*, **128** (3), 726–727.
- 13 Latroche, M., Surble, S., Serre, C., Mellot-Draznieks, C., Llewellyn, P.L., Lee, J.H., Chang, J.S., Jhung, S.H. and Ferey, G. (2006) *Angewandte Chemie, International Edition*, **45** (48), 8227–8231.
- 14 Krawiec, P., Kramer, M., Sabo, M., Kunschke, R., Frode, H. and Kaskel, S. (2006) *Advances in Engineering Materials*, **8** (4), 293–296.
- 15 Dinca, M., Yu, A.F. and Long, J.R. (2006) *Journal of the American Chemical Society*, **128** (27), 8904–8913.
- 16 Yang, Q.Y. and Zhong, C.L. (2005) *The Journal of Physical Chemistry. B*, **109** (24), 11862–11864.
- 17 Rowsell, J.L.C., Eckert, J. and Yaghi, O.M. (2005) *Journal of the American Chemical Society*, **127** (42), 14904–14910.
- 18 Panella, B. and Hirscher, M. (2005) *Advanced Materials*, **17** (5), 538–541.
- 19 Bordiga, S., Vitillo, J.G., Ricchiardi, G., Regli, L., Cocina, D., Zecchina, A., Arstad, B., Bjorgen, M., Hafizovic, J. and Lillerud, K.P. (2005) *The Journal of Physical Chemistry. B*, **109** (39), 18237–18242.
- 20 Ward, M.D. (2003) *Science (Washington, DC, United States)*, **300** (5622), 1104–1105.
- 21 Rosi, N.L., Eckert, J., Eddaoudi, M., Vodak, D.T., Kim, J., O’Keeffe, M. and Yaghi, O.M. (2003) *Science (Washington, DC, United States)*, **300** (5622), 1127–1130.
- 22 O’Keeffe, M., Eddaoudi, M., Li, H.L., Reineke, T. and Yaghi, O.M. (2000) *Journal of Solid State Chemistry*, **152** (1), 3–20.
- 23 Ferey, G. (2000) *Journal of Solid State Chemistry*, **152**, 37–48.
- 24 Mellot-Draznieks, C. and Ferey, G. (2005) *Progress in Solid State Chemistry*, **33**, 187–197.
- 25 Ferey, G. (2001) *Chemistry of Materials*, **13**, 3084–3098.
- 26 Yaghi, O.M., Li, H.L., Davis, C., Richardson, D. and Groy, T.L. (1998) *Accounts of Chemical Research*, **31** (8), 474–484.
- 27 Eddaoudi, M., Moler, D.B., Li, H.L., Chen, B.L., Reineke, T.M., O’Keeffe, M. and Yaghi, O.M., (2001) *Accounts of Chemical Research*, **34** (4), 319–330.
- 28 Kim, J., Chen, B.L., Reineke, T.M., Li, H.L., Eddaoudi, M., Moler, D.B., O’Keeffe, M. and Yaghi, O.M. (2001) *Journal of the American Chemical Society*, **123** (34), 8239–8247.
- 29 Hosseini, M.W. (2005) *Accounts of Chemical Research*, **38** (4), 313–323.
- 30 Vagin, S., Ott, A. and Rieger, B. (2007) *Chemie Ingenieur Technik*, **79** (6), 767–779.
- 31 Rowsell, J.L.C. and Yaghi Omar, M. (2004) *Microporous and Mesoporous Materials*, **73**, 3–14.
- 32 Eddaoudi, M., Kim, J., Wachter, J.B., Chae, H.K., O’Keeffe, M. and Yaghi, O.M. (2001) *Journal of the American Chemical Society*, **123** (18) 4368–4369.
- 33 Ni, Z., Yassar, A., Antoun, T. and Yaghi Omar, M. (2005) *Journal of the American Chemical Society*, **127**, 12752–12753.
- 34 Rosseinsky, M.J. (2004) *Microporous and Mesoporous Materials*, **73**, 15–30.
- 35 Kitagawa, S., Kitaura, R. and Noro, S. (2004) *Angewandte Chemie, International Edition*, **43** (18), 2334–2375.
- 36 Rao, C.N.R., Natarajan, S. and Vaidyanathan, R. (2004) *Angewandte*

- Chimie, International Edition*, **43** (12), 1466–1496.
- 37 Schueth, F., Sing, K.S.W. and Weitkamp, J. (2002) *Handbook of Porous Solids*, Vol. 2, Wiley-VCH Verlag GmbH, Weinheim, Germany.
 - 38 Rosi, N.L., Eddaoudi, M., Kim, J., O'Keeffe, M. and Yaghi, O.M. (2002) *CrystEngComm*, **4**, 401–404.
 - 39 Cheetham, A.K., Ferey, G. and Loiseau, T. (1999) *Angewandte Chemie, International Edition*, **38** (22), 3268–3292.
 - 40 Schlichte, K., Kratzke, T. and Kaskel, S. (2004) *Microporous and Mesoporous Materials*, **73** (1–2), 81–88.
 - 41 Chui, S.S.-Y., Lo, S.M.F., Charmant, J.P.H., Orpen, A.G. and Williams, I.D. (1999) *Science*, **283** (5405), 1148–1150.
 - 42 Li, H., Eddaoudi, M., O'Keeffe, M. and Yaghi, O.M. (1999) *Nature*, **402** (6759), 276–279.
 - 43 Eddaoudi, M., Li, H.L., Reineke, T., Fehr, M., Kelley, D., Groy, T.L. and Yaghi, O.M. (1999) *Topics in Catalysis*, **9** (1–2), 105–111.
 - 44 Yaghi, O.M., Li, G. and Li, H. (1995) *Nature*, **378** (6558), 703–706.
 - 45 Rosi, N.L., Kim, J., Eddaoudi, M., Chen, B.L., O'Keeffe, M. and Yaghi, O.M. (2005) *Journal of the American Chemical Society*, **127** (5), 1504–1518.
 - 46 Eddaoudi, M., Kim, J., Rosi, N., Vodak, D., Wachter, J., O'Keeffe, M. and Yaghi, O.M. (2002) *Science*, **295** (5554), 469–472.
 - 47 Seki, K. and Mori, W. (2002) *The Journal of Physical Chemistry B*, **106**, 1380–1385.
 - 48 Ferey, G., Mellot-Draznieks, C., Serre, C., Millange, F., Dutour, J., Surble, S. and Margiolaki, I. (2005) *Science*, **309** (5743), 2040–2042.
 - 49 Lebedev, O.I., Millange, F., Serre, C., Van Tendeloo, G. and Ferey, G. (2005) *Chemistry of Materials*, **17** (26), 6525–6527.
 - 50 Millward, A. and Yaghi Omar, M. (2005) *Journal of the American Chemical Society*, **127**, 17998–17999.
 - 51 Férey, G. (2007) *Journal de la Société Française de Chimie – L'actualité Chimique*, 304.
 - 52 Biemmi, E., Bein, T. and Stock, N. (2006) *Solid State Sciences*, **8**, 363–370.
 - 53 Eddaoudi, M., Li, H.L. and Yaghi, O.M. (2000) *Journal of the American Chemical Society*, **122** (7), 1391–1397.
 - 54 Clausen, H.F., Poulsen, R.D., Bond, A.D., Chevalier, M.S. and Iversen, B.B. (2005) *Journal of Solid State Chemistry*, **178**, 3342–3351.
 - 55 Edgar, M., Mitchell, R., Slawin, A., Lightfoot, P. and Wright, P.A. (2001) *Chemistry – A European Journal*, **7** (23), 5168–5175.
 - 56 Sabo, M., Henschel, A., Froede, H., Klemm, E. and Kaskel, S. (2007) *Journal of Materials Chemistry*, **17** (36), 3827–3832.
 - 57 Li, H., Eddaoudi, M., Groy, T.L. and Yaghi, O.M. (1998) *Journal of the American Chemical Society*, **120** (33), 8571–8572.
 - 58 Li, H.L., Davis, C.E., Groy, T.L., Kelley, D.G. and Yaghi, O.M. (1998) *Journal of the American Chemical Society*, **120** (9), 2186–2187.
 - 59 Rosi, N.L., Eddaoudi, M., Kim, J., O'Keeffe, M. and Yaghi, O.M. (2002) *Angewandte Chemie, International Edition*, **41** (2), 284–287.
 - 60 Hausdorf, S., Baitalow, F., Seidel, J. and Mertens, F. (2007) *Journal of Physical Chemistry A*, **111** (20), 4259–4266.
 - 61 Grzesiak, A., Uribe, F., Ockwig, N.W., Yaghi Omar, M. and Matzger, A.J. (2006) *Angewandte Chemie, International Edition*, **118**, 2615–2618.
 - 62 Hafizovic, J., Bjorgen, M., Olsbye, U., Dietzel, P.D.C., Bordiga, S., Prestipino, C., Lamberti, C. and Lillerud, K.P. (2007) *Journal of the American Chemical Society*, **129** (12), 3612–3620.
 - 63 Batten, S. (2005) *Journal of Solid State Chemistry*, **178**, 2475–2479.
 - 64 Rowsell, J.L.C., Millward, A., Park, K. and Yaghi Omar, M. (2004) *Journal of the American Chemical Society*, **126**, 5666–5667.
 - 65 Wang, Q.M., Shen, D., Bulow, M., Lau, M.L.L., Deng, S., Fitch, F.R., Lemcoff, N.O. and Semanscin, J. (2002) *Microporous and Mesoporous Materials*, **55**, 217–230.

- 66 Walton, K.S. and Snurr, R.Q. (2007) *Journal of the American Chemical Society*, **129** (27), 8552–8556.
- 67 Duren, T., Millange, F., Ferey, G., Walton, K.S. and Snurr, R.Q. (2007) *The Journal of Physical Chemistry C*, **111**, 15350–15356.
- 68 Seki, K. (2002) *Langmuir*, **18** (6), 2441–2443.
- 69 Wong-Foy, A.G., Matzger, A.J. and Yaghi, O.M. (2006) *Journal of the American Chemical Society*, **128** (11), 3494–3495.
- 70 Noro, S., Kitagawa, S., Kondo, M. and Seki, K. (2000) *Angewandte Chemie, International Edition*, **39** (12), 2081–2084.
- 71 Kondo, M., Okubo, T., Asami, A., Noro, S., Yoshitomi, T., Kitagawa, S., Ishii, T., Matsuzaka, H. and Seki, K. (1999) *Angewandte Chemie, International Edition*, **38** (1–2), 140–143.
- 72 Chen, B., Eddaoudi, M., Reineke, T.M., Kampf, J.W., O’Keeffe, M. and Yaghi, O.M. (2000) *Journal of the American Chemical Society*, **122** (46), 11559–11560.
- 73 Rowsell, J.L.C. and Yaghi, O.M. (2006) *Journal of the American Chemical Society*, **128** (4), 1304–1315.
- 74 Sudik, A.C., Millward, A.R., Ocking, N.W., Cote, A.P., Kim, J. and Yaghi Omar, M. (2005) *Journal of the American Chemical Society*, **127** (19), 7110–7117.
- 75 Barthelet, K., Marrot, J., Riou, D. and Ferey, G. (2002) *Angewandte Chemie, International Edition*, **41** (2), 281–284.
- 76 Barthelet, K., Marrot, J., Ferey, G. and Riou, D. (2004) *Chemical Communications*, (5), 520–521.
- 77 Devic, T., Serre, C., Audebrand, N., Marrot, J. and Ferey, G. (2005) *Journal of the American Chemical Society*, **127** (37), 12788–12789.
- 78 Lee, J., Li, J. and Jagiello, J. (2005) *Journal of Solid State Chemistry*, **178** (8), 2527–2532.
- 79 Choi, E.Y., Park, K., Yang, C.M., Kim, H., Son, J., Lee, S.W., Lee, Y.H., Min, D. and Kwon, Y. (2004) *Chemistry – A European Journal*, **10**, 5535–5540.
- 80 Mori, W., Sato, T., Ohmura, T., Kato, C.N. and Takei, T. (2005) *Journal of Solid State Chemistry*, **178**, 2555–2573.
- 81 Senkovska, I. and Kaskel, S. (2006) *European Journal of Inorganic Chemistry*, 4564–4569.
- 82 Fang, Q.R., Zhu, G.S., Jin, Z., Ji, Y.Y., Ye, J.W., Xue, M., Yang, H., Wang, Y. and Qiu, S.L. (2007) *Angewandte Chemie, International Edition*, **46** (35), 6638–6642.
- 83 Anokhina, E.V., Go, Y.B., Lee, Y., Vogt, T. and Jacobson, A.J. (2006) *Journal of the American Chemical Society*, **128** (30), 9957–9962.
- 84 Dietzel, P.D.C., Panella, B., Hirscher, M., Blom, R. and Fjellvag, H. (2006) *Chemical Communications*, (9), 959–961.
- 85 Sun, D., Collins, D.J., Ke, Y., Zuo, J.L. and Zhou, H.C. (2006) *Chemistry – A European Journal*, **12**, 3768–3776.
- 86 Pan, L., Olson, D.D., Ciemmolonski, L.R., Heddy, R. and Li, J. (2006) *Angewandte Chemie, International Edition*, **45**, 616–619.
- 87 Schuth, F. (2005) High-throughput experiments for synthesis and applications of zeolites, in *Zeolites and Ordered Mesoporous Materials: Progress and Prospects*, Vol. 157, Elsevier Science BV, Amsterdam, The Netherlands, pp. 161–180.
- 88 Sam Bergh, H. (2004) High-throughput workflow development: strategies and examples in heterogeneous catalysis, in *High-Throughput Screening in Chemical Catalysis* (eds A. Hagemeyer, P. Strasser and A. Volpe), Wiley-VCH Verlag GmbH, Weinheim, Germany, pp. 239–270.
- 89 Farrusseng, D. and Mirodatos, C. (2004) Combinatorial strategies for speeding up the discovery and optimization of heterogeneous catalysts on an academic scale: a case study of hydrogen purification for feeding PEM fuel cells, in *High-Throughput Screening in Chemical Catalysis* (eds A. Hagemeyer, P. Strasser and A. Volpe), Wiley-VCH Verlag GmbH, Weinheim, Germany, pp. 239–270.
- 90 Maxwell, I.E., van den Brink, P., Downing, R.S., Sijpkens, A.H., Gomez, S. and Maschmeyer, T. (2003) *Topics in Catalysis*, **24** (1–4), 125–135.

- 91 Cawse, J. (2003) *Experimental Design for Combinatorial and High Throughput Materials Development*, Wiley-VCH Verlag GmbH, Weinheim, Germany.
- 92 Bauer, S. and Stock, N. (2007) *Angewandte Chemie, International Edition*, **46**, 6857–6860.
- 93 Serre, C., Groves, J.A., Lightfoot, P., Slawin, A.M.Z., Wright, P.A., Stock, N., Bein, T., Haouas, M., Taulelle, F. and Ferey, G. (2006) *Chemistry of Materials*, **18** (6), 1451–1457.
- 94 Bauer, S., Bein, T. and Stock, N. (2005) *Inorganic Chemistry*, **44** (16), 5882–5889.
- 95 Forster, P.M., Stock, N. and Cheetham, A.K. (2005) *Angewandte Chemie, International Edition*, **44** (46), 7608–7611.
- 96 Stock, N. and Bein, T. (2005) *Journal of Materials Chemistry*, **15** (13), 1384–1391.
- 97 Stock, N. and Bein, T. (2004) *Angewandte Chemie, International Edition*, **43** (6), 749–752.
- 98 Go, Y.B., Wang, X.Q., Anokhina, E.V. and Jacobson, A.J. (2005) *Inorganic Chemistry*, **44** (23), 8265–8271.
- 99 Fletcher, A.J., Thomas, K.M. and Rosseinsky, M.J. (2005) *Journal of Solid State Chemistry*, **178** (8), 2491–2510.
- 100 Uemura, K., Kitagawa, S., Kondo, M., Fukui, K., Kitaura, R., Chang, H.C. and Mizutani, T. (2002) *Chemistry – A European Journal*, **8** (16), 3586–3600.
- 101 Kitaura, R., Seki, K., Akiyama, G. and Kitagawa, S. (2003) *Angewandte Chemie, International Edition*, **42** (4), 428–431.
- 102 Llewellyn, P.L., Bourrelly, S., Serre, C., Filinchuk, Y. and Ferey, G. (2006) *Angewandte Chemie, International Edition*, **45** (46), 7751–7754.
- 103 Loiseau, T., Serre, C., Huguenard, C., Fink, G., Taulelle, F., Henry, M., Bataille, T. and Ferey, G. (2004) *Chemistry – A European Journal*, **10**, 1373–1382.
- 104 Chen, B.L., Ma, S., Zapata, F., Fronczek, F.R., Lobkovsky, E.B. and Zhou, H.C. (2007) *Inorganic Chemistry*, **46** (4), 1233–1236.
- 105 Rowsell, J.L.C., Spencer, E.C., Eckert J., Howard, J.A.K. and Yaghi O.M. (2005) *Science*, **309** (1350–1354).
- 106 Hill, R.J., Long, D.L., Schroder, M. and Champness, N.R. (2005) *Journal of Solid State Chemistry*, **178**, 214–2419.
- 107 Serre, C., Pelle, F., Gardant, N. and Ferey, G. (2004) *Chemistry of Materials*, **16** (7), 1177–1182.
- 108 Alaerts, L., Seguin, E., Poelman, H., Thibault-Starzyk, F., Jacobs, P.A. and De Vos, D.E. (2006) *Chemistry – A European Journal*, **12** (28), 7353–7363.
- 109 Guo, X.D., Zhu, G.S., Li, Z.Y., Sun, F.X., Yang, Z.H. and Qiu, S.L. (2006) *Chemical Communications*, (30), 3172–3174.
- 110 Morra, G., Desmartin-Chomel, A., Daniel, C., Ravon, U., Farrusseng, D., Cowan, R., Krusche, M. and Mirodatos, C. (2008) *Chemical Engineering Journal*, **138** (1–3), 379–388.
- 111 Vimont, A., Goupil, J.M., Lavalley, J.C., Daturi, M., Surble, S., Serre, C., Millange, F., Ferey, G. and Audebrand, N. (2006) *Journal of the American Chemical Society*, **128** (10), 3218–3227.
- 112 Eddaoudi, M., Kim, J., O’Keeffe, M. and Yaghi, O.M. (2002) *Journal of the American Chemical Society*, **124** (3), 376–377.
- 113 Zou, R., Sakurai, H., Han, S., Zhong, R. and Xu, Q. (2007) *Journal of the American Chemical Society*, **129** (27), 8402–8403.
- 114 Di Nicola, C., Karabach, Y.Y., Kirillov, A.M., Monari, M., Pandolfo, L., Pettinari, C. and Pombeiro, A.J.L. (2007) *Inorganic Chemistry*, **46** (1), 221–230.
- 115 Horcajada, P., Surble, S., Serre, C., Hong, D.Y., Seo, Y.K., Chang, J.S., Greneche, J.M., Margiolaki, I. and Ferey, G. (2007) *Chemical Communications*, (27), 2820–2822.
- 116 Vimont, A., Leclerc, H., Mauge, F., Daturi, M., Lavalley, J.C., Surble, S., Serre, C. and Ferey, G. (2007) *Journal of Physical Chemistry C*, **111** (1), 383–388.
- 117 Millange, F., Serre, C. and Ferey, G. (2002) *Chemical Communications*, (8), 822–823.
- 118 Seo, J.S., Whang, D., Lee, H., Jun, S.I., Oh, J., Jeon, Y.J. and Kim, K. (2000) *Nature*, **404** (6781), 982–986.
- 119 Hayashi, H., Cote, A.P., Furukawa, H., O’Keeffe, M. and Yaghi, O.M. (2007) *Nature Materials*, **6** (7), 501–506.

- 120 Bradshaw, D., Claridge, J.B., Cussen, E.J., Prior, T.J. and Rosseinsky, M.J. (2005) *Accounts of Chemical Research*, **38** (4), 273–282.
- 121 Bradshaw, D., Prior, T.J., Cussen, E.J., Claridge, J.B. and Rosseinsky, M.J. (2004) *Journal of the American Chemical Society*, **126** (19), 6106–6114.
- 122 Kepert, C.J., Prior, T.J. and Rosseinsky, M.J. (2000) *Journal of the American Chemical Society*, **122** (21), 5158–5168.
- 123 Kepert, C.J. and Rosseinsky, M.J. (1998) *Chemical Communications*, (1), 31–32.
- 124 Dybtsev, D.N., Nuzhdin, A.L., Chun, H., Bryliakov, K.P., Talsi, E.P., Fedin, V.P. and Kim, K. (2006) *Angewandte Chemie, International Edition*, **45** (6), 916–920.
- 125 Xamena, F., Abad, A., Corma, A. and Garcia, H. (2007) *Journal of Catalysis*, **250** (2), 294–298.
- 126 Hermes, S., Schroder, F., Amirjalayer, S., Schmid, R. and Fischer, R.A. (2006) *Journal of Materials Chemistry*, **16** (25), 2464–2472.
- 127 Hermes, S., Schroter, M.K., Schmid, R., Khodeir, L., Muhler, M., Tissler, A., Fischer, R.W. and Fischer, R.A. (2005) *Angewandte Chemie, International Edition*, **44** (38), 6237–6241.
- 128 Mueller, U., Lobree, L., Hesse, M., Yaghi, O.M. and Eddaoudi, M. (2003) Process for epoxidation of organic compounds with oxygen or oxygen-delivering compounds using catalysts containing metal-organic framework (MOF) materials. 6624318.
- 129 George, S., Lipstman, S. and Golberg, I. (2006) *Crystal Growth & Design*, **6** (12), 2651–2654.
- 130 Golberg, I. (2005) *Chemical Communications*, 1243–1254.
- 131 Shmilovits, M., Diskin-Posner, Y., Vinodu, M. and Golberg, I. (2003) *Crystal Growth & Design*, **3** (5), 855–863.
- 132 Suslick, K.S., Bhyrappa, P., Chou, J.H., Kosal, M.E., Nakagaki, S., Smithenry, D.W. and Wilson, S.R. (2005) *Accounts of Chemical Research*, **38** (4), 283–291.
- 133 Mori, W., Takamizawa, S., Kato, C.N., Ohmura, T. and Sato, T. (2004) *Microporous and Mesoporous Materials*, **73** (1–2), 31–46.
- 134 Kato, C.N., Ono, M., Hino, T., Ohmura, T. and Mori, W. (2006) *Catalysis Communications*, **7**, 673–677.
- 135 Kato, C.N. and Mori, W. (2007) *Comptes Rendus Chimie*, **10** (4–5), 284–294.
- 136 Cho, S.H., Ma, B.Q., Nguyen, S.T., Hupp, J.T. and Albrecht-Schmitt, T.E. (2006) *Chemical Communications*, (24), 2563–2565.
- 137 Wu, C.D., Hu, A., Zhang, L. and Lin, W.B. (2005) *Journal of the American Chemical Society*, **127** (25), 8940–8941.
- 138 Wu, C.D. and Lin, W.B. (2005) *Chemical Communications*, (29), 3673–3675.
- 139 Lin, W.B. (2005) *Journal of Solid State Chemistry*, **178**, 2486–2490.
- 140 Cambor, M.A., Corma, A., Iborra, S., Miquel, S., Primo, J. and Valencia, S. (1997) *Journal of Catalysis*, **172** (1), 76–84.
- 141 Beyerlein, R.A., ChoiFeng, C., Hall, J.B., Huggins, B.J. and Ray, G.J. (1997) *Topics in Catalysis*, **4** (1–2), 27–42.
- 142 Ravon, U., Domine, M.E., Gaudillère, C., Desmartin-Chomel, A. and Farrusseng, D., (2008) *New Journal of Chemistry*, **32**, 937–940.
- 143 Huang, L.M., Wang, H.T., Chen, J.X., Wang, Z.B., Sun, J.Y., Zhao, D.Y. and Yan, Y.S. (2003) *Microporous and Mesoporous Materials*, **58** (2), 105–114.
- 144 Foster, M.D., Rivin, I., Treacy, M.M.J. and Friedrichs, O.D. (2006) *Microporous and Mesoporous Materials*, **90** (1–3), 32–38.
- 145 Millini, R., Frigerio, F., Bellussi, G., Pazzuconi, G., Perego, C., Pollesel, P. and Romano, U. (2003) *Journal of Catalysis*, **217** (2), 298–309.
- 146 Sugi, Y., Tawada, S., Sugimura, T., Kubota, Y., Hanaoka, T., Matsuzaki, T., Nakajima, K. and Kunimori, K. (1999) *Applied Catalysis A, General*, **189** (2), 251–261.
- 147 Perles, J., Iglesias, M., Martin-Luengo, M., Monge, M.A., Ruiz-Valero, C. and Snejko, N. (2005) *Chemistry of Materials*, **17**, 5837–5842.

8

Design of Bimetallic Catalysts: From Model Surfaces to Supported Catalysts

Jeffrey P. Bosco, Michael P. Humbert, and Jingguang G. Chen

8.1

Introduction

Many bimetallic catalysts have been shown to possess catalytic properties distinctly different than those of their parent metals [1]. In many cases, these unique properties result in activities and/or selectivities that exceed those achievable with a monometallic catalyst. The findings of these unexpected properties have inspired many extensive investigations on the possible applications of different bimetallic catalysts. However, it is difficult to know a priori how the electronic and chemical properties of a particular bimetallic catalyst will be modified relative to the parent metals. For this reason, the study of bimetallic surfaces and catalysis has gained considerable interest [2–5]. With the advances in surface science techniques and in computing power for elaborate calculations, the understanding of these bimetallic catalysts is being greatly advanced, but details about the novel reactivity are still not completely understood. It is generally accepted that there are two critical factors that contribute to the modification of the electronic and chemical properties of a metal in a bimetallic surface. First, the formation of the heteroatom bonds changes the electronic environment of the metal surface, giving rise to modifications of its electronic structure through the ligand effect. Second, the geometry of the bimetallic structure is typically different from that of the parent metals, for example, the average metal–metal bond lengths change. This gives rise to the strain effect that is known to modify the electronic structure of the metal through changes in orbital overlap [6]. One commonly used parameter to correlate changes in the electronic properties is the position of the surface d-band center with respect to the Fermi level. As this parameter has been shown to strongly correlate with the ability of the bimetallic surface to bind with adsorbates [6], the value of the surface d-band center may enable first-principles predictions of bimetallic surfaces that provide optimal binding strength and orientation of reactants, intermediates, and/or products to facilitate catalytic reactions.

In the current chapter, we will use Pt–Ni bimetallic catalysts as examples to demonstrate the correlation between fundamental understanding and the design of catalytic materials for hydrogenation reactions using the following combined

approaches: (1) fundamental surface science studies under ultrahigh vacuum (UHV) conditions, (2) density functional theory (DFT) modeling to correlate the electronic, structural and chemical properties of bimetallic surfaces, (3) synthesis and characterization of supported catalysts with conventional and synchrotron techniques, and (4) evaluation of the catalytic properties of supported catalysts using reactor studies.

In the next few sections, we will describe in detail each of the above approaches. In brief, the UHV surface science studies include the synthesis of a monolayer (ML) of Ni atoms either on the surface of Pt(1 1 1), designated as Ni–Pt–Pt(1 1 1), or in the subsurface region of Pt(1 1 1), designated as Pt–Ni–Pt(1 1 1); the binding strength of atomic hydrogen and the hydrogenation activity of cyclohexene are then determined experimentally on the monometallic and bimetallic surfaces. In the DFT modeling, the binding energies of atomic hydrogen and cyclohexene are compared on Ni–Pt–Pt(1 1 1), Pt–Ni–Pt(1 1 1), Pt(1 1 1), and Ni(1 1 1) to explain the unique low-temperature hydrogenation activity on the subsurface Pt–Ni–Pt(1 1 1) bimetallic structure. In the characterization of supported catalysts, results from conventional techniques, such as carbon monoxide (CO) chemisorption and transmission electron microscopy (TEM), are provided to compare the Pt–Ni bimetallic catalysts supported on γ -Al₂O₃. Additional characterization using extended X-ray absorption fine structure (EXAFS) is discussed to identify the presence or absence of the Pt–Ni bimetallic bonds in supported catalysts. Finally, the rates of cyclohexene hydrogenation on supported Pt–Ni bimetallic and the corresponding monometallic catalysts are compared to correlate with the UHV studies on model surfaces.

8.2

Experimental and Theoretical Methods

8.2.1

Experimental Techniques

The surface science results reported here were carried out in several UHV chambers, which were equipped with Auger electron spectroscopy (AES), low-energy electron diffraction (LEED), mass spectrometry (MS) for temperature-programmed desorption (TPD), and high-resolution electron energy loss spectroscopy (HREELS) for vibrational studies, as discussed in detail in previous publications [7]. The Ni films were prepared by resistively heating a tungsten wire with a high purity Ni wire (99.999% Ni, 0.25 mm diameter) wrapped around it. The TPD experiments were performed after cooling the crystal to 110 K and exposing the surface to H₂ and/or cyclohexene, followed by heating at a rate of 3 Ks^{−1}. Most of the bimetallic surfaces were synthesized by depositing atomically clean Ni atoms on a single crystal Pt(1 1 1) substrate. As described in detail in previous publications [8], the Ni–Pt–Pt(1 1 1) surface was prepared by depositing one monolayer of Ni on Pt(1 1 1) at 300 K, the subsurface Pt–Ni–Pt(1 1 1) structure was prepared by depositing one monolayer of Ni at 600 K, and the Ni(1 1 1) film was prepared by the deposition of a Ni film of more than six layers on Pt(1 1 1), which was characterized by the presence of a (1 1 1) LEED

pattern. The coverage of the Ni layer on Pt(1 1 1) was estimated using the reduction of the Pt (237 eV) AES peak intensity after deposition of Ni. In addition to deposition of Ni on Pt(1 1 1), the deposition of monolayer Pt on a Ni(1 1 1) substrate was also used in the cyclohexene TPD comparison made in Figure 8.3. This surface was synthesized and characterized in a manner similar to the Pt(1 1 1) experiments.

Supported Pt–Ni bimetallic catalysts were prepared by an incipient wetness method. The incipient wetness volume of dried γ -Al₂O₃ support was measured, and Pt and Ni solutions were then prepared accordingly by adding the necessary volume of deionized water to Pt(NH₃)₄(NO₃)₂ and Ni(NO₃)₂·6H₂O precursors, respectively. The γ -Al₂O₃-supported Pt–Ni bimetallic catalysts were prepared by sequential impregnation at two Pt/Ni atomic ratios, 3/1 and 1/1, with the Pt loading being constant at 5 wt%. The corresponding Ni loadings were 1.5 and 0.5 wt%, respectively. After the impregnation of the first precursor (Pt or Ni), the catalysts were dried at 383 K for 5 h followed by calcination in air at 563 K for 3 h. After this step, the second precursor (Ni or Pt) was impregnated, and the resultant solid mixture was again dried and calcined in air following the aforementioned procedure.

The metal dispersion of the catalysts was determined from CO chemisorption experiments using an Altamira Instruments (AMI-200ip) apparatus. A sample of 0.1 g was loaded into a quartz reactor and reduced in dilute hydrogen (50% H₂/He) at 723 K for 1 h. After cooling in He, pulses of CO in a He carrier gas were injected at 20 cm³ min^{−1} at room temperature through a sample loop and the signal was monitored with a thermal conductivity detector (TCD). The CO uptake was calculated by measuring the decrease in peak area due to adsorption in comparison with the area of a calibrated volume. By assuming a stoichiometry of one CO molecule per surface metal atom, the metal dispersion could be determined.

The supported catalysts were also characterized by high-angle annular dark-field scanning transmission electron microscopy (HAADF-STEM) using a JEOL 2010f electron microscope operating at 200 kV to determine the metal particle size on the support. The catalyst powders were sonicated in an ethanol solution for about 1 h. Immediately after sonication, two drops of the liquid were transferred onto a Lacey carbon support film on a copper grid. To be sure that the solvent was completely evaporated from the support, the TEM characterization was performed after 48 h of drying.

Extended X-ray absorption fine structure measurements were conducted on beamline X18-B at the National Synchrotron Light Source (NSLS), Brookhaven National Laboratory. The Pt L_{III}-edge EXAFS spectra were recorded using a double flat crystal Si (220) monochromator in the transmission mode at room temperature. Prior to the measurements, the samples were reduced *in situ* at 450 °C with dilute H₂ (5% H₂/He). The XDAP program, version 3.2, was used to analyze and fit the data. Briefly, the data reduction consisted of the following steps: spectra averaging, pre-edge subtraction, background determination, and normalization. The interatomic distance (*R*), the coordination number (CN), the difference of the Debye–Waller factor from the reference ($\Delta\sigma^2$), and the correction of the threshold energy (ΔE^0) were treated as free parameters during the fitting. The quality of the fit was estimated using the values of *k*³ variance (*V*_{*k*}²). The variance represents the residual between the

observed and calculated spectra in the fitted range, with low values of this parameter indicating a good agreement between the calculated model and experimental data. The reference spectrum for the Pt–Pt bond was obtained by measuring the spectrum for a Pt foil, while FEFF7 calculations of Pt–Ni interactions were used as the reference for the Pt–Ni contribution.

Fourier transform infrared (FTIR) spectroscopy was used to monitor the individual products and reaction kinetics of the disproportionation (i.e., self-hydrogenation) and hydrogenation of cyclohexene using a batch reactor system. For all of the reactor experiments, a small amount of supported catalyst was pressed into a pellet in direct contact with a rectangular tungsten mesh (2.4 cm × 1 cm, 100 mesh, 0.001 in wire diameter, Alfa Aesar). For the disproportionation of cyclohexene, a catalyst weight of ~40 mg was employed, whereas for the hydrogenation reaction, the amount was reduced to ~25 mg. Also connected to the mesh was a K-type thermocouple to monitor the temperature of the catalyst during reduction and reaction. The tungsten mesh was supported to a mounting bracket made of nickel connected at the end of a z-translating manipulator feedthrough. The feedthrough also had connections for resistive heating of the pressed sample through the supporting tungsten mesh. The design of this type of cell was based on a model reported elsewhere [9]. The stainless steel IR cell, consisting of BaF₂ windows, allowed for *in situ* reduction of samples and spectroscopic measurements of either surface species or gas-phase products. Gas-phase spectra were recorded with 4 cm⁻¹ resolution using a Nicolet-470 FTIR spectrometer equipped with an MCT-A (mercury cadmium telluride) detector. To remove water and other impurities, the cell was first evacuated to a pressure below 10⁻⁶ Torr for a minimum of 60 min. The catalyst was then reduced at 723 K in 30 Torr of hydrogen for 30 min followed by evacuation and a high temperature flash (723 K) to remove any surface species generated during reduction. This reduction cycle was repeated three times before performing the FTIR experiments. The gases and liquid vapors necessary for reduction, venting, adsorption, or hydrogenation reactions were admitted to the IR cell through a gas manifold.

For both the disproportionation and hydrogenation of cyclohexene, the gas-phase reaction products were monitored by recording gas-phase spectra (32 scans) every 30 s during the reaction. The purity of cyclohexene was verified *in situ* by comparing the IR spectrum with the standard reference reported in literature [10]. For each experiment, IR spectra were collected for 10 min prior to initiation of the reaction to determine an appropriate baseline. To begin the reaction, the reactant(s) were rapidly dosed into the IR cell containing the supported catalysts at room temperature and to a total initial pressure ranging from ~3.5 to 5.5 Torr. For the hydrogenation of cyclohexene, hydrogen gas and cyclohexene vapor were mixed at a partial pressure ratio of 2:1 within the gas manifold during the 10 min baseline collection period.

The concentrations of the three main gas-phase species during the disproportionation and hydrogenation reactions (cyclohexene, cyclohexane, and benzene) were estimated using the intensities of their vibrational modes at 1139 cm⁻¹ (ω CH₂ rock) [11], 1458 cm⁻¹ (–CH₂ deformation) [12], and 1810 cm⁻¹ (overtone of the C–C stretching mode at 993 cm⁻¹) [13], respectively. It is important to point out that the –CH₂ deformation mode at 1458 cm⁻¹ for cyclohexane is convoluted with both the

–CH₂ deformation feature at 1455 cm^{−1} for cyclohexene and the ring stretching and deformation feature at 1488 cm^{−1} for benzene. Therefore, contributions of the latter were subtracted when estimating the concentration of cyclohexane, as described previously [14]. These concentrations were then normalized to the weight of catalyst used in the experiment.

8.2.2

DFT Modeling

DFT was employed to calculate the binding energies of hydrogen and cyclohexene on the monometallic and bimetallic surfaces. The theoretical results discussed in this chapter were calculated using self-consistent periodic slab calculations with either the Dacapo or the VASP (Vienna *ab initio* Simulation Package) code [15–17]. The Kohn Sham equations were solved using a plane wave basis set with a cutoff energy of 396 eV, and the PW91 functional was used to describe the exchange correlation term. Vanderbilt ultrasoft pseudopotentials, as supplied by Kresse and Hafner [18, 19], were used to describe the core electrons and the nuclei of the atoms. A 3 × 3 × 1 Monkhorst–Pack *k*-point grid mesh was used to determine the electronic energies.

The adsorption of hydrogen and cyclohexene was studied using either 2 × 2 or 3 × 3 supercells that contained four atomic layers, with the top two layers allowed to relax in each case. A vacuum region of about six metal layers was used to separate the slabs to avoid any electronic interactions. Calculations for gas-phase hydrogen and cyclohexene were carried out implementing spin polarization, whereas the adsorbate–metal system calculations were carried out spin unpolarized, since the relative difference in the adsorption energies was found to be typically less than 5 kJ mol^{−1} [8, 20].

For the hydrogen–metal system, hydrogen was adsorbed at the threefold hollow site of the metal surface with a coverage of 1/9 ML. The adsorbate–slab system was then allowed to relax to its minimum energy configuration. The binding energy was calculated as the difference between the adsorbate–slab total energy and the sum of the total energy of gas-phase adsorbate and the bare slab. The binding of cyclohexene was studied on hydrogen coadsorbed surfaces. Cyclohexene was bonded in the di-σ configuration on the monometallic and the bimetallic surfaces in the presence of two coadsorbed hydrogen atoms. The hydrogen adatoms were bonded in the two threefold hollow sites nearest to the cyclohexene molecule to ascertain the effect of repulsion on the binding of cyclohexene.

8.3

Results and Discussion

8.3.1

UHV and DFT Studies on Pt–Ni Model Surfaces

Thermal desorption experiments were performed in combination with DFT modeling to characterize the chemical activities and structures of the model bimetallic

surfaces. Since hydrogen chemisorption on catalyst surfaces is a critical aspect of many catalytic processes, such as hydrogenation, the chemisorption properties of H_2 are examined. In addition, the hydrogenation of cyclohexene was used as a probe reaction to determine the chemical properties of the Pt–Ni bimetallic surface nanostructures.

8.3.1.1 Adsorption and Desorption of Hydrogen

Figure 8.1 shows a comparison of the TPD spectra of H_2 from clean Pt(1 1 1), surface monolayer Ni–Pt–Pt(1 1 1), subsurface monolayer Pt–Ni–Pt(1 1 1), and a thick Ni(1 1 1) film epitaxially grown on Pt(1 1 1). It is apparent that the desorption temperature of H_2 is significantly altered upon the formation of bimetallic surfaces. H_2 desorbs from the Pt–Ni–Pt(1 1 1) subsurface structure at a lower temperature than that from Pt(1 1 1) or Ni(1 1 1), while desorption from the Ni–Pt–Pt(1 1 1) surface structure occurs at a higher temperature than that of either parent metal surface.

Since the dissociative adsorption of H_2 on Ni(1 1 1) and Pt(1 1 1) is not an activated process [21], the desorption temperature of H_2 from these surfaces should, in principle, be related to the respective metal–H bond strengths. If one assumes that H_2 dissociation on the bimetallic surfaces is also not activated, then desorption temperatures in Figure 8.1 indicate a weaker metal–H bond on subsurface Pt–Ni–Pt(1 1 1), and a stronger metal–H bond on surface Ni–Pt–Pt(1 1 1) than on either Pt(1 1 1) or Ni(1 1 1).

Parallel DFT modeling is performed to understand the origin of the different hydrogen binding energies (HBE) from the four surfaces using the Dacapo-2.6 code

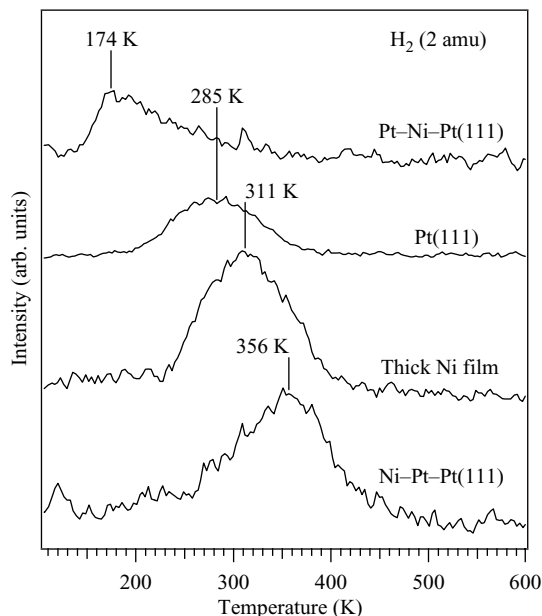


Figure 8.1 TPD results following the saturation exposure of H_2 at 100 K on different surfaces.

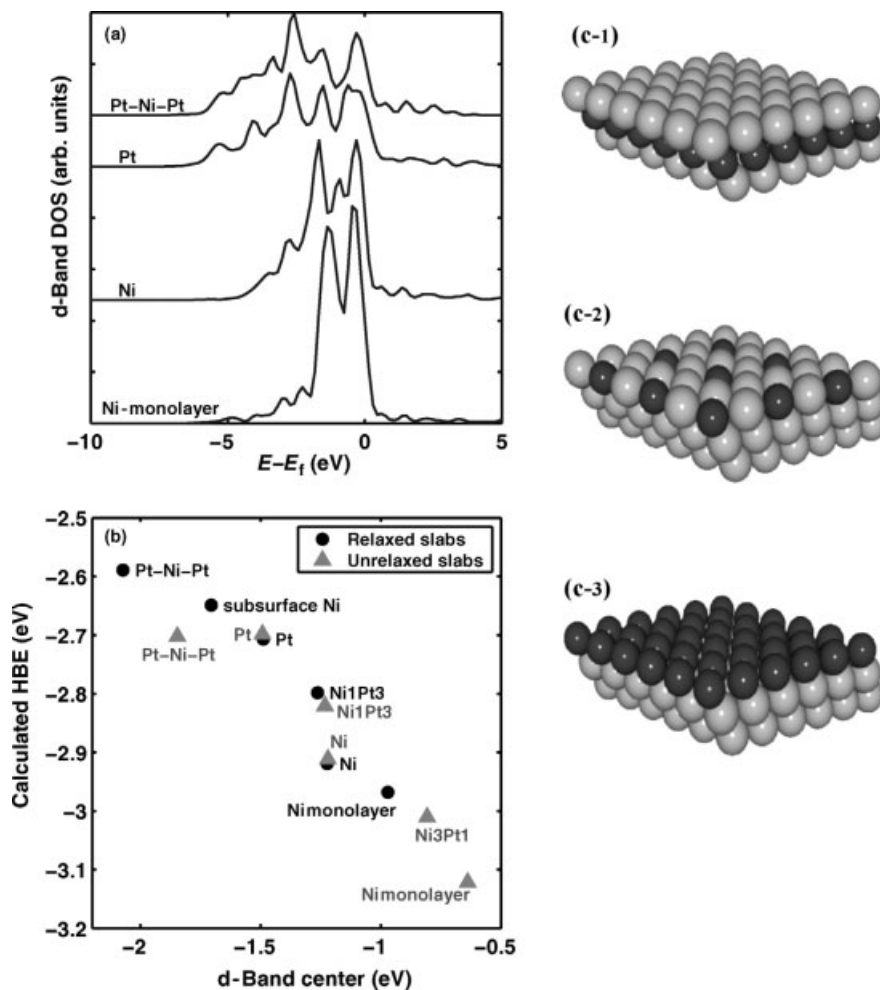


Figure 8.2 DFT calculations of the hydrogen binding energy (HBE) on Ni/Pt(111) surfaces with different surface nanostructures. The Ni atoms are the dark circles, whereas the Pt atoms are the light gray circles.

and with 2×2 supercells of three-layer slabs at a 0.25 ML coverage of hydrogen atoms [8]. Figure 8.2a shows the density of states (DOS), which is decomposed into contributions from different atomic orbitals by projection of the plane waves onto an atomic orbital basis set, as implemented by the Dacapo software, of the four surfaces. A comparison of the DOS clearly reveals significant differences in the electronic properties of the bimetallic surfaces. In comparison to Pt(111), the presence of subsurface Ni in Pt-Ni-Pt(111) tends to increase the intensity of low energy states at the expense of higher energy states in the surface Pt atoms, thus shifting the average energy of the surface Pt d-band away from the Fermi level. In contrast,

the Ni–Pt–Pt(1 1 1) d-band was narrower than Pt(1 1 1) and Ni(1 1 1), moving the d-band center closer to the Fermi level.

As has been demonstrated in many DFT modeling studies, the value of the surface d-band center is a very useful parameter to correlate the electronic properties of the bimetallic surfaces with the binding energies of adsorbates. The calculated HBE values as a function of the surface d-band center of various Pt–Ni surfaces are shown in Figure 8.2b. In addition to the surface and subsurface bimetallic structures, DFT modeling is also performed on intermixed Pt–Ni surface structures by incorporation of Ni into the Pt surface layer (e.g., Ni₁Pt₃, Ni₃Pt₁). The results show an approximately linear correlation between the HBE values and surface d-band center for both relaxed and unrelaxed surfaces, with Ni incorporated into the topmost Pt surface layer increasing the HBE and shifting the d-band center closer to the Fermi level in comparison to pure Pt, and subsurface Ni decreasing the HBE and shifting the d-band center away from the Fermi level. It is important to point out that the relaxation of the surface layers has a negligible effect on the calculated HBE values for the pure metal slabs (Pt and Ni). However, the HBE values on the bimetallic surfaces show a significant sensitivity to relaxation, as does the center of the d-band. In each case, relaxation reduces the magnitude of the HBE, with a corresponding change in the d-band center. The results in Figure 8.2b, as well as DFT modeling for many other bimetallic systems, indicate that allowing the surface layer or layers to relax is a critical requirement when performing DFT modeling on bimetallic surfaces.

The most important result is that the comparison of the DFT modeling (Figure 8.2b) and TPD (Figure 8.1) results provides verification of the existence of the Pt–Ni–Pt(1 1 1) subsurface structure. The presence of subsurface Ni in Pt(1 1 1) under the conditions used in these experiments is consistent with other studies of Pt–Ni alloys [22–25]. For example, for a Pt_{0.5}Ni_{0.5} alloy, it has been reported that the surface is ~88% Pt, the second layer is ~91% Ni, and the third layer is ~65% Pt [22]. The stability of Pt-terminated surfaces is also consistent with DFT modeling of the Pt–Ni–Pt(1 1 1) subsurface stability in vacuum and with adsorbed hydrogen.

To further verify the correlation between DFT modeling and TPD results, Kitchin *et al.* [8] calculated the heats of dissociative adsorption from the values of HBE on Pt(1 1 1), Ni(1 1 1), Pt–Ni–Pt(1 1 1), and Ni–Pt–Pt(1 1 1) surfaces. The barrier for desorption in this case is identical to the heat of dissociative adsorption of H₂, and is equal to the gas-phase dissociation energy minus twice the metal–H bond strength. These values are compared to the heat of adsorption from the TPD measurements using the Redhead equation for second-order desorption [26]. An identical trend is observed for the four surfaces between DFT modeling and TPD experiments [8].

8.3.1.2 Disproportionation and Hydrogenation of Cyclohexene

Similar to the trend in HBE as a function of d-band center, the binding energies of alkene molecules also decrease as the d-band center shifts away from the Fermi level. For example, the binding energy of cyclohexene on the Pt–Ni–Pt(1 1 1) subsurface structure is significantly lower than that on Pt(1 1 1) and Ni(1 1 1), whereas that on the Ni–Pt–Pt(1 1 1) surface structure is much stronger than on either of the parent metal surfaces [27]. In principle, the presence of weakly bonded hydrogen

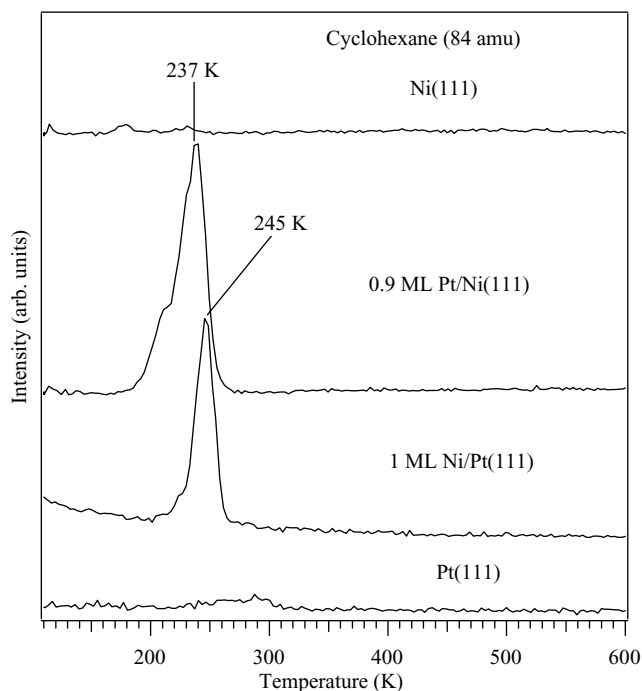


Figure 8.3 TPD spectra of cyclohexane (84 amu) desorption from the disproportionation of 3L cyclohexene on the Ni/Pt(1 1 1) and Pt/Ni(1 1 1) surfaces.

atoms and cyclohexene should favor the low-temperature hydrogenation of cyclohexene. We have used the disproportionation and hydrogenation of cyclohexene ($\text{c-C}_6\text{H}_{10}$) as a probe reaction to determine the hydrogenation activity of the Pt–Ni bimetallic surfaces. Figure 8.3 compares the TPD results following the desorption of the disproportionation product, cyclohexane, from the Ni–Pt(1 1 1) and Pt–Ni(1 1 1) surfaces. As shown in Figure 8.3, the disproportionation of cyclohexene does not occur on either Ni(1 1 1) or Pt(1 1 1) [28]. However, adding a monolayer coverage of Ni to Pt(1 1 1) or Pt to Ni(1 1 1) at 600 K changes the selectivity of that surface to produce cyclohexane. This low-temperature hydrogenation reaction pathway indicates that there is hydrogen available on the surface at temperatures as low as ~ 200 K, either from the dehydrogenation reaction to form benzene or from the background hydrogen in the chamber.

Results from vibrational spectroscopy also indicate that cyclohexene bonds more weakly on the Pt–Ni–Pt(1 1 1) subsurface structure [29]. Figure 8.4 shows the HREELS spectrum of cyclohexene on a 0.9 ML Pt–Ni–Pt(1 1 1) surface. For comparison, spectra of cyclohexene on clean Pt(1 1 1) and a thick Ni(1 1 1) film are also included in Figure 8.4. The spectra were taken after exposing the surfaces to 3L of cyclohexene at 80 K followed by heating the surface to 200 K. The spectrum of cyclohexene on the 0.9 ML Pt–Ni–Pt(1 1 1) surface indicates a weakly π -bonded intermediate, based on the appearance of the $\delta(\text{C}=\text{C})$ and $\nu(\text{C}=\text{C})$ vibrational modes

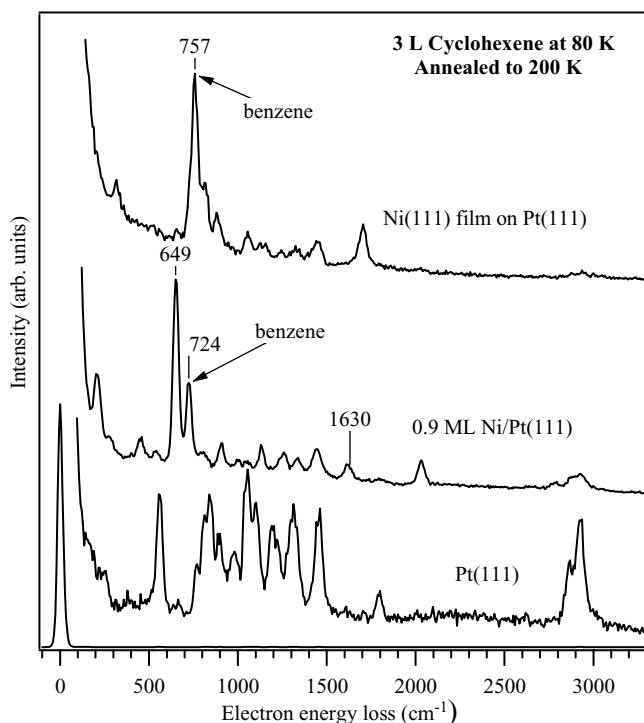


Figure 8.4 HREELS spectra of 3L cyclohexene on Pt(111), 0.9 ML Ni/Pt(111), and a Ni(111) film on Pt(111).

at 649, 724, and 1630 cm^{-1} . The presence of these modes indicates that C=C bonds in the cyclohexene molecule are intact, which is characteristic of a weakly bonded cyclohexene intermediate. In addition, after heating to temperatures higher than 200 K, HREELS spectra did not detect the presence of cyclohexene, indicating that the production of cyclohexene was a reaction-limited process [29]. On the Pt(111) surface, the vibrational modes characteristic of a weakly bonded cyclohexene molecule are not present. Instead, the spectrum is characteristic of a di- σ -bonded cyclohexene molecule. Furthermore, the spectrum on the thick Ni(111) film is consistent with the presence of chemisorbed benzene, indicating the thick Ni film is very reactive toward the dehydrogenation of cyclohexene. The drastic differences between the reactions of cyclohexene on the three surfaces further highlight the unique chemical properties of the Pt–Ni–Pt(111) surface [29].

To examine the bonding of cyclohexene on the Ni–Pt–Pt(111) surface, cyclohexene and preadsorbed hydrogen were dosed onto this surface, along with other Ni/Pt(111) bimetallic surfaces. Following this, it was found that hydrogen evolves from Ni–Pt–Pt(111) at 417 K (not shown), which is higher than the desorption temperature of hydrogen on this surface (355 K). The fact that hydrogen is desorbing at these high temperatures despite the lack of dehydrogenated products (not shown) is indicative of decomposition occurring on this surface, supporting the DFT prediction

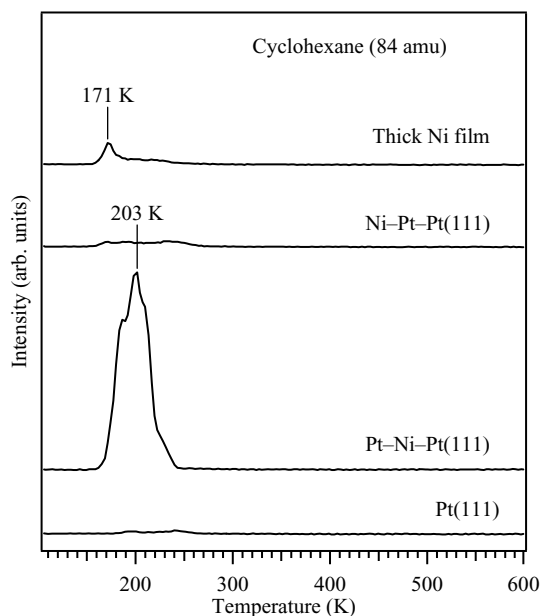


Figure 8.5 Hydrogenation of cyclohexene on Pt–Ni bimetallic surfaces.

that cyclohexene is strongly bonded to Ni–Pt–Pt(111). Figure 8.5 shows the cyclohexene desorption after dosing cyclohexene on the Ni/Pt(111) surfaces with preadsorbed hydrogen. By predosing the surfaces with hydrogen before cyclohexene exposure, the pathway toward hydrogenation is enhanced. In comparison, this low-temperature hydrogenation pathway does not occur on Pt(111) or Ni–Pt–Pt(111) and occurs only in trace amounts on thick Ni film. The absence of the hydrogenation pathway on these surfaces is most likely due to the strong bonding of hydrogen and cyclohexene, as predicted by the DFT calculations. Overall, the surface science and DFT results described in this section clearly indicated that the formation of the surface Pt–Ni–Pt(111) bimetallic structure results in a novel low-temperature hydrogenation pathway that is absent in both parent metals. The next challenge was to synthesize such bimetallic structures in supported Pt–Ni bimetallic catalysts, as described below.

8.3.2

Characterization and Reactor Studies of Supported Pt–Ni Catalysts

8.3.2.1 TEM and EXAFS Characterization of Ni/Pt/Al₂O₃ Catalysts

To correlate the reactivity seen on the model Ni/Pt(111) and Pt/Ni(111) surfaces with more realistic catalytic materials, we have synthesized and characterized supported Ni/Pt/alumina catalysts using EXAFS, TEM, and IR spectroscopy. Figure 8.6 shows the HAADF–STEM pictures of Ni–Pt/ γ -Al₂O₃ (Pt impregnated first) and Pt–Ni/ γ -Al₂O₃ (Ni impregnated first) samples for Pt/Ni atomic ratios of 1/1.

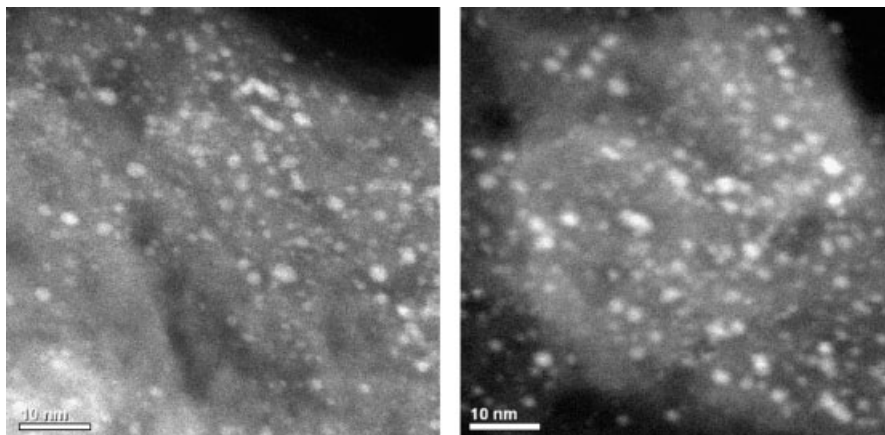


Figure 8.6 TEM images of Pt–Ni bimetallic particles on alumina support.

The samples were reduced in H_2 in the FTIR cell, although they were subsequently exposed to air during the sample preparation for TEM measurements. Since in the HAADF images the contrast arises due to difference in atomic number of the elements of interest (single heavy atoms on low- Z substrates) [30], the bright spots are most likely due to Pt and Ni particles distinguished from the low atomic number of the support ($\gamma\text{-Al}_2\text{O}_3$). The TEM images reveal a relatively uniform distribution of the metal particles, with an average metal particle size in the range of $\sim 2\text{--}3$ nm for both catalysts. The similar particle size distributions are consistent with the similar dispersion values for the two Pt–Ni bimetallic catalysts, which are determined from CO chemisorption to be approximately 24 and 25%, respectively, for the two catalysts [31].

Supported Pt–Ni catalysts were further characterized using EXAFS to assure the presence of Pt–Ni bonds. The best fit results are summarized in Table 8.1. In addition to the two catalysts with the Pt/Ni atomic ratio of 1/1, two catalysts, with the Pt/Ni ratio of 3/1, are also included to show the effect of impregnation sequence on the formation of the Pt–Ni bimetallic bonds. The EXAFS spectra were analyzed by assuming two contributions, Pt–Pt and Pt–Ni. For samples with a Pt/Ni ratio

Table 8.1 Results of Pt L_{III} -edge EXAFS fitting on 1/3Ni–1Pt/ $\gamma\text{-Al}_2\text{O}_3$, 1Pt–1/3Ni/ $\gamma\text{-Al}_2\text{O}_3$, 1Ni–1Pt/ $\gamma\text{-Al}_2\text{O}_3$, and 1Pt–1Ni/ $\gamma\text{-Al}_2\text{O}_3$.

Sample	1/3Ni–1Pt/ $\gamma\text{-Al}_2\text{O}_3$	1Pt–1/3Ni/ $\gamma\text{-Al}_2\text{O}_3$	1Ni–1Pt/ $\gamma\text{-Al}_2\text{O}_3$	1Pt–1Ni/ $\gamma\text{-Al}_2\text{O}_3$
$N(\text{Pt–Pt})$	8.0 ± 0.6	9.0 ± 0.4	8.2 ± 1.0	6.6 ± 1.6
$N(\text{Pt–Ni})$	0.8 ± 0.6	0	2.6 ± 1.1	4.1 ± 3.3
$R(\text{Pt–Pt})(\text{\AA})$	2.746 ± 0.002	2.75 ± 0.002	2.744 ± 0.003	2.739 ± 0.008
$R(\text{Pt–Ni})(\text{\AA})$	2.60 ± 0.03	—	2.58 ± 0.02	2.572 ± 0.04
$\sigma^2(\text{Pt–Pt})(\text{\AA}^2)$	0.0065 ± 0.0003	0.0064 ± 0.0002	0.0072 ± 0.0005	0.0076 ± 0.0011
$\sigma^2(\text{Pt–Ni})(\text{\AA}^2)$	0.013 ± 0.0066	—	0.0141 ± 0.0036	0.022 ± 0.009

of 3/1, the calculated values for the total Pt–M coordination numbers indicate that the average diameter of the nanoparticles in both cases can be estimated as about 3 nm, assuming a hemispherical cuboctahedral fcc structure [32]. In addition, a small coordination of Pt–Ni is observed on the 1/3Ni–1Pt/ γ -Al₂O₃, while no Pt–Ni bonds were found on the 1Pt–1/3Ni/ γ -Al₂O₃ sample. On the other hand, the results for the 1Ni–1Pt/ γ -Al₂O₃ and 1Pt–1Ni/ γ -Al₂O₃ samples confirmed the formation of Pt–Ni bonds in both the impregnation sequences. For example, for the 1Pt–1Ni/ γ -Al₂O₃ sample, the Pt–Ni bond length was found to be 2.57(4) Å, which is 0.07(4) Å longer than the Ni–Ni bond in the metallic Ni (2.49 Å) and 0.21(4) Å shorter than the Pt–Pt bond in metallic Pt (2.78 Å). The Pt–Pt bond length is 2.74(1) Å, which is 0.03(1) Å shorter than in the metallic Pt (2.78 Å). Both of these results suggest that Pt and Ni are in the alloy form. Furthermore, a good fit to the Pt L_{III}-edge data can only be obtained when both Pt–Pt and Pt–Ni contributions are included in the model, suggesting that the nanoparticles have both Pt and Ni atoms.

The four bimetallic catalysts listed in Table 8.1 as well as the monometallic catalysts were evaluated in the IR batch reactor for the disproportionation of cyclohexene. Figure 8.7 shows the rates of cyclohexane formation from the disproportionation of

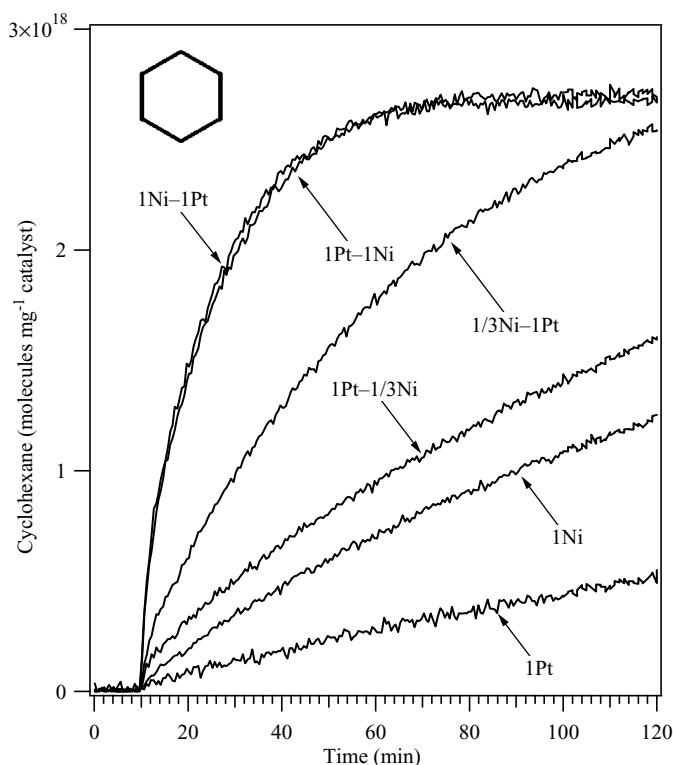


Figure 8.7 Cyclohexane formation during the cyclohexene disproportionation reaction at room temperature over different Ni/Pt supported catalysts.

Table 8.2 Results of first-order fitting for the cyclohexene disproportionation reaction over different Pt–Ni supported catalysts at room temperature.

Catalyst	k (s ⁻¹)
1Pt/ γ -Al ₂ O ₃	2.9×10^{-5}
1Ni/ γ -Al ₂ O ₃	7.2×10^{-5}
1/3Ni–1Pt/ γ -Al ₂ O ₃	3.3×10^{-4}
1Pt–1/3Ni/ γ -Al ₂ O ₃	1.1×10^{-4}
1Ni–1Pt/ γ -Al ₂ O ₃	1.2×10^{-3}
1Pt–1Ni/ γ -Al ₂ O ₃	1.1×10^{-3}

cyclohexene, in units of number of molecules per mg of catalyst, over the various Pt–Ni bimetallic catalysts and the corresponding monometallic catalysts. For the 1Ni–1Pt/ γ -Al₂O₃ and 1Pt–1Ni/ γ -Al₂O₃ catalysts, the conversion of cyclohexene to cyclohexane and benzene (not shown) reached 100% after ~60 min. In contrast, the monometallic Pt and Ni catalysts showed significantly lower rates for the conversion of cyclohexene. The conversion of cyclohexene on the 1/3Ni–1Pt/ γ -Al₂O₃ catalyst was significantly faster than that on 1Pt–1/3Ni/ γ -Al₂O₃. To obtain a more quantitative comparison, the conversion rate of cyclohexene on all of the catalysts was approximated by fitting the experimental results with the first-order kinetics. The rate constants from this fitting are listed in Table 8.2. The rate constants for cyclohexene conversion over the six catalysts followed the order of 1Pt/ γ -Al₂O₃ < 1Ni/ γ -Al₂O₃ < 1Pt–1/3Ni/ γ -Al₂O₃ < 1/3Ni–1Pt/ γ -Al₂O₃ < 1Pt–1Ni/ γ -Al₂O₃ \approx 1Ni–1Pt/ γ -Al₂O₃. The 1/3Ni–1Pt/ γ -Al₂O₃ catalyst clearly showed a higher disproportionation rate than 1Pt–1/3Ni/ γ -Al₂O₃. This can be explained by the presence of the Pt–Ni bimetallic alloy when Pt was impregnated first, as confirmed by the detection of the Pt–Ni bond from the EXAFS measurements.

Similar disproportionation rates, on the other hand, were observed on both 1Ni–1Pt/ γ -Al₂O₃ and 1Pt–1Ni/ γ -Al₂O₃ catalysts, which means that the formation of the bimetallic bonds on these Pt–Ni bimetallic catalysts does not depend strongly on the sequence in the impregnation of the metal precursors at the Ni metal loading used (1.5 wt% Ni). Again this is consistent with the EXAFS results, where the presence of the Pt–Ni bonds is observed in both catalysts. Correspondingly, the results in Figure 8.7 show no significant difference between the two 1/1 ratio catalysts in the overall activity for the disproportionation of cyclohexene and the estimated rate constants. As shown earlier, in Figure 8.5, the UHV surface science results indicate that the Pt-terminated bimetallic surfaces are much more active than Ni-terminated ones for the disproportionation of cyclohexene [28]. Therefore, the observation of similar disproportionation activities of the 1Ni–1Pt/ γ -Al₂O₃ and 1Pt–1Ni/ γ -Al₂O₃ suggests that the surfaces of both the catalysts are most likely terminated by Pt after the calcination and reduction cycles. The segregation of Pt atoms to the surface is consistent with our previous experiments under the DFT studies of the relative stability of the surface Ni–Pt–Pt(1 1 1) and subsurface Pt–Ni–Pt(1 1 1) structures, where the segregation of Pt is thermodynamically favored under UHV conditions

and in the presence of atomic hydrogen [8, 29, 33]. A similar finding has been reported for Pt–Ni catalysts supported on alumina for the reforming of methane. The authors concluded that the sequential impregnation of previously reduced Ni catalysts with Pt shows Pt atoms located preferentially on the surface of the Pt–Ni alloy [34].

In comparison, the physical and chemical probes described above demonstrate that the impregnation sequence has a significant effect on the formation of the Pt–Ni bimetallic bonds for catalysts with low Ni loading (~ 0.5 wt% Ni). With a Pt/Ni ratio of 3/1 (~ 0.5 wt% Ni), the formation of the Pt–Ni bimetallic nanoparticles is evident when Pt is impregnated first on the alumina support ($1/3\text{Ni}-1\text{Pt}/\gamma\text{-Al}_2\text{O}_3$), as confirmed by the detection of the Pt–Ni coordination in EXAFS (Table 8.2). In contrast, there is no evidence of bimetallic bond formation when the Ni precursor is impregnated first ($1\text{Pt}-1/3\text{Ni}/\gamma\text{-Al}_2\text{O}_3$). In addition, the disproportionation of cyclohexene on $1/3\text{Ni}-1\text{Pt}/\gamma\text{-Al}_2\text{O}_3$ shows a higher conversion rate than the $1\text{Pt}-1/3\text{Ni}/\gamma\text{-Al}_2\text{O}_3$ or $1\text{Pt}/\gamma\text{-Al}_2\text{O}_3$. These results suggest the lack of the formation of the bimetallic Pt–Ni bonds on the $1\text{Pt}-1/3\text{Ni}/\gamma\text{-Al}_2\text{O}_3$ catalyst. This could be due to the formation of Ni aluminate (NiAl_2O_4) species when Ni is impregnated first on the alumina support, due to the strong interaction of Ni with $\gamma\text{-Al}_2\text{O}_3$ as reported previously [35, 36]. According to Morikawa *et al.* [37] and Salagre *et al.* [38], Ni in NiAl_2O_4 is reducible only at temperatures above 873 K, which is higher than the reduction temperature of 723 K in the current study. In comparison, for a higher Ni loading (1.5 wt%) with a Pt/Ni ratio of 1/1 (5 wt% Pt), bimetallic Pt–Ni bonds are detected regardless of the impregnation sequence, suggesting that there is a threshold of Ni loading for the formation of the Pt–Ni bimetallic bonds. It is most likely that an initial threshold coverage of Ni interacts strongly with the support, producing either NiO or NiAl_2O_4 that prevents the reduction of Ni and therefore the formation of the Pt–Ni bimetallic bonds. When Pt is impregnated first, the strong interaction of Ni with the support seems to be reduced by the Pt precursor or the actual Pt oxide formed during the calcination step. This could explain the fact that the $1/3\text{Ni}-1\text{Pt}/\gamma\text{-Al}_2\text{O}_3$ catalyst shows the presence of the Pt–Ni bonds, and correspondingly an enhanced selectivity in the hydrogenation of acetylene and a higher disproportionation activity of cyclohexene than $1\text{Pt}-1/3\text{Ni}/\gamma\text{-Al}_2\text{O}_3$ or $1\text{Pt}/\gamma\text{-Al}_2\text{O}_3$.

Another explanation for the effect of impregnation sequence is the possible diffusion of Ni^{2+} ion into the tetrahedral and octahedral cavities of the $\gamma\text{-Al}_2\text{O}_3$ support. The ability of transition metal ions to enter the $\gamma\text{-Al}_2\text{O}_3$ lattice cavities should depend on the size of the ions. As reported by Yan *et al.* [39, 40], small ions such as Ni^{2+} or Co^{2+} with a radius of 0.69 Å are well known to enter the $\gamma\text{-Al}_2\text{O}_3$ matrix relatively easily, but the larger Pt^{2+} ion with a radius of 0.80 Å is unable to do so under the same conditions. The same argument could be applied in the current study. When the Ni^{2+} ion is impregnated first, all or a large fraction would enter the $\gamma\text{-Al}_2\text{O}_3$ cavities. On the other hand, if the Pt^{2+} is deposited first, it would remain outside the matrix and likely prevent subsequently deposited Ni^{2+} ion from entering the $\gamma\text{-Al}_2\text{O}_3$ cavities. The availability of both Ni and Pt outside the cavities would in turn facilitate the formation of the Pt–Ni bimetallic bonds, consistent with the results in the current study.

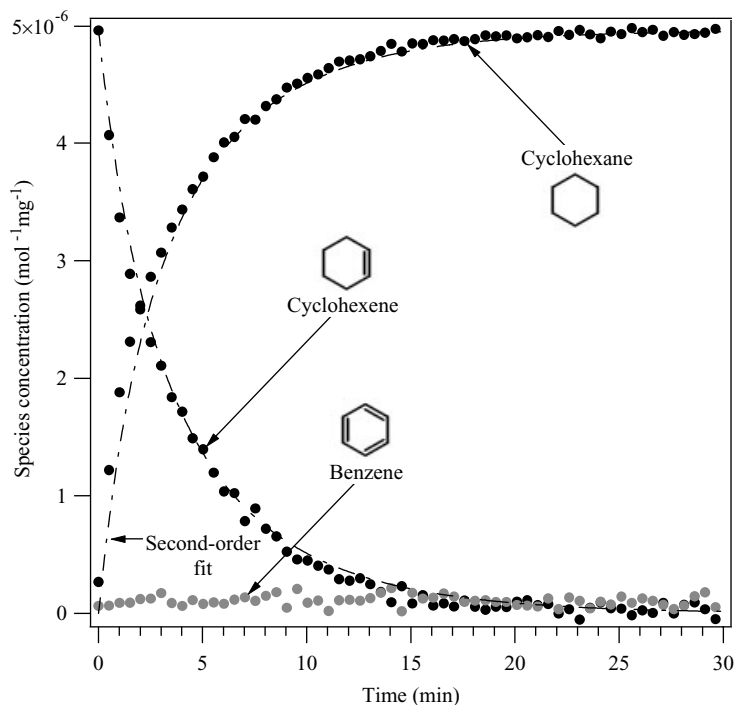


Figure 8.8 Second-order fit for the production of cyclohexane during the cyclohexene hydrogenation reaction over a 1Pt–1Ni/ γ - Al_2O_3 catalyst at room temperature.

Finally, we have also performed the hydrogenation of cyclohexene on the supported catalysts to further compare the hydrogenation activities of the bimetallic and monometallic catalysts. Figure 8.8 shows the gas-phase concentrations of cyclohexene and cyclohexane as a function of reaction time on the 1:1 Pt–Ni bimetallic catalyst. The solid lines in Figure 8.8 are from fitting the reaction rate with the second-order kinetics. Table 8.3 shows the rate constants from the fitting on several monometallic and bimetallic catalysts. Similar to the rates for the disproportionation reaction, the bimetallic catalysts show a significant increase in the hydrogenation rate. It is also interesting to point out that a 1/3Pt–1Ni/ γ - Al_2O_3 catalyst, with a Pt

Table 8.3 Results of second-order fitting for the cyclohexene hydrogenation reaction over different Pt–Ni supported catalysts at room temperature.

Catalyst	k ($\text{l mol}^{-1} \text{s}^{-1}$)
1Pt/ γ - Al_2O_3	20 710
1Ni/ γ - Al_2O_3	1712
1/3Pt–1Ni/ γ - Al_2O_3	22 030
1Pt–1Ni/ γ - Al_2O_3	36 240

loading 1/3 that in the monometallic Pt catalyst, shows a hydrogenation rate constant that is slightly higher than the Pt catalyst, demonstrating the possibility to significantly reduce the loading of Pt by the formation of the Pt–Ni bimetallic catalysts.

8.4

Conclusions

In the current chapter, we used the hydrogenation of cyclohexene on Pt–Ni bimetallic catalysts as an example to demonstrate the rational design of catalysts with desirable catalytic properties. The identification of the Pt–Ni bimetallic system as an efficient hydrogenation catalyst is first determined experimentally on model single crystal surfaces based on a novel low-temperature hydrogenation pathway. Subsequent DFT modeling attributes the novel hydrogenation pathway to the weaker binding of both atomic hydrogen and cyclohexene on the Pt–Ni–Pt(1 1 1) subsurface structure. Knowledge from these fundamental studies is then utilized to synthesize supported Pt–Ni bimetallic catalysts. TEM and CO chemisorption studies are utilized to assure the formation of well-dispersed bimetallic catalysts. Parallel EXAFS characterizations help to correlate the formation of the Pt–Ni bimetallic bonds to the Pt/Ni ratio and impregnation sequence in the catalyst synthesis. Finally, batch reactor studies of the hydrogenation of cyclohexene demonstrate the higher hydrogenation activity of the Pt–Ni bimetallic catalysts as compared to the monometallic Pt and Ni catalysts, confirming the prediction from the UHV surface science and DFT studies. Similar research approaches are currently used in our research group to identify various bimetallic catalysts for several types of reactions, including selective hydrogenation of molecules with multiple unsaturated bonds, reforming of oxygenates to produce H₂, and the identification of desirable bimetallic compositions and structures for fuel cell applications.

Acknowledgment

This work was funded by the Department of Energy, Office of Basic Energy Sciences (Grant No. DE-FG02-00ER15104).

References

- 1 Sinfelt, J.H. (1977) *Catalysis by Alloys and Bimetallic Clusters*, **10**, 15.
- 2 Madey, T.E., Nien, C.H., Pelhos, K., Kolodziej, J.J., Abdelrehim, I.M. and Tao, H.S. (1999) *Surface Science*, **438**, 191.
- 3 Campbell, C.T. (1990) *Bimetallic Surface-Chemistry*, **41**, 775.
- 4 Rodriguez, J.A. (1996) Physical and chemical properties of bimetallic surfaces. *Surface Science Reports*, **24**, 225.
- 5 Chen, J.G., Menning, C.A. and Zellner, M.B. (2008) *Surface Science Reports*, **63**, 201.
- 6 Kitchin, J.R., Norskov, J.K., Barteau, M.A. and Chen, J.G. (2004) Role of strain and ligand effects in the modification of the electronic and chemical properties of

- bimetallic surfaces. *Physical Review Letters*, **93**, 156801.
- 7 Khan, N.A., Murillo, L.E. and Chen, J.G. (2004) *The Journal of Physical Chemistry B*, **108**, 15748.
 - 8 Kitchin, J.R., Khan, N.A., Barteau, M.A., Chen, J.G., Yakshinskiy, B. and Madey, T.E. (2003) *Surface Science*, **544**, 295.
 - 9 Basu, P., Ballinger, T.H. and Yates, J.T. (1988) *Review of Scientific Instruments*, **59**, 1321.
 - 10 NIST Chemistry WebBook <http://webbook.nist.gov/>.
 - 11 Kiselev, A.V. and Lygin, V.I. (1975) *Infrared Spectra of Surface Compounds*, John Wiley & Sons, Inc., New York.
 - 12 Shimanouchi, T. (1972) *Tables of Molecular Vibrational Frequencies Consolidated*, National Bureau of Standards.
 - 13 Colthup, N.B., Daly, L.H. and Wiberley, S.E. (1990) *Introduction to Infrared and Raman Spectroscopy*, Academic Press, Inc., San Diego, CA.
 - 14 Khan, N.A., Murillo, L.E., Shu, Y.Y. and Chen, J.G.G. (2005) *Catalysis Letters*, **105**, 233.
 - 15 Kresse, G. and Hafner, J. (1993) *Physical Review B: Condensed Matter*, **47**, 558.
 - 16 Kresse, G. and Furthmuller, J. (1996) *Computational Materials Science*, **6**, 15.
 - 17 Kresse, G. and Furthmuller, J. (1996) *Physical Review B: Condensed Matter*, **54**, 11169.
 - 18 Vanderbilt, D. (1990) *Physical Review B: Condensed Matter*, **41**, 7892.
 - 19 Kresse, G. and Hafner, J. (1994) *Journal of Physics: Condensed Matter*, **6**, 8245.
 - 20 Goda, A.M., Barteau, M.A. and Chen, J.G. (2006) *The Journal of Physical Chemistry B*, **110**, 11823.
 - 21 Hammer, B. and Norskov, J.K. (1995) *Nature*, **376**, 238.
 - 22 Gauthier, Y., Baudoing, R., Joly, Y., Rundgren, J., Bertolini, J.C. and Massardier, J. (1985) *Surface Science*, **162**, 342.
 - 23 Bertolini, J.C. et al. (1982) *Surface Science*, **119**, 95.
 - 24 Detemmerman, L., Creemers, C., Vanhove, H., Neyens, A., Delichere, P., Massardier, J., Tardy, B., Abon, M. and Bertolini, J.C. (1983) *Vide-Science Technique et Applications*, **38**, 275.
 - 25 Gauthier, Y., Joly, Y., Baudoing, R. and Rundgren, J. (1985) *Physical Review B: Condensed Matter*, **31**, 6216.
 - 26 Redhead, P.A. (1962) Thermal desorption of gases. *Vacuum*, **12**, 203.
 - 27 Humbert, M.P., Murillo, L.E. and Chen, J.G. (2008) *ChemPhysChem*, **9**, 1262.
 - 28 Khan, N.A., Zellner, M.B., Murillo, L.E. and Chen, J.G.G. (2004) *Catalysis Letters*, **95**, 1.
 - 29 Hwu, H.H., Eng, J., Jr. and Chen, J.G. (2002) *Journal of the American Chemical Society*, **124**, 702.
 - 30 Williams, D.B. and Carter, C.B. (1996) *Transmission Electron Microscopy*, Plenum Press, New York.
 - 31 Shu, Y., Murillo, L.E., Bosco, J.P., Huang, W., Frenkel, A.I. and Chen, J.G. (2008) *Applied Catalysis A-General*, **339**, 169.
 - 32 Frenkel, A.I., Hills, C.W. and Nuzzo, R.G. (2001) *The Journal of Physical Chemistry B*, **105**, 12689.
 - 33 Menning, C.A. and Chen, J.G. (2008) *Journal of Chemical Physics*, **128**, 164703.
 - 34 Li, B.T., Kado, S., Mukainakano, Y., Miyazawa, T., Miyao, T., Naito, S., Okumura, K., Kunimori, K. and Tomishige, K. (2007) *Journal of Catalysis*, **245**, 144.
 - 35 Chen, Y.G. and Ren, J. (1994) *Catalysis Letters*, **29**, 39.
 - 36 Xu, Z., Li, Y.M., Zhang, J.Y., Chang, L., Zhou, R.Q. and Duan, Z.T. (2001) *Applied Catalysis A: General*, **213**, 65.
 - 37 Morikawa, K., Shirasaki, T. and Okada, M. (1969) *Advances in Catalysis*, (eds. Eley, D.D., Pines, H and Weisz, P.B.) 20 Academic Press Inc., 97–133.
 - 38 Salagre, P., Fierro, J.L.G., Medina, F., and Sueiras, J.E. (1996) *Journal of Molecular Catalysis A: Chemical*, **106**, 125.
 - 39 Yan, J.Y., Kung, H.H., Sachtler, W.M.H. and Kung, M.C. (1998) *Journal of Catalysis*, **175**, 294.
 - 40 Yan, J.Y., Kung, M.C., Sachtler, W.M.H. and Kung, H.H. (1997) *Journal of Catalysis*, **172**, 178.

9

Self-Assembled Materials for Catalysis

Kake Zhu, Donghai Wang, and Jun Liu

9.1

Introduction

Catalysis is pivotal to the world's economy and chemical industry. It was estimated that around 90% of the chemical products of current commercial processes are derived from heterogeneous catalytic processes [1]. Besides industrial applications to produce chemicals, catalysts also find applications in producing valuable pharmaceutical, automobile, food, and petrochemical products from raw materials. The deficiency of nonrenewable fossil energy sources (petroleum, coal, natural gas, etc.) in the near future and its environmental consequences, of global warming, present new challenges in catalyst development. Keys to most of the feasible processes to alternative fuels (hydrogen or methanol economy) are the design and function of novel catalysts [2–4]. From the “Green Chemistry” point of view, it is also essential to develop new catalysts and alternative processes that eliminate the utilization of toxics or produce harmful by-products [5]. Heterogeneous catalysis occurring on the surface of solids is stimulated by active sites, which catalyze a surface reaction by lowering the activation energy to a specific reaction pathway. The reaction pathway, in turn, determines what type and the yield of the products (activity and selectivity). Moreover, to reach the catalytically active sites, the reactants need to diffuse through the boundary layer surrounding the catalyst particle before intraparticle diffusion and chemical adsorption. The products will also need to experience a reverse process to leave the catalyst after the reaction [6]. Therefore, surface structure or chemistry controls the catalytic activity and selectivity kinetically. Tailoring the surface properties and structures of catalyst support provides an effect way to design catalysts with anticipated catalytic activity. Porosity, on the other hand, determines the mass transfer and heat transfer effects, which are crucial to the transport controlled reactions. Tailoring the porosity of catalysts also provides a way to achieve shape-selectivity through either sieving of substrates (intermediates) or products or tailoring the structure of transition states [7].

Most commercial catalysts are composed of high surface area support on which active species are well dispersed, so that the number of active sites is maximized.

These active species function in the form of small particles (normally in the nanometer-size range). The catalytic activity and selectivity are dependent on the size, shape, and surface structure of the active species, as well as their compositions. For instance, gold nanoparticles are found to be highly sensitive to their size during CO oxidation. Only the ones within the nanometer scale are active [8]. Single-site iron, copper, and titanium on mesoporous silica showed high activity in catalyzing oxidation of alkenes in the liquid phase [9]. Self-assembly has proven to be an effective way to produce microporous or mesoporous materials and nanoscale materials. The materials, when used as catalysts or support, paved new roads for designing heterogeneous catalysts at both surface structure and porosity levels. These newly developed materials have shown impressive improvements in comparison with their counterparts. They also offer precisely controlled synthesis of model catalytic systems and enable a better understanding of surface structure–porosity–catalytic activity relationships.

Among the high surface area catalysts widely used nowadays, zeolites prevail in the applications as catalysts and supports, as well as in separation and purifications. Zeolites are a series of crystalline microporous (<2 nm, according to IUPAC classifications) solids that possess high internal surface area, unique surface chemistry, precise pore channels (less than 0.8 nm) and cavities (typically, less than 1.5 nm) close to molecular scale, controlled framework structures, and tunable electron static field inside the microporous channels. This provides high shape and size selectivity for guest molecules [10]. These merits, together with their high thermal and hydrothermal stability, make zeolites almost ideal supports for catalysts. However, their major drawback of small pore channels imposes diffusion limitations and causes high back pressure in flow systems [11]. In order to facilitate the mass transportation of zeolites, mesoporous materials with pores (ranging from 2 to 50 nm) larger than micropores have been developed as a substitute for zeolites. On the other hand, creating additional porosity in zeolitic materials during the assembly of template with inorganic precursors offers an alternative method to improve diffusion. Besides porous solids, nanoparticles with surface functional groups do not have such a diffusion problem and become another possible solution to heterogenize active species as catalysts. In this chapter, we will briefly review some new developments on self-assembled nanostructured materials (i.e., nanoporous and nanoparticle-based materials) and their catalytic applications. As there are some reviews available for the metal-based nanoparticles as catalysts [12], we will mainly talk about oxides and related materials.

9.2

Mesocale Design

Self-assembly of cationic surfactant with inorganic siliceous precursor to form a mesophase was first found in a patent in 1971 [13a], which was left unknown due to the lacking of structural information. During 1989–1993, Kato and coworkers developed an intercalation method to synthesize ordered mesoporous silica from

polysilicate kanemite, whose series were named folded sheet mesoporous materials (FSM) [14]. When a similar method was developed in 1992 by Mobil researchers (MCM-41, MCM-48 and MCM-50) and the structure was well resolved, great efforts were made to understand the formation mechanism and its applications [13, 14]. MCM-41 shows a well-ordered hexagonal array of cylinder pores, with a quite narrow pore-size distribution. The pore walls are made up of noncrystalline amorphous silica. MCM-48 and MCM-50 are cubic and lamellar in their mesophase structure, respectively. After these earlier efforts, Stucky and Huo developed the surfactant–inorganic precursor interaction mechanism to extend the preparation to a variety of ionic surfactants, these interactions can be classified into S^+I^- , S^-I^+ , $S^+X^-I^+$, and $S^-M^+I^-$ pathways and be used for preparation of nonsiliceous mesoporous transition metal oxides and mixed oxides [15]. Pinnavaia and coworkers first used a nonionic template to prepare mesoporous materials through S^0I^0 hydrogen-bonding between polyethylene oxides and inorganic species. These mesoporous silica have a less-ordered wormhole-like structure, but the pore-size distribution of the material is reasonably narrow and the pore walls are thick compared with the ionic surfactant templated mesoporous materials, therefore, more thermally stable [16]. Later in 1998, Stucky and coworkers reported another mesoporous silica (e.g., SBA-15 and SBA-16) prepared from tri-block copolymer [17]. SBA-15 and SBA-16 possess a large pore size of above 6 nm, and are more thermally stable compared with previously reported ones. More interestingly, there are interconnected microchannels between the pores, thus forming a three-dimensional interconnected porous system. As far as formation mechanism is concerned, the Mobil researchers first proposed a liquid crystal templating (LCT) model, which suggests cylindrical micelles formed with the mediation of charged silicate clusters during formation of ordered hexagonal arrays. Polar groups of surfactants in the cylindrical micelles stretch outward, while the silicates fill the space in-between, subsequently [13c–d]. Davis and coworkers, based on their *in situ* observations on the formation of mesophase silica, proposed that the micelles formed when positively charged surfactants attract several layers of negatively charged silicate, which then self-assemble into ordered structures [18]. Currently the widely acceptable mechanism, the charge-density matching theory, was proposed by Stucky and coworkers, who suggested that the self-assembly occurs through a cooperative interaction between the organic templates and inorganic polyions during the hydrolysis of the precursors. The latter changed the charge density at their interface and tailored the subsequent mesophase, ranging from hexagonal, cubic, to lamellar mesophases. The ordering of micelles before inorganic wall formation is not necessary, and the rate-determining step controlling the formation of the mesophase is thus hydrolysis of the inorganic precursors [15, 19]. The Stucky mechanism was proved by *in situ* observations for mesophase formation and direct observations in later publications [19–21]. It is noteworthy to mention that the interactions between inorganic precursors are also important for the increased crosslinking on the pore walls, which controls the stability of the final porous solids [22].

Besides efforts to find new ways to tailor the structures and porosity of silica, at almost the same time, applications of these materials are under intense investigation

in the field of heterogeneous catalysis. Silica materials are covered by weak acidic silanols that are catalytically inert and have to be functionalized to be used as catalysts. Many methods are thereby being employed to modify the surfaces of the pore channels. These methods can be divided into the following two major categories: postsynthesis modifications on mesoporous materials, and *in situ* self-assembly functionalized mesoporous materials [21, 23]. Herein, we focus on the self-assembly functionalized catalytic materials. The following topics are elaborated: (1) inclusion of heteroatoms into the mesoporous silica walls; (2) nanoscale metal oxides embedded on the silica walls; (3) self-assembly of metal oxides into mesoporous solids, and (4) nonsiliceous mesoporous materials from molecular precursors.

9.2.1

Inclusion of Heteroatoms

9.2.1.1 Acid Sites

As acidic zeolite-based catalysts form a large category of heterogeneous catalysts and the small micropore size of zeolites limits larger molecules from approaching the active sites, it is intuitive to use aluminated mesoporous silica to circumvent such a problem. Similar to the case in zeolites, substitution of tetra-coordinated silicon by a trivalent atom will create an acidic proton to compensate for the charge balance. Al^{3+} , B^{3+} , Ga^{3+} , and Fe^{3+} have been extensively studied [24] as substitutes for tetra-coordinated Si^{4+} into mesoporous silica. Synthesis of the materials normally starts with alkoxides or salts in the presence of silica precursors. In the case of using MCM-48 as support, the following ordering of acid strength is evidenced: $\text{Al} > \text{Ga} > \text{Fe}$ [24f]. Two kinds of acid sites are observed for the substituted silica surfaces: the Brønsted sites and the Lewis sites, due to the coexistence of tetra-coordinated framework and extra-framework oxides. For instance, to the typical aluminated silica, two peaks can be observed by ^{27}Al MAS NMR. The one close to $\delta = 52$ ppm is from tetra-coordinated framework which creates Brønsted sites, while the other one from $\delta = 0$ ppm is from octa-coordinated extra-framework Lewis sites. Washing with NH_4Cl is found capable of removing some of the Lewis sites [24a]. For Al-containing MCM-41, it is also evidenced that calcination leads to exclusion of aluminum from the framework and causes loss of strong acid sites, consequently, and the acidity of acid site becomes much weaker compared with the same sites in zeolites, as a result of the noncrystalline nature of the pore walls [26]. When Al-SBA-15 is directly synthesized, it is found to be more chemically stable and thermally stable than MCM-41 [25]. As far as catalytic applications are concerned, the acid sites modified mesoporous silica are more active than zeolites for typical Brønsted sites catalyzed reactions, especially for reactions of larger molecules. For instance, cumene cracking is found to be much easier in Al-SBA-15 than Al-MCM-41. It can be attributed to the existence of larger pores and interconnecting small pores in SBA-15, which facilitates the mass transfer and therefore promotes both the conversion and selectivity [24a,g]. For Al-, Ga-, and Fe-substituted MCM-48, when used as catalyst for acetone conversion, the majority of active sites are composed of weak-to-medium acid sites, while minorities of strong acid sites coexist, which can be the reason for low selectivity [24f].

Attempts were made to prepare frameworks of crystalline pore walls or semi-crystalline walls in order to combine the merits of zeolites and mesoporous simultaneously [27, 23]. Kaliaguine group used SBA-15 and a housemade ZSM-5 gel as the starting material, and recrystallized the composite in glycerol to prepare such a composite material [27]. The use of both zeolitic and mesoscopic dual templates were also studied by several groups, but there is no direct evidence for homogeneous structure in the composites [27, 28], and there are doubts that these materials may be composed of mixtures of both components [11a]. Alternatively, creating additional porosity in zeolites is another option, as studied by several groups [29, 11a]. Some successful attempts from the self-assembly approach include using polymers as cotemplates [30] or silanes [31] as silica sources, which produce materials with both crystalline zeolite morphologies and mesoporosities. Figure 9.1 shows the structure of mesoporous beta zeolite from the co-template method. The mesoporous zeolite is highly crystalline and used as catalyst for alkylation of benzene, exhibiting improved activity and selectivity for the desired products (Figure 9.2) [30]. Ryoo and coworkers developed another method to synthesize mesoporous aluminated zeolites of MFI and LTA structures by using a silane-based surfactant [3-(trimethoxysilyl) propyl]hexadecyldimethylammonium chloride; from SEM and TEM images, the mesoporous zeolite could be identified intuitively (Figure 9.3). The catalytic syntheses of vesidryl and jasminaldehyde by acidic sites of MFI structure were compared with their noncrystalline counterparts and conventional zeolites, Table 9.1 shows these results: For large molecule substrates, the activity is prominent. Similarly, mesoporous H-ZSM-5 has shown improved activity and selectivity in the catalytic

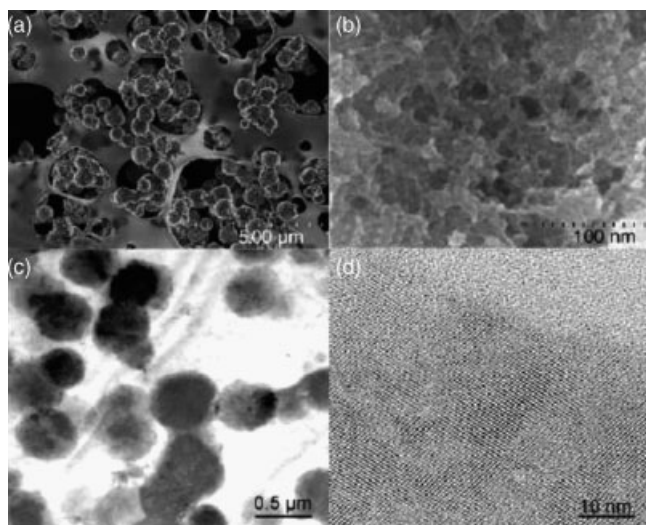


Figure 9.1 SEM and TEM images of hierarchical mesoporous zeolites Beta from tetraethyl-ammonium hydroxide and polydiallyldimethylammonium chloride bitemplating, which is highly crystalline as evidenced by HRTEM of (d) [30].

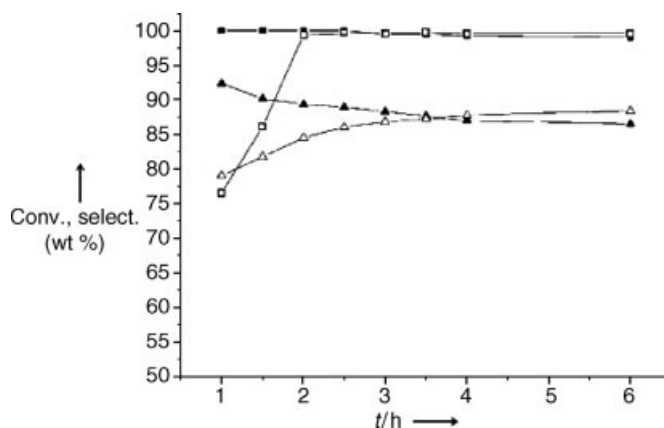


Figure 9.2 Reference [30], Catalytic conversions (conv. [wt%]) and selectivities (select. [wt %]) in the alkylation of benzene with propan-2-ol with various zeolites samples as a function of reaction time (reaction temperature: 200 °C; 4 : 1 benzene/propan-2-ol; reaction pressure: 2.0 MP). Conversion on Beta-H (solid square); selectivity on Beta-H (hollow square); conversion on Beta zeolite (solid triangle); selectivity on Beta zeolite (hollow triangle).

benzene alkylation to ethylbenzene due to highly crystalline pore walls and hierarchical porosity that make the acid sites strong and mass transportation easy, as evidenced by ^{27}Al MAS NMR and ammonia temperature programmed desorption (TPD) patterns [32].

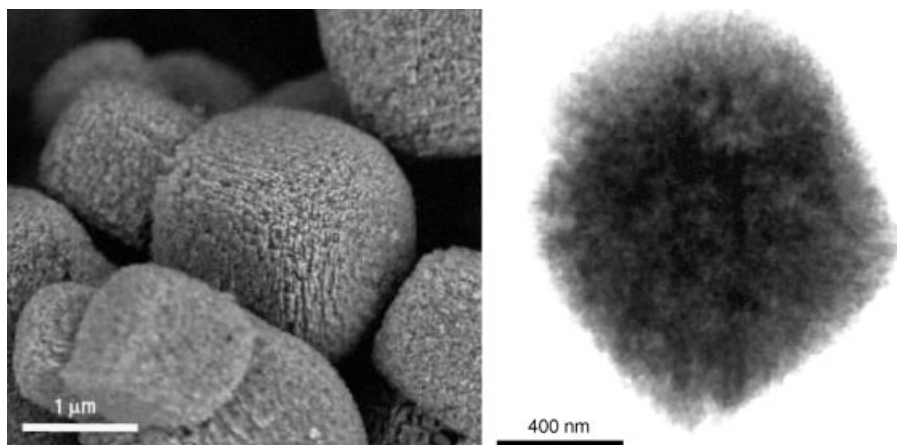
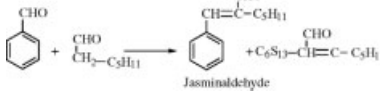
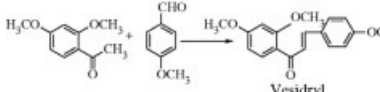


Figure 9.3 SEM and TEM images of crystalline zeolite with mesoporosity from [3-(trimethoxysilyl)propyl] hexadecyldimethylammonium chloride ($[(\text{CH}_3\text{O})_3\text{SiC}_3\text{H}_6\text{N}(\text{CH}_3)_2\text{C}_{16}\text{H}_{33}]\text{Cl}$, TPHAC) [31].

Table 9.1 Catalytic properties of mesoporous MFI zeolite and other aluminosilicate materials.

Reactions ^a	Mesoporous MFI zeolite	Bulk ZSM-5Al	MCM-41	SAM
Methanol to olefin/gasoline	86 (68/26/6) ^b	90 (67/28/5)	≤1 —	≤1 —
 Jasminaldehyde	98 (98) ^c	3.9 (69)	25 (79)	64 (75)
 Vesidryl	60	3.3	10	35

^aCatalytic activities were compared on the basis of the same weight of catalysts (see section “Methods” for reaction conditions). All catalysts had the same Si/Al = 20. The Brunauer–Emmett–Teller (BET) surface area was 590 for mesoporous MFI, 350 for ZSM-5, 948 for AlMCM-41, and 923 m² g^{−1} for SAM (MCM-41-type).

^bThe numbers in parentheses represent % selectivity (olefin/gasoline/others).

^cJasminaldehyde selectivity. All other numbers indicate the reactant conversion (%).

9.2.1.2 Dispersed Metal Oxides

Besides acid sites, other transition metals have also been included into mesoporous silica through self-assembly of metal alkoxide or salts together with siliceous sources. When combined with the high surface area of mesoporous supports, the transition metal-substituted mesoporous silica have shown many improved properties in heterogeneous catalysis [21, 23]. In Ti-MCM-41 and Ti-HMS, there are abundant tetra-coordinated Ti sites on surface of mesochannels that show superior activity in catalytic oxidation of 2,6-di-*tert*-butyl phenol to the corresponding quinone and the conversion of benzene to phenol. In the former case, conversion of 83% is achieved in Ti-HMS as compared to 6.5% of conventional TS-1, without sacrificing of selectivity (>95% for both) [33]. This extraordinary result is attributed to site-isolation of most active sites, predominance of 4-coordinated titanium species sitting independent of the framework claimed by the authors [33a,b]. However, Corma and coworkers found that the intrinsic catalytic activity was not as high when compared to the zeolitic counterpart TS-1. However, when large molecular substitutes participate, mesoporous Ti-containing materials were more catalytically active, due to the obstacles from microporosities of zeolites in mass transportation during reactions [33c]. Beside Ti-mesoporous silica, other transition metal-substituted mesoporous materials show similar improved catalytic properties by means of enhanced mass transport of large molecular reactants. When tungsten substituted mesoporous silica is used as catalyst for the selective oxidation of cyclopentene to glutaraldehyde in *tert*-butanol solvents, high selectivity and high conversion (85%) is achieved at a high H₂O₂ efficiency (60–77%) [34]. In the case of directly synthesized vanadium-containing mesoporous silica, most vanadium species are highly dispersed and no large aggregates are found at low contents, as shown by ⁵¹V NMR and Raman spectra. The V-containing mesoporous silica also exhibits high activity in liquid phase H₂O₂ oxidation of large molecules, such as cyclododecane and 1-naphthol [35].

Substitution of heteroatoms into the mesoporous silica walls, as one way to prepare heterogeneous catalysts, possesses the merits of simplicity in preparation, high dispersion, and versatility in structure control, but problems exist such as low-loading, low thermal or hydrothermal stability, lack of precise control over active sites, deep-embedded atoms being unavailable to substrates and leaching during reactions. It is desirable to develop methods to tailor the surface structures more precisely and to enhance the stability of these systems. Postsynthetic modifications (impregnation, ion exchange, ship-in-a-bottle synthesis, etc.) have been investigated to achieve this goal.

9.2.2

Embedded Nanoparticles

Although nanoscale metals have been used in heterogeneous catalysis for a long time, empirical methods do not provide precise control over catalyst sizes [36]. As nanoscale particles have high surface area, high surface-to-bulk atomic ratio (unsaturated surface atoms are more active), size and support effects are crucial to our understanding as well as applications. Combination of nanoparticles with mesoporous materials through self-assembly methods provides us a new way to design catalysts. Through the self-assembly approach, nanoparticles can be well dispersed within a high surface area support and the final material is no longer susceptible to sintering. Two categories of metal oxide precursor can be used: either molecule or nanoparticle. For instance, iron ethoxide can be used as a precursor to form iron oxide nanoparticles embedded on the aluminosilicate wall through self-assembly of copolymer and inorganic sources [37], and titanium isopropoxide can be used to synthesize anatase nanoparticle-embedded mesoporous silica [38]. Alternatively, preformed nanoparticles of CeO_2 are employed to self-assemble with tetraethyl orthosilicate (TEOS) by using poly(alkylene oxide) block copolymer as template in acidic media. A highly ordered hexagonal structured composite material is produced after calcination of organics. On the silica wall, discrete highly crystalline CeO_2 nanoparticles are embedded, which are stable up to 800°C due to the protection of thick pore walls. Such a composite material, by itself or after doping with vanadium, shows high activity in sulfur removal during gasoline cracking [39].

For metallic nanoparticles to be embedded into the inorganic wall, it is convenient to adopt some chelating reagents, which build up linking between the metal ions and inorganic wall. For example, with the help of bis[3-(triethoxysilyl)propyl]tetrasulfide, HAuCl_4 can be coprecipitate with TEOS during its hydrolysis, and be included into the silica wall of mesoporous silica SBA-15 [40]. Figure 9.4 shows the diagram of the preparation procedures. Gold ions are inserted into silica matrix and subsequently converted to metallic gold after removal of surfactant upon calcination. The ultrafine Au nanoparticles show improved thermal stability at silica surface. After calcinations at 500°C to remove the organics, the particles size is around 3 nm for a 1.5 wt% loading, which is the most favorable size for their catalytic activity [8]. As Au is found to be highly mobile on silica surfaces as a result of the weak acidic nature of its surfaces (low isoelectric point), it is hard to immobilize nanoparticles and prevent

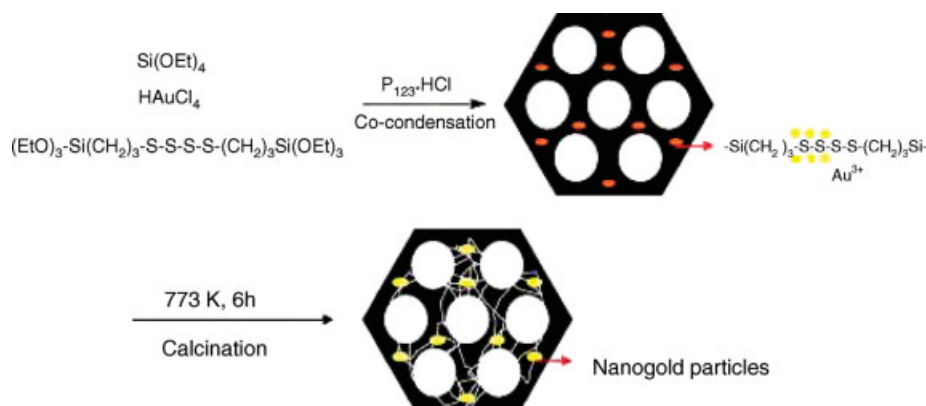


Figure 9.4 Graphical representation of the preparation processes for mesoporous silica catalysts with gold nanoparticles in the walls [40].

aggregation under reaction conditions [41], and thus the conventional loading method to confine gold nanoparticles within mesopores can hardly produce particles of around 2–3 nms [42]. The embedded Au nanoparticles are available to reactant substrates because of the interconnected micropores created by calcinations of polymer templates. The catalysts are found to have high activity ($\text{TOF} = 377$) for the aerobic oxidation of benzyl alcohols and cyclohexanol. No growth of particle size is observed after three catalytic cycles. Another case is Pt-embedded SBA-15 recently reported by Yang and Somorjai [43]. The authors first prepare a Pt colloid of controlled size (1.7–7.1 nm) with the assistance of poly(vinylpyrrolidone). The Pt nanoparticles are then dispersed in the synthetic gel of SBA-15 at neutral pH media, where NaF is used to mineralize siliceous source. During the preparation, neutral pH is adjusted to match the colloid stability with that of the mesophase micelles. Ethylene hydrogenation and ethane hydrogenolysis activity are tested. The former reaction is insensitive to particle size, while the latter is found to be more active as the particle size is decreased. This can be attributed to the roughness of surfaces for smaller particles, as shown by their CO adsorption of active surface area [43]. In this inclusion chemistry of nanoparticles in silica walls, SBA-15 is preferred because of the thick walls (3–4 nm) between channels and their thermal stability.

9.2.3

Nonsiliceous Mesoporous Materials

Nonsiliceous metal oxide synthesis and applications in catalysis attract much attention [21, 44]. Mesoporous transition metal oxides are attractive heterogeneous catalysts or catalyst support compared with the bulk oxides because they possess high surface area and expose large numbers of active sites. Moreover, their large pores are superior for mass transportation. Despite the lack of crosslinking between the metal oxides wall that makes them less stable and collapse after template removal [45], there are some successful examples in catalysis applications. For clarity of description, we

divide these examples into two parts with respect to the inorganic source: molecule self-assembly and nanoparticle self-assembly.

9.2.3.1 Molecule Self-Assembly to Mesoporous Catalysts

Metal alkoxides or chlorides that are normally used as sources self-assemble with organic surfactants including ionic and nonionic surfactants to synthesize mesoporous oxides catalysts. To prepare a V-TiO₂ catalyst with a BET surface area of more than 1000 m² g⁻¹, Yoshitake and coworkers [46] synthesized mesoporous mixed oxides by using dodecylamine as template and vanadium oxytriisopropoxide and titanium tetraisopropoxide as metal sources. Interestingly, the directly prepared catalyst has V⁴⁺ dominant on the surface, while the postsynthesized sample has a lot of the V⁵⁺ species. The catalyst V-TiO₂ catalyzed the propylene oxidation with a higher selectivity towards CO₂ than the postsynthesized ones. Kapoor and coworkers [47] studied the production of hydrogen through methanol decomposition over ultrafine Pd supported on mesoporous TiO₂, which showed superior catalytic activity to commercial ones. Serre and coworkers [48] reported preparation of thermally stable cubic and hexagonal mesoporous tin phosphates using SnF₄ as metal source and cationic surfactants as templates. The materials exhibit catalytic activity to the deNO_x reaction in the presence of ethane. Ammonia adsorption indicates that the surface are strong acidic, suggesting that these materials can also be used in acid sites catalyzed reactions. Preparation of mesoporous titanium phosphate in a similar way by using both cationic and anionic templates was achieved by Toyota researchers, the inorganic matrix also possesses ion exchange capabilities and the Ti and P are tetra-coordinated. When used to catalyze the oxidation of cyclohexene, it showed high activity and selectivity to 1,2-cyclohexanediol, as the active sites for this reaction is the tetra-coordinated Ti [49].

Besides being used as catalysts, these mesoporous oxides show improved catalytic behavior when used as supports. Mesoporous alumina-supported Ru is superior in olefin metathesis to other types of alumina [50], mesoporous ZrO₂ and CeO₂ prepared using inorganic salts are stable catalyst supports. For instance, Pd supported on ZrO₂ is better than nonporous supports when used in phenol hydrogenation, resulting from high dispersion [51]. Catalytic application of mesoporous materials are not limited to oxides; micro- and mesoporous silicon imido nitride from an organic self-assembly method promoted by potassium showed pore-size dependent selectivity towards products [52]. The mesoporous materials from molecule self-assembly are, nevertheless, noncrystalline in pore wall structure, which limited their applications to low temperatures and relatively mild conditions. It is, therefore, desirable to develop mesoporous materials with crystalline walls. One such endeavor is exemplified as to use a preformed crystalline nanoparticle as inorganic source, to self-assemble into mesoporous structures with the assistance of templates.

9.2.3.2 Nanoparticles Self-Assembly to Mesoporous Catalysts

Early efforts to prepare mesophased materials from nanoscale building blocks were made first by Ying and coworkers, who firstly synthesized a tungstated zirconium oxide through the self-assembly of copolymer surfactant with zirconium oxide colloid sol and ammonium metatungstate. The composite material is thermally stable but

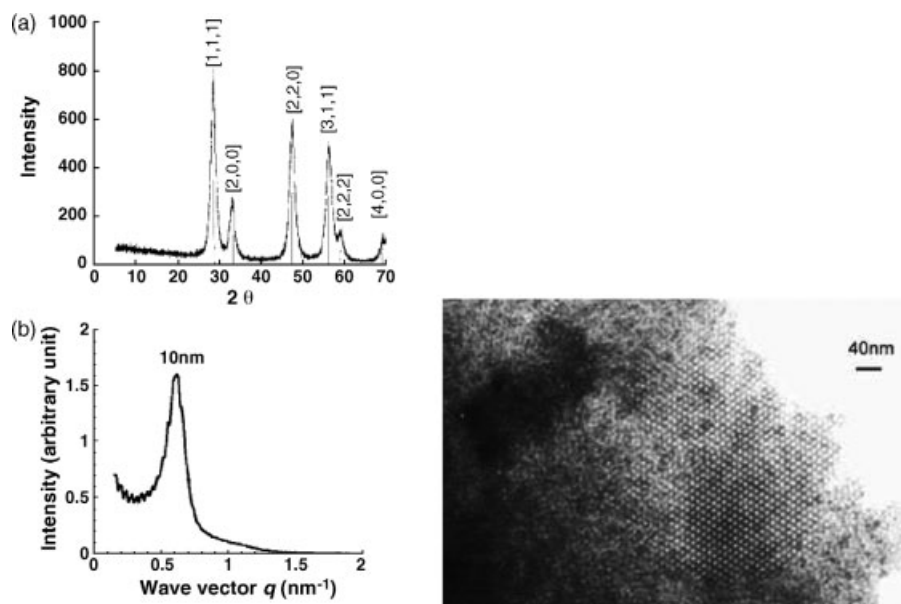


Figure 9.5 Low angle and wide angle XRD patterns, TEM images of self-assembled CeO_2 nanoparticles after calcination at 500°C [55].

not highly crystalline [53]. Corma and coworkers developed a method to synthesize mesoporous metal oxides ZrO_2 , CeO_2 , and $\text{CeO}_2\text{-Al}(\text{OH})_3$ using 3 nm CeO_2 , 5 nm ZrO_2 , and 3 nm $\text{Al}(\text{OH})_3$ colloids as starting materials, and copolymers as templates. Figure 9.5 shows the XRD patterns at both low angle and wide angle of CeO_2 together with the corresponding microscopic images. It is a well-ordered mesoporous structure with crystalline nature. To create strong interactions between nanoparticles and surfactants to facilitate the self-assembly, small bifunctional molecules are used. For example, $-\text{COOH}$ in 6-aminocaproic acid will combine with CeO_2 surface hydroxyl groups, while the amine interacts with poly(alkylene oxide) of the surfactants. When employed as photo anodes in photoelectrochemical solar cells, the novel mesoporous crystalline CeO_2 exhibits a photovoltaic response due to high surface area semiconductor properties [54, 55]. CeO_2 is a potential oxygen conductor and therefore suitable for aerobic oxidation support. When Au nanoparticles are loaded, the mesoporous CeO_2 was used to catalyze the selective aerobic oxidation of aliphatic and aromatic aldehydes. It exhibits better activity and selectivity than other reported catalysts. Furthermore, the catalysts can be recycled, due to the stability under reaction conditions [56].

9.2.4

Self-Assembly of Zeolite Seeds into Mesophase

Employing the nanosized zeolite seeds to prepare zeolites with hierarchical porous structures attracted much attention after the discovery of MCM-41, as a result of

failure of crystallization of walls of mesophase through postsynthesis. Pinnavaia and coworkers have used Y-zeolite seeds to prepare mesoporous Al-MSU-S. When a probe catalytic reaction of cumene cracking is used, improved activity is achieved using Al-MSU-S with respect to conventional Al-MCM-41; ^{27}Al MAS NMR shows that the chemical shift is closer to a structure of zeolitic structures and steaming stability is therefore enhanced. However, at above 800 °C, the low stability may result from carbon formation instead of framework stability [57]. When ZSM-5 or β -seeds are employed as a starting material to self-assemble to mesophase of MCM-41, the mesoporous material is found to be intrinsically stable and does not require the presence of occluded carbon for steam stability [58]. At almost the same time, Xiao and coworkers published similar methods for zeolite clusters to self-assemble into the BEA-structure. Catalytic activity of 2-butene in the alkylation of isobutane with butane, and 1,3,5-triisopropylbenzene were compared with zeolites and mesoporous counterparts. The improvement for mesoporous zeolites is dramatic in catalytic activity compared with conventional Al-MCM-41. It is impressive that the stability of the catalytic alkylation is the best of the three. The activity of HZSM-5 and Al-MCM-41 decays after 10 and 17 h, respectively, while the composite material shows little decay during the whole test period of 20 h [59].

9.2.5

Organic Functional Groups as Catalysts

Organic functionalizations of ordered mesoporous materials attracted great attention in the field of heterogeneous catalysis for their abilities to immobilize metal ion centers through chelating or anchoring of negatively charged polyoxometalates (POMs) (normally, through positively charged protonated amines by means of electric static interactions), or directly as metal-free catalysts. The functionalization of surface silanols is completed by either postsynthetic grafting of organosilanes or direct *in situ* synthesis of mesoporous silica with addition of the functional precursors [21, 23, 60]. For example, to add amine groups on the surface, 3-aminopropyltrialkoxysilane is used as a precursor, 3-mercapto- is the precursor for immobilization of thiol groups, and so on. Davis and coworkers designed a catalyst on mesoporous silica with discrete pairs of sulfonic acid and thiol groups for condensation of acetone and phenols. The bifunctional catalyst is three time more active than randomly distributed active sites [61]. The precise control of the synthetic procedure and precursor to design a catalyst at the nanoscale enables the positioning of active sites on the surface of support rather than sporadic dispersion, which is quite different from zeolite materials [62]. Another feature of mesoporous catalysts is heterogenization of chiral catalysis in nanopores. Most of the currently used enantioselective catalysts are from noble-metal-based organometallic molecule in homogeneous solutions, which possesses the disadvantage of difficulty in separation of the catalysts from products or substrates, recyclable use of catalysts, low costs, and so on. It is therefore highly desirable to develop a method for a heterogeneous system without loss of activity and selectivity in chiral catalysis. This has been exemplified by some groups. When cationic Rh(I) complexes containing the chiral diamino ligands and cyclooctadiene were tethered to

catalyze hydrogenation of methyl benzoylformate. The enantiomer excess (ee) values were actually boosted as compared with the homogeneous systems [63, 64]. Positively charged protonated amines can adsorb negatively charged polyoxometalates through attraction, which provides a way to load POMs on mesoporous silica with almost a monolayer dispersion inside the mesochannels. Negligible leaching was observed as a result of the strong interaction. The loaded POMs showed reasonably good activity for C–H bond activation and selective oxidation using H_2O_2 or air as the oxidants. It was found that for large substrates, large pore featured SBA-15 is more favorable than MCM-41 [65, 66]. The ship-in-a-bottle synthesis of catalysts taking advantage of high surface area of mesoporous materials and surface silanols to anchor designed active sites within a confined nanoscale space represents the future trend of heterogeneous catalysts.

9.3

Designing Catalysts at the Nanoparticle Surfaces

Catalytic studies of nanomaterials rely heavily on their preparation methods and stabilization approaches to avoid aggregating during reactions. So far, most of the catalysts using nanoparticles as active species originate from supported nanoparticles on high surface area porous solids, for which postsynthetic methods such as wet impregnation, grafting, and deposition are normally adopted. As an alternative, self-assembly of nanoscale building blocks to organized heterogeneous catalysts broadened our knowledge of preparation and showed extraordinary activity and selectivity in catalysis, given below in Section 9.3.1 are some examples.

9.3.1

Polyoxometalates: Nanoparticles with Cations

Polyoxometalates, a class of metal oxides with a great variety of compositions and structures, have showed catalytic activities for reactions such as olefin oxidations to epoxides, oxidative dehydrogenation of alkanes, or isomerizations by using their redox and acid properties. These compounds are themselves nonporous solids, and therefore, only a very few surface sites are available for substrates. To enlarge the surface area, besides supporting techniques, self-assembly techniques were developed [67, 68]. Substitution of protons in $\text{H}_3\text{PW}_{12}\text{O}_{40}$ with large Cs^+ cations will induce a self-assembly of the Keggin polyanions, and form a homogeneous composite material with interparticle mesoporosity. The polyanion emulates other solid acids such as zeolites or superacids such as $\text{SO}_4^{2-}/\text{ZrO}_2$ in catalytic activities, for isomerizations of *n*-pentane and *n*-hexane where coking was circumvented [68, 69]. Alternatively, Hill and coworkers recently designed POMs based catalysts through the cationic $(\text{Si}/\text{AlO}_2)^{n+}$ nanoparticle-induced self-assembly, in which positively charged nanoparticles with balanced Cl^- anions were ion-exchanged with POM anions driven by the greater strong interaction between nanoparticles and POM anions. An iron-containing POM was used for aerobic oxidation of tetrahydrothiophene to

tetrahydrothiophene oxide. The turnover number was promoted upon loading with respect to the homogeneous system, and the same trend was observed for 2-chloroethyl ethyl sulfide aerobic oxidation [70, 71].

9.3.2

Dendrimer-Stabilized Metal Nanoparticles

Metal nanoparticles are important to the application in catalysis with respect to conversion and yields due to their high surface area and size-dependent properties, however, selectivity is still a challenge [72]. Dendrimer entrapped metal nanoparticles have showed size selectivity in heterogeneous catalysis recently. Dendrimers are a series of macromolecules with specific molecular weight and structure. Their shape resembles trees or cauliflower and thus forms nanoscale spaces under the terminal layer between the branches. Once the metal particles are entrapped inside the internal spaces, only substrates smaller than the terminal gates could reach the catalytic center and proceed with the anticipated reactions, while the large ones are bounced backward. In an examination of hydrogenation of allyl alcohols by 2 nm Pd nanoparticles encapsulated within hydroxyl-terminated poly(amidoamine) dendrimers, Chung and coworkers found that the turnover frequency drops as the molecular size of substrates increases, or when the packing density on the dendrimer periphery is enhanced [73]. The preparation scheme is shown in Figure 9.6. This concept has been extended to bimetallic alloys or core-shell type nanoparticles. For the same type of hydrogenation reactions, a core-shell structure is superior to a mixed alloy [74]. Using nanoparticles as catalysts is one future trend for heterogeneous catalysis along with a focus on nanoscience and technology [72].

9.4

Perspectives

In summary, self-assembly of molecules, crystalline seeds, and nanoscale building blocks into organized mesoscopic structures opens up new routes for the tailoring of catalytic active structures and porosities simultaneously, which actually has boosted heterogeneous catalysts design from micrometer scale to the molecular and nanometer scale. The developments on the mechanism of self-assembly processes enabled us to design and synthesize new materials for catalysis-related applications. Numerous improvements in terms of basic understandings on structure–activity relationships, as well as new catalytic systems have been made [21, 23]. In spite of this progress, many challenges still exist: (1) Function-oriented multicomposites materials synthesis from self-assembly are needed. (2) The micro- and surface structures of some systems or formation mechanism are still not clear, and tailoring of active sites, their structure and spacing is difficult. (3) Stabilities of these meso- or nanomaterials can be a problem for their applications under critical reaction conditions, like high temperature, pressure, or under steaming. (4) Many nice lab syntheses will be hard at elevated scales. (5) Leaching is still a problem in liquid phase reactions, as a result of

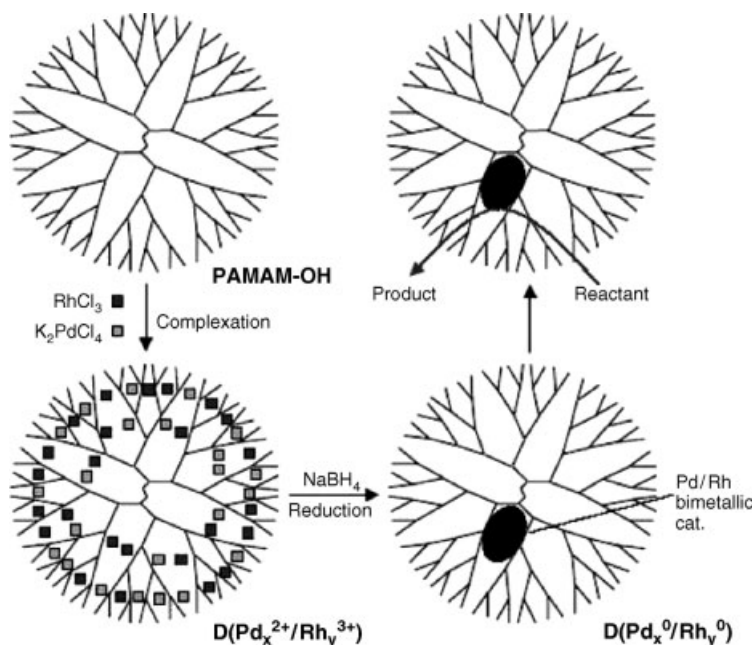


Figure 9.6 Method for nanoparticles encapsulated in PAMAM or PPI dendrimers: complexation of a metal cation to the inner nitrogen atoms of tertiary amines, then reduction to metals by NaBH_4 , and partial aggregation produces particles within the dendrimer, size and shape selectivity are achieved by peripheries [73].

the weak surface immobilization. (6) Cost needs to be reduced. (7) Environmental impact should be considered. Future efforts should be made toward finding solutions to these concerns in self-assembled materials, in particular, in heterogeneous catalysis.

References

- 1 National Research Council Panel on New Directions in Catalytic Sciences and Technology (1992) *Catalysis Looks to the Future*, National Academy Press, Washington D.C., p. 1.
- 2 Huber, G.W., Chheda, J.N., Barrett, C.J. and Dumesic, J.A. (2005) *Science*, **308**, 1446–1450.
- 3 Armor, J.N. (2005) *Catalysis Letters*, **101**, 131–135.
- 4 Olah, G.A. (2005) *Angewandte Chemie-International Edition*, **44**, 2636–2639.
- 5 Sheldon, R.A. (2007) *Green Chemistry*, **9**, 1273–1283.
- 6 Thomas, J.M. and Thomas, W.J. (1997) *Principles and Heterogeneous Catalysis*, VCH, Weinheim, p. 669.
- 7 (a) Jacobs, P.A., Martens, J.A., Weitkamp, J. and Beyer, H.K. (1981) *Faraday Discussions*, 353–369. (b) Haag, W.O., Lago, R.M., Weisz, P.B. (1981) *Faraday Discussions*, 317–330. (c) Derouane, E.G., Dejaive, P., Gabelica, Z. and Vedrine, J.C. (1981) *Faraday Discussions*, 331–344.

- (d) Thomas, J.M., Millward, G.R., Ramdas, S., Bursill, L.A. and Audier, M. (1981) *Faraday Discussions*, 345–352. (e) Corma, A., Rey, F., Valencia, S., Jorda, J.L. and Rius, J. (2003) *Nature Materials*, 2, 493–497.
- 8 (a) Bond, G.C. and Thompson, D.T. (1999) *Catalysis Reviews-Science and Engineering*, 41, 319–388. (b) Bell, A.T. (2003) *Science*, 299, 1688–1691.
- 9 (a) Nozaki, C., Lugmair, C.G., Bell, A.T. and Tilley, T.D. (2002) *Journal of the American Chemical Society*, 124, 13194–13203. (b) Fajdala, K.L., Drake, I.J., Bell, A.T. and Tilley, T.D. (2004) *Journal of the American Chemical Society*, 126, 10864–10866. (c) Maschmeyer, T., Rey, F., Sankar, G. and Thomas, J.M. (1995) *Nature*, 378, 159–162.
- 10 (a) Corma, A. (1997) *Chemical Reviews*, 97, 2373–2419. (b) Breck, D.W. (1974) in *Zeolite Molecular Sieves*, Robert E. Krieger Publishing Company, Inc., Malabar, FL.
- 11 (a) Tao, Y.S., Kanoh, H., Abrams, L. and Kaneko, K. (2006) *Chemical Reviews*, 106, 896–910. (b) van Donk, S., Broersma, A., Gijzeman, O.L.J., van Bokhoven, J.A., Bitter, J.H. and de Jong, K.P. (2001) *Journal of Catalysis*, 204, 272–280. (c) Herrmann, C., Haas, J. and Fetting, F. (1987) *Applied Catalysis*, 35, 299–310. (d) Perez-Ramirez, J., Kapteijn, F., Groen, J.C., Domenech, A., Mul, G. and Moulijn, J.A. (2003) *Journal of Catalysis*, 214, 33–45.
- 12 (a) Narayanan, R. and El-Sayed, M.A. (2005) *Journal of Physical Chemistry B*, 109, 12663–12676. (b) Ott, L.S. and Finke, R.G. (2007) *Coordination Chemistry Reviews*, 251, 1075–1100. (c) Astruc, D., Lu, F. and Aranzas, J.R. (2005) *Angewandte Chemie-International Edition*, 44, 7852–7872.
- 13 (a) Chiola, V., Ritsko, J.E. and Vanderpool, C.D. (1971) US Patent 3,556,725. (b) DiRenzo, F., Cambon, H. and Dutartre, R. (1997) *Microporous Materials*, 10, 283–286. (c) Kresge, C.T., Leonowicz, M.E., Roth, W.J., Vartuli, J.C. and Beck, J.S. (1992) *Nature*, 359, 710–712. (d) Beck, J.S., Vartuli, J.C., Roth, W.J., Leonowicz, M.E., Kresge, C.T., Schmitt, K.D., Chu, C.T.W., Olson, D.H., Sheppard, E.W., McCullen, S.B., Higgins, J.B. and Schlenker, J.L. (1992) *Journal of the American Chemical Society*, 114, 10834–10843.
- 14 (a) Yanagisawa, T., Shimizu, T., Kuroda, K. and Kato, C. (1990) *Bulletin of the Chemical Society of Japan*, 63, 988–992. (b) Inagaki, S., Fukushima, Y. and Kuroda, K. (1993) *Journal of the Chemical Society-Chemical Communications*, 680–682.
- 15 (a) Huo, Q.S., Margolese, D.I., Ciesla, U., Feng, P.Y., Gier, T.E., Sieger, P., Leon, R., Petroff, P.M., Schuth, F. and Stucky, G.D. (1994) *Nature* 368 317–321. (b) Huo, Q.S., Margolese, D.I. and Stucky, G.D. (1996) *Chemistry of Materials*, 8, 1147–1160.
- 16 (a) Bagshaw, S.A., Prouzet, E. and Pinnavaia, T.J. (1995) *Science*, 269, 1242–1244. (b) Tanev, P.T. and Pinnavaia, T.J. (1995) *Science*, 267, 865–867.
- 17 (a) Zhao, D.Y., Feng, J.L., Huo, Q.S., Melosh, N., Fredrickson, G.H., Chmelka, B.F. and Stucky, G.D. (1998) *Science*, 279, 548–552. (b) Zhao, D.Y., Huo, Q.S., Feng, J.L., Chmelka, B.F. and Stucky, G.D. (1998) *Journal of the American Chemical Society*, 120, 6024–6036.
- 18 Chen, C.-Y., Burkett, S.L., Li, H.-X. and Davis, M.E. (1993) *Microporous Materials*, 2, 21–34.
- 19 (a) Stucky, G.D., Monnier, A., Schuth, F., Huo, Q., Margolese, D., Kumar, D., Krishnamurthy, M., Petroff, P., Firouzi, A., Janicke, M. and Chmelka, B.F. (1994) *Molecular Crystals and Liquid Crystals Science and Technology Section A—Molecular Crystals and Liquid Crystals*, 240, 187–200; (b) Huo, Q.S., Margolese, D.I., Ciesla, U., Demuth, D.G., Feng, P.Y., Gier, T.E., Sieger, P., Firouzi, A., Chmelka, B.F., Schuth, F. and Stucky, G.D. (1994) *Chemistry of Materials*, 6, 1176–1191.
- 20 Firouzi, A., Kumar, D., Bull, L.M., Besier, T., Sieger, P., Huo, Q., Walker, S.A., Zasadzinski, J.A., Glinka, C., Nicol, J., Margolese, D., Stucky, G.D. and Chmelka, B.F. (1995) *Science*, 267, 1138–1143.
- 21 Taguchi, A. and Schuth, F. (2005) *Microporous and Mesoporous Materials*, 77, 1–45.

- 22 Tian, B.Z., Liu, X.Y., Tu, B., Yu, C.Z., Fan, J., Wang, L.M., Xie, S.H., Stucky, G.D. and Zhao, D.Y. (2003) *Nature Materials*, **2**, 159–163.
- 23 On, D.T., Desplandier-Giscard, D., Danumah, C. and Kaliaguine, S., (2003) *Applied Catalysis A – General*, **253**, 543–602.
- 24 (a) Yue, Y.H., Gedeon, A., Bonardet, J.L., Melosh, N., D’Espinose, J.B. and Fraissard, J. (1999) *Chemical Communications*, 1967–1968. (b) Tuel, A. (1999) *Microporous and Mesoporous Materials*, **27**, 151–169. (c) On, D.T., Joshi, P.N. and Kaliaguine, S. (1996) *Journal of Physical Chemistry*, **100**, 6743–6748. (d) Fricke, R., Kosslick, H., Lischke, G. and Richter, M. (2000) *Chemical Reviews*, **100**, 2303–2405. (e) Kosslick, H., Lischke, G., Walther, G., Storek, W., Martin, A. and Fricke, R. (1997) *Microporous Materials*, **9**, 13–33; (f) Kosslick, H., Lischke, G., Landmesser, H., Parltitz, B., Storek, W. and Fricke, R. (1998) *Journal of Catalysis*, **176**, 102–114. (g) Mokaya, R. and Jones, W. (1997) *Chemical Communications*, 2185–2186.
- 25 Gedeon, A., Lassoued, A., Bonardet, J.L. and Fraissard, J. (2001) *Microporous and Mesoporous Materials*, **44**, 801–806.
- 26 Corma, A., Fornes, V., Navarro, M.T. and Perezpariente, J. (1994) *Journal of Catalysis*, **148**, 569–574.
- 27 On, D.T. and Kaliaguine, S., (2002) *Angewandte Chemie-International Edition*, **41**, 1036–1040.
- 28 Huang, L.M., Guo, W.P., Deng, P., Xue, Z.Y. and Li, Q.Z. (2000) *Journal of Physical Chemistry B*, **104**, 2817–2823.
- 29 Jacobsen, C.J.H., Madsen, C., Houzvicka, J., Schmidt, I. and Carlsson, A. (2000) *Journal of the American Chemical Society*, **122**, 7116–7117.
- 30 Xiao, F.S., Wang, L.F., Yin, C.Y., Lin, K.F., Di, Y., Li, J.X., Xu, R.R., Su, D.S., Schlogl, R., Yokoi, T. and Tatsumi, T. (2006) *Angewandte Chemie-International Edition*, **45**, 3090–3093.
- 31 Choi, M., Cho, H.S., Srivastava, R., Venkatesan, C., Choi, D.H. and Ryoo, R. (2006) *Nature Materials*, **5**, 718–723.
- 32 Christensen, C.H., Johannsen, K., Schmidt, I. and Christensen, C.H. (2003) *Journal of the American Chemical Society*, **125**, 13370–13371.
- 33 (a) Tanev, P.T., Chibwe, M. and Pinnavaia, T.J. (1994) *Nature*, **368**, 321–323. (b) Zhang, W.H., Froba, M., Wang, J.L., Tanev, P.T., Wong, J. and Pinnavaia, T.J. *Journal of the American Chemical Society*, **118**, 9164–9171. (c) Corma, A., Navarro, M.T., Perezpariente, J. and Sanchez, F. (1994) in *Zeolites and Related Microporous Materials: State of the Art 1994*, Elsevier Vol. 84, pp. 69–75.
- 34 (a) Chen, H., Dai, W.L., Deng, J.F. and Fan, K.N. (2002) *Catalysis Letters*, **81**, 131–136. (b) Yang, X.L., Dai, W.L., Gao, R.H., Chen, H., Li, H.X., Cao, Y. and Fan, K.N. (2005) *Journal of Molecular Catalysis A – Chemical*, **241**, 205–214.
- 35 (a) Reddy, J.S. and Sayari, A. (1995) *Journal of the Chemical Society-Chemical Communications*, 2231–2232. (b) Reddy, J.S. and Sayari, A. (1995) *Journal of the Chemical Society-Chemical Communications*, 2231–2232.
- 36 Schlogl, R. and Abd Hamid, S.B. (2004) *Angewandte Chemie-International Edition*, **43**, 1628–1637.
- 37 Garcia, C., Zhang, Y.M., DiSalvo, F. and Wiesner, U. (2003) *Angewandte Chemie-International Edition*, **42**, 1526–1530.
- 38 Dong, W.Y., Sun, Y.J., Lee, C.W., Hua, W.M., Lu, X.C., Shi, Y.F., Zhang, S.C., Chen, J.M. and Zhao, D.Y. (2007) *Journal of the American Chemical Society*, **129**, 13894–13904.
- 39 Corma, A., Chane-Ching, J.Y., Airiau, M. and Martinez, C. (2004) *Journal of Catalysis*, **224**, 441–448.
- 40 Hu, J.C., Chen, L.F., Zhu, K.K., Suchopar, A. and Richards, R. (2007) *Catalysis Today*, **122**, 277–283.
- 41 Wolf, A. and Schuth, F. (2002) *Applied Catalysis A: General*, **226**, 1–13.
- 42 Zhu, K.K., Hu, J.C. and Richards, R. (2005) *Catalysis Letters*, **100**, 195–199.
- 43 Song, H., Rioux, R.M., Hoefelmeyer, J.D., Komor, R., Niesz, K., Grass, M., Yang, P.D. and Somorjai, G.A. (2006) *Journal of the*

- American Chemical Society*, **128**, 3027–3037.
- 44 Schuth, F. (2001) *Chemistry of Materials*, **13**, 3184–3195.
 - 45 Yang, P.D., Zhao, D.Y., Margolese, D.I., Chmelka, B.F. and Stucky, G.D. (1999) *Chemistry of Materials*, **11**, 2813–2826.
 - 46 Yoshitake, H. and Tatsumi, T. (2003) *Chemistry of Materials*, **15**, 1695–1702.
 - 47 Kapoor, M.P., Ichihashi, Y., Kuraoka, K. and Matsumura, Y. (2003) *Journal of Molecular Catalysis A – Chemical*, **198**, 303–308.
 - 48 Serre, C., Auroux, A., Gervasini, A., Hervieu, M. and Ferey, G. (2002) *Angewandte Chemie-International Edition*, **41**, 1594–1597.
 - 49 Bhaumik, A. and Inagaki, S. (2001) *Journal of the American Chemical Society*, **123**, 691–696.
 - 50 Onaka, M. and Oikawa, T. (2002) *Chemistry Letters*, 850–851.
 - 51 Velu, S., Kapoor, M.P., Inagaki, S. and Suzuki, K. (2003) *Applied Catalysis A: General*, **245**, 317–331.
 - 52 Farrusseng, D., Schlichte, K., Spliethoff, B., Wingen, A., Kaskel, S., Bradley, J.S. and Schuth, F. (2001) *Angewandte Chemie-International Edition*, **40**, 4204–4207.
 - 53 Wong, M.S., Jeng, E.S. and Ying, J.Y. (2001) *Nano Letters*, **1**, 637–642.
 - 54 Corma, A., Atienzar, P., Garcia, H. and Chane-Ching, J.Y. (2004) *Nature Materials*, **3**, 394–397.
 - 55 Chane-Ching, J.Y., Cobo, F., Aubert, D., Harvey, H.G., Airiau, M. and Corma, A. (2005) *Chemistry – A European Journal*, **11**, 979–987.
 - 56 Corma, A. and Domine, M.E. (2005) *Chemical Communications*, 4042–4044.
 - 57 Liu, Y., Zhang, W.Z. and Pinnavaia, T.J. (2000) *Journal of the American Chemical Society*, **122**, 8791–8792.
 - 58 Liu, Y., Zhang, W.Z. and Pinnavaia, T.J., (2001) *Angewandte Chemie-International Edition*, **40**, 1255–1258.
 - 59 Zhang, Z.T., Han, Y., Zhu, L., Wang, R.W., Yu, Y., Qiu, S.L., Zhao, D.Y. and Xiao, F.S., (2001) *Angewandte Chemie-International Edition*, **40**, 1258–1302.
 - 60 Liu, J., Shin, Y., Nie, Z.M., Chang, J.H., Wang, L.Q., Fryxell, G.E., Samuels, W.D. and Exarhos, G.J. (2000) *Journal of Physical Chemistry A*, **104**, 8328–8339.
 - 61 Margelefsky, E.L., Zeidan, R.K., Dufaud, V. and Davis, M.E. (2007) *Journal of the American Chemical Society*, **129**, 13691–13697.
 - 62 Dufaud, V. and Davis, M.E. (2003) *Journal of the American Chemical Society*, **125**, 9403–9413.
 - 63 Li, C., Zhang, H.D., Jiang, D.M. and Yang, Q.H. (2007) *Chemical Communications*, 547–558.
 - 64 Raja, R., Thomas, J.M., Jones, M.D., Johnson, B.F.G. and Vaughan, D.E.W. (2003) *Journal of the American Chemical Society*, **125**, 14982–14983.
 - 65 Kaleta, W. and Nowinska, K. (2001) *Chemical Communications*, 535–536.
 - 66 Chen, L.F., Zhu, K., Bi, L.H., Suchopar, A., Reicke, M., Mathys, G., Jaensch, H., Kortz, U. and Richards, R.M. (2007) *Inorganic Chemistry*, **46**, 8457–8459.
 - 67 Mizuno, N. and Misono, M. (1998) *Chemical Reviews*, **98**, 199–217.
 - 68 Mizuno, N., Yamaguchi, K. and Kamata, K. (2005) *Coordination Chemistry Reviews*, **249**, 1944–1956.
 - 69 Liu, Y.Y., Koyano, G., Na, K. and Misono, M. (1998) *Applied Catalysis A–General*, **166**, L263–L265.
 - 70 Okun, N.M., Anderson, T.M. and Hill, C.L. (2003) *Journal of the American Chemical Society*, **125**, 3194–3195.
 - 71 Okun, N.M., Anderson, T.M. and Hill, C.L. (2003) *Journal of Molecular Catalysis A – Chemical*, **197**, 283–290.
 - 72 Astruc, D., Lu, F. and Aranzas, J.R. (2005) *Angewandte Chemie-International Edition*, **44**, 7852–7872.
 - 73 Khung, Y.M. and Rhee, H.K. (2003) *Journal of Molecular Catalysis A–Chemical*, **206**, 291–298.
 - 74 Scott, R.W.J., Wilson, O.M., Oh, S.K., Kenik, E.A. and Crooks, R.M. (2004) *Journal of the American Chemical Society*, **126**, 15583–15591.

10

Theory-Aided Catalyst Design

Matthew Neurock

10.1

Introduction

The design of new catalytic materials can be broadly categorized by two rather different approaches, namely, combinatorial screening and scientific discovery. The former involves very rapid synthesis and testing of tens to hundreds of thousands of material samples for specific properties. It is based on the premise that faster is better and that rapid automated testing will readily narrow down phase space to find new material leads that can then be tested by more classical kinetic studies. The approach was adapted from combinatorial drug discovery methods that have had some success in identifying new target molecules. The application of combinatorial screening to heterogeneous catalysis has been more difficult due to the structural complexity of the materials, the reaction conditions, the physico-chemical steps that comprise the catalytic cycle, and the active sites that carry out both selective and unselective reactions [1–12]. Despite the complexity, there are a number of catalytic materials that have been discovered by such methods and a number of companies which have adopted this technology [4–13]. The second and more classic approach to catalyst design is based on hypothesis-driven research involving detailed characterization studies, rigorous kinetic analyses, and mechanistic studies to determine how a particular catalytic reaction proceeds and establish the factors that control the catalytic behavior [1–3, 6, 8–10, 13]. The latter approach is based on the premise that fundamental knowledge will establish the factors that control the catalytic performance and aid in the discovery process. For catalysis, this requires an in-depth understanding of the nature of the active site and its local reaction environment, and their collective influence on the elementary steps that govern catalytic reactions. This knowledge-based approach requires detailed characterization along with rigorous kinetic analyses in which hypotheses are generated and tested to establish the critical factors and material features that control catalysis. This involves a significant effort that can last over years or even decades. There are a number of known examples where this knowledge-based approach has led to important catalyst discoveries [6, 8–10].

These two approaches present the two extremes in catalyst development today and as such bracket most of the catalyst discovery approaches that are currently employed. This is shown schematically in Figure 10.1, which presents what we define as the “materials discovery cone,” where the number of materials tested is plotted (x-axis) against the knowledge acquired (y-axis). The top of the cone represents combinatorial approaches that involve very rapid screening of different material compositions but generate very little knowledge. The bottom of the cone perhaps refers to the sole researcher who has worked for years to elucidate the fundamental factors that control a particular catalytic reaction. There is a tremendous amount of knowledge about how

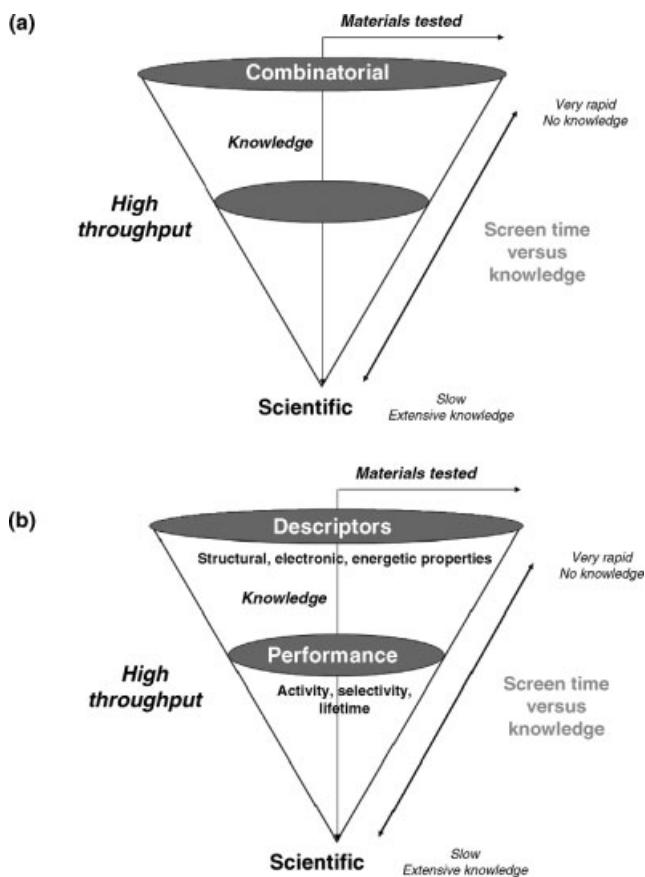


Figure 10.1 Schematic depiction of the current methods for catalyst discovery. (a) The experimental catalyst discovery cone is bracketed by combinatorial discovery approaches that rapidly synthesize and screen many different materials in order to systematically map out the phase space. The bottom of the cone involves more traditional scientific discovery that is based

on the development and application of knowledge. (b) The computational catalyst discovery cone is bracketed by methods that rapidly calculate simple descriptors in order to rapidly scan the phase space or through detailed *ab initio* methods that are used to determine catalytic mechanisms.

the particular catalytic reaction proceeds, but the results tend to be limited to just a few materials. One could argue at great length the merits and drawbacks of both approaches. The compromise between the two is the more pragmatic high-throughput approach that combines knowledge with rapid catalytic testing, under more realistic conditions and tries to capitalize on the best of both approaches. It has generated perhaps the greatest industrial following. The number of materials that can be rapidly tested and the degree of knowledge acquired from the experiments dictate the specific positioning along the discovery cone in Figure 10.1a.

The tremendous advances in computing that have taken place over the past two decades have made theory and simulation valuable partners with experiment and have enabled the transition from an era of fundamental understanding and elucidation to one of theory-driven materials discovery. *Ab initio* methods together with coarse-grained simulations are being used not only to elucidate the properties and reactivity of molecules and materials but also to begin tailoring the design of new materials [14, 15]. The use of theory and simulation in materials discovery can be categorized much in the same way as the one presented for experimental discoveries using a very similar material discovery cone as is shown in Figure 10.1b.

There have been a number of advances in combining theory and simulation to provide fundamental structural descriptors with which to rapidly test the structural, electronic, and the chemical properties of a large array of molecules to understand their reactivity [5]. Much of this effort has been focused on the development of structure–property and structure–activity relationships that are subsequently used together with theory and simulation to rapidly screen different molecules to establish potential new leads.

The development of a set of similar simple descriptors to describe heterogeneous catalyzed reactions has been much more challenging, since catalytic behavior usually does not correlate with the properties of the bulk materials. There may be important *chemical* descriptors, however, that can be used to help screen for important catalytic properties [1–3]. This will undoubtedly require more detailed information about the nature of the active site and its complex nanoscale environment, since they control the rate at which elementary catalytic steps proceed. The complexity of the active site and its environment, however, typically obscures our ability to isolate such descriptors from experimental analyses alone.

At the opposite end of the computational discovery cone is purely knowledge-driven discovery. This might involve the use of *ab initio* methods to elucidate all possible reaction paths and establish the full potential energy surface. In addition, *ab initio* methods can be used to determine surface coverage, alloying, particle size and morphology, and support effects [14]. The degree of fundamental knowledge would be very high and would likely lead to suggestions for other metal systems that might be more active. The effort, however, could take years just to elucidate one catalytic system over a single supported metal catalyst, and thus the degree of screening might be very limited.

The optimal balance between the two approaches might involve the use of *ab initio* methods to determine the best potential catalytic descriptors or the use of kinetic simulations to test how changes in the catalyst influence its activity or selectivity.

In the past 5 years, there has been an increasing shift to *ab initio* studies where theory and simulation are used to carry out some of the first elements for catalyst design [14–21]. These studies lie at different points along the hierarchical knowledge axis of the materials discovery funnel, in terms of the number of systems screened and the available information that is ultimately uncovered. Herein, we present a series of different example studies from the literature and from our own work and describe their relative positioning along the discovery funnel as well their impact on catalyst development and future directions.

10.2

Catalytic Descriptors

As already discussed above, classic structural and chemical property descriptors tend to fail when used in the context of heterogeneous catalyst design due to the complexity of the catalyst and the influence of structure and function within the catalytic cycle. A longstanding goal in heterogeneous catalysis has been to tie the structural, compositional, or bulk electronic properties of metals and alloy systems to their catalytic performance [14]. Catalytic performance, however, is typically not governed by the bulk properties of a material. As such, these efforts have often failed. Most of the experimental high-throughput and combinatorial approaches have therefore focused solely on establishing very simple descriptors such as catalyst composition with which to assess catalytic performance. Modeling has thus not played any real role in connecting to these high-throughput efforts. One approach, would be to use theory to elucidate the factors that control a particular reaction and establish the controlling structural features. There is the hope that, for a specific class of reactions, a general or universal descriptor or set of descriptors based on electronic properties, chemical bonding, bond energies, or kinetics can be used to explain the observed catalytic behavior and guide the search for new materials.

10.2.1

Electronic Descriptors

Hammer and Nørskov have elegantly shown through the use of formal chemisorption theory that the d-band center of a metal can be tied to the intrinsic strength of the chemical bond that forms between the metal and an adsorbate. The d-band center has proven to be an ideal descriptor of the adsorption properties as well as the intrinsic reactivity of different metal surfaces [22–24]. The formal relationship between the d-band center and the metal–adsorbate bond energy can be derived from a tight binding analysis of coupling of the d-band of the metal with the one-electron state of the adsorbate. The resulting binding energy is given in Equation 10.1:

$$E_{\text{d-hyb}} = \frac{2(1-f)\beta V_{\text{ad}}^2}{\epsilon_{\text{d}} - \epsilon_{\text{a}}} + 2(1+f)\alpha\beta V_{\text{ad}}^2 \quad (10.1)$$

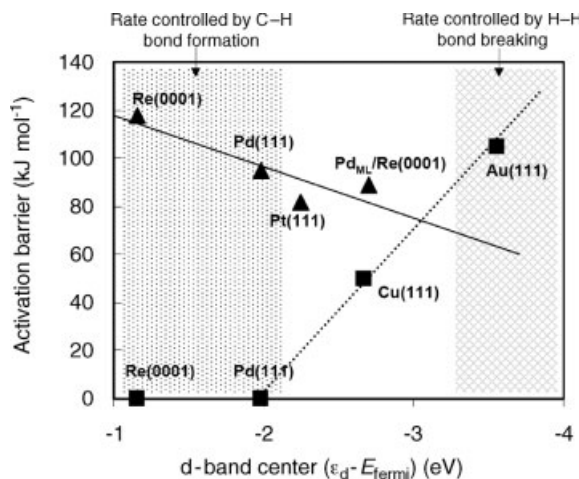


Figure 10.2 The correlation of DFT-calculated activation barriers for the addition of the first hydrogen to maleic anhydride and the activation of molecular hydrogen with the d-band center of the metal surface. (Source: Ref. [26]).

where f is the fractional filling of the d states, V_{ad}^2 refers to the square of the coupling d-matrix elements, ϵ_d is the energy level for the center of the d-band, and ϵ_a is the energy level of the one-electron state of the adsorbate. The first term on the right-hand side of Equation 10.1 is the result of the attractive bonding interactions, whereas the second term is the result of Pauli repulsion. This equation reduces to a direct correlation between the center of the d-band, ϵ_d , and strength of the metal adsorbate bond when the relative changes in the latter term are small.

The d-band center has been used to correlate with the adatom binding energies, molecular adsorption energies, overall reaction energies, and activation barriers for bimetallic pseudomorphic overlayers and metal alloys. For example, we present in Figure 10.2 the correlation between the activation barriers for the addition of hydrogen to maleic anhydride adsorbed on to Pd monolayers supported on different substrates, together with the barriers for the dissociation of hydrogen over these surfaces against the d-band center projected onto the surface metal layer. There have been a number of studies and reviews on the use of the d-band center to catalytic systems that we refer the interested reader to [22–25]. While the d-band center has proven to be an outstanding descriptor of surface reactivity, we will not focus on it here but will adopt a more pragmatic approach of using energy descriptors such as the adatom binding energy.

10.2.2

Energetic Descriptors

The catalytic activity and selectivity for a heterogeneous catalyzed reaction is ultimately controlled by the kinetics of the elementary steps that govern the surface chemistry. The kinetics for many reactions is controlled by a single rate-determining step that can

be described by a small number of parameters such as the pre-exponential factor, activation barrier, and equilibrium constant. While *ab initio* methods can be used to calculate the activation barriers and equilibrium constants, this requires a rather significant effort and would not be considered rapid screening. It has been shown experimentally and theoretically that the rate constant for a particular reaction in many cases obeys a very simple Brønsted–Evans–Polyani (BEP) relationship whereby the activation barrier is linearly proportional to the heat of reaction [14, 25, 27]:

$$\Delta E_{\text{act}} = \alpha \Delta H_{\text{RXN}}. \quad (10.2)$$

Theory can then be used to more rapidly calculate the heat of reaction for a wide range of systems. There are now a number of examples in the literature where theory has been used quite successfully to demonstrate that the BEP relationship for many reaction systems. While the BEP relationship is based on theoretical constructs and applies to most catalytic systems, it requires that the systems and materials examined fall within a particular reaction family so that any entropic changes that exist between different materials are also linearly related to the changes in enthalpy [27].

10.2.3

Adsorption Energies or Binding Energies

An even simpler descriptor than the heat of reaction would be to use the heat of adsorption of a probe molecule to elucidate the nature of the adsorbate–metal bond strength. It has been found that many reaction steps are governed by the heat of adsorption of the reactants or products depending upon whether the reaction follows an early or late transition state [14, 25, 27]. This can be simplified further in a number of cases to the binding energy of the reactant or product. We have shown previously that reactant, product, or adatom binding energies can serve as key descriptors for catalytic reactions over metals and metal alloy surfaces [14, 27, 28].

We illustrate this here by using the hydrogenation and dehydrogenation of ethylene as a probe reaction due to its importance in the conversion of other hydrocarbon and larger oxygenate intermediates. In the catalytic hydrogenation of olefins, alkenes, aromatic, and other similar hydrocarbons, one must make C–H or X–H bonds as well as break M–H and H–H bonds on the surface. The catalytic kinetics are thus governed by Sabatier’s principle, which indicates that optimal surface is one that can activate the reactants and subsequently allow the associative coupling of surface fragments or desorption of the products to occur as well. As such, there is an optimal metal–adsorbate surface bond strength that controls the surface chemistry. If this interaction is too strong, the surface is poisoned by intermediates or products that form (H^* or C_2H_x^* for this reaction), whereas if the interaction is too weak, it becomes difficult to activate the reactant (H_2 for this reaction). The metal–adsorbate bond is governed by the nature of the atom that interacts with surface. As such, the adsorption energy is directly related to the binding energy of the adatom that anchors the adsorbate to the surface. This idea was originally proposed sometime ago by Shustorovich and Sellers for the development of the bond order conservation (BOC) model [29, 30].

For hydrogenation, this involves the M–H or the M–C bond energy. We can show this by making a series of simplifying assumptions, starting with the assumption that the changes in the activation barrier for different materials are linearly correlated with the changes in the overall reaction energy ($\Delta E_{\text{act}} = \alpha \Delta H_{\text{RXN}}$) [27]. The activation barriers for the hydrogenation of ethylene to ethyl nicely follow the BEP relationship and scale linearly with the heat of reaction, as shown in Figure 10.3a.

A close analysis of the BEP relationship for this first hydrogen addition step, given in Equation 10.3 indicates that the heat of reaction is controlled by the adsorption energy, or the hydrogen binding energy, of the alkyl intermediates as they are the most strongly adsorbed to the metal surface:

$$\Delta E_{\text{act}} = \alpha[(\Delta H_{\text{RC}^*-(\text{CH}_3)}) - \Delta H_{(\text{CH}-\text{CH}_2^*)} - \Delta H_{(\text{RCH}-\text{CH}_2^*)}] \quad (10.3)$$

The activation energies can therefore be linearly related to the alkyl and hydrogen adsorption energies. The barriers also appear to correlate very well with the calculated ethylene adsorption energies as shown in Figure 10.3b [27].

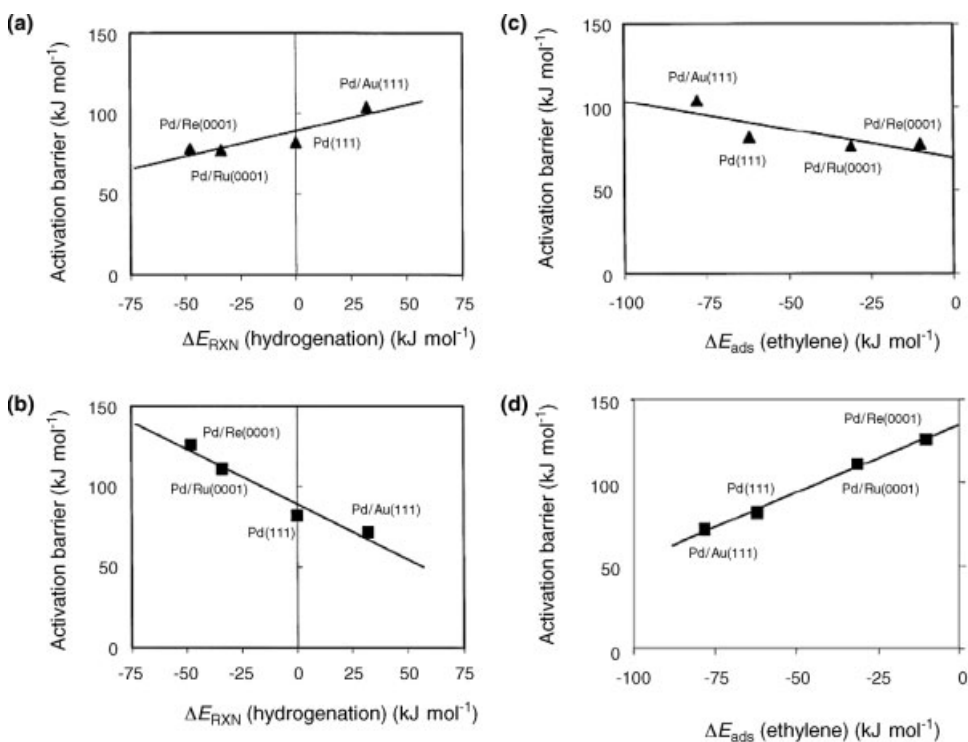


Figure 10.3 Theoretically calculated Brønsted–Evans–Polanyi relationships for the hydrogenation of ethylene and the C=H activation of adsorbed ethyl to ethylene over pseudomorphic overlayers of Pd on Re, Ru, Pd, and Au. The correlation between the activation energy for the correlation between the

hydrogenation of absorbed vinyl to ethylene and (a) its heat of reaction and (b) the heat of adsorption of ethylene as well as the correlation between the activation energy for hydrogenation of ethylene to vinyl and (c) its heat of reaction and (d) the heat of adsorption of ethylene [27].

The correlation can be extended further to show that the metal–carbon and metal–hydrogen bond strength, which governs the adsorption of ethylene and hydrogen, also correlates with the reported activation energies. The M–C and the M–H binding energies can thus be used as predictors that screen various different reactions [27].

The correlation of the barriers with the adatom binding energies should not be too surprising, since Shustorovich and Sellers recognized this over 20 years ago in their pioneering work on the BOC approach [29, 30]. This approach effectively describes the adsorption energies for different molecular intermediates in terms of the bond energy between the M–X bond strength, where X is the atom of the adsorbate bound to the metal. Similar ideas were used to extend this approach to the prediction of activation barriers. BOC thus uses the adatom binding energies on a metal surface together with gas-phase dissociation energies to estimate elementary reaction barriers over different metal surfaces.

We extended our earlier studies on the hydrogenation and dehydrogenation of olefins to the hydrogenolysis of various oxygenates including maleic anhydride [26, 31–33] and acetic acid [34] that are controlled by a similar balance of bond making and breaking processes. Hydrogenolysis, however, is different from hydrogenation as it requires the hydrogenation of both oxygen and carbon sites as well as the ability to break both C–H and C–O bonds. The DFT-calculated results revealed that pseudomorphic overlayers of Pd on Re and Ru were active for hydrogenation due to the weaker M–C and M–H bonds to these surfaces, which enhances the elementary hydrogen addition steps [26, 31–34]. The C–O and C–H activation steps involved in hydrogenolysis, however, require that some of the Re be present in the surface layer to carry out these heterolytic bond activation steps. The DFT-calculated results suggest that the most active catalytic material involves Pd_{ML}/Ru or Pd_{ML}/Re with atomically dispersed Re or Ru in the Pd surface layer.

While the examples presented here were some of the first theoretical efforts to demonstrate the importance of the metal–adsorbate and M–X bond energies in controlling the optimal balance necessary to achieve Sabatier's principle, they were limited to small data sets. As such, they helped to demonstrate the ideas but were not used to screen a large number of systems.

10.2.4

High-Throughput Screening

Nørskov and colleagues have made the most significant advances in moving the concept of descriptors into the realm of catalyst design [15, 19–21, 35–38]. They clearly demonstrated that density functional theory can be used to rapidly calculate and screen hundreds of metal alloys to determine the binding energies of adsorbates and reaction energies of the controlling reaction energies. By combining the results with other important properties such as catalyst cost and Pareto-optimal simulation methods, they were able to suggest a series of novel alloy materials with optimal catalytic functionality for the methanation of CO [19, 21], ammonia synthesis [20, 37–39], and hydrogen evolution [36]. This is a hypothesis-driven approach whereby

detailed theoretical results were carried out first to elucidate the elementary steps that control the specific reaction to help choose the appropriate energetic descriptors.

As an example, we will discuss the approach and findings for the methanation reaction [19, 21]. A set of rigorous density functional theory calculations were carried out to show that the reaction is controlled by the ability of the metal surface to dissociate CO and ultimately remove the C* and O* products that form. These two steps are actually linearly correlated with one another since the transition state that governs the CO activation is a very late transition state that is very similar to the product state. The activation barrier for CO dissociation was found to be linearly correlated with the overall reaction energy in accordance with the Brønsted–Evans–Polyani relationship, as shown in Figure 10.4a [19]. Since both the dissociation and the removal

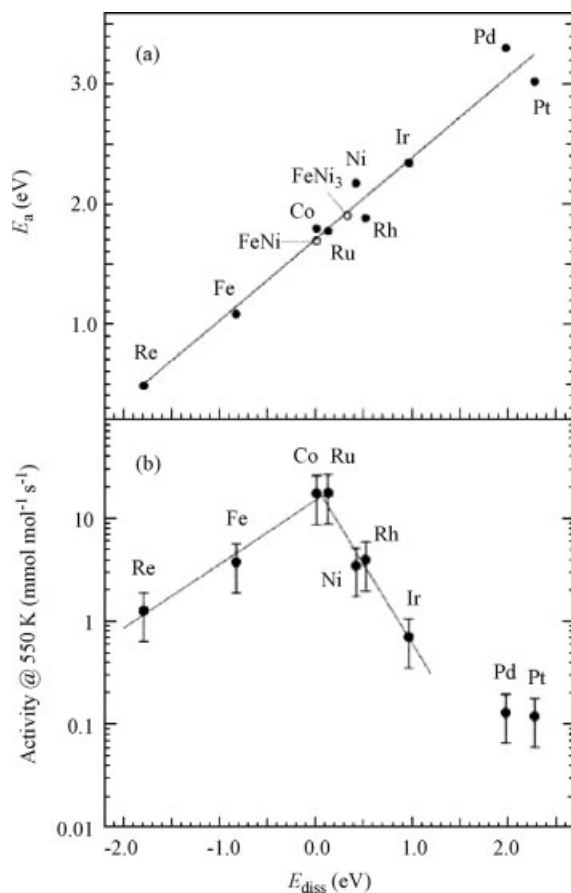


Figure 10.4 (a) BEP relationship for the activation of CO over different closed-packed transition metal surfaces. (b) A comparison of measured catalytic activities for methanation and the CO dissociation energy shows the volcano relationship following the Sabatier's principle [19].

steps are correlated with one another, the catalytic activity can be described by a single property, the CO dissociation energy. The actual experimental methanation activities over different supported metal particles demonstrated a classic volcano-shaped curve when plotted against the CO dissociation energy, as shown in Figure 10.4b. This is indicative of the Sabatier's principle. The metals on the left-hand side readily dissociate CO but are limited by the removal of C^* and O^* from the surface. The metals on the right, however, are limited by their ability to dissociate CO. The most active metals appear to be Co and Ru that have optimal metal–adsorbate bond energies whereby the surface can activate CO and still allow for the removal of carbon and oxygen [19]. The optimal dissociation energy was calculated to be 0.06 eV.

The dissociation energy was then used as a descriptor to screen 117 different alloys of the form A_xB_{1-x} , where x was chosen to be 0, 0.25, 0.5, and 1.0 and comprised the following metals: Ni, Pd, Pt, Co, Rh, Ir, Fe, Ru, and Re [19]. The results indicate that the best alloys combine metals from the left-hand side of the Sabatier curve with those on the right. Cost estimates for each metal were used to establish a multidimensional optimization problem whereby the optimal solution is one based on Pareto-optimal set.

The results, shown in Figure 10.5, plot the cost of the alloy against the descriptor value, which in this case is the dissociation energy of the reaction [19, 21]. Based on the activity descriptor (ΔE_{diss}) alone, the most active metals are Ru and Co. The cost of both Ru and Co, however, is rather high. The optimal materials are those at the bottom left corner or the Pareto-optimal “knee,” which are alloys of iron and nickel (FeNi_3 and NiFe) as they balance both cost and activity. These alloys were subsequently

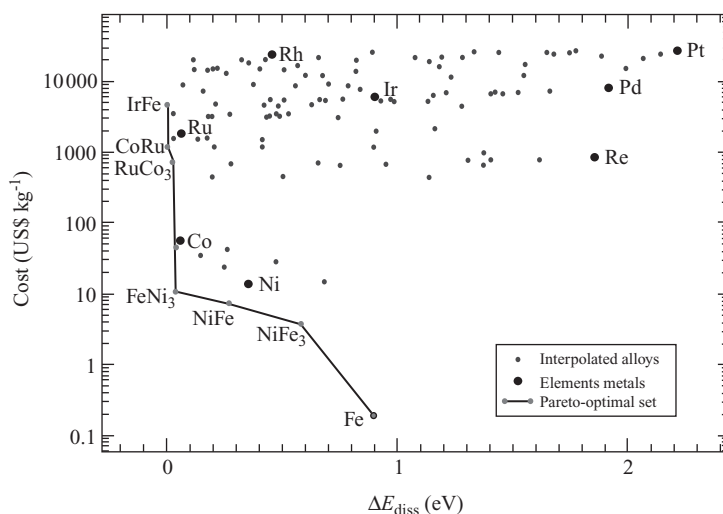


Figure 10.5 Pareto-optimal plot comparing the price for over 117 different metal alloys of the form A_xB_{1-x} (where $x = 0, 0.25, 0.5, 1.0$) against the CO dissociation energy, which serves as a descriptor of the actual catalytic activity [19].

synthesized and tested experimentally [19, 21]. They indeed demonstrated activities almost as good as Co. These FeNi alloy catalysts, however, are significantly cheaper.

The authors used a similar approach to screen alloys in the search for new catalytic materials for ammonia synthesis [38]. A rigorous analysis of the mechanism for ammonia synthesis over different metals indicates that the dissociation of the N_2 and the stability of NH and N surface intermediates limit the rate [20, 37–39]. The authors show that ammonia synthesis activity clearly follows a volcano curve when plotted against the nitrogen binding energy, as shown in Figure 10.6. The nitrogen binding energy therefore proved to be a valuable predictor of the activity and was thus

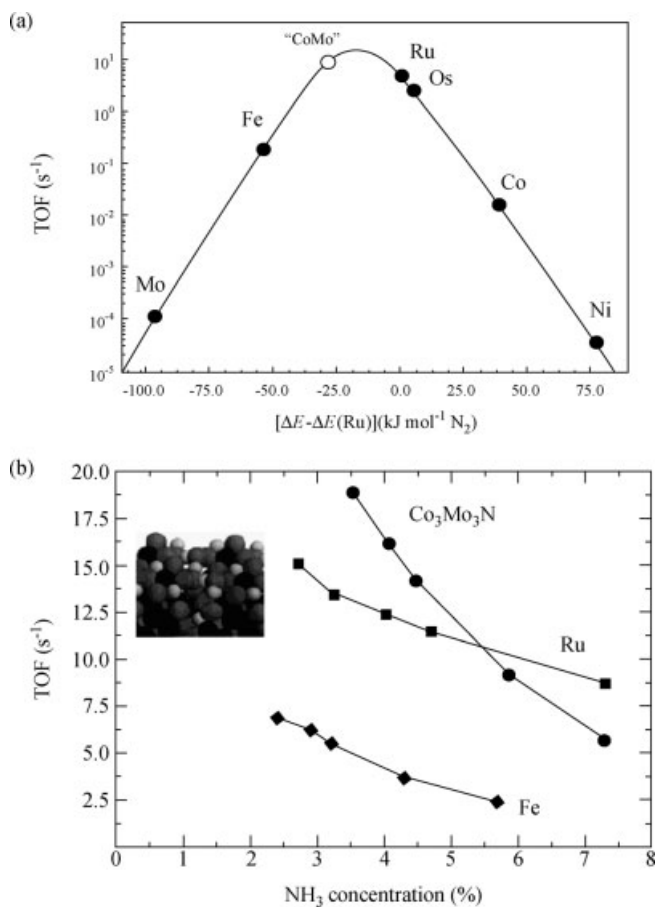


Figure 10.6 Comparison of the measured catalytic turnover frequencies for ammonia synthesis versus DFT-calculated nitrogen adsorption energies over different metals. (b) The plot of the measured turnover frequency for ammonia synthesis over Co_3Mo_3N , Ru, and Fe catalysts indicates that the Co_3Mo_3N system is more active than Ru and Fe at low NH_3 concentrations [38].

subsequently used to test a number of different metals and alloys. The results indicate that a CoMo alloy would lead to significant enhancements in the rate. This suggests that optimal material is one that directly combines a metal having a strong metal–nitrogen bond (Mo) with that having a weak metal–nitrogen bond. This was subsequently verified by means of experiments [35, 38], whereby alloying Co with Mo leads to a catalyst with TOF exceeding both Ru and Fe, at least at lower NH_3 concentrations. The active catalyst was later revealed to be a cobalt–molybdenum nitride ($\text{Co}_3\text{Mo}_3\text{N}$).

The studies presented here show how theory can be used to not only elucidate mechanisms but also aid in catalyst discovery through hypothesis-driven computational screening. It is important to note that there were significant theoretical efforts that went into first establishing the controlling catalytic steps and identifying the critical bond energies, which can be used successfully as descriptors. As such, the approach can be characterized as hypothesis-driven high-throughput computational screening, which would lie somewhere in the middle of the knowledge axis of the materials discovery cone outlined in Figure 10.1.

10.3

High-Throughput Simulation and Design

The use of “intelligent” descriptors is clearly an important approach that will aid in providing potential leads for new catalytic materials. There are some limitations, however, with this approach as it involves rapid screening and does not take into account the reaction environment or its influence on the catalytic performance. The foundation of the descriptor approach, or at least its initial applications, is that the most predominant factor that changes in moving from one metal to the next is the adsorbate–metal bond strength, and this governs the intrinsic reactivity. Changes in the metal, however, can also lead to a number of other changes in the reaction environment including changes in surface coverage, adlayer composition, particle size and morphology, and support interactions that can significantly alter the surface chemistry and kinetics. While some of these effects may be captured by descriptors, a number of them are not. The descriptor approach tries to balance the rigorous description of the elements that control catalysis with the ability to rapidly screen hundreds to thousands of systems.

A second approach that has emerged is the one that tries to provide a more complete description of the reaction environment but does so at the expense of the ability to rapidly screen as many systems as possible in a very short time. For lack of a better name, we refer to this approach as high-throughput simulation. We have developed and used such an approach to elucidate a number of different catalytic systems including olefin and alkyne hydrogenation, Fischer–Tropsch synthesis, vinyl acetate (VA) synthesis, NO_x reduction, and CO oxidation as well as the design of alloy surfaces [1–3, 14, 16, 40–49]. The approach takes the basic premise that catalysis is controlled by kinetics and that a comprehensive kinetic model is essential to the understanding of catalysis.

Most of the kinetic models that have been developed in catalysis are based on deterministic kinetics, which follows the time-dependent behavior of gas-phase concentrations and surface coverages. The atomic structure and composition of the catalyst in such models are averaged over and essentially removed or buried into macroscopic rate constants. As such, there is no clear way in which to use these models to carry out catalyst design or screening, since the macroscopic rate constants on which they are based are devoid of structure. A second and potentially more useful approach to modeling the kinetics for complex systems is to adopt stochastic kinetic methods that explicitly allow direct incorporation of atomic structure. Stochastic methods provide an exact mathematical treatment of the reaction kinetics [14]. For complex systems, stochastic approaches can be more accurate than deterministic models since they rigorously follow all of the individual molecular transformations and the specific influence of the surface atomic structure and composition on these transformations [14].

We have developed an *ab initio* kinetic Monte Carlo (KMC) simulation that integrates first-principles theoretical results into a stochastic kinetics framework, to follow the dynamic changes in the surface adlayer as a function of time, process variables, and catalytic structure. The simulations track the individual molecular transformations over different surface sites and can be used to follow the influence on catalyst structure and composition on reactivity [3, 16, 41–49]. *Ab initio* methods are used to calculate (1) the adsorption energies for all reactants, intermediates, and products, (2) the overall reaction energies and activation barriers for all potential pathways, and (3) the influence of coverage effects over a series of different metals. Pre-exponential factors are estimated from statistical mechanics. The results provide a fairly comprehensive database, which is subsequently used as an input for KMC simulations and to establish more coarse-grained models that can estimate energies for systems that arise in carrying out specific simulations. The simulations can be used to specifically determine the primary metal that should be used, the surface structure, an appropriate second metal, and the surface composition and specific atomic connectivity, thus defining the surface alloy. The simulations can then follow the individual molecular transformations over the surface and thus predict the turnover frequency, the selectivity and the molecular product distributions that result for different metal alloys run at different process conditions. Simulation results offer a wealth of molecular and kinetic details that can be used to elucidate the structural and compositional factors that control the surface chemistry. The drawbacks of this approach are that it requires a significantly greater number of calculations to be carried out before the simulations can take place to determine the kinetics and the influence of the local coverage and surface structure. Once these calculations are completed through, one can simulate the composition and structure of the alloy of interest and, in addition, effectively transfer the model to other metals and alloys. The full kinetic simulations can be almost as time consuming as the *ab initio* calculations. So, while the approach adds more sophistication into the design of metal ensembles, it is slower than the descriptor methods described above. The application of the high-throughput simulation approach is highlighted in the next two sections for the design of surface ensembles to carry out NO_x decomposition [3, 46] and VAM synthesis [16, 50].

10.3.1

NO Decomposition

The catalytic decomposition of NO_x into N_2 and O_2 under lean operating conditions is critical for the commercialization of lean-burn engines [51–53]. Current three-way exhaust catalysts effectively convert NO_x into N_2 and O_2 but are rapidly poisoned by oxygen under lean conditions. Supported Rh, for example, is inactive. Although Pt/ Al_2O_3 shows activity, it is significantly inhibited by oxygen. Current solutions to operating under lean conditions include the use of a sacrificial reductant or NO_x storage and reduction (NSR) methods. While these strategies are very promising, there are still efforts for finding materials that carry out direct NO_x reduction. This includes the design of alloys that can activate NO and resist oxygen poisoning. One potential solution might be to alloy a metal that can readily activate the NO bond (such as Pt, Pd, or Rh) with a more inert group IB metal (Cu, Ag, or Au) to weaken the metal–oxygen bond strength and promote the desorption of oxygen.

A number of *ab initio* DFT calculations were carried out to determine the kinetics of the sequence of elementary steps presented in Table 10.1 over different Pt surfaces and at different oxygen and NO surface coverages to understand the surface chemistry and establish the kinetics under more realistic conditions [3, 46]. Results were used to fit the more coarse-grained bond order conservation and Merck molecular force field models to follow through-surface and through-space interactions to fully capture the effects of coverage.

While the simulations required a significant initial effort to establish the kinetics and interaction models, the results were used directly in the kinetic Monte Carlo simulation to specifically follow molecular transformations that occur on the surface. The simulation could then be used as a virtual experiment to explore how changes in the process variables controlled the macroscopic kinetic behavior as well as the molecular pathways and kinetics. By systematically changing the temperature and

Table 10.1 The activation barriers (E_{for} and E_{rev}) and the pre-exponential factors (ν_{for} and ν_{rev}) or sticking coefficients (S_0) for the forward and reverse elementary steps in the catalytic decomposition of NO over Pt [46].

Reaction	E_{for} (kcal mol ⁻¹)	E_{rev} (kcal mol ⁻¹)	ν_{for} (s ⁻¹)	$S_{0,\text{for}}$ (s ⁻¹)	ν_{rev} (s ⁻¹)	$S_{0,\text{rev}}$ (s ⁻¹)
$\text{NO}(\text{g}) + * \leftrightarrow \text{NO}^*$	0.0	51.2	—	0.7	1×10^{13}	—
$\text{NO}^* + * \rightarrow \text{N}^* + \text{O}^*$	25.6	5.0	1×10^{13}	—	1×10^{13}	—
$\text{NO}^* + \text{O}^* \rightarrow \text{NO}_2^* + *$	31.7	11.7	1×10^{13}	—	1×10^{13}	—
$\text{NO}^* + \text{N}^* \rightarrow \text{N}_2\text{O}^* + *$	33.9	22.2	1×10^{13}	—	1×10^{13}	—
$\text{NO}^* + \text{NO}^* \rightarrow \text{N}_2\text{O}^* + \text{O}^*$	37.5	0.0	1×10^{13}	—	1×10^{13}	—
$\text{N}_2\text{O}^* \rightarrow \text{N}_2(\text{g}) + \text{O}^*$	0.0	24.6	1×10^{13}	—	1×10^{13}	—
$\text{N}^* + \text{N}^* \rightarrow \text{N}_2(\text{g}) + 2^*$	9.0	33.7	1×10^{13}	—	—	0.1
$\text{O}^* + \text{O}^* \leftrightarrow \text{O}_2(\text{g}) + 2^*$	0.0	52.2	1×10^{15}	—	—	0.1
$\text{NO}_2^* \rightarrow \text{NO}_2(\text{g}) + *$	28.4	0.0	1×10^{13}	—	—	1.0
$\text{N}_2\text{O}^* \rightarrow \text{N}_2\text{O}(\text{g}) + *$	6.3	0.0	1×10^{13}	—	—	1.0

the partial pressures, we can determine the apparent activation barriers and reaction orders. Results of such simulations are shown in Figure 10.7 for both the NO decomposition and the NO oxidation reaction. The apparent activation barrier to NO dissociation was found to be $7.4 \text{ kcal mol}^{-1}$ at P_{NO} of 0.468 Torr and P_{O_2} of 60.8 Torr, which are conditions of interest for deNOx [3, 46]. At lower temperatures, NO

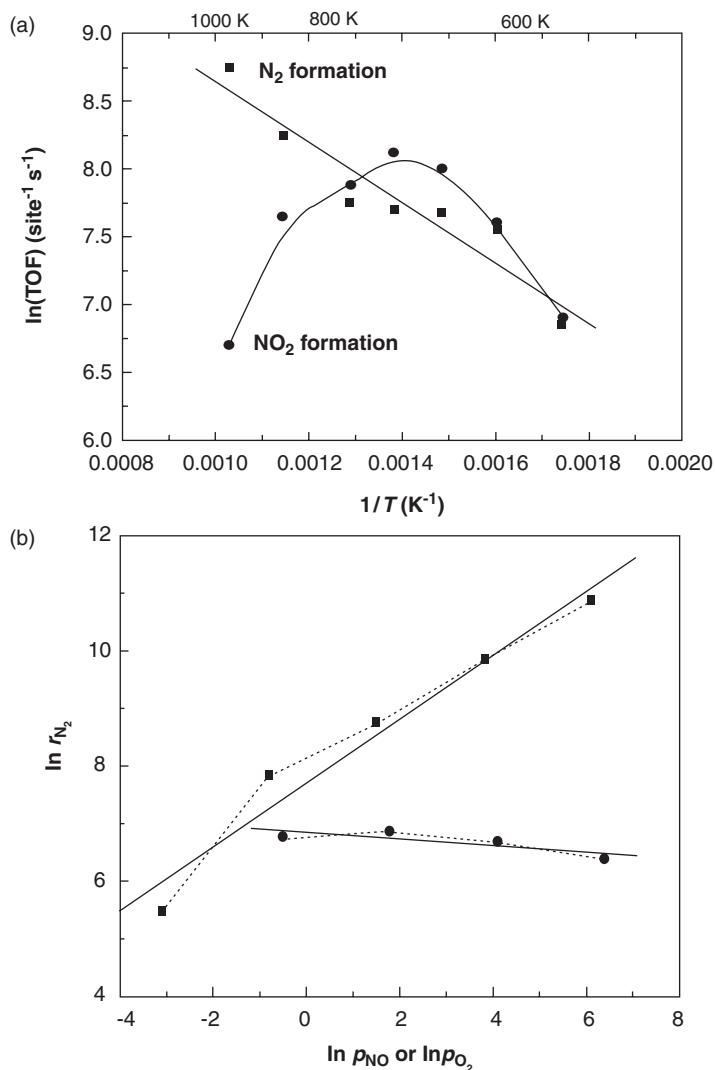


Figure 10.7 DFT-KMC simulated kinetic results for NO decomposition over Pt. (a) Turnover frequencies and apparent activation barriers for N_2 and NO_2 formation over Pt(100) at $T = 723 \text{ K}$, $P_{\text{NO}} = 0.47 \text{ Torr}$, and $P_{\text{O}_2} = 60.8 \text{ Torr}$. (●, NO_2 ; ■, N_2). (b) Simulated apparent reaction orders for P_{NO} (■) and P_{O_2} (●) [46].

oxidation showed significantly higher rates. The rates for NO oxidation, however, decreased significantly as the temperature was increased. Higher temperatures significantly enhanced the back reaction, which involves the decomposition of NO_2 to form NO and oxygen. This is consistent with experimental evidence. The reaction is calculated to be nearly first order in NO (0.9) and negative half order in oxygen (-0.4). We demonstrated that the fourfold sites on the Pt(100) surface had unique reactivity for activating the NO bond [54]. NO preferentially adsorbs on the bridge sites and dissociates over the fourfold site, whereby the nitrogen and the oxygen produced through reaction were stabilized at the bridge sites and do not share metal atoms [54]. A key issue in this system is that both the atomic oxygen that forms and the NO reactant prefer to adsorb at Pt bridge sites. Oxygen tends to win out and inhibits the adsorption of NO onto the surface [3, 46].

The simulations were used to analyze NO decomposition under lean conditions over Pt, PtAu, PtAg, and PtCu alloy surfaces [3]. A number of different alloy compositions and specific atomic configurations were generated and subsequently simulated to establish the ones that would demonstrate both optimal activity and selectivity. These systems were all screened at a constant temperature and NO and O_2 partial pressures. Simulations were run for times long enough to achieve steady state before analyzing the turnover frequencies and selectivities to products. In general, alloying Au into Pt increased the turnover rate for nearly all of the compositions examined, as shown in Figure 10.8. The catalytic activities improved by nearly a factor of 4 over a narrow range of Au compositions (40–60%).

The results clearly revealed that different Au configurations lead to significantly different selectivities even when the Pt and Au compositions were the same. For

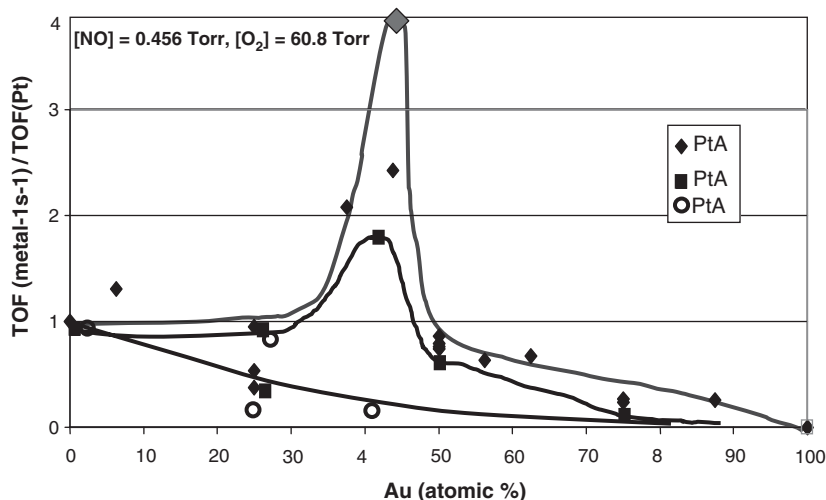


Figure 10.8 The effect of alloying different compositions of Au [3] Ag and Cu onto the Pt(100) surface on the turnover frequency for NO decomposition. TOF are reported relative to the TOF for NO decomposition over pure Pt(100).

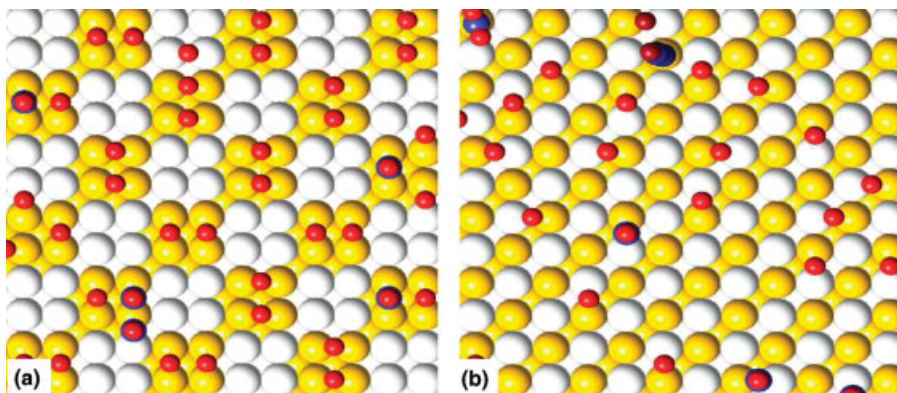


Figure 10.9 The adlayer for the most active PtAu alloy found. The Pt_4Au_4 ensemble and PtAu well-dispersed alloys under steady-state conditions. (a) The Pt–Pt bridge sites on the Pt_4Au_4 ensembles tend to be poisoned by oxygen. (b) The removal of the Pt–Pt bridge sites on the dispersed PtAu alloy prevents oxygen poisoning but leads to greater NO_2 formation [3].

example simulations carried out over a $\text{Pt}_{50\%}\text{Au}_{50\%}$ configuration in which the Au and Pt form segregated 2×2 surface ensembles, as shown in Figure 10.9a, resulted in turnover frequencies that were very similar to those calculated over pure Pt [3]. This might be expected since the bridging Pt sites are still present in these large surface ensembles and are still poisoned by oxygen. This suggested that well-dispersed PtAu alloys that remove the Pt=Pt bridge sites might be more active since the substitution of Au for Pt in the bridge sites should reduce the binding energy of oxygen at these sites, prevent oxygen poisoning and ultimately increase the surface coverage of NO. A snapshot from the simulation over this surface is shown in Figure 10.9b. Results show that while this alloy is more active, it is less selective, thus forming more NO_2 than N_2 . NO does not actively dissociate over the Pt=Au bridge sites. On the contrary, the weaker NO^* and O^* bonds at the bridge sites allow them to react together much more readily to form NO_2 .

The most active and selective surface had a composition of $\text{Pt}_{56.2\%}\text{Au}_{43.8\%}$ and a unique structural configuration where Pt atoms in the surface were arranged into a specific “+”-shaped ensemble and surrounded by Au [3]. This structure is shown in Figure 10.10. The site maintains Pt bridge sites that are necessary for the adsorption of NO. Surrounding these Pt sites with Au atoms helps prevent these sites from being poisoned by oxygen. Molecular oxygen is less likely to dissociate at these sites since the active fourfold Pt sites are not present. Any oxygen that does dissociate at these “+” sites is fairly labile. One of the oxygen adatoms that forms is forced away from the Pt “+” ensemble and onto the Au sites that border its periphery to prevent the strong repulsive interactions associated with having two oxygen atoms share the same Pt atoms. The oxygen atoms that spill over the Au sites are weakly bound and readily recombine and desorb as O_2 . NO, can now adsorb at the Pt–Pt bridge sites and react with coadsorbed NO to form N_2O . The lateral interactions between two NO molecules are significantly

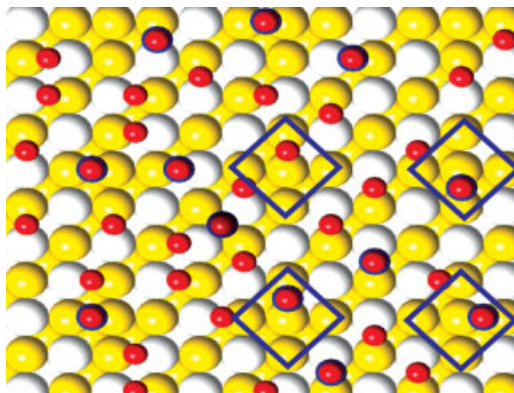


Figure 10.10 Snapshot of the adlayer that forms on the most active PtAu alloy surface that was found. The unique “+”-ensemble in the $\text{Pt}_{56.2\%}\text{Au}_{43.8\%}$ surface alloy, which is highlighted, results in Pt–Pt bridge sites that can activate NO but avoid poisoning by oxygen [3].

weaker. At higher temperatures, N_2O can dissociate on the surface to form $\text{N}_2(\text{g})$ and adsorbed atomic oxygen. NO can also dissociate at these “+” sites. The resulting oxygen adatom that forms can spill over onto the Au sites, where it can be associatively removed as O_2 . Atomic nitrogen also recombines with other nitrogen adatoms to form N_2 . By closer analysis of the alloy, we find that the presence of Au decreases the oxygen binding energy as well as the amount of oxygen that forms on the surface. This decreased oxygen surface coverage then leads to a concomitant increase in the NO adsorption energy. The “+” ensemble analyzed here was found to be the most active surface ensemble of all those examined as it increased the TOF by a factor of 4 [3].

Simulations carried out over a wide range of PtAg and PtCu alloys resulted in trends very similar to those found for PtAu, as shown in the other two curves in Figure 10.8. The turnover frequencies over PtAg and PtCu, however, were found to be lower than those over the PtAu alloys and resulted in the following order of increasing TOF: $\text{PtCu} < \text{PtAg} < \text{PtAu}$. This increase nicely corresponds to the decrease in the oxygen binding energy on each of these surfaces. The active ensemble was found to be the same on all three alloys.

Results presented here demonstrate that theory and simulation can be used to not only screen particular alloys but also explore different surface compositions as well as specific atomic assemblies. As such, one can think of “patterning” the metal surface so as to allow the spatial separation of the product molecules or intermediates from the reactant molecules on the surface. More generally, what appears to be critical for lean NO_x decomposition is the ability to dissociate NO and rapidly expel the atomic oxygen that forms onto neighboring sites that have weaker oxygen binding energies. While all three of the alloy surfaces examined demonstrated improved catalytic activities, the increase in the TOF is at best only four times that of the parent Pt metal. It is difficult to fully remove oxygen from the Pt sites. Results suggest that further increases in the TOF would be difficult to achieve with metals or alloys alone and that a more active

system might require a bifunctional surface with metal sites to be in close proximity to an oxide regions to enable the spillover of oxygen to the oxide away from the metal.

10.3.2

Vinyl Acetate (VAM) Synthesis

In this second example, we present the results from *ab initio* based kinetic Monte Carlo simulations that were carried out to suggest novel PdAu alloys that could selectively enhance the activity and the selectivity for the synthesis of vinyl acetate. VAM synthesis, which involves the acetoxylation of ethylene in the presence of oxygen, is typically carried out over supported Pd and PdAu alloys and used in the production of adhesives, paints, and films [55–57]. The optimal catalysts tend to contain Pd that is alloyed with Au. While there have been a number of important studies on the influence Pd/Au composition, the optimal Pd and Au composition and atomic assembly is still debated. Recent experimental studies by Chen *et al.* [58] suggest that the most active surface for VAM synthesis predominantly consists of Au and contains noncontiguous Pd dimer pairs. This is consistent with the fact that high Au coverages would significantly reduce carbon formation and help maintain a high activity. There is still some debate, however, as to whether these surfaces would be the most active or could be maintained under operating conditions. The catalytic reaction is thought to proceed over supported Pd by one of the two mechanisms. Both mechanisms suggest that acetic acid readily dissociates to form surface acetate intermediates. In the first mechanism, which was attributed to Samanos and is highlighted in Figure 10.11a, ethylene coadsorbs and reacts directly with the surface acetate to form an acetoxyethyl intermediate that undergoes a subsequent β C–H scission to form VAM [14, 57]. In the second mechanism, which is attributed to Moiseev or Nakamura and highlighted in Figure 10.11b, a C–H bond of ethylene is

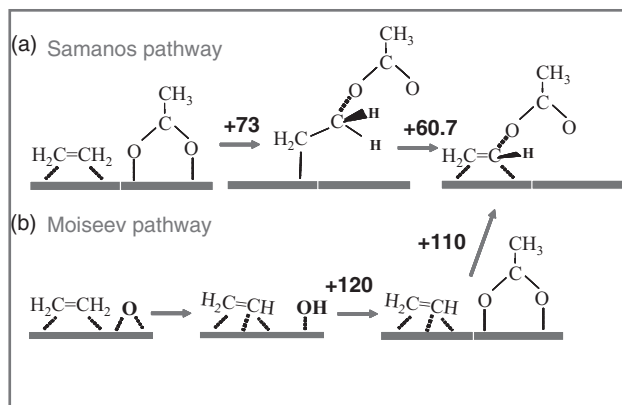


Figure 10.11 The major steps in the two predominant mechanisms proposed for VAM synthesis over Pd. (a) Samanos mechanism and (b) Moiseev or Nakamura mechanism [57].

activated first resulting in the formation of a surface vinyl intermediate that subsequently reacts with coadsorbed acetate to form VAM. Density functional theoretical calculations were used together with *in situ* RAIRS spectroscopy and deuterium labeling studies to show that the mechanism over Pd proceeds through the Samanos route [57].

The activation barriers, overall reaction energies, and rate constants for the forward and reverse elementary steps in both mechanisms over Pd were determined from DFT calculations [16]. Theory was also used to determine the kinetics for the unselective pathways that lead to CO_2 and surface carbon formation and to show that the larger Pd ensembles catalyzed the unselective pathways [41]. Subsequent calculations were carried out to analyze the influence of surface coverage as well as alloying different amounts of Au into the surface on its reactivity. These results were used to help parameterize the more coarse-grained bond order conservation and Merck molecular force field models used to treat lateral interactions and alloying effects “on-the-fly” in the kinetic Monte Carlo simulations [16, 50].

The *ab initio* results along with the coarse-grained models were incorporated into the kinetic Monte Carlo simulation to provide the intrinsic kinetic data. The simulations were carried out to track the individual molecular transformations along with the micro- and macroscopic kinetics. By changing the temperature and the pressure, the simulations were used to determine the apparent activation barriers and the overall reaction orders. Figure 10.12a depicts a snapshot of the working Pd surface simulation [16]. The pure Pd surface is covered in acetate and oxygen intermediates that block the adsorption of ethylene. At low temperatures, the turnover rate to form VAM is limited by the ability to adsorb ethylene onto the surface. This adsorption of ethylene and the TOF can be improved significantly by

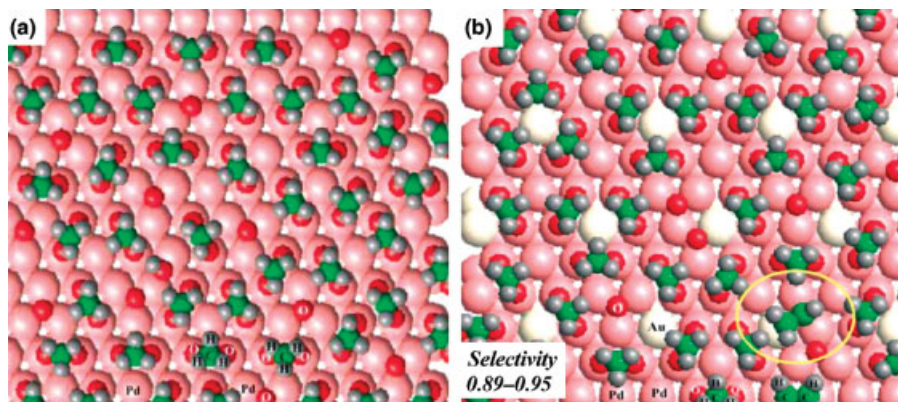


Figure 10.12 The effects of alloying Au into Pd. Snapshots of the steady-state adlayer that forms on (a) pure Pd(100) and (b) $\text{Pd}_{66.7\%}\text{Au}_{33.3\%}$ well-dispersed alloy for the synthesis of VA ($T = 473\text{ K}$, $P_{\text{C}_2\text{H}_4} = 3800\text{ Torr}$, $P_{\text{AcOH}} = 1520\text{ Torr}$, $P_{\text{O}_2} = 608\text{ Torr}$). The addition of Au opens up sites in the acetate and oxygen adlayer, which increases ethylene adsorption. This results in an increase in both the activity and the selectivity [16].

increasing the partial pressure of ethylene. This is well established commercially as the reaction is run at very high partial pressures of ethylene. Higher ethylene pressures, however, tend to result in significant carbon formation, which can lead to inhibition and production of CO_2 [16, 50].

Most of the current commercial VAM catalysts alloy Pd with Au to improve VAM yields. Simulations were used to explore the influence of alloying the surface with small amounts of Au. Both acetate and oxygen bind strongly to Pd and prefer to adsorb solely on the Pd sites. Ethylene, on the contrary, is more weakly held to the surface and indiscriminately adsorbs on both Pd and Au. The presence of Au atoms in the surface therefore creates sites that can exist in the acetate and oxygen adlayer unoccupied where ethylene can adsorb and subsequently react with neighboring acetate to form VAM. This is seen quite clearly in the snapshot of the working surface at steady-state conditions, depicted in Figure 10.12b, where acetate and oxygen are bound to Pd and only ethylene and vinyl intermediates are bound to Au. The presence of Au in the adlayer also breaks up the large Pd ensembles that are generally responsible for unselective CO_2 production. This increase in both activity and selectivity was observed in the transient kinetic experiments performed by Provine *et al.* [59]. This is also consistent with the classic work by Boudart who has shown that the addition of Au to Pd increases the rate and selectivity for hydrogen oxidation [60, 61].

Simulations were subsequently used to screen different Au compositions and configurations. Results indicate that the optimal configurations are those in which Au is well dispersed and forms small islands with radii no larger than about four Au atoms within the Pd surface. Islands that are smaller than four Au atoms are still somewhat limited by the amount of ethylene that can adsorb into the dense adlayer. Islands that are too large decrease the effective Pd–Au contacts. The surface here is alloyed to optimize the coadsorption of the two reactants, acetate and ethylene. The TOF increased by a factor of 4 and the selectivity improved by 5% of the Au ensembles, as presented in Figure 10.13.

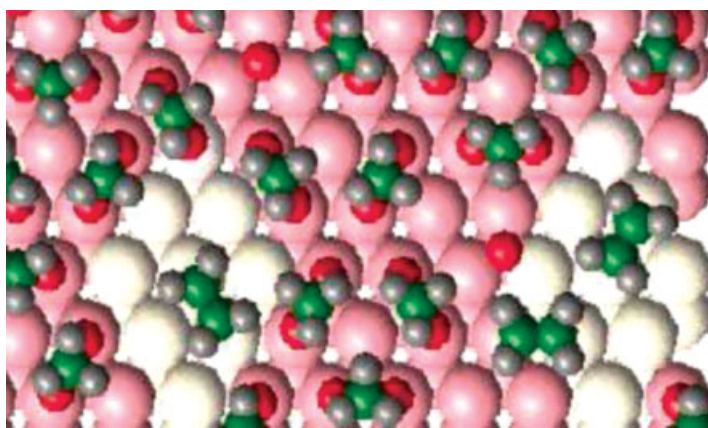


Figure 10.13 Snapshot of the steady-state adlayer on the active nine-atom Au ensembles embedded into the Pd surface [42].

10.4

Controlled Patterning

The two example systems presented above suggest that one can begin to screen not only for the best compositions but also for the optimal atomic configurations of the surface alloy that lead to enhanced catalytic performance. By patterning the surface, one can think of controlling the self-assembly of molecules in the adlayer to drive particular reactions. In the first example, Au was added to help remove the product as well as other potentially reactive intermediates present in the feed, which prevent the adsorption and activation of the reactant. The strongly bound oxygen product that forms upon O_2 activation poisons the surface and must therefore be removed from the reactive ensemble. The optimal alloy here is one that allows for the adsorption and decomposition of NO but prevents the dissociation of the O_2 in the feed or allows the facile recombination of oxygen atoms and desorption of O_2 from the surface. In the second catalytic system presented, the acetate and oxygen reactants block the surface and prevent the coreactant ethylene from adsorbing. The goal in this system was to allow ethylene to adsorb while still enabling the close proximity of the acetate and oxygen coreactants. This involved directly embedding sites within the adlayer that enable the weakly held reagent (ethylene) to adsorb in the sea of acetate surface intermediates.

10.5

Catalyst Synthesis and Stability

In all of the examples presented and the approaches discussed, we ignored two very important issues: (1) Can the alloys suggested from theory and simulation actually be synthesized and (2) are the suggested alloys and specific configurations stable under reaction conditions? The calculations reported were carried out under the premises that one wants to generate as many new ideas as possible and without constraints on the screening process introduced by bulk properties of the metals. Most active metal catalysts are supported nanometer-size clusters whereas most of our information on the stability of the metal, alloys, and oxides is predominantly based on properties of bulk materials. We did not want to limit the search based on what is known only for the bulk. In many cases, alloy compositions can be synthesized and stabilized at the nanoscale especially if one includes the vast array of supports that can be used as well. For example, in the NO decomposition example presented above, it is well established that Pt and Au do not form bulk alloys and one could suggest that the proposed alloys would not form based on what is known from bulk thermodynamic data. A number of very recent experimental studies, however, demonstrate that such clusters of Pt and Au can be stabilized [62–65] and are currently being used as electrocatalysts for fuel cells.

Theory and simulation are also being used to explore issues of stability and synthesis. This requires more rigorous simulations and is thus considered as a subsequent test of the alloy compositions and structures that might be generated from the initial screening. We have shown, for example, that the PdAu and PtAu complexes similar to those identified above can be formed by going to small nanometer particles

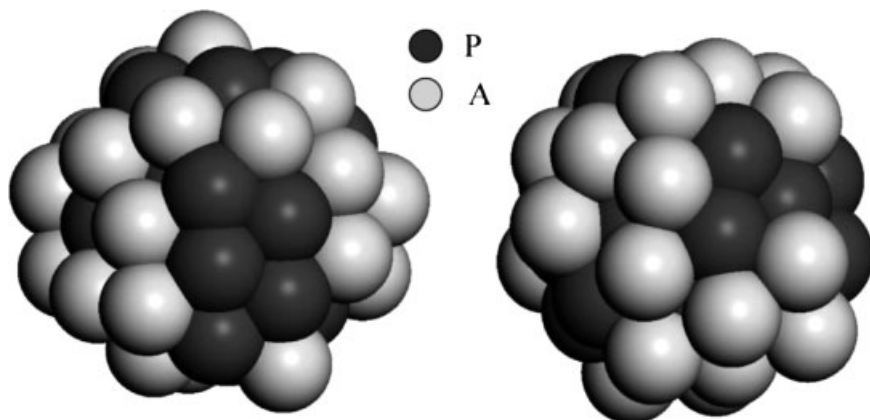


Figure 10.14 Optimal atomic structure of the $\text{Pt}_{40\%}\text{Au}_{60\%}$ nanoparticle alloy that forms as a result of the deposition of Pt onto an Au nanoparticle, which is followed by a high-temperature simulated annealing.

by sequentially depositing Au onto the surface in controlled amounts. Simulated annealing studies were carried out to show that by depositing a limited amount of Au onto a Pt particle, the resulting thermodynamically favored alloy nanoparticle is one in which the core is Pt and the outside is made up of a Pt ensemble that takes on some of the same characteristics of “+” active surface site involved in NO_x decomposition. This can clearly be seen in Figure 10.14, which is an optimal structure for the $\text{Pt}_{40\%}\text{Au}_{60\%}$ particle found from simulated annealing studies.

There is also some work that is being carried out to develop descriptors that can be calculated more rapidly to assess this directly in the initial screen itself, which would limit the phase space to material that thermodynamically has the potential to be synthesized.

10.6 Conclusions

Both the catalytic descriptor and high-throughput simulation design approaches to screening metals and alloys discussed in this chapter are based on the fundamental understanding of the mechanism and result in the generation of significant knowledge. They thus lie somewhere between the combinatorial and hypothesis-driven scientific approaches presented as the two extremes of the discovery funnel in Figure 10.1. The use of catalytic descriptors can rapidly screen many more material systems but requires more simplifying assumptions to describe the catalytic behavior with just one or two descriptors. The high-throughput simulations, on the other hand, require much more information concerning coverage effects and alloying to elucidate the mechanism prior to any screening. Full-scale kinetic simulations are then used to analyze different metals and alloys. While this is based on more

fundamental knowledge, the number of systems that can be screened is much smaller. Both approaches have demonstrated valuable insights and guidance into new metal alloys and hold tremendous promise for the development of novel catalytic materials. They attempt to provide an optimal balance of fundamental knowledge and rapid screening capabilities. As the goal is to guide the development of new catalytic materials, there is no single optimal approach. The use of both approaches should therefore prove to be invaluable.

Acknowledgments

I am grateful for the financial support of the ideas presented herein from US Department of Energy, Office of Basic Energy Sciences, Division of Chemical Science (DE-FG02-05ER15700) and the Army Research Office (MURI award: DAAD-19-03-1-0169) as well as the computational support from the Environmental Molecular Sciences Laboratory at Pacific Northwest Laboratory. I would also like to thank Professor Enrique Iglesia, Dr Laurent Kieken, Dr Jan Lerou, Dr Donghai Mei, and Professor Eddy Tysoe for invaluable discussions.

References

- 1 Iglesia, E., Kieken, L. and Neurock, M. (2004) Knowledge-based process for the development of materials. US Patent 6,763,309.
- 2 Kieken, L., Iglesia, E., Neurock, M. and Trenkle, J.M. (2003) Method and system for the development of materials. US Patent 6,647,342.
- 3 Kieken, L.D., Neurock, M. and Mei, D.H. (2005) Screening by kinetic Monte Carlo simulation of Pt–Au(1 0 0) surfaces for the steady-state decomposition of nitric oxide in excess dioxygen. *The Journal of Physical Chemistry B*, **109** (6), 2234–2244.
- 4 Hagemeyer, A., Jandeleit, B., Liu, Y.M., Poojary, D.M., Turner, H.W., Volpe, A.F. and Weinberg, W.H. (2001) Applications of combinatorial methods in catalysis. *Applied Catalysis A: General*, **221**, (1–2), 23–43.
- 5 Burello, E. and Rothenberg, G. (2006) *In silico* design in homogeneous catalysis using descriptor modelling. *International Journal of Molecular Sciences*, **7** (9), 375–404.
- 6 Maier, W.F., Stowe, K. and Sieg, S. (2007) Combinatorial and high-throughput materials science. *Angewandte Chemie-International Edition*, **46**, 6016–6067.
- 7 Koyama, M., Tsuboi, H., Endou, A., Takaba, H., Kubo, M., Del Carpio, C.A. and Miyamoto, A. (2007) Combinatorial computational chemistry approach for materials design: applications in deNO_x catalysis, Fischer–Tropsch synthesis, lanthanoid complex, and lithium ion secondary battery. *Combinatorial Chemistry & High Throughput Screening*, **10** (2), 99–110.
- 8 Corma, A. and Serra, J.M. (2005) Heterogeneous combinatorial catalysis applied to oil refining, petrochemistry and fine chemistry. *Catalysis Today*, **107–108**, 3–11.
- 9 Schuth, F. and Demuth, D. (2006) High-throughput-experimentation in heterogenic catalysis. *Chemie Ingenieur Technik*, **78** (7), 851–861.
- 10 Schuth, F., Baumes, L., Clerc, F., Demuth, D., Farrusseng, D., Llamas-Galilea, J.,

- Klanner, C., Klein, J., Martinez-Joaristi, A., Procelewska, J., Saupe, M., Schunk, S., Schwickardi, M., Strehlau, W. and Zech, T. (2006) High throughput experimentation in oxidation catalysis: higher integration and "intelligent" software. *Catalysis Today*, **117** (1–3), 284–290.
- 11 Oh, K.S., Kim, D.K., Maier, W.F. and Woo, S.I. (2007) Discovery of new heterogeneous catalysts for the selective oxidation of propane to acrolein. *Combinatorial Chemistry & High Throughput Screening*, **10** (1), 5–12.
 - 12 Gobin, O.C., Joaristi, A.M. and Schuth, F. (2007) Multi-objective optimization in combinatorial chemistry applied to the selective catalytic reduction of NO with C₃H₆. *Journal of Catalysis*, **252** (2), 205–214.
 - 13 Caruthers, J.M., Lauterbach, J.A., Thomson, K.T., Venkatasubramanian, V., Snively, C.M., Bhan, A., Katare, S. and Oskarsdottir, G. (2003) Catalyst design: knowledge extraction from high-throughput experimentation. *Journal of Catalysis*, **216** (1–2), 98–109.
 - 14 van Santen, R.A. and Neurock, M. (2006) *Molecular Heterogeneous Catalysis: A Mechanistic and Computational Approach*, VCH-Wiley Verlag GmbH, Weinheim
 - 15 Johannesson, G.H., Bligaard, T., Ruban, A.V., Skriver, H.L., Jacobsen, K.W. and Norskov, J.K. (2002) *Physical Review Letters*, **88**, 25506.
 - 16 Neurock, M. (2003) Perspectives on the first principles elucidation and the design of active sites. *Journal of Catalysis*, **216** (1–2), 73–88.
 - 17 Neurock, M., Wasileski, S.A. and Mei, D. (2004) From first principles to catalytic performance: tracking molecular transformations. *Chemical Engineering Science*, **59** (22–23), 4703–4714.
 - 18 van Santen, R.A. and Neurock, M. (1995) Concepts in theoretical heterogeneous catalytic reactivity. *Catalysis Reviews: Science and Engineering*, **37** (4), 557–698.
 - 19 Andersson, M.P., Bligaard, T., Kustov, A., Larsen, K.E., Greeley, J., Johannessen, T., Christensen, C.H. and Norskov, J.K. (2006) Toward computational screening in heterogeneous catalysis: Pareto-optimal methanation catalysts. *Journal of Catalysis*, **239** (2), 501–506.
 - 20 Hellman, A., Baerends, E.J., Biczysko, M., Bligaard, T., Christensen, C.H., Clary, D.C., Dahl, S., van Harreveld, R., Honkala, K., Jonsson, H., Kroes, G.J., Luppi, M., Manthe, U., Norskov, J.K., Olsen, R.A., Rossmeisl, J., Skulason, E., Tautermann, C.S., Varandas, A.J.C. and Vincent, J.K. (2006) Predicting catalysis: understanding ammonia synthesis from first-principles calculations. *The Journal of Physical Chemistry B*, **110** (36) 17719–17735.
 - 21 Kustov, A.L., Frey, A.M., Larsen, K.E., Johannessen, T., Norskov, J.K. and Christensen, C.H. (2007) CO methanation over supported bimetallic Ni–Fe catalysts: from computational studies towards catalyst optimization. *Applied Catalysis A-General*, **320**, 98–104.
 - 22 Hammer, B. and Norskov, J.K. (1995) Electronic factors determining the reactivity of metal surfaces. *Surface Science*, **343** (3), 211–220.
 - 23 Ruban, A., Hammer, B., Stoltze, P., Skriver, H.L. and Norskov, J.K. (1997) Surface electronic structure and reactivity of transition and noble metals. *Journal of Molecular Catalysis A: Chemical*, **115** (3), 421–429.
 - 24 Hammer, B. and Norskov, J.K. (2000) Theoretical surface science and catalysis – calculations and concepts. *Advances in Catalysis*, **45**, 71–129.
 - 25 Norskov, J.K., Bligaard, T., Logadottir, A., Bahn, S., Hansen, L.B., Bollinger, M., Bengaard, H., Hammer, B., Sljivancanin, Z., Mavrikakis, M., Xu, Y., Dahl, S. and Jacobsen, C.J.H. (2002) Universality in heterogeneous catalysis. *Journal of Catalysis*, **209** (2), 275–278.
 - 26 Pallassana, V. and Neurock, M. (2000) First-principles periodic density functional study of the hydrogenation of maleic anhydride to succinic anhydride over palladium(111). *The Journal of Physical Chemistry B*, **104** (40), 9449–9459.

- 27 Pallassana, V. and Neurock, M. (2000) Electronic factors governing ethylene hydrogenation and dehydrogenation activity of pseudomorphic Pd–ML/Re (0001), Pd–ML/Ru(0001), Pd(111), and Pd–ML/Au(111) surfaces. *Journal of Catalysis*, **191** (2), 301–317.
- 28 van Santen, R.A. and Neurock, M. (2007) Theory of surface chemical reactivity. *Russian Journal of Physical Chemistry B*, **1** (4), 261–291.
- 29 Shustorovich, E. (1988) Bond-order conservation approach to chemisorption of polyatomic-molecules – effective partitioning of 2-center bond-energies. *Surface Science*, **205** (1–2), 336–352.
- 30 Shustorovich, E. and Sellers, H. (1998) The UBI-QEP method: a practical theoretical approach to understanding chemistry on transition metal surfaces. *Surface Science Reports*, **31** (1–3), 5–119.
- 31 Pallassana, V., Neurock, M. and Coulston, G.W. (1999) Theoretical density functional analysis of maleic anhydride chemisorption on Pd(111), Re(0001), and bimetallic Pd–ML/Re (0001) and Pd–ML//Mo(110) pseudomorphic overlayers. *The Journal of Physical Chemistry B*, **103** (42), 8973–8983.
- 32 Pallassana, V. and Neurock, M. (1999) Theoretical density functional study of the hydrogenation of maleic acid over Pd and Re surfaces. *Chemical Engineering Science*, **54** (15–16), 3423–3431.
- 33 Pallassana, V., Neurock, M. and Coulston, G. (1999) Towards understanding the mechanism for the selective hydrogenation of maleic anhydride to tetrahydrofuran over palladium. *Catalysis Today*, **50** (3–4), 589–601.
- 34 Pallassana, V. and Neurock, M. (2002) Reaction paths in the hydrogenolysis of acetic acid to ethanol over Pd(111), Re (0001), and PdRe alloys. *Journal of Catalysis*, **209** (2), 289–305.
- 35 Boisen, A., Dahl, S., Norskov, J.K. and Christensen, C.H. (2005) Why the optimal ammonia synthesis catalyst is not the optimal ammonia decomposition catalyst. *Journal of Catalysis*, **230** (2), 309–312.
- 36 Greeley, J. and Norskov, J.K. (2007) Large-scale, density functional theory-based screening of alloys for hydrogen evolution. *Surface Science*, **601** (6), 1590–1598.
- 37 Hellman, A., Honkala, K., Remediakis, I.N., Logadottir, A., Carlsson, A., Dahl, S., Christensen, C.H. and Norskov, J.K. (2006) Insights into ammonia synthesis from first-principles. *Surface Science*, **600** (18), 4264–4268.
- 38 Jacobsen, C.J.H., Dahl, S., Clausen, B.S., Bahn, S., Logadottir, A. and Norskov, J.K. (2001) Catalyst design by interpolation in the periodic table: bimetallic ammonia synthesis catalysts. *Journal of the American Chemical Society*, **123** (34), 8404–8405.
- 39 Honkala, K., Hellman, A., Remediakis, I.N., Logadottir, A., Carlsson, A., Dahl, S., Christensen, C.H. and Norskov, J.K. (2005) Ammonia synthesis from first-principles calculations. *Science*, **307** (5709), 555–558.
- 40 Hansen, E. and Neurock, M. (1999) Predicting lateral surface interactions through density functional theory: application to oxygen on Rh(100). *Surface Science*, **441** (2–3), 410–424.
- 41 Hansen, E. and Neurock, M. (2001) First-principles based kinetic simulations of acetic acid temperature programmed reaction on Pd(111). *The Journal of Physical Chemistry B*, **105** (38), 9218–9229.
- 42 Hansen, E.W. and Neurock, M. (1999) Modeling surface kinetics with first-principles-based molecular simulation. *Chemical Engineering Science*, **54** (15–16), 3411–3421.
- 43 Hansen, E.W. and Neurock, M. (2000) First-principles-based Monte Carlo methodology applied to O/Rh(100). *Surface Science*, **464** (2–3), 91–107.
- 44 Hansen, E.W. and Neurock, M. (2000) First-principles-based Monte Carlo simulation of ethylene hydrogenation kinetics on Pd. *Journal of Catalysis*, **196** (2), 241–252.
- 45 Mei, D., Sheth, P.A., Neurock, M. and Smith, C.M. (2006) First-principles-based

- kinetic Monte Carlo simulation of the selective hydrogenation of acetylene over Pd(1 1 1). *Journal of Catalysis*, **242** (1), 1–15.
- 46 Mei, D.H., Ge, Q.F., Neurock, M., Kieken, L. and Lerou, J. (2004) First-principles-based kinetic Monte Carlo simulation of nitric oxide decomposition over Pt and Rh surfaces under lean-burn conditions. *Molecular Physics*, **102** (4), 361–369.
 - 47 Mei, D.H., Hansen, E.W. and Neurock, M. (2003) Ethylene hydrogenation over bimetallic Pd/Au(1 1 1) surfaces: application of quantum chemical results and dynamic Monte Carlo simulation. *The Journal of Physical Chemistry B.*, **107** (3), 798–810.
 - 48 Neurock, M. and Hansen, E.W. (1998) First-principles-based molecular simulation of heterogeneous catalytic surface chemistry. *Computers & Chemical Engineering*, **22**, S1045–S1060.
 - 49 Neurock, M. and Mei, D.H. (2002) Effects of alloying Pd and Au on the hydrogenation of ethylene: an *ab initio*-based dynamic Monte Carlo study. *Topics in Catalysis*, **20** (1–4), 5–23.
 - 50 Hansen, E. (2001) *Methodology for Stochastic Simulations of Surface Kinetics*, University of Virginia.
 - 51 Kaspar, J., Fornasiero, P. and Hickey, N. (2003) *Catalysis Today*, **77**, 419.
 - 52 Burch, R. (2004) *Catalysis Reviews*, **46**, 271.
 - 53 Epling, W.S., Campbell, L.E., Yezerets, A., Currier, N.W. and Parks, J.E. (2004) *Catalysis Reviews: Science and Engineering*, **46**, 163.
 - 54 Ge, Q. and Neurock, M. (2004) Structure dependence of NO adsorption and dissociation on platinum surfaces. *Journal of the American Chemical Society*, **126** (5), 1551–1559.
 - 55 Neurock, M., Provine, W.D., Dixon, D.A., Coulston, G.W., Lerou, J.J. and van Santen, R.A. (1996) First principle analysis of the catalytic reaction pathways in the synthesis of vinyl acetate. *Chemical Engineering Science*, **51** (10), 1691–1699.
 - 56 Kragten, D.D., van Santen, R.A., Neurock, M. and Lerou, J.J. (1999) A density functional study of the acetoxylation of ethylene to vinyl acetate catalyzed by palladium acetate. *The Journal of Physical Chemistry A*, **103** (15), 2756–2765.
 - 57 Stacchiola, D., Calaza, F., Burkholder, L., Schwabacher, A.W., Neurock, M. and Tysoe, W.T. (2005) Elucidation of the reaction mechanism for the palladium-catalyzed synthesis of vinyl acetate. *Angewandte Chemie-International Edition*, **44** (29), 4572–4574.
 - 58 Chen, M.S., Kumar, D., Yi, C.W. and Goodman, D.W. (2005) The promotional effect of gold in catalysis by palladium–gold. *Science*, **310** (5746), 291–293.
 - 59 Provine, W.D., Mills, P.L. and Lerou, J.J. (1996) Discovering the role of Au and KOAc in the catalysis of vinyl acetate synthesis. 11th International Congress on Catalysis – 40th Anniversary, Vol. 101, Parts A and B, pp. 191–200.
 - 60 Lam, Y., Criado, J. and Boudart, M. (1977) *Nouveau Journal de Chimie*, **1**, 461.
 - 61 Boudart, M. and Djega-Mariadassou, G., (2008) *Kinetics of Heterogeneous Catalyzed Reactions*, Princeton University Press.
 - 62 Lee, J.K., Lee, J., Han, J., Lim, T.H., Sung, Y.E. and Tak, Y. (2008) Influence of Au contents of AuPt anode catalyst on the performance of direct formic acid fuel cell. *Electrochimica Acta*, **53** (9), 3474–3478.
 - 63 Zhou, S.H., Jackson, G.S. and Eichhorn, B. (2007) AuPt alloy nanoparticles for CO-tolerant hydrogen activation: architectural effects in Au–Pt bimetallic nanocatalysts. *Advanced Functional Materials*, **17** (16), 3099–3104.
 - 64 Bus, E. and van Bokhoven, J.A. (2007) Hydrogen chemisorption on supported platinum, gold, and platinum–gold-alloy catalysts. *Physical Chemistry Chemical Physics*, **9** (22), 2894–2902.
 - 65 Choi, J.H., Park, K.W., Park, I.S., Kim, K., Lee, J.S. and Sung, Y.E. (2006) A PtAu nanoparticle electrocatalyst for methanol electrooxidation in direct methanol fuel cells. *Journal of the Electrochemical Society*, **153** (10), A1812–A1817.

Keywords/Abstract

Dear Author,

Please check and/or supply keywords and an abstract. These will not be included in the print version of your chapter but in the online version.

If you do not supply an abstract, the section heading will be used instead.

Abstract

Detailed knowledge of reaction intermediates, mechanisms, and kinetics is essential to understanding how elementary molecular transformations control catalysis and establishing the structural features that control catalyst performance. Theory and simulation have proven to be quite successful in modeling the elementary steps that control these transformations. This knowledge can be used to aid in the design of new catalytic materials. Here we discuss two different approaches that are being used to screen novel compositions and atomically structured materials for enhanced catalytic activity and selectivity. The first approach is based on defining relevant reactivity descriptors that can be rapidly calculated to test thousands of candidate materials. The second approach uses more detailed simulations to follow molecular transformations and their kinetics over different alloy surfaces. These two approaches demonstrate that there is a tradeoff between knowledge and speed. Both approaches show great promise in aiding catalytic materials discovery.

Keywords: catalyst design; computational screening; density functional theory; quantum chemical; descriptors; kinetic Monte Carlo; Brønsted–Evans–Polanyi relationship; methanation; ammonia synthesis; NO decomposition; vinyl acetate synthesis; alloys.

11

Use of *In Situ* XAS Techniques for Catalysts' Characterization and Design

Christophe Geantet and Jean-Marc M. Millet

11.1

Introduction

Today, a large number of physical techniques are used to study solid catalysts and catalytic systems. These techniques, which are continuously evolving, have their advantages and disadvantages, but some of them are extremely powerful and efficient because they are specific to one element, are without interference, and provide both structural and electronic information. These include the X-ray absorption techniques and magnetic resonance techniques such as nuclear magnetic resonance (NMR) and nuclear gamma X-ray resonance (NGR). However, the two latter techniques cannot be applied in most catalytic reaction conditions and to the study of all types of elements; furthermore, both lack time and spatial resolution.

Like all physical characterization techniques, the X-ray absorption spectroscopy (XAS) is based on the interaction of matter with an X-ray beam. When the energy of the X-ray beam matches the core electron energy of the atom studied, photon absorption accompanied by the expulsion of one of these electrons may be observed. An absorption spectrum consists of two main regions. The first region occurs before and close to the absorption edge. It involves electron excitations to unoccupied bound states below the vacuum level and to bond and quasibond or continuum states, giving peaks that start to superimpose onto a smooth atomic contribution of the absorption spectrum. The second one, which starts 40–60 eV above the edge and goes up to hundreds of electron volts, involves the modulation of the X-ray adsorption of the atoms by its neighbors. Depending upon the region studied, the absorption technique is named XANES (X-ray absorption near-edge spectroscopy) and EXAFS (extended X-ray absorption fine structure spectroscopy).

Obviously, both techniques differ in energy of the final states of electrons sampled. At very high energies in the continuum of the electrons participating in EXAFS, the effect on the neighboring atoms becomes very small. The electron states approximate the plane waves that are simply scattered by atoms. The electronic information is enclosed in the low-lying extended states, as these states contain bonding information. The states populated by XANES are included in the last category. Therefore,

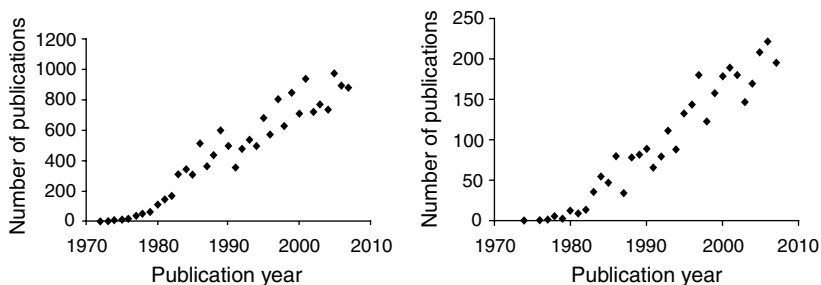


Figure 11.1 Number of publications identified by Science Finder database using search key “exafs” (on the left) and “exafs and catalysis” (on the right).

XANES contains local geometrical as well as electronic information whereas EXAFS provides information about the local geometrical structure around the photoexcited atom.

The development of synchrotron radiation facilities (SRFs) has greatly expanded the use of XAS technique since laboratory facilities cannot compete in terms of energy resolution and intensity. Among XAS users, the catalysis community is one of the major actors with approximately 20% of the published articles (Figure 11.1). From the early use of SRF, the father of the modern theory of EXAFS, F.W. Lytle and coworkers [1–3], applied EXAFS to catalytic systems, and the use of this technique has steadily grown ever since.

Recent technological improvements have made XAS as one of the most efficient techniques to study and design catalysts. An overview of some of these improvements and new capabilities are described in this chapter and their value in catalyst characterization is illustrated. These new capabilities offered by XAS are related to the common use of third-generation rings and the emergence of several new equipment, and most of the examples are drawn from measurements performed at the European Synchrotron Radiation Facility (ESRF; Grenoble, France). These examples have also been chosen to demonstrate the high adaptability of the techniques to the investigation of catalysts under working conditions and the ease of coupling with other techniques.

11.2

The X-Ray Absorption Techniques

11.2.1

Principles and Feasibility

The Fermi golden rule and the one-electron dipole approximation describe the variation of the absorption coefficient μ with energy during the interaction of a photon with a core electron (commonly 1s or 2p level):

$$\mu(E) \propto \langle \psi_{\text{exc}} | O_{\text{dip}} | \psi_{\text{fond}} \rangle^2 \delta(h\nu - E_{\text{exc}} + E_{\text{fond}}) \quad (11.1)$$

The Dirac δ function describes the energy conservation and $\delta(h\nu - E_{\text{exc}} + E_{\text{fond}})$ represents the density of states, Ψ_{fond} is the initial state core orbital with an energy, E_{fond} , Ψ_{exc} is the final state photoelectron wave function with a kinetic energy E_{exc} , and O_{dip} is dipolar interaction operator that mainly governs the phenomena. Like other spectroscopies, these transitions follow selection rules $\Delta L = \pm 1$, $\Delta j = \pm 1, 0$, $\Delta s = 0$, $\Delta m = 0$. Thus, in the framework of dipolar interaction, excitation of a K-edge (1s) will probe specifically p unoccupied orbitals.

When the excitation energy remains close to the edge, the amplitude of the signal is directly proportional to the empty states located above the Fermi level. Thus, XANES is a probe of the electronic properties of the matter, and theoretical calculations can model the shape and fine structures of an adsorption edge. Adequate software based on mono-electronic approach such as FEFF 8 or FDMNES can model these fine structures and give a complete understanding of the electronic properties of the sample [4]. Another way is the full description of the band structure by means of conventional softwares (Gaussian, VASP) introducing an excited state in the starting model. In fact, the electric operator is not restricted to dipolar interactions and also contains further quadrupolar terms that may generate in the XANES signal characteristic pre-edge features (or due to hybridization of p - d orbitals in the final state).

When the energy of the ejected photoelectron becomes much higher, the photoelectron spherical wave acts as a probe of the local structure around the absorbing atom. $\langle \Psi_{\text{exc}} | O_{\text{dip}} | \Psi_{\text{fond}} \rangle$ term is proportional to a so-called interference function $\chi(E)$ that is a sin function modulation superimposed onto the atomic background $\mu_0(E)$. Thus, the total absorption corresponds to $\mu(E) = \mu_0(E)(1 + \chi(E))$. It is this interference function that contains the structural information of interest, that is, the distance and number of neighboring atoms. In fact, this function expresses the interaction of the ejected photoelectron wave, thus, it is necessary to convert the x -axis from photon energy in electron volt to the corresponding wave vector of the ejected photoelectron $k(\text{\AA}^{-1})$ according to the relation:

$$k = [8\pi^2 m E_{\text{cin}} / h^2]^{1/2} \# (0.2624 E_{\text{cin}})^{1/2} \quad (11.2)$$

with $E_{\text{cin}} = E_{\text{ph}} - E_0$ (E_{ph} energy of the incident photon, E_0 energy of the absorption edge). This electron wave is backscattered by the neighboring atoms and goes back to the absorbing atoms (simple diffusion). The XAFS spectrum is defined as the normalized oscillatory structure occurring from these backscattered waves. The interference function is the superposition of all contributions of j atoms located at R_j distances. The total interference function of an atom i surrounded by j neighboring atoms is given by the following equation:

$$\chi(k) = S_0^2 \sum_j N_j A_j(k) (1/kR_j^2) \exp(-2R_j/\lambda_{\text{mfp}}) \exp(-2k^2 s_j^2) \sin[2kR_j + \phi_{ij}(k)] \quad (11.3)$$

The scale factor S_0^2 is a many-body effect due to the relaxation of the system in response to the creation of the core hole ($0.7 < S_0^2 < 1$ usually), N_j is the number of j atoms located at R_j distance, and $A_j(k)$ reflects the ability of j atom to backscatter the incoming wave and hence is primarily responsible for the intensity of the EXAFS signal. The $(1/kR_j^2)$ term corresponds to the spherical wave factor.

The sin function presents a structural and an electronic factor. $2kR_j$ is the phase shift introduced by a wave of wave number k traveling the distance $2R_j$. $\phi_{i,j}(k)$ is an additional shift occurring from the fact that the electron moves out and into the varying potentials of the absorbing atom (twice) and backscattering atoms.

Two dampening factors $\exp(-2R_j/\lambda_{\text{mfp}})$ and $\exp(-2k^2\sigma_j^2)$ explain why EXAFS spectroscopy gives a highly localized structural data (restricted at a maximum to 1 nm). The first term reflects the decay due to the free mean path or finite lifetime of the photoelectron. The second term representing the Debye–Waller broadening is partly due to thermal effects. In this classical equation, it is assumed that both thermal vibration and static disorder follow a Gaussian expression. This theoretical equation of the EXAFS signal is used in the dedicated software for the simulation of the EXAFS experimental functions. Thus, structural parameters are deduced.

11.2.2

Data Acquisition

Most of the conventional XAS data acquisitions are performed either on transmission mode or on fluorescence mode depending on the absorption of the sample or the concentration of the absorbing element. In transmission mode, the loss of intensity is related to Lambert–Beer's law:

$$I(E)/I_0(E) = e^{-\mu(E)x} \quad (11.4)$$

where I_0 and I are the photon intensities before and after the passage of the beam through the sample of thickness x . Thus, the absorption $\mu(E)$ in transmission mode is expressed as a function of $\ln I_0(E)/I(E)$. Since the attenuation of intensity is determined by the thickness and nature of the matter traversed by the X-ray beam, it is necessary to estimate the absorbance and calculate it from tabulated atomic absorption coefficients.

If the nature of the sample (thickness, concentration, etc.) does not allow recording of the absorption in transmission mode, the detection of fluorescence issued from the specific emission of the element studied is performed at 90 °C according to the incident beam (to minimize Compton emission of photons). Thus, the absorption is expressed as a function of the ratio $\mu(E) = I(E)/I_0(E)$ in some cases, self-absorption of fluorescence photons may occur and corrections should be performed.

Spectra are generally recorded over an energy range going from 200 eV before the edge to 800–1000 eV after the edge and without too many difficulties either under gas or liquid reaction media when using dedicated cells *in situ* (Table 11.1). This

Table 11.1 Typical recording conditions used with respect to a reference edge.

	Starting energy	Final energy	Increment (eV)
Pre-edge	−200	−20	5.0
XANES	−20	+30	0.5
EXAFS	+30	# 800	0.05 Å ^{−1}

advantage is crucial for studying catalysts since spectra can possibly be recorded under working conditions with almost no restrictions in terms of reaction temperature or pressure.

11.2.3

Spectral Analysis and Interpretations

As already mentioned above, XANES spectrum is a highly sensitive image of the electronic properties of the sample. Qualitative analysis can be easily done as well as the chemiometric extraction of the contribution of specific features (obtained from references), which give the distribution of various chemical states of the excited atom (see examples below). Furthermore, several softwares are now easily available and may provide simulations to help proposed models. Concerning EXAFS, data analysis is based on a two-stage procedure.

The first stage corresponds to the extraction of the interference function from the experimental data:

$$\chi(E) = (\mu(E) - \mu_0(E)) / \mu_0(E) \quad (11.5)$$

where $\mu_0(E)$ stands for the absorption of the free atom. To proceed to this extraction, several steps are required. At first the threshold energy E_0 is determined. In practice, it is generally considered that the middle point of the edge (maximum of the first derivative) is a good first approximation of E_0 . This parameter will be later optimized in the curve fitting procedure. The second stage of the data treatment involves the estimation of $\mu_0(E)$. This is obtained from the extrapolation of pre-edge absorption (often linear) and extraction of the background $\mu_0(E)$ from the EXAFS oscillating part by using polynomial or cubic spline methods (Figure 11.2).

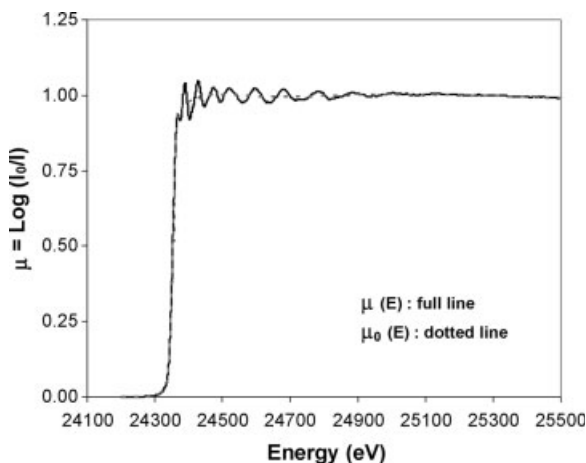


Figure 11.2 Typical absorption spectrum recorded at Pd K-edge.

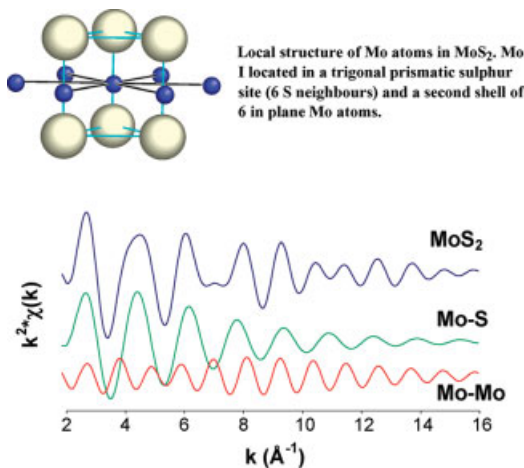


Figure 11.3 Interference function of MoS₂ sample at Mo K-edge as a sum of Mo–S and Mo–Mo contributions.

In fact, the expression of interest is $\chi(k)$, which is obtained from the conversion into k space using the following expression:

$$k = \sqrt{\frac{2m}{\hbar^2}}(E - E_0)^{1/2} \quad (11.6)$$

where E_0 is the threshold energy above which the photoelectron is emitted. The oscillating interference function contains the mixture of several contributions of neighboring atoms as illustrated in Figure 11.3 demonstrating the local environment of Mo in MoS₂ structure. In this model, the interference function is the sum of the Mo–S contributions and Mo–Mo contributions, which are identified below. The specific contribution of the combination of the phase shifts and backscattering amplitudes will introduce in the total interference function reinforcement or extinction of oscillations.

Analyses and understanding of EXAFS signal was deeply improved in 1975 by the introduction of Fourier transform (FT) analysis [5]. An FT of the EXAFS signal with respect to k will transform the oscillations in the reciprocal space (\AA^{-1}) into a corresponding pseudoradial distribution function in the real space (\AA):

$$k^n \chi(k) = 1/\sqrt{2\pi} \int_{R_{\min}}^{R_{\max}} \text{FT}(r) e^{-2ikr} dr \quad (11.7)$$

For MoS₂ sample (see Figure 11.3), for instance, the first peak corresponds in the case of MoS₂ to the Mo–S contributions, the second to Mo–Mo ones. Due to the FT operation, a real part and an imaginary part are obtained. The imaginary part is often used as a guide for the location of the surrounding atoms (more precise than the amplitude). The oscillation function is also often weighted by k^n . This weighting compensates the reduction of the oscillations in the high k region and emphasizes the contribution of heavy atoms.

Furthermore, *ab initio* multiple scattering simulations are able to distinguish contributions coming from simple diffusion from those coming from multiple diffusions, thus allowing a complete fitting of the spectra.

The final stage involves a curve fitting analysis of the experimental data. A set of parameters for one or several shells is used as a starting point and required phase and amplitude files are employed. Simulation is based on the standard EXAFS equation, and a minimization method is applied to find out the experimental shell parameters (N , r , σ , ΔE_0). Details of analytical methods currently used are given in classical textbooks [6–9], and many free and friendly softwares are available for data treatment [10].

An alternative to classical interpretation of the wave functions by Fourier transform analysis based on the use of continuous wavelet analysis has recently been proposed. This new analytical method is an efficient method for analyzing “frequency-modulated” signals. In the case of XAS, it provides an informative 3D view of the signals in (k , R) space and the corresponding dependency of each EXAF component [11, 12]. Whatever the technique used (micro XAS, QXAS, etc.) accumulation of data requires adequate software to proceed to the data analysis. In most of the cases, XAS and principal component analysis tools (PCA) in tandem are able to provide unique information in terms of speciation with micro XAS or XANES studies or structural modification upon gas or reactant or temperature modifications during time-resolved studies [13, 14].

11.3

Recent Applications of X-Ray Absorption Techniques to the Design of Heterogeneous Catalysts

The improvements in sources, mirrors, monochromators, and detectors always provide more efficient tools in terms of energy resolution, spatial resolution, time resolution, and sensitivity. We will try to illustrate in the following paragraphs these progresses through examples mostly dealing with catalysts under reaction or during activation. In these examples, XAS is often coupled with other techniques to allow a better characterization of the catalysts or the collection of the information on the complete catalytic process.

11.3.1

Time Resolution

The monitoring of the activation or catalytic processes and the impact of reactants on the catalysts requires accurate time resolutions. With that respect the time-resolved XAS is well adapted and present the great advantage that it can be performed in the condensed phase and at low concentration.

There are two different technical approaches to make the technique time resolved. The first one, called Quick EXAFS (QEXAFS) was developed by R. Fhram in the 1980s [15]. In conventional XAS, a double-mirror monochromator is moved step by

step to select the monochromatic wavelength that will excite the sample; under these conditions, optimizing signal-to-noise ratio, a typical acquisition time of several tenths of minutes is used. Instead of a step-by-step movement, it is also possible to apply a continuous rotation of this monochromator and to acquire simultaneously the intensities. This provides the record of data within a few seconds. Recently, cam-driven monochromators were developed allowing data acquisition in millisecond range [16]. In this case, signal-to-noise ratio diminishes and some information is lost; nevertheless, both XANES signals and interference functions can be obtained and used to follow the dynamics of transformation of a catalytic system.

The alternative way to explore time resolution is dispersive X-ray absorption spectroscopy (DAXS). Unlike QEXAFS, which relies on the mechanical rotation of the monochromator, DXAFS uses a bent crystal focusing the polychromatic beam of the synchrotron ring on the sample. A position sensitive detector measures simultaneously the transmitted energies.

This scheme presents a high stability in focal spot position and in energy scale because there are no moving components and a high acquisition speed as all energy points are acquired rigorously in parallel.

In the following section, we will illustrate the two experimental approaches, QEXAFS and DXAS, with two different examples. The first approach deals with the use of QEXAFS to study the *in situ* sulfidation of an industrial CoMo on alumina hydrotreating catalyst. Hydrotreatment (HDT) is the removal of organic sulfur, nitrogen, oxygen, and metals from petroleum crudes at high hydrogen pressure. Since the first processes were developed before the second world war, hydrotreatment grew steadily and represents now more than 50% of the total refining capacities. The trend to tighten the legislation toward lowering the sulfur content in fuels (10 ppm of sulfur in gasoline and gas oil by 2009 in the EC) and the necessity to convert heavier fractions of crude oil explain the expansion of HDT processes over the years. In hydrodesulfurization (HDS), CoMo sulfide catalysts supported on alumina are used, and the structure of the active phase has been investigated since the 1970s. It is now well established that the active phase consists of the so-called "CoMoS," which means the decoration of MoS₂ nanoslabs by Co atoms at the periphery of the particles. XAS and Mössbauer spectroscopy were the two techniques used to describe this unique structural configuration of the active sites (now supported by theoretical calculations). In most cases, the activation of catalysts, provided in an oxidized state by the manufactures, is performed *in situ*, in the HDT reactor by using (in the case of gas-oil production) an SRGO spiked with a sulfiding agent (dimethyl disulfide in Europe). An alternative is to provide the refiners a catalyst that has already been sulfided *ex situ* [17]. To understand this process, we have studied the *in situ* sulfidation of a CoMo/Al₂O₃ catalyst by QXAS [18].

A CoMo on alumina industrial catalyst (Co 3 wt%, Mo 12.3 wt%) and a Co on alumina (3 wt%) catalyst were studied during *in situ* sulfidation by an H₂/H₂S (10%) gas mixture flowed from RT up to 400 °C. Samples were pressed into pellets and mounted on a dedicated sulfidation cell. A QEXAFS spectra was recorded for 30 seconds, each 10 °C of the heating ramp of sulfidation. Figure 11.4 compares the absorption data in transmission mode for XAFS (45 min) and QEXAFS (30 s).

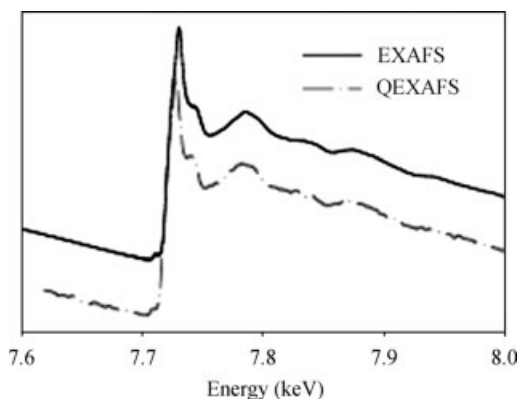


Figure 11.4 Comparison of XAFS and QEXAFS modes recorded at room temperature at Co K-edge of absorption for CoMo/Al₂O₃ catalyst in its initial oxide form.

Even if the signal-to-noise ratio is decreased in fast acquisition mode, reliable XAFS information is obtained. Both XANES and EXAFS can be used to get useful information on the kinetics of sulfidation of Co atoms in both solids.

A first interpretation is provided by the analysis of the intensity of the white line in the XANES spectra. Co in oxide form either in Co or in CoMo on alumina presents a strong white line due to Co 1s–4p transition, whereas in the sulfided state the white line disappears. This effect is a measurement of the change in the partial density of the final states located above the Fermi level. Figure 11.5 illustrates the evolution of the white line during the sulfidation reaction of the Co/Al₂O₃ sample. To compare the intensities, the edge jump is normalized to the room temperature. White line intensity (the difference between the flat absorption before the edge and the maximum of absorption after the edge I_{wl}) is normalized by the white line intensity of the oxide form at room temperature. Results obtained are similar to those obtained after a shape renormalization of the absorption spectra. Comparison of the sulfidation treatment with that performed under He shows that even at room temperature the Co atoms in CoMo catalyst react with H₂/H₂S (Figure 11.6). Above 250 °C, no variation of the white line intensity is observed suggesting that sulfidation of Co is complete. The Co/Al₂O₃ presented a different behavior; white line modification was noticeable and abrupt: modification of Co environment starts at 150 °C and finishes at 250 °C. Measurements performed during cooling of a sulfided CoMo sample under H₂/H₂S from 400 °C to room temperature showed that temperature has no effect on the edge jump of the sulfided CoMo sample.

Similar observations have been made after treatment of the EXAFS oscillations. Replacement of O atoms by S atoms in the coordination sphere of Co atoms shifted the first peak of the Fourier transform uncorrected from phase shift (Figure 11.7). A program using an automatic extraction of the RDF and the distance of the main peak, including phase shift correction, was used during the experiments to get a rapid overview of the modification of Co atoms neighboring during the sulfidation process. Figure 11.7 shows that the first-neighbor distance rapidly rises up to the value of

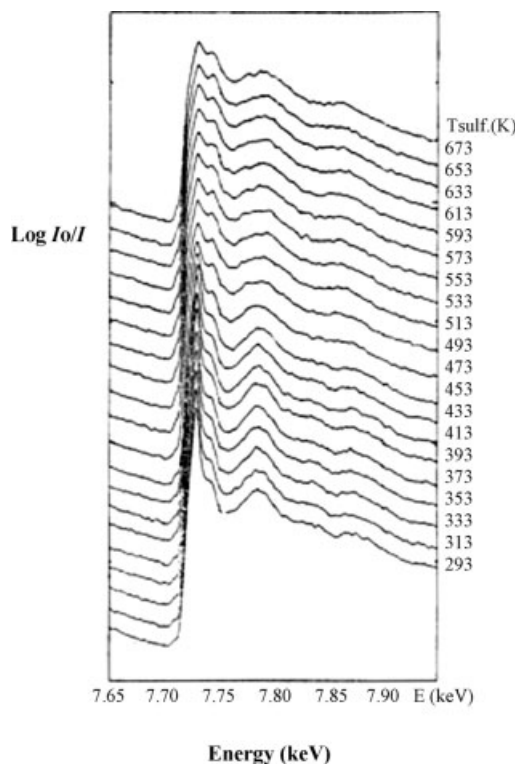


Figure 11.5 *In situ* QEXAFS at Co K-edge of the sulfidation of a Co on alumina catalyst.

Co–S distance in CoMo catalyst, whereas for Co alone, a temperature of 200 °C is needed to perform the sulfidation. Thus, both techniques, in a perfect agreement, give the same image of a fast sulfidation process for the CoMo catalysts starting at room temperature and a sudden reaction at circa 200 °C for the Co on alumina

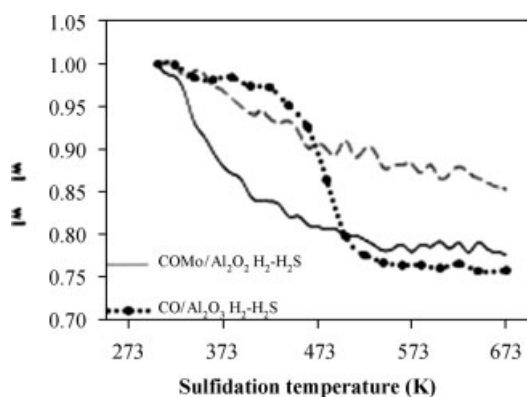


Figure 11.6 Evolution of white line intensity versus temperature of a CoMo/Al₂O₃ catalyst under H₂/H₂S and He and comparison with Co on alumina sample under H₂/H₂S.

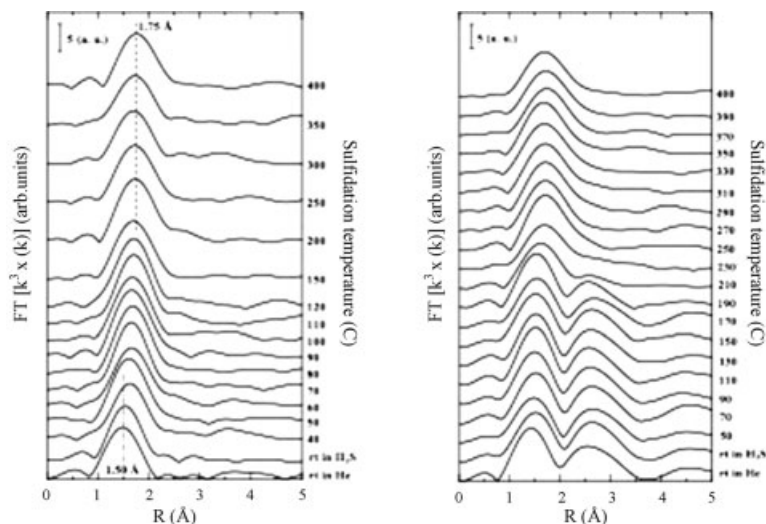


Figure 11.7 Fourier transforms of the Co K-edge k^3 -weighted Quick EXAFS functions of an oxide CoMo/ Al_2O_3 (left) and Co/ Al_2O_3 (right) catalysts during sulfidation at rising temperature.

catalysts. This example illustrates the considerable advantage of using QEXAFS for understanding the activation of catalysts.

The use of dispersive X-ray absorption spectroscopy is illustrated with the following example dealing with the study of the behavior of molybdenum oxide under reductive and oxidative atmosphere [19]. The bulk structure of molybdenum trioxide under reductive and oxidative reaction conditions was investigated *in situ* by DXAS at the Mo K-edge. Reduction and reoxidation of MoO_3 at 500 °C with H_2 and O_2 (100%, 1 atm), respectively, XAS experiments were carried out at the Mo K-edge (19.999 keV) utilizing an energy-dispersive spectrometer (ESRF, ID24) equipped with a curved Si(111) polychromator in transmission mode. Figure 11.8 shows the evolution of Mo K-edge

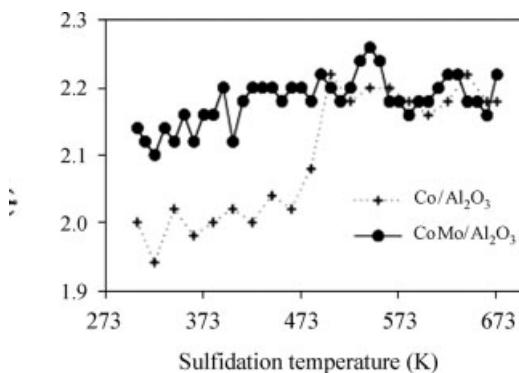


Figure 11.8 Evolution of the distance of the maximum of the first peak of the FT of EXAFS signal corrected from Co–S phase shift.

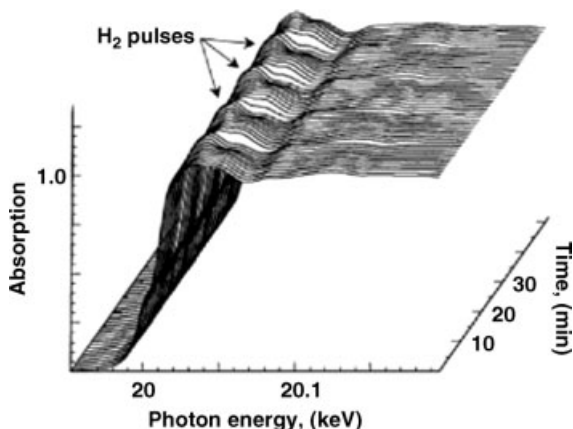


Figure 11.9 Evolution of Mo K-edge XANES of MoO_{3-x} during several reduction and oxidation cycles with H_2 and O_2 , respectively [18].

XANES spectra measured during a series of H_2 and O_2 pulses at 500°C over a period of 50 min with a time resolution of 15 s per spectrum. Like in the previous example, the evolution of the white line intensity corresponds to the alternative reduction or reoxidation of MoO_{3-x} sample. The reduction or reoxidation of MoO_{3-x} also causes a shift in the Mo K-absorption edge to lower or higher photon energies, respectively, and Figure 11.9 depicts Mo K-edge-shift data corresponding to absorption spectra, together with the normalized mass spectrometer signal coupled to the *in situ* XAS cell for H_2 and O_2 . It can be seen from Figure 11.10 that reduction and reoxidation of Mo oxide proceeded rapidly (subminute scale) under the conditions employed.

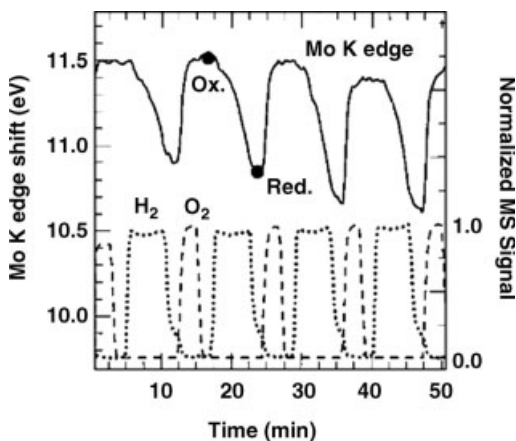


Figure 11.10 Mo K-edge position (relative to the first inflection point in the Mo metal K-edge XANES at 19 999 eV) of MoO_{3-x} during reduction and oxidation obtained from corresponding XANES spectra in Figure 11.9. Oxidized and reduced states of Mo are indicated. Normalized O_2 and H_2 MS signals are shown [19].

A survey of the application of time-resolved EXAFS to homogeneous systems reveals a marked preference for a given experimental variant according to the material phase under study [20]. QEXAFS is found to predominate in the solid state, EDE in the liquid phase: it is in the liquid phase, with its intrinsic spatial homogeneity, that the constraints of the dispersive approach are least problematic.

11.3.2

High-Resolution XANES

Recent development of third-generation synchrotron source with increased brilliance of sources enables the measurement of trace elements by XANES at a few parts per million level when combined with modern, highly efficient detectors. Furthermore, progress in optical devices allowed to strongly increase the energy resolution that, due to the difference of EXAFS, is crucial for XANES measurements. This energy resolution ΔE , dominated by the divergence of the beam, is proportional to the photon energy E and $\Delta E/E$, easily reaches now 10^{-4} – 10^{-5} , which corresponds to ΔE lower than 1 eV at low energy ($E = 10$ keV), and a factor 3–5 better than the intrinsic spectral broadening at any K or L absorption edge.

Although XANES has been used less frequently in the past to characterize catalysts because of the lack of a standard tool to analyze the experimental data, today theoretical calculation of XANES without any adjustable parameters, that is, by means of first-principles calculations, is now possible and should boost the use of XANES to characterize catalysts [4].

XANES can be a powerful tool to characterize elements in catalysts determining their oxidation state, local site symmetry, and orbital occupancy (part II) and it has proved particularly helpful in probing different elements in the multicomponent MoVTe(Sb)NbO-based catalysts for light alkanes' oxidation and characterizing their behavior under oxidative or reductive atmosphere. The related study has been used to exemplify the powerful analytical perspective of XANES to the in-depth characterization of an active catalytic phase, stressing the importance of *in situ* study.

The multicomponent MoVTe(Sb)NbO molybdate-based catalysts have been shown to be efficient for the partial oxidation of light alkanes. These catalysts, first patented for propane ammoxidation to acrylonitrile, are also active for the oxidation of propane to acrylic acid and the oxidative dehydrogenation of ethane [21–23]. The active phase of these catalysts is an oxide solid solution containing the four metallic elements: Mo, V, Te or Sb and Nb. This phase, called M1 phase, has a formula reported as $(\text{AO})_{2-2x}(\text{A}_2\text{O})_x\text{M}_{20}\text{O}_{56}$, where $\text{A} = \text{Sb, Te, M} = \text{Mo, V, Nb}$ and $0 < x < 1$ and into which V/Mo and Nb/Mo ratios can slightly vary [24, 25]. The structure can be described as a network of MO₆ octahedra ($\text{M} = \text{Mo, V, Nb}$) sharing corners and edges forming pentagonal, hexagonal, and heptagonal channels in the [001] direction. The first channel type contains Nb and oxygen; the second, Sb or Te and oxygen; and the third one is empty. The presence of several elements, each of them with several possible oxidation states, does not allow a redox titration of each element in the solid and it is the only technique specifically and independently applicable to each element among which XANES appeared very efficient that allowed to characterize the M1

phase [26]. In the case of an Sb-containing M1 phase (M1(Sb)) such characterization at room temperature led to the formula $[\text{Sb}^{5+}\text{O}]_{1.0}[\text{Sb}^{3+}\text{O}_{0.5}]_{0.8}\text{V}^{4+}_{3.4}\text{V}^{5+}\text{Mo}^{6+}\text{Mo}^{5+}_{14.5}\text{Nb}_{2.2}\text{O}_{56}$, where Sb, V, and Mo cations are present with two valence states. The goal of this *in situ* characterization by XAS is described in this example was to determine the valence state of these cations in reaction conditions and to understand how a structure built from corner-sharing octahedra could support a high concentration of oxygen vacancies, which is often a common trait of efficient oxidation catalysts. XAS was measured under working conditions at the K-edges of V and Mo and the L_1 -edge of Sb and was combined for the first time with electrical conductivity measurements [27].

The experiment consisted in recording XANES spectra at the three edges of an M1(Sb) phase sample with the composition given above at different temperatures (25–380 °C) and under different atmospheres (pure He, pure O_2 , and two gas mixtures containing propane and oxygen in different ratios). The former gas mixture ($\text{O}_2/\text{C}_3\text{H}_8/\text{He} = 10/5/85$) is the most common for the process of propane oxidation to acrylic acid; the latter ($\text{O}_2/\text{C}_3\text{H}_8/\text{He} = 7.5/7.5/85$) is enriched with propane. The list of successive treatments used to determine the nature of the chemical processes taking place in the catalyst under real working conditions and the processes controlling the mobility of oxygen in the catalyst structure is shown in Figure 11.11a. The *in situ* cell and setup used (ESRF beamline ID26) allowed XAS measurements every 63 s at different temperatures under atmospheric pressure gas

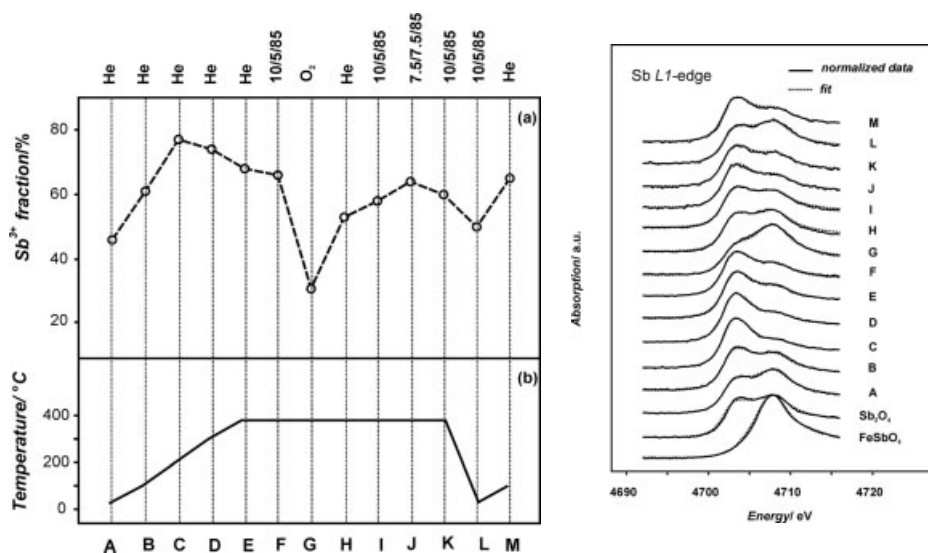
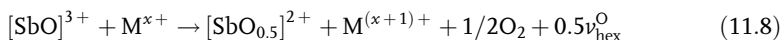


Figure 11.11 (a) Sb L_1 -edge XANES spectra of the M1 phase under different redox conditions and the spectra of the reference samples. Solid lines show experimental data; dotted lines show best fit. The letters A–M correspond to the temperature and atmospheres given in (b) with the evolution of the fraction of Sb^{3+} cations in the structure of the M1 phase calculated from the fit of the spectra [27].

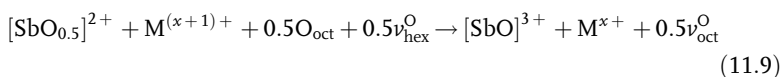
flows and simultaneously allowed electrical conductance measurements. Reactivity of the catalyst was controlled by online gas-phase analysis using a mass spectrometer to study catalytic and electronic properties of the active phase in dynamic conditions.

The Sb L₁-edge spectra (4.660–5.600 keV) showed a prepeak corresponding to a transition from the 2s_{1/2} level into unoccupied 5p states whose energy depends on the presence or lack of the 5s electrons. The position of the Sb L₁-edge varied by 4 eV for a Sb^{III} and a Sb^V cation and the relative ratio of Sb^{III} and Sb^V in a compound could be determined by fitting this prepeak considering a combination of two peaks whose relative areas are proportional to the relative amount of the two cations. The analysis of K-edge XANES spectra of V and Mo was based on the observations of the pre-edge and edge positions [28].

First the sample was heated under He up to 380 °C. Although no change in the sample was expected during this treatment, a strong reduction of Sb was observed (Figure 11.11b). Although it was thought that such reduction might be related to the presence of hydrogen in the bronze-like structure of M1, it was shown that it resulted from a self-reduction with the formation of O₂ evidenced by TG-TDA coupled with mass spectrometry [28]:



where M = V, Mo and $\nu_{\text{hex}}^{\text{O}}$ are oxygen vacancies in the hexagonal channels. At 300–380 °C, antimony reoxidized but to a lesser extent than it was reduced. This reoxidation corresponded to an equilibration of oxygen content in the structure with the diffusion of O²⁻ from the octahedral network into the hexagonal channels, where antimony cations are located:



where M = V, Mo and $\nu_{\text{oct}}^{\text{O}}$ are oxygen vacancies in the octahedral network. The oxygen vacancies formed in the hexagonal channel are located between two antimony atoms and removal of oxygen leads to the reduction of Sb⁵⁺ to Sb³⁺ and to the formation of the [Sb³⁺O_{0.5}]²⁺ species. Theoretically, only half the oxygen atoms can be removed from the channels, otherwise the coordination number of Sb³⁺ would be too low. Since the [Sb⁵⁺O]³⁺ and [Sb³⁺O_{0.5}]²⁺ structures are charged differently, removal of oxygen from the hexagonal channels should be accompanied by the oxidation of Mo or V atoms from the octahedral network. However, below 380 °C no reactivity of vanadium was observed and the mean oxidation state of vanadium remained close to 4+. If it had participated in Equation 11.8 as the M cation, an oxidation of 17.6% of V would have been taken place, which would have been unambiguously detected. Therefore, it has been proposed that Mo was involved in the reaction although no oxidation of Mo was observed. Nevertheless, taking into account the proportion of Mo in the oxides and the stoichiometry of Equation 11.8, only 3.7% of molybdenum would be oxidized, which is almost undetectable by XANES.

At 380 °C, antimony also reversibly changes its oxidation state depending on the partial pressures of oxygen and propane in the atmosphere. This proves that oxygen

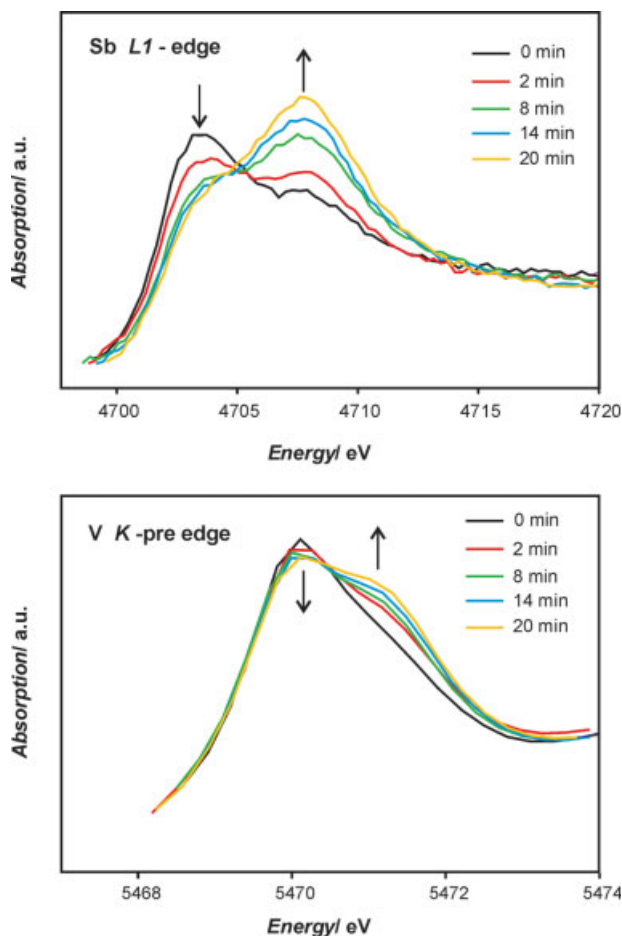


Figure 11.12 Time variation of Sb L₁-edge and V K-edge XANES spectra of the M1 phase in O₂ atmosphere at 380 °C [27].

from the hexagonal channels participates in the redox process of the M1(Sb) phase taking place under the working conditions. These results prove very high oxygen mobility in the phase. Moreover, they clearly demonstrate that it is worthless to study this catalyst *ex situ*.

Oxidation of the catalyst has been studied by switching the catalytic reaction mixture gas flow for a pure oxygen gas flow. The XANES spectra at V K-edge and Sb L₁-edge during exposure of the sample in O₂ atmosphere are shown in Figure 11.12. Variations were observed at the V K-edge and Sb L₁-edge during exposure of the sample in O₂ atmosphere but not at the Mo K-edge (Figure 11.13). The kinetics of the oxidation of Sb and V together with the data of conductivity measurements is presented in Figure 11.14. The M1 phase reached equilibrium in 20–25 min. This length of time is required for the diffusion of oxygen from the surface to the bulk of

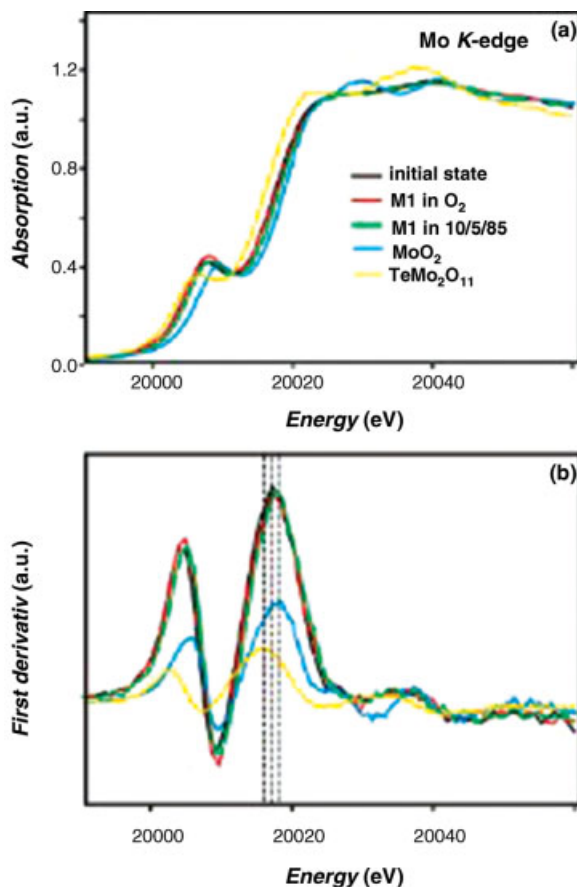


Figure 11.13 (a) Mo K-edge XANES spectra of M1 phase in the initial state at 25 °C and under steady-state conditions in the 10/5/85 mixture and O₂ atmosphere at 380 °C compared with the spectra of the reference samples. (b) First derivatives of the XANES data. Dashed lines indicate positions of the edge jumps [27].

the M1 crystallites. The electrical conductivity changes synchronously with Sb and V oxidation states and the concentration of oxygen vacancies in the structure, which is normal for *n*-type semiconductors (Figure 11.14). If Sb and V oxidations proceed at almost the same speed, oxygen exchange seems faster through the hexagonal channels since only Sb changes its oxidation state at low temperatures (100–300 °C). Furthermore, if the contributions of the Sb and V cations to the redox process are compared in terms of electrons donated, the Sb cations contribute almost twice the number of V cations, although they are more than four times fewer in number. These results demonstrated that hexagonal channels where Sb cations are located play a role as oxygen reservoirs in the M1 structure. The changes

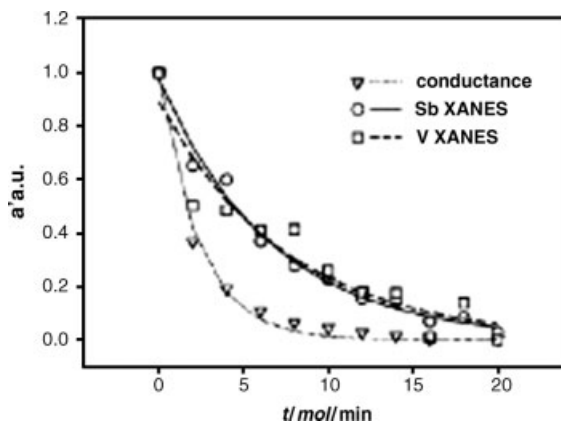


Figure 11.14 Analysis of variation of conductance and XANES spectra (at Sb L_{1-} and V K-edges) of the M1 phase in O_2 at $380^\circ C$ using an exponential decay function. Points show the experimental data; lines indicate the best fit [27].

observed were all reversible when the catalyst was alternately exposed to He and 10/5/85 atmosphere. The propane conversion at $380^\circ C$ with the 10/5/85 gas mixture was around 16%, which is slightly lower than that obtained in a fixed-bed reactor in the same conditions (19%) but the carbon-containing products detected by mass spectrometry correspond to those generally observed (acrylic and acetic acids, CO, CO_2 , and propene).

When the oxygen-to-propane ratio was reduced from 10/5 to 7.5/7.5, a slight reversible reduction of antimony was observed, showing that the catalyst bulk is sensitive to the redox catalytic atmosphere and correspondingly equilibrated. At the end of the experiment, the catalyst was cooled at room temperature under the reaction gas mixture. After the switch to a pure He atmosphere, the catalyst was again heated at $100^\circ C$. A reduction of Sb similar to that observed at the beginning of the experiment was observed. This demonstrates the reversibility of Equation 11.8 and again points to the need for studying the oxidation state of the metallic elements of such type of catalysts in reaction conditions.

This study shows that XAS coupled with conductivity measurements could be applied to understand a mechanism of catalytic processes under dynamic operational conditions. The simultaneous use of these techniques allowed to observe the mobility of different types of oxygen in the complex structure of the M1(Sb) phase in reaction conditions and to demonstrate that hexagonal channels play the role of oxygen reservoirs. Finally, this study demonstrated how XAS measurements can contribute to determine the electronic structure of a complex redox active phase, and the results obtained may be considered for designing a new preparation method starting from elements' precursors with their *in situ* relative oxidation state, foreseeing the possibility and extent of isovalent cationic substitutions or even undertaking a theoretical modeling of the active solid phase.

11.3.3

High Detection Sensitivity

Using SR sources, concentrations of elements of 10^8 atoms cm^{-2} or femtogram level can be detected with accurate detectors and methods such as total reflection X-ray fluorescence [30]. If impurity detection is not a main objective in catalyst studies, XAS might be able to characterize active phases or dopants with very low concentrations. Thus, compared to other characterization techniques, XAS is able to measure parts per million or parts per billion concentrations of elements in a complex matrix under *in situ* conditions.

The following example, dealing with cracking catalysts, will illustrate the ability of XAS to characterize diluted samples. Fluidized catalytic cracking (FCC) is economically the most important catalytic process; it converts heavy petroleum feedstock into gasoline range hydrocarbons, that is, C_{20} – C_{40} and above downsized into C_5 – C_{10} range. Cracking reactions involve C–C bond rupture catalyzed by acid sites. Thus, cracking catalysts are solid acids that include especially SiO_2 – Al_2O_3 and Y zeolites formed into microspheres (40–120 μm). Over 1500 tons per day of such FCC catalysts are consumed worldwide in processing more than 14 million barrels per day of oil. Crackers operate at 520–550 °C under 2–3 atm, with a catalyst-to-oil ratio of 4–6 and very short contact time (a few seconds). During this short residence time, catalyst accumulates appreciable amount of coke (about 1%) leading to a loss of activity. Therefore, the catalyst is routed to a regenerating procedure where the coke is burned at a temperature of 650–750 °C. Following regeneration, the fluid catalyst is returned to the cracking section. Additional thermal stability of the catalyst is provided by ion exchanging zeolite with rare earth ions such as La^{3+} or Ce^{3+} . To facilitate the regeneration process and reduce its cycle time, Pt is sometimes added at a very low content (0.05 wt%).

We have studied the *in situ* reduction of such La-stabilized FCC catalysts, which also contain 500 ppm of platinum as determined by chemical analysis. X-ray absorption spectroscopy measurements were performed at FAME beamline station at the ESRF (French Collaborative Research Group) at Pt L_3 -edge in the fluorescence detection mode performed with a 30-elements solid-state detector (Canberra). The reduction procedure was done under a flow of pure hydrogen at atmospheric pressure from room temperature and up to 300 °C. A dedicated *in situ* T-shaped quartz cell was used and sample was introduced as a self supported pellet. Figure 11.15 compares the FT of the catalyst before and after *in situ* reduction with H_2 , for 2 h at 300 °C. We can see that even with such low concentration of Pt, accurate data could be obtained. By direct visualization of the FT, we can notice that starting from the oxidic state, reduction at 300 °C created a main contribution corresponding to Pt–Pt metallic state but an oxidic contribution still remained. Data treatment provides the structural information as summarized in Table 11.2. The average Pt–Pt coordination number was close to 4.6 suggesting from classical $N = f(\text{particle size})$ relationship an average size of metallic Pt of 2 nm [31]. This information cannot be achieved by means of transmission electron microscopy (TEM) since the concentration of Pt is very low. Few particles are observed either by bright field conventional imaging or by high-angle annular dark field

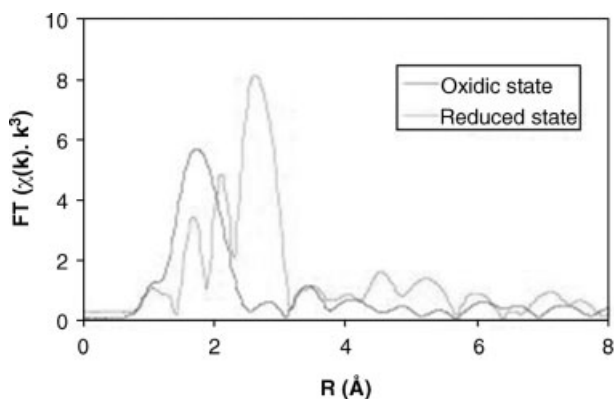


Figure 11.15 Fourier transform $\chi(k)$ at Pt L_3 -edge of oxide state and *in situ*-reduced Pt (500 ppm)-doped FCC catalyst.

detection (HAADF) detection, which specifically images heavy atoms. Statistics from the images for getting an average size of Pt particles cannot be performed. XAS is a unique way that can provide indirectly this information. We can also notice an oxidic contribution that is supposed to correspond to highly dispersed Pt in the zeolite matrix as it was also observed with higher loadings (close to 1 wt%) after *in situ* reduction [31–33]. However, due to the complexity of the catalysts, we can also consider other specific interactions with the silica alumina or the rare earth oxide.

11.3.4

Spatial Resolution

Early synchrotron rings provided X-ray beams of centimeter diameter size that with increasing brilliance were reduced to millimeter size by the use of slits. With the third generation of synchrotron rings, two bendable mirrors are often located before and after the monochromator for beam collimation and to obtain a vertical focus. A beam size around $250\ \mu\text{m} \times 150\ \mu\text{m}$ can thus be focalized on the sample. A microfocalization apparatus (such as the Kirkpatrick–Baez system) allows decreasing the size of the beam in the range of $20\ \mu\text{m} \times 20\ \mu\text{m}$ with full flux and close to $1\ \mu\text{m} \times 1\ \mu\text{m}$ with slits. This kind of spatial resolution permits scanning of the sample and consequently

Table 11.2 Structural parameters derived from EXAFS at Pt L_3 -edge of Pt-doped FCC catalysts.

	Pt–O shell			Pt–Pt shell		
	$R(\text{Pt–O})$ (Å)	$N(\text{O})$	$\sigma^2 \times 10^3$ (Å ²)	$R(\text{Pt–Pt})$ (Å)	$N(\text{Pt})$	$\sigma^2 \times 10^3$ (Å ²)
Oxidized state	2.39	6	2.8	–	–	–
Reduced state	2.45	4.9	2.10	2.789	4.6	3.56

$\Delta R = \pm 0.01\ \text{\AA}$, $\Delta N = \pm 0.7$, $\Delta(\sigma^2) = \pm 0.5 \cdot 10^{-3}\ \text{\AA}^2$.

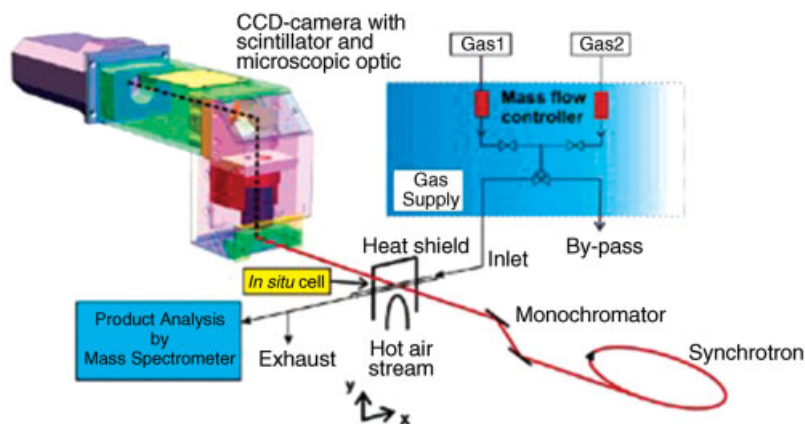


Figure 11.16 Experimental setup for 2D mapping studies in the micrometer scale [39].

spatial elemental mapping according to the probed edge. Thus, the term of micro-XAS was proposed to describe this approach, which brings a chemical state complementary analysis to the elemental one brought by X-ray fluorescence (XRF), for instance. Up to now, micro-XANES has only been applied to environmental science for the study of the speciation of Cr in particulate matter ($7\text{ }\mu\text{m} \times 7\text{ }\mu\text{m}$) or geology for the analysis of a natural rock thin section (below $5\text{ }\mu\text{m} \times 5\text{ }\mu\text{m}$) [34, 35]. Estimated spot sizes of $2\text{ }\mu\text{m} \times 1\text{ }\mu\text{m}$ are expected in near future [36].

Another technological alternative consists of a full-field imaging with a 2D detector such as a charge-coupled device (CCD) camera coupled by means of a microscope to a scintillation screen [37]. Thus, the spatial resolution of this configuration coming from the detection system is estimated to a few micrometers. Such 2D mapping approach combines a parallel data acquisition leading to short recording times (30 s). Figure 11.16 illustrates this kind of experimental setup used for the study of the ignition of Rh/Al₂O₃ catalysts during partial oxidation of methane [38]. The spatially resolved 2D monitoring is in the range of $10\text{ }\mu\text{m}$. The X-ray energy was scanned in the XANES region around the Rh K-edge (from 23.190 to 23.375 keV with 1 eV step). After correction of the readout noise, integral absorption was obtained for each pixel and XANES spectra were compared with reference oxide and metallic states. The characteristic white line of an oxidic state clearly differentiates the nature of the chemical state compared to the metallic one. The absorption as a function of the position of the catalyst in the reactor (x , y) can thus be obtained.

A catalyst Rh/Al₂O₃ (2.5 wt%) was placed in a capillary tube (about 10 mm bed length) and reacted with a 6 vol% CH₄, 3 vol% O₂, in He mixture at 283 °C. Online gas analysis was performed with a mass spectrometer. The distribution of Rh chemical state along the reactor evidenced a gradient state stable for several hours and depended on the reaction temperature.

This example nicely illustrates the potential of *in situ* mapping technique brought by SR sources and opens many perspectives, for instance, for the characterization of structured catalysts (monolith, microreactors).

11.3.5

Coupling of Techniques

While the techniques described so far are powerful and sensitive enough to characterize catalysts, elucidating the active sites and related reaction mechanism in catalysis need sometime their coupling with other techniques. The potential of coupling of techniques involving XAS to study catalysts in the reaction conditions has been explored during the past decade and new instrumental setup combining two or three operando spectroscopic techniques or diffraction in one-spectroscopic reaction cell have been developed.

The first explored and most trivial combination, investigated in the beginning of the 1990s in the field of catalysis, was XAS–XRD coupling. Thus, a full description of the structural evolution from a highly disordered state up to a well-ordered state during a temperature treatment (activation or reactivity) was applied for the study of methanol synthesis catalysts or doped zeolite's stability [39–43]. Later on, several other combination techniques were developed. For example, UV–Vis/Raman/XAFS has been fruitfully combined in one-spectroscopic reaction cell to study hydration effects on the molecular structure of silica-supported vanadium oxide catalysts [44]. As shown in Section 11.3.4, XANES spectroscopy has been coupled with a CCD camera to obtain a 2D map of the Rh-oxidation state in a catalyst bed during the catalytic reaction [38]. In Section 11.3.3, it was coupled with electronic conductivity measurement device [27].

As pointed out in reviews dealing with the subject, the crucial advantage of such multiple coupling is that spectroscopic and catalytic data are obtained from the same catalyst for which identical reaction conditions are guaranteed [45, 46]. This is illustrated in the following example concerning the *in situ* study of Cu–CeO₂ catalysts used for the water–gas shift (WGS) reaction ($\text{CO} + \text{H}_2\text{O} \rightarrow \text{CO}_2 + \text{H}_2$). It demonstrates how powerful the XAS techniques could be to identify the active species and determine the roles of different components in a complex catalyst when coupled with other techniques.

The WGS reaction is processed industrially to purify hydrogen obtained from reforming and which contains up to 10% of CO and whatever the re-formed product, crude oil, coal, natural gas, wood, or biomass. CuO–CeO₂ mixed oxides have been shown to be active and selective in the WGS reaction by several research teams [47–54]. The roles played by ceria and copper in this reaction had not been ascertained and either metallic Cu or Cu⁺ was proposed as active site.

To solve this problem, Wang *et al.* studied two catalysts corresponding to copper oxide supported on ceria 5% CuO_x/CeO₂ and to a mixed oxide solid solution Ce_{0.8}Cu_{0.2}O₂ *in situ* under different reaction conditions by time-resolved EXAFS and XANES, time-resolved synchrotron X-ray diffraction (S-XRD), infrared spectroscopy (DRIFTS), and effluent gas analysis by mass spectroscopy [55]. S-XRD is similar in design to conventional XRD revealing the interatomic spacing, atomic identities, and positions of atoms within a crystal and thus identifying phases. However because of the high intensity and the wavelength tunability, S-XRD allows circumventing several limitations of the conventional techniques such as the long time required and

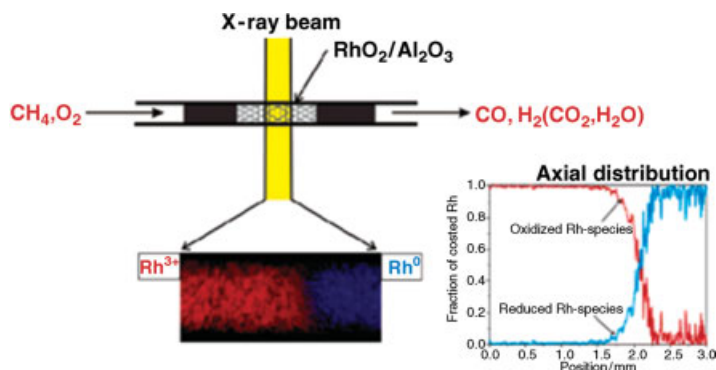


Figure 11.17 2D mapping illustration of the chemical distribution of Rh in Rh/Al₂O₃ sample along the catalytic reactor during the ignition process of partial oxidation of methane [39].

the use of a large volume of sample. It offers exceptional resolution even on very small samples containing only a few grains of a particular phase. This ability and the excellent detectors for S-XRD allowed the identification and quantification of trace amounts of phases that were not detected by other means. In this study, it was the time resolution of the technique that was advantageously used to characterize the catalysts. In parallel, DRIFTS was used to characterize the species adsorbed at the surface of the catalysts and mass spectroscopy was used to follow the activity and selectivity of the catalysts.

The EXAFS spectra at Cu K-edge of the two compounds after WGS reaction at room temperature exhibit a main peak between 1.1 and 2.0 Å corresponding to the first Cu–O coordination shell and is similar to that of CuO [56] (Figure 11.18a). With temperature, the Cu–O peak decrease was observed combined with an increase in the Cu–Cu peak in metallic copper. In the case of the 5% CuO_x/CeO₂ sample, copper oxide was directly transformed to copper metal whereas in the case of the Ce_{0.8}Cu_{0.2}O₂ solid solution the intermediate formation of Cu₂O characterized by a peak at 3.1 Å was observed at 100 °C (Figure 11.18b). However, the recording of the H₂ and CO₂ concomitantly formed as a function of time at the different temperatures clearly showed that this intermediate phase was not active and that the active phase was metallic copper (Figure 11.19). The results were confirmed by *in situ* X-ray diffraction showing at room temperature the presence of the phase CeO₂ and CuO in the case of the supported oxide and of only CeO₂ in the case of the solid solution and at high temperature the presence of metallic Cu besides CeO₂.

The phase composition and the nature of the active phase were not the only information obtained from this experiment with coupled techniques. In parallel to the EXAFS study at Cu-K-edge, XANES spectra were recorded at the Ce L₃-edge. The Ce L₃-edge is used as a “fingerprint” to characterize the electronic properties of ceria-based materials [57]. The electronic transitions behind these XANES features are complex. In pure stoichiometric CeO₂, the Ce L₃-edge exhibits two peaks, labeled B1 and C [57]. The Ce L₃-edge XANES spectra from the Ce_{0.8}Cu_{0.2}O₂ sample in the

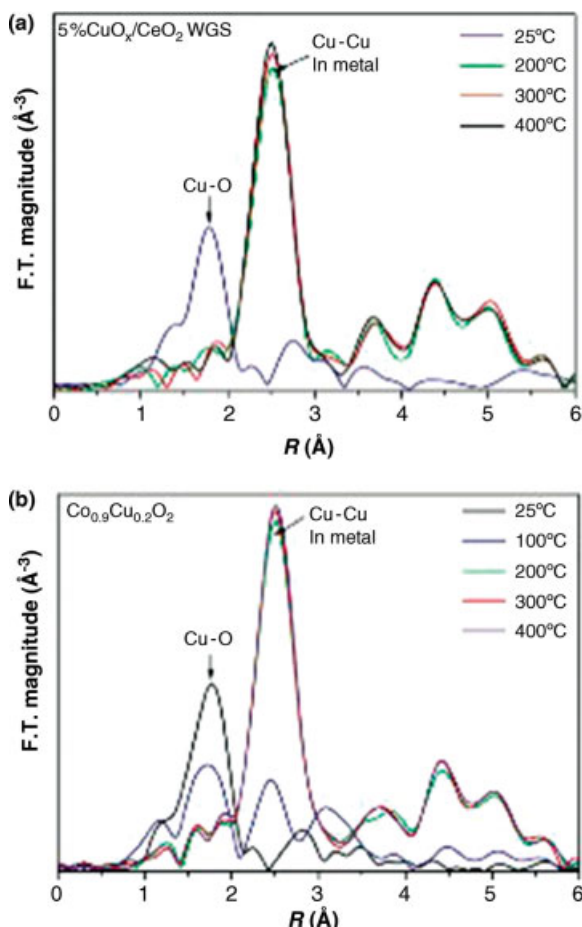


Figure 11.18 (a) Fourier transforms of Cu K-edge EXAFS spectra collected over 5% CuO_x/CeO₂ after water–gas shift reaction at different temperatures. (b) Cu K-edge EXAFS spectra collected over Ce_{0.8}Cu_{0.2}O₂ after water–gas shift reaction at different temperatures [55].

reaction conditions at different temperatures has been compared with the spectrum for a Ce(NO₃)₃·6H₂O reference (Figure 11.20a). The two main peaks in the spectrum of the sample at room temperature are separated by 7 eV and correspond to those evidenced in bulk CeO₂ (B1 and C). On the basis of the comparison of the intensities of the spectra near the Ce³⁺ position, it was possible to confirm that Ce³⁺ and oxygen vacancies were formed during the WGS reaction. The amount of oxygen vacancies and Ce³⁺ were seen to increase with reaction temperature up to 300 °C but decreased at higher temperatures, especially above 400 °C. When the Ce_{0.8}Cu_{0.2}O₂ catalyst was exposed to 5% CO in He, the amount of Ce³⁺ formed was larger than for the experiments in Figure 11.20a and increased continuously with the temperature of

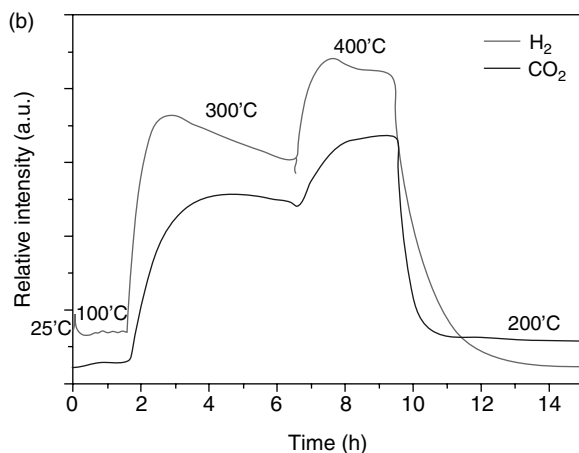


Figure 11.19 Relative concentration of H_2 and CO_2 products as a function of time at different temperatures during the water–gas shift reaction [55].

exposure. These results show that ceria was oxidized by H_2O under the WGS reaction, with oxygen vacancies and Ce^{3+} being eliminated especially at high temperature.

The Ce $\text{L}_{3\text{-edge}}$ XANES spectrum of the 5% $\text{CuO}_x/\text{CeO}_2$ sample has been compared with those of $\text{Ce}_{0.8}\text{Cu}_{0.2}\text{O}_2$, and a ceria sample with similar particle size (ceria nano) during the WGS reaction at 300 °C (Figure 11.20b). Reference spectra for bulk ceria and $\text{Ce}(\text{NO}_3)_3 \cdot 6\text{H}_2\text{O}$ are also shown in the figure and used as standards. The peak intensities at the Ce^{3+} position for the samples followed the order $\text{Ce}_{0.8}\text{Cu}_{0.2}\text{O}_2 > 5\% \text{CuO}_x/\text{CeO}_2 > \text{nano ceria}$, pointing out the improved ceria reducibility for the Cu-containing ceria samples, as reported by other authors [53, 58]. In accordance with this, the closer interaction between copper and ceria in the mixed-metal oxide can explain the higher ceria reducibility (Figure 11.20b).

The formation of oxygen vacancies has been confirmed by S-XRD during the WGS. Figure 11.21 shows the variation of the lattice parameters for ceria and metallic Cu for $\text{Cu}_{0.2}\text{Ce}_{0.8}\text{O}_2$ in different gases at 300 °C. The sample was first heated to 300 °C in He, and no metallic Cu was observed (Figure 11.21b). Metallic copper was formed as soon as the gas was switched to CO, stayed through the WGS reaction and H_2O exposure, and disappeared after O_2 oxidation. The disappearance of metallic Cu and the practical recovery of the initial lattice parameter in an oxygen environment confirm that reduction and oxidation of Cu and Ce in $\text{Ce}_{0.8}\text{Cu}_{0.2}\text{O}_2$ are easily reversible [59] and certainly explain the misinterpretation of the nature of the active species in the literature.

If the lattice of the formed metallic Cu did not change under different gas environments of CO and H_2O , in contrast, the ceria lattice varied significantly (Figure 11.21a) with an increase after exposure to CO and a decrease in H_2O . This clearly indicated that CO reduced ceria and H_2O oxidized it. CO created oxygen vacancies and H_2O eliminated them. A comparison of the ceria lattices in

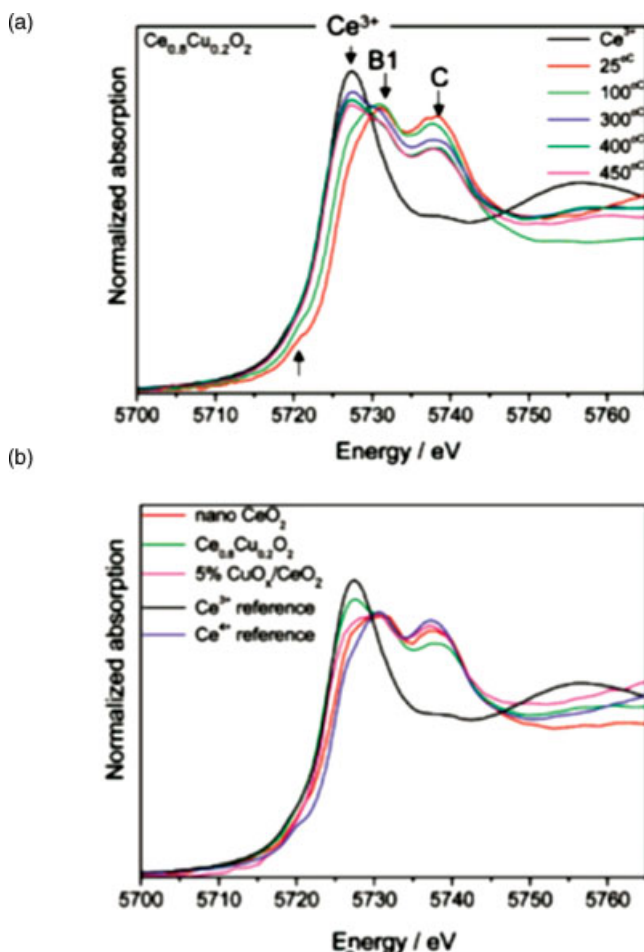


Figure 11.20 (a) Ce L₃-edge XANES spectra collected over $\text{Ce}_{0.8}\text{Cu}_{0.2}\text{O}_2$ after water-gas shift reaction at different temperatures. (b) Ce L₃-edge XANES spectra collected over 5% $\text{CuO}_x/\text{CeO}_2$, $\text{Ce}_{0.8}\text{Cu}_{0.2}\text{O}_2$, and nano- CeO_2 after water-gas shift reaction at 300 °C; CeO_2 and $\text{Ce}(\text{NO}_3)_3 \cdot 6\text{H}_2\text{O}$ are given as references for Ce^{4+} and Ce^{3+} spectra [55].

Figure 11.21a for oxidation in water and O_2 indicates that H_2O does not completely reoxidize the CeO_{2-x} . The ceria lattice parameter under the WGS reaction reflects a combination of the effects of CO reduction and H_2O oxidation, implying that oxygen vacancies are involved in the chemistry of the process.

If the techniques used *in situ* allowed to unambiguously determine that the active species in WGS reaction over mixed copper and cerium oxide or CeO_2 supported oxide was Cu^0 , they also demonstrated that interactions with the CeO_2 support were necessary to obtain high catalytic properties. The active phase could be described as metal nanoparticles dispersed on partially reduced ceria, the later phase undergoing

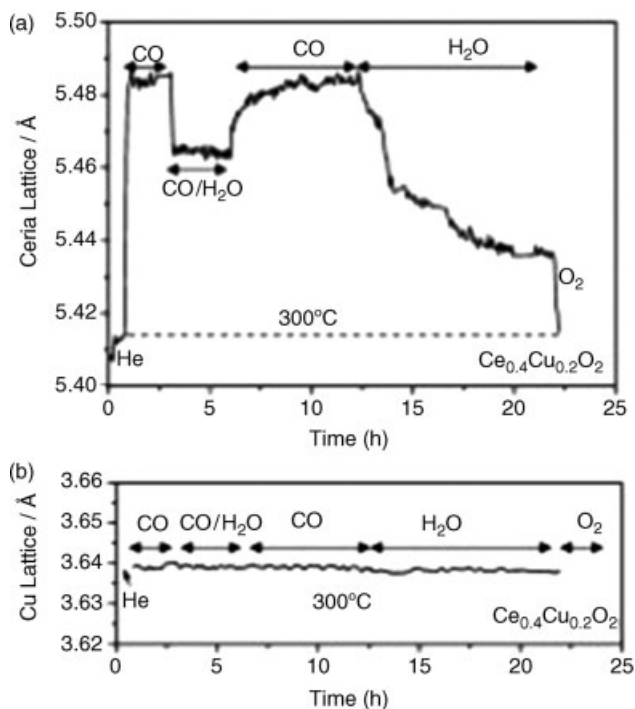


Figure 11.21 Lattice parameters during the gas-switch experiments over $\text{Ce}_{0.8}\text{Cu}_{0.2}\text{O}_2$ at 300°C : (a) ceria and (b) metallic copper [55].

the combined effects of CO reduction and H_2O oxidation, with oxygen vacancies involved in the chemistry of the processes.

Furthermore it illustrates, as did several other examples presented, the efficiency of coupling these physical techniques with techniques in characterizing their catalytic properties. In that respect, this case study also shows the importance of characterizing the catalysts in reaction conditions and how well adapted the synchrotron techniques arose to be for such studies. The coupling of techniques described here appears particularly efficient as it allows a complete dynamic view of the catalytic reaction, each technique allowing the follow up of a specific aspect: (i) the phase composition of the catalysts (S-XRD), (ii) the characteristics of these phases like the local environment of cations in these phases (XANES-EXAFS), (iii) the adsorbed surface species (DRIFTS), and (iv) the products of the reaction (mass spectrometry).

11.4

Perspective

The various examples described in detail in the above section illustrate how the recent progress made in the development of the XAS techniques can efficiently be applied to

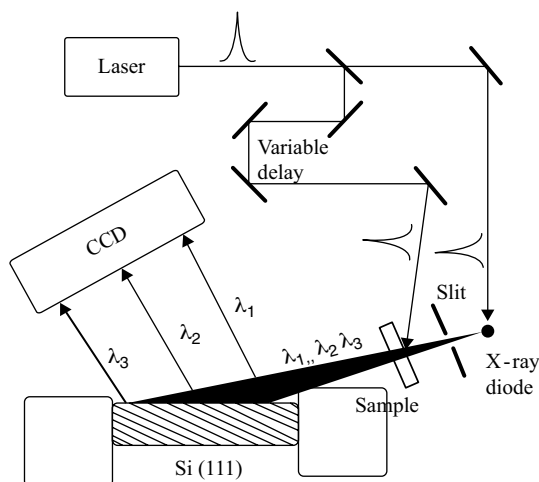


Figure 11.22 Time-resolved ultrafast dispersive X-ray absorption spectrometer [62].

the characterization of catalysts. Some of these progresses have yet not yet been implemented but should be in the next few years. They are discussed in this section.

11.4.1

Time-Resolved Ultrafast X-Ray Absorption Spectroscopy

We have seen that the time resolution of the XAS techniques could be considerably increased allowing the *in situ* monitoring of activation or deactivation of catalysts. Recent techniques allow to further increase this time resolution. A schematic representation of an ultrafast X-ray absorption spectrometer is presented in Figure 11.22 [60]. This spectrometer is equipped with a laser-driven X-ray diode. The X-ray continuum generated by the laser-pumped X-ray diode has an energy spectrum similar to that of a tungsten X-ray tube but with a pulse duration of 12 ns at a repetition rate of 300 Hz. The divergent X-ray continuum beam was formed by a slit situated between the diode and the sample. After passing through the sample X-ray pulse was reflected by a Si(1 1 1) crystal. The energy resolution of the system was found to be in the range 5–9 eV depending on the X-ray wavelength.

This technique of ultrafast XAS has recently been used to study the mechanisms of photolysis of CBr_4 in solution in cyclohexane [61]. The FT EXAFS spectra at Br K-edge of CBr_4 obtained before and after irradiation clearly show changes in the coordination shell (Figure 11.23). These changes have been analyzed and attributed to dissociation of CBr_4 into CBr_3 radical and Br atom.

This new technique is in constant progress with the use of efficient focusing lens and femtosecond laser-driven X-ray sources. Intense ultrashort X-ray pulses of characteristic lines and continua, in the kilo electron volt range, with subpicosecond duration can be formed from the interaction of high-power femtosecond laser pulses with solid and liquid targets and used for X-ray diffraction and absorption studies

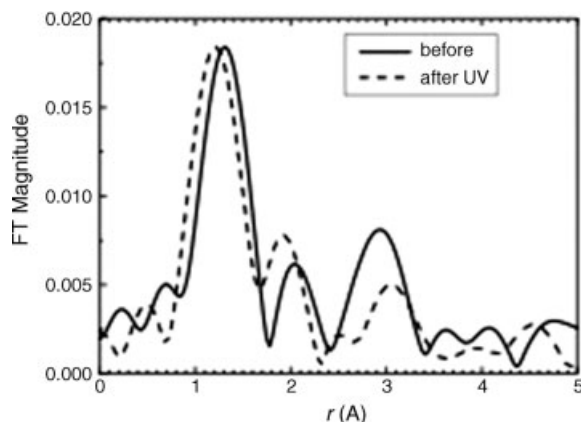


Figure 11.23 Radial distribution function of carbon tetrabromide, before and after UV irradiation [61].

with a picosecond time resolution [62]. A pump/probe technique has also been applied to hard X-ray diffraction and absorption studies [60]. In this case, the ultrashort X-ray pulses were used to probe the structural changes as a function of time after excitation and, therefore, they were precisely synchronized with the exciting optical pulses. The synchronization could be achieved because both the X-ray and optical pulses are generated from the same laser source. These new experimental systems will certainly find application in catalysis in the coming years. Their structure could help identify transient state for active sites and describe its structure and consequently allow to structurally probe the catalytic act at a molecular level.

11.4.2

X-Ray Emission Spectroscopy (XES) and Resonant Inelastic X-Ray Scattering Spectroscopy (RIXS)

We have seen that after the creation of a hole in the 1s shell, photons with different energies are emitted, forming a K fluorescence emission spectrum (Figure 11.24) [63]. These strongest K fluorescence lines result from 2p–1s transitions ($K\alpha$ lines), but weaker lines are also observed corresponding to transitions from high orbitals ($K\beta$ lines). For 3d elements, $K\beta$ main lines ($K\beta_{1,3}$ and $K\beta'$) correspond to the 3p–1s transition, whereas $K\beta$ satellite lines ($K\beta_{2,5}$ and $K\beta''$) correspond to the valence-to-core transitions. The valence-to-core transitions are chemically sensitive fluorescence lines, because the character of the valence orbitals changes the most for different chemical species. The $K\beta$ satellite region is divided into the $K\beta''$ or crossover peak at lower fluorescence (or higher binding) energies and the $K\beta_{2,5}$ structure immediately below the Fermi level.

Detectors used up to now did not allow separating spectral features within the $K\alpha$ and $K\beta$ groups and furthermore did not allow detecting changes of the spectral shape due to the chemical environment. New emission spectrometer using a spherically bent Johann type Bragg crystal allows now to analyze the fluorescence from the

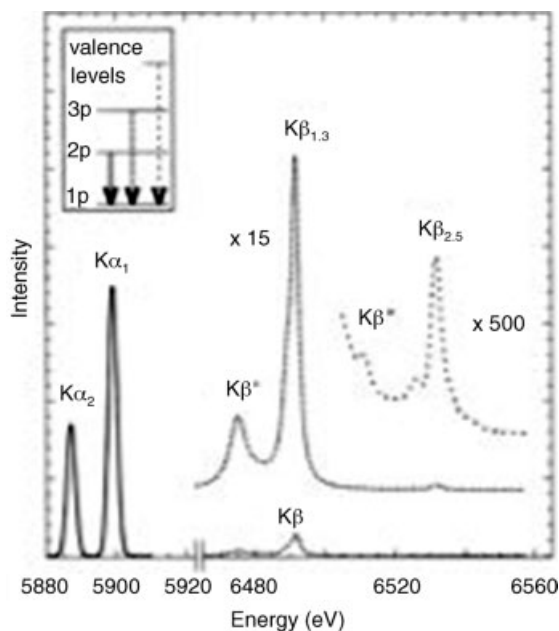


Figure 11.24 Typical K-emission spectrum of transition metal compound (MnF_2). The $K\alpha$ spectrum was simulated by using the known $K\alpha/K\beta$ integrated intensity ratio of 7.7. The peaks $K\alpha_1$ and $K\alpha_2$ are a result of the spin-orbit interaction in the $2p^5$ core hole. The main $K\beta$ lines are split by the 3p–3d exchange interaction into a $K\beta_{1,3}$ peak and a $K\beta'$ feature. These are shown magnified by a factor 15 (dashed line). The much weaker $K\beta_{2,5}$ and $K\beta''$ features that are not visible in the main figure are shown magnified by a factor 500 (dotted line) [62].

sample and reflect it onto a photon detector (Figure 11.25) leading to a new spectroscopy called X-ray emission spectroscopy (XES).

The valence-to-core transitions ($K\beta_{2,5}$ and $K\beta''$) for 3d elements are chemically sensitive because the character of the valence orbitals differs from one chemical species to another. This is illustrated in Figure 11.26 showing the $K\beta$ satellite lines of different chromium compounds (Cr , Cr_2O_3 , CrN , and Cr_3C_2) [64]. For the different

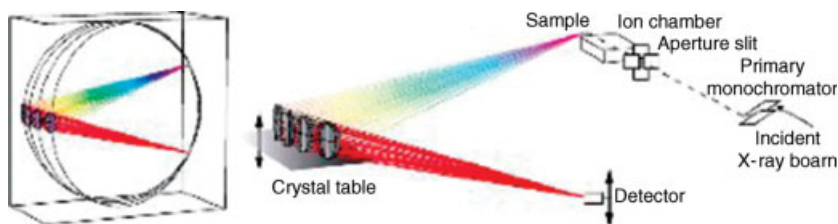


Figure 11.25 Experimental setup at a storage ring beamline. The arrows indicate the motion of the components when a spectrum of the emitted X-rays is recorded. The insert shows the orientation of the Rowland circles for the four analyzer crystals [63].

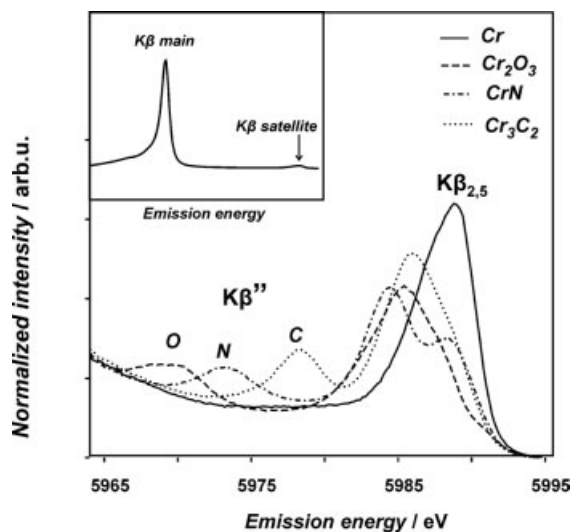


Figure 11.26 $K\beta$ satellite lines of Cr, Cr_2O_3 , CrN, and Cr_3C_2 . O, N, and C indicate the positions of the crossover ($K\beta''$) peaks of oxygen, nitrogen, and carbon ligands. The main $K\beta$ lines of Cr are shown in the inset [64].

ligands, the relative shifts between the crossover fluorescence energies correspond mainly to the shift in 2s binding energies of atomic species. One can see in Figure 11.26 that the shape of spectra and the position of the $K\beta''$ peak depend on the local environment of Cr. The position of the $K\beta''$ can consequently be used as a fingerprint of the presence of Cr–O, Cr–N, or Cr–C bonds in a sample, which is very difficult to distinguish by conventional X-ray absorption spectroscopy. The same type of results have been obtained for other transition elements as well such as Mn [63, 65]. The technique can thus advantageously be used to characterize catalysts having catalytic sites corresponding to metallic cations with the formation of several different types of bonds, for example, oxycarbides, oxynitrides, or oxysulfides. In these cases, it is rather difficult to characterize the environment of cations, which can change in reaction conditions. In that respect, XES appears as a very efficient technique to study such environments.

The analysis of the X-ray emission after 1s core hole creation that leads to the XES spectroscopy described above does not need a tunable incident X-ray source. However, it can be combined with EXAFS or XANES spectroscopy to enhance the power of the later techniques. The chemical sensitivity of the $K\beta$ emission can be combined with EXAFS to gather local information on one element in a given chemical environment. Such “selective” EXAFS technique is achieved by tuning the emission analyzer to a particular fluorescence energy. The fluorescence intensity is then recorded while the incident energy is scanned across the EXAFS range. The contributions from the different sites to such a fluorescence-detected absorption scan depend on the chosen emission energy. The technique can thus be applied to any type

of sample that can be measured in conventional fluorescence-detected absorption spectroscopy, with the only limitation of the $K\beta$ lines of the sites being impossible to separate.

The electronic states that give rise to the edge of an absorption spectrum are resonantly excited states that subsequently decay. The energy that is released in the decay process can be carried either by an electron that is promoted into the continuum or by a photon. In the later case, the process can be viewed as an inelastic scattering of the incident photon at the resonance energy of the metal ion (resonant X-ray inelastic scattering spectroscopy or RIXS).

In the study of the edge of an absorption by RIXS, the incident energy and the emitted energy are varied. The recorded intensity is proportional to both of them and is plotted against a two-dimensional grid. This technique, which has been well described in Ref. [63], allows to evidence and analyze all the resonant excitations to the lowest unoccupied electronic state corresponding to transitions intensities of which are very small and masked in conventional absorption spectroscopy by the more intense main edge. A lot of information on the local electronic configuration of the metal ion and thus on the metal oxidation state, site symmetry, and crystal-field splitting becomes accessible. It is obvious that all this information gained in catalytic reaction conditions will be useful to better describe catalytic sites.

11.5

Conclusions

In this chapter, we outlined the growing importance of XAS techniques in catalysts' characterization and exemplify how some of the experimental progresses in these techniques led to new developments and uses of the techniques to understand the activation, reaction, or deactivation catalytic processes. Applications to investigations of catalysts under controlled conditions or under catalytic reaction conditions are now commonly performed with *in situ* cells more and more well adapted to catalysis and allowing coupling with various other techniques. These applications will continue to benefit from the constant progresses made in energy, time, and space resolution, and new techniques such as those put in perspective at the end of the chapter will continue to merge. These techniques will allow a more accurate determination of oxidation states of the metals, quantification of coordination, and local symmetry site populations in static and dynamic conditions for a better understanding of the catalysts at work and the design of more efficient ones.

Acknowledgments

The authors thank the managers and local contacts of beamlines BM30B (FAME) and ID26 at the European Synchrotron Radiation Facility in Grenoble (France) who provided help and support in the realization of experiments.

References

- 1 Lytle, F.W., Sayers, D.E. and Moore, E.B., Jr. (1974) *Applied Physics Letters*, **24** (2), 45.
- 2 Lytle, F.W., Via, G.H. and Sinfelt, J.H. (1977) *Journal of Chemical Physics*, **67** (8), 3831.
- 3 Bassi, I.W., Lytle, F.W. and Parravano, G.J. (1976) *Catalysis*, **42** (1), 139.
- 4 Rher, J.J. and Ankudinov, A.L. (2005) *Coordination Chemistry Reviews*, **249** (1–2), 131.
- 5 Little, F.W., Sayers, D.E. and Stern, E.A. (1975) *Physical Review B: Condensed Matter*, **11**, 4825.
- 6 Teo, B.K. (1986) *Inorganic Chemistry Concepts*, Vol. 9, Springer-Verlag, Berlin.
- 7 Koningsberger, D.C. and Prins, R.(eds) (1988) *X-Ray Absorption: Principles, Applications, Techniques of EXAFS, SEXAFS and XANES*, Vol. 92, Chemical Analysis, John Wiley & Sons, Inc., New York.
- 8 Baruchel, J., Lehmann, M.S., Regnard J.R. and Schlenker C.(eds) (1993) *Neutron and Synchrotron Radiation for Condensed Matter Studies*, Vol. I, Les Editions de Physique, Springer-Verlag, Berlin.
- 9 Iwasawa, Y.(ed.) (1996) *X-ray Absorption Fine Structure for Catalysts and Surfaces*, World Scientific, Singapore.
- 10 <http://www.esrf.eu/computing/scientific/exafs/gnxs.html>.
- 11 Yamagushi, K., Ito, Y. and Mukoyama, T. (1999) *Journal of Physics B: Atomic Molecular and Optical Physics*, **32**, 1393.
- 12 Munoz, M., Argoul, P. and Farges, F. (2003) *The American Mineralogist*, **88**, 694.
- 13 Wasserman, S.R. (1997) *Journal de Physique IV*, **7**, 203.
- 14 Wasserman, S.R., Allen, P.G., Shuh, D.K., Bucher, J.J. and Edelstein, N.M. (1999) *Journal of Synchrotron Radiation*, **6**, 284.
- 15 Frahm, R. (1988) *Nuclear Instruments & Methods in Physics Research Section A: Accelerators Spectrometers Detectors and Associated Equipment*, **270**, 578.
- 16 Frahm, R., Richwin, M. and Lützenkirchen-Hecht, D. (2005) *Physica Scripta*, **T115**, 974.
- 17 1077085, US6559092 B1 patents assigned to Eurecat Co.
- 18 Geantet, C., Soldo, Y., Glasson, C., Matsubayashi, N., Lacroix, M., Proux, O., Ulrich, O. and Hazemann, J.L. (2001) *Catalysis Letters*, **73**, 95.
- 19 Ressler, T., Timpe, O., Neisius, T., Find, J., Mestl, G., Dieterle, M. and Shloegl, R. (2000) *Journal of Catalysis*, **191**, 75.
- 20 Newton, M.A., Dent, A.J. and Evans, J. (2002) *Chemical Society Reviews*, **31**, 83.
- 21 Ushikubo, T., Oshima, K., Ihara, T. and Amatsu, H. (1996) US Patent 5,534,650 assigned to Mitsubishi Chemical Co.
- 22 Botella, P., Garcia-Gonzalez, E., Dejoz, A., Lopez Nieto, J.M., Vazquez, M.I. and Gonzalez-Calbet, J. (2004) *Journal of Catalysis*, **225**, 428.
- 23 Ueda, W., Oshihara, K., Vitry, D., Hisano, T. and Kayashima, Y. (2002) *Catalysis Surveys From Japan*, **6** (1–2), 33.
- 24 De Santo, P., Buttrey, J., Grasselli, R.K., Lugmair, C.G., Volpe, A.F., Togy, B.H. and Vogt, T. (2004) *Zeitschrift für Kristallographie*, **219**, 152.
- 25 Baca, M. and Millet, J.M.M. (2005) *Applied Catalysis A: General*, **279**, 67.
- 26 Millet, J.M.M., Baca, M., Pigamo, A., Vitry, D., Ueda, W. and Dubois, J.L. (2003) *Applied Catalysis A: General*, **244**, 359.
- 27 Savova, O., Deniau, B. and Millet, J.M.M. (2007) *Journal of Physical Chemistry C*, **111**, 1444.
- 28 Wong, J., Lytle, F.W., Messner, R.P. and Maylotte, D.H. (1984) *Physical Review B: Condensed Matter*, **30**, 5596.
- 29 Deniau, B., Bergeret, G., Jouguet, B., Dubois, J.L. and Millet, J.M.M. (2008) *Topics in Catalysis*, **50**, 33.
- 30 Comin, F., Mangiagalli, P., Navizet, M. and Apostolo, G. (1999) *Microelectronic Engineering*, **45** (2–3), 265.
- 31 de Graaf, J., van Dillen, A.J., de Jong, K.P. and Koningsberger, D.C. (2001) *Journal of Catalysis*, **203**, 307.
- 32 Deutsch, S.E., Miller, J.T., Tomishige, K., Iwasawa, Y., Weber, W.A. and Gates, B.C.

- (1996) *Journal of Physical Chemistry*, **100**, 13408.
- 33 Keegan, M.B.T., Dent, A.J., Blake, A.B., Conyers, L., Moyes, R.B., Wells, P.B. and Whan, D.A. (1991) *Catalysis Today*, **9**, 183.
 - 34 Werner, M.L., Nico, P.S., Marcus, M.A. and Anastasio, C. (2007) *Environmental Science & Technology*, **41**, 4919.
 - 35 Munoz, M., De Andrade, V., Vidal, O., Lewin, E., Pascarelli, S. and Susini, J. (2006) *Geochemistry, Geophysics, and Geosystems*, **7** (11), 1.
 - 36 Pascarelli, S., Mathon, O., Munoz, M., Mairs, T. and Susini, J. (2006) *Journal of Synchrotron Radiation*, **13**, 351.
 - 37 Rau, C., Somogyi, A. and Simionivici, A., (2003) *Nuclear Instruments & Methods in Physics Research Section B: Beam Interactions with Materials and Atoms*, **200**, 444.
 - 38 Grunwaldt, J.D., Hannemann, S., Schroer, C.G. and Baiker, A. (2006) *Journal of Physical Chemistry. B*, **110** (17), 8674.
 - 39 Clausen, B.S., Steffensen, G., Fabius, B., Villadsen, J., Feidenhans'l, R. and Topsøe, H. (1991) *Journal of Catalysis*, **132**, 524.
 - 40 Clausen, B.S., Topsøe, H. and frahm, R. (1998) *Advances in Catalysis*, **42**, 315.
 - 41 Grunwaldt, J.D. and Clausen, B.S. (2002) *Topics in Catalysis*, **18**, 37.
 - 42 Sankar, G., Thomas, J.M., Rey, F. and Greaves, G.N. (1995) *Journal of the Chemical Society: Chemical Communications*, 2549.
 - 43 Kappen, P., Tröger, L., Zink, H., Materlik, G., Sankar, G. and Thomas, J.M. (1999) *Topics in Catalysis*, **8**, 1.
 - 44 Keller, D.E., Visser, T., Soulimani, F.F., Koningsberger, D.C. and Weckhuysen, B.M. (2007) *Vibrational Spectroscopy*, **43** (1), 140.
 - 45 Tinnemans, S.J., Mesu, J.G., Kervinen, K., Visser, T., Nijhuis, A.T., Beale, A.M., Keller, D.E., van der Eerden, M.J. and Weckhuysen, B.M. (2006) *Catalysis Today*, **113** (1–2), 3.
 - 46 Sankar, G., Raja, R., Thomas, J.M. and Gleeson, D. (2001) *Catalysis by Unique Metal Ion Structures in Solid Matrices*, Vol. 13, NATO Science Series II: Mathematics, Physics and Chemistry, Kluwer Academic Publishers, pp. 95–114.
 - 47 Shido, T. and Iwasawa, Y. (1993) *Journal of Catalysis*, **141**, 71.
 - 48 Liu, W. and Flytzani-Stephanopoulos, M. (1995) *Journal of Catalysis*, **153**, 304.
 - 49 Bulezin, T., Gorte, R. and Graham, G.W. (1998) *Applied Catalysis B: Environmental*, **15**, 107.
 - 50 Tschöpe, A., Schaadt, D., Birringer, R. and Ying, J.Y. (1997) *Nanostructured Materials*, **9**, 423.
 - 51 Ovensen, C.V., Stolze, P., Norskov, J.K. and Cambell, C.T. (1992) *Journal of Catalysis*, **134**, 445.
 - 52 Hilaire, S., Wang, X., Luo, T., Gorte, R. and Wagner, J. (2001) *Applied Catalysis B: Environmental*, **215**, 271.
 - 53 Li, Y., Fu, Q. and Flytzani-Stephanopoulos, M. (2000) *Applied Catalysis B: Environmental*, **27**, 179.
 - 54 Fu, Q., Weber, A. and Flytzani-Stephanopoulos, M. (2001) *Catalysis Letters*, **77**, 87.
 - 55 Wang, X., Rodriguez, J.A., Hanson, J.C., Gamarra, D., Martinez-Arias, A. and Fernandez-Garcia, M. (2006) *Journal of Physical Chemistry B*, **110**, 428.
 - 56 Wang, X., Hanson, J.C., Frenkel, A.I., Kim, J.-Y. and Rodriguez, J.A. (2004) *Journal of Physical Chemistry B*, **108**, 13667.
 - 57 Fernandez-Garcia, M. (2002) *Catalysis Reviews: Science and Engineering*, **44**, 59.
 - 58 Martinez-Arias, A., Fernandez-Garcia, M., Conesa, J.C. and Munuera, G. (2006) *The Journal of Physical Chemistry B*, **110**, 428.
 - 59 Wang, X., Rodriguez, J.A., Hanson, J.C., Gamara, D., Fernandez-Garcia, M. and Martinez-Arias, A. (2005) *The Journal of Physical Chemistry B*, **109**, 19595.
 - 60 Chen, L.X., Hager, J.H., Jennings, G., Gosztola, D.J., Munkholm, A. and Ressler, J.P. (2001) *Science*, **292**, 262.
 - 61 Tomov, I.V. and Rentzepis, P.M. (2004) *Chemical Physics*, **299**, 203.
 - 62 Schonlein, R.W., Chattopadhyay, S., Chong, H.H.W., Glover, T.E., Heimann,

- P.A., Shank, C.V., Zholents, A.A. and Zolotarev, M.S. (2000) *Science*, **287**, 2237.
- 63** Glatzel, P. and Bergmann, U. (2005) *Coordination Chemistry Reviews*, **249**, 65.
- 64** Safonov, V.A., Ludmila, N., Vykhodtseva, N., Polukarov, Y.M., Safonova, O.V., Smolentsev, G., Sikora, M., Eeckhout, S.G. and Glatzel, P. (2006) *The Journal of Physical Chemistry B*, **110**, 23192.
- 65** Bergmann, U., Horne, C.R., Collins, T.J., Workman, J.M. and Cramer, S.P. (1999) *Chemical Physics Letters*, **302**, 119.

12

Catalyst Design Through Dual Templating

Moises A. Carreon and Vadim V. Guliants

12.1

Introduction

Ordered periodic mesoporous inorganic oxides were first reported by the researchers at Mobil Research and Development Corporation [1]. These materials, with well-defined pores up to about 3 nm in diameter and high surface areas ($>1000 \text{ m}^2 \text{ g}^{-1}$), belong to the family of the so-called M41S aluminosilicate molecular sieves, which break past the pore size constraints of microporous zeolites. The preparation of the M41S phases represents a new approach in organic-template-assisted synthesis, where, instead of individual organic molecules (as in the case of zeolites), self-assembled molecular aggregates or supramolecular assemblies are employed as the structure-directing agents. The discovery of M41S silicas has stimulated the search for other ordered mesostructured materials with nonsilicate compositions over the last years [2]. Figure 12.1a illustrates the general self-assembly route for mesostructured metal oxides. Mesoporous mixed metal oxides are particularly promising as heterogeneous catalysts because of their high surface areas, tunable surface compositions, metal oxidation states (via organic–inorganic interfacial chemistry), and wall structure nature (amorphous or nanocrystalline). Furthermore, their electronic properties and the surface structure, which are critical parameters for the catalytic performance of any catalyst, are expected to change greatly in the nanoregime [3] thereby offering new, exciting possibilities for the molecular engineering of mixed metal oxides with unique catalytic properties.

Colloidal arrays of monodispersed spheres (polystyrene, poly(methyl methacrylate), or silica) have been used to prepare ordered macroporous materials with 3D structures [4]. This macroscale templating approach consists of the three distinct processing steps depicted in Figure 12.1b. First, the interstitial voids of the monodisperse colloidal sphere (approximately 100 nm–50 μm in diameter) arrays are filled with precursors of various classes of materials, such as ceramics, semiconductors, metals, monomers, and so on. In the second step, the precursors condense around the spheres and form a solid framework. Finally, the spheres are removed by either calcination or solvent

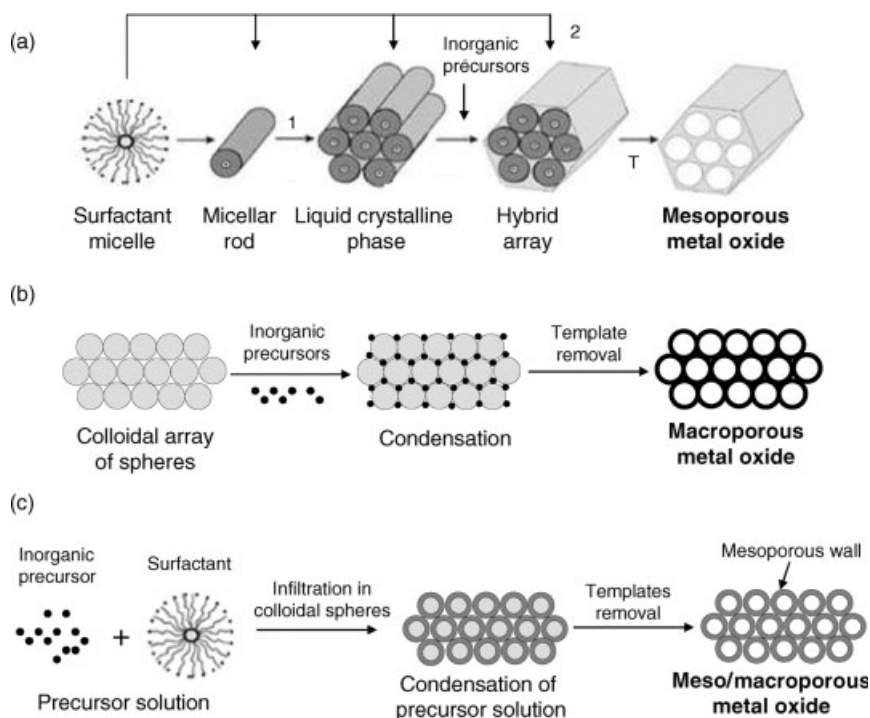


Figure 12.1 General synthesis approaches for (a) the self-assembly of mesoporous metal oxides via (1) preexisting liquid crystalline phase and (2) the formation of inorganic precursor-coated surfactant species, (b) ordered macroporous metal oxides employing colloidal arrays of monodispersed spheres as templates, and (c) meso/macroporous metal oxides by dual templating approach.

extraction to form the 3D ordered macroporous structures. The control over wall thickness, pore size, and elemental and phase compositions makes colloidal sphere array templating a versatile, attractive, and flexible route for the synthesis of highly ordered macroporous catalysts with fine-tuned pore and framework architectures.

Another class of materials possessing bimodal mesoporous–macroporous structures can be prepared by dual templating, using supramolecular mesoscale assemblies of surfactants in conjunction with colloidal sphere arrays to introduce macroscale organization. The resulting high surface area bimodal periodic pore structure is expected to enhance accessibility and molecular transport of guest molecules within the pore network due to the presence of *macropores*, while catalytic active sites will reside in the *mesopores*, making these materials highly attractive for catalytic applications (Figure 12.1c). In this study, we first describe the meso- and macroscale templating approaches separately as individual components of the dual templating approach. Then, we focus our discussion on dual templating by colloidal arrays of monodispersed spheres and mesostructure-directing agents. Finally, emerging *catalytic applications* of these porous materials are presented.

12.2

Surfactant-Assisted Self-Assembly of Mesoporous Metal Oxides

12.2.1

Fundamentals

Typically, the original M41S family of mesoporous molecular sieves is synthesized by reacting a silica source (e.g., tetraethylorthosilicate (TEOS), Ludox, fumed silica, sodium silicate), an alkyltrimethylammonium halide surfactant (e.g., cetyltrimethylammonium bromide (CTAB)), a base (e.g., sodium hydroxide or tetramethylammonium hydroxide (TMAOH)), and water at $\geq 100^\circ\text{C}$ for 24–144 h. The as-synthesized product contains occluded organic surfactant, which is removed by calcination at 500°C in air to yield an ordered mesoporous material. Two main mechanistic routes have been proposed for the formation of these materials.

Figure 12.1a shows the “liquid crystal templating” (LCT) formation mechanism proposed by the Mobil researchers, based on the similarity between liquid crystalline surfactant assemblies (i.e., lyotropic phases) and M41S [1]. Two mechanistic pathways were proposed by the Mobil researchers to explain the formation of MCM-41 containing two-dimensional hexagonal arrays of cylindrical mesopores: (1) via condensation and cross-linking of the inorganic species at the interface with a preexisting hexagonal lyotropic liquid crystal (LC) phase and (2) via ordering of the surfactant molecules into the two-dimensional hexagonal mesophase mediated by the inorganic species and followed by their condensation and cross-linking. In both pathways, the inorganic species, which are negatively charged at the high synthesis pH preferentially interact with the positively charged alkyl ammonium head groups of the surfactants and condense into a solid, continuous framework. The resulting organic–inorganic mesostructure could be viewed as a hexagonal array of surfactant micellar rods embedded in a silica matrix. The surfactant removal produces the open mesoporous MCM-41 framework. These mesophases with pore sizes $>2.5\text{ nm}$ display type IV nitrogen adsorption–desorption isotherms characteristic of mesoporous materials with ordered unimodal pore size distribution. However, most likely pathway 1 did not take place in the Mobil syntheses because the surfactant concentrations used were far below the critical micelle concentration (CMC) required for the hexagonal LC formation [5]. The second mechanistic pathway of LCT was proposed as a cooperative self-assembly of the alkyl ammonium surfactant and the silicate precursor species below the CMC. It is well established that no preformed LC phase is necessary for the MCM-41 formation. We have reviewed the various proposed formation mechanisms of ordered mesostructured phases [6].

12.2.2

Thermal Stability Considerations

The high thermal stability of mesoporous phases is perhaps the most critical requirement for their applications in heterogeneous catalysis. In general, the thermal stability of mesostructured metal oxide phases will depend on (1) the degree of charge

matching at the organic–inorganic interface, (2) the interactions strength between inorganic species and surfactant head groups, (3) the Tamman temperature of the metal oxide, (4) the flexibility of the M–O–M bond angles in the constituent metal oxides, and (5) the occurrence of redox reactions in the metal oxide wall.

The *charge matching at the organic–inorganic interface* allows control over the wall composition and facilitates cross-linking of the inorganic species into a robust mesostructured framework. The knowledge of the *electrokinetic behavior* of the inorganic species in solution (i.e., the isoelectric points [7]) is required for fine-tuning electrostatic and other interactions at the inorganic–organic interface to obtain thermally stable mesoporous phases. The presence of strong *covalent bonds* between metal oxide species and surfactant head groups, for example, metal–N bonds, means that harsh conditions, such as combustion, are required for surfactant removal, leading typically to collapse of the mesostructure. On the other hand, metal oxide species should possess low lattice mobility at elevated temperatures to prevent transformation of the mesostructured metal oxides into more thermodynamically stable dense phases. The mobility of metal ions or atoms in a crystalline metal oxide increases considerably in the vicinity of its Tamman temperature (defined as $0.5\text{--}0.52T_m$, where T_m is the metal oxide melting point). Therefore, the low Tamman temperature of several transition metal oxides [8] translates into a limited thermal stability of the corresponding mesostructures. The isoelectric points and Tamman temperatures of common transition metal oxides are shown in Table 12.1. *Nonflexible M–O–M bond angles* that are unable to accommodate the curvature of the inorganic–organic interface may result in the formation of only lamellar or dense metal oxide phases. Finally, the structural collapse of mesophases may be caused by *redox reactions* occurring in the metal oxide wall during surfactant removal or catalytic reaction.

Table 12.1 Isoelectric points and Tamman temperatures of common transition metal oxides.

Metal oxide	Isoelectric point	Tamman temperature (K)
V ₂ O ₅	0.5	472
MoO ₃	<0.5	534
WO ₃	0.5 (hydrous)	873
Nb ₂ O ₅	<0.5	892
Fe ₂ O ₃	8.7 (α -Fe ₂ O ₃) 6.7 \pm 0.2 (γ -Fe ₂ O ₃)	919
MnO	4.0–4.5 (MnO ₂)	962
TiO ₂	4.7 (natural rutile) 6.2 (synthetic rutile anatase)	1064
NiO	10.3 \pm 0.4	1129
ZrO ₂	4.0 (natural mineral) 6.7 (Zr(NO ₃) ₄ + NaOH)	1492
MgO	12.4 \pm 0.3	1563
Y ₂ O ₃	8.9 (hydrous)	—

12.2.3

Mesostructuring via Evaporation-Induced Self-Assembly

We have reviewed the guiding principles for the synthesis of *binary and mixed metal oxide mesostructures* relevant to applications in catalysis [6]. Here we focus our discussion on the so-called evaporation-induced self-assembly (EISA), which has emerged as a powerful synthesis approach to design mesoporous functional oxides as fibers, particles, and films [9]. EISA relies on using very dilute surfactant solutions ($C_0 \ll \text{CMC}$, where C_0 is the initial surfactant concentration and CMC is the critical micelle concentration) from which a liquid crystalline mesophase is gradually developed upon solvent evaporation. Slow coassembly between the inorganic network and liquid crystalline phase leads to the formation of well-defined mesostructures possessing long-range order (Figure 12.2). One of the great advantages of EISA is that this highly efficient and flexible method allows one to rationally target a particular mesostructure by appropriately adjusting chemical (i.e., sol-gel hydrolysis-condensation reactions and relative quantities of surfactant and inorganic precursor) and processing (diffusion of alcohol, water, catalysts to or from the surface) parameters. For many structure-sensitive applications (such as in heterogeneous catalysis), it is highly desirable to have a well-defined crystalline phase. In this respect, EISA is an ideal approach for

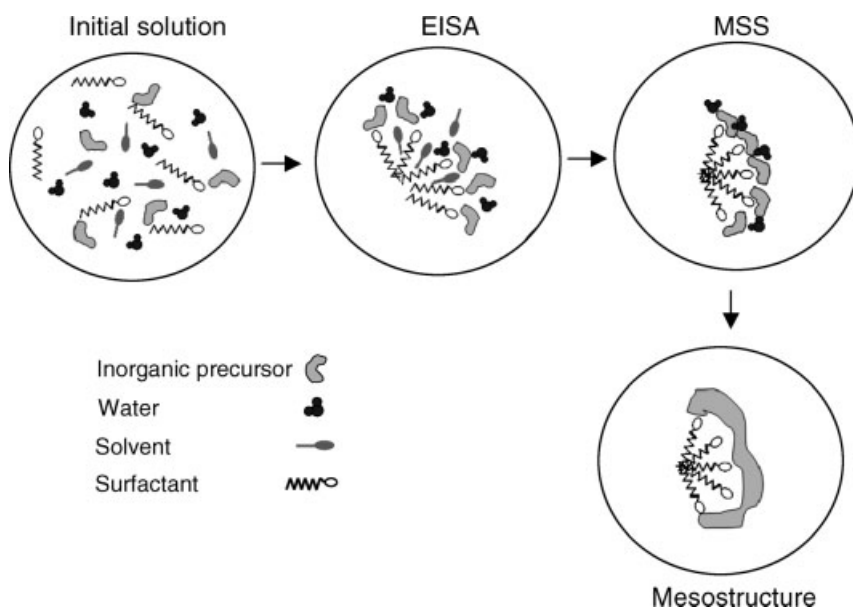


Figure 12.2 Schematic representation of EISA for the preparation of ordered mesostructures: (a) initial solution composed of the inorganic precursor, water, solvent (alcohol), and surfactant, (b) evaporation takes place and micelles gradually form above the CMC (EISA),

(c) the inorganic framework is not fully condensed, and the control of the final mesostructure can be adjusted (modulable steady state (MSS)) [9d], and (d) the inorganic framework condenses forming the final mesostructure.

the molecular design of *nanocrystals* possessing remarkable order in the mesoscale regime.

A wide variety of metal oxides displaying highly ordered pore nanoarchitectures, flexible compositions, and nanocrystallinity have been prepared by this method. We will next review some catalytically relevant mesoporous transition metal oxides prepared via EISA. To date, most research efforts on mesostructured transition metal oxides by EISA have been focused on titania [9e, 10–15].

Hexagonal mesoporous titania displaying high surface areas (up to $370 \text{ m}^2 \text{ g}^{-1}$) and 2.0–2.5 nm pores was prepared by EISA [10a]. The authors proposed a formation pathway for these mesophases, in which hydrolysis of a Ti precursor leads to the formation of Ti-hydroxochloroalkano species, which condensed into colloidal Ti-*oxo* nanobuilding blocks (NBBs). The solvent evaporation induces the formation of a liquid crystalline mesophase by the assembly of the Ti-*oxo* nanobuilding blocks around the tubular micelles. Bromide and chloride anions helped counterbalance the positive charges of the surfactant (CTAB) and NNB. The amorphous nature of the resultant mesophase limited the use of this material for practical applications in which a well-developed crystalline structure is required. Later, the same research group reported the synthesis of mesoporous nanocrystalline anatase films [10b]. In their approach, poly(ethylene oxide)-based surfactants were used to direct the synthesis. A careful control over synthesis conditions and postsynthesis treatments led to the formation of anatase nanocrystals in the mesoporous walls. Alternatively, phosphorus could be introduced in the titania framework to form self-standing mesoporous titania–phosphorus oxide films containing anatase nanocrystals via EISA [11]. In this case, the presence of phosphate prevented excessive crystal growth and improved the thermal stability of the final mesostructure. As in the previous example, a triblock copolymer surfactant was employed to direct the synthesis. The coexistence of amorphous and rutile phases in mesoporous titania films synthesized by EISA have been reported [12]. Unfortunately, these materials were composed of lamellar mesophases, which limits their practical applications. Various synthesis modifications have led to improved mesoporous nanocrystalline titania phases. For example, it has been shown recently that postsynthesis modification of mesoporous titania with NH_4OH helps in stabilizing anatase nanocrystals in the mesostructure [13]. The resultant mesostructures had high surface areas (up to $573 \text{ m}^2 \text{ g}^{-1}$). Ozin's group reported the synthesis of highly crystalline and well-ordered periodic mesoporous nanocrystalline anatase films displaying 2D hexagonal and 3D cubic pore structures [14]. The high quality mesostructures were obtained by controlling the temperature and relative humidity, as well as by using 1-butanol as a solvent, which enhanced the microphase separation between the surfactant and the inorganic precursor, and consequently created a highly condensed inorganic framework. Recently, EISA has been used to prepare ultrathin mesostructured nanocrystalline anatase films [15]. In this approach, KLE (diblock copolymer) and Brij-58 led to spherical and cylindrical micelles, respectively. The synthesis approach employed by the authors led to 17–18 nm thick titania films displaying a monolayer or bilayer of highly ordered mesopores arranged on a 2D cubic lattice in which the inorganic matrix was composed of ~ 6 –10 nm anatase crystals.

Other transition metal oxides have been successfully mesostructured by EISA [15–21]. Brezesinski *et al.* [15] reported the synthesis of large pore (10–25 nm) and highly ordered mesostructured ultrathin films of WO_3 , CeO_2 , and MoO_3 employing KLE and Brij-58 as structure-directing agents. Interestingly, these three mesostructures displayed well-developed nanocrystalline monoclinic, cerianite, and fcc phases for WO_3 , CeO_2 , and MoO_3 , respectively. Recently, nanocrystalline mesostructured Y_2O_3 films doped with rare earth metals and displaying 10–17 nm crystals and 8.5–14 nm pores have been reported [16]. Nanocrystalline mesostructured CeO_2 , ZrO_2 , and CeO_2 – ZrO_2 thin films with ordered arrays of nanopores and displaying crystal sizes in the 2–10 nm range have been synthesized [17]. The successful preparation of these mesophases was mainly attributed to the KLE surfactant employed in the synthesis. It was proposed [17] that KLE accelerates the mesostructure formation, avoiding the insufficient buildup or loss of mesostructure typically observed when other surfactants are used. Also, KLE polymer is more thermally stable, and, therefore, it may maintain the mesostructural order even beyond the onset of the metal oxide crystallization. Mesostructured nanocrystalline γ - Al_2O_3 with ellipsoidal disk-shaped pores (\sim 9–29 nm) and interconnecting windows of 2 or 5 nm in diameter has been synthesized employing KLE-22 and KLE-23 surfactants [18]. Mesoporous films composed of 7–10 nm crystals of α - Fe_2O_3 with average pore diameter of \sim 10 nm were synthesized employing a novel PIB–PEO (poly(isobutylene)-block-poly(ethylene oxide)) copolymer and KLE [19]. The retention of the structural order in these films was attributed to high thermal stability of the surfactants.

Mixed mesoporous Nb–M (M = V, Mo, Sb) metal oxides with surface areas up to $200 \text{ m}^2 \text{ g}^{-1}$, pore sizes in the 5–14 nm range, and high pore volumes ($0.46 \text{ cm}^3 \text{ g}^{-1}$) have been prepared by EISA [20]. Examples of mesostructured multimetallic mixed oxides prepared by EISA have been reported by Sanchez's group [21]. In this report, ordered nanocrystalline mesoporous films composed of SrTiO_3 , MgTa_2O_6 , and $\text{Co}_x\text{Ti}_{1-x}\text{O}_{2-x}$ were prepared employing a designed nonionic block copolymer surfactant composed of hydrogenated poly(butadiene)-block-poly(ethylene oxide) designated as KLE3739. Optimal conditions for film deposition deduced from *in situ* time-resolved SAXS, optimal conditions for annealing deduced from *in situ* time-resolved simultaneous WAXS and SAXS, and the use of KLE3739 allowed the formation of these highly crystalline mesostructures. Table 12.2 summarizes some of the relevant work done on the preparation of mesoporous transition metal oxide films and particles by EISA.

12.3

Colloidal Sphere Templating of Macroporous Metal Oxides

Colloidal crystals consisting of three-dimensional ordered arrays of monodispersed spheres can be used as templates for the preparation of highly ordered macroporous inorganic solids that exhibit tightly controlled pore sizes and highly ordered 3D porous structures. In the macroscale templating route, the interstitial voids of the monodisperse sphere arrays are first filled with precursors (ceramics, semiconductors, metals, monomers) followed by their condensation around the spheres to form a

Table 12.2 Mesoporous transition metal oxide films and particles prepared by EISA.

Structure	Precursors	Substrate	Deposition method	Reference
TiO ₂ 2D hexagonal and wormlike particles	Ti(EtO) ₄ , CTAB, HCl, H ₂ O	None	Casting	[10a]
TiO ₂ 2D hexagonal and 3D cubic films	TiCl ₄ , Ti(EtO) ₄ , F-127, P-123, Brij-56, Brij-58 EtOH, H ₂ O	Si wafers, fused silica, or glass	Dip coating	[10b]
TiO ₂ hexagonal films	Ti(EtO) ₄ , PCL, P-123, EtOH, HCl, H ₂ O	None	Casting	[11]
TiO ₂ lamellar films	TiCl ₄ , Brij-58, EtOH, H ₂ O	Si wafers, (1 0 0) Si, glass	Dip coating	[12]
TiO ₂ mesoporous nonperiodic particles	Titanium tetraisopropoxide, HDA, CTAB, EtOH, NH ₄ OH, H ₂ O	None	Casting	[13]
TiO ₂ 3D hexagonal, 2D hexagonal, and 3D cubic films	Ti(OEt) ₄ , P-123, BuOH, HCl, H ₂ O	Glass	Spin coating	[14]
TiO ₂ 1D hexagonal and 2D cubic films	TiCl ₄ , KLE, EtOH, THF, H ₂ O	Si, glass	Dip coating	[15]
WO ₃ , MoO ₃ , and CeO ₂ 1D hexagonal and 2D cubic films	WCl ₆ , MoCl ₅ , CeCl ₃ ·7H ₂ O, KLE, EtOH, THF, H ₂ O	Si wafers, glass	Dip coating	[15]
Y ₂ O ₃ doped with Eu, Sm, and Er mesoporous nonperiodic films	YCl ₃ ·6H ₂ O, EuCl ₃ ·6H ₂ O, KLE-22, EtOH, NH ₄ OH, H ₂ O	Si wafers	Dip coating	[16]
CeO ₂ , ZrO ₂ , and CeO ₂ -ZrO ₂ cubic (bcc) films	CeCl ₃ ·7H ₂ O, ZrCl ₄ , KLE block copolymer, EtOH, THF, H ₂ O	Si wafers	Dip coating	[17]
Al ₂ O ₃ cubic (fcc) films	AlCl ₃ ·6H ₂ O, KLE22, KLE23, EtOH, H ₂ O, NH ₄	Si wafers	Dip coating	[18]
Fe ₂ O ₃ and FeOOH mesoporous films	FeCl ₃ , PIB-PEO, KLE, EtOH, THF, H ₂ O	Si wafers, glass	Dip coating	[19]
Nb-M oxides particles (M = V, Mo, Sb)	NbCl ₅ , V ₂ O ₅ , VOSO ₄ , MoO ₃ , Sb ₂ O ₃ , P-123, EtOH	None	Casting	[20]
SrTiO ₃ , MgTa ₂ O ₆ , and Co _x Ti _{1-x} O _{2-x} 3D and 2D pore arrangements, films	SrCl ₂ ·6H ₂ O, TiCl ₄ , CoCl ₂ , Mg(OH) ₂ , Ta(OC ₂ H ₅) ₅ , THF, EtOH, H ₂ O	Si wafers	Dip coating	[21]

solid framework. Finally, the spheres are removed by either thermal or chemical means. The final inorganic structure after the removal of spheres, contains a macroporous ordered interconnected pore structure.

The success of forming macroporous ordered structures is mainly determined by van der Waals interactions, wetting of the template surface, filling of the voids between the spheres, and volume shrinkage of the precursors during the solidification process. Typical colloidal-crystal templates used to prepare 3D macroporous materials include monodisperse polystyrene (PS), poly(methyl methacrylate) (PMMA), and silica spheres. Prior to precursor infiltration, these monodisperse spheres are ordered into close-packed arrays by sedimentation, centrifugation, vertical deposition, or electrophoresis [22]. Several synthesis methods have been used in the past to prepare 3D macroporous inorganic materials including sol-gel, salt precipitation, nanocrystal infiltration, and polymerization [4].

The ability to manipulate wall thickness, pore size, and elemental and phase compositions makes the macrotemplating route a flexible and attractive technique for the synthesis of highly ordered macroporous materials with fine-tuned pore and framework architectures. For instance, the wall thickness of macroporous structures can be controlled by the hydrolysis/condensation rates of the inorganic precursors [23], the packing of the PS spheres [24], and by forming core-shell structures at the sphere surface (i.e., deposition of polyelectrolyte multilayers at the sphere surface) [25]. The pore size can be easily manipulated in the range of the sphere sizes, which are typically between 100 nm and 50 μm in diameter. Even smaller ~ 20 nm spheres can be prepared and used to template small-pore materials [4]. Furthermore, it is possible to build macroporous structures containing a specific crystalline phase by incorporating nanoparticles of desired phases in the voids of sphere arrays [26]. Depending on the choice of the inorganic sources and template removal method, various crystalline phases can be obtained [24]. This suggests that the most critical aspects in the preparation of these macroporous structures are the ability of precursors to infiltrate and condense in the voids of colloidal sphere arrays without swelling or destroying these arrays, which serve as a template, as well as the ability to avoid excessive crystal growth, which leads to a decrease in macroporosity and structural order. We have reviewed the synthesis methods that have been used in the past to prepare *macroporous inorganic frameworks* employing colloidal sphere arrays as macroscale templates with compositions relevant to catalysis [6].

12.4

Dual Templating of Metal Oxides

Herein we review only the use of *colloidal sphere arrays* as macroscale templates in combination with mesostructure-directing agents. The use of other macroscale templates such as emulsions, foams, vesicles, polymeric membranes, and so on is outside the scope of this study. These methods have been recently reviewed by Yuan and Su [27].

Dual templated metal oxides can be prepared by combining the surfactant-assisted self-assembly and colloidal sphere templating methods. The pioneering work on the

synthesis of ordered dual templated structures was first reported by Stucky's group [28]. In this report, close-packed arrays of latex spheres formed by capillary forces were infiltrated with a sol-gel block copolymer-precursor solution. Cross-linking and polymerization of the inorganic precursor species led to the formation of a hybrid meso/macroporous oxide. The removal of the latex spheres and surfactant by calcination produced hierarchical ordered metal oxides with remarkable order in the meso- (~ 10 nm pore size) and macroscale (100 nm pore size) porous regimes. Most research into dual templating of metal oxides using colloidal sphere arrays has been done on silica [28–38]. We will next briefly describe relevant work regarding these silica-based bimodal pore structures.

Macroporous (140 nm and dual 80 nm–140 nm) silica structures possessing ordered hexagonal mesoporous (~ 7 nm) walls have been reported employing colloidal arrays of sedimented PS spheres and Pluronic P123 as templates [29]. Smaller mesopore sizes can be obtained employing CTAB as mesostructure-directing agent. For example, Sanchez's group has reported interconnected ~ 115 nm macroporous silica displaying walls composed of 3.9 nm wormlike mesopores [30].

Ionic liquids (low melting point organic salts) have been successfully used as mesostructure-directing agents for the synthesis of bimodal porous silicas [31]. In this case, the ionic liquid 1-hexadecyl-3-methylimidazolium-chloride produced lamellar mesostructure (with the presence of microporosity) between 175 nm macropores. Interestingly, the combination of this ionic liquid with a triblock copolymer (KLE) and polystyrene spheres produced 360 nm macroporous silica structures with walls composed of bimodal mesopores (large spherical ~ 12 nm mesopores and small elongated ~ 2 – 3 nm mesopores located between the larger mesopores) [32]. Cosurfactants (*n*-butanol, *n*-pentanol), triblock copolymers (P-123 and F-127) as mesostructure-directing agents, and colloidal PS spheres have been successfully employed for the preparation of dual templated silicas with macropore sizes in the 200–800 nm range and 3–8 nm mesopores [33]. Significant microporosity was also observed for these materials associated with the presence of the alcohols.

Meso/macroporous silica films have been prepared by spin-coating infiltration (SCI) approach [34]. In this method, mesostructure-directing agent-precursor solutions are infiltrated within the array of the PS colloidal crystal film. The SCI approach allows a homogeneous infiltration of the voids present in colloidal crystal films leading to high-quality periodic films in the dual meso- and macroporous regimes. The method was successfully used to prepare 1–10 μm films displaying ~ 375 nm macropores with walls composed of ~ 6 nm hexagonal mesopores. Recently, several mesostructure-directing agents have been used for the synthesis of these dual porous silica phases, including block copolymers, such as Pluronic F-127, Pluronic P-123, KLE, SE (poly(styrene)-poly(ethylene oxide)) [35], and poly(oxyethylene) surfactant Brij-56 [36]. The use of these surfactants enabled control over the pore size of the mesostructure in the ~ 2 – 22 nm range.

In these previous examples, the bimodal porous structures were prepared by infiltration of a gel solution containing inorganic precursors and mesostructure-directing agents in the voids of the colloidal sphere arrays followed by condensation of inorganic precursors. Alternatively, it has been shown that mixing of the colloidal

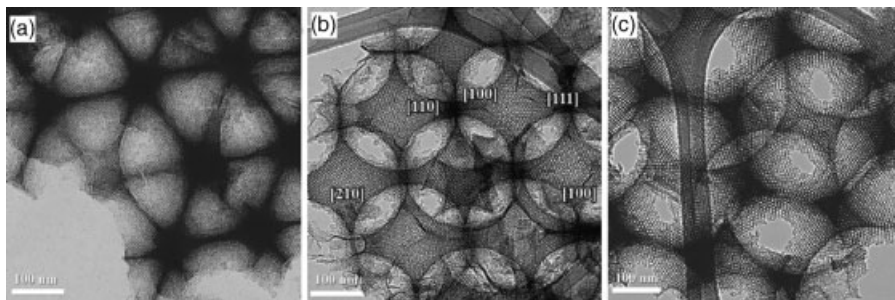


Figure 12.3 TEM images of ordered meso/macroporous silica structures obtained by dual templating displaying (a) wormhole, (b) cubic, and (c) hexagonal mesostructures in the macropore walls [36].

sphere arrays with micellar solutions prior to the addition of inorganic precursors produces bimodal porous structures [37]. In this report, ~ 200 – 300 nm macroporous silica with ~ 2 – 2.3 nm cubic mesoporous walls were prepared employing CTACl (cetyltrimethylammonium chloride as surfactant). This synthesis approach was used to produce ordered dual templated silicas displaying ~ 220 nm macropores and a hexagonal MCM-41 type mesostructure with 2.7 nm mesopores [38].

The dual templating approach has been successfully extended to the synthesis of silica–alumina composites [39]. Ordered arrays of poly(methyl methacrylate) spheres were impregnated with Al and Si source–CTAB gel solution to produce ~ 150 nm macroporous silica–alumina structures with disordered mesoporous walls. Figure 12.3 shows the transmission electron microscopy (TEM) images of tridimensionally ordered macroporous silica with different wall mesoporosities [36]. Table 12.3 summarizes the relevant work done on dual templated silica-based oxides, employing colloidal sphere arrays as macroscale templates in combination with diverse mesostructure-directing agents.

12.5

Catalytic Applications

Finely tuned meso- and macroporous structures, controlled metal oxide wall structures and compositions, high surface areas, and enhanced accessibility of the active surface sites are some of the properties that make these ordered porous metal oxides highly attractive for a wide range of catalytic applications. We will next review the emerging applications of these ordered porous metal oxides in catalysis.

12.5.1

Mesoporous Metal Oxides

Examples of catalytic mesoporous silicates have been reviewed by Sayari [40]. Here, we discuss only the relevant work done on mesoporous transition metal oxides. Only

Table 12.3 Ordered porous silicas obtained by dual templating approach employing colloidal arrays of spheres as macroscale templates in combination with mesostructure-directing agents.

Mesopore size/macropore size	Mesostructure-directing agent	Colloidal array of spheres	Reference
11 nm cubic mesostructure/100 nm	Pluronic F-127	200 nm PS spheres ordered by capillary forces	[28]
~7 nm hexagonal mesostructure/140 and 80–140 nm	Pluronic P-123	210 nm sedimented PS spheres	[29]
3–9 nm wormhole mesostructure/120 nm	CTAB	140 nm sedimented PS spheres	[30]
2.7 nm lamellar mesostructure/175 nm	HMC	200 nm sedimented PS spheres	[31]
Dual: 12 nm and 2–3 nm disordered mesostructure/360 nm	HMC + copolymer KLE	560 nm suspended PS spheres	[32]
3–8 nm linear and disordered mesostructure/200–800 nm	Pluronic F-127, Pluronic P-123	485–805 nm centrifuged PS spheres	[33]
6 nm hexagonal (MCM-41 and SBA type) mesostructure/375 nm	Pluronic F-127	300–600 nm PS spheres ordered by capillary forces	[34]
Dual: 6–22 nm and 2–3 nm disordered mesostructure/90–1000 nm	Pluronic F-127, Pluronic P123, HMC copolymer KLE, CTAB, and copolymer SE	100–900 nm sedimented PS and PMMA spheres	[35]
2.5–5.1 nm cubic, hexagonal, and wormhole mesostructure/340–370 nm	Brij-56, Pluronic P-123	400 nm sedimented PMMA spheres	[36]
2–2.3 nm cubic mesostructure/200–300 nm	CTACl	400 nm suspended PS spheres	[37]
2.7 nm hexagonal mesostructure/220 nm	CTACl	200–350 nm centrifuged PS spheres	[38]
~3.3–3.5 nm disordered mesostructure ^a /150 nm	CTAB	275 nm centrifuged PMMA spheres	[39]

HMC, 1-hexadecyl-3-methylimidazolium-chloride; PS, polystyrene; PMMA, poly(methyl methacrylate).
^aSilica-alumina composite.

a few reports exist on catalytic applications of mesoporous transition metal oxides. The photocatalytic behavior of mesoporous TiO_2 films has been reported [41]. It was found that the photocatalytic activity of the films for the oxidation of NO_x was higher for the mesoporous films than for conventional gel films, due to the higher surface areas and pore architectures of the mesoporous films. Mesoporous Ta_2O_5 doped with NiO was found to display higher photocatalytic activity than nonporous amorphous and crystalline NiO– Ta_2O_5 [42]. It was claimed that the higher surface areas and better NiO dispersion over the mesoporous Ta_2O_5 host were responsible for the superior catalytic performance of these materials. The photocatalytic activity of mesoporous phosphated TiO_2 and Nb_2O_5 catalysts has been studied in the dehydrogenation of 2-propanol to acetone [43]. Surprisingly, a lower activity of the mesoporous Ti and Nb oxides was observed than for the bulk anatase phase. The amorphous nature of mesoporous walls and the surface defects in these mesoporous oxides were probably responsible for the recombination of photogenerated electron–hole pairs and the poor catalytic performance.

Recently, the photocatalytic activity of mesoporous nanocrystalline titania films has been reported by independent research groups [13, 14b, 44]. In these reports, superior photocatalytic efficiency has been observed for the mesoporous nanocrystalline films prepared via EISA as compared to conventional and nonperiodic nonporous nanocrystalline titania. For example, it was found that NH_4OH -modified mesoporous nanocrystalline titania degraded rhodamine 6G faster than commercially available Degussa P25 titania [13]. Periodic ordered hexagonal and cubic nanocrystalline anatase films (Figure 12.4) photodegraded methylene blue approximately two times faster than nanocrystalline titania [14b]. Mesoporous titania comprised of ~ 7.5 nm crystals displayed improved photocatalytic performance for methylene blue degradation as compared to a TiO_2 control sample [44]. Superior photocatalytic activity in all these systems may be related to the periodic open porous structures with organized framework of nanocrystals, which provide facile diffusion pathways for guest molecules.

Mesoporous Fe_2O_3 – TiO_2 has been used as a catalyst for the oxidation of cyclohexane to cyclohexanol and cyclohexanone [45]. These mesoporous catalysts displayed slightly higher (by 5%) cyclohexane conversion under the same conditions as compared to catalysts, in which Fe_2O_3 was incorporated into nonporous TiO_2 . Vanadium oxide incorporated into mesoporous TiO_2 has been studied as a catalyst for propene combustion [46]. It was found that the rate of propane combustion to CO and CO_2 was about 18 times higher for mesoporous VO_x – TiO_2 catalysts than for a conventional VO_x – TiO_2 catalyst (i.e., a nonporous TiO_2 matrix). High surface areas displayed by these mesoporous catalysts and improved dispersion of active surface sites in the mesoporous hosts were responsible for their enhanced catalytic performance.

Gulianti's group has reported the catalytic performance of several mesoporous mixed metal oxides in alkane oxidation, including vanadium–phosphorous oxide (VPO) [47], niobium–M oxides ($\text{M} = \text{V}, \text{Mo}, \text{Sb}$) [20], and cobalt–nickel oxides [48]. Mesostructured vanadium–phosphorous oxide was evaluated in the oxidation of *n*-butane to maleic anhydride [47]. The selectivities to maleic anhydride of up to 40 mol% were observed at 673 K at about 10% *n*-butane conversion. A conventional organic VPO catalyst containing well-crystallized vanadyl(IV) pyrophosphate, the

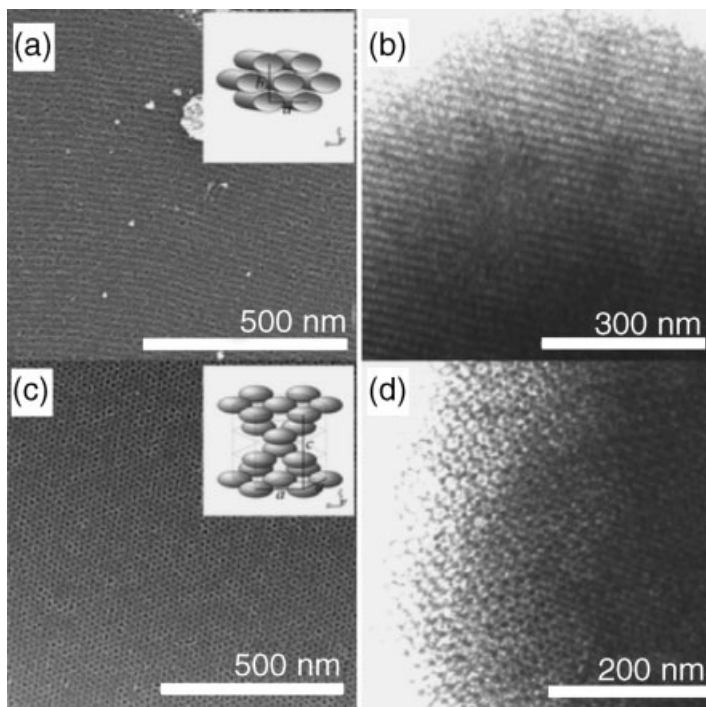


Figure 12.4 HRSEM and STEM images of hexagonal mesoporous nanocrystalline TiO_2 (a and b) and cubic mesoporous nanocrystalline TiO_2 (c and d) employed as catalysts for the photooxidation of methylene blue [14b].

proposed active and selective phase for *n*-butane oxidation to maleic anhydride, displayed the selectivity to maleic anhydride of 50 mol% under the same reaction conditions. Limited thermal stability of mesostructured VPO phases during *n*-butane oxidation led to a gradual loss of the structural order and poor catalytic performance. These results further suggested that crystalline vanadyl(IV) pyrophosphate is required for this alkane oxidation reaction. Thermally stable mesoporous mixed metal Nb–M (M = V, Mo, Sb) oxide catalysts were evaluated in the oxidative dehydrogenation (ODH) of propene to propylene [20]. It was found that the mesoporous Nb–Mo–O catalyst containing molecularly dispersed MoO_x species showed higher propane ODH activity than supported $\text{MoO}_x/\text{Nb}_2\text{O}_5$, in which molybdenum oxide was present as MoO_x species and MoO_3 crystals. Mesoporous nanocrystalline cobalt–nickel oxides were studied as catalysts in the combustion of propane [48]. These mesoporous phases composed of 8–11 nm Co–Ni–O spinel nanocrystals displayed a higher rate of propane combustion to CO and CO_2 as compared to a conventional dense spinel. This improved catalytic behavior may be related to their morphological and structural features, such as large surface area and mesoporous structure, and to the relatively small size of spinel crystallites. Table 12.4 summarizes examples of catalytic applications of mesoporous metal oxides.

Table 12.4 Catalytic applications of mesoporous metal oxides.

Mesostructure ^a	Reaction	Product	Activity/selectivity	Reference
TiO ₂	NO photooxidation	NO ₂	15% NO removal, 10% NO ₂ generation	[41]
NiO–Ta ₂ O ₅	Water photocatalytic decomposition	H ₂ + O ₂	515 $\mu\text{mol h}^{-1}$ H ₂ , 272 $\mu\text{mol h}^{-1}$ O ₂	[42]
PO ₃ –TiO ₂ –Nb ₂ O ₅	2-Propanol dehydrogenation	Acetone	Quantum yield ^b : 0.0089 (TiO ₂), 0.45 (Degussa P25), 0.0041 (Nb ₂ O ₅), 0.217 (Nb ₂ O ₅)	[43]
TiO ₂	Photocatalytic degradation of rhodamine 6G	CO ₂ + H ₂ O	~30% decomposition after 1 h irradiation	[13]
TiO ₂	Photocatalytic degradation of methylene blue	CO ₂ + H ₂ O	Apparent rate constants $k = 15\text{--}25 \text{ min}^{-1} \text{ cm}^{-3}$ TiO ₂	[14b]
TiO ₂	Photocatalytic degradation of methylene blue and lauric acid	CO ₂ + H ₂ O	Decomposition of MB up to ~100 mmol g ⁻¹ TiO ₂ ; NA for lauric acid	[44]
Fe ₂ O ₃ –TiO ₂	Cyclohexane oxidation	Cyclohexanol, cyclohexanone, isobutyraldehyde, acetic acid	Conversion = 25.8%; selectivity to cyclohexanol and cyclohexanone = 90%	[45]
VO _x –TiO ₂	Propene oxidation	CO + CO ₂	Activity (min^{-1}): CO = 0.091, CO ₂ = 0.279; selectivity to CO ₂ = 75%	[46]
VPO	<i>n</i> -Butane oxidation	Maleic anhydride	<i>n</i> -Butane conversion = 10%; selectivity to maleic anhydride = 40%	[47]
Nb–M (M = V, Mo, Sb) oxides	Propane oxidative dehydrogenation	Propylene	Propane conversion: Nb–V oxide = 6–12%, Nb–Mo oxide = 9%; selectivity to propylene: Nb–V oxide 46–72%, Nb–Mo oxide = 56%, no activity for Nb–Sb oxide	[20]
Co–Ni oxide	Propane oxidation	CO + CO ₂	C ₃ combustion rate = 3.59 mmol m ⁻² s ⁻¹ ; CO ₂ /CO selectivity = 2.2	[48]

^aLetters in bold refer to the mesoporous oxides.^bQuantum yield defined as the molecules of acetone formed per incident photon.

12.5.2

Macroporous Metal Oxides

Few examples of catalytic applications have been reported for bulk macroporous solids. Stein's group employed ordered macroporous silica as a support for catalytically active species [49, 50]. It was found that γ - $\text{SiW}_{10}\text{O}_{36}$ polyoxometalate clusters incorporated into the walls of macroporous silica exhibited catalytic activity for the epoxidation of cyclooctene [49]. In a different study, they compared the catalytic activity of different macro-, meso-, and nonporous silicas doped with transition metal-substituted polyoxometalates (TMSPs) [50]. The macroporous structure displayed $\sim 62\%$ cyclohexene conversion as compared to $\sim 47\%$ cyclohexene conversion observed for nonporous silica. The greater catalytic activity of the open macroporous structure was related to the higher number of TMSP clusters anchored in its surface. The same research group reported the catalytic performance of ordered macroporous crystalline sulfated zirconia in the isomerization of *n*-butane [51]. It was found that the catalytic activity was highly dependent on the sulfate density and calcination temperature. However, no comparison with nonporous sulfated zirconia was presented.

Macroporous VPO phase (Figure 12.5) represents the first example of a macroporous mixed metal oxide employed in the selective oxidation of lower alkanes [52]. The catalytic performance of this VPO phase was evaluated in the partial oxidation of *n*-butane to maleic anhydride. The observed yield of maleic anhydride was greater than 55 mol% for macroporous VPO [52]. Under similar reaction conditions, the yield of maleic anhydride was circa 40 mol% for the conventional organic VPO catalyst. The ordered open pore structures, high surface areas ($>40\text{ m}^2\text{ g}^{-1}$), and the presence of nanocrystalline $(\text{VO})_2\text{P}_2\text{O}_7$ in the macroporous VPO phase led to the observed improved catalytic performance. Recently, three dimensionally ordered macroporous perovskite-type $(\text{La}_{1-x}\text{Sr}_x\text{FeO}_3)$ phases have been employed as catalysts for carbon particle combustion, which represents a model reaction of particulate matter exhausted from diesel engines [53]. It was found by TG-DTA that the

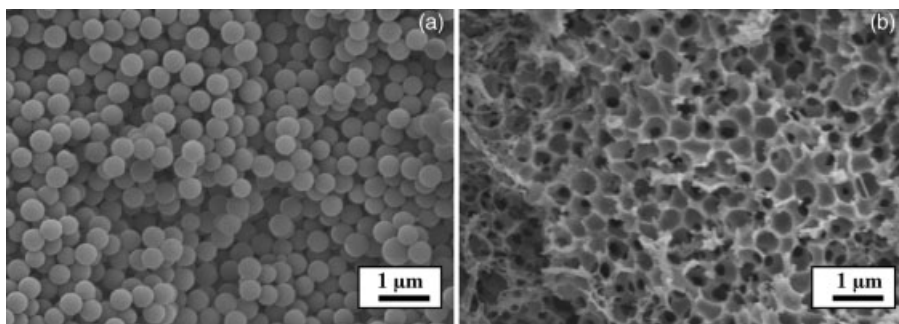


Figure 12.5 SEM images of (a) sedimented colloidal array of $\sim 400\text{ nm}$ PS spheres used as template for the synthesis of macroporous VPO and (b) macroporous VPO employed as catalyst for *n*-butane oxidation to maleic anhydride [24, 52].

Table 12.5 Catalytic applications of macroporous metal oxides.

Macrostructure	Reaction	Product	Activity/selectivity	Reference
γ -SiW ₁₀ O ₃₆ -SiO ₂	Cyclooctene epoxidation	Cyclooctene oxide	Conversion = 24%; selectivity to epoxide = 100%	[49]
TMSP-SiO ₂ ^a	Cyclohexene epoxidation	Cyclohexene oxide	Conversion ~62%; selectivity to epoxide = 100%	[50]
SO ₄ -ZrO ₂	<i>n</i> -Butane isomerization	Isobutane	Activity ~0.57 mmol g ⁻¹ cat h ⁻¹ ; selectivity to isobutene ~92%	[51]
VPO	<i>n</i> -Butane oxidation	Maleic anhydride	<i>n</i> -Butane conversion 90%; selectivity to maleic anhydride = 65%	[52]
La _{1-x} Sr _x FeO ₃	Carbon combustion	CO ₂ + H ₂ O	Carbon weight loss ~8%	[53]

^aTMSP = Transition metal-substituted polyoxometalates.

macroporous phases displayed higher catalytic activity for the combustion of nanosized carbon as compared to nonporous perovskite phase. Superior catalytic performance was attributed to the periodic ordered macrostructure, which facilitated guest molecules transport through the macropores. Table 12.5 shows examples of catalytic applications of macroporous metal oxides.

12.5.3

Metal Oxides Obtained via Dual Templating

Dual templated oxides are highly promising for catalytic applications, despite the fact that current literature shows the lack of reports of catalytic applications of these bimodal meso- and macroporous oxides. In principle, the presence of *interconnected ordered macropores* will enhance the diffusion of guest molecules, leading to higher reactant conversions, while highly *ordered mesopores* with controlled pore architectures providing high surface areas will represent regions where the active sites could potentially be located.

To date, research efforts have been centered mainly on the synthesis of dual templated silicas, which can be readily used as supports for various catalytically active species. However, the preparation of dual templated oxide phases containing transition metals remains highly challenging. Recently, the synthesis of thermally stable hierarchically ordered meso/macroporous MoVTaNbO_x phases by dual templating has been reported [54]. To our knowledge, this is the first successful example of a transition metal oxide system displaying ordered bimodal pore size synthesis employing colloidal arrays of polystyrene spheres and nonionic surfactants as mesostructure-directing agents. The 200 nm macroporous structure was composed of ~8 nm mesoporous walls. Interestingly, the mesoporous walls were composed of ~45 nm crystals corresponding to the rutile phase (Figure 12.6). Although the meso/macroporous MoVTaNbO_x catalysts lacked the active and selective M1 phase for

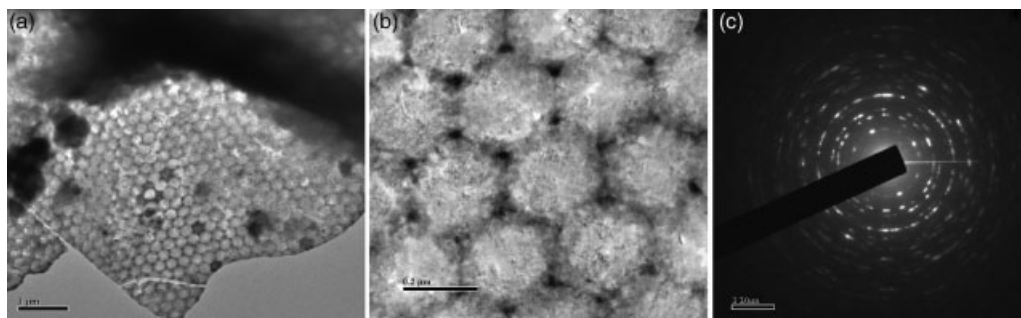


Figure 12.6 TEM images (a and b) and selected area electron diffraction pattern showing the polycrystalline nature (c) of meso/macroporous MoVTeNbO_x synthesized by dual templating and employed as a catalyst for propane ammoxidation to oxidation to acrylonitrile [54].

propane ammoxidation, they displayed activity and selectivity in propane ammoxidation to acrylonitrile.

12.6

Concluding Remarks

The molecular design of high surface area, three dimensionally periodic macroporous structures (~100–1000 nm) composed of ordered mesoporous walls (~2–20 nm) prepared in the presence of colloidal arrays of monodispersed spheres and diverse mesostructure-directing agents, has emerged as an attractive synthesis approach for the hierarchical design of dual porous oxides for several potential nanotechnological applications. In particular, these novel phases are highly promising as heterogeneous catalysts, which can be designed with adjustable macro- and mesopore dimensions as well as controlled mesopore architectures. These remarkable structural characteristics are expected to enhance the mass-transfer rates of guest molecules leading to improved catalytic performances. The molecular design of bimodal porous oxides with *controllable pore structures* in the macro and meso regimes displaying *crystallinity*, *thermal stability*, and *compositions relevant to catalysis* is still challenging. The successful preparation of these *dual templated phases* will lead to molecularly engineered porous catalysts with unique structural and compositional properties for a wide range of industrially relevant catalytic reactions.

References

- 1 (a) Kresge, C.T., Leonowicz, M.E., Roth, W.J., Vartuli, J.C. and Beck, J.S. (1992) *Nature*, **359**, 710–712; (b) Beck, J.S., Vartuli, J.C., Roth, W.J., Leonowicz, M.E., Kresge, C.T., Schmitt, K.D., Chu, C.T.-W., Olson, D.H., Sheppard, E.W., McCullen, S.B., Higgins, J.B. and Schlenker, J.L. (1992) *Journal of the American Chemical Society*, **114**, 10834–10843; (c) Kresge, C.T., Leonowicz, M.E., Roth, W.J. and Vartuli,

- J.C. (1992) US Patent 5,098,684 (Mobil Oil Corp.).
- 2 Schüth, F. (2001) *Chemistry of Materials*, **13**, 3184–3195.
- 3 Bell, A.T. (2003) *Science*, **299**, 1688–1691.
- 4 Stein, A. and Schroden, R.C. (2001) *Current Opinion in Solid State & Materials Science*, **65**, 553–564.
- 5 Vartuli, J.C., Kresge, C.T., Leonowicz, M.E., Chu, A.S., McCullen, S.B., Johnson, I.D. and Sheppard, E.W. (1994) *Chemistry of Materials*, **6**, 2070–2077.
- 6 Carreon, M.A. and Gulians, V.V. (2005) *European Journal of Inorganic Chemistry*, **1**, 27–43.
- 7 (a) Hunter, R.J. (1981) *Zeta Potential in Colloid Science: Principles and Applications*, Academic Press, London, New York; (b) Parks, G.A. (1965) *Chemical Reviews*, **65**, 177–198.
- 8 Weast, R.C., Astle, M.J. and Beyer, W.H. (1986) *CRC Handbook of Chemistry and Physics: A Ready-Reference Book of Chemical and Physical Data*, 67th edn, CRC Press, Boca Raton, FL.
- 9 (a) Lu, Y., Ganguli, R., Drewien, C.A., Anderson, M.T., Brinker, C.J., Gong, W., Guo, Y., Soye, H., Dunn, B., Huang, M.H. and Zink, J.I. (1997) *Nature*, **389**, 364–368; (b) Lu, Y., Fan, H., Stump, A., Ward, T.L., Rieker, T. and Brinker, C.J. (1999) *Nature*, **398**, 223–226; (c) Brinker, C.J., Lu, Y., Sellinger, A. and Fan, H. (1999) *Advanced Materials*, **11**, 579–585; (d) Cagnol, F., Grosso, D., Soler-Illia, G.J. de A.A., Crepaldi, E.L., Babonneau, F., Amenitsch, H. and Sanchez, C. (2003) *Journal of Materials Chemistry*, **13**, 61–66; (e) Grosso, D., Cagnol, F., Soler-Illia, G.J. de A.A., Crepaldi, E.L., Amenitsch, H., Brunet-Bruneau, A., Burgeois, A. and Sanchez, C. (2004) *Advanced Functional Materials*, **14**, 309–322.
- 10 (a) Soler-Illia, G.J. de A.A., Louis, A. and Sanchez, C. (2002) *Chemistry of Materials*, **14**, 750–759; (b) Crepaldi, E.L., Soler-Illia, G.J. de A.A., Grosso, D., Cagnol, F., Ribot, F. and Sanchez, C. (2003) *Journal of the American Chemical Society*, **125**, 9770–9786.
- 11 Yun, H., Zhou, H. and Honma, I. (2004) *Chemical Communications*, 2836–2837.
- 12 Henderson, M.J., Gibaud, A., Bardeau, J.-F. and White, J.W. (2006) *Journal of Materials Chemistry*, **16**, 2478–2484.
- 13 Beyers, E., Cool, P. and Vansant, E.F. (2007) *Microporous and Mesoporous Materials*, **99**, 112–117.
- 14 (a) Choi, S.Y., Lee, B., Carew, D.B., Mamak, M., Peiris, F.C., Speakman, S., Chopra, N. and Ozin, G.A. (2006) *Advanced Functional Materials*, **16**, 1731–1738; (b) Carreon, M.A., Choi, S.Y., Mamak, M., Chopra, N. and Ozin, G.A. (2007) *Journal of Materials Chemistry*, **17**, 82–89.
- 15 Brezesinski, T., Groenewolt, M., Gibaud, A., Pinna, N., Antonietti, M. and Smarsly, B.M. (2006) *Advanced Materials*, **18**, 2260–2263.
- 16 Castro, Y., Julian-Lopez, B., Boissiere, C., Viana, B., Grosso, D. and Sanchez, C. (2007) *Microporous and Mesoporous Materials*, **103**, 273–279.
- 17 Brezesinski, T., Antonietti, M., Groenewolt, M., Pinna, N. and Smarsly, B. (2005) *New Journal of Chemistry*, **29**, 237–242.
- 18 Kuemmel, M., Grosso, D., Boissiere, C., Smarsly, B., Brezesinski, T., Albouy, P.A., Amenitsch, H. and Sanchez, C. (2005) *Angewandte Chemie-International Edition*, **44**, 4589–4592.
- 19 Brezesinski, T., Groenewolt, M., Antonietti, M. and Smarsly, B. (2006) *Angewandte Chemie-International Edition*, **45**, 781–784.
- 20 Yuan, L., Bhatt, S., Beaucage, G., Gulians, V.V., Mamedov, S. and Soman, R.S. (2005) *The Journal of Physical Chemistry. B*, **109**, 23250–23254.
- 21 Grosso, D., Boissiere, C., Smarsly, B., Brezesinski, T., Pinna, N., Albouy, P.A., Amenitsch, H., Antonietti, M. and Sanchez, C. (2004) *Nature Materials*, **3**, 787–792.
- 22 Xia, Y., Gates, B., Yin, Y. and Lu, Y. (2000) *Advanced Materials*, **12**, 693–713.
- 23 Holland, B.T., Blanford, C.F., Do, T. and Stein, A. (1999) *Chemistry of Materials*, **11**, 795–805.

- 24 Carreon, M.A. and Guliants, V.V. (2002) *Chemistry of Materials*, **14**, 2670–2675.
- 25 Wang, D., Caruso, R.A. and Caruso, F. (2001) *Chemistry of Materials*, **13**, 364–371.
- 26 (a) Subramanian, G., Manoharan, V.N., Thorne, J.D. and Pine, D.J. (1999) *Advanced Materials*, **11**, 1261–1265; (b) Vlasov, Y.A., Yao, N. and Norris, D.J. (1999) *Advanced Materials*, **11**, 165–169.
- 27 Yuan, Z.Y. and Su, B.L. (2006) *Journal of Materials Chemistry*, **16**, 663–677.
- 28 Yang, P., Deng, T., Zhao, D., Feng, P., Pine, D., Chmelka, B.F., Whitesides, G.M. and Stucky, G.D. (1998) *Science*, **282**, 2244–2246.
- 29 Luo, Q., Li, L., Yang, B. and Zhao, D. (2000) *Chemistry Letters*, 378–379.
- 30 Lebeau, B., Fowler, C.E., Mann, S., Farcet, C., Charleux, B. and Sanchez, C. (2000) *Journal of Materials Chemistry*, **10**, 2105–2108.
- 31 Zhou, Y. and Antonietti, M. (2003) *Chemical Communications*, 2564–2565.
- 32 Kuang, D., Brezesinski, T. and Smarsly, B. (2004) *Journal of the American Chemical Society*, **126**, 10534–10535.
- 33 (a) Sen, T., Tiddy, G.J.T., Casci, J.L. and Anderson, M.W. (2003) *Angewandte Chemie-International Edition*, **42**, 4649–4653; (b) Sen, T., Tiddy, G.J.T., Casci, J.L. and Anderson, M.W. (2004) *Chemistry of Materials*, **16**, 2044–2054.
- 34 Villaescusa, L.A., Mihi, A., Rodríguez, I., García-Bennett, A.E. and Miguez, H. (2005) *The Journal of Physical Chemistry. B*, **109**, 19643–19649.
- 35 Sel, O., Kuang, D., Thommes, M. and Smarsly, B. (2006) *Langmuir*, **22**, 2311–2322.
- 36 Li, F., Wang, Z., Ergang, N.S., Fyfe, C.A. and Stein, A. (2007) *Langmuir*, **23**, 3996–4004.
- 37 Danumah, C., Vaudreuil, S., Bonneviot, L., Bousmina, M., Giasson, S. and Kaliaguine, S. (2001) *Microporous and Mesoporous Materials*, **44–45**, 241–247.
- 38 Oh, C., Baek, Y. and Ihm, S. (2005) *Advanced Materials*, **17**, 270–273.
- 39 Gundiah, G. (2001) *Bulletin of Materials Science*, **24**, 211–214.
- 40 Sayari, A. (1996) *Chemistry of Materials*, **8**, 1840–1852.
- 41 Yusuf, M.M., Imai, H. and Hirashima, H. (2002) *Journal of Sol–Gel Science and Technology*, **25**, 65–74.
- 42 Takahara, Y., Kondo, J.N., Takata, T., Lu, D. and Domen, K. (2001) *Chemistry of Materials*, **13**, 1194–1199.
- 43 Stone, V.F., Jr and Davis, R.J. (1998) *Chemistry of Materials*, **10**, 1468–1474.
- 44 Sakatani, Y., Grosso, D., Nicole, L., Boissiere, C., Soller-Illia, G.J. de A.A. and Sanchez, C. (2006) *Journal of Materials Chemistry*, **16**, 77–82.
- 45 Perkasa, N., Wang, Y., Koltypin, Y., Gedanken, A. and Chandrasekaran, S. (2001) *Chemical Communications*, **11**, 988–989.
- 46 Yoshitake, H. and Tatsumi, T. (2003) *Chemistry of Materials*, **15**, 1695–1702.
- 47 Carreon, M.A., Guliants, V.V., Pierelli, F. and Cavani, F. (2004) *Catalysis Letters*, **92**, 11–16.
- 48 Carreon, M.A., Guliants, V.V., Yuan, L., Hughett, A.R., Dozier, A., Seisenbaeva, G.A. and Kessler, V.G. (2006) *European Journal of Inorganic Chemistry*, **24**, 4983–4988.
- 49 Schroden, R.C., Blanford, C.F., Melde, B.J., Johnson, B.J.S. and Stein, A. (2001) *Chemistry of Materials*, **13**, 1074–1081.
- 50 Johnson, B.J.S. and Stein, A. (2001) *Inorganic Chemistry*, **40**, 801–808.
- 51 Al-Daous, M.A. and Stein, A. (2003) *Chemistry of Materials*, **15**, 2638–2645.
- 52 Carreon, M.A. (2003) PhD Thesis, University of Cincinnati.
- 53 Sadakane, M., Asanuma, T., Kubo, J. and Ueda, W. (2005) *Chemistry of Materials*, **17**, 3546–3551.
- 54 Yuan, L. (2007) PhD Thesis, University of Cincinnati.

Index

a

ab initio methods 232f, 243, 249f, 265
 absorption coefficient 260, 262
 absorption edge 259, 270f
 absorption spectrum 259, 263, 290
 ACH, *see* aluminum chlorhydrol
 acid sites 216, 218f, 222
 acidity 38, 95f, 162, 179f, 188, 216
 activation barrier 235ff, 243f, 250
 activation energy 16, 25, 87, 135, 213, 237f
 adatom binding energy 235f, 238
 adenosine triphosphate 141f
 adlayer 117f, 130, 242f, 247f, 250f
 adsorbate-metal bond strength 236, 242
 adsorption
 – energies 235ff, 241, 243
 – geometry 120ff
 – heat 236f
 – isotherms 166, 169, 172f, 297
 – strength 18, 126f
 adsorption-desorption equilibrium 123, 134
 AES, *see* Auger electron spectroscopy
 age distribution 102, 105f
 aging 86f, 91f, 97, 110
 air grid 106
 air jet index 106
 air jet method 106
 air-to-fuel ratio 92
 Al₂O₃, *see* aluminum oxide
 alkene hydrogenation 74, 77
 alkoxides 216, 219, 222
 aluminum oxide 1, 5f, 18, 26, 33f, 40f, 89, 101f, 196f, 205ff, 244, 266ff, 277, 279, 281, 301f
 aluminum chlorhydrol 107
 amino acids 62f, 68, 114f, 127, 132f

anatase films 300, 307
 anchoring 1, 5, 7, 16, 18, 118, 121, 133, 185, 224f, 310
 API 108f
 ATP, *see* adenosine triphosphat
 attenuated total reflection infrared (ATR-IR) 120, 122, 126
 attrition 26, 86, 91f, 106f
 Auger electron spectroscopy 196f
 autonomous motion 141f, 148, 157
 azimuthal rotation 132f, 153

b

backbone rigidity 66, 78
 backscattering 261f, 264
 base metals 90f
 BEP, *see* Brønsted-Evans-Polyani relationship
 BET, *see* Brunauer-Emmett-Teller
 binder 106f
 binding energy 234ff, 241, 247f, 287, 289
 bioelectrochemical propulsion 150
 biological motors 141f, 158
 biomimetics 28, 184
 block copolymers 215, 220, 301, 304
 boiling point 101, 107f
 bond order conservation model (BOC) 236, 238
 bond-node pore network model 40f
 branches 59f, 64, 66f, 78
 bridge sites 246f
 Brij-56 302, 304, 306
 Brij-58 300f
 Brønsted-Evans-Polyani relationship 236f, 239
 Brunauer-Emmett-Teller 86, 166, 187
 bubble propulsion 144, 148f
 bulk diffusivity 30

c

calcination 2, 37, 88, 103, 107ff, 197, 208f, 216ff, 223, 295ff, 304, 310
 carbon monoxide 89, 92, 95, 108, 196, 211, 214, 238f, 242, 276, 283f, 309
 catalysis
 – Brønsted acid 181
 – chiral 224
 – enantioselective 182
 – enzymatic 25, 34
 – Lewis acid 180f
 catalyst
 – automobile 89f
 – bimetallic 61, 71ff, 78, 195ff
 – bimodal 40, 42ff, 48
 – CoMo 266ff
 – cracking 277
 – eggshell 35
 – enantioselective 114f, 134f
 – equilibrium 101ff, 109
 – FCC 41f, 277f
 – mesoporous 26, 38, 49, 307
 – metal-free 224
 – microporous 26, 38
 – monometallic 72, 74f, 195f, 199, 207ff
 – multicomponent 271
 – particulate 84, 87, 91f, 106
 – porosity 30
 – powder 83f
 – preparation 84f
 – stability 252f
 – synthesis 252f
 – testing 85f
 – three-way 92, 244
 – vanadium-phosphorous oxide 307f, 310f
 catalytic applications 296, 305, 307ff
 cavities 163, 169, 172, 180f, 209, 214
 CCD camera, *see* charge-coupled device camera
 CDU 104f
 cerium oxide (CeO₂) 220, 222f
 cetyltrimethylammonium bromide 297, 300, 302, 304f
 cetyltrimethylammonium chloride 305f
 CH₃OH temperature-programmed surface reaction spectroscopy (CH₃OH-TPSR) 2, 15f
 channel diameter 41f, 45, 47
 channel wall thickness 43, 47, 303
 characteristic length scale 30
 charge-coupled device camera 279f, 286
 charge-density matching theory 215
 chemical vapor deposition 1
 chemisorption 86, 89, 108, 173, 181, 196f, 200, 204, 206, 211, 231

chiral metal complexes 113f
 chiral modification 113ff
 chiral modifiers 114f, 118, 121, 128, 131ff
 chiral sites 130, 132
 cinchona alkaloids 114ff, 123, 125f, 130, 134f
 cinchonidine 115ff, 135
 cinchonine 115, 117f, 125, 127
 cleavage 62, 78
 CMC, *see* critical micelle concentration
 CO, *see* carbon monoxide
 co-catalyst 114
 [Co^{III}–(salen)] complexes 61
 CO₂ capture 161, 167, 169, 171ff, 189
 coadsorption 118f, 126, 131f, 247, 249f
 coarse-grained models 233, 243f, 250
 coke 27, 41, 87, 93f, 101, 103f, 108f, 277
 combinatorial methods 167ff, 189, 231f, 234, 253
 combustion 38, 101, 298, 307f, 310f
 combustion engine 89f
 commercialization 83f, 94f, 101, 107, 109f
 computational density functional theory 2, 6, 9f, 18, 130, 196, 199ff, 208, 211, 235, 241, 244f, 250
 concentration gradient 143f
 connectivity 28, 30f, 38f, 41
 Conradson carbon 107f
 continuum model 31f, 39, 41, 43
 conversion rate 25, 208f
 conversion-selectivity profile 85
 coordination number 197, 273, 277
 cordierite 91
 core electron 259f
 core hole 261, 288f
 core-shell nanoparticles 74f, 79, 226
 coverage 1f, 17, 118f, 122, 127, 129ff, 197, 199, 201, 203, 209, 233, 242f, 247ff, 253
 CPS, *see* cyclic propylene steaming
 cracking 95, 100ff
 critical micelle concentration (CMC) 297, 299
 cross-linking 59, 77f, 215, 221, 297f, 304
 crude oil 40, 100, 107, 266, 280
 CTAB, *see* cetyltrimethylammonium bromide
 CTACL, *see* cetyltrimethylammonium chloride
 CVD, *see* chemical vapor deposition
 cyclic propylene steaming 103f
 cyclohexane 198f, 203f, 207f, 210, 309
 cyclohexene 65, 70, 196ff, 202ff, 207ff, 311

d

D, *see* fractal dimension of the surface
 1,4DBC, *see* 1,4-dicarboxylicbenzyl acid
 D_e, *see* effective diffusivity

- deactivation 25, 27, 29f, 36, 39f, 47, 83, 86f, 91, 94, 96f, 101ff, 286, 290
 - Debye-Waller broadening 262
 - decomposition
 - methanol 222
 - of hydrogen peroxide 143, 146, 150
 - of nickel 104
 - of nitrogen oxides 243ff, 252ff
 - site 25
 - sugar 38
 - surface 17f
 - temperature 162
 - dehydrogenation 93ff, 103, 225, 236, 238, 307f
 - dendrimer encapsulated nanoparticles 71ff
 - dendrimer synthesis 60
 - dendrimers 59ff, 226f
 - dendrons 62, 65f, 77
 - deNO_x reaction 222, 245
 - DENs, *see* dendrimer encapsulated nanoparticles
 - density of states 201
 - deposition 3f, 6, 38, 103f, 151, 153, 155, 196f, 225
 - descriptors
 - catalytic 233ff, 253
 - chemical 233
 - electronic 234
 - energetic 235f, 239
 - DFT, *see* computational density functional theory
 - diatomic oscillator 3, 4, 7
 - 1,4-dicarboxylicbenzyl acid (1,4DBC) 162, 183
 - dielectric constant 123
 - diesel 100f, 108, 310
 - diffuse reflectance infrared Fourier transform spectroscopy 120, 122, 173, 280f, 285
 - diffusiophoresis 144f, 150
 - Dirac δ function 261
 - dispersion limit 1, 3
 - dispersive X-ray absorption spectroscopy 266, 269
 - disproportionation 198, 202f, 207ff
 - dissociation energy 238f
 - distortion 10, 13f
 - D_m, *see* bulk diffusivity
 - DOS, *see* density of states
 - downstream 93f
 - DRIFTS, *see* diffuse reflectance infrared Fourier transform spectroscopy
 - DRS, *see* UV-Vis diffuse reflectance spectroscopy
 - drunkard's walk model of diffusion 27
 - DSG, *see* dynamic shadowing growth
 - dual templating 295ff
 - dusty-gas model 41
 - duty cycle 83, 86f, 89, 91f, 107
 - DXAS, *see* dispersive X-ray absorption spectroscopy
 - dynamic shadowing growth 151f
- e**
- E_{act}, *see* activation energy
 - E_{cat}, *see* equilibrium catalyst
 - edge energy 14f
 - ee, *see* enantiomeric excess
 - effective diffusivity 30, 34, 36, 40, 43
 - effective medium approach 31
 - effectiveness factor, η 35, 39ff
 - E_g, *see* edge energy
 - EISA, *see* evaporation-induced self-assembly
 - electrical conductivity measurement 272ff, 280
 - electron density 18f
 - electronegativity 5, 18f
 - EMA, *see* effective medium approach
 - embedded nanoparticles 220f
 - enantiomeric excess 115, 121, 123, 125, 128, 131, 185, 225
 - enantiomers 113, 115, 128, 135
 - enantioselectivity 114, 121, 123f, 126, 128, 130, 132ff
 - encapsulation 64, 71ff, 114, 227
 - enediolate 118f
 - enzymes 28, 60, 179
 - ϵ , *see* catalyst porosity
 - equilibrium catalyst 101ff, 108f
 - η , *see* effectiveness factor
 - European Synchrotron Radiation Facility (ESRF) 260, 269, 272, 277
 - evaporation-induced self-assembly 299f, 307
 - excitation 259, 261, 287, 290
 - extended X-ray absorption fine structure (EXAFS) 196f, 205f, 208f, 211, 259
- f**
- faujasite 36, 38, 42
 - FCC, *see* fluid catalytic cracking
 - feed effects 107f
 - feed rate 84, 100
 - Fermi level 195, 201f, 261, 267, 287
 - Fischer-Tropsch synthesis 242
 - fluid catalytic cracking 93, 100ff, 277
 - folded sheet mesoporous materials 215
 - fouling 26
 - Fourier transform 145, 264f, 267, 269, 277f, 282, 286

Fourier transform infrared spectroscopy 198, 206
 fractal dimension of the surface 33
 Fréchet-type dendrimers 59, 64, 66
 FSM, *see* folded sheet mesoporous materials
 FT, *see* Fourier transform
 FTIR, *see* Fourier transform infrared spectroscopy
 fuel cells 83, 211, 252

g

gasoline 90, 93, 100f, 104, 108f, 219f, 266, 277
 gate opening 169, 172
 gold gear 150
 grafting 38, 182, 184, 224f

h

H-BEA 186f
 HAADF-STEM, *see* high-angle annular dark-field scanning transmission electron microscopy
 HBE, *see* hydrogen binding energy
 HDS, *see* hydrodesulfurization
 HDT, *see* hydrotreatment
 heat of adsorption 236f
 heat of reaction 236f
 heteroatoms, inclusion of 216ff
 N-heterocyclic carbenes 64f
 high throughput experimentation 84f, 88, 95, 167, 232f, 238
 high throughput simulation 242ff
 high-angle annular dark-field scanning transmission electron microscopy 197, 205, 278
 high-resolution electron energy loss spectroscopy 196, 203f
 higher generation dendrimers 59, 61, 69
 highway network 27, 36ff
 HKUST-1 162, 166, 169, 171, 180, 188
 hollow cage 77f
 homometallic dendrimers 70
 hot spots 88, 94
 HPNPP, *see* 2-hydroxypropyl-p-nitrophenyl phosphate
 HREELS, *see* high-resolution electron energy loss spectroscopy
 HTE, *see* high throughput experimentation
 hydrocarbon 87, 89, 92, 99, 104, 108
 hydrodemetallation 40
 hydrodesulfurization 266
 hydrogen binding energy 200f
 hydrogen peroxide 143ff, 148f, 153, 155f, 219, 225

hydrogenation 73ff, 114ff, 183f, 188, 195ff, 200, 202ff, 209f, 221f, 225f, 236f, 242
 hydrogenolysis 238
 hydrophobic pocket 60
 hydrosilylation 64f, 78
 hydrothermal stability 94ff, 214, 220
 hydrotreatment 266
 2-hydroxypropyl-p-nitrophenyl phosphate 62
 hypothesis-driven research 231, 238, 242
 hysteresis 166, 169, 172

i

impregnation 103f, 183, 197, 205ff, 211
 inclusion of heteroatoms 216ff
 interatomic distance 197
 intercalation 165
 interfacial tension gradients 144, 149
 interference function 261, 263f, 266
 interpenetration 162, 165, 169, 171
 interweaving 171
 intrinsic activity 25, 27, 36, 219
 ionic liquid 304
 IRMOF, *see* isorecticular compound metal open framework
 isobutene 93f, 97ff
 isoelectric point 220, 298
 isorecticular compound metal open framework 162f, 166, 171f, 178, 185f, 189
 isotopic exchange 2f, 7, 9f, 12f, 18

k

K β main lines 287f
 K β satellite lines 287f
 K-edge 261, 263f, 267ff, 272ff, 281f, 286
 Keggin structure 6, 8, 225
 α -ketoesters 114f, 118, 121, 134
 β -ketoesters 114f, 127, 130, 134
 kinetic Monte Carlo Simulation (KMC) 243f, 245, 249f
 kinetics 87f, 94f, 168, 198, 208, 210, 231, 233f, 242ff, 249ff, 267, 274
 KLE 300f, 304
 Knudsen diffusion 32f
 k_{rds} , *see* rate constant for the rate-determining step

l

L, *see* characteristic length scale
 lambda-sweep method 105
 lamellar structure 298, 300, 302, 304
 Langmuir surface 167, 184
 Langmuir-Hinshelwood-Hougen-Watson models 28
 large pore channels 34, 36ff

latex 37
 lattice parameters 283f
 LCO, *see* light cycle oil
 LCT, *see* liquid crystal templating
 leaching 220, 225f
 lean conditions 244, 246, 248
 LEED, *see* low-energy electron diffraction
 lepidine 121, 126f
 Lewis acid 95, 107f, 180
 ligand-to-metal charge transfer 14
 light cycle oil 104, 108f
 linkage 78
 linkers 163, 165, 167, 171f, 174f, 179, 183f
 liquefied petroleum gas 100f, 104, 109
 liquid crystal templating 215, 297
 LMCT, *see* ligand-to-metal charge transfer
 lock-and-key hypothesis 25
 long-range order 117f, 127, 129f, 133, 135, 299
 low-energy electron diffraction 118, 129, 131, 196
 low-generation dendrimers 60
 LPG, *see* liquefied petroleum gas

m

M1 phase 271ff
 M1(Sb) phase 272, 274, 276
 M₂(CO₂)₄ paddle wheel 162f, 171
 M41S 297, 299
 MAA, *see* methylacetoacetate
 MARI, *see* most abundant reaction intermediate
 mass spectrometry 196, 270, 273, 276, 279f, 285
 mass transfer 87f, 110, 213, 216, 312
 MCM-41 26, 30, 37f, 215f, 219, 223f, 297, 305
 MCM-48 37, 215f
 MCM-50 215
 Merck molecular force field models 244, 250
 mesophase 214f, 221ff
 mesopores 26f, 30ff, 36f, 296f, 300, 304f, 311f
 mesoporous silica 214f, 219ff, 224f, 305
 mesoporous transition metal oxide films 301f
 mesostructure 295ff, 303f, 307f, 311f
 mesostructure-directing agent 296, 303f, 311f
 metal open framework 161ff
 methanation 238f
 methane monooxygenase 60
 methanolysis 65
 methyl pyruvate 116ff
 methyl tert-butyl ether 93
 methylacetoacetate 127f, 131f

MFI 217, 219
 micellar templating 37
 micelles 215, 221, 296f, 299f, 305
 Michaelis-Menten kinetics 69
 Mitchell method 103f
 modifiable steady state 299
 MOF, *see* metal open framework
 Moiseev mechanism 249
 molecular sieves 297, 299
 molybdenum oxide 2f, 8ff, 15, 18, 298, 301f, 308
 monolayer 1f, 131, 196f, 200, 203, 225, 235, 300
 monolayer coverage 1
 Monte Carlo simulations 32f, 130, 243f, 245, 249f
 MoO₃, *see* molybdenum oxide
 Mössbauer spectroscopy 266
 most abundant reaction intermediate 15
 MoVTenbO_x phases 271, 311f
 MS, *see* mass spectrometry
 MSS, *see* modifiable steady state
 MTBE, *see* methyl tert-butyl ether

n

Nakamura mechanism 249
 nanobuilding block 300
 nanocage 77f
 nanomotors 141ff
 nanoparticles 26, 71ff, 207, 209, 214, 220ff, 225f, 284
 nanopores 27, 31f, 36ff
 nanorod 142ff, 151ff, 157
 nanoscale 25, 27, 29, 41, 50, 141, 161, 179, 214ff, 220, 222ff, 233, 252
 naphthylethylamine 118, 120f, 124
 National Synchrotron Light Source 197
 NBB, *see* nanobuilding block
 near-edge extended X-ray absorption fine structure (NEXAFS) 121
 NGR, *see* nuclear gamma X-ray resonance
 NHC, *see* N-heterocyclic carbenes
 Ni-porphyrin 104f
 nitrogen oxides 40, 45, 47f, 242ff, 307
 NMR, *see* nuclear magnetic resonance spectroscopy
 NO_x decomposition 243f, 248, 253
 NO_x storage and reduction 244
 NO_x, *see* nitrogen oxides
 NSLS, *see* National Synchrotron Light Source
 NSR, *see* NO_x storage and reduction
 nuclear gamma X-ray resonance 259
 nuclear magnetic resonance spectroscopy 86, 216, 218f, 224

o

oblique angle deposition (OAD) 151f
 ODH, *see* oxidative dehydrogenation
 olefins 93, 98, 100f
 oligomerization 64f
 oxidative dehydrogenation 308f
 oxide ligands 1ff

p

PAMAM, *see* polyamidoamine
 parent metals 195, 200, 202, 205, 248
 Pareto-optimal set 238, 240
 particle size 26, 39, 42
 patterning 248, 252
 PCA, *see* principal component analysis
 Pellet-Particle model 39f, 45
 pellets 35f, 94, 110
 percolation threshold 30f
 periphery 60f, 64ff, 73, 78, 226f, 247, 266
 perovskite structure 310f
 perturbed silica vibrations 4, 6
 petroleum 83, 91, 100ff, 213, 266, 277f
 PFG NMR, *see* pulsed-field gradient nuclear magnetic resonance spectroscopy
 ϕ , *see* Thiele modulus
 photocatalytic activity 307
 photovoltaics 29, 34
 pillars 162, 170f, 184
 pilot plant 93, 95, 97, 109f, 163
 Pluronic F-127 304, 306
 Pluronic P-123 304, 306
 PMMA, *see* poly(methyl methacrylate)
 poisoning 25, 86f, 108, 236, 244, 247f
 polarity 123, 163f, 171f
 polarity gradients 66f, 78
 polyamidoamine 59, 61, 69, 71f, 77, 227
 poly(methyl methacrylate) 295, 303, 305f
 polyoxymetalate 224f
 polypropyleneimine 59, 227
 polystyrene 37, 295, 303f, 311
 POM, *see* polyoxymetalate
 pore
 – architecture 36, 41, 307, 311
 – blockage 25, 30f
 – diameter 33, 37f
 – diffusion 87
 – morphology 28, 32
 – network 27, 30ff, 39f, 43, 50
 – shape 32, 39
 pore-size distribution 215, 297
 postsynthesis 216, 220, 222, 224f, 300
 power plant 40, 45, 47f
 PPI, *see* polypropyleneimine

pre-exponential factor 236, 243, 244
 precious metals 90f
 pressure drop 88, 90f, 94f
 pressure swing adsorption 167f, 171, 173, 175, 177f, 188f
 principal component analysis 265
 promoters 85, 95
 propylene 93f, 104
 PS, *see* polystyrene
 PSA, *see* pressure swing adsorption
 pseudomorphic overlayers 235, 237f
 pseudoradial distribution function 264
 Pt-Al₂O₃ 116, 120, 122f, 125f
 pulsed-field gradient nuclear magnetic resonance spectroscopy 36, 42
 pyridoxamine 68f

q

quick extended X-ray absorption fine structure (QEXAFS) 265ff, 271
 quinoline 117f, 121, 123f, 126f

r

racemic mixtures 113
 RAIRS, *see* reflection-absorption infrared spectroscopy
 Raman spectroscopy 2ff, 14, 18, 280
 Raney nickel 127
 rate constant for the rate-determining step 15f
 Re₂O₇, *see* rhenium oxide
 reaction rate 25, 31, 34, 39f, 43, 61, 67f, 73, 76, 88, 210
 reactors
 – fixed-bed 26, 35, 84, 88, 93f, 123, 276
 – monolith 26, 35, 47f, 84, 88, 91f, 279
 – membrane 26, 61
 – slurry 26, 84
 refining 100ff
 reflection-absorption infrared spectroscopy 118, 121, 123f, 126, 129, 131f, 250
 regeneration 41, 83f, 93f, 105, 277
 resonant inelastic X-ray scattering spectroscopy (RIXS) 287, 290
 rhenium oxide 2f, 11f, 18
 rolling nanospring 153
 rutile phase 298, 300, 311

s

S-XRD, *see* synchrotron X-ray diffraction
 Sabatier's principle 236, 238f
 Samanos mechanism 249f
 SAXS, *see* small angle X-ray scattering

- SBA-15 30, 37f, 215f, 220f, 225
 SBA-16 37, 215
 SBU, *see* single building unit
 scale-up 29, 83, 88, 94, 101, 105, 109f
 scanning electron microscopy 155, 157, 217f
 scanning tunnel microscopy 117f, 129f
 SCI, *see* spin-coating infiltration
 screening 84f, 97, 105, 110
 selective catalytic reduction (SCR) 1, 47f
 self-assembly 214ff, 219f, 222f, 225f, 252, 297f, 299f, 303
 self-electrophoresis 144f, 148, 151f, 155
 SEM, *see* scanning electron microscopy
 semiconductors 275, 295, 301
 SERS, *see* surface-enhanced Raman spectroscopy
 SFA, *see* smooth field approximation
 shell cross-linking 77f
 ship-in-a-bottle synthesis 72, 220, 225
 silicon dioxide 1ff, 41, 277, 311
 silsesquioxanes 6
 single building unit 162, 164, 181ff
 single crystals 130, 135, 174, 178, 185, 196, 211
 sintering 86f, 90f, 220
 SiO₂, *see* silicon dioxide
 site isolation 64f, 219
 slip velocity 146, 150
 slip-stream testing 87
 small angle X-ray scattering 301
 small pore channels 214
 smooth field approximation 31
 space velocity 85f
 spatial distribution 28, 31, 41
 spatial resolution 259, 265, 278f
 spin-coating infiltration 304
 spinel crystals 308
 spray drying 107, 109
 SRF, *see* synchrotron radiation facility
 stabilizers 91, 95
 steady-state conditions 17f, 83, 246f, 250f
 steaming 103ff
 steric hindrance 116, 119, 186f
 Stille coupling 72
 STM, *see* scanning tunnel microscopy
 sulfidation, of CoMo 266ff
 sulfur 90, 98, 107, 109
 surface
 – area 1, 27, 29, 33, 36, 44, 71, 91f, 102, 106f, 166f, 183ff, 213ff, 225f, 295f, 300f, 305, 307f, 310f
 – coverage 1, 233, 242f, 248, 250
 – dioxo species 9f, 18
 – modifiers 4, 7f, 10, 14, 17
 – monoxo species 10, 14, 18
 – roughness 28, 32f, 50, 221
 – trioxo species 11, 18
 surface-enhanced Raman spectroscopy 122, 124f
 surfactant 37, 214f, 217, 220, 222f, 296ff, 303f, 311
 Suzuki coupling 72f, 183
 λ -sweep method 105
 synchrotron radiation facility 260
 synchrotron X-ray diffraction 280f, 283, 285
 synergistic effect 76, 179
- t**
 Tamman temperature 298
 tartaric acid (TA) 114f, 117, 127ff, 182
 τ , *see* tortuosity factor
 TCD, *see* thermal conductivity detector
 TCPP, *see* 5,10,15,20-tetra(carboxyphenyl) porphyrin
 TDEP, *see* template-directed electroplating
 TEM, *see* transmission electron microscopy
 temperature-programmed desorption 196f, 200, 202f, 218
 template-directed electroplating 151
 tetraethylorthosilicate (TEOS) 220, 297
 5,10,15,20-tetra(carboxyphenyl) porphyrin 183f
 thermal conductivity detector 197
 thermal shock 90f
 thermal stability 91, 94ff, 188, 214, 220f, 277, 297, 300f, 308, 313
 thermodynamics 94f
 Thiele modulus 30, 35, 43ff, 50
 3D transmission electron microscopy (3D TEM) 36, 41
 three-way catalyst 92, 244
 time-resolved ultrafast dispersive X-ray absorption spectrometry 286
 titanium dioxide (TiO₂) 1, 5, 7, 18, 48, 222, 298, 302, 307f
 TMSP, *see* transition metal-substituted polyoxometalates
 TOF, *see* turnover frequency
 TON, *see* turnover number
 tortuosity factor 30
 TPD, *see* temperature-programmed desorption
 transamination 68f
 transesterification 182
 transition metal oxides 2, 5, 16, 215, 221, 298, 300f, 305, 307, 311
 transition metal-substituted polyoxometalates 310f
 transition state 61, 64, 67, 187, 213, 236, 239

transmission electron microscopy 86, 131,
152f, 155, 196f, 205f, 211, 217f, 223, 259,
277, 305, 312
transmission mode 262, 266, 269
TUD-1 38
tungsten oxide 3, 5f, 298, 301
turnover frequency 17f, 75f, 221, 226, 241f,
245ff, 250f
turnover number 181, 184, 226
turnover rates 27, 73
TWC, *see* three-way catalyst
2P model 127f

u

ultrahigh vacuum (UHV) 121, 124, 130, 196,
199, 208f, 211
unit cell size (UCS) 102, 106
upstream 86, 93, 107
UV-Vis diffuse reflectance spectroscopy 2, 4,
14f

v

V_2O_5 , *see* vanadium oxide
VA, *see* vinyl acetate
VAM synthesis 243, 249f
vanadium-phosphorous oxide 307f, 310f
vanadium oxide 2f, 5ff, 15, 18, 48, 280, 298
velocity 144f, 150
vinyl acetate 242, 249f
VPO, *see* vanadium-phosphorous oxide

w

washcoats 88, 91f
water-gas shift reaction (WGS reaction) 280ff
wide angle X-ray scattering (WAXS) 301
 WO_3 , *see* tungsten oxide
working capacity (WC) 178
working selectivity (WS) 178
wormhole structure 215, 304f

x

X-ray absorption near-edge spectroscopy
(XANES) 259ff, 265f, 270ff, 283f, 289
X-ray absorption spectroscopy (XAS) 259ff
X-ray beam 259, 262, 278
X-ray diffraction (XRD) 86, 89, 165, 174ff,
185, 187, 223, 281
X-ray emission spectroscopy (XES) 287f
X-ray fluorescence (XRF) 279
X-ray photoelectron diffraction (XPD) 130
X-ray photoelectron spectroscopy (XPS) 86
o-xylene oxidation 1

z

zeolite 25, 32, 36f, 41, 93, 101ff, 162ff, 171f,
178f, 181f, 185ff, 214, 216ff, 223f, 277f,
297
zeolite imidazole framework (ZIF) 182
zirconium dioxide (ZrO_2) 1, 4f, 7, 18, 222f,
225, 298, 301f, 311
ZSM-5 41, 217, 219, 224